Photo-dissociation for studying the astrophysical $^{12}\mathrm{C}(\alpha,\gamma)^{16}\mathrm{O}$ reaction and the structure of $^{12}\mathrm{C}$

Kristian Charles Zajdek Haverson

A thesis submitted in partial fulfilment of the requirements of

Sheffield Hallam University

for the degree of Doctor of Philosophy

November 2025

In collaboration with the University of Connecticut & the University of Warsaw

Dedicated to Natasha

Abstract

This thesis uses Time Projection Chambers (TPCs) operating in γ beams to study nuclear reactions critical to stellar helium burning and to elucidate the structure of ^{12}C. Two photo-dissociation reactions were investigated —$^{16}\mathrm{O}(\gamma,\alpha_0)^{12}\mathrm{C}$ and $^{12}\mathrm{C}(\gamma,\alpha_0)^{8}\mathrm{Be}$ —both time-reversed analogues of reactions that occur in stars. The first determines the uncertainty in the carbon-to-oxygen ratio during helium burning, emphasised by W. Fowler in his Nobel Prize speech to be of "paramount importance" in nuclear astrophysics. The second was used to probe the clustered structure of ^{12}C, and to provide insight into the Hoyle state, without which life would not exist.

Two experiments were performed at the High Intensity Gamma-ray Source (HIγS) facility at Duke University. The first used an Optical Time Projection Chamber (OTPC) with an N_2O + N_2 active gas target, to measure four angular distributions from the $^{16}\mathrm{O}(\gamma,\alpha_0)^{12}\mathrm{C}$ reaction between the broad $J^\pi(1^-)$ resonance at E_x = 9.59 MeV and narrow $J^\pi(2^+)$ resonance at E_x = 9.84 MeV. New methods were developed to extract reliable values of the $E1$–$E2$ mixing phase angle (ϕ_{12}) in agreement with elastic scattering data, addressing a long-standing inconsistency in the field. The second experiment used the Warsaw electronic Time Projection Chamber (eTPC) with a CO_2 active gas target, measuring angular distributions from $E_x = 8.51 - 13.9$ MeV. This provided higher statistics both at lower astrophysically relevant energies and at higher energies for the $^{16}\mathrm{O}(\gamma,\alpha_0)^{12}\mathrm{C}$ reaction, where the latter provided data able to constrain the background terms in an R-matrix analysis. Angular distributions for $^{12}\mathrm{C}(\gamma,\alpha_0)^{8}\mathrm{Be}$ were also investigated. Resonance parameters for the Algebraic Cluster Model-predicted $J^\pi_n(2^+_2)$ Hoyle band excitation and the $J^\pi_n(1^-_1)$ bending band excitation in ^{12}C were extracted. No evidence was found to confirm the $J^\pi_n(2^+_3)$ state predicted by the same model.

Declaration

I hereby declare that:

1. I have not been enrolled for another award of the University, or other academic or professional organisation, whilst undertaking my research degree.

2. None of the material contained in the thesis has been used in any other submission for an academic award.

3. I certify that this thesis is my own work. The use of all published or other sources of material consulted have been properly and fully acknowledged. I confirm that I have sought and obtained copyright permission for any third-party materials included in this thesis. The data presented in this thesis were obtained and analysed in collaboration with Sheffield Hallam University, the University of Warsaw, and the University of Connecticut at the HIγS facility in Durham, North Carolina, USA. The University of Warsaw designed and constructed the electronic time projection chamber (eTPC) used in this work, with the gas system provided by the University of Connecticut. I participated in two data collection campaigns using this detector. The University of Warsaw also developed the base software for raw event processing and the Monte Carlo framework employed in this thesis. The University of Connecticut, in collaboration with HIγS, designed and built the optical time projection chamber (OTPC) used in this work. The OTPC data were collected in 2011, prior to my involvement in the collaboration. I led the analysis efforts for both experimental datasets presented in this thesis. Contributions from colleagues in the collaboration are appropriately referenced throughout the text. I used AI at AITS 2 (AI for Shaping) of the Artificial Intelligence Transparency Scale (AITS). I acknowledge the use of claude.ai for sentence structure, grammar, and spelling.

4. The work undertaken towards the thesis has been conducted in accordance with the SHU Principles of Integrity in Research and the SHU Research Ethics Policy, and ethics approval has been granted for all research studies in the thesis, as shown in the table below.

Ethics Review Ref. No.	**Title of Research Study**	**Approval Date**
ER49343498	Evaluating the $^{12}C(\alpha,\gamma)^{16}O$ cross-section and the cluster structure of ^{12}C.	07/12/2022

5. The word count of the thesis is 38670.

Name: Kristian Charles Zajdek Haverson
Date: 30/11/2025
Award: PhD
Director of Studies: Dr Robin Smith
Second Supervisor: Professor Andy Alderson
Advisor: Professor Moshe Gai

Acknowledgements

First, I would like to thank my supervisor, Dr Robin Smith, for his guidance and encouragement over the past few years. This work and the opportunities I have had would not have been possible without him. I am particularly thankful for his willingness to answer physics and analysis questions well beyond the 9-5. I am grateful to my advisor, Professor Moshe Gai, for facilitating my work on these data, for his invaluable advice and insight, and for always encouraging me to aim high. My thanks also extend to Professor Andy Alderson for his support and for making time to help with any challenges I encountered. I have learned a great deal from this experience. My thanks go to all those involved in the collaboration from both the University of Warsaw and the University of Connecticut, especially the other PhD students — Mateusz, Sarah, and Deran. I would also like to thank Dr Kevin Ching Wei Li for offering his expertise and guidance with the intricacies of R-matrix analyses.

It goes without saying that my time at Sheffield Hallam University would not have been the same without my office mates, Joel Hirst, Harry Saxton, and Raphael Fortulan. Thank you all for the friendship, support (IT and otherwise), and especially the Thursday pub trips—let's hope pints stay this price for the foreseeable (£5–6 for a good one, circa 2025).

I would also like to thank my Mum and extended family for their unconditional love and support throughout my studies. Your belief in me has been a constant, and I am forever grateful for everything you have done to help me reach this point.

Last, but by far not least, special thanks go to my partner, Natasha Flett. This journey certainly would not have been possible without your enduring patience, encouragement, and love; it truly means the world to me. Thank you for making this possible. That being said, I genuinely hope you don't find yourself bored enough to read this.

Publications

Experiment 1

Haverson, K.C.Z., Smith, R., Gai, M. *et al.* Background-free ^{12}C(α, γ) angular distribution measurements with a time projection chamber operating in gamma beams. *Commun. Phys.* **9**, 27 (2026). https://doi.org/10.1038/s42005-025-02458-7

Experiment 2

Haverson, K.C.Z. & Cwiok, M., *et al. Working title:* Measurement of the ^{12}C(α, γ_0)^{16}O cross section from $E_x = 8.5 - 13.9$ MeV using the Warsaw active target time projection chamber. *In preparation.*

Haverson, K.C.Z., *et al. Working title:* Studying the clustered structure of ^{12}C through photo-dissociation. *In preparation.*

Contents

List of Figures

List of Tables

Abbreviations

ADC Analog-to-Digital Converter

AGB Asymptotic Giant Branch

AGET ASIC for GET

AsAd ASIC & ADC

ASIC Application-Specific Integrated Circuit

BBN Big-Bang Nucleosynthesis

BGO Bismuth Germanium Oxide

cm Centre-of-Mass

CNO Carbon-Nitrogen-Oxygen

CoBo Concentration Board

DAQ Data Acquisition

DSSD Double Sided Silicon Strip Detector

eTPC Electronic Time Projection Chamber

FEL Free Electron Laser

FPGA Field-Programmable Gate Array

GCR Galactic Cosmic Ray

Geant4 GEometry ANd Tracking 4

GEM Gas Electron Multiplier

GET General Electronics for TPCs

HB Horizontal Branch

HIγS High Intensity Gamma Source

HPGe High Purity Germanium

HRD Hertzsprung–Russell Diagram

ISM Interstellar Medium

LiBeB Lithium-Beryllium-Boron

MPAD Mirror Paddle Detector

MS Main Sequence

MWPC Mulit-Wire Proportional Chamber

NaI(Tl) Sodium Iodide doped with Thallium

OTPC Optical Time Projection Chamber

PCB Printed Circuit Board

PDF Probability Density Function

PID Particle Identification

PMT Photomultiplier Tube

PSD Pulse Shape Discrimination

RGB Red Giant Branch

SPAD Single Paddle Detector

SRIM Stopping and Range of Ions in Matter

SVM Support Vector Machine

TPC Time Projection Chamber

TUNL Triangle Universities Nuclear Laboratory

UTR Upper Target Room

Symbols

$E_{\mathbf{cm}}^{\mathbf{eff}}$	Effective centre-of-mass energy
$E_{\mathbf{cm}}^{\mathbf{inc}}$	Incident beam energy in the centre-of-mass
$E_{\mathbf{cm}}^{\mathbf{tpc}}$	Effective centre-of-mass energy reconstructed in the TPC
E_R	Observed resonance energy
E_γ	Nominal gamma-ray energy
E_λ	Formal resonance energy
E_x	Excitation energy in the compound nucleus
J_n^π	Total angular momentum quantum number J and parity π of the nth nuclear state
P_ℓ	Nuclear penetrability
$P_\nu(\cos\theta)$	Legendre polynomial of order ν
Q	Reaction Q-value
S_ℓ	Shift factor
Γ	Observed partial width
Γ_λ	Formal partial width
η	The Sommerfeld parameter
γ^2	Observed reduced width
γ_λ^2	Formal reduced width
$d\sigma/d\Omega$	Differential cross section
σ	Cross section
a_c	Channel radius
k	Wave number
$\mathcal{L}$	Integrated luminosity

Part I

Theory & Background

1

Nuclear Astrophysics

Astrophysics is a multidisciplinary field spanning many areas of physics, including cosmology, astronomy, particle physics, and nuclear physics, all of which share the common aim of describing the structure of the universe. Nuclear astrophysics aims to explain phenomena, such as the origins of the universe's nuclear abundances, the energy sources within stars, and stellar evolution, using nuclear (quantum) processes.

1.1 Introduction

One process that significantly affects observed nuclear abundances is Big Bang Nucleosynthesis (BBN). In the early universe, about 3 minutes after the initial Big Bang event, the universe had expanded and cooled to $\sim 10^9$ K. This satisfied the conditions to permit the survival of primordial nuclei, marking the start of BBN. Protons and neutrons[1] fuse to synthesise (weakly bound, ∼2.2 MeV) deuterium, now cool enough to survive

[1] $p + p$ or $n + n$ also possible but less likely due to involvement of the weak nuclear force.

photo-dissociation by high-energy photons long enough to allow for successive capture reactions [1], initiating the BBN reaction chain shown in the left panel of figure 1.1.

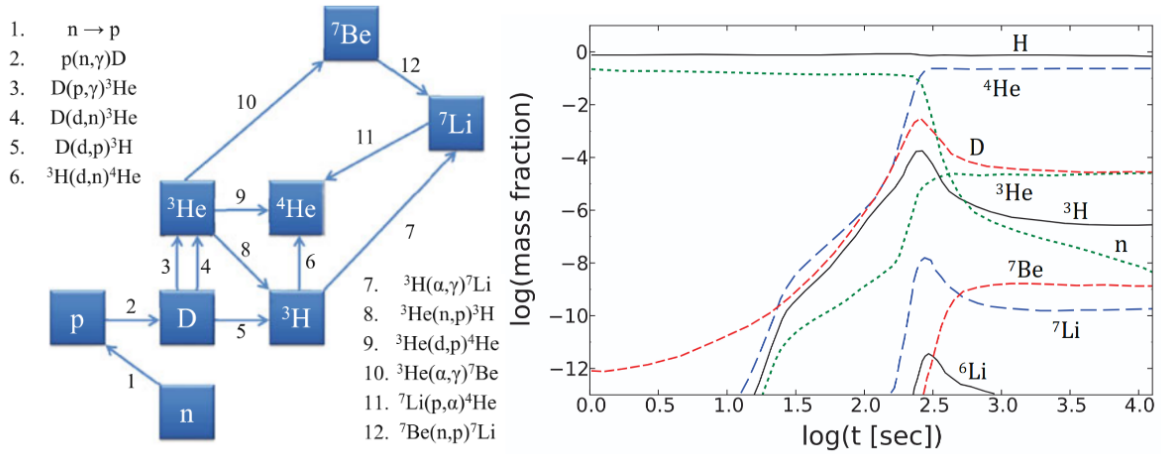

Figure 1.1: Big-Bang Nucleosynthesis. Left: The chain of nuclear reactions occurring during BBN is shown. This figure was taken from reference [2]. **Right:** The time evolution of mass fractions for light elements during BBN is shown. This figure was taken from reference [3].

The most abundant reaction products surviving from this phase are ^{1}H (75% by mass) and ^{4}He (25% by mass). This is shown in the right panel of figure 1.1, which displays the fractional abundances during BBN for $\eta = (6.07 \pm 0.07) \times 10^{-10}$ [4]. The parameter η is the baryon-to-photon ratio, which is a key parameter in BBN that determines the abundances of light nuclei. Most reactions in the early stages proceed through simple α, proton, or neutron capture. The lack of stable nuclei at $A = 5$ and $A = 8$ create a significant bottleneck for the formation of heavy nuclei during BNN as these would require rarer three-body reactions, or those involving $^{2/3}$H or ^{3}He nuclei [5]. As temperatures dropped during the universe's expansion, these reactions ceased, fixing the abundances of the synthesised light elements at this stage.

Predictions made from BBN models perform well at reproducing the observed light element abundances in the universe [6], but still face open challenges such as the primordial lithium problem. The abundance of ^{7}Li in low-metallicity (first generation) stars remains approximately constant—a feature known as the *Spite plateau* [7], considered to reflect the primordial abundance of ^{7}Li. Recent observations from such stars have determined the

lithium-to-hydrogen ratio to be Li/H = $(1.58^{+0.35}_{-0.28}) \times 10^{-10}$ [8], whereas BBN calculations predict a value of Li/H = $(4.283^{+0.335}_{-0.292}) \times 10^{-10}$ [9], leaving a factor of three discrepancy.

The synthesis of heavier elements was theorised to take place in stellar interiors, as outlined in the seminal work of Burbidge, Burbidge, Fowler, and Hoyle (B^2FH) [10]. As the universe aged, the first stars formed and provided sites for stellar nucleosynthesis. Here, nuclear fusion reactions synthesised elements from ^{12}C to ^{56}Fe. When these stars exhausted their nuclear fuel and die, they spread heavy elements throughout the interstellar medium (ISM), providing the "seeds" for future generations. Beyond ^{56}Fe, fusion becomes endothermic, so heavier elements must be produced from other sources. Two such sources are the slow neutron capture process (s-process) in Asymptotic Giant Branch (AGB) stars and the rapid neutron capture process (r-process), thought to occur in explosive events such as core-collapse supernovae and neutron-star mergers [11]. In both cases, new elements are synthesised through successive neutron capture followed by β-decay.

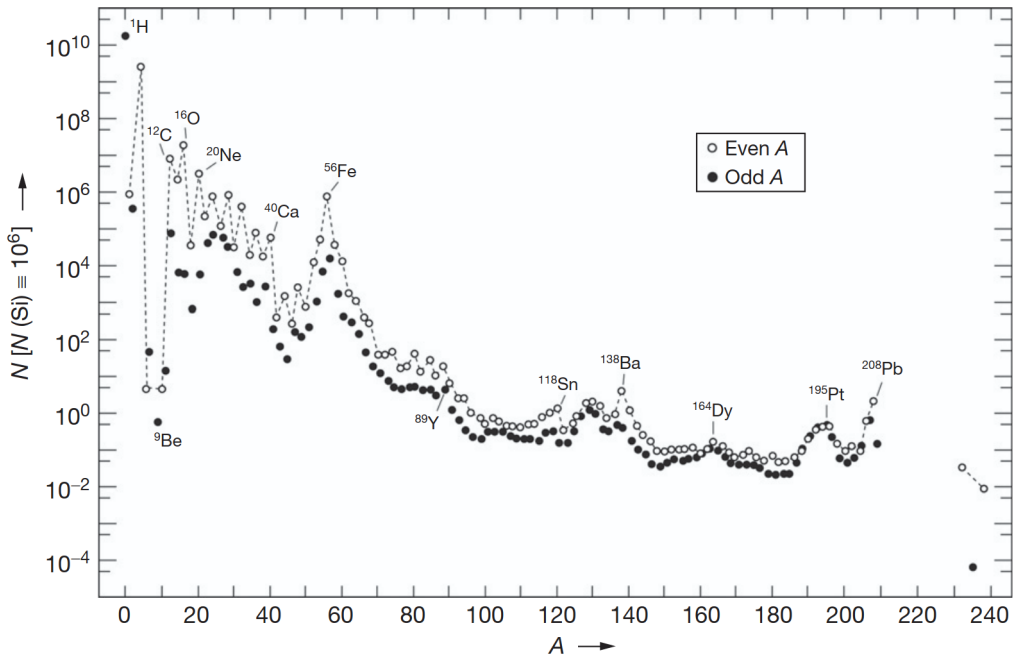

Figure 1.2: Abundances of Elements: Plot showing the observed abundances of nuclei in the solar system. Hollow circles represent even-mass nuclei and black circles represent odd-mass nuclei. Even-mass nuclei are more abundant than odd-mass, following the Oddo-Harkins rule [12]. The data were tabulated by reference [13], and the figure was taken from reference [14].

Light nuclei such as lithium, beryllium, and boron (LiBeB) are produced in the ISM through ongoing galactic cosmic ray (GCR) spallation reactions. These processes are responsible for most of ^{6}Li, ^{9}Be, ^{10}B, and ^{11}B, and contribute to the production of some ^{7}Li in the solar system [15, 16].

The culmination of these processes results in the observed elemental abundances in our solar system, as shown in figure 1.2. Reflecting contributions from BBN, cosmic-ray spallation, and stellar nucleosynthesis.

1.2 The Hertzsprung-Russel Diagram

A star's luminosity (radiative power), L, depends on its radius, R, and surface temperature, T, such that $L = 4\pi R^2 \sigma T^4$, where σ is the Stefan-Boltzmann constant. This relationship is central to the Hertzsprung-Russell diagram (HRD), a powerful tool for classifying and studying stellar evolution. On the HRD, the vertical axis shows luminosity (or absolute magnitude M_V), and the horizontal axis shows surface temperature (or colour index $B-V$) [11].

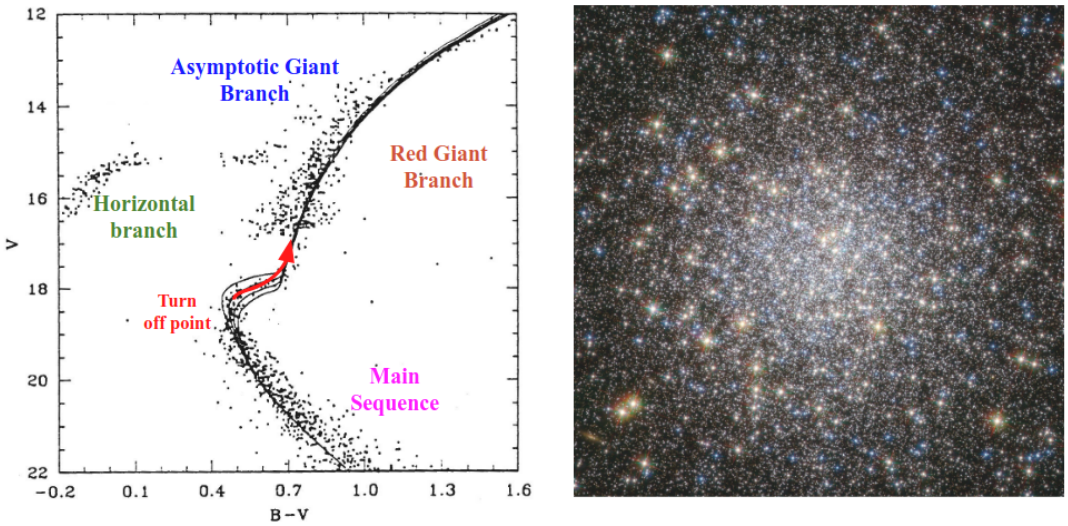

Figure 1.3: Messier 5 Globular Cluster. Left: The Messier 5 globular cluster HRD is shown, adapted from reference [17]. Here, the horizontal axis shows the colour index and the vertical axis the absolute magnitude. The regions corresponding to main sequence (pink), red giant (orange), horizontal branch (green), and asymptotic giant branch (blue) stars are indicated. The so-called "turn-off point" is also shown in red, which indicates when stars leave the main sequence. **Right:** The Hubble Space Telescope image of the Messier 5 globular cluster, taken from reference [18], is shown.

One important HRD is shown in figure 1.3. This figure depicts the globular cluster M5 (Messier 5, NGC 5904), located in the constellation Serpens, which was first discovered by Gottfried Kirch in 1702. The right panel shows the Hubble photograph of the cluster, and the left panel displays an HRD of 15,000 stars in the cluster. The HRD clearly marks stellar regions for various evolutionary phases. The Main Sequence (MS) extends from cool (red), dim stars in the lower right to hotter (blue), more luminous stars in the upper left[2].

1.3 Stellar Evolution

This section details the evolutionary stages of stars, from formation to stellar death, and discusses the nuclear burning phases. To provide context, figure 1.4 illustrates the evolutionary track of a $1M_{\odot}$ star on an HRD.

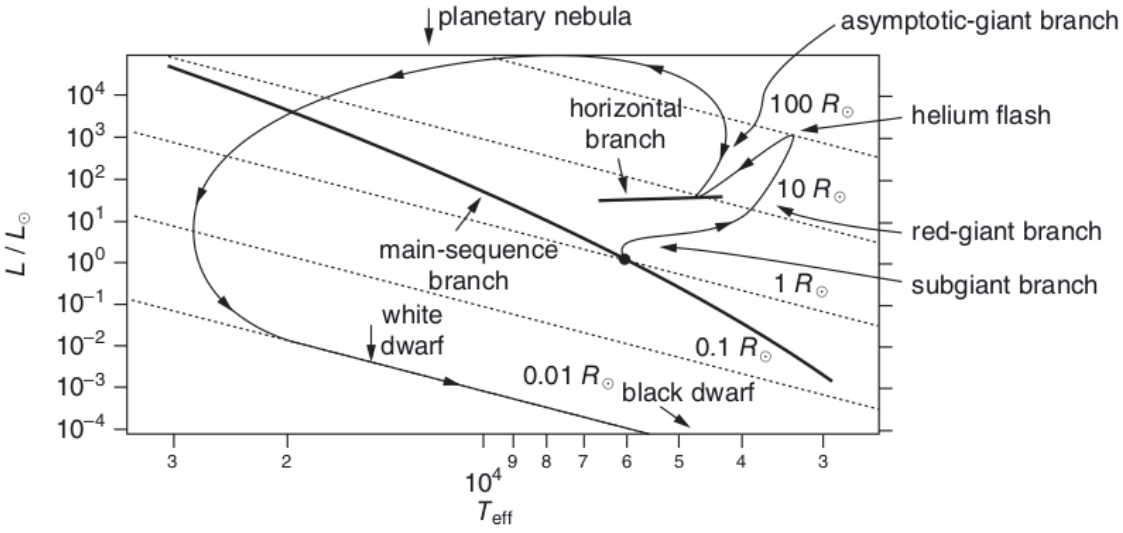

Figure 1.4: Hertzsprung-Russell Diagram Illustration: An HRD showing the evolutionary track of a $1M_{\odot}$ star, taken from reference [20]. The track follows the star (from the bottom right) as it moves off the main sequence (black line), passes through the red giant phases, crosses the horizontal branch, and ends as a black dwarf.

[2]Of note is the so-called "Turn off point" (where the stars leave the main sequence) [19], shown by the red arrow. This feature was used by King *et al.* in their 1988 paper [17] to estimate the universe's age to be about 13 billion years old, when at that time it was considered to be only 8 billion years old. Today, the age of the universe is thought to be 13.7 billion years old.

1.3.1 Path to Main Sequence

Star formation begins in the ISM, where large clouds of gas composed primarily of hydrogen and helium at typical temperatures of ~ 100 K coalesce. They become gravitationally unstable and contract, creating a protostar with a cool, dense core surrounded by a protostellar disc [1]. As gravity overcomes the outward thermal pressure of the gas molecules, the protostar continues to contract, raising its core temperature. For massive protostars ($M > 0.08\ M_{\odot}$), contraction continues until core temperatures reach $\sim 10^7$ K, at which point hydrogen burning commences. This marks the onset of stellar thermonuclear reactions and places the star on the MS. The energy released through fusion reactions halts further gravitational collapse, establishing a state of hydrostatic equilibrium. For protostars with $M < 0.08\ M_{\odot}$, this criterion is not met, and they form failed stars known as brown dwarfs [19, 20].

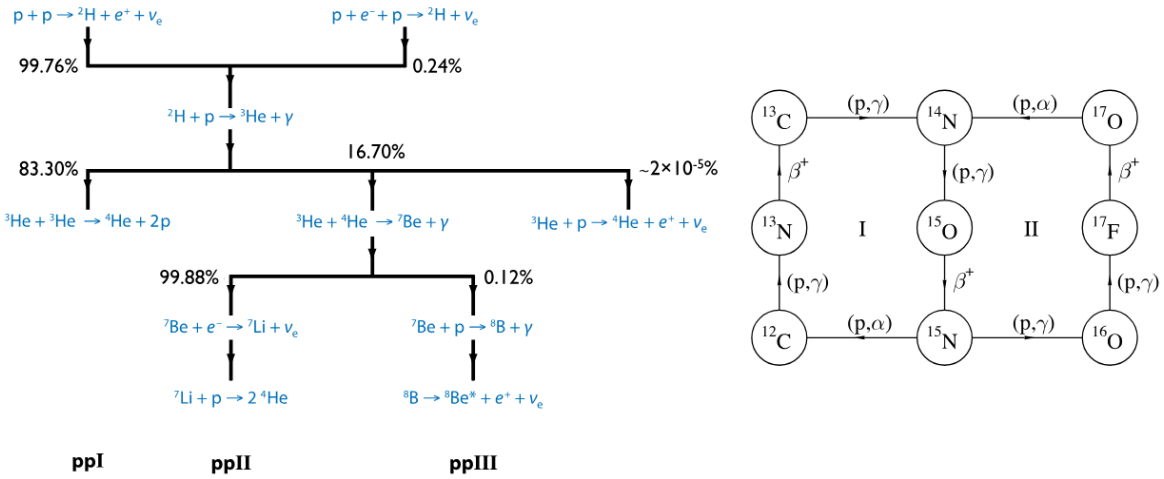

Figure 1.5: Hydrogen Burning Reaction Chains. Left: The three proton-proton (pp) decay chains (ppI, ppII, ppIII) are shown. The branching percentage for each path is given. **Right:** The Carbon-Nitrogen-Oxygen (CNO) cycle is shown. The circles represent the compound nuclei, and the paths are indicated with reaction type and arrows showing the direction. Both figures were taken from reference [21].

Hydrogen burning proceeds through two different reaction mechanisms. For first-generation stars, the only fuel source available is hydrogen, which fuses to generate energy through the pp chains, as shown in the left panel of figure 1.5, to synthesise ^{4}He. For subsequent-generation stars, depending on their initial composition, fusion may also occur

through the Carbon-Nitrogen-Oxygen (CNO) cycle, to produce ^{4}He [1]. However, due to the higher Coulomb barrier, the CNO cycle requires slightly higher temperatures of $\sim 1.4 \times 10^7$ K [22]. The CNO cycle is shown in the right panel of figure 1.5.

1.3.2 Red Giant to Horizontal Branch

Once the hydrogen in the core is exhausted, low mass stars ($M < 0.5\ M_\odot$) end their nuclear burning phase here, as they don't have sufficient mass to fuse ^{4}He in their core [20]. More massive stars move from the MS onto the Red Giant Branch (RGB), as shown in figure 1.6. Under this regime, the star will continue to gravitationally collapse without a fuel source until the remaining hydrogen, in a shell surrounding an inert helium core, is ignited. The energy produced by this burning causes the outer layers to expand and cool (becoming redder), while becoming highly luminous [1, 19].

When the core reaches a sufficiently high temperature, $\sim 10^8$ K [19], helium ignition occurs through the triple-alpha (3α) process, synthesising ^{12}C. After 3α ignition, stars move across the Horizontal Branch (HB), where at temperatures of $\sim 2 \times 10^8$ K, the $^{12}\mathrm{C}(\alpha,\gamma)^{16}\mathrm{O}$ reaction competes to destroy the synthesised oxygen. Stars in this phase shrink in radius, become hotter, and grow fainter [1, 20].

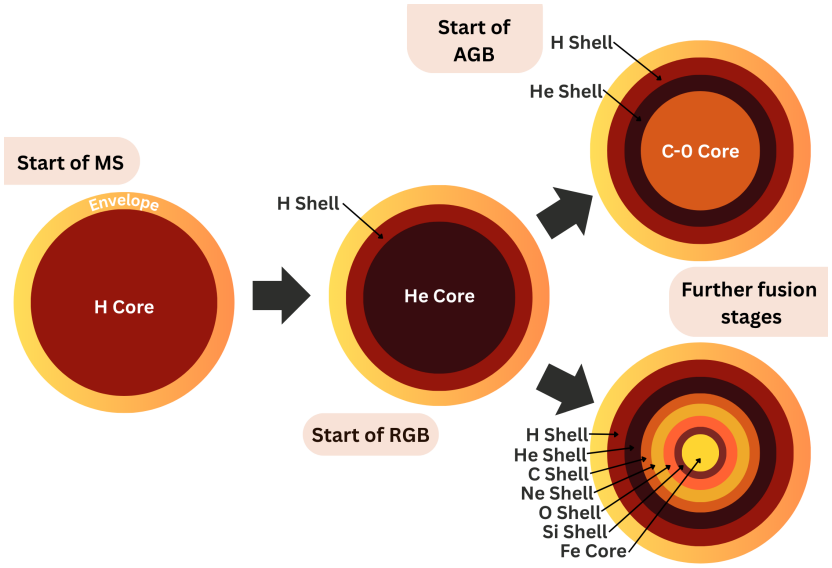

Figure 1.6: Stellar Evolution Pathway: Diagram showing the general structure of a star at different stages in its evolution, for different possible pathways. This illustration was inspired by figure 1.3 of reference [23], which assumes the helium burning leads to C/O $\gg 1$ (defined later).

1.3.3 Asymptotic Giant Branch

After the helium in the core is exhausted, stars leave the HB. Stars with $M < 10\ M_{\odot}$ will enter Asymptotic Giant Branch (AGB) phase. This stage is characterised by double-shell burning, with hydrogen fusion occurring in the outer shell and helium fusion in an inner shell, both surrounding an inert carbon-oxygen core (top path in figure 1.6). These stars will expand and cool again, becoming very luminous [1, 11].

1.3.4 Further Burning & Type II Supernova

Stars with $M > 10\ M_{\odot}$, leaving the HB, undergo further burning stages (bottom path in figure 1.6). Working progressively through carbon, neon, oxygen, and finally silicon. As a result, an onion-like structure forms, with burning from previous stages still occurring in shells above the active burning core. Following silicon burning, the core consists primarily of iron. Because it has the highest binding energy per nucleon, iron cannot release energy through fusion. Without an energy source, the star contracts rapidly, and the core collapses. The outer layers are ejected into the ISM by a powerful rebounding shock wave from the collapse in an event called a Type II (core-collapse) supernova [20].

The fate of the dense core is dependent on the ratio of Carbon-to-Oxygen (C/O) at the end of stellar helium burning. It determines whether the remnant becomes a neutron star (C/O>1) or a black hole (C/O<1) [24].

1.3.5 Type Ia Supernovae

Another class of supernova of interest is the Type Ia supernova [25]. Type Ia supernovae form during the evolution of binary star systems, where a white dwarf accretes mass from a nearby companion star. Just before it reaches the Chandrasekhar limit ($1.4M_{\odot}$), carbon burning is ignited, starting a runaway thermonuclear reaction. This results in an explosive supernova event, in which no remnant remains [26].

An important property of Type Ia supernovae is their light-curve; they all peak at similar luminosities, meaning they can be used as so-called “standardisable candles”, marking distances in the universe [20, 27]. One parameter that is cited to cause variation in said light

curves is the C/O ratio at the end of stellar helium burning. The C/O ratio, along with the initial density of the white dwarf and its metallicity, influences the abundance of ^{56}Ni [28], and the photons emitted through the decay of ^{56}Ni define the peak of the light curves.

Example light-curves are shown in figure 1.7, each colour group tracks a different supernova over multiple days on the x-axis and magnitude on the y-axis. The left panel shows the raw data, which indicates that not all events have the same magnitude. There is a relation, however, between the magnitude and the rate of decline (width) of the light-curves. This can be used to define a so-called "stretch factor" [26], which corrects the data such that they line up (thus and are standardisable), as shown in the right panel. The peak corresponds to photons emitted through decay of ^{56}Ni, and the tail from those emitted from ^{56}Co.

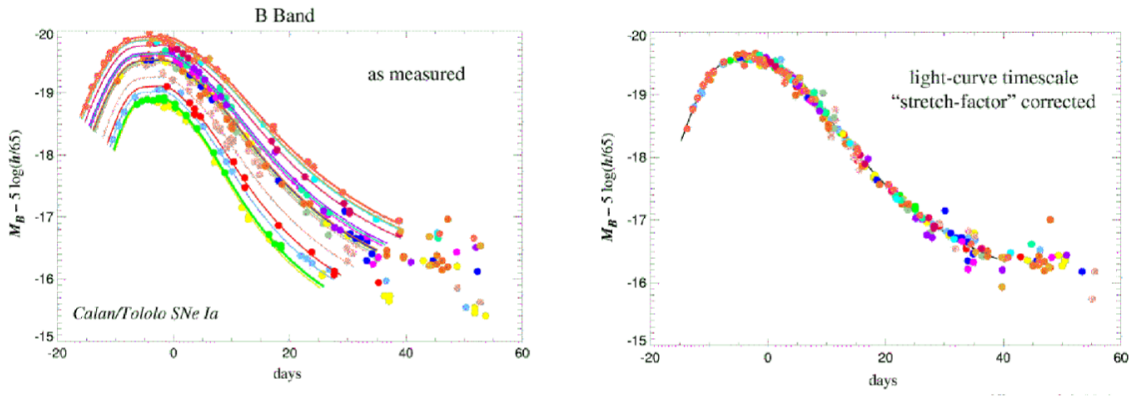

Figure 1.7: Type-Ia Supernova Light Curves: The figure shows both the raw and corrected light-curves observed from different type-Ia nova events. This figure was taken from reference [29].

1.4 Thermonuclear Reactions

Stellar nucleosynthesis proceeds through nuclear reactions in stellar interiors. The outcome of stellar evolution depends on the rates at which these reactions occur — a key input to stellar models.

To understand stellar evolution, it is therefore pertinent to review different reaction mechanisms, their contribution to the reaction cross section, and how this affects reaction rate calculations. This section of the thesis reviews both resonant and non-resonant

processes, as well as tools useful in analysing these reactions. These include the single-level R-matrix formalism and partial-wave decomposition.

The aforementioned reaction mechanisms are illustrated in figure 1.8, for the $^{17}\mathrm{O}(p,\gamma)^{18}\mathrm{F}$ capture reaction. The left panel depicts the resonant capture process, and the middle panel shows the non-resonant, or direct capture, process. Each of their contributions to the reaction cross section (depicted here as S-factor, discussed later) is shown in the right panel.

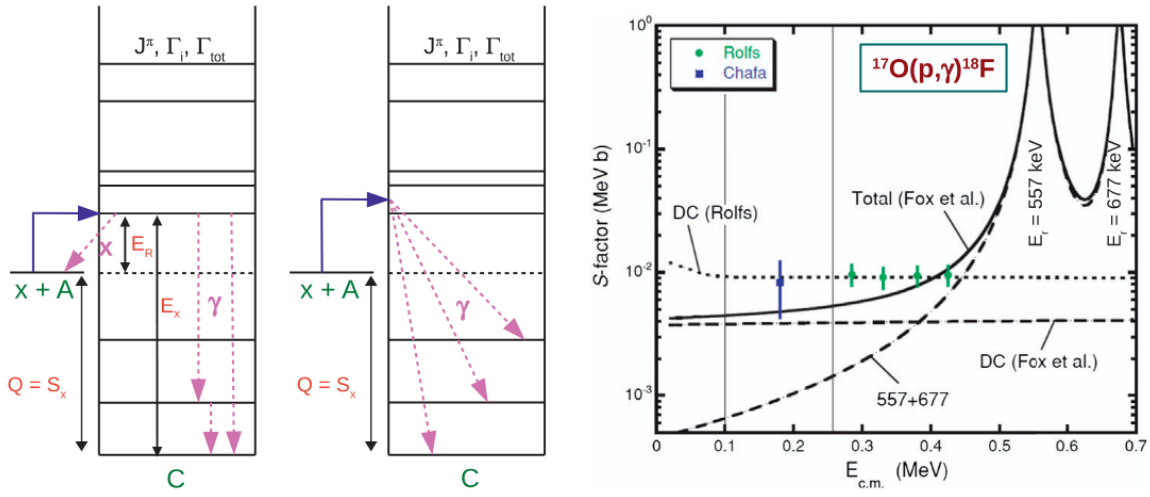

Figure 1.8: Outline of Nuclear Reaction Mechanisms & Cross section Contributions: The image taken from reference [30] to illustrate different capture mechanisms. **Left:** Resonant capture of entrance channel $X + A$ to a state in the compound nucleus C is shown, with possible decays, γ or X emission, indicated. **Centre:** Direct capture is shown, where the entrance channel steps straight to the exit channel with the emission of a γ. **Right:** The different contributions to the reaction cross section (shown here as S-factor, discussed later), for $^{17}\mathrm{O}(\mathrm{p},\gamma)^{18}\mathrm{F}$ are shown. Direct capture (labelled DC) varies slowly, whereas resonant capture exhibits a resonant structure.

1.4.1 Reaction Rate

The total reaction rate between particles a and b in stellar interiors, denoted r_{ab} depends on the number densities per cubic centimetre n_a and n_b, respectively, and the reaction rate per particle pair $\langle \sigma v \rangle$ [1], such that

$$r_{ab} = \frac{n_a n_b \langle \sigma v \rangle}{(1 + \delta_{ab})}. \tag{1.4.1.1}$$

Here, the Kronecker delta δ_{ab} is included to correct for double-counting of identical particles. The average reaction rate per particle pair, $\langle \sigma v \rangle$, is obtained by integrating over the reaction cross section, $\sigma(v)$, which is the intrinsic interaction probability, with the velocity distribution in the stellar plasma $v\phi(v)$, as shown below.

$$\langle \sigma v \rangle = \int_0^\infty v\phi(v)\sigma(v)\, dv. \tag{1.4.1.2}$$

Here, v is the average velocity, and $\phi(v)$ is the probability density function of stellar velocities. The velocity distribution is modelled by the Maxwell-Boltzmann distribution

$$\phi(v) = 4\pi \left(\frac{\mu}{2\pi k_B T}\right)^{3/2} v^2 \exp\left(-\frac{\mu v^2}{2k_B T}\right) \tag{1.4.1.3}$$

where $\mu = m_a m_b/(m_a + m_b)$ is the reduced mass of the interacting particles, k_B is the Boltzmann constant, and T is the temperature. With knowledge that $E = \frac{1}{2}\mu v^2$, equation (1.4.1.2) can be reparameterised in terms of energy,

$$\langle \sigma v \rangle = \left(\frac{8}{\pi\mu}\right)^{1/2} (k_B T)^{-3/2} \int_0^\infty \sigma(E) E \exp\left(-\frac{E}{k_B T}\right) dE. \tag{1.4.1.4}$$

The energy dependence of the reaction rate is determined by the terms in the integrand. Thus, the reaction rate strongly depends on both the reaction cross section and the temperature distribution.

1.4.2 Non-resonant Reactions

The first class of reactions to consider are the non-resonant kind. An astrophysically important example is direct capture (others include pickup, stripping, and coulomb excitation [31]). These reactions are "direct" as they occur in a single step from the entrance channel to the exit channel. For direct capture the entrance channel, $a + b$, will step directly to the final state, C, with the emission of a γ-ray [1].

As with any reaction, resonant or not, as the particles in the entrance channel approach to interact, they must overcome both the Coulomb potential and the centrifugal potential.

Since nuclear reactions in stellar interiors occur at relatively low energies, much below the Coulomb barrier ($E \ll E_C$), the reaction must proceed through quantum mechanical tunnelling. To determine the energy range at which reactions proceed in stellar interiors, George Gamow [32] first derived the approximate tunnelling probability for s-wave nuclei (no centrifugal barrier, $\ell = 0$, where ℓ is the orbital angular momentum quantum number) as

$$P(E) = \exp(-2\pi\eta(E)), \tag{1.4.2.1}$$

where, $\eta = Z_a Z_b e^2 \sqrt{\mu/(2E)}/\hbar$ is the Sommerfeld parameter which has its usual definition [33]. It is therefore immediately clear that the non-resonant cross section at astrophysical energies will drop exponentially as

$$\sigma \propto \exp(-2\pi\eta). \tag{1.4.2.2}$$

The full form can be expressed as,

$$\sigma(E) = \frac{1}{E}\exp(-2\pi\eta)S(E), \tag{1.4.2.3}$$

where $1/E$ is a geometric factor arising from the de Broglie wavelength of the particle, and $S(E)$ is the astrophysical S-factor, which only contains information about the nuclear interactions.

Direct reactions can occur at any bombardment energy, and their contribution to the S-factor varies smoothly with energy. An example direct capture contribution, labelled DC, is shown by Fox *et al.* in figure 1.8.

The Gamow Window

The reaction rate per particle pair from equation (1.4.1.4) can then be written as

$$\langle \sigma v \rangle = \left(\frac{8}{\pi\mu}\right)^{1/2} \frac{1}{(k_B T)^{3/2}} \int_0^\infty S(E) \exp\left[-\frac{E}{k_B T} - 2\pi\eta(E)\right] dE. \tag{1.4.2.4}$$

For reactions with a slowly varying S-factor, it can be treated as constant and removed from the integral. Therefore, the reaction rate is dominated by two exponential terms in the integrand: The Maxwell–Boltzmann velocity distribution (favouring lower energies) and the Coulomb barrier penetration term (favouring higher energies).

Evaluating the product of these contributions defines the Gamow peak, indicated by the red peak in figure 1.9. This is the range of energies where reactions most effectively occur in stellar interiors. The energy at which the product is maximal, E_0 in the figure, is known as the Gamow energy.

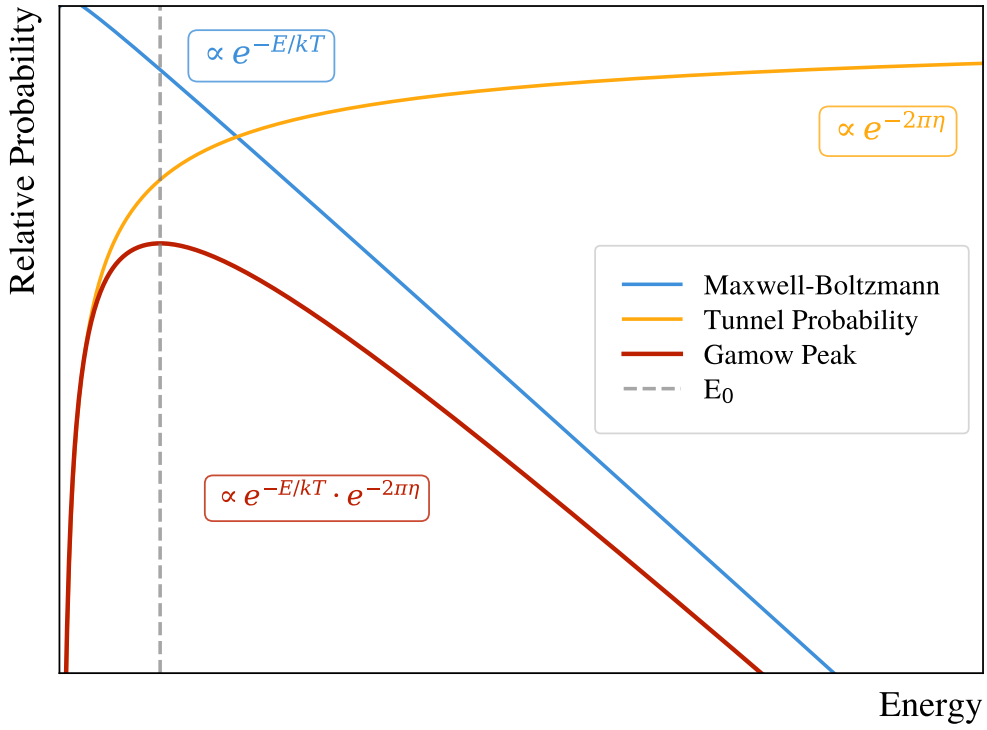

Figure 1.9: The Gamow Window: The Gamow peak for arbitrary temperature is shown in red. This is calculated as the product of the temperature distribution (blue) and Gamow tunnelling probability (yellow). The Gamow energy, the point at which the Gamow peak is maximal, is indicated by a dashed grey line. A log scale is applied to the y-axis.

1.4.3 Resonant Reactions

Another class of reactions is the resonant kind. These are a two-step process, in which the entrance channel first forms an excited state in the intermediate compound nucleus before decaying through the exit channel. For example, resonant radiative capture is denoted

$$a + b \rightarrow C^* \rightarrow C + \gamma, \tag{1.4.3.1}$$

where $a + b$ is the entrance channel, C^* the excited compound nucleus, C the compound nucleus in its ground state, and γ is the emitted photon.

For such a process to occur, standard conservation laws of angular momentum and parity must be met, and the relative energy between a and b must be close to the resonance energy, denoted E_R and defined as $E_R = E_x - Q$, where Q is the reaction Q-value, and E_x is the excitation energy in the compound nucleus. When these conditions are met, the wave functions inside and outside the potential barrier match, leading to a rapid change in the reaction cross section [34]. Example resonant contributions are shown by Fox *et al.* in figure 1.8.

Before defining the energy dependence of the cross section, simple conclusions about the nature of a resonance can be drawn simply through Heisenberg's uncertainty principle

$$\Delta\ t\Delta\ E \geq \frac{\hbar}{2}. \tag{1.4.3.2}$$

This states that a resonance with well-defined energy (narrow state) will have a longer lifetime, while a state with poorly defined energy will have a shorter lifetime.

The energy dependence of an (α, γ_0) radiative capture reaction cross section for a narrow isolated resonance (no overlapping states) is given by the single-level Breit-Wigner formula,

$$\sigma(E) = \frac{\pi}{k^2} \frac{2J_{C^*} + 1}{(2J_a + 1)(2J_b + 1)} \frac{\Gamma_a \Gamma_\gamma}{(E - E_{\mathrm{R}})^2 + \Gamma^2/4}. \tag{1.4.3.3}$$

Here k is the wave number of the entrance channel, and J_{C^*}, J_a, and J_b are the total angular momentum quantum numbers of the excited state, the projectile and the target,

respectively. The quantities Γ_a and Γ_γ are the partial widths, representing the probabilities of forming and decaying from the excited state through the respective channels. The total width is given by $\Gamma = \sum_i \Gamma_i$, summing over all open channels. The shape obtained by equation (1.4.3.3) will be Lorentzian in nature, and perfectly symmetric. One can use equation (1.4.3.3) and equation (1.4.2.4) to define the reaction rate when a narrow resonance is near the Gamow window.

1.4.4 Single-level R-matrix

The Breit-Wigner approximation for the resonance shape is only valid for narrow states. For broad resonances, one must account for the energy dependence of the partial widths. The following example continues for (α, γ_0) radiative capture.

Energy Dependence

Charged particle. For a charged particle channel (in this case the α channel) the partial width is given by [31]

$$\Gamma_\alpha(E) = 2P_\ell(E)\gamma_\alpha^2, \tag{1.4.4.1}$$

where $P_\ell(E)$ is the penetrability for angular momentum ℓ at energy E and γ_α^2 is the reduced α width, where the latter contains information about the nuclear interior.

The penetrabilities are calculated using the regular and irregular Coulomb wave functions $F_\ell(\rho, \eta)$ and $G_\ell(\rho, \eta)$, which are solutions to the Schrödinger equation with a Coulomb potential, using [35]

$$P_\ell(E) = \frac{\rho}{F_\ell^2(\rho, \eta) + G_\ell^2(\rho, \eta)}. \tag{1.4.4.2}$$

In the preceding equation $\rho = ka_c$, where a_c is the channel radius (defined later) and is typically calculated as $a_c = r_0(A_1^{1/3} + A_2^{1/3})$, where A_n is the mass number of nucleus n. The value of r_0 is usually between $\sim 1.2 - 1.4$ fm.

Due to the penetrabilities, as one goes higher in energy the probability of tunnelling increases; therefore, for broad states, the cross section lineshape will become asymmetric. The energy dependence of the charged particle width of a state located at resonance energy E_R is given by [31]

$$\Gamma_\alpha(E) = \Gamma_\alpha(E_R)\frac{P_\ell(E)}{P_\ell(E_R)}. \tag{1.4.4.3}$$

Electromagnetic. The radiative partial width also has energy dependence. It can be written in terms of the decay constant, $\lambda(\bar{\omega}LE)$, which gives the probability for the emission of electromagnetic radiation in a transition between two states per unit time [19, 31]

$$(2J_f + 1)\ \Gamma_\gamma(E) = \hbar\,\lambda(\bar{\omega}LE). \tag{1.4.4.4}$$

Here, J_f is the angular momentum quantum number of the final state, and the decay constant, given by

$$\lambda(\bar{\omega}LE) = \frac{8\pi(L+1)}{L[(2L+1)!!]^2}\frac{1}{\hbar}\left(\frac{E_\gamma(E)}{\hbar c}\right)^{2L+1} B(\bar{\omega}L), \tag{1.4.4.5}$$

where L is the multipolarity, E_γ is the gamma-ray energy, and $B(\bar{\omega}L)$ is the reduced transition probability, where $\bar{\omega} = E$ for electric or M magnetic transitions.

Using equations (1.4.4.4) and (1.4.4.5) the energy dependence of the radiative width of a state located at E_R is given by [31]

$$\Gamma_\gamma(E) = \Gamma_\gamma(E_R)\left(\frac{E+Q}{E_R+Q}\right)^{2L+1},$$

where Q is the reaction Q value.

Single-Level Parameterisation

To incorporate the aforementioned energy dependence and obtain a more representative lineshape for modelling the cross section, the Wigner-Eisenbud parametrisation [36] of the

phenomenological R-matrix theory (one with arbitrary boundary conditions) can be used. The isolated single-level R-matrix model is briefly outlined here. The reader is referred to references [19, 35, 37] for a complete and rigorous discussion of R-matrix theory.

In R-matrix theory, the space is divided into two regions by the channel radius a_c. Where $r < a_c$, complicated many-body physics are involved. Whereas, for $r \geq a_c$, only Coulomb interactions are considered. In this formalism, solutions to the Schrödinger equation are obtained separately in each region, and the wave functions and their derivatives are matched at $r = a_c$. The result of this process yields the *formal* expression for the (α, γ_0) reaction cross section as shown in equation (1.4.4.6) [19], where all *formal* parameters (defined later) are denoted with a λ subscript.

$$\sigma(E) = \frac{\pi}{k^2} \frac{2J_{C^*} + 1}{(2J_\alpha + 1)(2J_b + 1)} \frac{\Gamma_{\lambda\alpha}\Gamma_{\lambda\gamma}}{(E - E_\lambda - \Delta_\lambda(E))^2 + \Gamma_\lambda^2/4}. \tag{1.4.4.6}$$

The parameters E_λ, $\Gamma_{\lambda\alpha}$, $\Gamma_{\lambda\gamma}$, are the *formal* resonance energy and *formal* partial widths for the α and γ channels respectively, and Γ_λ is the *formal* total width. The energy shift $\Delta_\lambda(E)$, included to ensure proper wavefunction matching at a_c, is defined as

$$\Delta_\lambda(E) = -\gamma_{\lambda\alpha}^2[S_\ell(E) - B]. \tag{1.4.4.7}$$

Here, $\gamma_{\lambda\alpha}^2$ is the *formal* reduced α width, B is the arbitrary boundary condition, and $S_\ell(E)$ is the shift factor, which is given by

$$S_\ell(E) = \frac{\rho[F_\ell(\eta,\rho)F'_\ell(\eta,\rho) + G_\ell(\eta,\rho)G'_\ell(\eta,\rho)]}{F_\ell(\eta,\rho)^2 + G_\ell(\eta,\rho)^2}. \tag{1.4.4.8}$$

Whilst the shift factor is solely dependent on conditions outside the nucleus, the energy shift itself, equation (1.4.4.7), is also dependent on the internal nuclear conditions through the reduced α width. It should be noted that this formalism cannot account for the γ channel contribution in the same way as the α channel, in equation (1.4.4.7). However, as discussed in reference [35], since γ widths are typically orders of magnitude smaller than charged particle widths, this omission is practically insignificant.

Formal and observed parameters. The *formal* parameters in equation (1.4.4.6), which are varied to reproduce experimental data, depend on both the channel radius a_c and the boundary condition B. Due to the arbitrary choice of the latter, they need not have any direct physical significance. To obtain physically meaningful *observed* resonance parameters (E_R, γ_α^2, Γ_γ) independent of B and a_c, a conversion is required.

The observed resonance energy, E_R, is defined to be located where the cross section is maximal, where

$$E_R - E_\lambda - \Delta_\lambda(E_R) = 0. \tag{1.4.4.9}$$

One can use the Thomas approximation [35] to linearise the shift factor in the vicinity of the resonance to yield

$$S_\ell(E) \approx S_\ell(E_\lambda) + (E - E_\lambda)\frac{dS_\ell}{dE}\bigg|_{E_\lambda}, \tag{1.4.4.10}$$

using this and expression (1.4.4.9), the following relation between observed and formal resonance energy is obtained

$$E_R = E_\lambda - \frac{\gamma_{\lambda\alpha}^2[S_l(E_\lambda) - B]}{1 + \gamma_{\lambda\alpha}^2 \frac{dS_\ell}{dE}\Big|_{E_\lambda}}. \tag{1.4.4.11}$$

A similar expression can be obtained for the observed reduced α width

$$\gamma_\alpha^2 = \frac{\gamma_{\lambda\alpha}^2}{1 + \gamma_{\lambda\alpha}^2 \frac{dS_\ell}{dE}\Big|_{E_\lambda}}, \tag{1.4.4.12}$$

and the observed partial γ width

$$\Gamma_\gamma = \frac{\Gamma_{\lambda\gamma}}{1 + \gamma_{\lambda\alpha}^2 \frac{dS_\ell}{dE}\Big|_{E_\lambda}}. \tag{1.4.4.13}$$

The *observed* parameters obtained this way should be independent of B and a_c. Practically,

due to the linear approximation of the shift factor, there can still be some residual a_c dependence that should be taken into account.

Multi-level Parametrisation

When analysing non-isolated resonances (multi-level) one must be aware of possible interference scenarios. Resonances with the same J^π can exhibit interference effects in the angle-integrated cross section, σ, and resonances with dissimilar J^π can exhibit interference effects in the differential cross section ($d\sigma/d\Omega$). For complex cases where many channels and/or interference effects are considered, codes such as `AZURE2` [38] should be used.

1.4.5 Partial-wave Decomposition

A reaction's differential cross section can be exploited to extract the different partial-wave contributions. In the following section, the channel-spin formalism for partial-wave decomposition, as shown by Carr *et al.*. [39], is used to derive the angular distributions corresponding to $E1$, $E2$, and $E1 - E2$ mixing.

Using γ beams to excite a compound nucleus decaying into two $J^\pi(0^+)$ nuclei, as is the focus of this work, affords a relatively simple reaction mechanism: No $J^\pi(0^+)$ states can form in the compound nucleus, and only decays through natural parity states are possible, as parity is restricted by $\Pi \equiv (+)(+)(-1)^l$ for electric or $\Pi \equiv (+)(+)(-1)^{l+1}$ for magnetic transitions. Therefore, assuming $E3$ transitions are orders of magnitude less probable, one expects only $E1$ and $E2$ transitions to contribute.

The shape of the angular distribution for a given reaction channel has the general form

$$W(\theta) = \sum_\nu \left\{ \sum_{ij} A_{t_i t_j \nu} \mathrm{Re}\left[\langle S_{t_i} \rangle \cdot \left\langle S_{t_j} \right\rangle \right] \right\} P_\nu(\cos\theta), \tag{1.4.5.1}$$

where t_i denotes the set of quantum numbers describing the reaction of channel i, and the matrix element is S_{t_i}. The $P_\nu \cos(\theta)$ term are the Legendre polynomials of order ν, defined in table 1.1. Finally, $A_{t_i t_j \nu}$ are the angular distribution coefficients for a given order and set of reaction channels.

ν	$P_\nu(\cos(\theta))$
0	1
1	$\cos(\theta)$
2	$\frac{1}{2}(3\cos^2(\theta)-1)$
3	$\frac{1}{2}(5\cos^3(\theta)-3\cos(\theta))$
4	$\frac{1}{8}(35\cos^4(\theta)-30\cos^2(\theta)+3)$

Table 1.1: Legendre Polynomials: A table of Legendre polynomials of order 0 to 4.

Each reaction channel is described by the set of quantum numbers, t_i, defined as, $t_i \equiv \{P_i, L_i, J_i^{\pi_i}, \ell_i, s_i\}$, where

- P_i is the parity of the entrance channel.
- L_i is the multipolarity of the excitation.
- $J_i^{\pi_i}$ is the intrinsic angular momentum and parity of the intermediate excited state.
- ℓ_i is the orbital (relative) angular momentum between the two decay products in the exit channel.
- s_i is the channel spin.

The two channel sets for $E1$ and $E2$ transitions are $t_1\,\{1,1,1-,1,0\}$ and $t_2\,\{1,2,2+,2,0\}$. Equation (1.4.5.1) is expanded over these channel sets, to give

$$W(\theta) = \sum_\nu \Big\{ A_{11\nu}\mathrm{Re}\left[\langle S_1\rangle^2\right] + A_{12\nu}\mathrm{Re}\left[\langle S_1\rangle \cdot \langle S_2\rangle\right] + A_{21\nu}\mathrm{Re}\left[\langle S_2\rangle \cdot \langle S_1\rangle\right] + A_{22\nu}\mathrm{Re}\left[\langle S_2\rangle^2\right] \Big\} P_\nu(\cos\theta). \tag{1.4.5.2}$$

Using the relation

$$C_{t_1t_2} = \begin{cases} A_{t_1t_2} & t_1 = t_2 \\ 2A_{t_1t_2} & t_1 \neq t_2, \end{cases} \tag{1.4.5.3}$$

equation (1.4.5.2) can be simplified to

$$W(\theta) = \sum_{\nu} \left\{ C_{11\nu} \mathrm{Re}\left[\langle S_1 \rangle^2\right] + C_{12\nu} \mathrm{Re}\left[\langle S_1 \rangle \cdot \langle S_2 \rangle\right] + C_{22\nu} \mathrm{Re}\left[\langle S_2 \rangle^2\right] \right\} P_\nu(\cos\theta). \quad (1.4.5.4)$$

Next, the summation over allowed values of ν are expanded, where values from $\nu = 0$ to $\nu = 2l$ are considered, with l defined to be the maximum allowed change in angular momentum. The C coefficients are then either evaluated from the tables listed in reference [39], or computed using the related A coefficients from the following formula

$$\begin{aligned} A_{t_1 t_2} = {} & (-1)^{s-j_1-1}(-1)^{p_1+p_2} \\ & \times \left[(2\ell_1+1)(2\ell_2+1)(2L_1+1)(2L_2+1)\right]^{1/2} \\ & \times (2J_1+1)(2J_2+1)(2v+1) \\ & \times \begin{pmatrix} \ell_1 & \ell_2 & \nu \\ 0 & 0 & 0 \end{pmatrix} \begin{pmatrix} L_1 & L_2 & \nu \\ -1 & 1 & 0 \end{pmatrix} \\ & \times \begin{Bmatrix} \ell_1 & J_1 & s \\ J_2 & \ell_2 & \nu \end{Bmatrix} \begin{Bmatrix} L_1 & J_1 & j_A \\ J_2 & L_2 & \nu \end{Bmatrix}. \end{aligned} \quad (1.4.5.5)$$

In the equation above, the matrices in parentheses and braces are the Wigner 3-j symbols and the Wigner 6-j symbols, respectively, which are used in angular momentum coupling. It is worth noting that terms with even ν containing non-interfering amplitudes, and odd ν terms with interfering amplitudes, always evaluate to zero.

By evaluating the A coefficients, equation (1.4.5.4) becomes

$$\begin{aligned} W(\theta) = {} & \left(3\mathrm{Re}\left[\langle S_1 \rangle^2\right] + 5\mathrm{Re}\left[\langle S_2 \rangle^2\right]\right) P_0(\cos\theta) + \left(6\sqrt{3}\mathrm{Re}\left[\langle S_1 \rangle \cdot \langle S_2 \rangle\right]\right) P_1(\cos\theta) \\ & + \left(-3\mathrm{Re}\left[\langle S_1 \rangle^2\right] + \frac{25}{7}\mathrm{Re}\left[\langle S_2 \rangle^2\right]\right) P_2(\cos\theta) + \left(-6\sqrt{3}\mathrm{Re}\left[\langle S_1 \rangle \cdot \langle S_2 \rangle\right]\right) P_3(\cos\theta) \\ & + \left(-\frac{60}{7}\mathrm{Re}\left[\langle S_2 \rangle^2\right]\right) P_4(\cos\theta). \end{aligned} \quad (1.4.5.6)$$

Then, writing the equation in terms of reaction amplitudes, using $\mathrm{Re}[\langle S_1 \rangle \cdot \langle S_2 \rangle] = |S_1|\,|S_2| \cos\phi_{12}$, where ϕ_{12} is the mixing angle between the amplitudes (interference), one

obtains, after rearranging, the following form. As first shown by Dyer and Barnes [40]

$$W(\theta) = \left(3S_1^2 + 5S_2^2\right)P_0(\cos\theta) + \left(\frac{25}{7}S_2^2 - 3S_1^2\right)P_2(\cos\theta) + \left(-\frac{60}{7}S_2^2\right)P_4(\cos\theta) + 6\sqrt{3}S_1S_2\cos\phi_{12}\Big(P_1(\cos\theta) - P_3(\cos\theta)\Big).$$

Using the relation between the partial-wave amplitudes and cross sections, $\sigma_i = \sigma_{tot}\ell(\ell+1)S_i^2$, one obtains the parametrisation as shown in Assunção *et al.* [41]

$$W(\theta) = \sigma_{E1}W_{E1}(\cos\vartheta) + \sigma_{E2}W_{E2}(\cos\vartheta) + \sqrt{\sigma_{E1}\sigma_{E2}}\cos\phi_{12}\,W_{12}(\cos\vartheta), \tag{1.4.5.7}$$

where, the individual angular distributions W_{E1}, W_{E2}, and the interference term W_{12} are defined as follows

$$W_{E1}(\cos\theta) = P_0(\cos\theta) - P_2(\cos\theta)\,, \tag{1.4.5.8}$$

$$W_{E2}(\cos\theta) = P_0(\cos\theta) + \frac{5}{7}P_2(\cos\theta) - \frac{12}{7}P_4(\cos\theta)\,, \tag{1.4.5.9}$$

$$W_{12}(\cos\theta) = \frac{6}{\sqrt{5}}\Big(P_1(\cos\theta) - P_3(\cos\theta)\Big). \tag{1.4.5.10}$$

The angle-dependent interference between the partial-waves introduces an asymmetry about $\theta = 90°$ in the angular distributions. This can be seen in figure 1.10 for both signs of interference.

1.5 The Carbon-Oxygen Ratio

Carbon and oxygen are two of the most abundant elements in the universe, and are essential to life. The ratio of these nuclei (the C/O ratio) at the end of stellar helium burning is a critically important astrophysical quantity. As William Fowler noted in his 1984 Nobel lecture, "the ratio of ^{12}C to ^{16}O in helium burning is of paramount importance in nuclear astrophysics" [42] – a statement which remains true today.

The C/O ratio has far-reaching consequences when modelling phenomena across astrophysics. It affects the light curves of Type Ia supernovae, which have been instrumental

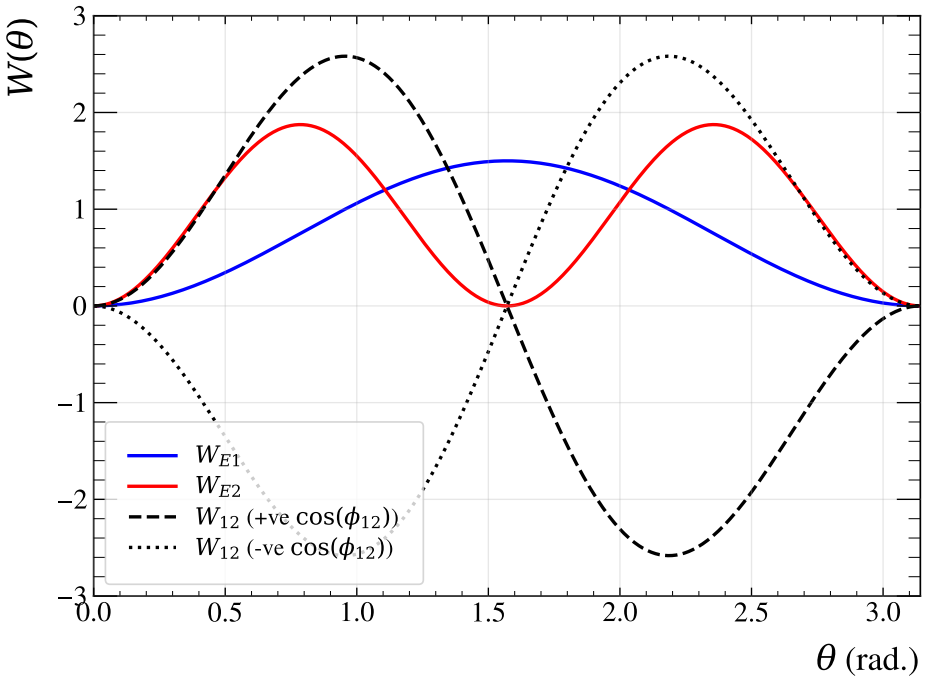

Figure 1.10: Angular Distributions Examples: The individual angular distributions from equation (1.4.5.7) are shown. The $E1$ contribution is shown in blue, and the $E2$ in red. The mixing term is given in black, where the positive interference is shown as a dashed line, and the negative interference as a dotted line.

in studying the accelerated expansion of the universe [43] and, more recently, used to investigate whether dark energy is time-varying rather than a cosmological constant [44]. Additionally, this ratio influences the mass of the stellar core prior to core-collapse supernova events, determining whether the remnant is a neutron star (C/O>1) or a black hole (C/O<1) [24]. Furthermore, recent work has shown that it can shift the predicted black hole mass gap caused by Pair-instability supernovae (PISN) by up to 50 $M_\odot$ [45].

The C/O ratio is governed by the nuclear reactions that produce and destroy carbon and oxygen during helium burning. The triple-alpha (3α) process synthesises ^{12}C, while the $^{12}\mathrm{C}(\alpha,\gamma)^{16}\mathrm{O}$ reaction destroys it to produce oxygen. Although the subsequent $^{16}\mathrm{O}(\alpha,\gamma)^{20}\mathrm{Ne}$ reaction is also possible to destroy oxygen, its comparatively low cross section at helium burning temperatures (higher coulomb barrier) means it does not significantly affect the C/O ratio [46].

In determining the uncertainty of the C/O ratio, the 3α rate is known to approximately 10% precision at helium burning temperatures [47], while dominant uncertainty comes

from the $^{12}\mathrm{C}(\alpha,\gamma)^{16}\mathrm{O}$ with values of around 20% [48] – this is twice the 10% precision reportedly required for accurate stellar modelling [49]. The following sections describe these reactions in detail, including the compound nuclei they populate, relevant theoretical aspects and previous measurements.

1.6 The $^{12}\mathrm{C}(\alpha,\gamma)^{16}\mathrm{O}$ Reaction

As first noted by Hoyle [50], then much later Fowler [42], the $^{12}\mathrm{C}(\alpha,\gamma)^{16}\mathrm{O}$ reaction would be the most effective at competing against the 3α process. Unlike the 3α process, there are no resonances at helium-burning temperatures. Therefore, the reaction cross section drops with the Coulomb barrier penetrability to $\sim 10^{-17}$ b, making direct measurements at the Gamow window impossible with current technology.

It is important to understand the allowed transitions determined by the conservation laws of angular momentum and parity. In the case of this reaction, only excited states of natural parity can be populated in the $^{16}\mathrm{O}$ compound nucleus. This constraint arises because both $^{12}\mathrm{C}$ and the α particle are even-even nuclei with 0^+ ground states [3]. As the total angular momentum of the system must be conserved, it follows that the angular momentum of the excited state, J, must equal the relative orbital angular momentum ℓ of the interacting nuclei. The parity of this state is given by $(-1)^\ell$. Therefore, states of natural parity are produced. For decays of these states directly to the 0^+ ground state of $^{16}\mathrm{O}$, only electric multipole transitions are allowed [51].

Naively, one might expect the $E1$ transitions to dominate the $^{12}\mathrm{C}(\alpha,\gamma)^{16}\mathrm{O}$ reaction because of the lower centrifugal barrier compared to the $E2$ transitions. However, this is not the case due to isospin selection rules. The electromagnetic interaction operator can be decomposed into isoscalar (IS, $T = 0$) and isovector (IV, $T = 1$) components. The IS component treats protons and neutrons the same, whereas the IV component distinguishes between them. The isospin projection is defined as $T_3 = {}^1\!/_2(N - Z)$, so self-conjugate nuclei, such as $^{16}\mathrm{O}$, have $T_3 = 0$. For self-conjugate nuclei, the IV part of the electromagnetic transition operator vanishes between states of the same isospin

[3] As is the case for all even-even nuclei in their ground states, the protons and neutrons couple to a total angular momentum of $0\hbar$.

($\Delta T = 0$). The remaining IS component of the $E1$ operator vanishes in the long-wavelength limit [52]. Together, these yield the selection rule that $\Delta T = 0$ $E1$ transitions between self-conjugate nuclei are forbidden. Since all states in ^{16}O below the proton separation threshold ($S_p = 12.13$ MeV) have isospin $T = 0$, this implies that $E1$ transitions between these states should be forbidden. In practice, however, these low-lying states in ^{16}O are not isospin-pure due to mixing with higher-lying $T = 1$ states of the same J^π [53]. This isospin mixing permits $E1$ transitions to occur, albeit at a greatly reduced rate.

The dominant contributions approaching the Gamow window come from $E1$ and $E2$ radiative capture to the ground state of ^{16}O, dubbed ^{12}C(α,γ_0)^{16}O. These transitions account for more than 90% of all capture events, while cascade transitions (through successive γ decays before reaching the ground state) contribute the remaining fraction [51].

The level scheme for ^{16}O is shown in figure 1.11, where astrophysically relevant levels (and those which this work is sensitive to) are detailed. Contributions to the cross section of interest come from the high energy tails of two sub-threshold ($S_{\alpha_0} = 7.16$ MeV) resonances, $J^\pi(2^+)$ at $E_x = 6.92$ MeV and a $J^\pi(1^-)$ at 7.12 MeV, and are influenced by their interference with the low energy tails of higher lying resonances. These are namely the $J^\pi(1^-)$ states at $E_x = 9.59$ MeV ($\Gamma = 420$ KeV), $E_x = 12.44$ MeV ($\Gamma = 91$ KeV), and $E_x = 13.09$ MeV ($\Gamma = 130$ KeV), as well as the $J^\pi(2^+)$ states at $E_x = 9.85$ MeV ($\Gamma = 0.625$ KeV), $E_x = 11.52$ MeV ($\Gamma = 71$ KeV), and $E_x = 13.02$ MeV ($\Gamma = 150$KeV). The energies and widths were taken from reference [54].

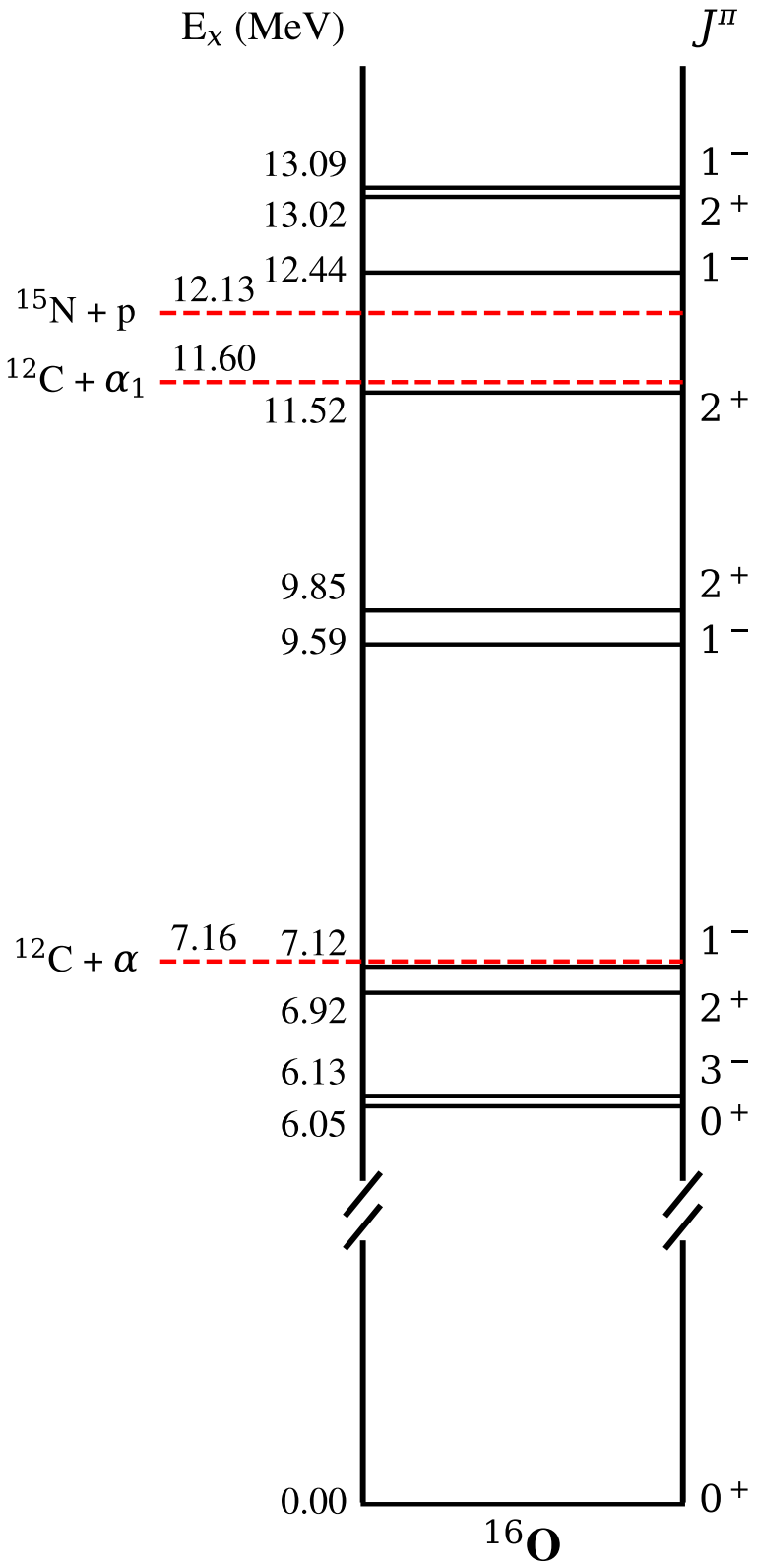

Figure 1.11: Level Structure for ^{16}O: The level scheme for the ^{16}O compound nucleus is shown; all relevant resonance information has been taken from the TUNL database [54].

1.6.1 Previous Measurements of $^{12}C(\alpha,\gamma)^{16}O$

The combination of the complicated level structure of ^{16}O with no resonant processes at the Gamow window, means that high-quality angular distributions from direct measurements are needed in order to separate the partial-wave contributions at higher energies, facilitating extrapolation down to the Gamow window using R-matrix theory. The current "global-fit" fit to the so-called world data are shown in figure 1.12. The data in this figure do not represent all data that were included in this fit, nor those listed in this review.

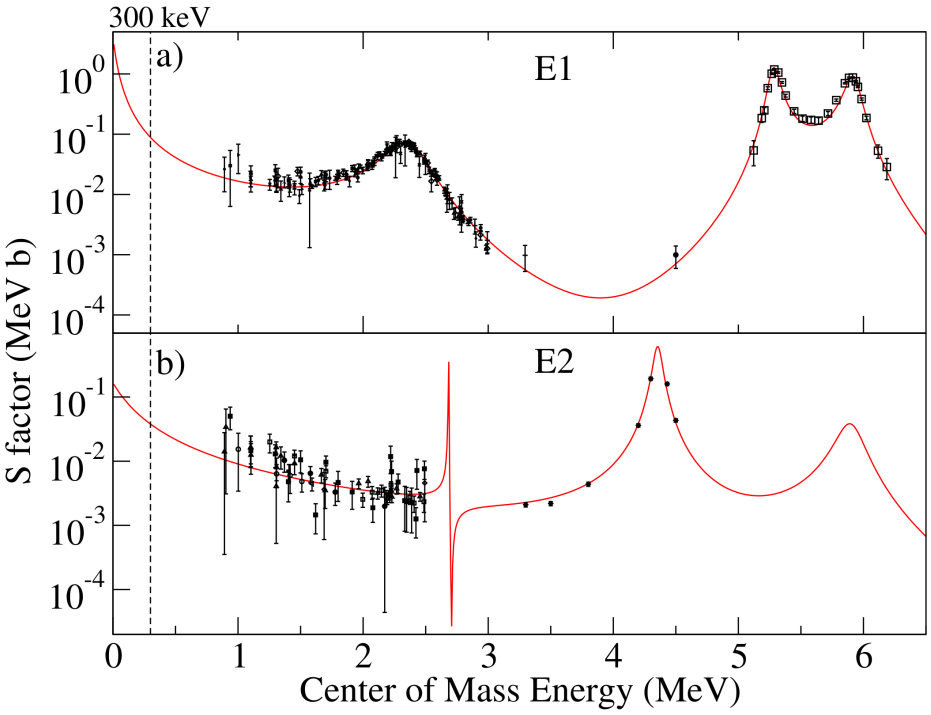

Figure 1.12: R-matrix Fit to the $^{12}C(\alpha,\gamma_0)$ World Data: This plot shows the R-matrix fit (red line) to the $^{12}C(\alpha,\gamma_0)$ world data, which was taken from [46]. The E1 contributions in the top panel are from references [41, 55–64]. Whereas the E2 contributions in the bottom panel are from [41, 56, 58, 60, 61, 63, 65].

Indirect Measurements

Information about the reaction can be constrained through indirect measurements probing the same compound nucleus. Significant effort has been put into studying beta-delayed particle emission [66–71], as well as transfer reactions [72–78] which are vital in constraining information about the sub-threshold states.

Another key indirect channel is elastic scattering $^{12}C(\alpha,\alpha)$ [79–81], which again can be used to constrain the R-matrix fit, but also provides information about the predicted partial-wave interference using the extracted phase shifts through Watson's theorem (discussed later). Of note was the measurement by Tischhauser *et al.* [79], who measured elastic scattering for alpha energies from 2.6 to 8.2 MeV, over angles from 24 to 166 degrees using an array of 32 silicon detectors. They measured the differential cross sections with the highest available precision to date for this channel.

Direct Measurements

Low energy measurements. While direct $^{12}C(\alpha,\gamma)$ measurements have been conducted previously, for example shown in reference [82], the first undertaken specifically for astrophysical purposes were performed by Dyer and Barnes [40], where a beam of α particles was impinged on a carbon target, and the γ-rays were detected using NaI(Tl) detectors. The main issue reported with the direct approach is the considerable background from the competing $^{13}C(\alpha,n)$ reaction, which has a cross section an order of magnitude higher, as shown in figure 1.13. To overcome this, they used a ^{13}C-depleted target and implemented time-of-flight (TOF) techniques to gate away from neutron events. The result of this was four angular distributions over the broad 1^- region, from 1.41 to 2.94 MeV in the centre-of-mass.

Measuring and reporting angular distributions around the broad 1^- region has been done extensively, using germanium [41, 56, 58, 60, 61, 83, 84], BaF_2 [65], or NaI(Tl) [59] detectors. With only Makii using TOF for background reduction, the rest typically opted to use depleted ^{13}C targets alone. It should be noted that no matter the level of depletion, ^{13}C build-up will occur over the course of the experiment. The usefulness of severely depleted ^{12}C targets is therefore questionable for experiments typically spanning several weeks or months.

Others report using inverse kinematics to measure this reaction, where a carbon beam impinges on a windowless gas ^4He target, and γ-rays are detected with germanium [55], BGO [62], and NaI(Tl) [85] detectors. However, no typical angular distributions are

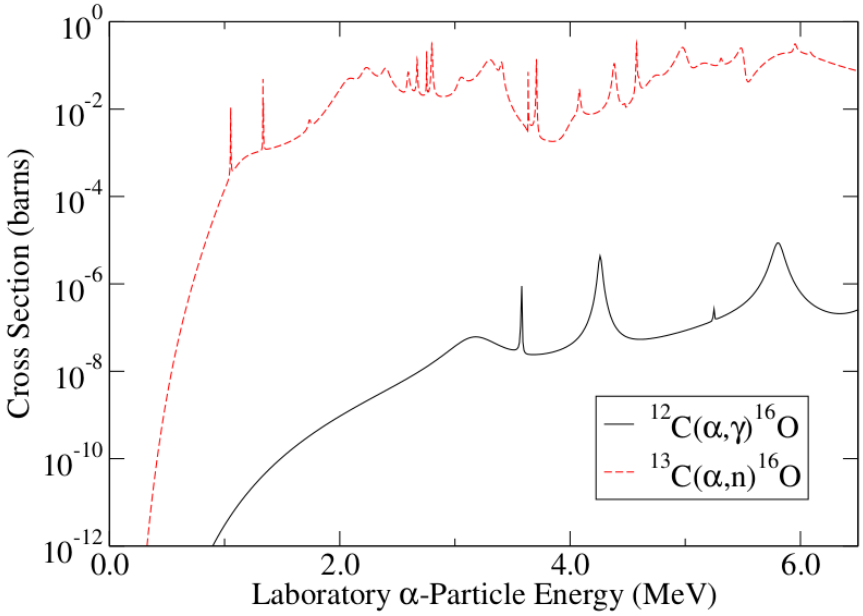

Figure 1.13: Comparison of ^{12}C(α,γ) and ^{13}C(α,n) Cross Sections: This figure shows the cross section for the reaction of interest (black-solid) against the cross section for a prominent background contribution (red-dashed). This plot was taken from reference [46].

obtained, as they only measure the total yield and the yield at 90 degrees ($E1$). Yamaguchi *et al.* [86] have reported similar measurements in inverse kinematics for the total reaction cross section.

Of note is also Jaszczak *et al.* [87], who measured the total integrated cross section in forward kinematics with NaI(Tl) detectors, using γ/n Pulse Shape Discrimination (PSD) for ^{13}C gating. Other analyses focus on cascade transitions [88, 89].

Mixing angle and data quality. One issue in the field is the incorrect treatment when it comes to fitting angular distributions, therefore in separating the partial-wave contributions. Even if one is to assume all background from ^{13}C(α,n) has been removed, these data still may not be suitable for extrapolation due to other uncharacterised systematic uncertainties. Such can be examined by the way of the mixing phase angle in equation (1.4.5.7), ϕ_{12}.

A theoretical relationship established in the literature states that the interference phase (mixing angle) of radiative capture partial-waves can be obtained from the phase

shifts extracted from $^{12}\mathrm{C}(\alpha,\alpha)$ elastic scattering data using

$$\phi_{12} = \delta_2 - \delta_1 + \arctan\left(\frac{\eta}{2}\right), \tag{1.6.1.1}$$

where δ_1 and δ_2 are the measured p- and d-wave elastic scattering phase shifts respectively, and η is the Sommerfeld parameter. Typical values of the $\arctan\left(\frac{\eta}{2}\right)$ term, in the energy range considered, are between $40 - 60°$. It is noted that only the absolute value of $\cos\phi_{12}$ can be obtained from the phase shifts. The sign must be extracted from capture/photo-dissociation data.

This expression was originally given by Barker (via private communication as referenced in [40]) and subsequently used by Dyer and Barnes [40] to compare experimentally determined capture reaction ϕ_{12} values with those calculated from elastic scattering data using single-level R-matrix theory. Barker [90] later demonstrated that this relationship also holds for multi-level R-matrix theory and is independent of the chosen channel radius. This is again discussed later by Barker and Kajino [91].

Brune [92] then highlighted that the general validity of equation (1.6.1.1) can be established through the earlier work of Knutson [93]. In order to reduce the number of free parameters when analysing p-d radiative capture data, Knutson applied Watson's theorem [94] to relate the radiative capture phases to elastic scattering phases in d-p reactions.

Watson's theorem was originally formulated for π-meson photoproduction. It was stated that given certain restrictions and symmetries, such as charge independence, probability conservation (a unitary scattering matrix), and time-reversal invariance, the phases of the meson partial-waves in the final state, following photo-production, are shifted relative to each other by an amount equal to the meson scattering phase shifts [94].

The limitations and conditions of Watson's theorem are discussed in references [92, 93], and listed here:

1. The cross section must be small enough that it can be approximated by first-order perturbation theory.

2. No other reaction channels (other than scattering) can be open.

Gai [95] points out that the ability to accurately extract ϕ_{12} serves as a critical test of the quality of the capture data, as disagreement with values extracted from elastic scattering indicates the presence of unaccounted systematic errors in the dataset. The alternative is to disagree with fundamental symmetries.

Some analyses of $^{12}\mathrm{C}(\alpha,\gamma)$ data indeed fit a partial-wave decomposition keeping ϕ_{12} as a free parameter [41, 60, 61, 65]. The extracted values are shown in figure 1.14 against the prediction of ϕ_{12} using the scattering data of Tischhauser [79] and equation (1.6.1.1). The values extracted from the analysis of Dyer and Barnes agree relatively well with the theoretical predictions, although statistical errors are large. The data of Assunção *et al.* deviate significantly from theoretical predictions despite having very small statistical error bars. The measurements by Plag *et al.* show much better agreement with predictions, however, they do not cover the region of disagreement, close to the 1^- resonance. Redder *et al.* performed multiple measurements that either deviate significantly from predictions, or exhibit a constant trend at approximately $\phi_{12} = 20°$. The data of Ouellet *et al.* show a trend of general agreement, large errors, and they don't measure over the challenging 1^- region.

Unfortunately, a common approach in the literature when analysing capture datasets, using a partial-wave decomposition, is to "fix" ϕ_{12} to match the prediction from equation (1.6.1.1) when fitting equation (1.4.5.7) [58, 59]. Alternatively, this done implicitly when including the elastic scattering channel in an R-matrix fit. In these examples, no quality checks can be made. Fortunately, the analysis of [41] reported both. As pointed out by Gai [95], when fixing ϕ_{12}, this dataset shows a difference by a factor of ~ 3 in the extracted ratio of partial $E1/E2$ cross sections. This highlights that fixing ϕ_{12} is only a reasonable approach if the inability to extract ϕ_{12} from the capture data is due to large statistical uncertainties. If there are systematic errors (which appears to be the case with the data of Assunção *et al.* [41]), fixing ϕ_{12} in this way will only serve to further propagate these uncertainties into the extracted partial cross sections.

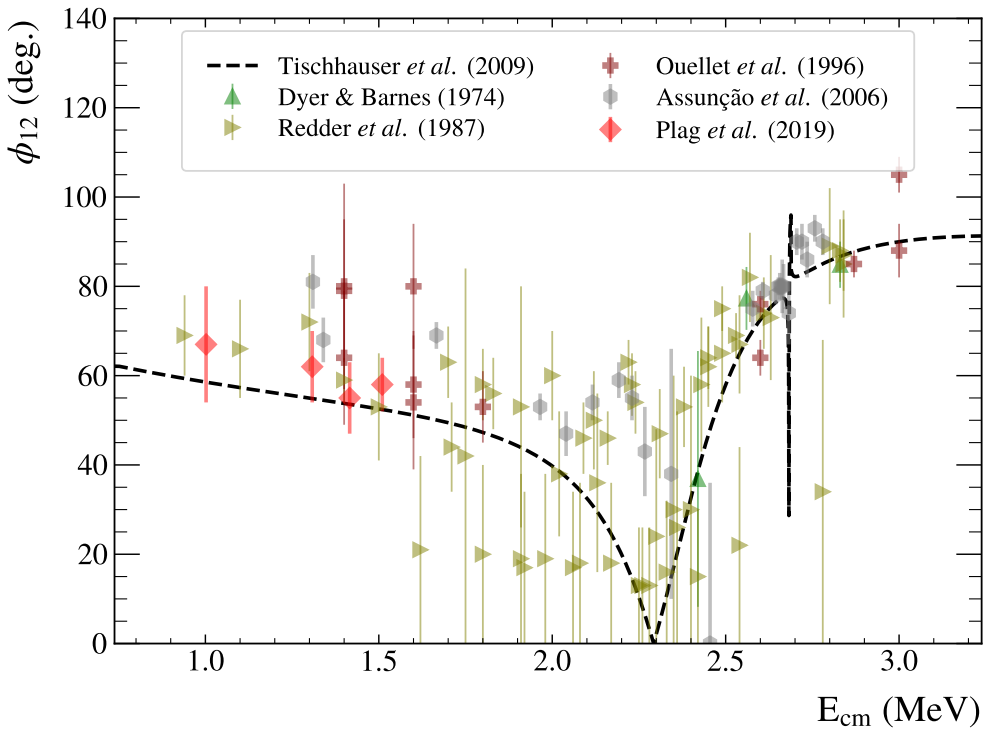

Figure 1.14: Current Status of ϕ_{12}: The experimentally measured ϕ_{12} values from various capture reaction experiments [40, 60, 61, 65] are compared to the predictions from scattering data (dashed black line) from reference [79] in the region of interest, obtained using equation (1.6.1.1).

High energy measurements. The lack of high-quality, high-energy measurements ($E_{cm} > 3.5$ MeV) is also an issue. The resonances themselves are either poorly constrained or unmeasured in the off-resonance region, leading to the need for arbitrary background terms to be added in the R-matrix fit.

The only direct measurement that constrains the $E_x = 11.52$ MeV $J^\pi(2^+)$ state, just below the α_1 threshold, in the global-fit is that of Brochard *et al.* [64]; No angular distributions were measured, and instead, the angle-integrated yield was reported. Similarly, the high-energy $J^\pi(1^-)$ resonances are primarily by contained by the data of Schürmann *et al.*, who measured in inverse kinematics, detecting the γ-rays with NaI(Tl) detectors while also gating on the recoiling ^{16}O. No typical angular distributions were reported, an unfolding approach was used where they simulated the γ-ray spectra for different $E1$ and $E2$ contributions, which were fitted to the data. They note that above $E_{\rm cm} = 4$ MeV that ϕ_{12} was fixed using equation (1.6.1.1) and the data of Tischhauser*et al.* [79]. It is unclear

whether they do this above the α_1 threshold, where the equation no longer holds.

Considerable time has been put into measurements of both the on and off-resonance regions at high-energy. The effort was led by Dr Ching Wei Li's group at the University of Oslo. Data were collected at the iThemba Tandertron in 2025, where they detected γ-rays with $LaBr_3$ detectors, and used PSD to gate away the ^{13}C background [96].

Time Reverse

Photo-dissociation reactions are the time-reverse of radiative capture, where a photon is incident on a target nucleus, the energy is distributed across all nucleons, and it breaks up into daughter nuclei. This method has been published once before to study this reaction for astrophysical purposes [97].

The shape of the differential cross sections obtained from these two reaction mechanisms are identical due to time-reversal invariance of both strong nuclear and electromagnetic interactions [98]. However, the angle-integrated cross sections are different, but simply related by the principle of detailed balance, if measuring over all azimuthal angles ϕ[4]. This energy-dependent detailed balance factor, f_{db}, is a calculable ratio of the forward capture and reverse photo-dissociation cross sections [99], and is obtained as follows

$$\sigma_{\alpha\gamma}(E_{cm}) = \frac{2(2J_{^{16}\mathrm{O}}+1)}{(2J_{^{12}\mathrm{C}}+1)(2J_{\alpha}+1)}\frac{k_{\gamma}^2}{k^2}\sigma_{\gamma\alpha}(E_{cm}), \tag{1.6.1.2}$$

where J is the angular momentum quantum number, $\sigma_{\gamma\alpha}$ is the photo-dissociation cross section, $\sigma_{\alpha\gamma}$ is the radiative capture cross section, and k and k_{γ} are wave numbers of the γ and ^{12}C+α channel respectively. These are defined as

$$k_{\gamma} = \frac{E_{\gamma}}{\hbar c} = \frac{E_{\mathrm{cm}} - Q}{\hbar c}, \quad k = \sqrt{\frac{2\mu E_{\mathrm{cm}}}{\hbar^2}}, \tag{1.6.1.3}$$

where μ is the reduced mass of ^{12}C + α. Substituting the appropriate angular momentum

[4]The technicality arises due to azimuthal angle dependence of the differential cross section $\frac{d\sigma}{d\Omega}$, which is dependent on the polarisation of the γ beam used [92].

quantum numbers and simplifying, the following is obtained

$$\sigma_{\alpha\gamma}(E) = \frac{E_\gamma^2}{c^2 \mu E_{\rm cm}} \sigma_{\gamma\alpha}(E). \tag{1.6.1.4}$$

The detailed balance factor is therefore given by

$$f_{db}(E_{\rm cm}) = \frac{\sigma_{\gamma\alpha}(E_{\rm cm})}{\sigma_{\alpha\gamma}(E_{\rm cm})} = \frac{1}{c^2\mu}\frac{E_\gamma^2}{E_{\rm cm}}, \tag{1.6.1.5}$$

and energy dependence is shown in figure 1.15.

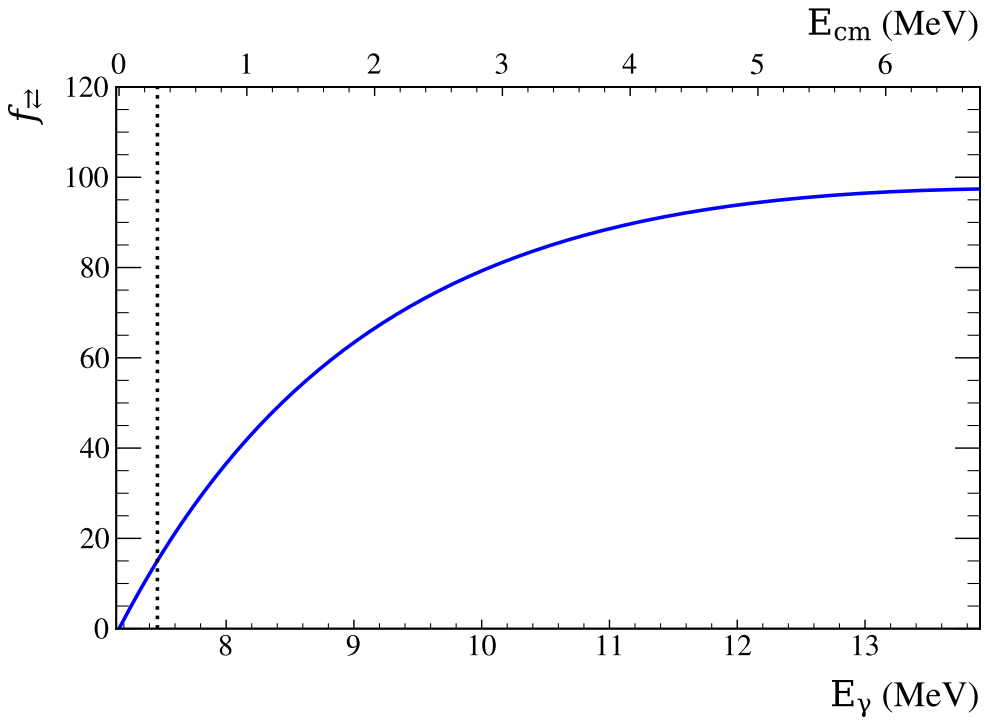

Figure 1.15: Detailed Balance Factor: Energy dependence of the detailed balance factor relating the ^{12}C(α,γ) capture and ^{16}O(γ,α) photo-dissociation cross sections. The vertical dashed line shows the approximate position of the Gamow window.

Measuring the time-reversed reaction of ^{12}C$(\alpha,\gamma)^{16}$O yields a significant increase in the cross section, as shown by the R-matrix fits in figure 1.16, potentially yielding better experimental statistics than measuring the forward reaction. When studying this reaction, while ^{16}O can, in principle, be excited to states of any J^π (aside from 0^+), decays to two $J^\pi(0^+)$ particles (^{12}C and α in their ground states) are only permitted from states

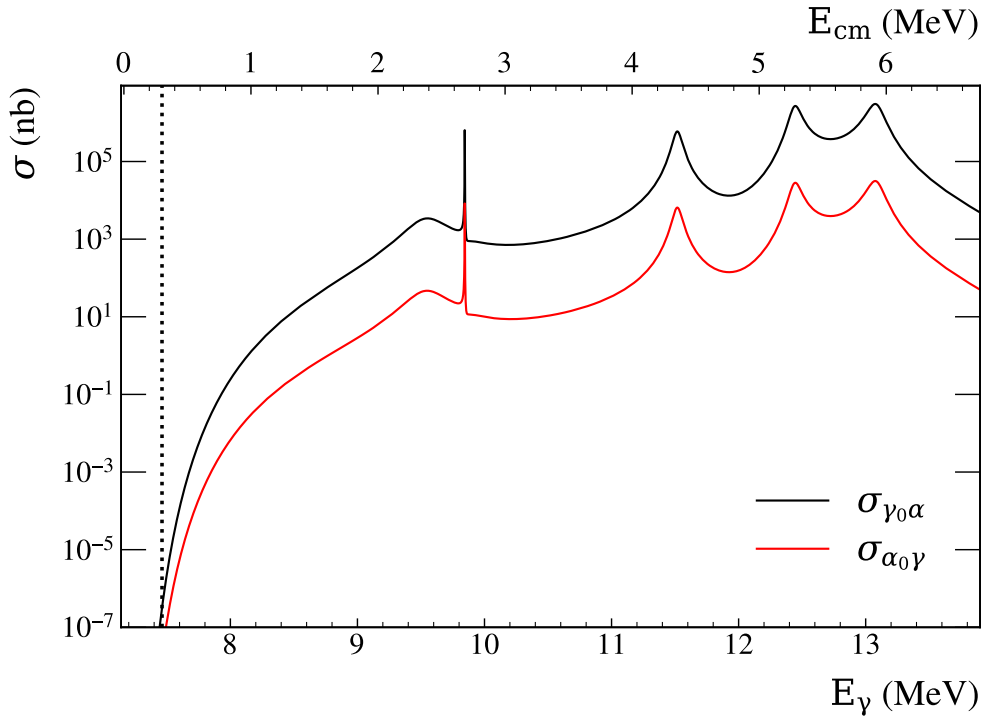

Figure 1.16: Cross Section Comparison: Theoretical cross sections for the capture (red) and photo-dissociation reactions (black), with the Gamow window indicated by the vertical dotted line. The data were taken from reference [46].

of natural parity. Thus by selecting photo-dissociation events in which ^{16}O decays into $^{12}C_{g.s.}$ and an α particle, electric multipole ground state transitions are selectively focused on, dubbed $^{16}O(\gamma,\alpha_0)^{12}C$. It is important to note that while typically only $E1$ and $E2$ transitions are considered, contributions from $E3$ transitions are still possible (although unlikely). Still, this being the case, there are no known $J^{\pi}(3^{-})$ resonances in ^{16}O in the energy range considered in this experiment [100].

1.7 The Triple-alpha Process

The process which synthesises ^{12}C is dubbed the triple alpha process, 3α, where α particles capture to form ^{8}Be, then again to form ^{12}C, emitting two γ's or an electron-positron pair:

$$\alpha + \alpha \rightarrow {}^{8}\mathrm{Be}, \tag{1.7.0.1}$$

$${}^{8}\mathrm{Be} + \alpha \rightarrow {}^{12}\mathrm{C} + \gamma + \gamma, \tag{1.7.0.2}$$

$${}^{8}\mathrm{Be} + \alpha \rightarrow {}^{12}\mathrm{C} + e^{+}e^{-}. \tag{1.7.0.3}$$

This two-step process was first suggested by Salpeter [101] and Öpik [102] in the 1950s to account for the mass gap at $A = 8$, noting that the half-life of ^{8}Be would be sufficiently long to allow for an equilibrium concentration of ^{8}Be to form and an additional α-capture reaction to occur. It was later shown by Hoyle [103] that this mechanism alone could not reproduce the observed abundance of ^{12}C [1]. Hoyle therefore proposed the existence of a $J^{\pi}(0^{+})$ resonance [50] (with no centrifugal barrier) in ^{12}C just above the $\alpha + {}^{8}$Be threshold (7.37 MeV), at an excitation energy of $E_x = 7.68$ MeV, lying close to the Gamow window for helium-burning temperatures (centre $\approx$ 85 keV, width $\approx$ 60 keV) [104].

Hoyle convinced Dunbar *et al.* [105] to search for this state, as noted in the review paper of Freer and Fynbo [104]. Dunbar *et al.* used the $^{14}\mathrm{N}(d,\alpha)^{12}\mathrm{C}$ reaction to probe the compound nucleus, detecting the α particles using a magnetic spectrometer. The state was identified at $E_x = 7.68(2)$ MeV with a width less than 25 keV, dubbed the Hoyle state. A later measurement by Cook *et al.* [106], studied the state by measuring α particles proceeding the beta decay of ^{12}B. They were able to successfully assign it as $J^{\pi}(0^{+})$ with an excitation energy of 7.653(8) MeV.

At helium burning temperatures critical for the C/O ratio, $10^{8}/10^{9}$ K, the synthesis of ^{12}C is characterised primarily by the resonant structure of the Hoyle state. The width dominating the resonant structure is the radiative width, the sum of the γ-decay and pair production widths. The study of which has drawn significant effort in order to reduce uncertainties in its characterisation [107–109]. The current uncertainty is reported

to be 10% [47]. At temperatures above $\sim 10^9$ K, the reaction proceeds via higher-lying resonances that are not as well constrained due to their broad overlapping nature. Accurate characterisation of these states is critical for understanding the astrophysical sites where such burning occurs, including helium flashes during the AGB phase and explosive burning events.

1.7.1 The Algebraic Cluster Model of ^{12}C

The known level scheme for ^{12}C is shown in figure 1.17. States of astrophysical interest, or those to which this analysis is sensitive, are shown. The first exited state, of $J^\pi(2^+)$, is at $E_x = 4.44$ MeV, next is the Hoyle state at $E_x = 7.65$ MeV just above the α decay thresholds ($S_{3\alpha}$=7.38 MeV and $S_\alpha = 7.28$ MeV). The second $J^\pi(2^+)$ is reportedly situated at $E_x = 9.87$ MeV, close to the very broad $\Gamma \simeq 3000$ KeV $J^\pi(0^+)$ state. Then, higher in energy is the first $J^\pi(1^-)$ state at $E_x = 10.85$ MeV. All values were taken from TUNL [54].

Some insight into the observed resonances of ^{12}C can be gained by considering its physical structure, namely that it exhibits clustering properties of an α-conjugate nucleus. Clustering phenomena appear throughout nature, in shoals of fish, galaxies, molecules, etc, so it may not be a leap to think of ^{12}C as a system made up of clusters of three α particles. The first idea that nuclei have preformed sub-clusters came from Hafstad and Teller [110], who saw that even-even nuclei, with structure that can be explained as multiples of α particles, displayed a linear trend between their binding energy and the number of hypothesised α particle bonds [104]. They believed that these nuclei in their ground states indeed existed as clusters, which later fell out of favour and was replaced by the single-particle shell description [104]. The notion of clustering gained traction again when Ikeda *et al.* [111] proposed that cluster formations appear close to decay thresholds. This idea is displayed in the Ikeda diagram as shown in figure 1.18. For the case of ^{12}C, one can think that when the excitation in the nucleus gets close to the decay threshold, the internal structure could change such that it becomes a system of three α particles.

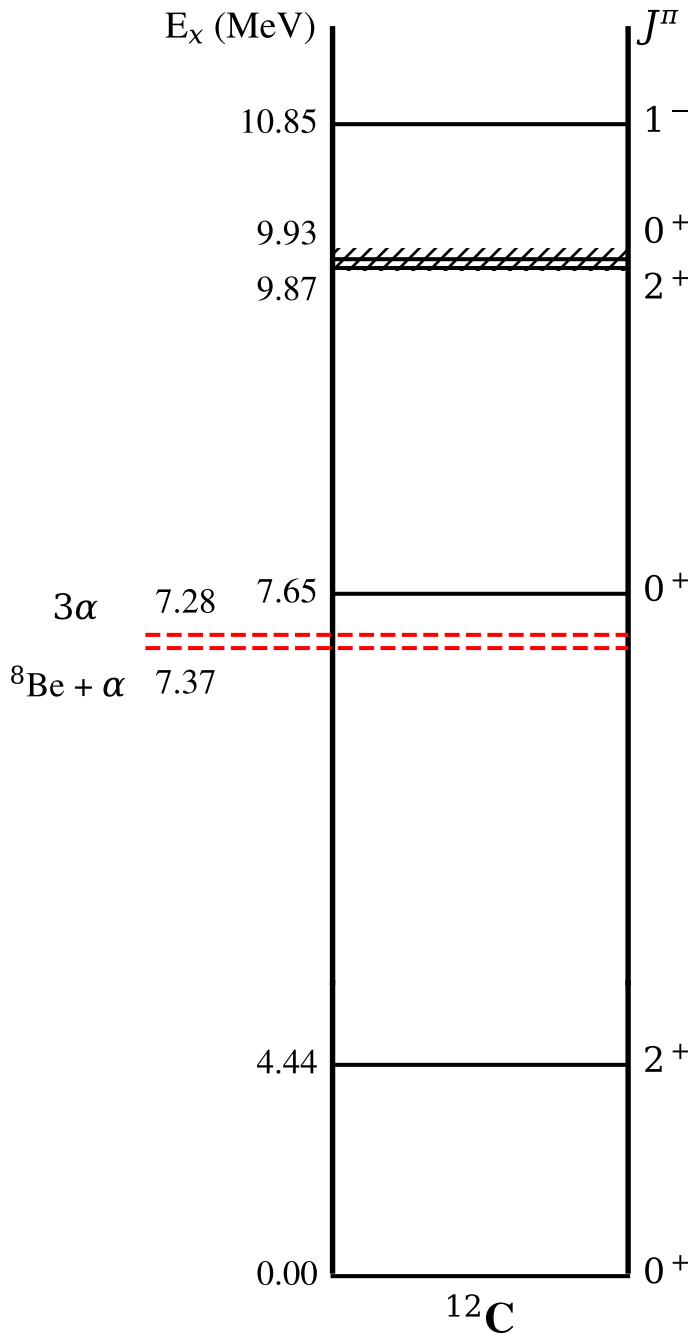

Figure 1.17: Level Structure for ^{12}C: The known level structure for ^{12}C is shown for states of relevance. All resonance information was obtained from the TUNL database [54].

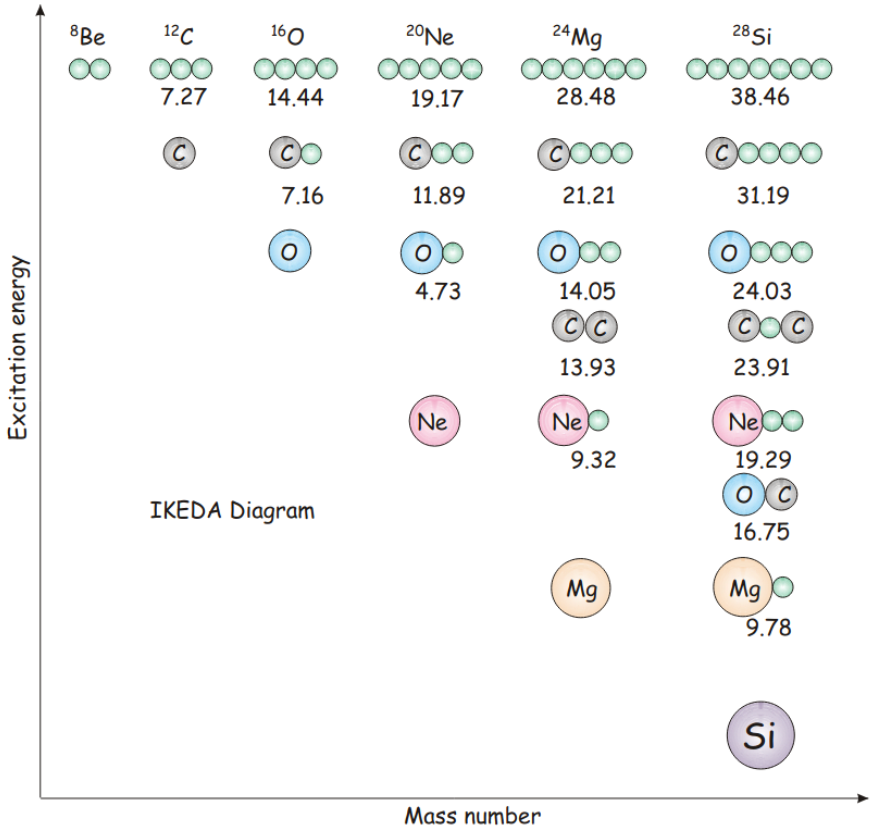

Figure 1.18: The Ikeda Diagram: The Ikeda diagram is shown, illustrating possible cluster configurations of different nuclei. This plot was taken from reference [104].

Hence, due to the Hoyle state's proximity to the 3α threshold, it is commonly believed to be an alpha-clustered state [104]. It was predicted by Morinaga [112] to be a linear chain of alpha particles, although the exact structure of the clustered state is debated still today [113]. There are many models used to study the structure of ^{12}C, such as the *ab initio* no-core shell model (NCSM) [114], *ab initio* Effective Field Theory (EFT) calculations on the lattice [115], the fermionic molecular dynamics (FMD) model [116], the Bose-Einstein Condensate (BEC) model [117], and the algebraic cluster model (ACM) [118, 119]. Each of these models predicts different 3α structures of ^{12}C. The following section focuses on the ACM.

The Algebraic Cluster Model

The ACM postulates that ^{12}C has a molecular-like structure consisting of three α particles arranged in an equilateral triangle with D_{3h} geometric symmetry [120]. Rotations and vibrations of this triangular configuration are predicted to give rise to the excited states.

Rotations of the triangular structure, illustrated in the blue box of figure 1.19, lead to characteristic energy levels: rotations around the line passing through one α particle give rise to $J^\pi(0^+, 2^+, 4^+)$ states. Rotations in the plane, where angular momentum is distributed equally among the three α particles, produces a $J^\pi(3^-)$ state. Combinations of these rotational modes yield higher-lying $J^\pi(4^-)$ and (5^-) states [104].

Classically, a body rotating with moment of inertia $\mathcal{I}$ and angular frequency ω has kinetic energy given by

$$E_k(\omega) = \frac{1}{2}\mathcal{I}\omega^2. \tag{1.7.1.1}$$

Since $J = \mathcal{I}\omega$, this can be expressed as

$$E_k(\omega) = \frac{J^2}{2\mathcal{I}}. \tag{1.7.1.2}$$

In the quantum mechanical case, the operator $\hat{J}^2$ has eigenvalues $\hbar^2 J(J+1)$, giving

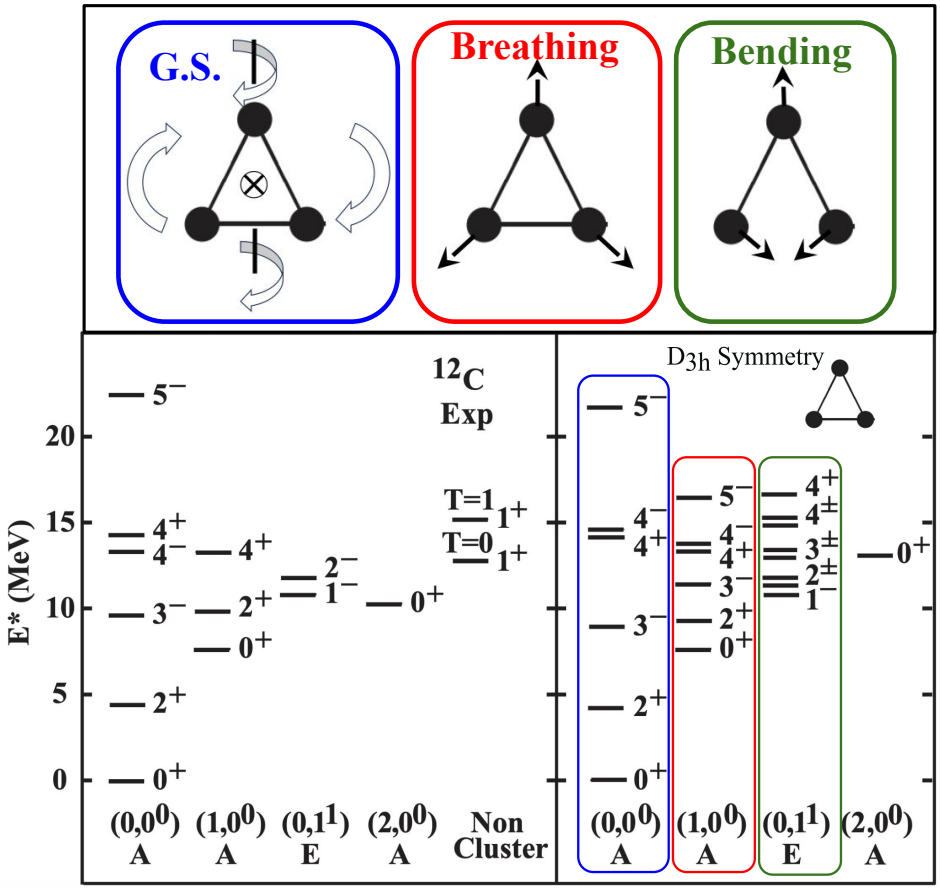

Figure 1.19: The Algebraic Cluster Model of ^{12}C: The upper panel shows different intrinsic structures: ground state (with possible rotations), breathing mode, and bending mode. The lower panels show the levels predicted by the ACM, compared with experimental data, adapted from reference [120].

rise to the rotational energy expression

$$E(J) = \frac{\hbar^2}{2\mathcal{I}} J(J+1). \tag{1.7.1.3}$$

States sharing the same moment of inertia (intrinsic structure) but differing in angular momentum will therefore have energies that follow this pattern, and are said to belong to a rotational band. If the band is built upon an excited state, the expression generalises to

$$E(J) = E_0 + \frac{\hbar^2}{2\mathcal{I}} J(J+1), \tag{1.7.1.4}$$

where E_0 denotes the energy of the band-head.

The energy levels arising from the aforementioned rotations of the ^{12}C ground state configuration are shown in the blue box at the bottom right of figure 1.19. The states that form the ground state band have been experimentally confirmed [120].

The ACM predicts that the Hoyle state has a different intrinsic configuration compared to those in the ground state band. Due to its $J^{\pi}(0^{+})$ assignment, it cannot possess rotational angular momentum; instead, it corresponds to a *breathing-mode* vibrational excitation of the triangular structure, shown in the red box of figure 1.19. This excitation mode involves oscillations of the α particles, resulting in an increased average radius compared to the ground-state configuration. The Hoyle state is predicted by the ACM to have its own rotational excitations, forming a second rotational band. The predicted states are indicated in the lower red box of figure 1.19.

A third family of excitations are predicted, known as the *bending band*, to occur when two of the α particles bend away from the third, as illustrated in the green box of figure 1.19. This mode gives rise to characteristic states also shown in 1.19.

The energy-spin relation from experimental data, corresponding to each of the aforementioned rotational bands predicted by the ACM, is shown in figure 1.20.

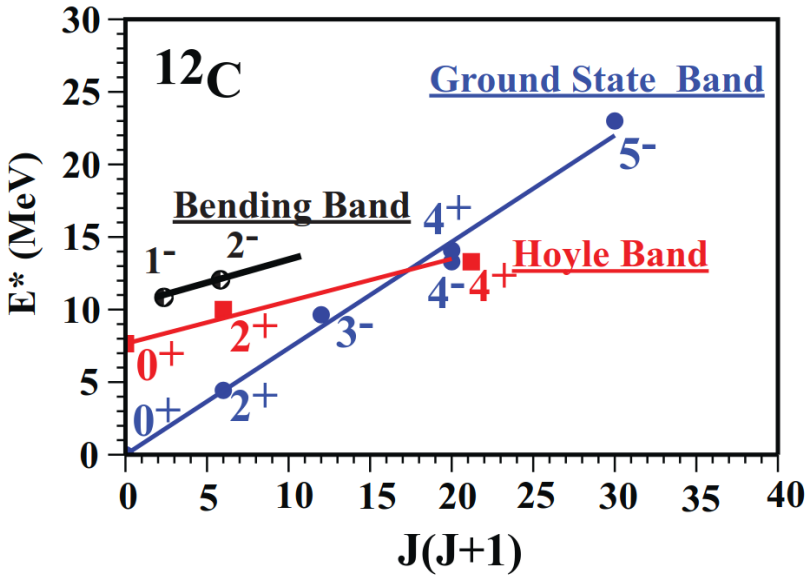

Figure 1.20: Rotational Bands of ^{12}C: The experimentally measured states are shown grouped into their rotational bands as predicted by the Algebraic Cluster Model. This figure was taken from reference [120].

The present study has three primary objectives:

1. To remeasure the $J^\pi(1^-)$ state in the bending band and search for the corresponding $J^\pi(2^+)$ in a parity doublet.

2. To remeasure the $J^\pi(2^+)$ state in the Hoyle band, which has important implications for understanding the intrinsic structure of the Hoyle state, and for high-energy helium burning processes.

1.7.2 Previous Measurements of the $J^\pi_n(2^+_2)$

While the $J^\pi_n(1^-_1)$ of the bending band has been measured with relative ease [121–123], this is not the case for the $J^\pi_n(2^+_2)$ of the Hoyle band, as it resides in a region where there are broad overlapping states. Historically, there have been many conflicting reports of the $J^\pi_n(2^+_2)$, which are reviewed here. Measurements of the $J^\pi_n(2^+_2)$ state in ^{12}C can be broken down into four categories: inelastic scattering, β-delayed α-decay, experiments involving ^{3}He beams incident on boron targets, and photo-dissociation.

Inelastic Scattering

The first collaboration to find experimental evidence for the $J^\pi_n(2^+_2)$ state was Itoh *et al.* [124], using (α, α') scattering; impinging a ^{12}C target with 386 MeV α beams. Measurements were taken at angles 0 to 10°, using the GRAND RAIDEN spectrometer [125]. They noted the $J^\pi_n(2^+_2)$ state was submerged in a very broad $J^\pi(0^+)$ state. A second experiment was performed with improved statistics [113], through these data, they were able to determine it to have $E_x = 9.84 \pm 0.06$ MeV with $\Gamma = 1.01 \pm 0.15$ MeV. The energy and width were extracted using Gaussian fits.

Next, Freer *et al.* [126] performed a ^{12}C(p,p') experiment using 66 MeV and 200 MeV protons generated with the Separated Sector Cyclotron (SSC) accelerator at iThemba LABS. Using the K600 magnetic spectrometer [127, 128] to detect the protons. Through an R-matrix analysis they obtained E_x=9.6(1) MeV with a Γ = 600(100) keV for the $J^\pi_n(2^+_2)$ state, but again submerged beneath a large $J^\pi(0^+)$ background.

Zimmerman *et al.* [129] then conducted another ^{12}C(p,p') measurement at the Yale tandem using 25 MeV protons, detecting protons using the Yale Enge Split Pole Spectrometer. By fitting "asymmetric Lorentzians" to the data they were able to extract $E_x = 9.6$ MeV for the $J^\pi_n(2^+_2)$ state, but do not quote a width. Instead, they state their results are consistent with the Freer *et al.* [126] measurement of $\Gamma = 600$ KeV.

Freer *et al.* [130] then reanalysed the preceding α scattering datasets [113, 124, 126] to obtain $E_x = 9.75(0.15)$ MeV with a $\Gamma = 750(150)$ keV. The data were fitted using a single-level R-matrix model, using the Wigner-Eisenbud parametrisation.

Li *et al.* [131] used both ^{12}C(α, α') and ^{14}C(p,t) reactions to study the origins of monopole strength in ^{12}C between 7 and 13 MeV. However, the $J^\pi_n(2^+_2)$ was also measured. The beam was produced at iThemba using the SSC, with ejectiles detected in the K600 spectrometer and coincidence measurements of ^{12}C decay products using the CAKE double-sided silicon strip detector (DSSD) array [132]. Beam energies of 67.5 and 100 MeV for protons, and 118, 160, 196, and 200 MeV for alphas were used. To extract parameters from the data, a multi-channel R-matrix fitting procedure using the Wigner-Eisenbud parametrisation was employed. A unique treatment of penetrabilities was used: The standard form to calculate penetrabilities, equation (1.4.4.2), does not account for the excitation structure of the decay products, and is only strictly correct if the daughter states are infinitely narrow. They make the argument that decays through both the ground state, $J^\pi_n(0^+_1)$, due to its ghost, and broad ($\Gamma = 1.513(15)$ MeV) first excited, $J^\pi_n(2^+_1)$ state at $E_x = 4.03(10)$ MeV, of ^{8}Be do not fulfil this condition. Thererefore, they account for the excitation function of ^{8}Be in the calculation of the penetrabilities. The lineshapes for the ^{8}Be ground and first exited state can be found in figure 1.21[5]. Two results were reported for the $J^\pi_n(2^+_2)$ state. One for a fit where the additional monopole strength interfered ($9.830 \pm 0.008 \pm 0.032$ MeV, $\Gamma = 981 \pm 19 \pm 53$ keV), and another when it did not ($9.890 \pm 0.008 \pm 0.007$ MeV, $\Gamma = 1425 \pm 19 \pm 161$ keV). The first error listed is statistical and the second is systematic.

[5]What is noted is that for decays through the ground state of ^{8}Be, in the energy region considered in this work, the difference in penetrabilities is negligible.

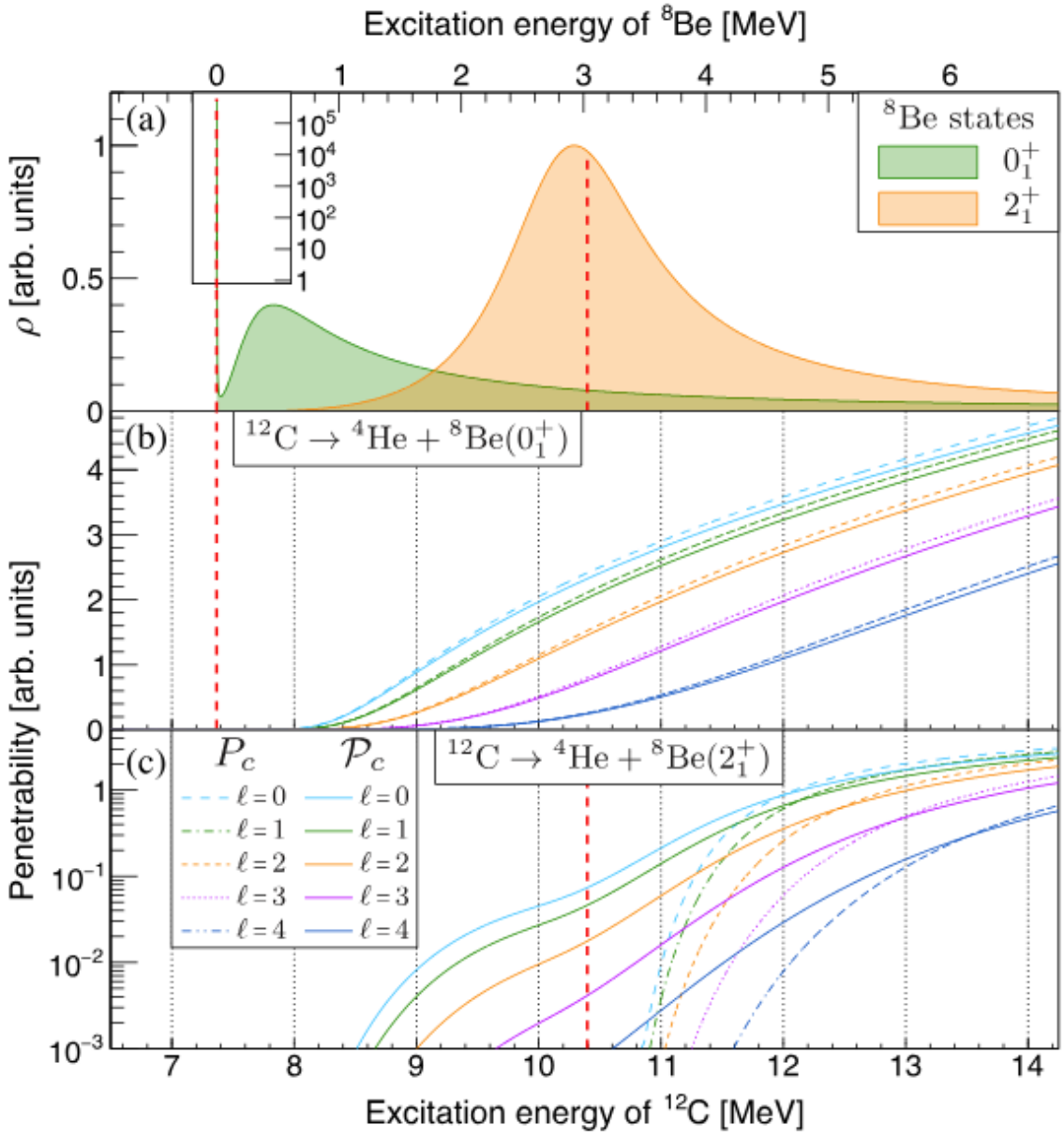

Figure 1.21: Alternative Treatment of ^{12}C Penetrabilities: The top panel shows the linesahpes for the ^{8}Be ground state and first excited state using an $\alpha - \alpha$ channel radius of 6 fm. The centre and bottom panels show the ^{12}C penetrabilities for α_0 (decays through the ^{8}Be ground state) and α_1 (decays through the first excited state of ^{8}Be), respectively, using an $\alpha - ^8$Be channel radius of 6 fm. This plot was taken from reference [131].

The β-delayed α-emission

Measurements were conducted by Diget *et al.* [133] and Fynbo *et al.* [134], who were the first to look for the state using beta-delayed alpha emission from ^{12}B and ^{12}N. The experiments were performed at ISOLDE CERN for ^{12}B (using 1 GeV proton-induced spallation reactions on a thick Ta target) and at IGISOL at Jyväskylä for ^{12}N (using the ^{12}C(p,n)^{14}N reaction with 40 MeV protons). The ^{12}C excitation spectrum was reconstructed by detecting all α particles using DSSDs. These analyses reported no sign of the $J^{\pi}_{n}(2^{+}_{2})$ in these data, and Fynbo *et al.* [134] indicated the state is unlikely to exist. The same group again studied ^{12}N and ^{12}B beta decay with higher statistics, in the paper of Hyldegaard *et al.* [135], and did find an indication of the $J^{\pi}_{n}(2^{+}_{2})$. The data were analysed using a multi-channel, multi-level R-matrix fit and the alternative Brune parametrisation [136]. They obtained $E_x = 11.1 \pm 0.3$ MeV with an observed width of $\Gamma = 1.4 \pm 0.4$ MeV.

Helium-3 Beams

Other experiments were performed by impinging ^{3}He beams onto boron targets [137, 138]. In the work of Smit *et al.* the ^{11}B(^{3}He,d)^{12}C reaction was studied at iThemba [137] using a beam energy of 44 MeV, analysing the deuterons with the K600 magnetic spectrometer. An R-matrix analysis of these data was stated to give a resonance energy for the $J^{\pi}_{n}(2^{+}_{2})$ state of $E_x = 9.7$ MeV.

Alcorta *et al.* [138] searched for the state again using ^{3}He beams, but instead using the ^{10}B(^{3}He,p)^{12}C and ^{11}B(^{3}He,d)^{12}C reactions, detecting the alphas from ^{12}C decay and the protons using DSSDs. They restricted their analysis to gate on events in which at least two α particles are detected, in coincidence with a proton or deuteron. They reported no sign of the $J^{\pi}_{n}(2^{+}_{2})$ state.

Photo-dissociation Measurements

A previous photo-dissociation measurement was reported by Zimmerman *et al.* [139, 140]. One drawback in the prior methods is that the $J^{\pi}_{n}(2^{+}_{2})$ is submerged in the dominant broad $J^{\pi}(0^{+})$. Using photo-dissociation, as the γ excites the $J^{\pi}(0^{+})$ nucleus, no $J^{\pi}(0^{+})$

states can be populated, so the significant broad background is removed. No other constraints on excitations are held, but higher J states are suppressed. When decaying, the allowed transitions depend on the decay method. One can decay directly through democratic methods into three alpha particles. As each is a $J^\pi(0^+)$ nucleus in its ground state, only transitions of natural parity are allowed. This is also the case for sequential decays through ^{8}Be when in its ground state. However, ^{8}Be has a very broad first excited state. If the decay proceeds through that state, no such restriction is made, and the angular distributions will be considerably harder to analyse. However, in the energy range considered, it is typically easy to gate away from decays through the excited state in ^{8}Be, as Zimmerman does [139, 140].

Zimmerman conducted a study using the OTPC (detector in experiment one of this thesis) and measured the $J^\pi_n(2^+_2)$, and $J^\pi_n(1^-_1)$, resonances unambiguously [139, 140]. However, several issues arise with this analysis. The efficiency correction used to normalise the data was done incorrectly, so the reported cross sections are incorrect, as discussed later. Furthermore, when fitting the data with R-matrix, the level shift was dropped, so the parameters extracted are also incorrect. For completeness, they are listed as: $E_x = 10.13^{+0.06}_{-0.05}$ MeV and $\Gamma = 2.08^{+0.33}_{-0.28}$ MeV. It is also noted that a comparison was made between the extracted $E1 - E2$ mixing phase angle, ϕ_{12}, with that calculated using equation (1.6.1.1). However, the conditions for this equation to be valid are not met in this case, as other decay modes are open.

Overview

An overview of the extracted resonance parameters from analyses reporting the $J^\pi_n(2^+_2)$ is shown in figure 1.22, and tabulated in table 1.2.

Study	E_x (MeV)	Γ (keV)
Itoh *et al.*(2004) [113, 124]	9.84 ± 0.06	1010 ± 150
Freer *et al.*(2009) [126], Zimmerman *et al.*(2011) [129]	9.60 ± 0.10	600 ± 100
Freer *et al.*(2012) [130]	9.75 ± 0.15	750 ± 150
Li[1] *et al.*(2022) [131]	9.830 ± 0.033	981 ± 56
Li[2] *et al.*(2022) [131]	9.890 ± 0.011	1425 ± 162
Hyldegaard *et al.*(2010) [135]	11.10 ± 0.30	1400 ± 400
Smit *et al.*(2012) [137]	9.70	—
Zimmerman *et al.*(2013)[140]	$10.13^{+0.06}_{-0.05}$	2080^{+330}_{-260}

Table 1.2: Resonance Parameters of the ^{12}C $J^\pi_n(2^+_2)$ State: Excitation energy, E_x, and width, Γ, for this level are listed from various studies. The superscripts for the Li *et al.* measurements indicate different interference scenarios, explained in the text.

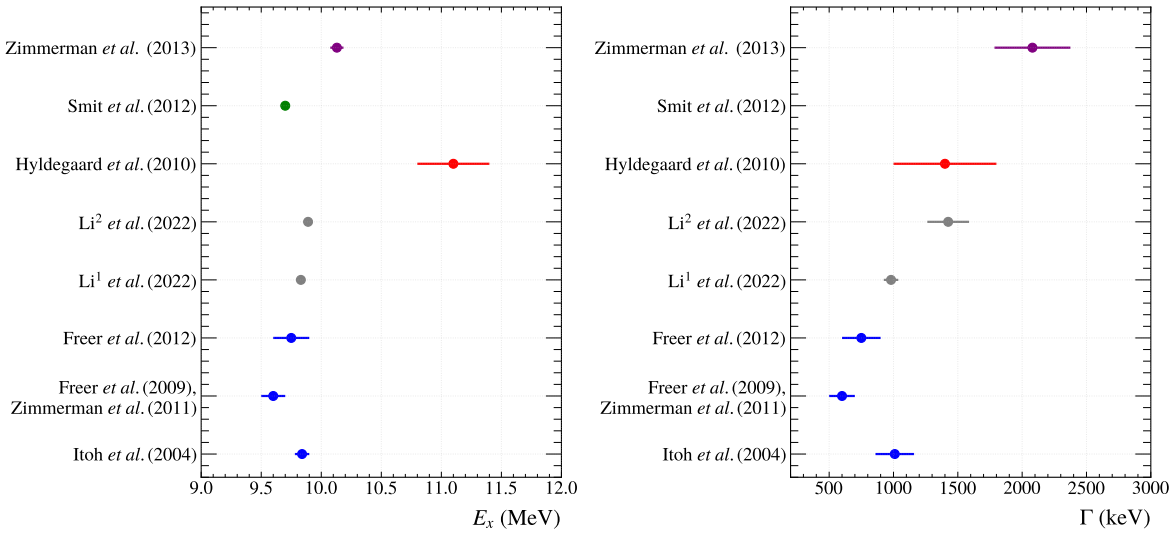

Figure 1.22: Resonance Parameters of the ^{12}C $J^\pi_n(2^+_2)$ State: Excitation energy, E_x, and width, Γ, for this level are plotted from various studies. The superscripts for the Li *et al.* measurements indicate different interference scenarios, explained in the text.

2

Time Projection Chambers

This section details the technological advancements that led to the Time Projection Chamber (TPC), outlines the principles of gaseous detectors, and describes the general operational principles of TPCs.

2.1 Historical Developments

To study the physical properties of nuclei and nuclear reactions, physicists need methods to observe and record particle interactions. To this end, they design particle detectors that exploit the known properties of particle interactions in matter. This section outlines key detection technologies developed for this purpose, leading to the development of the TPC.

The Cloud Chamber

The cloud chamber [141, 142], also referred to as the Wilson chamber, was developed by C.T.R. Wilson in the early 1900s, and was one of the earliest gaseous particle detectors.

A sealed chamber was saturated with water vapour, such that when charged particles propagated through the medium, condensation would form, tracing out the paths of ionisation. These tracks were then recorded using continuous photographic methods. For this work, enabling the unprecedented direct visual observation of particle tracks, Wilson received the 1927 Nobel Prize in Physics [143]. An example cloud chamber is presented in the left panel of figure 2.1.

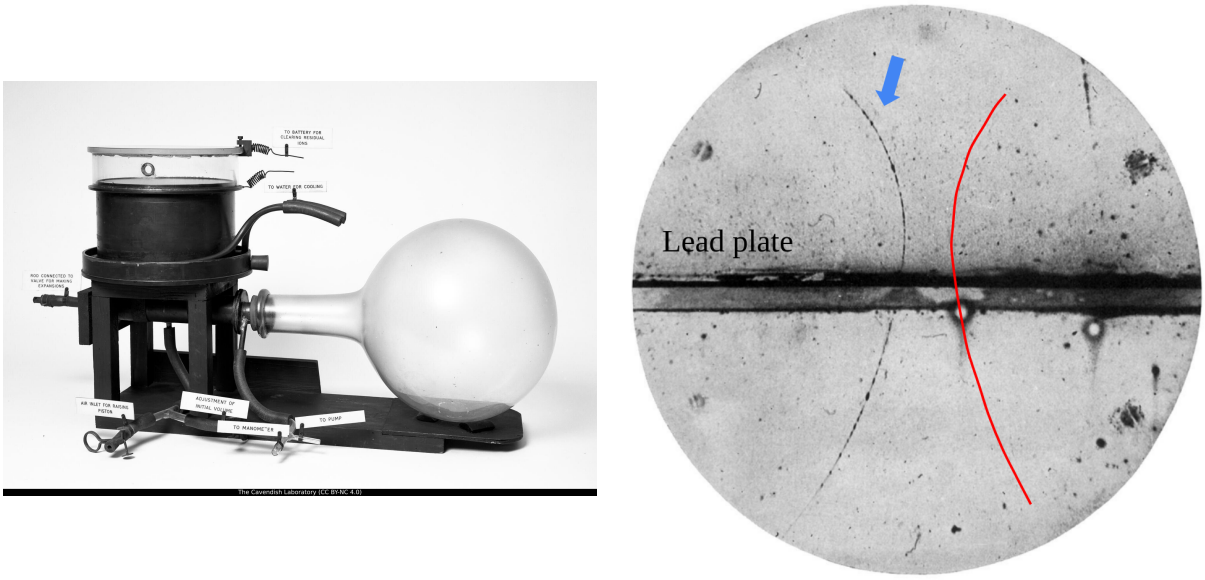

Figure 2.1: The Cloud Chamber. Left: Photograph of a cloud chamber from the Cavendish Laboratory, University of Cambridge (Cambridge University Library, CC BY-NC 3.0). **Right:** A positron captured in a cloud chamber - the horizontal line indicates 6 mm lead plate, and the blue arrow points to the faint positron track, travelling from lower to upper hemisphere. The red line shows the electron trajectory of the same energy. A B-field of 1.5 T points into the page. The original image was taken from reference [144].

Later, his concept was adapted by Carl Anderson, who surrounded his chamber with a large electromagnet ($B = 1.5$ T) to force ions to follow helical paths, enabling the determination of charge/mass from the particle trajectories [144]. To determine the direction of travel of the charged particle, Anderson added a 6 mm thick lead plate in the centre of the chamber. Particles would lose energy when passing through the plate, and particles with less energy would curve more in the magnetic field. Using this technique, Anderson observed positively charged tracks that were too faint to be protons. This led to the discovery of the positron (predicted by Paul Dirac 1928 [145]) as shown in the right panel of figure 2.1. Anderson received the Nobel Prize in 1936 for this work.

The Spark Chamber

Another key step toward the TPC was the spark chamber. Developed in the late 1940s, the spark chamber consisted of a stack of parallel plates in a gas-filled volume. Situated above and below the chamber were two scintillators connected to photomultiplier tubes (PMTs). When charged particles are measured in coincidence with both scintillators, a trigger signal is sent, and a high voltage is applied across the plates. This causes sparking across the plates in the region where the electron-ion pairs are, leaving a visible track that is then photographed for analysis. This design enabled triggered readout rather than continuous monitoring, as in the previous method. Leon M. Lederman, Melvin Schwartz, and Jack Steinberger used this technique in their experiments to discover the muon neutrino [146].

Multi-Wire Proportional Chamber

A significant technological advancement was the invention of the Multi-Wire Proportional Chamber (MWPC) [147], which enabled high-resolution, position-sensitive electronic readout and eliminated the need for photographic film for data acquisition. Georges Charpak was awarded the 1992 Nobel Prize in Physics [148] for this achievement.

The MWPC consists of a gas-filled volume with thin, parallel anode wires suspended between two cathode planes, across which a potential difference is applied. Charged particles traversing the gas, produce ionisation, liberating electrons that drift toward the anode wires, where rapid acceleration due to the high potential difference leads to avalanche multiplication. Each wire functions as an independent proportional counter, providing position sensitivity in one dimension, with resolution constrained by wire spacing (typically several millimetres) [149]. An additional two-dimensional readout is possible by including an orthogonal wire plane. Depth (drift) information requires multiple wire chamber layers to determine signal arrival time differences, but this approach increases system complexity and cost.

The Drift Chamber

To address the limitations of the MWPC, Walenta, Heintze, and Schuerlein developed the drift chamber [150] in 1971. This detector featured a large gas volume with a uniform drift region across which a drift voltage was applied. Incident particles would first pass through a scintillator, providing the start signal. The ionisation electrons produced within the detector volume, due to interactions of the incident particle, would drift toward the anode, where they were amplified and recorded. Given the known drift velocity and electric field, the timing information enabled spatial reconstruction along the drift direction. The drift chamber reduced the number of required electronics channels relative to the MWPC, while achieving position resolutions of 300–400 μm in the drift direction [149].

The Time Projection Chamber

These technological advances were all critical in developing the TPC, which was first conceptualised and designed by David R. Nygren at Lawrence Berkeley National Laboratory (LBNL) in 1974. The original TPC design [151] comprised a spectrometer system, intended to suppress track diffusion and thereby improve resolution, over a long drift volume.

It has MWPCs at the cathode to provide two-dimensional in-plane sensitivity, using an electronic readout based on charge-coupled device (CCD) technology. Timing information, coupled with an external trigger, provided the out-of-plane information. This combination enabled full three-dimensional particle tracking capability. The first operational TPC, built for the PEP-4 experiment, is described in reference [152] and served as the central tracking detector for studies of electron-positron collisions at the SLAC National Accelerator Laboratory.

2.2 Principles of Gas-filled Detectors

Gas-filled detectors are widely used for particle detection. This section briefly explains their operational principles relevant to this thesis, based on the following texts [34, 153, 154].

When charged particles propagate through an "absorber" material, they will interact in different ways, but primarily through Coulomb interactions. The main contributions from these interactions are the ionisation and excitation of electrons in the outermost shell of the absorber material's atoms. These processes are denoted as

$$X + p \rightarrow X^* + p \quad \text{(excitation)}, \tag{2.2.0.1}$$

$$X + p \rightarrow X^+ + p + e^- \quad \text{(ionisation)}, \tag{2.2.0.2}$$

where X is the absorber atom, p is the incident charged particle, X^* denotes an excited atom, and X^+ represents a positive ion. Due to the ionisation, many electron-ion pairs form along the primary charged particle's trajectory. These electrons can then be detected as a current signal, providing indirect information about the energy deposited and the spatial location of said deposits.

2.2.1 Regions of Operation

The response of a gas-filled detector to incident radiation depends on its operating mode, determined by the level of bias applied across its active region. This is illustrated schematically in figure 2.2, which delineates the various operational modes into distinct regions. A summary of these regions is provided below [153].

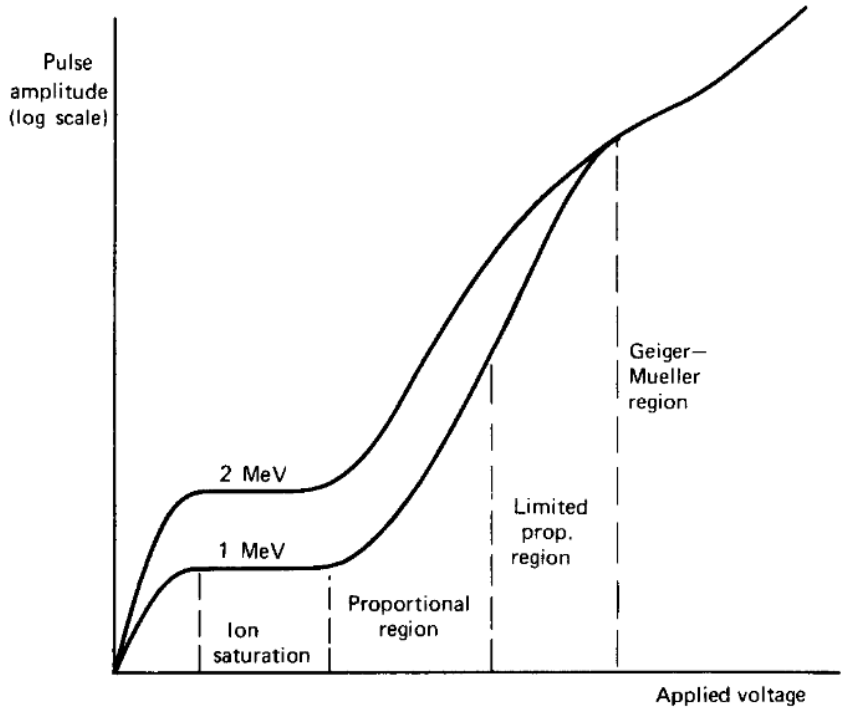

Figure 2.2: Regions of Operation: Plot showing the regions of operation for gaseous detectors. The plot was taken from reference [153].

- **Recombination Region (not shown on the plot):** At low applied voltage, the electric field is insufficient to fully prevent recombination of the electron-ion pairs before they reach the electrodes [1]. The collected charge is less than expected based on the number of ion pairs initially produced.

- **Ionisation Saturation:** By increasing the voltage the electric field is raised enough to suppress recombination, allowing all primary ionisation charges to be collected. The use of detectors operating in this region, such as ionisation chambers, are ideal when the original deposited energy is significant. This is the operational region for the drift portion of a TPC.

- **Proportional Region:** At higher voltages, electrons gain sufficient energy between collisions to ionise other gas molecules, leading to gas multiplication/avalanche formation. The number of collected electrons becomes proportional to the number of primary ion pairs. Proportional counters operate in this region and are typically

[1] Assuming a simple geometry the electric field across a detectors sensitive volume, E, is given by the drift voltage, V_d, divided by distance between electrodes, d, such that $E = V_d/d$.

used where the initial amount of deposited energy is low. This is the operational region for the multiplication section of a TPC.

- **Limited Proportionality Region:** Further voltage increase introduces non-linear effects, primarily due to the space charge effect, where the accumulation of slow-moving positive ions distorts the local electric field. This reduces the proportionality of the output signal [154].

- **Geiger-Müller (GM) Region:** Beyond this point, avalanches continue until the space charge reduces the electric field enough to stop further multiplication. This results in the same output signal no matter the initial ionisation. Geiger-Müller counters operate in this region and are used to determine whether charged particles have passed through their volume. However, they do not provide information about the deposited energy.

2.2.2 Charged Particle Interactions with Matter

As mentioned, charged particles interact with matter through the Coulomb force. The two most likely interactions are elastic scattering of primary charged particles by the absorber atoms and inelastic collisions between the primary charged particles and the electrons in the absorber material's outer shell. In a typical experiment, particles are usually moving too fast for elastic collisions to contribute meaningfully. Therefore, inelastic interactions dominate.

Ionisation & Excitation

The most common inelastic collisions are excitation and ionisation. Excitation is a resonant process where the primary charged particle transfers only enough energy to excite an electron in the outer shell of the absorber material to a higher energy level. In ionisation, the primary particle provides enough energy to remove the electron entirely from the atom [154].

If sufficient energy above threshold is transferred to the electrons from this primary ionisation, they may go on to liberate more electrons through ionisation (secondary ionisation). These high-energy electrons are called delta rays. They typically have a short range, so their contribution to ionisation is localised near the primary charged particle track.

Particle Range

As the initial charged particle propagates through the material, it interacts numerous times through the processes above, its kinetic energy is dispersed through inelastic collisions, and its velocity decreases, and eventually comes to rest. The range of the charged particle, the total distance it travels in the material before stopping, is characteristic of both the material, particle type, and its initial energy. Therefore, by measuring the total distance a particle travels in a material, one can calculate the energy loss and infer the initial energy deposited [154].

Angular Straggling

As mentioned, particles also interact through elastic (Rutherford [155]) scattering from target nuclei, the differential cross section of which is defined as

$$\frac{d\sigma}{d\Omega} = \left(\frac{Z_1 Z_2 e^2}{4\pi\epsilon_0 \cdot 4E}\right)^2 \frac{1}{\sin^4(\theta/2)}, \tag{2.2.2.1}$$

where Z_1 is the atomic number of the incident particle, Z_2 is the atomic number of the target nucleus, ϵ_0 is the permittivity of free space, E is the kinetic energy of the incident particle, e is the electron charge, and θ defines the scattering angle. After a charged particle undergoes many collisions, it will deviate from its original trajectory by some angle θ. This is depicted in figure 2.3.

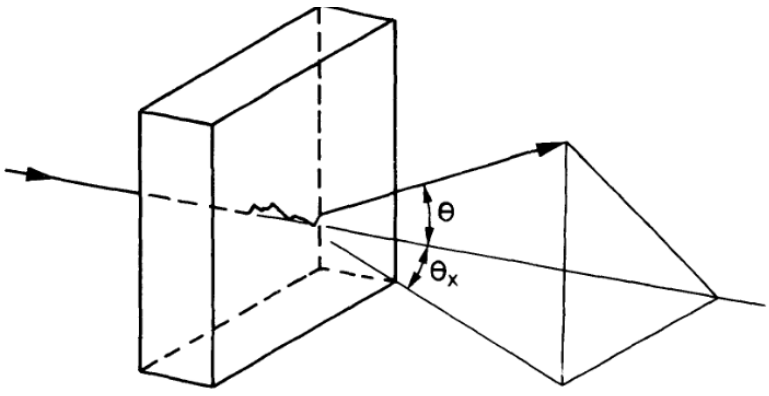

Figure 2.3: Particle Angular Straggling: Plot illustrating the effect of angular straggling, which was taken from reference [154].

A Gaussian approximation for the width of the distribution obtained from multiple Coulomb scatterings onto a plane is given by the following σ (in radians)

$$\sigma = 15\frac{\sqrt{X/X_0}}{p\beta}. \tag{2.2.2.2}$$

Here X is the thickness of the scatterer material and X_0 is its radiation length. The value p is the incident particle momentum, and β is its velocity. Reference [156] also outlines other versions of this simple formula for better approximations.

Stopping Power

Another characteristic quantity used to describe energy loss is known as stopping power, which is the energy lost per unit distance travelled by the particle, denoted by $-\frac{dE}{dx}$. This can be decomposed into two main sources

1. **Electronic stopping power**: arising from inelastic collisions causing electron excitation and ionisation.

2. **Nuclear stopping power**: arising from elastic collisions with recoiling target nuclei.

As noted previously, inelastic collisions dominate. Therefore, electronic stopping power is the dominating contribution. Under this assumption, formulae were developed to parametrise stopping power. First derived by Bohr [157, 158] using a classical argument, this formulation works well for heavy particles such as α-particles but breaks down for smaller particles due to the neglect of quantum mechanical effects. Bethe later derived a formula using principles of quantum mechanics, valid for relativistic particles [154], which is given by

$$-\frac{dE}{dx} = \frac{4\pi e^4 z^2}{m_e v^2} NZ \left[\ln\left(\frac{2m_e v^2}{I}\right) - \ln\left(1 - \frac{v^2}{c^2}\right) - \frac{v^2}{c^2}\right]. \tag{2.2.2.3}$$

Here, e is the elementary charge, z is the charge number of the incident ion, m_e is the electron mass, v is the velocity of the incident particle, N is the number density of target atoms, Z is the atomic number of the target material, I is the mean excitation potential of the target, and c is the speed of light.

A practical tool, developed by Ziegler and Manoyan, called SRIM [159], tabulates stopping powers and ranges of particles across a wide range of compounds and is commonly used in particle and nuclear physics. The SRIM code can also be used to obtain longitudinal and lateral straggling, and ranges of ions through matter. An example energy-loss curve, known as a Bragg curve, for an α particle in CO_2 at 1 atm pressure was obtained from SRIM, and is shown in figure 2.4. The Bragg curve exhibits characteristic behaviour as the primary charged particle slows down in the target [153].

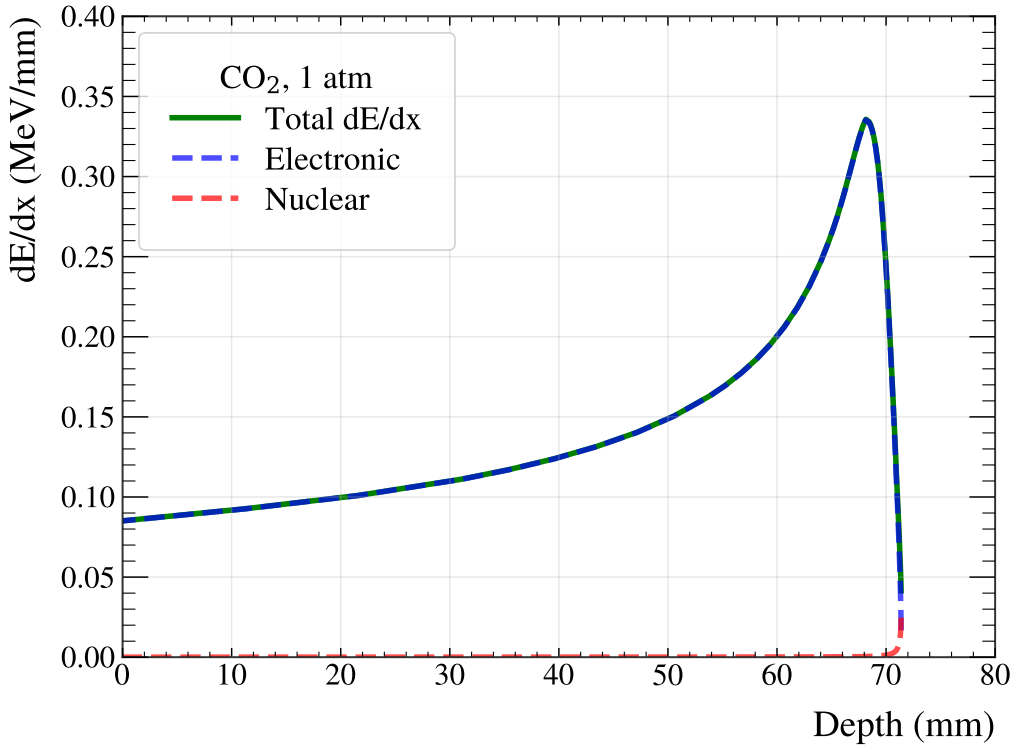

Figure 2.4: Stopping Power Bragg Curve: The electric and nuclear stopping powers for a 10 MeV α particle in CO_2 at 1 atm, obtained using SRIM.

2.2.3 Charge Transport and Collection

W-Value & Fano Factor

Some gas-filled detectors measure the energy of an event by directly counting the ionisation electrons, rather than inferring it from the track length. Therefore, it is important to define the average energy deposited per electron–ion pair, known as the W-value [153,

154]. The W-value is not simply the ionisation energy, as energy is also lost through other processes such as excitation of atomic electrons. Consequently, the W-value is always higher than the ionisation energy. For a given gas, the W-value remains approximately constant and can be obtained experimentally or through simulation using transport codes such as `Garfield++` [160].

The resolution of a detector, R, that collects electron-ion pairs assuming Poisson statistics is defined as

$$R = \frac{2.35}{\sqrt{N}}, \tag{2.2.3.1}$$

where N is the number of charge carriers. However, in some cases, the resolutions obtained from experimental data exhibit deviations from this behaviour. The value that relates the observed variance and that predicted by Poisson statistics is called the Fano factor, F [154]. The corrected resolution is therefore defined as [153]

$$R = 2.35\sqrt{\frac{F}{N}}. \tag{2.2.3.2}$$

The Fano factor is therefore an important consideration when selecting fill gas.

Diffusion

The electron-ion pairs that are liberated in the gas volume will begin to diffuse from regions of high density to regions of low density. Therefore, an initially point-like track will spread out over time, following a Gaussian profile sometimes referred to as an electron cloud. The width of this distribution increases with time and is given by

$$\sigma(t) = \sqrt{2Dt}, \tag{2.2.3.3}$$

where t is the diffusion time, and D is the diffusion constant. A simple approximation for D can be derived from kinetic gas theory [154] under the assumption that the velocity of the ions follows a Maxwell-Boltzmann distribution. In this case, the diffusion

constant is approximately

$$D \simeq \frac{1}{3} v\lambda, \tag{2.2.3.4}$$

where λ is the mean free path (the average distance an ion travels between collisions), and v is the mean velocity of the ions. For realistic cases, for example, when an external electric field is applied, the diffusion constant D is typically calculated using transport codes, such as `GARFIELD++` [160].

Drift

If an external electric field is applied across the gas volume, the recombination of electron-ion pairs is reduced, and the charged particles will accelerate and drift to the anode/cathode. They will also be slowed down through interactions in the gas. The average drift velocity, v_d, achieved is defined as

$$v_d = \frac{\mu E}{p}, \tag{2.2.3.5}$$

where E is the electric field strength, p is the gas pressure, and μ is the charge mobility. This equation is valid at typical operating pressures of gaseous detectors, where the number of electron collisions is high.

Avalanche Multiplication

Typically, the signal induced by the electron-ion pairs will be too small to generate a measurable signal. To overcome this charge multiplication is used to amplify the signal. This is when detectors are said to operate in the proportional region. Charge multiplication will occur when the primary electrons gain sufficient energy, through an applied electric field, to ionise additional gas molecules themselves. This in turn produces secondary electrons, and those produce tertiary and so on, initiating an (Townsend) avalanche process.

2.3 The Time Projection Chamber

A TPC [161] is a fluid-filled particle tracking detector that provides users with three-dimensional particle tracking information, in *x, y, z*, where *z* is the drift direction. This technology typically enables particle position determination, momentum reconstruction, and charge identification on an event-by-event basis, using a variety of sensors.

There are many types of TPC, such as active target TPCs (AT-TPC) [162–164] where the fill fluid is both the target and the detection medium, TPCs that have an externally applied magnetic field that use mass-charge of particles for particle identification (PID) and for transverse diffusion suppression [165], and dual-phase TPCs that contain both a liquid and a gas for delayed timing information [166].

The general structure of a TPC consists of three main areas:

- **The drift volume**, which operates in the proportional region. In this volume, the primary charged particles ionise the gas, and the electrons diffuse to form an electron cloud (or track). An electric field is applied across this volume, maintained by a drift cage, to drift the electrons to the readout plane.

- **The avalanche multiplication region**, which operates in the proportional region. It is here where the electrons are multiplied to produce a measurable signal. Typical technologies include avalanche grids, Gas Electron Multipliers (GEMS) [167], and Micromegas (MM) [168], where the latter is also a readout technology.

- **The readout plane**, which can consist of electronic technology such as pixels [169] or overlapping strips [163], providing coupled *x, y, z* information. Alternatively, there is optical readout technology, typically consisting of a camera, CCD [162]or sCMOS [170], for in-plane detection and PMTs [162, 170] for out-of-plane information.

An illustration of a TPC is shown in figure 2.5 that outlines these general areas. It shows charge particles induced by a neutral beam entering its volume.

The main advantages of TPCs remain consistent across these different configurations. They excel at recording both high-multiplicity events with complex tracks and simple particle interactions with equal detail, all within 4π solid-angle coverage using a single

detector. However, a significant challenge lies in post-processing the data, specifically in reconstructing the desired physical quantities from recorded particle tracks.

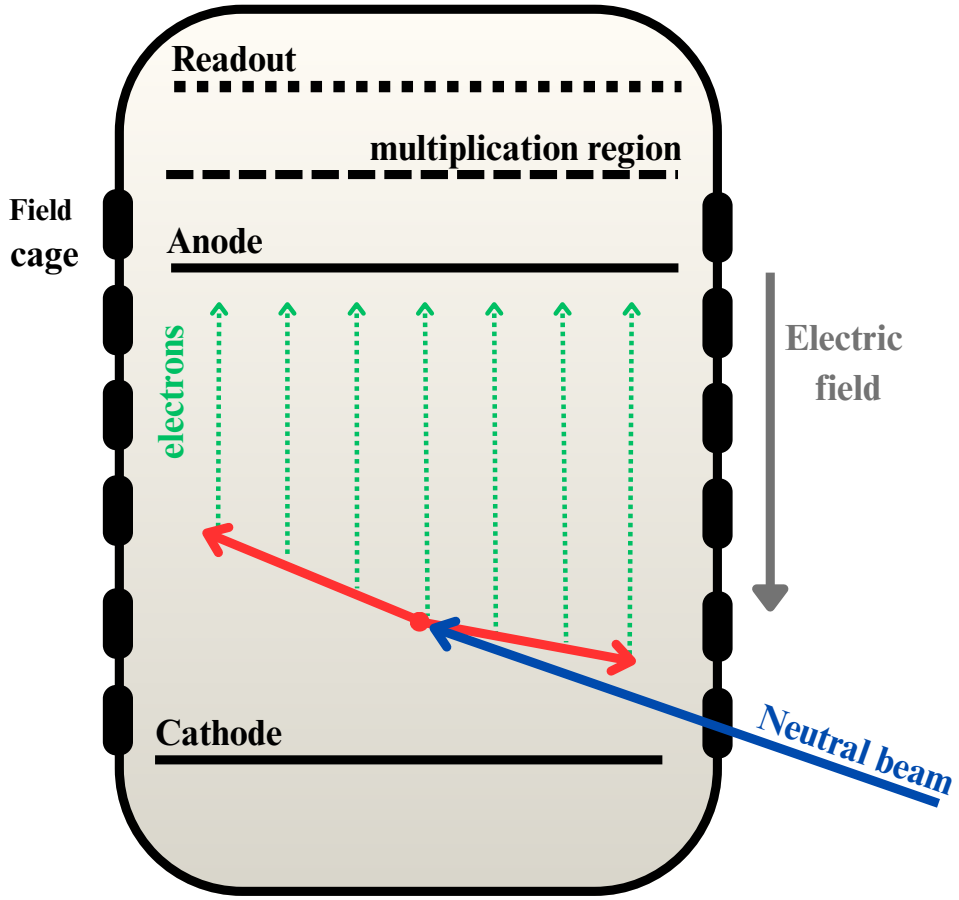

Figure 2.5: Time Projection Chamber Schematic: A generalised schematic of an active target time projection chamber is shown. A neutral beam enters the chamber (blue), causing some reaction that results in charged particle production (red). The induced ionisation (green) is shown to drift towards the readout plane due to an applied electric field.

A variety of methods are used for reconstruction and identification, such Bragg-curve fitting and vertex-endpoint identification [164]. As well as more recently, machine learning based approaches [171, 172]. However, these are often limited by the small sample size of labelled training data.

3

The HIγS Facility

Both experiments in this thesis used γ beams [1] produced by the High Intensity γ-ray Source (HIγS) facility, located at Duke University in North Carolina. The facility is a joint initiative between the Duke Free Electron Laser Laboratory (DFELL), and the Triangle Universities Nuclear Laboratory (TUNL). The facility operates as an electron-photon collider, using the Compton back-scattering technique to boost Free Electron Laser (FEL) light from relativistic electron bunches to generate quasi-monoenergetic γ beams. These beams can be either linearly or circularly polarised, cover an energy range of 1–100 MeV, and achieve intensities of up to $\sim 10^9$ γ/s. The energy resolution of the beam, defined as $\Delta E/E$ (with ΔE = FWHM), typically falls between 0.8% to 10%. An overview of the experimental hall is shown in figure 3.1 [173].

An overview of the interactions of photons with matter is given, before discussing beam production, and then detailing the experimental setup for both experiments in this thesis.

[1] As they are commonly referred to, even though they do not arise from inside a nucleus.

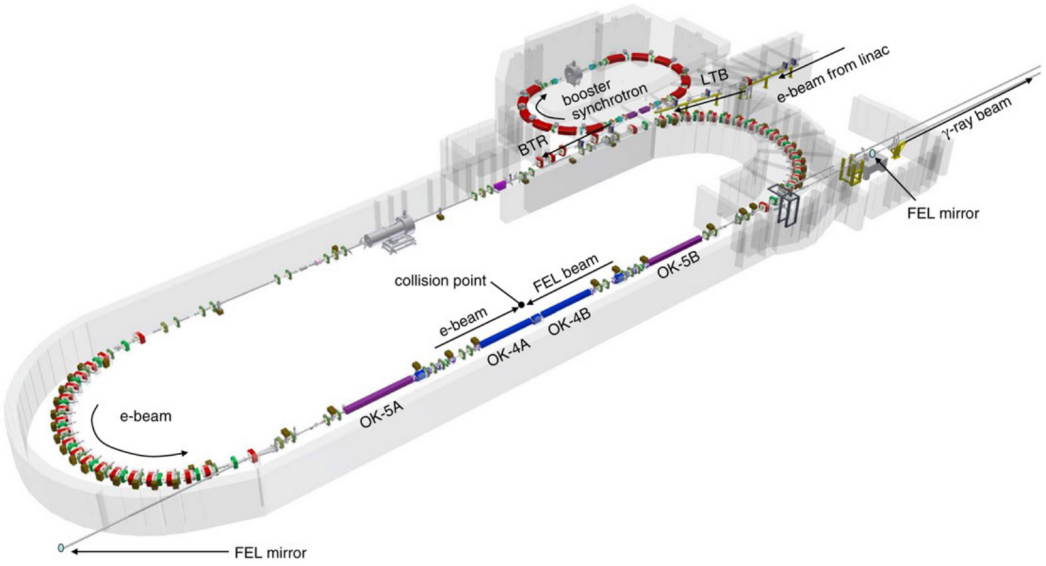

Figure 3.1: The HIγS Facility: An overview of the beamline is presented, the figure was taken from reference [173]. It highlights the initial linear accelerator, the booster synchrotron, the main storage ring and collision point, as well as the γ beam passing through the mirror directed towards the upper target room.

3.1 Photon Interactions with Matter

As photons are charge-neutral, they do not interact inelastically with the electrons in an absorber material, as charged particles do. Instead, photons interact predominantly through the photoelectric effect, Compton scattering, and pair production[2]. Compared to charged particle interactions, the aforementioned processes have, in general, a much lower cross section; therefore, photon beams are much more penetrating. Also, these interactions remove photons from the beam entirely, either through scattering or absorption. The relation of intensity before and after transmission through a material of thickness x, is given by

$$I = I_0 e^{-\mu x}, \tag{3.1.0.1}$$

where I is the transmitted intensity, I_0 is the initial intensity, and μ is the linear attenuation coefficient. Where the latter is characteristic of the material and the photon energy. It is sometimes also represented as the mass attenuation coefficient, μ/ρ, where ρ is the material's density [153].

[2]Photo-dissociation interactions are also possible.

Each of the aforementioned processes will contribute to the attenuation coefficient differently, these contributions are shown in figure 3.2.

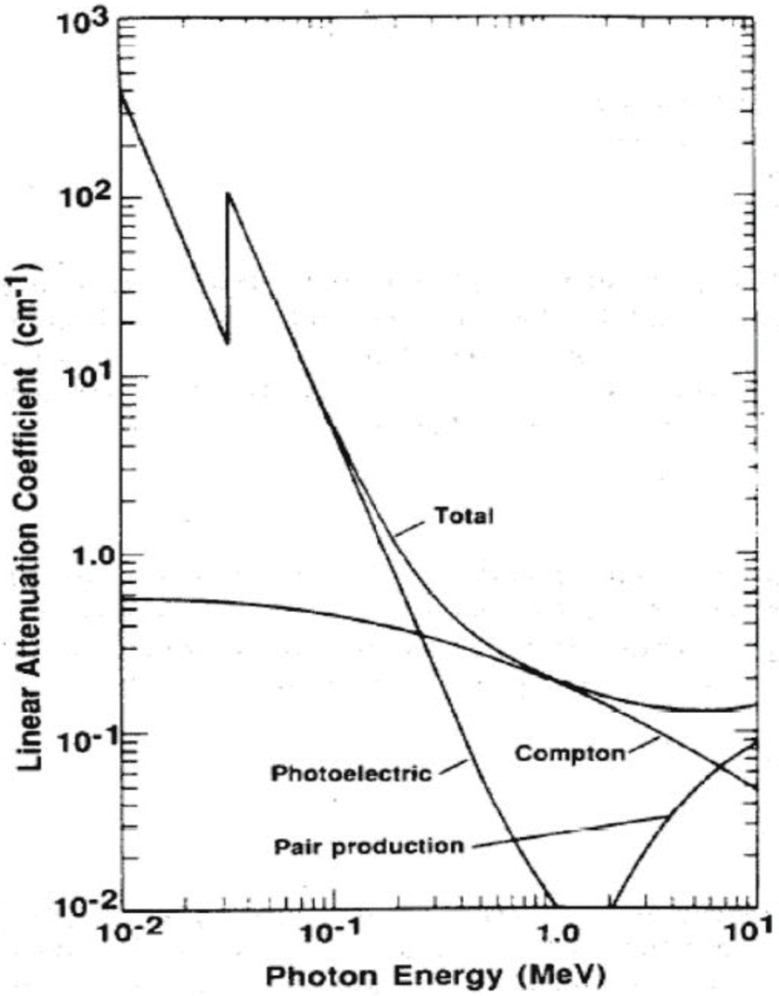

Figure 3.2: Photon Interaction Contributions to Attenuation Coefficient: A figure showing the contribution to the linear attenuation coefficient for Compton scattering, pair production and photoelectric effect, for NaI. This figure was taken from reference [174].

The Photoelectric Effect

In the photoelectric effect, a photon interacts with an atom where it is completely absorbed, ejecting a photoelectron from a bound shell to conserve energy and momentum. For this effect to take place, the photon must have an energy closely matching the energy needed to overcome the electron's binding energy, E_b. For example, in figure 3.2, you can see that the photoelectric effect contribution to the mass attenuation coefficient

spikes when the photon energy matches that of a given shell. In this process, the photoelectron will be emitted with energy

$$E_e = hv - E_b, \tag{3.1.0.2}$$

where h is the Planck constant, v the frequency of the photon, and hv is the photon energy. The hole left in place of the ejected electron will be filled by another atomic electron from a less-bound shell, releasing a characteristic X-ray [153]. In the spectra of photon detectors, the full-energy peak arises predominantly from energy deposited through the photoelectric effect.

Compton Scattering

Compton scattering can occur when a photon strikes an electron in an atom's outer shell. In this process, some energy is transferred to the electron as it is ejected from the nucleus, altering the trajectory of the incident photon. This process is outlined in figure 3.3, and typical contribution to the attenuation coefficient given in figure 3.2.

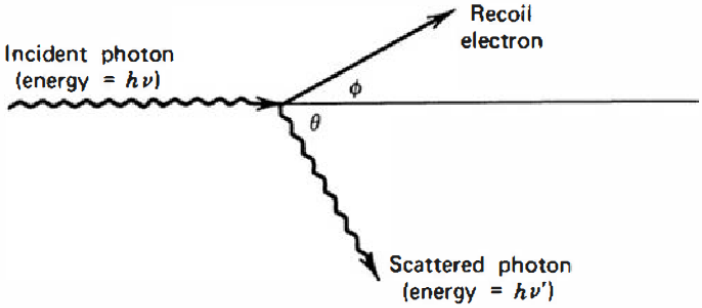

Figure 3.3: Compton Scattering: A simple plot that illustrates Compton scattering, by showing an incident and scattered photon and recoil electron. This figure was taken from [153].

The energy of the scattered photon, $E' = hv'$, with incident energy, $E = hv$, will depend on the scattering angle of the photon, θ, such that

$$E' = \frac{E}{1 + \frac{E}{m_0 c^2}(1 - \cos\theta)}, \tag{3.1.0.3}$$

where m_0 is the electron rest mass, and c is the speed of light. The energy deposited from Compton scattering forms a broad Compton continuum up to the Compton edge [153].

Pair Production

Pair production can take place when a photon, which has more energy than twice the rest mass of an electron (1.022 MeV), passes through the Coulomb field of a nucleus. Here, the photon disappears and is replaced with an electron-position pair. While the electron can deposit its full energy into the material, the positron pair will annihilate with another electron, producing two 511 keV photons that may escape the material. This can cause two escape peaks to form in photon detector spectra [153].

3.2 Beam Production

The production of γ beams at HIγS begins with the generation and acceleration of electrons in a linear accelerator (LINAC). A lanthanum hexaboride photo-cathode electron gun emits electrons in bunches via the photoelectric effect, using a pulsed N_2 laser [140]. These electron bunches are accelerated within the LINAC, reaching energies in the range of 0.18–0.28 GeV [173].

The electron beam is then injected into a booster ring, of circumference 31.902 m, where its energy is increased to 1.2 GeV. Subsequently, the electrons are transferred to the main storage ring, which has a circumference of 107.46 m. During operation, the storage ring is continuously topped up with full-energy electrons from the booster ring through a periodic injection process. This procedure typically requires five minutes per cycle.

Radio-frequency (RF) cavities are positioned along the curved sections of the storage ring, which are used to bunch the electrons and compensate for energy losses due to emission of synchrotron radiation. The straight section of the storage ring, which leads to the γ beam-line, houses several optical klystrons (OK-4 or OK-5), also referred to as "wigglers". These produce magnetic fields to induce rapid oscillatory motion of the electrons, resulting in the emission of FEL light. The polarisation of the emitted light can be either linear or circular, depending on the wigglers used [140].

The HIγS operates in a dual-bunch mode, whereby two electron bunches circulate concurrently within the storage ring. The FEL light produced by the first electron bunch travels along a 53.73-metre-long optical cavity and is reflected by a FEL mirror located at the end of the cavity. This process is timed such that the reflected light then interacts with the second electron bunch at the centre of the cavity. The resulting collision induces Compton backscattering, which boosts the energy of the photons. These higher energy γ beams then propagate down the beam-line and pass through the FEL mirror, towards the target room. The energy of the γ beam is controlled by varying the energy of the incident FEL laser [173].

The equation that determines the energy of the γ beams, in the case where the scattering angle θ is small, is given by

$$E_\gamma \simeq \frac{4\gamma^2 E_{FEL}}{1 + \gamma^2\theta^2 + E_{FEL}/E_e}, \tag{3.2.0.1}$$

where γ is the Lorentz factor of the relativistic electrons, E_{FEL} is the energy of the FEL photons, and E_e is the energy of the electrons involved in the scattering. Since HIγS operates with head-on collisions between the FEL photons and electron bunches, the scattering angle θ is effectively zero. Photons scattered at non-zero angles, and thus possessing lower energies, are removed by the collimators located further down the beam-line.

3.3 Experimental Set-up

The experimental set-up at HIγS was similar for both experiments detailed in this thesis. The TPCs in question were each located in the upper target room (UTR) of the facility, with a number of different detectors and equipment for beam characterisation. Both setups are described here.

3.3.1 Experimental Setup - OTPC

The OTPC experiment was set up as shown in figure 3.4.

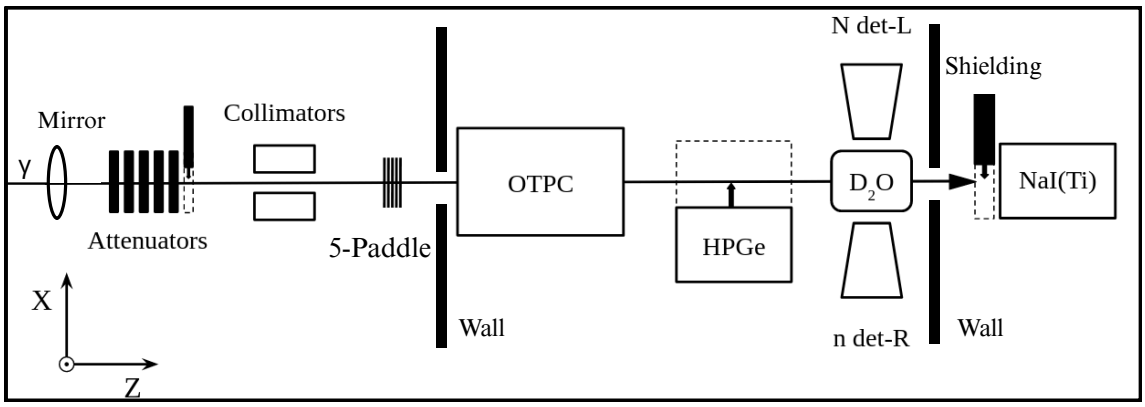

Figure 3.4: The HIγS Beamline Detector Setup Overview: The setup for the OTPC experiment is shown. The beam passes through the mirror, the movable attenuator station, the collimator station, and then through the relative flux monitor 5-paddle system. It then passes through the OTPC, the movable HPGe station, then through a heavy water cell surrounded by neutron detectors, and finally into the shielded NaI(Tl) station.

1. The γ beam produced through Compton backscattering of FEL light from electron bunches passes through the FEL mirror and propagates down the beamline towards the UTR.
2. The beam passes through the attenuator station, where a set of five copper attenuators can be remotely moved into the beamline to reduce the intensity.
3. The beam passes through a series of collimators used to reduce the energy spread of the beam by limiting its angular spread (see equation (3.2.0.1)).
4. Next, the beam passes through the five-paddle plastic scintillator system, which provides real-time monitoring of the relative beam intensity by detecting Compton scattering of particles produced when the gamma beam passes through a radiator material on the beam line. This system can also be scaled offline to measure the full beam intensity.
5. The beam then travels through the Optical Time Projection Chamber (OTPC), where a very small fraction of the beam will interact in the gas.
6. The remaining vast majority of the beam then enters the High Purity Germanium (HPGe) station, which is used for beam energy measurements. This detector is also capable of being moved in and out of the beam-line as needed.
7. The beam passes through a heavy water cell positioned centrally along the beam-line. Surrounding the cell are two neutron detectors that were previously used to validate

intensity measurements [140].

8. Finally, a large sodium iodide detector (NaI(Tl)) used for intensity scaling is located at the end of the beam-line, which has a thick wall that can be moved into its path to function as a beam dump.

3.3.2 Experimental Setup - eTPC

The eTPC experiment, overviewed in figure 3.5, was set up similarly with a few differences, discussed here. The 5-paddle system was removed and replaced with the mirror paddle (MPAD) and single paddle (SPAD) detectors. The former monitors relative beam intensity by detecting particles produced through Compton scattering on the FEL mirror at 40° to the beamline, and the latter SPAD monitors relative intensity through Compton scattering directly in the beamline. The heavy-water cell flux-monitoring system was removed and replaced with both a ^{235}U fission chamber and a gold foil. Both can be used to monitor the beam intensity.

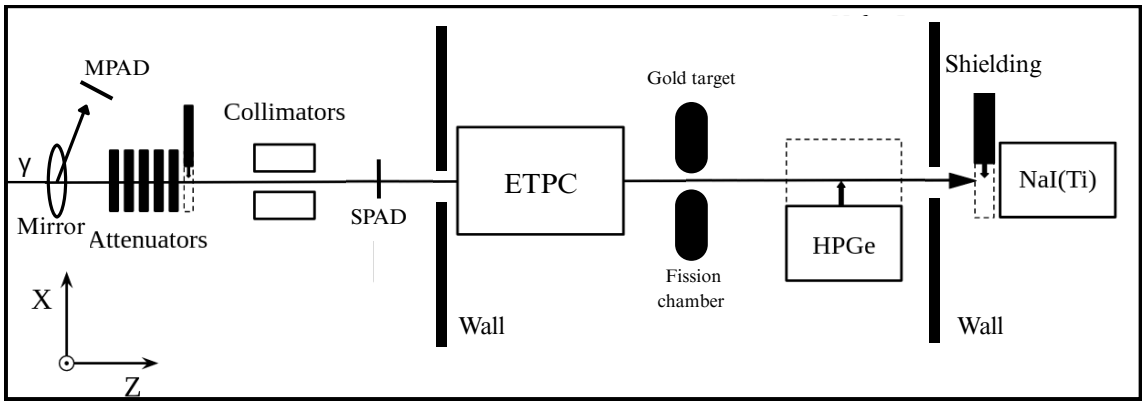

Figure 3.5: The HIγS Beamline Detector Setup Overview: The setup for the eTPC experiment is shown. The beam passes through the mirror, where Compton-scattered γ-rays are detected at 45° using the MPAD system. The beam then passes through the movable attenuator station, the collimator station, and the relative flux monitor SPAD system. It then passes through the eTPC, the station which houses the gold target and fission chamber, then the movable HPGe station, and finally into the shielded NaI(Tl) station.

3.3.3 Detector Systems & Equipment

The following section provides a description of each detector system used in this analysis and outlines its basic operational principles.

Sodium Iodide Detector

Situated furthest downstream is a large, high-efficiency, cylindrical NaI(Tl) scintillation detector, with a diameter of 25.4 cm and depth of 30.48 cm, shown pictured in the left panel of figure 3.6. This detector can be used to measure the total beam intensity of the incident photon beam.

Scintillation detectors operate by converting the energy deposited from ionising radiation into scintillation light. These scintillation photons are then converted into electrons, which are multiplied using a photo-multiplier tube (PMT). The recorded signal at the anode, which is related to the initial energy deposited by the photon, is read out and processed [153]. A schematic overview of the operation of a generic scintillation detector is shown in the right panel of figure 3.6.

This detector was selected due to its high photon detection efficiency, attributed to the high linear attenuation coefficient of NaI(Tl) coupled with the substantial detector size. However, due to the high beam intensity delivered during experiments the beam cannot be measured directly by this detector without attenuation. Failure to appropriately attenuate the beam would lead to rate-dependent dead-time effects and cause damage to the crystal. The beam was therefore only measured when heavily attenuated. While the beam was operating at full intensity the detector was protected using a movable shield.

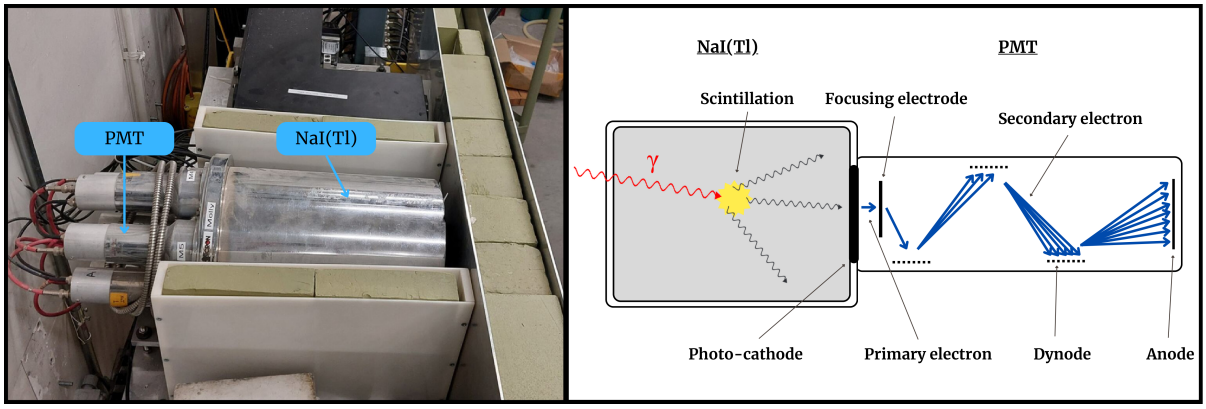

Figure 3.6: Sodium Iodide Detector. Left: A picture of NaI(Tl) detector with protective shield in place. **Right:** A diagram illustrating the operating principle of a scintillation detector. An incident γ ray (red) interacts in the NaI(Tl) crystal, producing electrons primarily via the photoelectric effect. These electrons excite the crystal, leading to the emission of scintillation light (black), which is then captured and amplified by the photomultiplier tube .

Copper Attenuators

Attenuation of the beam was achieved by moving a series of remotely controlled thick copper attenuators into the beam-line, with thicknesses listed in table 3.1.

Copper Attenuator	Thickness (cm)
1	2.45
2	8
3	8
4	8
5	8
6	4.9

Table 3.1: Beam attenuators: A list of the thicknesses of the copper attenuator used at HIγS.

Paddle System

For relative beam intensity measurements different *paddle* systems were used. The *five-paddle* system is described fully in [175]. Briefly, this system consists of a series of low-efficiency plastic scintillator paddles positioned in the beam-line to provide continuous relative intensity measurements. Three paddles are placed in front of a radiator material. When a high-energy photon from the beam interacts with this radiator, it can knock off electrons (or positrons) through the photoelectric effect, Compton scattering, or the

pair production process. A triple coincidence of signals from these three paddles is required to register a photon event.

An additional "veto" paddle is positioned behind the radiator to reject background events not originating from the radiator material. A fifth paddle is placed behind the veto paddle, which is used for an additional coincidence while calibrating. The left panel of figure 3.7 shows a photograph of a single paddle in the beamline, while the right panel depicts the overall design of the paddle system. The latter was taken from reference [175].

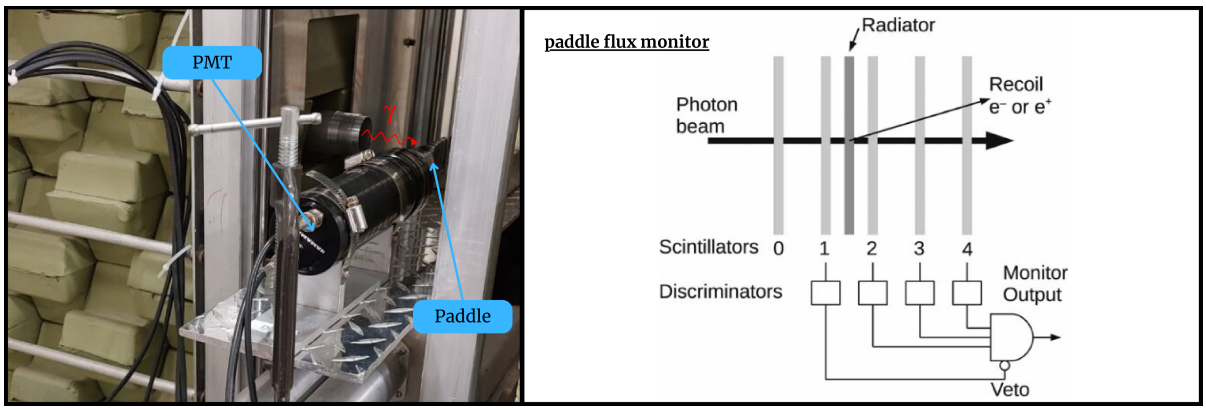

Figure 3.7: Plastic Scintillation 5-Paddle System. Left: Photograph of a single paddle in the beam-line. **Right:** Shows the design of 5-paddle system taken from [175].

The SPAD and MPAD systems function similarly to this, but without the veto functionality, and without the radiator.

High Purity Germanium

For energy measurements, a High Purity germanium (HPGe) detector was used, and is shown in the left panel of figure 3.8. An HPGe detector was selected because of its high intrinsic resolution, due to the large number of detected charge carriers (electron-hole pairs) per incident photon.

These HPGe detectors are a type of semiconductor detector that functions similarly to a reverse-biased PN diode. When incident ionising radiation interacts with the material, electron-hole pairs are liberated within the depletion region between the p-type and n-type material. The generated free charge carriers then drift under the influence of the intrinsic electric field and the applied reverse bias. The measured current pulses are therefore

related to the energy deposited in the detector and hence, to the energy of the incident photons. The small band gap of these detectors permits the liberation of a large number of charge carriers, leading to good intrinsic energy resolution [153].

For the OTPC experiment (experiment 1), an annular NaI(Tl) detector was mounted and used for Compton background suppression by anti-coincidence gating with the HPGe detector. Both detectors were situated on a movable workstation that could be remotely controlled to move in and out of the beamline. These detectors also required an attenuated beam for operation.

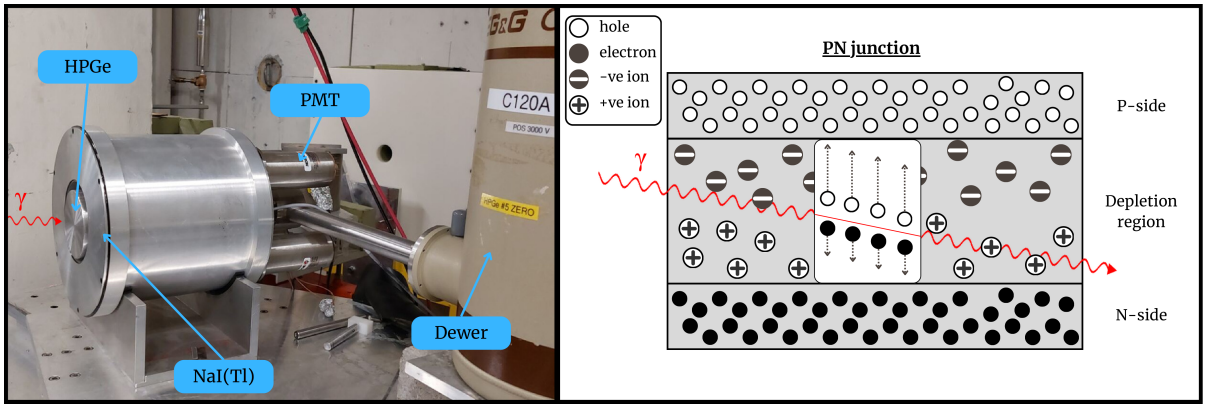

Figure 3.8: High-purity germanium detector. Left: Photograph of the HPGe, NaI(Tl) annulus, and liquid nitrogen dewar is shown. **Right:** Operational principle of a basic PN junction as a γ detector is illustrated.

Part II

Experiment 1: Optical Time Projection Chamber

4

Experimental Details

The chapter provides details on the OPTC detector used in this part of the thesis, defines the coordinate system used, and provides an overview of the experiment.

4.1 Optical Time Projection Chamber

The work presented in this section of the thesis relies on data acquired using an active-target Optical Time Projection Chamber (OTPC) as a charged particle detector, shown set up at the HIγS facility in figure 4.1. This detector was designed and built [1] with the primary purpose to provide high-precision tracking of charged particle decay products resulting from photo-dissociation reactions using high-energy γ beams.

The detector has been successfully used in two previous studies. Smith *et al.* [97] performed the first proof-of-principle measurement of the $^{16}\mathrm{O}(\gamma, \alpha_0)$ reaction, demonstrating

[1] In collaboration with the University of Connecticut (UConn), the High Intensity gamma Source (HIγS) facility, Brookhaven national Labs, CERN, the Weizmann Institute, the Université Libre de Bruxelles, and the Université Catholique de Louvain[176].

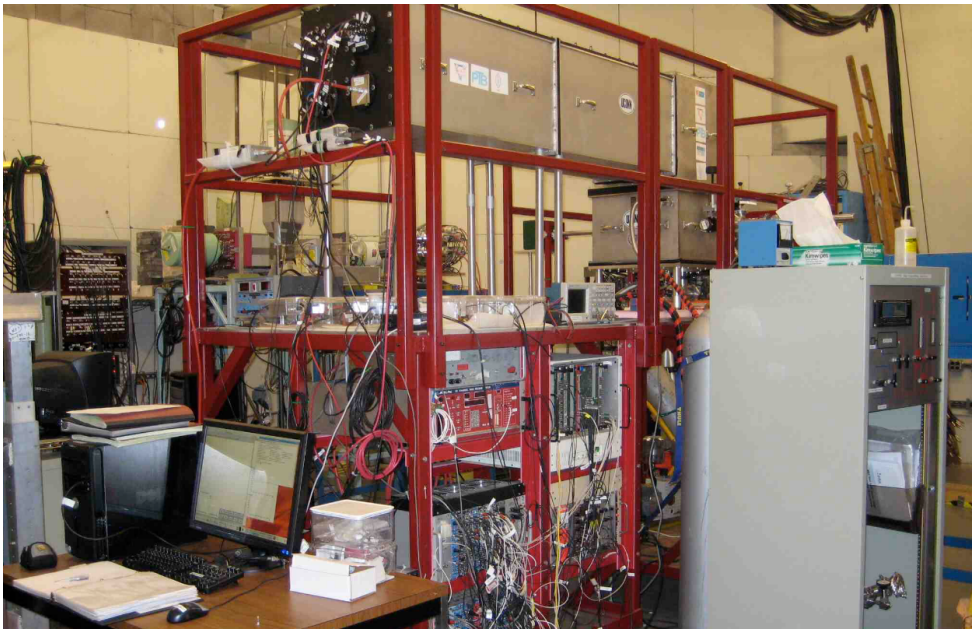

Figure 4.1: Photograph of the OTPC: The detector is shown in the HIγS Upper Target Room (UTR), alongside the electronics rack, and data acquisition (DAQ) PC. The photograph was taken from reference [176].

that the $^{12}C(\alpha, \gamma_0)$ reaction could be studied accurately via the inverse process. While Zimmerman *et al.* [139, 177] investigated the structure of ^{12}C, as discussed in the ^{12}C review section of this work. Both studies were conducted during the same experimental campaign using a $CO_2(80\%)$ + $N_2(20\%)$ active gas target. The present work builds upon the Smith *et al.* measurement by obtaining angular distributions over the same energy range with significantly improved statistics, and implementing an energy calibration of the OTPC.

A schematic overview of the internal structure of the OTPC is shown in figure 4.2. The main regions of the detector include the drift volume, charge multiplication region, and optical readout system. The following text provides an overview of these regions. Further information can be found in references [140, 176].

4.1.1 Drift Volume

Active Volume

The drift volume, which constitutes the active region of the detector, has dimensions of 30 cm length (aligned with the beam axis), 30 cm width, and 21 cm drift height. Two

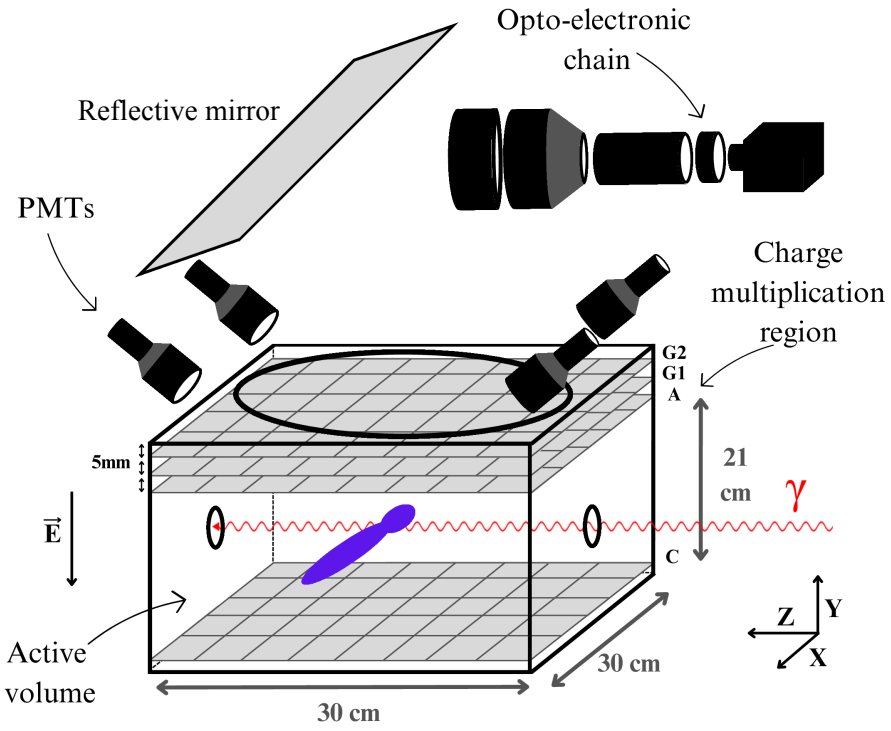

Figure 4.2: Illustrated Overview of the OTPC: The key features of the OTPC are shown. These include the active volume, anode (A), cathode (C), charge multiplication avalanche grids (G1/2), and the readout system (PMTs and the opto-electronic chain). This figure was taken from reference [178].

stainless steel wire grids form the anode (ceiling) and cathode (floor) of the active volume. These grids have a wire spacing of 500 μm and a thickness of 50 μm (pitch 550 μm). The walls of the drift volume are comprised of double-sided Printed Circuit Board (PCB), with 66 parallel copper strips embedded into the circumference. The strips have a width of 2.5 mm and a spacing of 0.4 mm (pitch 2.9 mm). Each strip connects to an adjacent strip through 1 MΩ resistors, and the final strips to the grids through 5 MΩ resistors. This set-up forms a voltage divider circuit which, through controlled voltage steps, maintains a uniform electric field within the drift volume [176].

Beam Entrance

The OTPC features 15 mm diameter entrance/exit holes in the drift cage walls. The γ beam (and α calibration source) enters/exits here after first passing through 1 mm thick aluminium windows, which are situated 64/70 cm away from the active volume at the end of two sections of metal tubing. Having the windows far from the active

volume prevents beam-induced charged particles from the aluminium from reaching the sensitive region. Additionally, a permanent magnet was positioned downstream of the entrance window to help deflect charged particles [176].

Gas Target

For the experiment described in this work, the chamber was filled with a mixture of 80% N_2O plus 20% N_2. The N_2 component was selected out of necessity for an organic scintillator, as this is essential for the operation of an optical TPC. It also benefits by not adding any additional background targets that are not already in the gas mixture. The N_2O was chosen as it contains the target nuclei ^{16}O, while also removing a prominent background of ^{12}C that was present in previous analyses where CO_2 was used as the primary target [97]. To maintain the purity of the target gas, the gas flow rate was set at 100-200 cm^3/min (at stp) [140].

Electron Drift

As the charged reaction products, induced via γ beam or calibration source interaction, pass through the active volume, they will ionise the target gas, resulting in a cloud of free electrons within the drift volume. While the physical drift length, l, of the OTPC is 21 cm, the effective "recordable" length, ℓ, is determined by the maximum possible recordable length in the time projection (the time window), w, the sampling rate of the electronics, f_s, and the electron drift velocity, v_{drift}

$$\ell = \frac{w \times v_{\text{drift}}}{f_s}. \tag{4.1.1.1}$$

It is therefore important to select an appropriate pressure and drift voltage that allows for both the physical containment of the electron cloud and ensures it remains within the time window defined by ℓ. For this experiment, a pressure of 100 Torr was used, with the anode grid biased at -1000 V and the cathode grounded, establishing the drift field. The drift velocity for these settings, $v_{\text{drift}} = 11.58$ μm/ns, was obtained using the

`Magboltz` [179] code. The drift velocity was later verified using the experimental data. These settings satisfy the condition that $l \approx \ell$.[2]

4.1.2 Charge Multiplication

The tracks drift upwards under the influence of the applied electric field across the grids towards the readout system. As it stands, not enough charge is deposited to induce a signal in the readout elements without amplification; the current measured on the grids will be below threshold, and minimal scintillation light is produced.

The charge multiplication region consists of two parallel-plane avalanche grids mounted 5 mm above the anode grid, with a 5 mm spacing between them. A steep potential gradient is established across these grids, with applied voltages of 3.8 kV and 6.5 kV, respectively. This creates an electric field strong enough to trigger an avalanche, leading to electron multiplication.

4.1.3 Readout System

The readout system comprises multiple charge- and photo-sensitive components that together provide sufficient information for particle-track reconstruction.

In addition to the charge signal that is read out from both the avalanche grids (providing a coarse measurement of energy), the avalanche process creates scintillation light by exciting the N_2 molecules, which then decay and emit light. The N_2 gas as an organic scintillator is transparent to this emitted light. The wavelengths of the light emitted are at 337 nm, with smaller yet visible contributions at 377 nm and 391 nm [140].

This measurable scintillation light propagates through the drift chamber and exits through a 2.5-cm-thick, 40-cm-diameter quartz window at the top of the chamber. Here, it is detected by two photosensitive systems, which form the optical readout chain, as described below [176].

[2]The PMTs used to record the time projection have a time window of 2150 bins, and a sampling rate of 100 MHz in the flash ADC $\therefore \ell$=25 cm. If $l > \ell$, tracks would be truncated; if $l < \ell$, time resolution would be reduced.

Time Projection

Four Hamamatsu R1033 photomultiplier tubes (PMTs) are positioned above this window to detect the scintillation light. The signals from all four PMTs are digitised using a 100 MHz flash ADC and stored, providing information about the time projection (out-of-plane dimension) of the particle tracks [176].

Optical Detection System

The in-plane information of the track is captured by a charge-coupled device (CCD) camera as part of a so-called "optoelectronic chain", based on technology developed for the CERN Hybrid Oscillation Research ApparatUS (CHORUS) experiment [180].

The chain consists of the following components: a mirror, a large primary quartz lens array, an electric de-magnifier (Hamamatsu V4440U), a set of commercial secondary lenses, gated image intensifier (photocathode, Microchannel Plate (MCP), and P46 phosphor screen), and the CCD camera [176].

The light, after passing through the quartz window, is reflected 90° by the mirror. Here it is, then focused by the primary lens array, reducing the image size by a factor of 4, onto the photocathode of the electric de-magnifier. Electrons are then emitted via the photoelectric effect, and accelerated to strike a phosphor screen, which converts them back into light while further reducing the image size by a factor of six [3] [140].

The resulting light passes through additional quartz lenses and reaches the photocathode of the gated image intensifier. If a valid trigger signal is received from the final avalanche grid, the gate bias is raised, opening the intensifier for a 50 ns window [140]. During this interval, the incoming light is converted to electrons, which are multiplied within the MCP and then strike a second phosphor screen, converting the signal back into photons. These photons are channelled via fibre bundles to the CCD camera, where the final image is recorded

Although the CCD is capable of capturing images at 1344 ×1024 pixel resolution with 16-bit depth, the resolution was reduced to 672× 512 pixels with 12-bit depth to

[3] A slow decay time, 50 μs, P11 phosphor was used to allow a delayed trigger signal to reach the gated image intensifier.

reduce dead time effects related to frame rate. Using this configuration, the frame rate was limited to 28.4 frames per second [140].

4.2 Experiment

4.2.1 Experimental Overview

The goal of this study was to measure the $^{12}C(\alpha,\gamma_0)$ cross section in a region where the broad $J^\pi(1^-)$ at $E_x = 9.585$ MeV and the narrow $J^\pi(2^+)$ at $E_x = 9.8445$ MeV states overlap. To achieve this the ^{16}O photo-dissociation differential cross sections were measured at four nominal γ-beam energies, $E_\gamma = 9.38, 9.50, 9.70$, and 9.80 MeV. These energies are shown as dashed lines in figure 4.3 against the partial cross sections from reference [46]. The aim was to overcome the disagreement, shown by many previous alpha capture measurements, between the measured phase angle, ϕ_{12}, between the $E1$ and $E2$ partial wave components and the predictions obtained from scattering data.

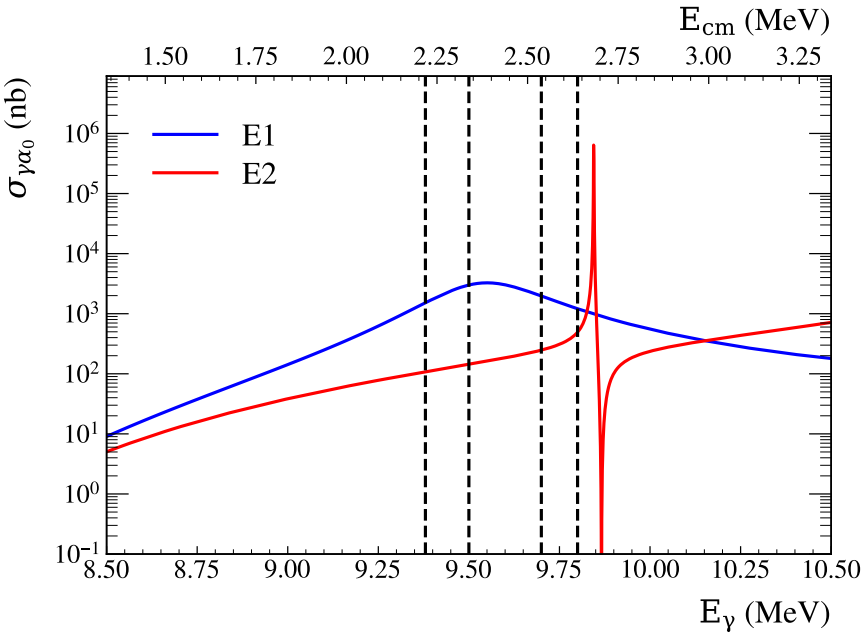

Figure 4.3: Experimental Measurement Points for the OTPC: Plot showing the nominal energies probed in this experiment (dashed vertical lines) against the $E1$ (blue) and $E2$ (red) fit lines for the $\sigma_{\gamma\alpha_0}$ cross sections on a log-scale. The fit lines were taken from reference [46]. The x-axis is shown in terms of both the centre-of-mass energy and the γ beam energy.

4.2.2 Coordinate System

The OTPC detector uses two right-handed polar coordinate systems, as shown in figure 4.4.

- (θ, ϕ): Used for physics results, where θ is the angle measured from the incoming γ-beam, and ϕ is the azimuthal angle measured as a rotation about the z (beam) axis. The solid angle term is given by $d\Omega = \sin\theta \, d\theta \, d\phi$.
- (α, β): Defined as a consequence of the design of the detector, α is measured as a rotation in the $z - x$ plane from the incoming γ-beam, and β is measured purely as the angle out of the $z - x$ plane. The solid angle term is given by $d\Omega = \cos\beta \, d\alpha \, d\beta$.

The relation of these two coordinate systems is given by

$$\begin{aligned} \sin\theta \ \cos\theta &= \sin\alpha \ \cos\beta \\ \sin\theta \ \sin\phi &= \sin\beta \\ \cos\theta &= \cos\alpha \ \cos\beta. \end{aligned} \tag{4.2.2.1}$$

The Cartesian coordinates are defined as

$$\begin{aligned} x &= r\cos\phi\sin\theta \\ y &= r\sin\phi\sin\theta \\ z &= r\cos\theta. \end{aligned} \tag{4.2.2.2}$$

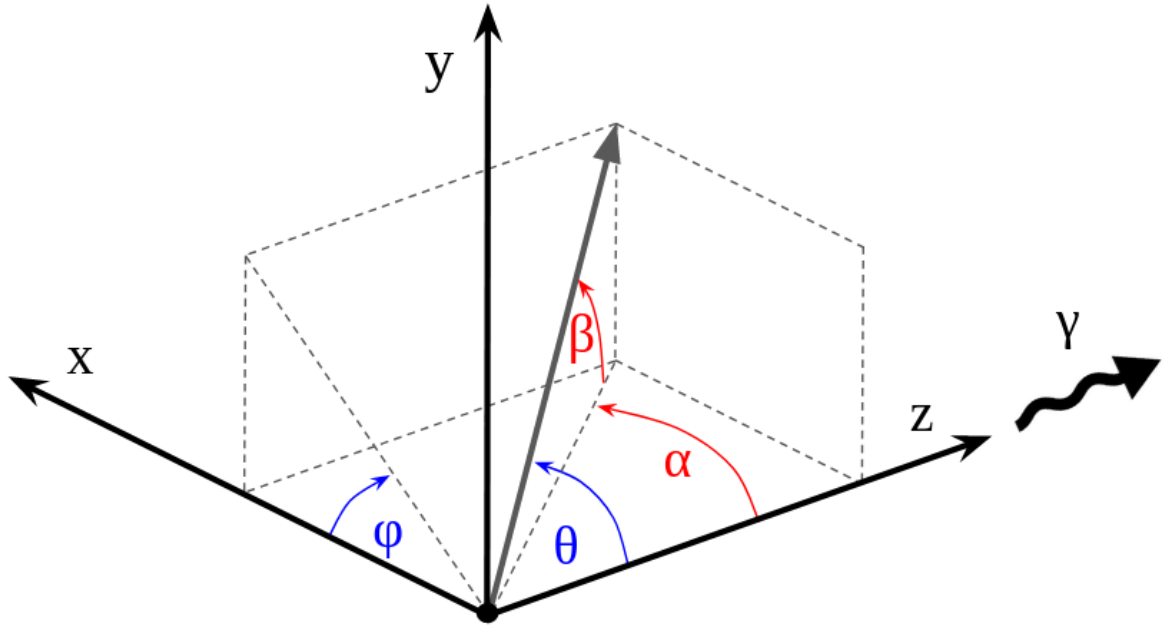

Figure 4.4: Detector Coordinate System for the OTPC: Plot shows the relation between the (θ, ϕ) physics coordinate system and the (α, β) detector coordinate system.

5

Analysis

This chapter details the analysis steps required to extract photo-dissociation cross sections. First, the HIγS beam characterisation is described. Subsequently, track reconstruction methods are presented, including calibration and resolution extraction. The event selection procedure to isolate ^{16}O photo-dissociation events is then explained, and finally, the centre-of-mass energy calibration procedure is detailed.

The majority of the analysis conducted in this section was performed using a combination of custom-written batch-processing tools for event reconstruction and the extraction of relevant observables from the OTPC data, written in C++ using the ROOT framework. Spectral analysis of the beamline detectors and subsequent OTPC analysis were performed using the standard set of Python-based scientific libraries.

5.1 Beam Characterisation

Accurately characterising the beam energy and intensity throughout the experiment is a critical step in the analysis. The beam intensity, measured using the large NaI(Tl) and paddle systems, is used to determine absolute cross section normalisation. Although the total cross section in this energy region is well known, reproducing it here provides essential validation that the correct reaction channel is being measured with minimal background. Furthermore, the beam energy profiles are necessary to know the distribution of energies delivered to the OTPC. This is useful for distributing luminosity when calculating cross sections, and for OTPC energy reconstruction validation. This section details the methods used to monitor and characterise these beam properties throughout the experiment.

5.1.1 Energy

The γ beam energy spectra were measured by illuminating a highly attenuated beam onto a high-resolution HPGe detector. Example raw and anti-coincidence Compton-suppressed spectra are shown in the left and right panels of figure 5.1, respectively. Whilst the beam parameters could be extracted from the anti-coincidence spectrum alone, this was done only for validation.

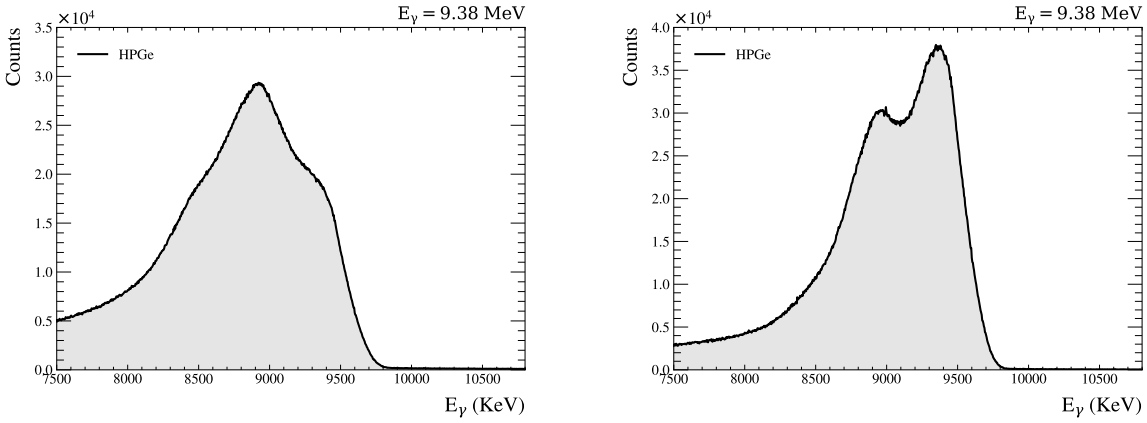

Figure 5.1: HPGe spectra for $E_\gamma = 9.38$ MeV. Left: Showing the raw HPGe measured spectrum. **Right:** The anti-coincidence HPGe spectrum obtained using the NaI Compton annulus.

Unfolding

To extract the true profile of the photo-peak, the raw HPGe spectra were unfolded using the HORST code [181]. The response matrices used included a 10 mm collimator diameter and 20 mm detector offset from the beam axis. The outputted unfolded distributions were then fitted with a skewed Gaussian to parametrise the energy profile. This general procedure is detailed in appendix B.

Time-weighting

Before fitting, if a given run spanned many hours, multiple beam measurements were made. In this case, each unfolded beam profile was normalised, denoted by $H(E)$, weighted, and summed to obtain an effective unfolded beam profile $\langle H(E) \rangle$. They were weighted according to the associated relative beam intensity measured in the paddles, I_{pad}, and the OTPC measurement time, such that over n runs the average profile is obtained using equation (5.1.1.1). An example resulting distribution is shown in figure 5.2.

$$\langle H(E) \rangle = \sum_{\text{run}=0}^{n} H(E) I_{\text{pad}} t_{\text{TPC}}. \tag{5.1.1.1}$$

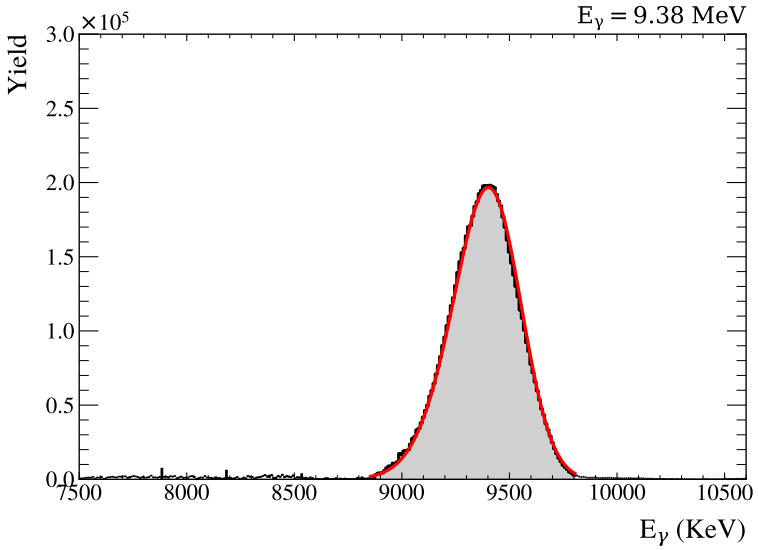

Figure 5.2: Unfolded HPGe Spectrum: The spectrum from $E_\gamma = 9.38$ MeV is shown after applying the HORST unfolding procedure (grey). This is fitted with the Skewed Gaussian equation (5.1.1) (red), with parameters given in table 5.1.

Parametrised Beam Profile

The unfolded spectra were fitted with skewed Gaussian distributions, defined as,

$$G(x \,|\, \xi, \omega, \alpha) = \frac{1}{\omega\sqrt{2\pi}} \exp\Big[-\frac{1}{2}\Big(\frac{x-\xi}{\omega}\Big)^2 \Big]\Big[1 + \mathrm{erf}\Big(\alpha \frac{x-\xi}{\omega\sqrt{2}}\Big)\Big],$$

where ξ represents the location parameter, ω the scale parameter, and α the shape parameter controlling the skewness. The mean (μ) and standard deviation (σ) of the distribution are obtained by

$$\mu = \xi + \omega\delta\sqrt{\frac{2}{\pi}}, \quad \sigma = \omega\sqrt{1 - \frac{2\delta^2}{\pi}},$$

where

$$\delta = \frac{\alpha}{\sqrt{1+\alpha^2}}.$$

The fitted parameters and their associated uncertainties obtained for each nominal beam energy are presented in table 5.1.

E_γ (MeV)	ζ (MeV)	ω (KeV)	α	μ (MeV)	σ (keV)
9.38	9.51(1)	208(2)	-1.29(4)	9.38(1)	161(2)
9.50	9.63(1)	220(3)	-1.35(5)	9.49(1)	169(3)
9.70	9.83(1)	227(2)	-1.40(3)	9.68(1)	173(2)
9.80	9.97(1)	185(2)	-2.09(5)	9.83(1)	129(2)

Table 5.1: Energy Profile Fit Parameters: Skewed Gaussian distribution parameters and their errors. Errors on all parameters are statistical from the fit. The error on the location parameter, ζ, has been added in quadrature with 10 keV reflecting contributions from the calibration error [140].

5.1.2 Intensity

At the time of the experiment, two methods of beam intensity monitoring were used

1. **Paddle Ratio Method**: A scaling between the rate measured in the relative intensity monitors (paddles) and the rate in the large NaI(Tl) detector was established under attenuated conditions. This allows the unattenuated paddle counts to be scaled to the full intensity.

2. **Attenuator Extrapolation Method**: The rate recorded in the large NaI(Tl) using an attenuated beam is extrapolated to full intensity using the measured copper attenuation coefficients.

Paddle Ratio Method

NaI(Tl) detector calibration and corrections The large NaI(Tl) detector was calibrated using natural background lines from ^{208}Tl and ^{40}K, plus the full-energy photopeak obtained from unfolded HPGe spectra. An example NaI(Tl) spectrum, denoted $N(E)$, is shown in figure 5.3.

To determine the rate in the NaI(Tl) from an attenuated beam, the total counts above background ($\sim$3.5 MeV) were obtained by direct integration, whilst counts below 3.5 MeV were estimated by fitting and integrating a Lorentzian tail, $L(E)$. Other contributions from background were assumed to be negligible. Under that assumption the total recorded counts, N_{NaI}, is given by

$$N_{\mathrm{NaI}} = \int_0^{3.5} L(E)dE + \sum_{E=3.5}^{12.5} N(E). \qquad (5.1.2.1)$$

The rate was then calculated using the measurement time, t, which was determined using a 60 Hz clock ($t = N_{clock}/60$). However, several corrections were then applied to obtain the true γ rates. These are listed below.

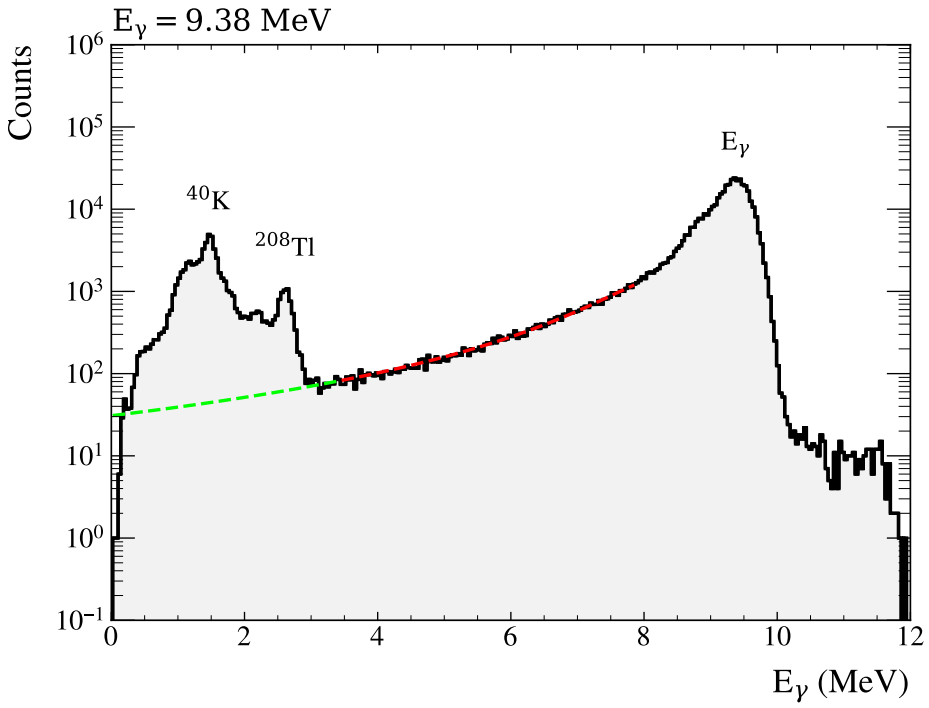

Figure 5.3: Sodium Iodide γ Spectrum: An example energy spectrum from the HIγS NaI(Tl) detector. The red/green line shows an extrapolation of the Compton continuum below the lower energy background peaks.

1. **Live-time Correction**: The data acquisition system used a trigger-veto method to account for detector dead time. Random pulser signals were continuously injected into the system throughout the measurement. Some were injected during detector dead time when a real signal is recorded (the random signal is vetoed) and others during detector live time (the random signal is triggered). The live-time fraction is therefore $f_{LT} = N_{veto}^{Rand}/N_{trig}^{Rand}$, where N_{veto}^{Rand} and N_{trig}^{Rand} are the number of vetoed and triggered random pulser events, respectively.

2. **Detection Efficiency**: The vast majority of incident photons interact in the NaI(Tl) detector. Simple efficiency corrections were obtained using the attenuation factor, $\epsilon = 1 - e^{-(\mu/\rho)x\rho}$, where μ/ρ is the mass attenuation coefficient, ρ is the density (3.67 g/cm^3), and x is the crystal thickness (30.48 cm). Using NaI crystal parameters, and NIST mass attenuation coefficients [182], the efficiencies were calculated at each beam energy and found to be consistently 98.4 %.

3. **Target Attenuation**: For runs with the D_2O target cell in place (density: 1.11 g/cm^3, thickness: 4.47 cm), a fraction of photons are attenuated before reaching the NaI detector. The fraction of transmitted $\gamma's$, $A = e^{-(\mu/\rho)x\rho}$, accounts for this attenuation. The number of attenuated photons was calculated using mass attenuation coefficients from NIST [182], and the transmission fractions are shown in table 5.2.

E_γ (MeV)	A
9.38	0.89780(2)
9.50	0.89820(1)
9.70	0.89900(1)
9.80	0.899500(1)

Table 5.2: Attenuation Coefficients for the Heavy Water Cell: The calculated efficiency values for the D_2O cell for each beam energy are listed. The calculations were done using the attenuation coefficients for H_2O acquired from the NIST database [182].

The fully corrected NaI(Tl) rate is therefore defined as

$$R_{\mathrm{NaI}} = \frac{N_{NaI}}{t\ f_{LT}\ \epsilon\ A}. \tag{5.1.2.2}$$

Where the calculated errors on R_{NaI} include the errors on the total counts, measurement time, live-time fraction, efficiency, and target attenuation.

Paddle corrections For the same measurement, the rates recorded in the paddles were also obtained. The counts were taken from the scalers, and rates were calculated using a 60 Hz clock. The same live-time fraction procedure was applied here, but the correction was minimal due to the plastic scintillators' fast response. No attenuation/transmission corrections were needed. However, a small background subtraction of 0.7 Hz [183] was applied. This 0.7 Hz rate was previously determined as the background rate of the paddles in the absence of any beam. The rate in the paddle is therefore given by

$$R_{\mathrm{pad}} = \frac{N_{pad}}{t\ f_{LT}} - 0.7. \tag{5.1.2.3}$$

Normalisation factor Several intensity measurements were conducted successively with varying levels of attenuation, achieved by using different combinations of the copper attenuators. Consequently, each configuration corresponded to a different beam rate. For each nominal beam energy, the corrected paddle rates, R_{pad}, are plotted against the corrected NaI(Tl) rates, R_{NaI}. This is shown for $E_\gamma = 9.38$ MeV in figure 5.4[1].

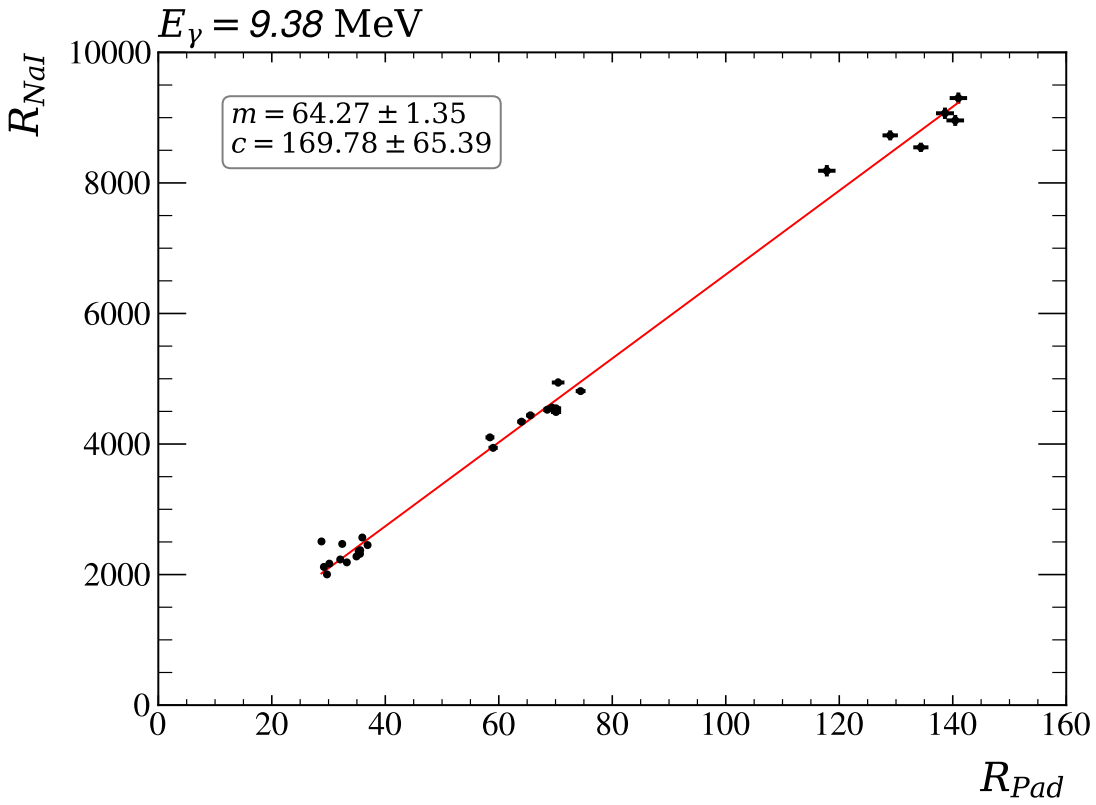

Figure 5.4: Sodium Iodide Rate Vs. Paddle Rate: The relationship between the rates measured in both the NaI(Tl) and the plastic scintillator paddles is shown, post corrections, for a run taken with a heavily attenuated beam. The linear relationship, gradient (m) and offset (c), between the two rates demonstrates that live-time corrections are functioning appropriately. The fitted linear model parameters are shown in plot.

A linear fit to these data, gradient (m) and offset (c), extracts the calibration required to scale the rates from the paddle detectors, obtained during unattenuated runs, to the full beam intensity. It is noted that an approximation was used to correct the data, as the number of measured unattenuated γ's in the paddles is of the order of billions; therefore,

[1]The linearity of the data demonstrates the effectiveness of the applied rate-dependent corrections.

the intercept is negligible. The extracted normalisation factors are listed in table 5.3[2].

E_γ (MeV)	m
9.38	64(1)
9.50	65(4)
9.70	72(3)
9.80	N/A

Table 5.3: Paddle Method Intensity Calibration: The table presents the multiplicative calibration factors, obtained for each nominal beam energy, needed to scale rates in the paddle detectors to full beam intensity.

Beam intensity. The unattenuated paddle rates, R^u_{pad} were then scaled to absolute intensities observed in the OTPC, as $I = m \cdot R^u_{pad}$. The values for m were taken from table 5.3. Figure 5.5 shows typical intensity variations for a single nominal beam energy.

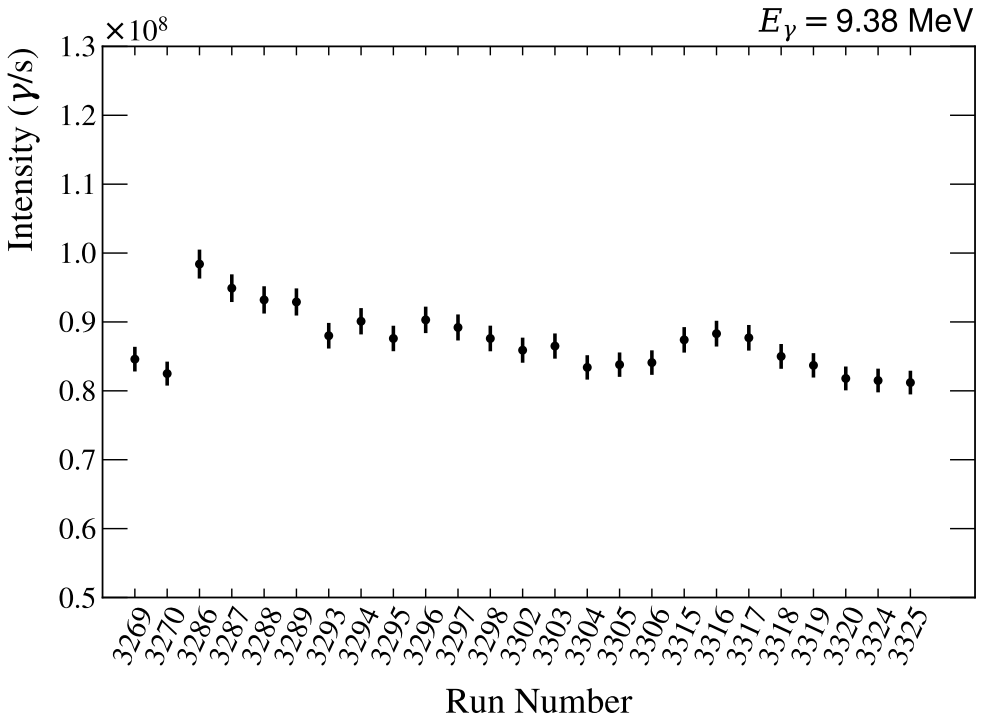

Figure 5.5: Absolute Beam Intensity - Paddle Method: Calibrated intensity measurements for different $E_\gamma = 9.38$ MeV runs spanning approximately two hours. The observed variation in intensity is consistent with that expected from the beamline being periodically "topped-up" with electrons.

[2]This method does not require any knowledge of the attenuation coefficients of the copper attenuators.

Attenuator Extrapolation Method

This method directly extrapolates the rates recorded in the NaI(Tl) under different levels of attenuation to the full beam intensity.

Copper attenuation characterisation. For accurate extrapolation, historical data [184] measuring the linear attenuation coefficients of the HIγS copper attenuators were analysed. These data were recorded across various campaigns, shown in blue figure 5.6, measuring the linear attenuation coefficients of the copper attenuators under different conditions for different beam energies. The red points are the linear attenuation coefficients from NIST [182], calculated using the copper density (8.96 g/cm^3). A linear model was

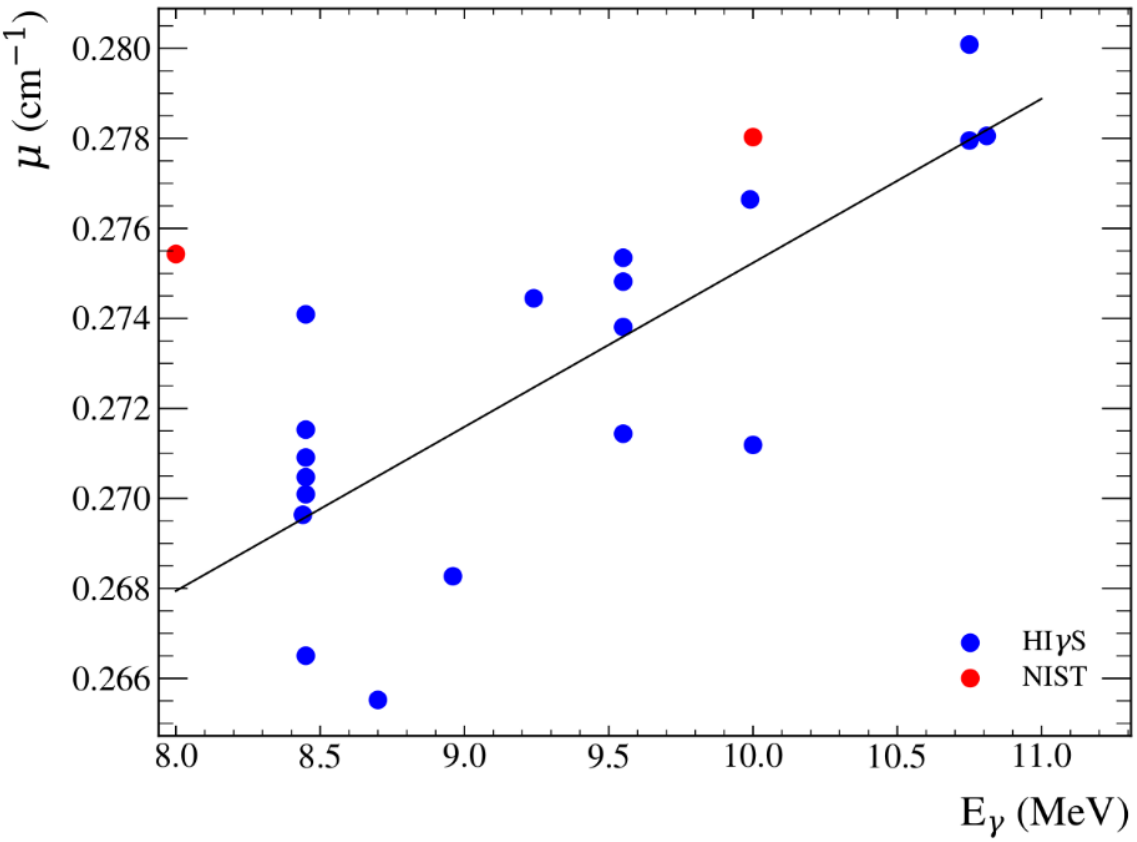

Figure 5.6: Measured Copper Linear Attenuation Coefficients: The linear attenuation coefficients for the HIγS copper attenuators are shown (blue) [184] compared with values from the NIST database [182] (red). A linear model (black line) was fitted phenomenologically to extract values in the region of interest.

fitted to the HIγS data, and the linear attenuation coefficient for each beam energy

was obtained and listed in table 5.4.

E_γ	μ (cm^{-1})
9.38	0.273(6)
9.50	0.273(6)
9.70	0.274(6)
9.80	0.275(6)

Table 5.4: Copper Attenuation Coefficients: The calculated linear attenuation coefficients for the HIγS attenuators are listed.

Intensity Extrapolation Multiple NaI measurements were taken in succession using varying thicknesses of copper attenuators, as listed in table 3.1. The rates recorded in the NaI(Tl) were corrected using the same methods as listed in the previous section. After this, the following relation holds true

$$\ln(R_{\mathrm{NaI}}) = -\mu x + \ln(I), \tag{5.1.2.4}$$

where x is the copper thickness, R_{NaI} is the corrected NaI(Tl) count rate, and I is the unattenuated beam intensity incident in the OTPC.

For each series of measurements, of varying thickness at a given beam energy, $\ln(R_{\mathrm{NaI}})$ was plotted against copper thickness x. A linear model was fitted to these data using a fixed value of μ, taken from table 5.4. An example of this analysis for the E_γ=9.38 MeV data is shown in figure 5.7. The extracted intercept C was used to obtain the unattenuated TPC intensity, as $I = \exp(C)$. Uncertainty propagation was performed using Monte Carlo techniques, incorporating both the statistical uncertainty from the fit and the uncertainty in μ.

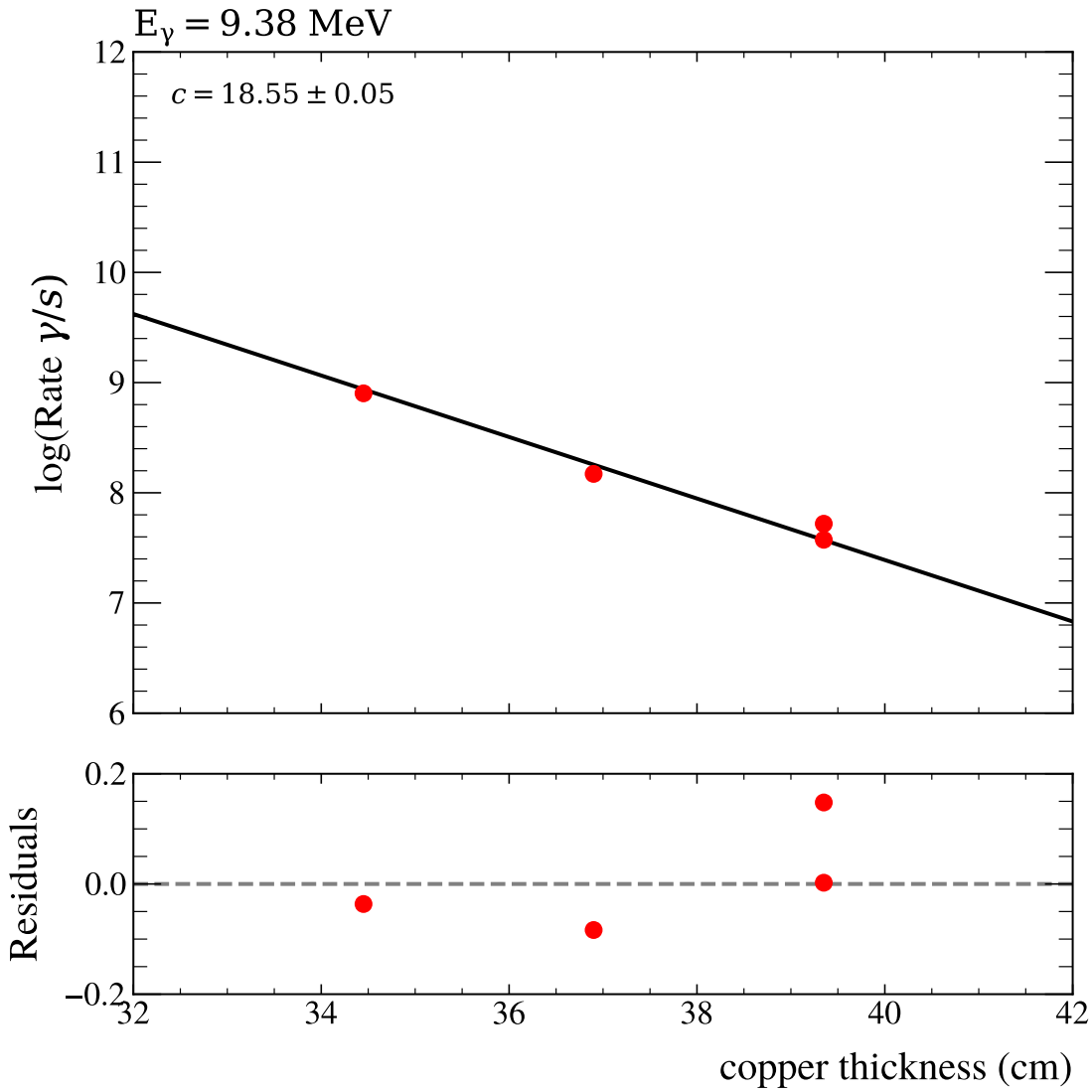

Figure 5.7: Beam Intensity Extrapolation. Upper: The log(Rate) as measured in the NaI(Tl) detectors is plotted as a function of copper attenuator thickness. These data are fitted with a linear model, fixing the gradient with μ values from table 5.4, to extract beam intensity at zero attenuator thickness. **Lower:** This panel shows the residuals from the fit in the upper panel.

Beam intensity. Figure 5.8 compares the absolute beam intensities obtained using this attenuation method with those derived from the paddle method. The large errors from the attenuator method are attributed to the relatively high uncertainty in the copper attenuation coefficients and the limited number of measurements at too few different copper thickness values. As such, the paddle method was used where possible.

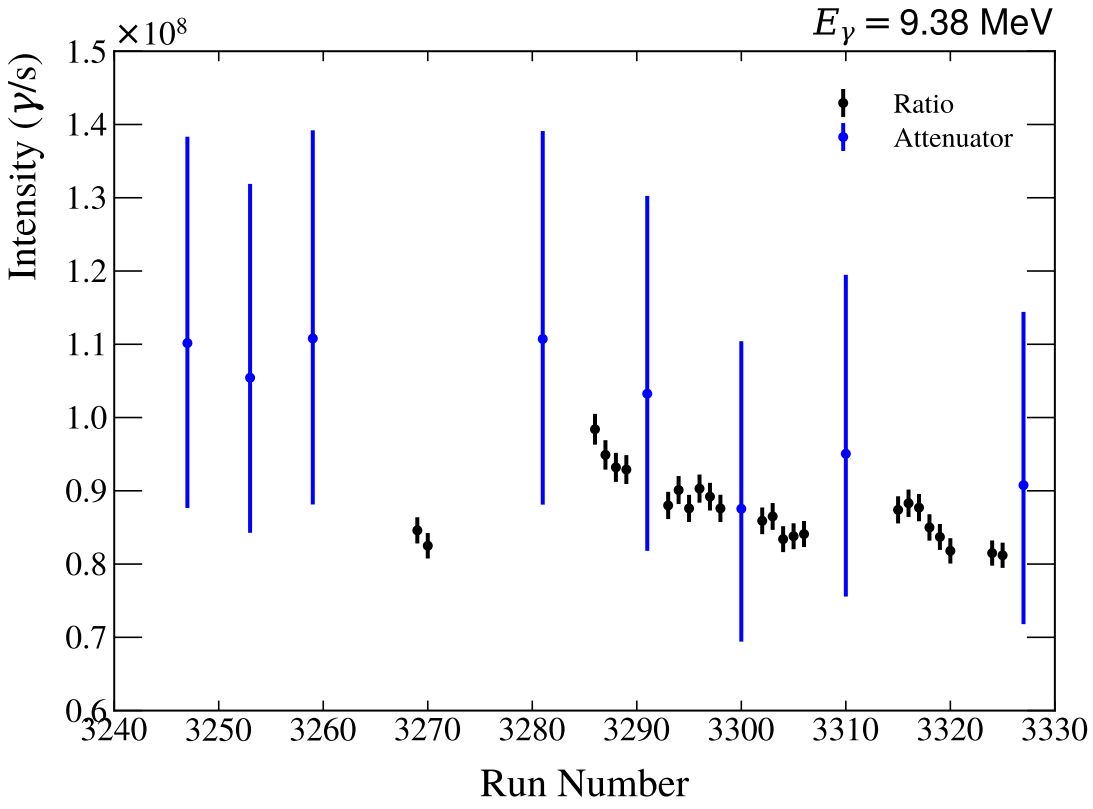

Figure 5.8: Comparison of Beam Intensity Methods: Absolute beam intensity measured for different $E_\gamma = 9.38$ MeV runs, for both the paddle and extrapolation methods is shown.

5.1.3 Luminosity

As there were many beam intensity runs, a useful and practical quantity to tabulate for cross section normalisation is the total number of γ's in the beam for a given beam energy. For a single run, it is calculated as $N_\gamma = I_{TPC}\ t_{TPC}$, where I_{TPC} is the intensity measured for an OTPC run and t_{TPC} is the associated OTPC run time [3]. The total number in the beam for a whole beam energy is obtained by summing over all runs for that energy. Table 5.5 presents the final N_γ values using the paddle method, whilst table 5.4 shows results from the attenuation method.

E_γ (MeV)	N_γ	σN_γ	Percentage Error %
9.38	1.645×10^{13}	9.047×10^{10}	0.55
9.50	5.654×10^{12}	1.310×10^{11}	2.32
9.70	1.079×10^{13}	3.711×10^{11}	3.44

Table 5.5: Table of Paddle Method Calculated N_γ: Number of γ's in the beam calculated using the paddle method, and its error is listed for each beam energy.

E_γ (MeV)	N_γ	Lower Error	Upper Error	Lower Error (%)	Upper Error (%)
9.38	1.92×10^{13}	3.95×10^{12}	4.94×10^{12}	20.6	25.8
9.50	6.50×10^{12}	1.38×10^{12}	1.75×10^{12}	21.2	27.0
9.70	1.32×10^{13}	2.72×10^{12}	3.41×10^{12}	20.6	25.8
9.80	2.40×10^{12}	4.74×10^{11}	5.91×10^{11}	19.7	24.6

Table 5.6: Table of Extrapolation Method Calculated N_γ: Number of γ's in the beam calculated using the extrapolation method and its error is listed for each beam energy.

Cross sections were calculated, as detailed in appendix A.2, using $\sigma = N/\mathcal{L}$, where N is the number of events of interest, and $\mathcal{L}$ is the integrated luminosity. Here, $\mathcal{L}$ is related to the previously calculated N_γ through

$$\mathcal{L} = N_\gamma\ n\ x. \tag{5.1.3.1}$$

[3] In total E_γ=9.38 ran for 192255 seconds, E_γ=9.50 for 48072 seconds, E_γ=9.70 for 73279 seconds, and E_γ=9.80 for 101457 seconds.

Here, n denotes the number of ^{16}O targets per cubic centimetre, with x representing the active OTPC length of 20 cm. This is shorter than the full length of the OTPC, which is explained later in the data reduction section.

For the gas mixture of 80% N_2O + 20% N_2 at 100 Torr, $n = 2.8 \times 10^{18}$. Consequently, $T = 5.7 \times 10^{19}$ targets per cm^2. Using the values presented in table 5.5 when possible, otherwise using the values in 5.6, the luminosities for each run were calculated and are given in table 5.7.

E_γ	$\mathcal{L}$ (cm^{-2})
9.38	$9.3\times10^{32}\pm5.1\times10^{30}$
9.50	$3.2\times10^{32}\pm7.4\times10^{30}$
9.70	$6.1\times10^{32}\pm2.1\times10^{31}$
9.80	$1.4\times10^{32}{}^{+3.3\times10^{31}}_{-2.7\times10^{31}}$

Table 5.7: Table of calculated integrated luminosities: Luminosity values for each nominal beam energy for the OTPC analysis.

5.2 Track Reconstruction

This section is split into four main components. First, the standard image-processing procedure for isolating tracks induced by (γ, α) reactions is given. Second, the calibration procedures for converting PMT-measured time bins and CCD-measured pixels to physical track lengths in mm are described. Third, methods for extracting the in-plane angle, α, the out-of-plane angle β, the total track length, and the approximate vertex position are presented. Finally, energy and angular resolutions are discussed.

5.2.1 Image Processing

This analysis step aimed to isolate the track in the CCD image, which was optimised for ^{16}O photo-dissociation events. The CCD in the OTPC uses an 8-bit camera to capture grey-scale images of the x-z horizontal plane. This is triggered by a leading-edge discriminator, set to 800 keV on the anode grid.

At the start of each run, a blank exposure is taken to obtain a reference image for background subtraction. This so-called "flat-field" correction is applied to all subsequent events, accounting for both overactive pixels and ambient light leaking into the optics chain. An example of a corrected image is shown in figure 5.9A.

To optimise processing time, the image was compressed by a factor of four. This is shown in figure 5.9B. Using the compressed image, the average background value and standard deviation were extracted. Then, a threshold was set at six standard deviations above the mean background level. The resulting image is shown in figure 5.9C. In order to isolate the charge belonging to the main particle-track, a recursive clustering algorithm was used. The image was scanned with a 3×3 grid, and any pixels with fewer than five non-zero neighbours were set to zero. The cleaned image, shown in figure 5.9D, served as a mask, which was applied to the flat-field-corrected image to restore the original image's resolution (figure 5.9E). Next, all charge outside of the largest cluster was set to zero. Then, a final finer recursive scan was applied to the restored image. The fully cleaned track is shown in figure 5.9F.

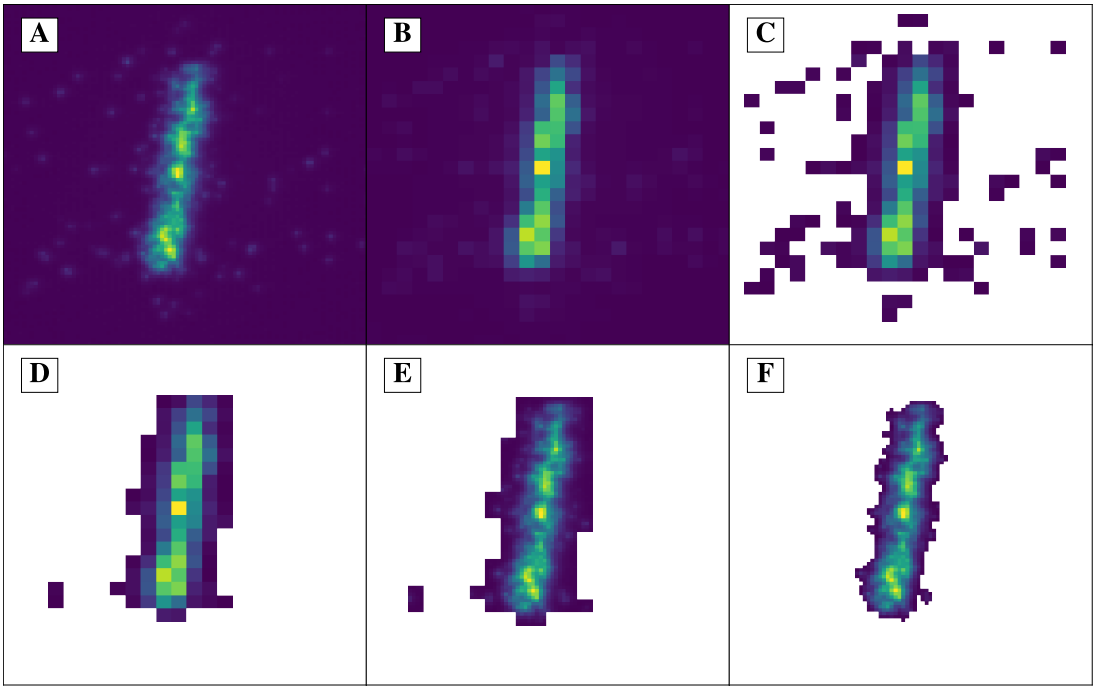

Figure 5.9: Image Processing Steps in the OTPC: A series of CCD images illustrating the image processing steps used to isolate the track in the OTPC are shown. These steps are discussed in the text. This figure was taken from reference [178].

5.2.2 Calibration

To extract physically meaningful quantities from the CCD image and PMT spectra, a calibration was needed to convert the native pixel and time-bin units to lengths in mm.

CCD calibration

The CCD "pixel-to-mm" calibration was obtained through a so-called "z-scan", where a mono-energetic Gd-148 ($E = 3.18$ MeV) α source was held inside the OTPC active volume using a magnetic source holder and moved along the z axis (beam axis). Images were taken at four different z-positions. For each z-position, the corresponding pixel associated with the origin of the alpha track in the CCD image was identified. A plot was made of the known z-position in mm against the reconstructed source position in the CCD image in pixels. The conversion factor, the gradient of the linear fit to the data, is found to be $f_{Im} = 0.74(1)$ mm per pixel, as shown in figure 5.10.

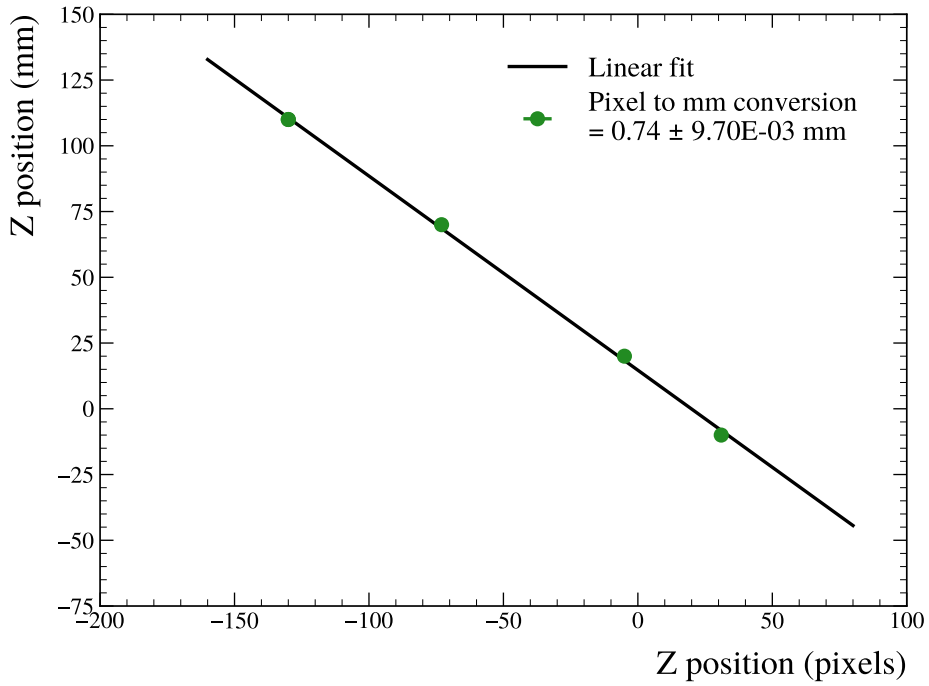

Figure 5.10: Z-scan OTPC CCD Calibration: Plot of the known z-position of the alpha source holder in mm on the vertical axis. Against the extracted z-position of the source in pixels, obtained from the CCD image on the horizontal axis. A linear fit was used to determine the pixel-to-mm conversion factor from the slope.

Time Calibration

The PMT "time-to-mm" calibration was obtained using the `Magboltz` code. The drift velocity of electrons in the gas was found to be $v_{\text{drift}} = 11.58\mu$m/ns. As the PMT signal was read out using a digitiser with a 100 MHz sampling rate, and the PMT channels have $10ns$ per bin, the multiplicative channel-to-mm calibration factor was found to be $f_{Ti} = 0.1158$ mm per time-channel.

5.2.3 Feature Extraction

The following methods were used to reconstruct the events in the OTPC, in order to separate reaction channels and extract physical observables. As mentioned, in the OTPC the angles α and β are reconstructed, as they are natively bound to the x−y plane and z direction, respectively. However, due to poor resolution in the drift direction (see section 5.2.4) both angles were extracted from the CCD image.

The α angle is a rotation in-plane, as shown by the red fit line on the left-hand side of figure 5.11. The out-of-plane angle, β, was obtained by fitting Bragg curves, calculated using `SRIM`, to the projection of the charge in the CCD along the direction of the track. This is shown in the right-hand side of figure 5.11.

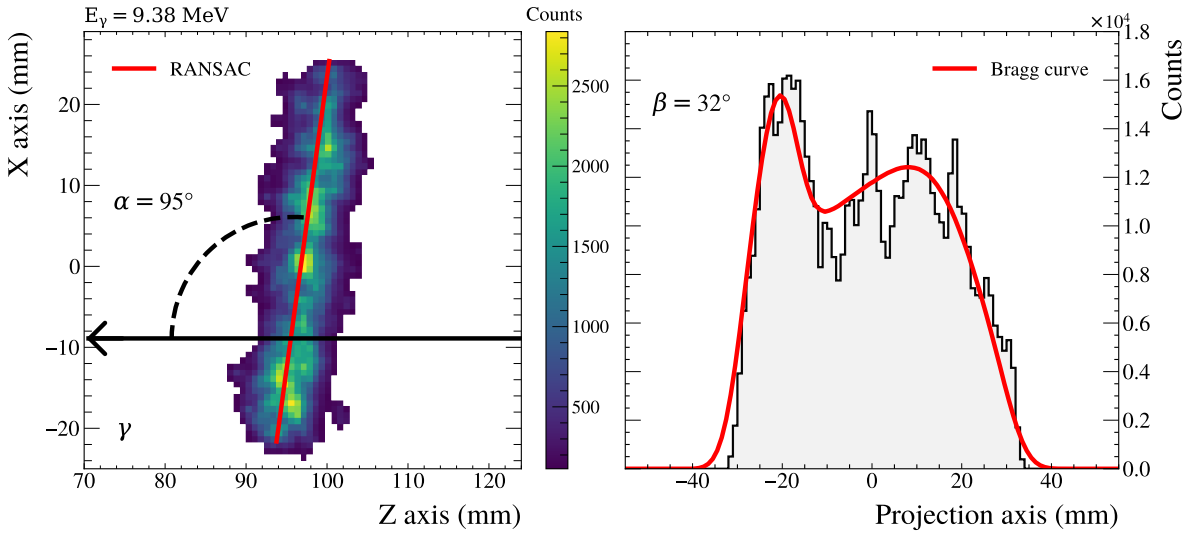

Figure 5.11: Angle Reconstruction in the OTPC. Left: The reconstructed α angle is obtained using RANSAC fitting on the charge in the CCD. **Right:** The reconstructed β angle is obtained by fitting Bragg curves to the image projection along the RANSAC line. The data shown were obtained at $E_\gamma = 9.38$ MeV. This figure was taken from reference [178].

RANSAC Fitting

To extract the α angle from the CCD image (using the CCD image at the stage shown in figure 5.9F), a straight line was fitted using a Random Sample Consensus (RANSAC) algorithm. The RANSAC algorithm iteratively performed a χ^2 minimisation on random subsets of the data. Each fit is scored based on the number of inliers from the full dataset. This method effectively ignores any remaining outliers or noise in the image. The 1σ error on the gradient was extracted using standard χ^2 methods. A successful fit is shown as the red line in the left panel of figure 5.11.

Bragg Curve Fitting

The charge in the CCD image was projected onto the RANSAC-fitted line, providing a one-dimensional model of the Bragg curve of the ion(s) of interest. The projection was fit using χ^2 minimisation with the lineshapes generated using `SRIM` energy-loss tables. Before fitting, these lineshapes were convolved with the OTPC image resolution (discussed later). A successful fit is shown as the red line in the right panel of figure 5.11.

Track Length & Vertex Extraction

To extract the track length in the CCD image, the charge in the image (at the stage presented in figure 5.9E) was projected onto the RANSAC-fitted line. The total track length was extracted by finding the first and last bin above 10% of the maximum charge deposited. A similar method of track length extraction was used for the PMT waveform, with a threshold of 15% of the maximum charge deposited. The lengths extracted from the image and the PMT were added in quadrature to obtain the total-track length in mm.

As an approximation, the vertex location in the $x - z$ plane was taken to be the brightest pixel remaining in the CCD image after cleaning. It was found, from `SRIM` calculations, that the vertex would consistently lie within a few mm of the maximum energy deposition of the heavy ion (^{12}C).

5.2.4 Resolutions

A mono-energetic alpha source, ^{148}Gd, was used to extract various detector resolutions. Figure 5.12 shows four plots corresponding to the "flattest" $\beta = 0$ event. This was identified by iterating over all events and finding the one with the narrowest time-projection and a $\beta = 0$ assignment, determined via an α-particle lineshape fit to the image projection.

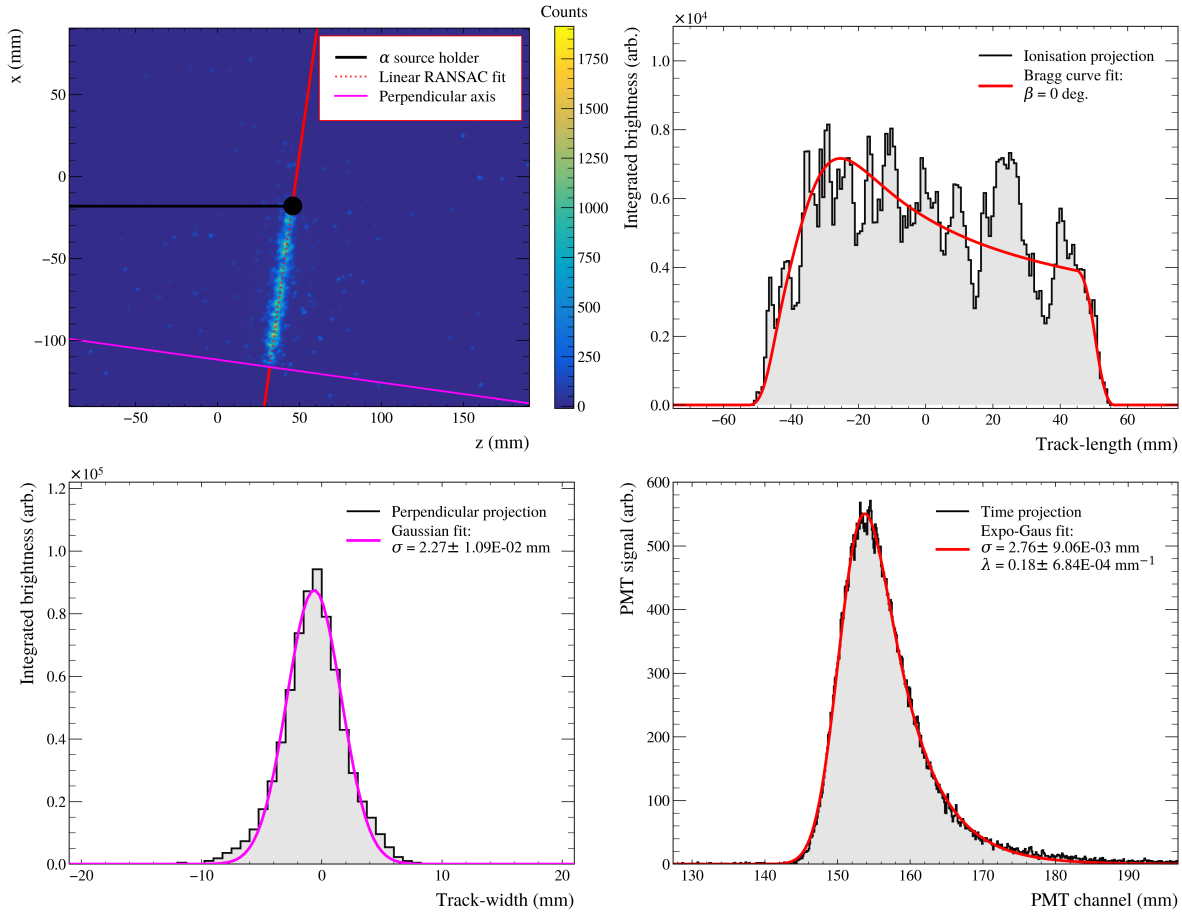

Figure 5.12: Flat α-track Reconstructed in the OTPC. Top-left: The CCD image of an α track is shown. The RANSAC-fitted line is in red, the line perpendicular to this is in pink, and the source holder is added in black for illustration. **Top-Right:** The charge in the CCD image is projected onto the RANSAC line, resulting in the experimental Bragg curve seen here. The so-called "towers" in this projection are due to the bundles of fibre-optic cables that direct the light in the opto-electronic chain. This projection is fitted with the Bragg curve lineshapes obtained from `SRIM` to extract the out-of-plane angle, β. **Bottom-left:** The charge in the CCD image is shown projected onto the pink line. This is fitted with a Gaussian distribution to extract the image resolution. **Bottom-right:** The time-projection of the same event is shown here, fitted with an exponentially-modified Gaussian to extract the time resolution and decay constant.

Figure 5.12 a shows the CCD image of an α track, with the source holder in black added for illustrative purposes. The charge from this track was projected onto the red RANSAC fitted line, yielding the experimental Bragg curve in figure 5.12 b. This projection was fit with α-track Bragg curve lineshapes, smeared by the image resolution, σ_{Image}, to obtain the $\beta = 0$ angle assignment.

The image resolution was found by examining the widths of tracks in the CCD image, as shown in figure 5.12 c. This was obtained by projecting the image onto the axis

perpendicular to the RANSAC line (pink line in figure 5.12 a). The image resolution was obtained by fitting this projection with a Gaussian profile; this procedure was done for many events, shown in figure 5.13, and the average was found to be $\sigma_{Image} = 2.5$ mm.

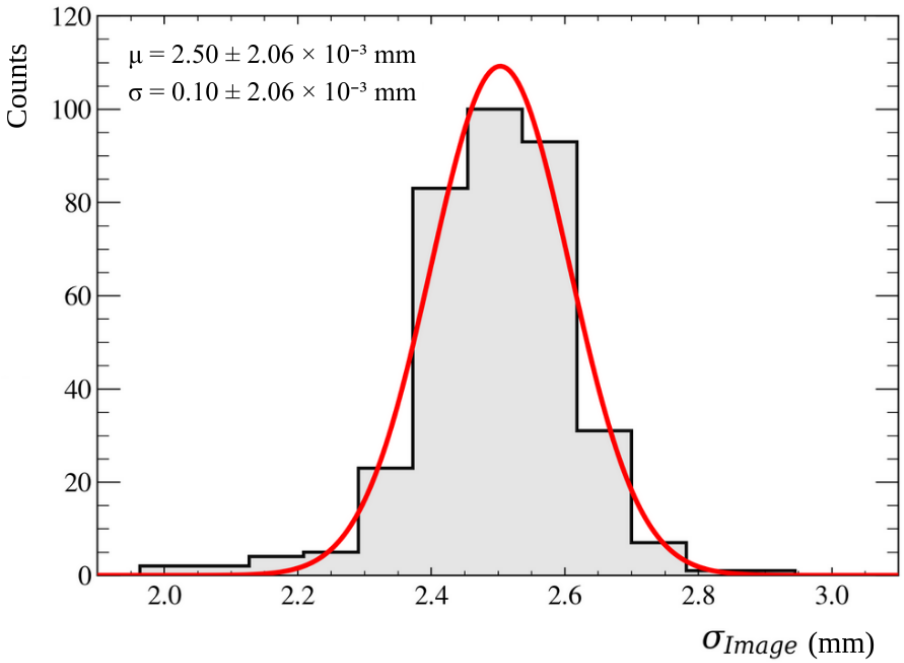

Figure 5.13: Resolution from α particle track widths: A histogram of individual σ_{Image} values obtained by Gaussian fits to a large sample of α particle track widths.

Finally, the time projection of the "flattest" track is shown in figure 5.12 d. This was fitted with an exponentially modified Gaussian to extract σ_{Time} and the decay parameter λ [4]. The time resolution was found to be $\sigma_{Time} = 2.76$ mm.

Energy Resolutions

In the OTPC, there are several different metrics related to the energy deposited; these include integrated PMT signal, integrated CCD charge, grid signal, and total track length. The resolution of each of these was determined using the mono-energetic alpha source, as shown in figure 5.14. The resolutions are reported as absolute and fractional values. Here fractional resolution is defined as FWHM/$\mu = \sigma\frac{2\sqrt{2\ln 2}}{\mu}$, where σ is the

[4]Note that in the CO_2 data [176] the time resolution was found to be Gaussian in shape. In N_2O, on the other hand, the time projections were all found to be smeared by an exponential tail. This is likely due to the fact that N_2O has a large electron attachment cross section, causing electrons to be removed from the track during drift.

Gausssian standard deviation and μ is the mean. Far and away, the best measure of energy in the OTPC is the track length. In the data analysis, all of these metrics were used to isolate the events of interest.

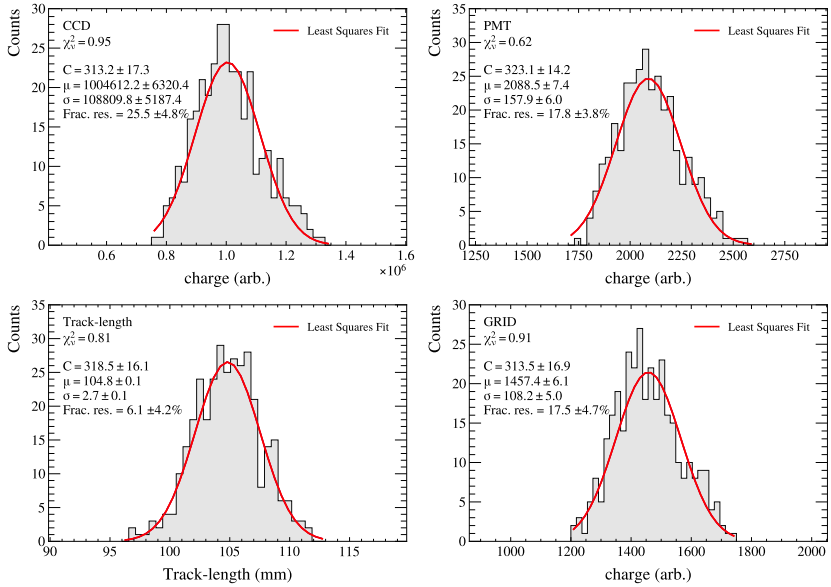

Figure 5.14: Raw Energy Resolutions in the OTPC: Absolute and fractional resolutions are shown for multiple different energy metrics extracted from the OTPC. **Top-left:** Integrated CCD charge is shown with a fractional resolution of 26%. **Top-right:** Integrated PMT signal is shown with a fractional resolution of 18%. **Bottom-left:** Total track length is shown with a fractional resolution of 6%. **Bottom-right:** Grid signal is shown with a fractional resolution of 18%.

Angular Resolution

Properly quantifying angular resolution is an essential step in the analysis, as the key physics are extracted from the angular distributions. Angular resolution subtly alters the shape of the measured angular distributions and must be accounted for when fitting them.

Resolution in α. To evaluate the α angle resolution "beam" data were examined. This is because the α particles from the calibration source were emitted in a narrow in-plane cone from the source holder. The resulting α range covered was relatively narrow. To obtain the resolution in α, the RANSAC fitting procedure was performed multiple times on a group of the same events to determine the range of solutions it converged to, and whether this had β angle dependence. Figure 5.15 shows this procedure, for $E_\gamma = 9.38$ MeV, for

β angles within the range 20-40°. The reasons for considering only this range in β are discussed later. It can be seen that the error on the α fit does not vary much with α itself in any systematic way. It is also shown that the average error in α does not vary much with β. The error-weighted average value of σ_α was found to be 3.4°.

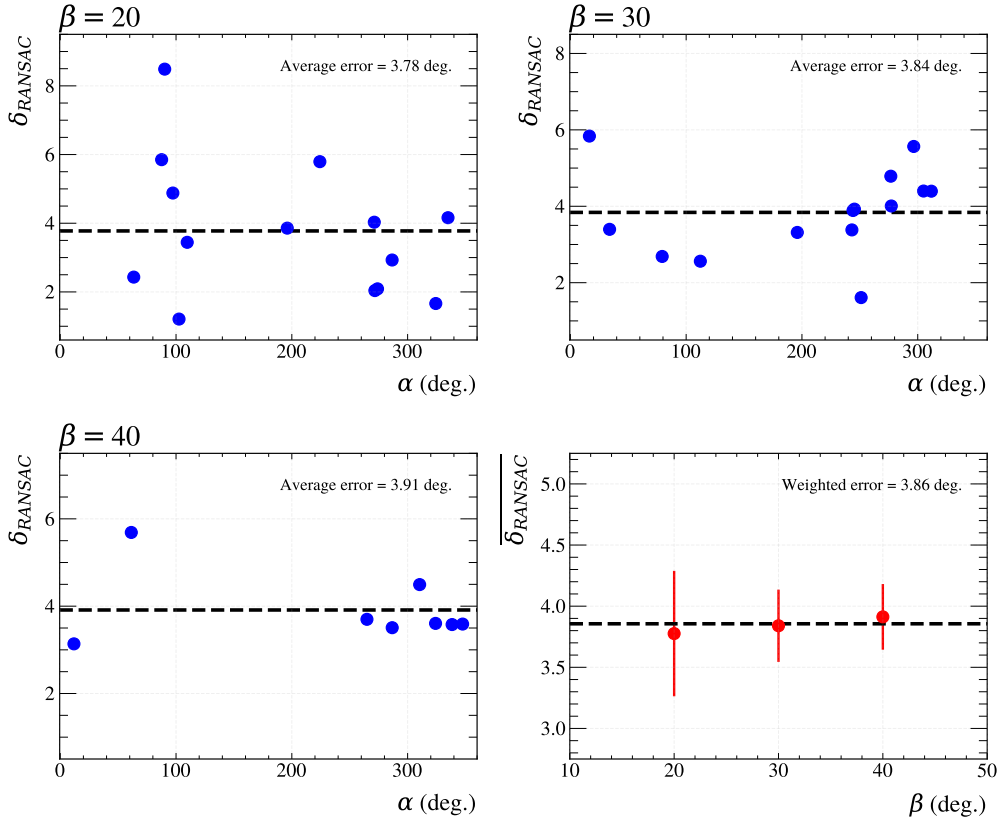

Figure 5.15: Tracking α Angle Resolution in the OTPC: The first three panels show the average reconstructed α value against its error. This was obtained by fitting the same events multiple times with the RANSAC procedure, for different β angles. The average α error at each β angle is obtained through a linear fit (black dotted line). The last panel shows the average α error as a function of β. The linearity of this confirms that the α error does not vary with β in the considered range.

Resolution in β. To ascertain the error on the out-of-plane angle β, the α-source calibration data were used. The α-particle lineshape (Bragg curve) for different β angles was fitted to the track projection and varied until the best fit was obtained. To extract errors on β a normalised χ^2 profile, χ^2/χ^2_ν, was used. This scaling was done to account for

unrealistic χ^2 scores caused by the "towers" in the CCD data[5]. Absolute 1σ errors were obtained by stepping in β until χ^2/χ^2_ν changed by one unit. Example profiles are shown in figure 5.16 for different β angles. The average of the lower and upper errors was taken.

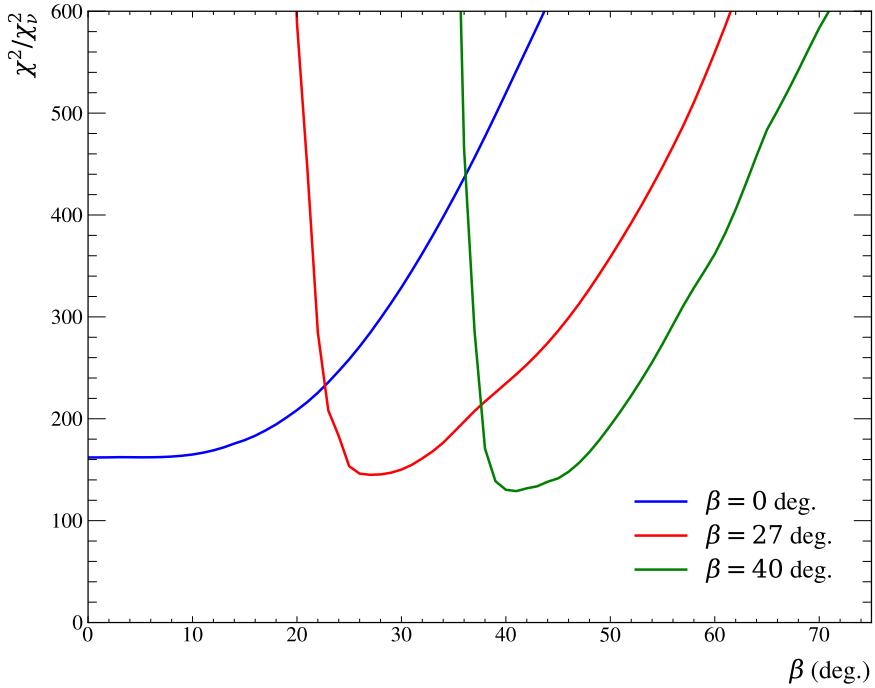

Figure 5.16: The β Angle Resolution Extraction Procedure: The figure shows three normalised error profiles obtained when fitting Bragg-curves to extract the out-of-plane angle β. The goodness-of-fit metric is defined as χ^2/χ^2_ν, this was due to unrealistic χ^2 scores caused by artefacts in the CCD image.

What is observed from figure 5.16 is that at low β there is a reduction in sensitivity to changes in β. This is made more evident by tracking the average β error as a function of β for many events, as is shown in figure 5.17. This is expected, as the β angle depends on the cosine of the out-of-plane gradient; a slight change in the gradient near $\beta = 0$ results in a significant change in the extracted angle. It was determined that at $\beta < 20°$, the extraction procedure had insufficient sensitivity to β. Thus, a lower limit was placed here when analysing beam data. The average β resolution for data above $\beta = 20$ degrees was found to be 1.2°.

[5]The towers in the image are due to the bundling of the fibre optic cables that direct light onto the CCD camera. This results in light buckets that produce unphysical hotspots in the image [140, 176]

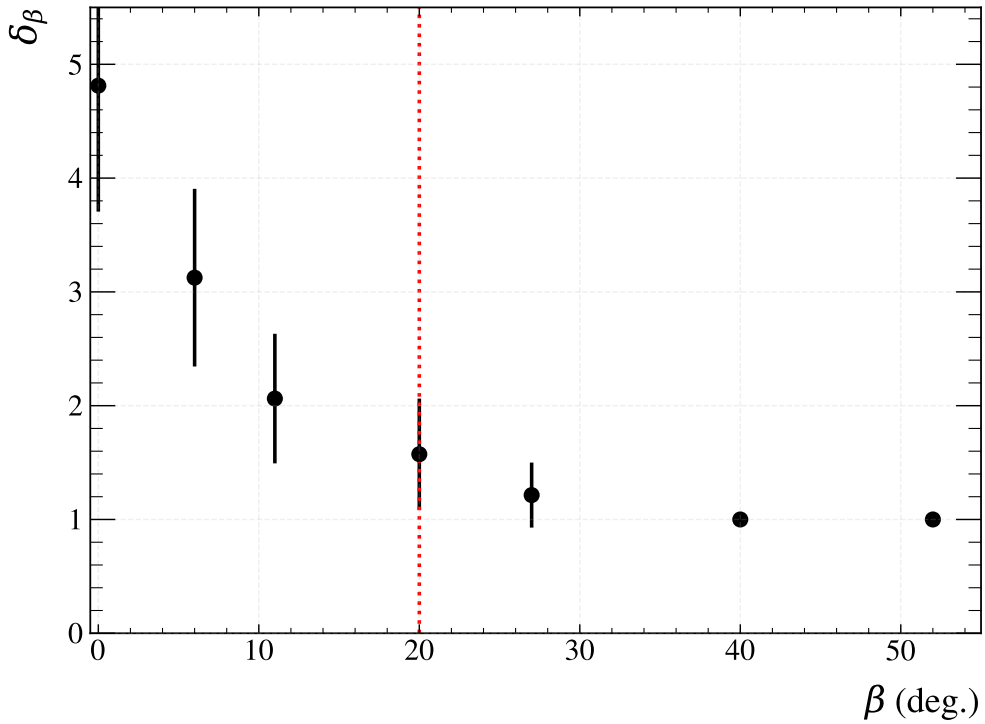

Figure 5.17: Tracking β Angle Resolution. The extracted β error is shown as a function of β angle, as determined from α-source calibration data. The red dotted line at $\beta = 20$ indicates the threshold set to guarantee good angular resolution.

Efficiency in α. For large β angles, the ability to reliably extract the α angle diminishes, as the visible track length in the detector plane becomes too short.

At large β values, the visible in-plane track length reduces to the point where it is impossible to reliably extract the α angle since the direction of the track becomes ambiguous. When analysing angular distributions of beam data, an upper limit of $\beta = 42°$ was set, as was done in previous work [97, 139]. This threshold was determined by manually analysing a sample of events and noting whether the α angle extracted was reliable. Figure 5.18 presents these data, showing the α angle extraction efficiency for different β values. The figure shows the percentage of confidently-assigned α angles as a function of β angle. Beyond $\beta = 42°$, the α efficiency drops significantly [6].

[6] It should be noted that due to solid angle effects, few events are expected as β approaches 90°, so this cut is not overly restrictive in terms of cutting out valid events.

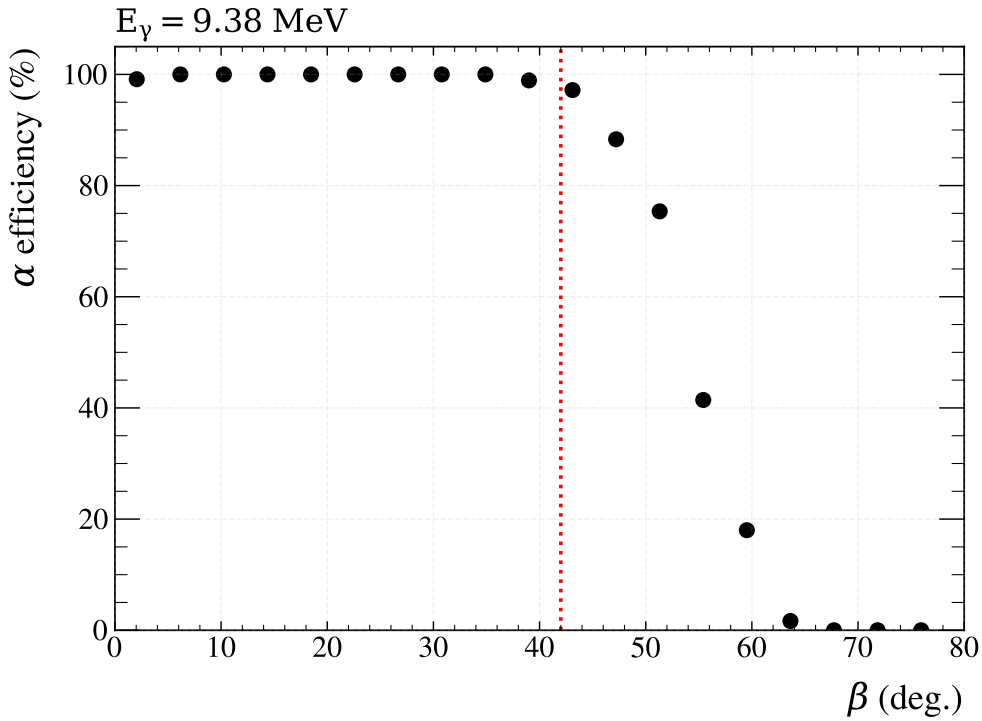

Figure 5.18: Upper Limit of β Angle: The ability to extract the in-plane angle α is shown to drop considerably after $\beta = 42°$, this defines the upper limit on β.

Resolution in θ. The extracted angle-independent errors on reconstructed lab angles β (1.2°) and α (3.4°) are propagated to θ, using standard partial differential methods. Figure 5.19 shows the error on θ for each combination of α and β assuming the values listed above. It is noted that the error on θ does indeed vary depending on the reconstructed OTPC angles. Weighting this distribution by the experimentally observed events yields the estimated average θ errors listed in table 5.8. However, these are not used in the analysis and are only included as an indication of resolution. Later, to correct for the shape of the fit function when analysing the θ angular distributions, a Monte Carlo efficiency correction is applied that accounts for the varying resolution in θ.

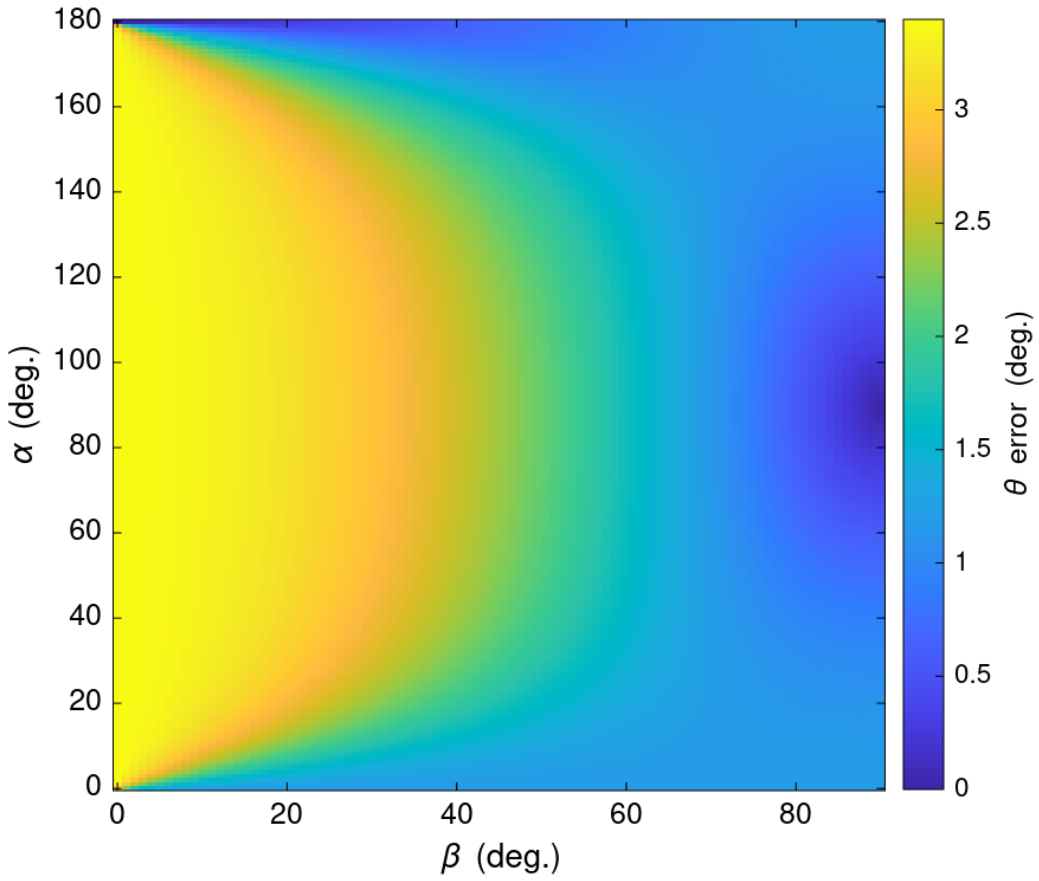

Figure 5.19: Reconstruction Errors Propagated to θ: The heatmap shows the error on θ for each combination of α and β, assuming the errors on those angles as given in the text.

E_γ (MeV.)	1-$\sigma\theta$ error (deg.)
9.38	2.77
9.50	2.77
9.70	2.58
9.80	2.40

Table 5.8: Table of θ Resolutions: The approximate average θ resolution extracted empirically from data is given.

5.3 Event Selection

This section identifies sources of background and how they manifest in the data. It then outlines the software and fiducial volume cuts implemented to isolate a clean sample of ^{16}O events.

5.3.1 Event Classifications

The chosen gas mixture, N_2O+N_2, introduces several sources of background. Within the considered energy range, background events are primarily due to various photodissociation reactions, including (γ, α), (γ, n), and (γ, p) reactions, as well as some cosmic-ray-induced interactions.

Figure 5.20 shows the open photo-dissociation reaction channels, grouped by target nuclei on the horizontal axis and reaction Q-values on the vertical axis. The reactions are colour-coded according to their decay products: α decays (blue), neutron decays (red), and proton decays (green).

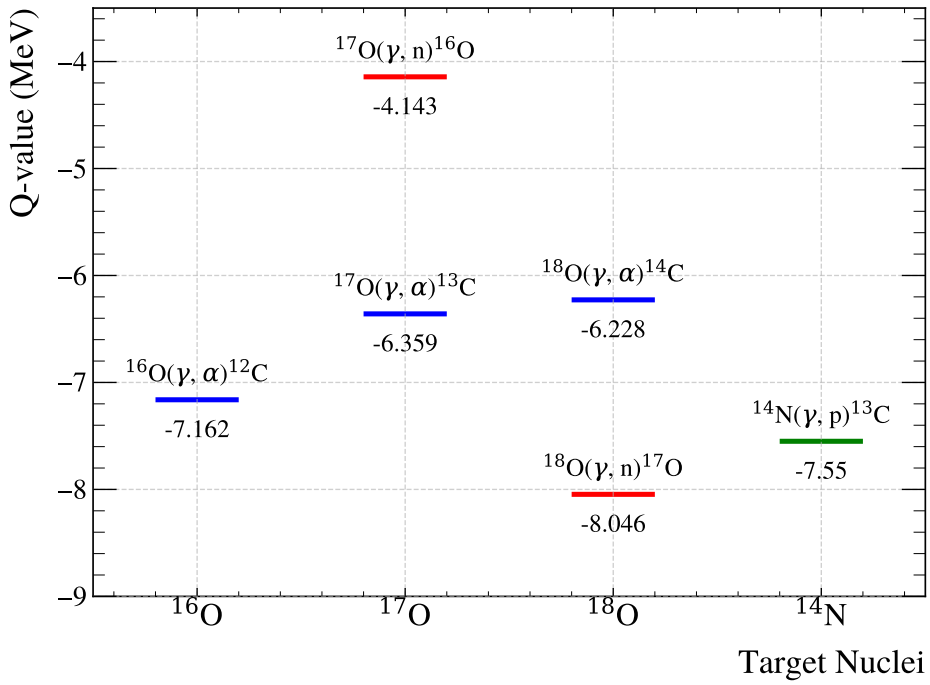

Figure 5.20: Open Photo-dissociation Reaction Channels: All open photo-dissociation reaction channels are listed with their Q-values, as a function of Target nuclei: α decays in blue, n decays in red, and p decays in green.

Each event category has distinct characteristics; these features were used to remove the background events through various cut conditions. Each type of background observed is listed below, with examples of how they manifest are shown in figure 5.21.

- (γ, n) **Reactions:** These were effectively removed by online triggers during the experiment. In these processes, the neutron carries the majority of the energy from the reaction. This leaves the recoiling heavy ion with minimal energy, which is typically below the 800 keV grid trigger.

- (γ, α) **Reactions:** The background oxygen isotopes ($^{17/18}$O) are distinguishable from ^{16}O due to their different Q-values, which result in different energy depositions and track lengths. These differences were exploited in offline software cuts.

- **Cosmic ray events:** A small fraction of additional events observed in the detector were induced by cosmic rays. Unlike beam-related events, cosmic events show no correlation with the beam direction and could therefore be easily identified and removed offline.

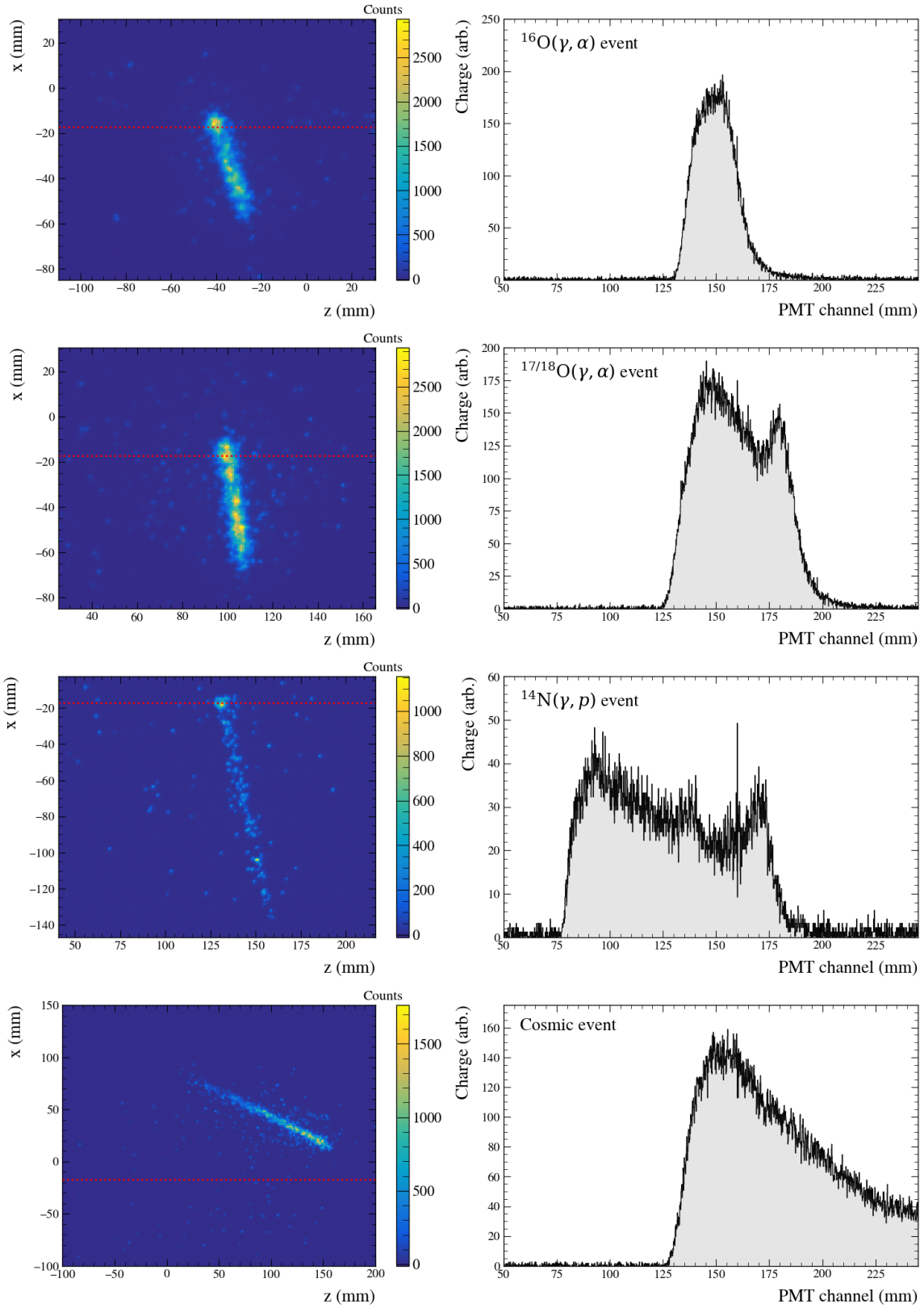

Figure 5.21: Reactions Observed in the OTPC: The CCD images and time projections associated with each common type of reaction recorded in the OTPC are shown. The red line indicates the beam's path through the detector. Categories are listed in the right panel on each row.

5.3.2 Data Reduction

All events that passed the online charge trigger (grid signal) were recorded to disk and subsequently reconstructed. Following reconstruction, the data were analysed to establish offline trigger conditions and fiducial cuts designed to isolate ^{16}O events. These selection steps are listed in the order they were applied.

Initial Selection

An initial selection was made by applying a graphical cut around two distinct features in the track-length versus grid-signal spectrum, as shown in figure 5.22. Track length here is the total track length of the event, as measured from the end of the light ion to the end of the heavy ion. The grid-signal is the charge deposited on the final Avalanche grid. The two features in the acceptance region correspond to ^{16}O and $^{17/18}$O photo-dissociation events, while most of the remaining (rejected) events correspond to ^{14}N photo-dissociation.

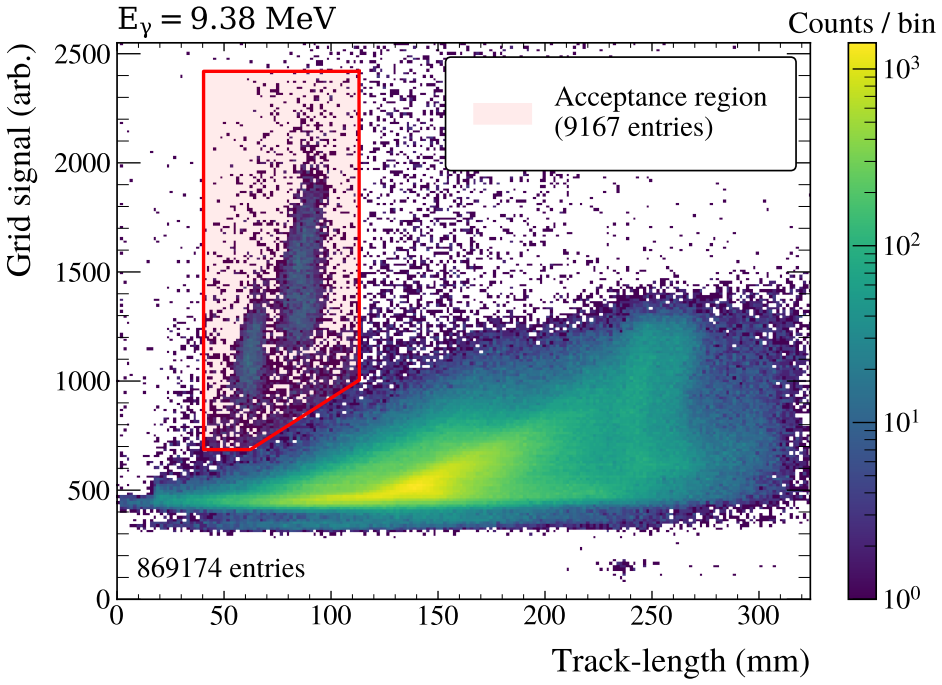

Figure 5.22: Data Cut 1) Track-length vs. Grid-signal: The spectrum shows distinct features corresponding to oxygen isotopes, and a broad region corresponding to background events. The applied acceptance region is indicated in red, and the total number of events before and after the cut is given. This figure was taken from reference [178].

Fiducial Volume

Event vertices were recorded throughout the entire length of the OTPC active volume without loss of detection efficiency. However, events that occur near the edge of the active volume, for certain scattering angles, may escape, resulting in truncated reconstructed track lengths. This means that an $^{17/18}$O photo-dissociation event, which typically has a longer track length than an ^{16}O event, may have a shortened reconstructed track length. This leads to ambiguities in the track-length spectra and, therefore, event identification. This effect is illustrated in the z-vertex versus track-length distribution shown in figure 5.23. For all beam energies, the central 20 cm region is selected, removing all events outside this region. This is to ensure that all events that occur in the extremes, where increased isotope mixing occurs, are removed.

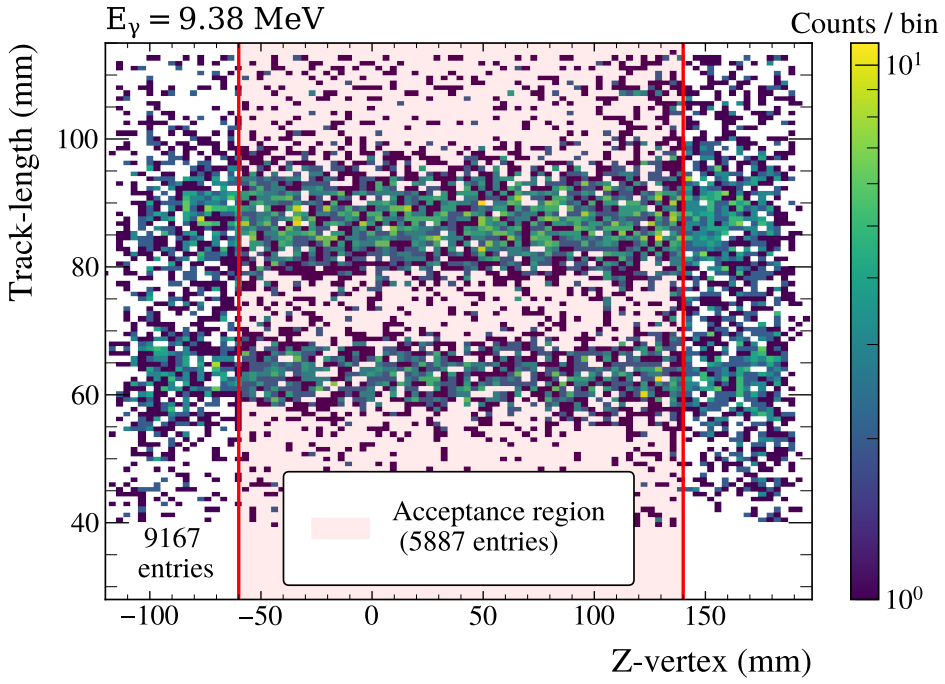

Figure 5.23: Data Cut 2) z-Vertex Cut: The vertex fiducial cut is highlighted in red. All events beyond this region are removed from the analysis, due to the increased overlap between ^{16}O and $^{17/18}$O photo-dissociation events. This figure was taken from reference [178].

CCD & Track Length Background Rejection

Further background was removed by analysing the CCD images. The proton tracks from (γ, p) events appear fragmented in the CCD images due to low gas gain and the low proton stopping power. This can be exploited using the cluster cleaned images, as the (γ, p) events will undergo more "cleaning" than the (γ, α) events. This results in an image with a much smaller remaining charge cluster, which, when integrated, yields a clear separation from the remaining (γ, α) events. The integrated CCD charge is plotted against track length in figure 5.24, with the acceptance region highlighted.

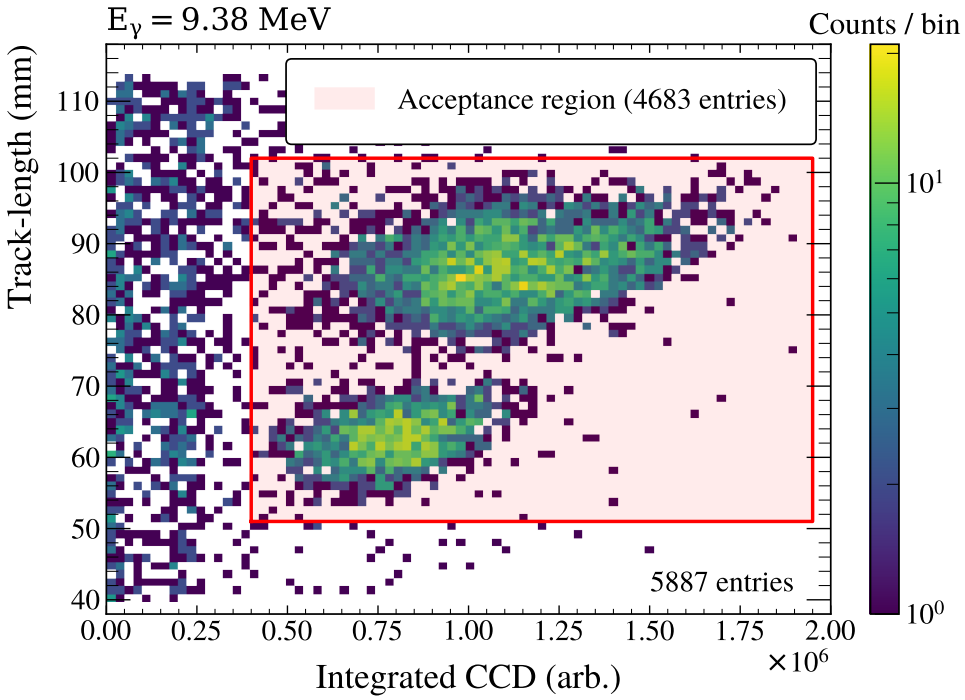

Figure 5.24: Data cut 3) CCD vs. track-length cut: Cluster-cleaned CCD charge versus track length plot showing the separation between (γ, α) and (γ, p) events. The applied acceptance region is indicated in red, and the total number of events before and after the cut is given. This figure was taken from reference [178].

Particle Identification Confirmation

To validate that the remaining events were predominantly from the photo-dissociation of oxygen isotopes, the track lengths were decomposed into temporal (out-of-plane) and spatial (in-plane) components. Figure 5.25 shows a plot of in-plane length versus out-of-plane track lengths. The theoretical predictions for all ^{16}O, ^{17}O, and ^{18}O events are overlaid in red, confirming the event selection. These calculations were based on a simple simulation that generates events across a range of α and β angles. The α+C Bragg curves for each reaction are generated both in-plane and out-of-plane, then smeared by the experimental resolutions. Then, the track lengths were extracted using the same method as applied to the real data.

Furthermore, the agreement between predictions and the data confirms that the correct drift velocity, obtained from `Magboltz`, was used. If an incorrect drift velocity had been applied, the data would appear systematically longer or shorter along the time axis compared to the predictions.

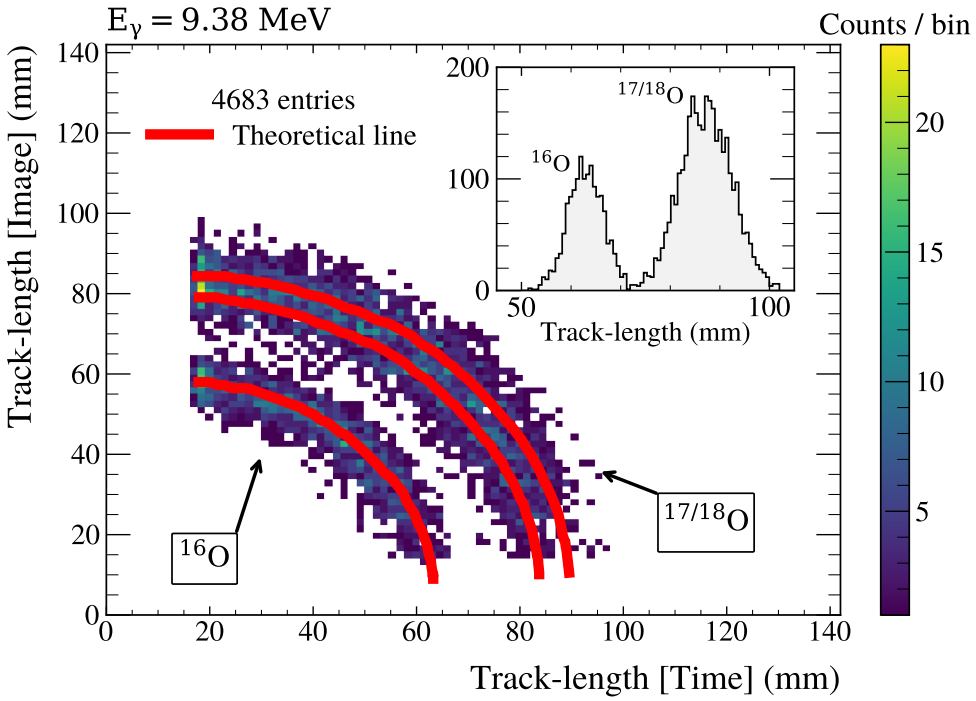

Figure 5.25: Oxygen Isotope Confirmation: The decomposed track lengths are shown compared with theoretical predictions, indicating correct isotope identification. Due to their relatively similar Q-values ^{17}O and ^{18}O events are unresolved. The inset shows a histogram of the total track length. This figure was taken from reference [178].

Grid vs Track Length Isotope Selection

The confirmed region of ^{16}O was selected by gating on the grid-signal versus track-length plot, as shown in figure 5.26. To obtain this acceptance region, the data are first projected onto the x-axis and fit with a Gaussian. Then, after placing a centroid $\pm$ 3σ cut based on this fit, the remaining data were projected onto the y-axis. This distribution was fitted with a Skewed Gaussian plus linear background, and a further centroid $\pm$ 3σ cut was placed based on the second fit. The resulting acceptance region is highlighted. This plot clearly demonstrates a virtually background-free isolation of the ^{16}O photo-dissociation reaction events.

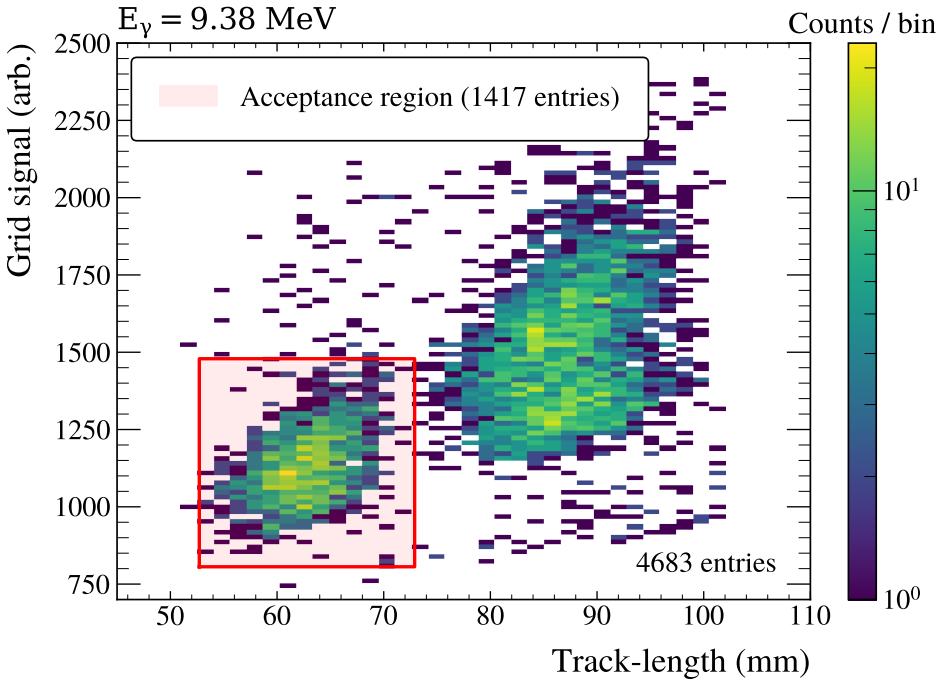

Figure 5.26: Data Cut 4) Grid vs. Track-length Cut. A cut is placed, highlighted in red, to isolate the ^{16}O photo-dissocation events from the other oxygen isotopes. The total number of events before and after the cut is given. This figure was taken from reference [178].

Beam Position Cut

A final cut was based on an event's spatial position relative to the beam axis. Figure 5.27 a shows the x-vertex versus z-vertex distribution of all remaining events, illustrating the beam's path through the detector's active volume. The x-vertex projection, shown in figure 5.27 b, was fitted with two Gaussian functions sharing a common centroid (μ) parameter. This model accounts for non-physical broadening in the vertex reconstruction, attributed to the tower effects in the CCD image. A selection of $\mu \pm 6\sigma_2$ was applied to remove events far from the nominal beam position, where σ_2 is the standard deviation of the narrower peak. This acceptance region is shown in figure 5.27 a.

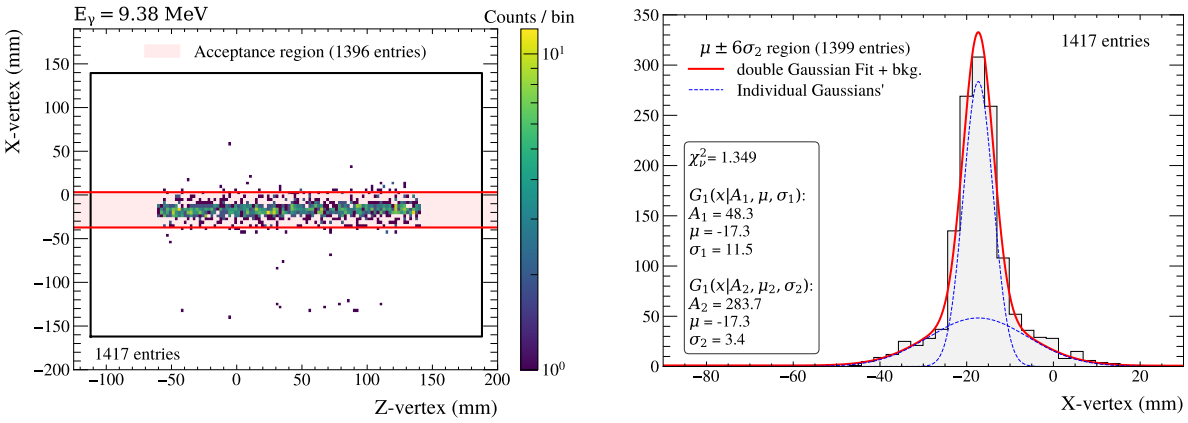

Figure 5.27: Data Cut 5) Beam Position. Left: The distribution of event vertices is shown across the detector's active volume, with the acceptance region highlighted in red. This figure was taken from reference [178]. **Right:** The projection of this distribution onto the y-axis is shown. This projection is fitted with a model, as described in the text, to ascertain an appropriate cut value.

Overview

An overview of the reduction in event counts for the $E_\gamma = 9.38$ MeV dataset is shown in figure 5.28. The plot shows both the absolute number of remaining events after each cut and the percentage remaining after each cut.

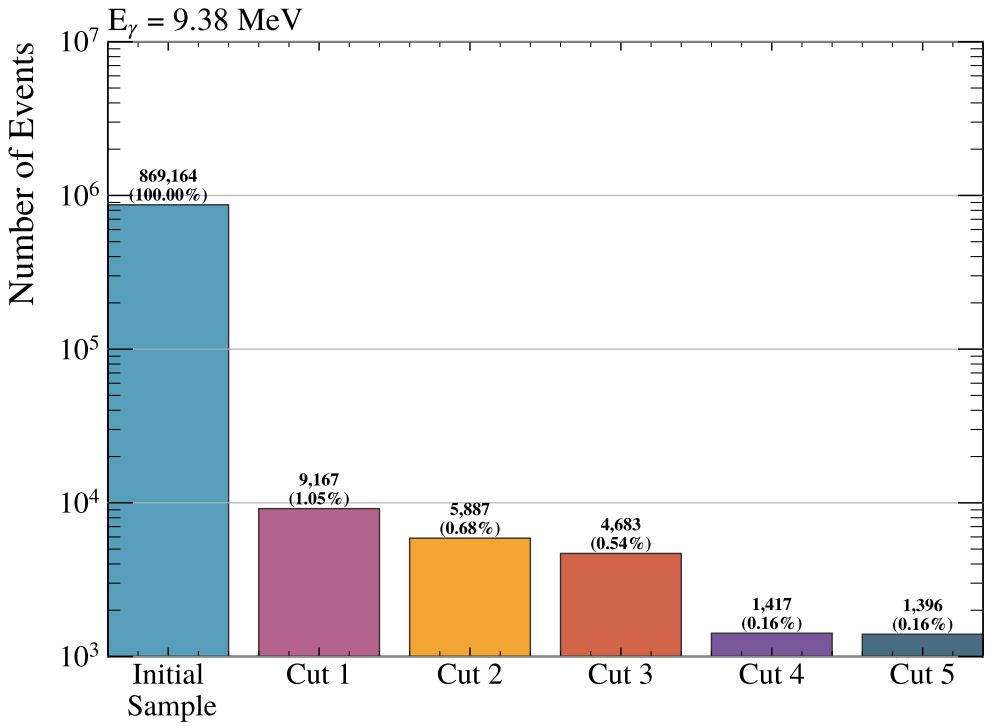

Figure 5.28: OTPC Event Reductions: This chart presents the number of events remaining after each sequential cut applied to isolate the $^{16}O(\gamma, \alpha)$ events. The cuts on the x-axis are: (1) Initial Selection, (2) Fiducial Volume, (3) CCD & Track Length Background Rejection, (4) Grid vs Track Length Isotope Selection, (5) Beam Position Cut.

5.4 Energy Scale

5.4.1 Calibration

For each event, the total track length is obtained by adding the length in the image and in the time projection in quadrature. The extracted length will be greater than expected due to their resolutions (reconstruction and drift effects). Therefore, a small systematic offset from the true track length is expected. The total track-length spectra obtained for $E_\gamma = 9.50$ MeV is shown in figure 5.29.

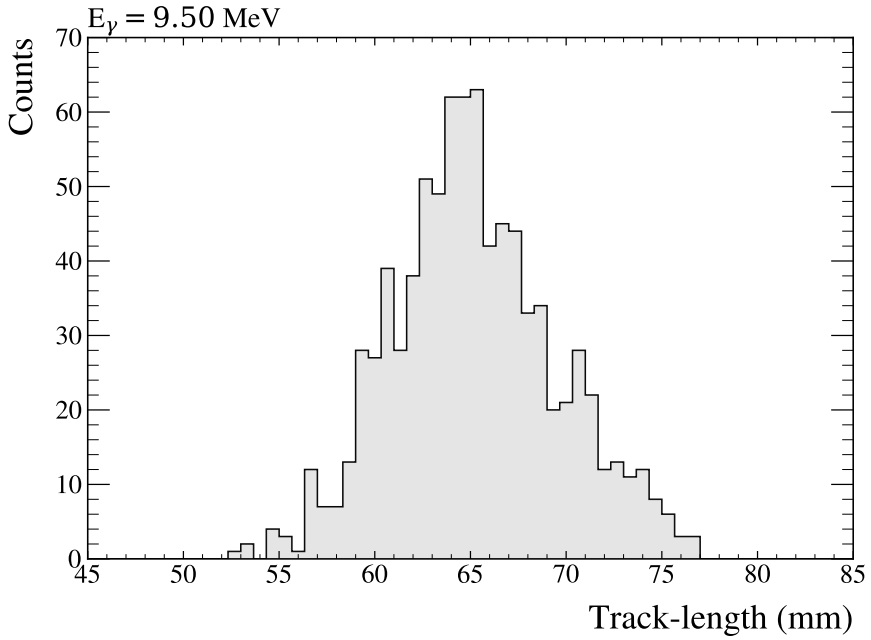

Figure 5.29: Raw Track Lengths: The total track-length spectra for ^{16}O events obtained at $E_\gamma = 9.5$ MeV is shown.

Kinematic Conversion

For each event, the total track length and lab scattering angle θ_{lab} are reconstructed. This lab angle is boosted to the centre-of-mass using the mean beam energy from the HPGe fits, obtaining θ_{cm}. Due to the poor CCD image resolution, the ^{12}C portion of the track manifests as largely co-linear, so it has little effect on the extraction of the scattering angle.

To calculate the true energy of an event, one needs to calculate the track length of only the α portion of the track. Exploiting 2-body kinematics of the $^{16}O(\gamma,\alpha)^{12}C$ reaction and `SRIM` energy-loss tables, a relation was obtained between centre-of-mass energy, centre-of-mass scattering angle, and overall track length. This was subsequently applied to all events to extract the nominal centre-of-mass energy. This is shown in figure 5.30 for two example scattering angles.

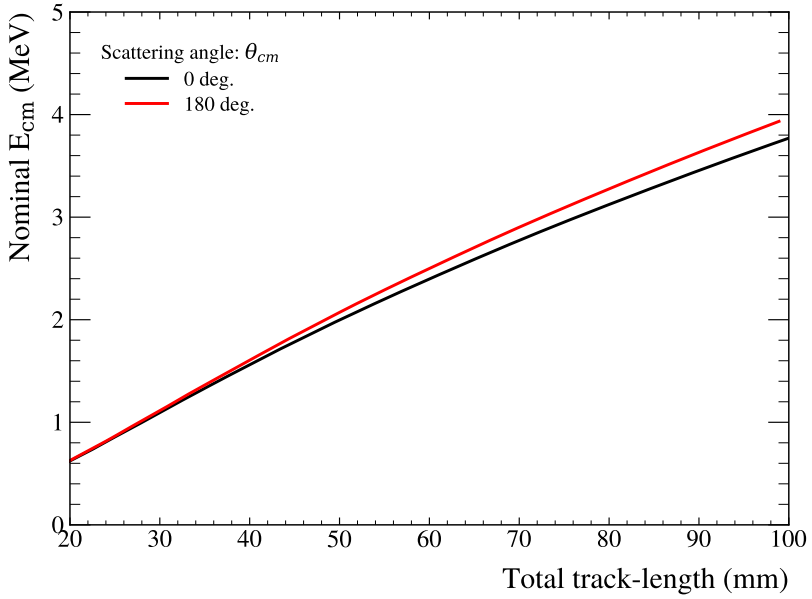

Figure 5.30: Kinematic Conversion: The conversion from track length to nominal centre-of-mass energy based on 2-body kinematics and `SRIM` energy-loss tables.

As previously mentioned, for events with $\beta > 42°$ and $\beta < 20°$, the resolution in the extracted polar angle is reduced. Despite the reduction in angular resolution for certain track orientations, this was not a large effect, and simply manifested as a reduction in the centre-of-mass energy resolution. For example, the difference in calculated centre-of-mass energy for a typical track length of 60 mm is 100 keV for the most unlikely and extreme case, where events have the θ angle wrongly reconstructed by 180°.

The reconstructed nominal centre-of-mass energies for $E_\gamma = 9.50$ MeV are shown in figure 5.31.

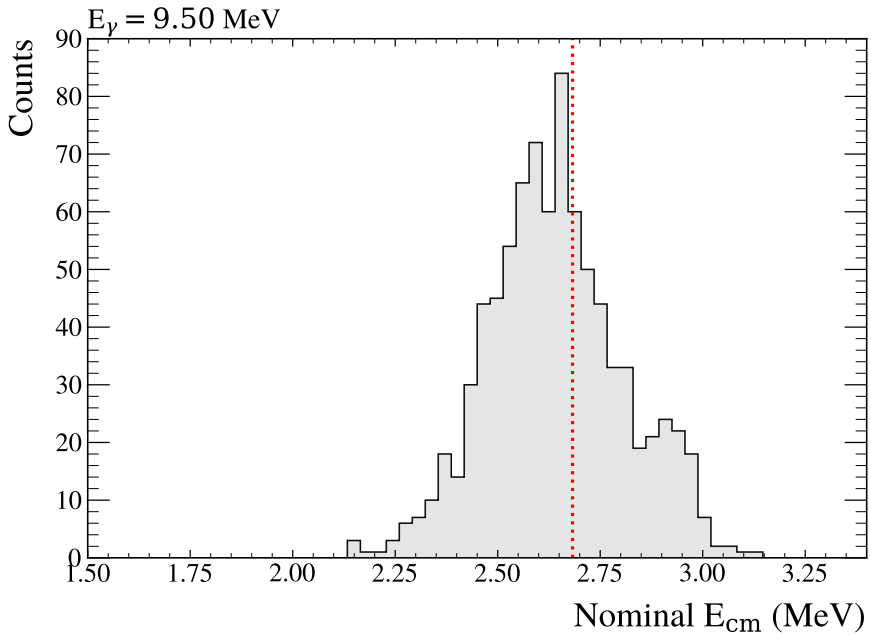

Figure 5.31: Nominal Centre-of-mass Energies: Reconstructed nominal centre-of-mass energies as measured by the OTPC. The centroid of the narrow 2^+ in ^{16}O is shown as a red dotted line.

Energy Calibration

The small bump in the right-hand side of the energy spectra of figure 5.31 should line up with the red dotted line; this is the location of the narrow 2^+ in ^{16}O at $E_{\mathrm{cm}} = 2.68$ MeV. To account for the systematic shift observed in the reconstructed energies (due to resolution effects), a calibration is needed.

Calibration Data. The narrow 2^+ state is measured at the two highest beam energies, this serves as one calibration point. Similarly, the position of the broad 1^- state at the two lowest energies, and the 3.18 MeV gadolinium alpha peak (from the calibration runs), provide three additional calibration points.

The 2^+ state is narrow, so the expected values were taken from TUNL [54]. For the 1^- state, a parametrisation of the known total cross section (see appendix C) was folded with the measured beam energy distribution for the $E_\gamma = 9.38$ & 9.50 MeV runs. The expected centroids were then extracted from the resulting distributions. The

gadolinium calibration point accounted for the recess of the source holder, which cuts out a small section of the track.

The TPC centroids were extracted using simple Gaussian fits, one example is shown later in figure 5.34

Calibration Fit The calibration from the nominal centre-of-mass to true centre-of-mass energy is shown in figure 5.32. The fit has a χ^2_ν of 1.7. The extracted fit parameters are $m = 0.9734$, $c = 0.3215$, with the following correlation matrix

$$\mathrm{Cov}(m, c) = \begin{pmatrix} 0.00488925 & -0.00197369 \\ -0.00197369 & 0.00080147 \end{pmatrix}$$

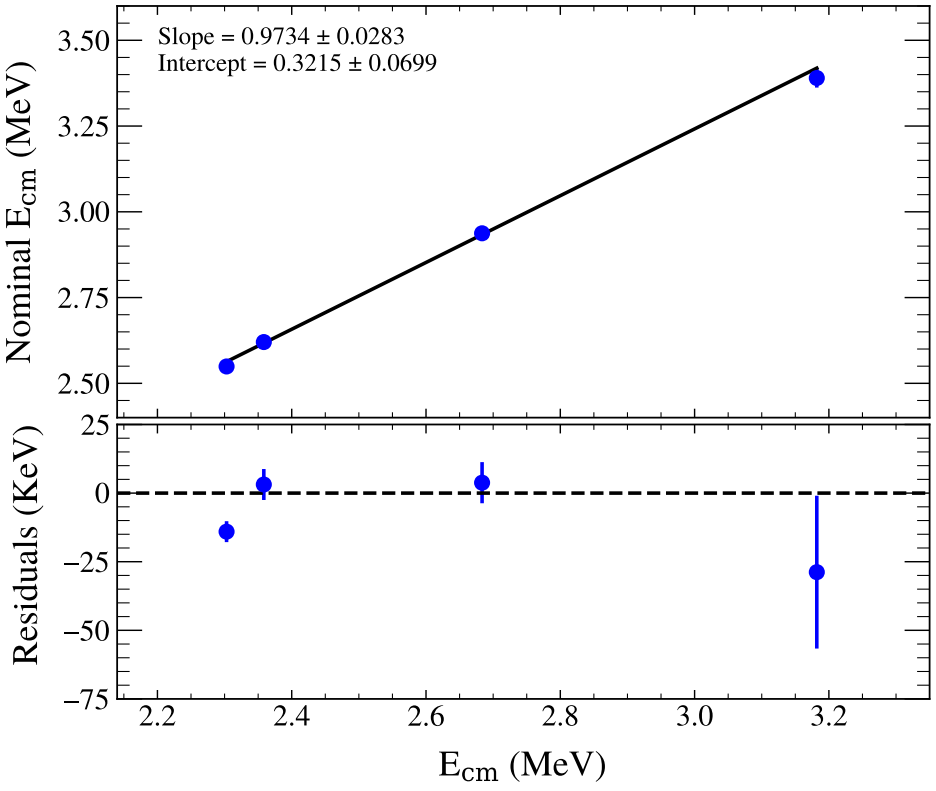

Figure 5.32: OTPC Energy Calibration: The calibration for OTPC reconstructed nominal centre-of-mass energy to true centre-of-mass energy, accounting for reconstruction bias.

The calibration gradient is very close to unity, suggesting that the conversion from track length to centre-of-mass energy is robust. The main effect is an approximately 300 keV shift, which accounts for the reconstruction bias due to resolution effects. Since the track length resolution would increase all track lengths by a similar amount, it is reasonable that a simple energy shift would be required for all data. The fully calibrated E_{cm} spectrum is shown in figure 5.33.

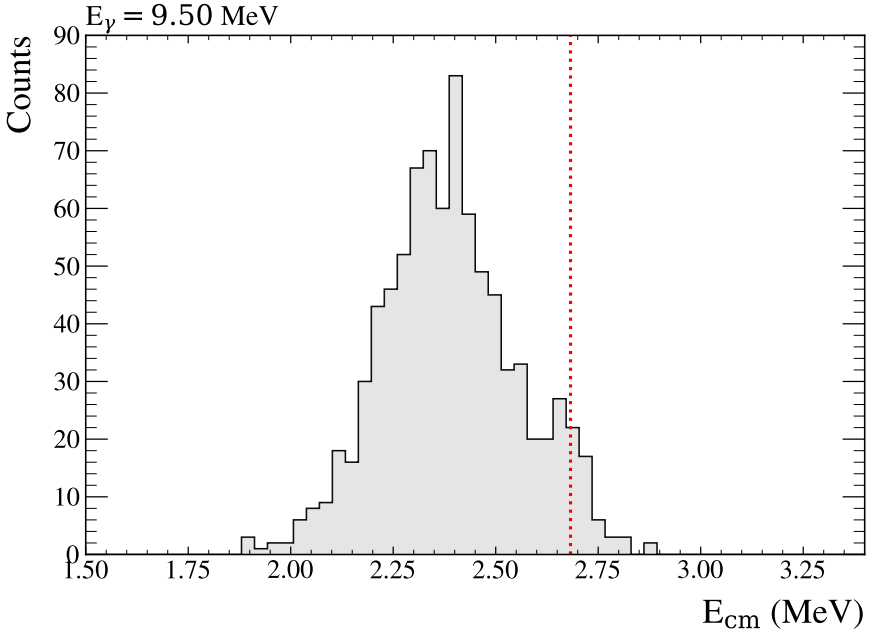

Figure 5.33: Calibrated Centre-of-mass Energies: Calibrated centre-of-mass energies as measured by the OTPC. The centroid of the narrow 2^+ in ^{16}O is shown as a red dotted line.

5.4.2 Centre-of-mass Energy Resolution

To obtain the OTPC centre-of-mass energy resolution, the narrow 2^+ resonance at 2.68 MeV was used. As this state has a vanishingly small natural width of $\Gamma = 0.625$ keV [54], it can be used to approximate the detector resolution. A fit is shown in figure 5.34 using two Gaussians, where the extracted resolution of $\sigma \approx 67$ keV was obtained.

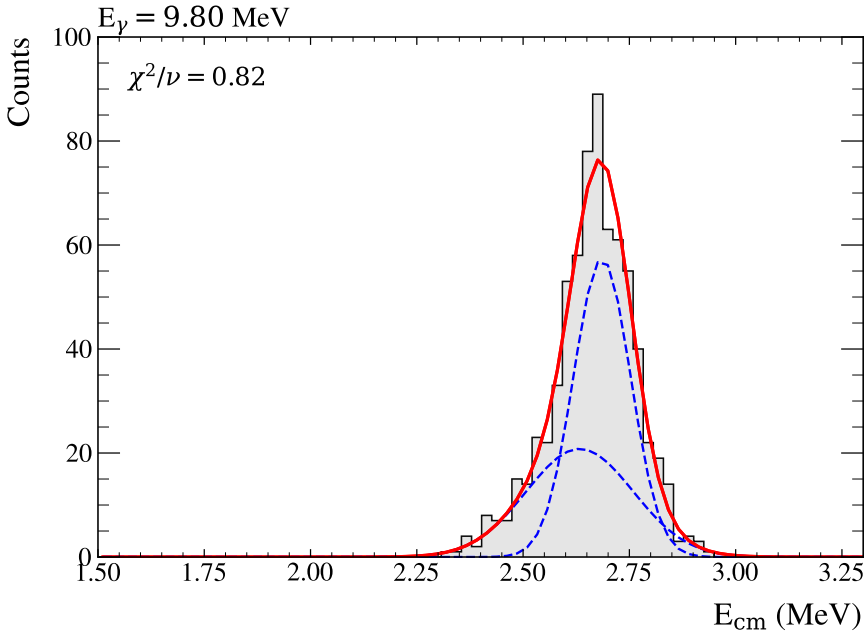

Figure 5.34: Calibrated Centre-of-mass Energy Resolution: The Calibrated centre-of-mass energy spectrum measured at $E_\gamma = 9.80$ MeV, was used to obtain the TPC energy resolution. Two Gaussians were fitted, shown as blue dotted lines, to model the background and extract the observed width of the narrow 2^+.

5.5 Cross sections of ^{16}O Photo-dissociation

This section presents several angular distribution analyses using variations of the $E1-E2$ mixing partial-wave decomposition 1.4.5. The data are fitted using a one-degree binned negative log likelihood procedure; further details on both are given in appendix A, and should be read in full before continuing. The polar-angle distribution is given again here for convenience

$$\begin{aligned} W(\theta) = \sigma_{E1} W_{E1}(\cos\vartheta) + \sigma_{E2} W_{E2}(\cos\vartheta) \\ + \sqrt{\sigma_{E1}\sigma_{E2}}\cos\phi_{12}\, W_{12}(\cos\vartheta). \end{aligned} \tag{5.5.0.1}$$

This formula consists of three individual angular distributions: a pure $E1$ contribution W_{E1}, a pure $E2$ contribution W_{E2}, and the interference term W_{12}. These are defined in terms of Legendre polynomials $P_l(\cos\theta)$.

An efficiency correction is applied when fitting the angular distributions to account for the loss of events due to the β fiducial cuts. It also corrects for the change in shape due to angular resolution. The procedure yields the efficiency profile $\epsilon(\theta)$, and is described in appendix D. When fitting the data, the profile is applied directly to the fit function to preserve Poisson statistics. But when viewing the angular distributions, the data are corrected, and the fit function is normalised to the same area.

5.5.1 Method-1: Beam-by-beam Analysis

First, all data at each beam energy are considered, and the θ_{cm} angular distributions are fitted with the standard partial wave decomposition equation (5.5.0.1). The fits for each beam energy are shown in figure 5.35. The extracted energy-averaged fit parameters and associated uncertainties are presented in table 5.9 at their incident energy.

E_γ (MeV)	$E_{\mathrm{cm}}^{\mathrm{inc}}$ (MeV)	$\langle\phi_{12}\rangle$ (deg.)	$\frac{\langle\sigma_{E2}\rangle}{\langle\sigma_{E1}\rangle}$	χ^2_ν
9.38	2.22(1)	$39.96^{+11.97}_{-38.24}$	$0.11^{+0.08}_{-0.06}$	2.47
9.50	2.32(1)	$68.46^{+6.42}_{-6.54}$	$0.31^{+0.18}_{-0.14}$	1.83
9.70	2.52(1)	$81.41^{+3.43}_{-3.44}$	$1.03^{+0.25}_{-0.2}$	0.56
9.80	2.67(1)	$78.68^{+8.26}_{-8.85}$	$2.93^{+2.44}_{-1.18}$	0.78

Table 5.9: Summary of Energy-Averaged Fit Parameters from Method 1:. The table lists the fit parameters and their associated errors from the standard partial-wave decomposition. The energies indicated are the nominal beam energy and the incident energy, as described in appendix A.1.

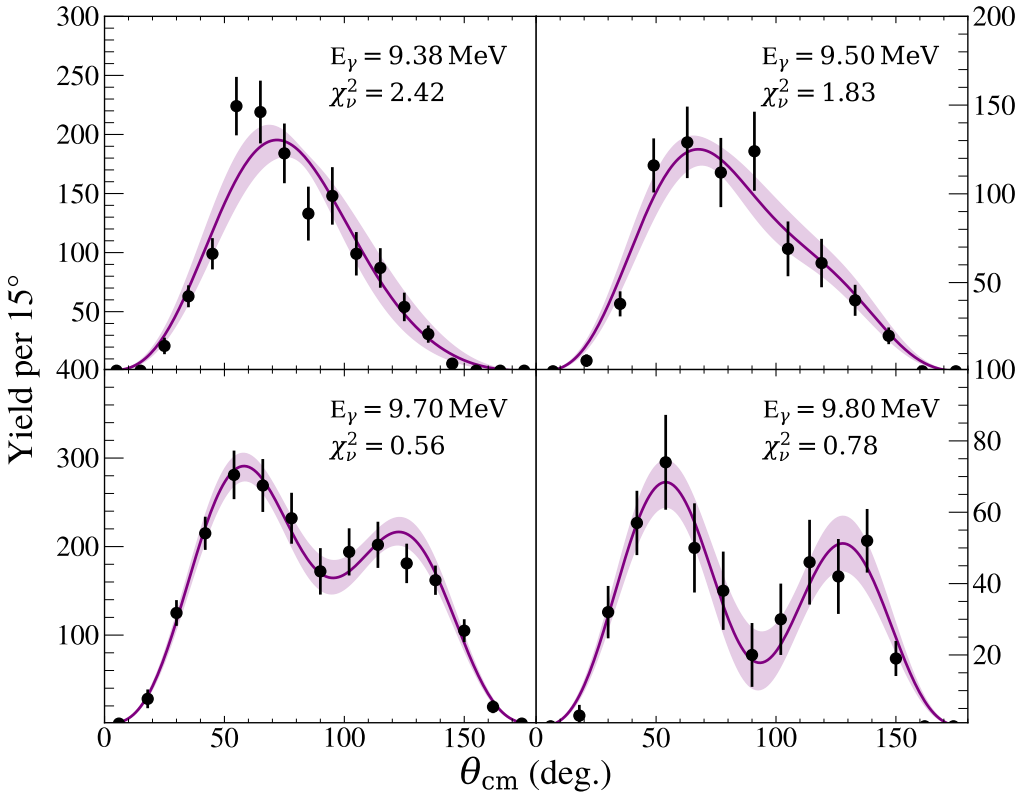

Figure 5.35: Angular Distributions Method-1: The fits to the angular distributions are shown using equation (5.5.0.1). Each panel states the reduced chi-squared metric and the nominal beam energy. The error band comes from varying the parameters within their 1σ errors.

Uncertainties. As there are only two fitted parameters, it is convenient to visualise their behaviour using a contour map. These can be used to identify parameter errors, including parameter correlation, and help investigate regions where the fit struggles. The contour areas are found by varying the fit parameters until the $-\mathcal{L}$ changes from its minimum by an amount described in table A.2. Two examples of contour regions are presented.

The left panel of figure 5.36 is from an $E1$-dominated distribution, and the right panel is from an $E2$-dominated distribution. While 1σ errors were obtained from both plots, the extreme correlation in the $E1$-dominated distribution is clear.

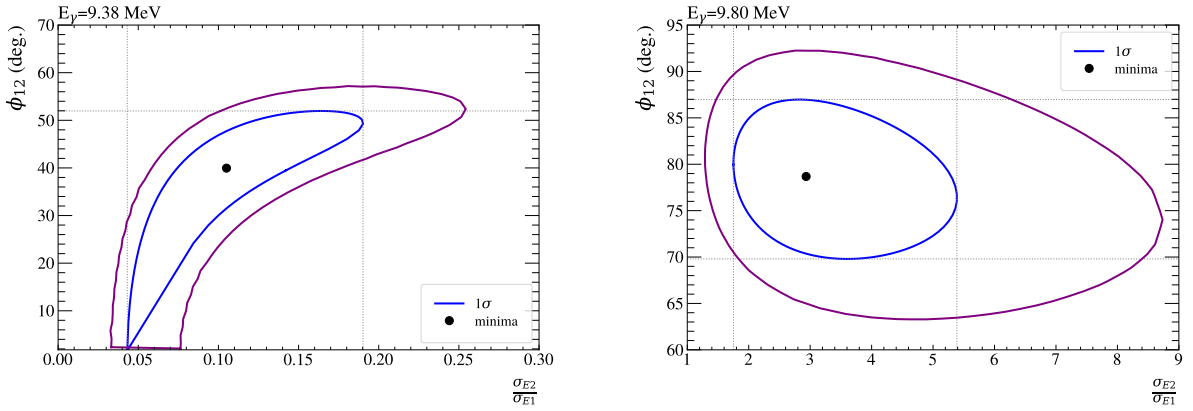

Figure 5.36: Angular Distribution Contour Regions - Method 1. Left: Contour region from the fit to the $E1$-dominated $E_\gamma = 9.38$ MeV angular distribution, showing high parameter correlation and large uncertainties. **Right:** Contour region from the fit to the $E2$-dominated $E_\gamma = 9.85$ MeV angular distribution, showing low parameter correlation and smaller uncertainties.

Comparison with theory. The extracted effective fit parameters are plotted at their measured incident energy and compared with energy-averaged theory in figure 5.37. As the current method uses energy obtained solely from the beam profile $G(E)$, the response is trivial and expressed as

$$\langle \cos\phi_{12} \rangle = \frac{\int_0^\infty \cos\phi_{12}(E)\,\sqrt{\sigma_1(E)\,\sigma_2(E)}\,G(E)\,dE}{\sqrt{\langle\sigma_1\rangle\,\langle\sigma_2\rangle}\int_0^\infty G(E)\,dE} \tag{5.5.1.1}$$

and

$$\langle \sigma_L \rangle = \frac{\int_0^\infty \sigma_L(E) G(E)\,dE}{\int_0^\infty G(E)\,dE}. \tag{5.5.1.2}$$

This is described in appendix A.3. To calculate these theoretical expectation values, the cross sections are taken from reference [46], and the phase shifts from reference [79]. The grey lines represent the intrinsic predictions that would be observed with perfect energy resolution. The central orange line corresponds to the theory averaged over a

Gaussian beam profile with the average beam width. The shaded error band reflects the uncertainty due to the range of possible beam widths.

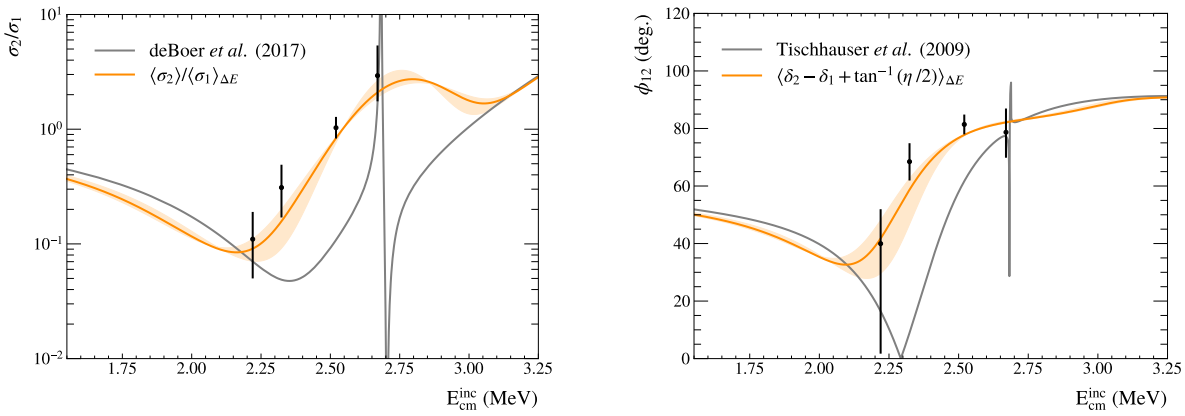

Figure 5.37: Energy-Averaged Angular Distribution Fit Parameters from Method-1: The extracted energy-averaged fit parameters, $\langle\sigma_2\rangle/\langle\sigma_1\rangle$ (**left**) and $\langle\phi_{12}\rangle$ (**right**) from table 5.9 are plotted. They are compared with the energy-averaged theoretical predictions (orange line), obtained using equations (5.5.1.2) and (5.5.1.1) respectively. The error band corresponds to the range in beam widths.

Unfolding. The error band shown above is only an approximation based on the average Gaussian width of the beam profiles. Instead, the more appropriate method is to calculate the point-by-point response using the exact beam profile. This can be used for comparison or to unfold the experimental data. The procedure as outlined in reference [185], and described in appendix A.3 was used to unfold the experimental data. The multiplicative correction factor and unfolded results are shown in figure 5.38, with values summarised in table 5.10.

E_γ (MeV)	E_{cm}^{eff} (MeV)	$f_{cor}^{\phi_{12}}$	ϕ_{12} (deg.)	$f_{cor}^{\sigma_2/\sigma_1}$	$\frac{\sigma_2}{\sigma_1}$
9.38	2.31(1)	0.11(5)	$4.36\ ^{+1.31}_{-4.17}$	0.62(3)	$0.07\ ^{+0.05}_{-0.04}$
9.50	2.39(1)	0.52(3)	$35.41^{+3.32}_{-3.38}$	0.29(3)	$0.09^{+0.05}_{-0.04}$
9.70	2.57(1)	0.881(7)	$71.75\ ^{+3.02}_{-3.03}$	0.17(5)	$0.18^{+0.04}_{-0.03}$
9.80	2.66(03)	0.934(1)	$73.55^{+7.72}_{-8.27}$	0.29(5)	$0.84^{+0.70}_{-0.34}$

Table 5.10: Summary of Unfolded Fit Parameters from Method-1: The table lists the deconvolution values, and the fit parameters with their associated errors from the partial-wave decomposition after unfolding. The energies indicated are the nominal beam energy and the incident energy, as described in appendix A.3.

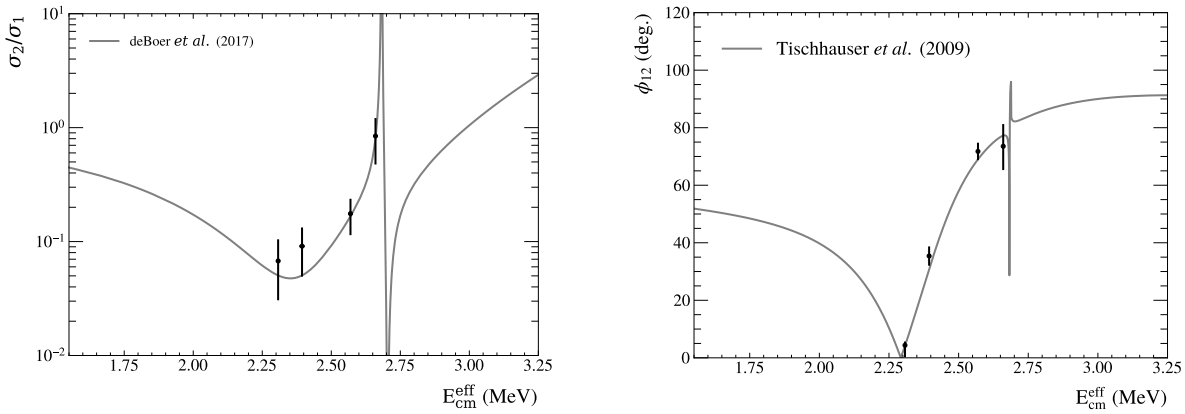

Figure 5.38: Unfolded Angular Distribution Fit Parameters from Method-1: The unfolded fit parameters, σ_2/σ_1 (**left**) and ϕ_{12} (**right**) from table 5.10 are plotted. They are both compared with the theoretical predictions (grey line).

5.5.2 Method-2: beam-by-beam Incoherent $E2$

The analysis above shows agreement with ϕ_{12}, as predicted from scattering data. However, comparison with theory—and hence any unfolding—relies on knowing the energy dependence of the underlying σ_{E1} and σ_{E2}. The results should be validated without relying on the underlying theory.

To achieve this, one is forced to make the assumption that the product of the $E1$ and $E2$ cross sections do not vary significantly across the energy width of the beam. If this assumption holds, the cross sections can be taken out of the integral in equation (5.5.1.1), reducing it to a simple convolution

$$\langle \cos\phi_{12} \rangle = \frac{\int_0^\infty \cos\phi_{12}(E)\, G(E)\, dE}{\int_0^\infty G(E)\, dE}. \tag{5.5.2.1}$$

The assumption was made that contributions from the narrow 2^+ resonance to the angular distributions are incoherent. It was then possible to model the angular distribution using two terms. The standard $E1-E2$ mixing term $W(\theta)$, and a pure $E2$ term $W_2(\theta)$ to account for the narrow 2^+ state. The resulting fitting angular distributions is

$$N\Big(\theta|\frac{\sigma_{E2}}{\sigma_{E1}},\phi_{12}\Big) = (1-a_2)\frac{W(\theta)\,\epsilon(\theta)\,\sin\theta}{\int_0^\pi W(\theta)\,\epsilon(\theta)\,\sin\theta\,d\theta} + a_2\frac{W_2(\theta)\,\epsilon(\theta)\,\sin\theta}{\int_0^\pi W_2(\theta)\,\epsilon(\theta)\,\sin\theta\,d\theta}. \tag{5.5.2.2}$$

Here, a_2 is the fraction of the total distribution pertaining to the narrow 2^+ resonance.

Obtaining a_2

The fraction of incoherent $E2$ from this narrow resonance was approximated using the calibrated centre-of-mass energy spectra as measured in the OTPC (before β cuts were applied). The lineshapes obtained in appendix C are folded with the beam profiles, convolved with the OTPC resolution and normalised to unity. They were then fitted by varying their amplitudes independently. A small gain and offset was included to account for the error in the calibration to each beam energy. These fits are shown in figure 5.39, and the extracted fit parameters are given in table 5.11.

E_γ	$E1$ counts	$E2$ counts	$E2/E1$	a_2
9.38	1370(38)	0.00(2)	0.00(0)	0.00(0)
9.50	730(27)	100(12)	0.12(2)	0.14(2)
9.70	1490(43)	940(37)	0.39(2)	0.63(3)
9.80	180(21)	500(25)	2.7(4)	0.73(5)

Table 5.11: Proportions of Incoherent $E2$ from OTPC Spectra: The fully calibrated OTPC spectra have been fitted with a model of the underlying cross sections, after folding with the beam profile and convolving with the OTPC resolution. This process approximates the total proportions of counts related to the broad $J^\pi(1^-)$ and narrow $J^\pi(2^+)$ states, listed here as $E1$ and $E2$ respectively.

Table 5.11 lists the counts in both peaks, the $E2/E1$ ratio, and $a2 = \frac{E2}{E1+E2}$. It is noted that the fraction of $E2/E1$, for $E_\gamma = 9.80$ MeV, using this method, is comparable to that obtained by the fit to the scattering angle listed in table 5.9. This justifies the approach for other energies.

Fitting

The data at the lowest three beam energies are fitted with equation 5.5.2.2, by fixing the pure $E2$ contribution from table 5.11. Data at $E_\gamma = 9.80$ MeV were not fit because they contain mainly $E2$ from the narrow resonance, so that a stable fit couldn't be obtained in the way described. The fits in are shown in figure 5.40, and extracted fit parameters in table 5.12.

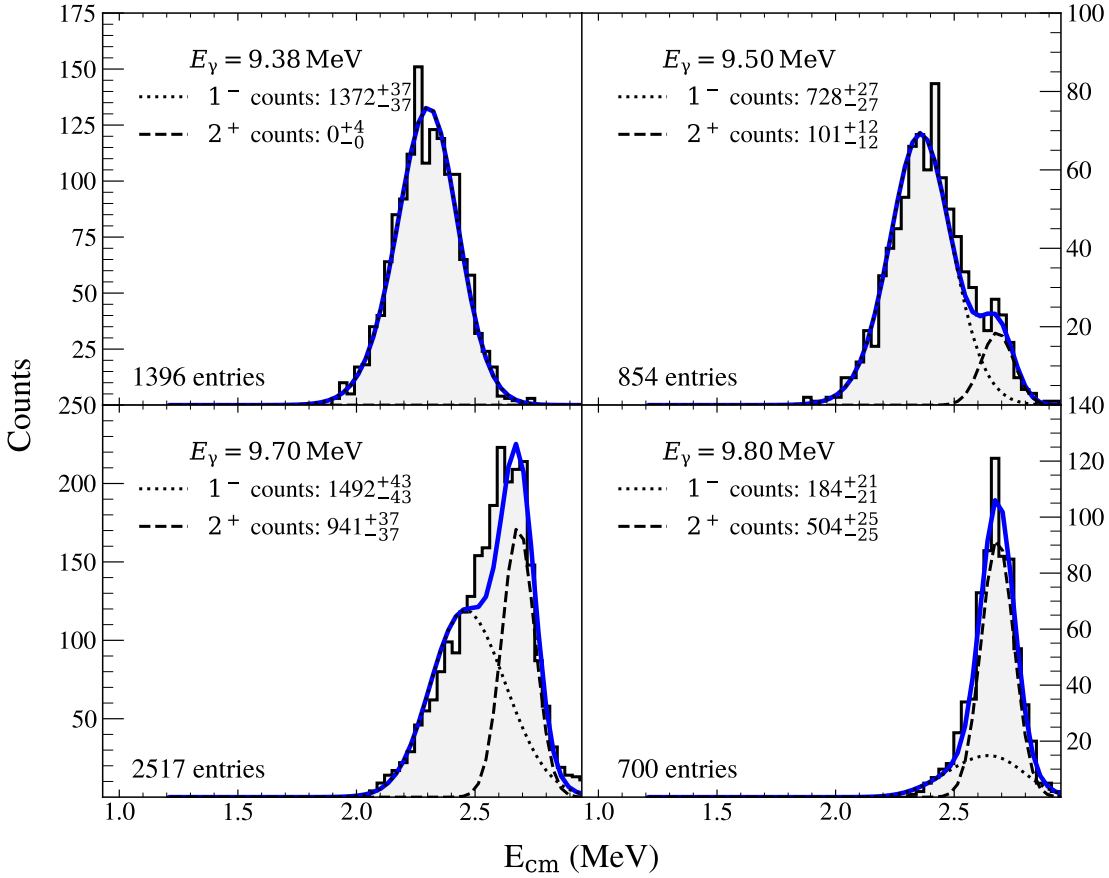

Figure 5.39: Lineshape fits to the OTPC spectra. Each panel shows an OTPC-reconstructed energy spectrum for a given nominal beam energy (grey histogram). The spectra are fitted with a cross section model after applying detector effects (blue), from which the total counts associated with the broad $J^\pi(1^-)$ state (black dotted) and the narrow $J^\pi(2^+)$ state (black dashed) are extracted. This figure was taken from reference [178].

E_γ (MeV)	E_{cm}^{inc} (MeV)	ϕ_{12} (deg.)	$\frac{\sigma_{E2}}{\sigma_{E1}}$	χ^2_ν
9.38	2.22(1)	$39.96^{+11.97}_{-38.25}$	$0.11^{+0.08}_{-0.06}$	2.42
9.50	2.32(1)	$58.34^{+10.87}_{-29.99}$	$0.15^{+0.16}_{-0.12}$	1.82
9.70	2.52(1)	$72.22^{+7.39}_{-8.94}$	$0.25^{+0.16}_{-0.13}$	0.57

Table 5.12: Summary of Energy-Averaged Fit Parameters from Method-2:. The table lists the fit parameters and their associated errors from the partial-wave decomposition. The energies indicated are the nominal beam energy and the incident energy. The errors on the fit parameters include the contribution from the a_2 parameter.

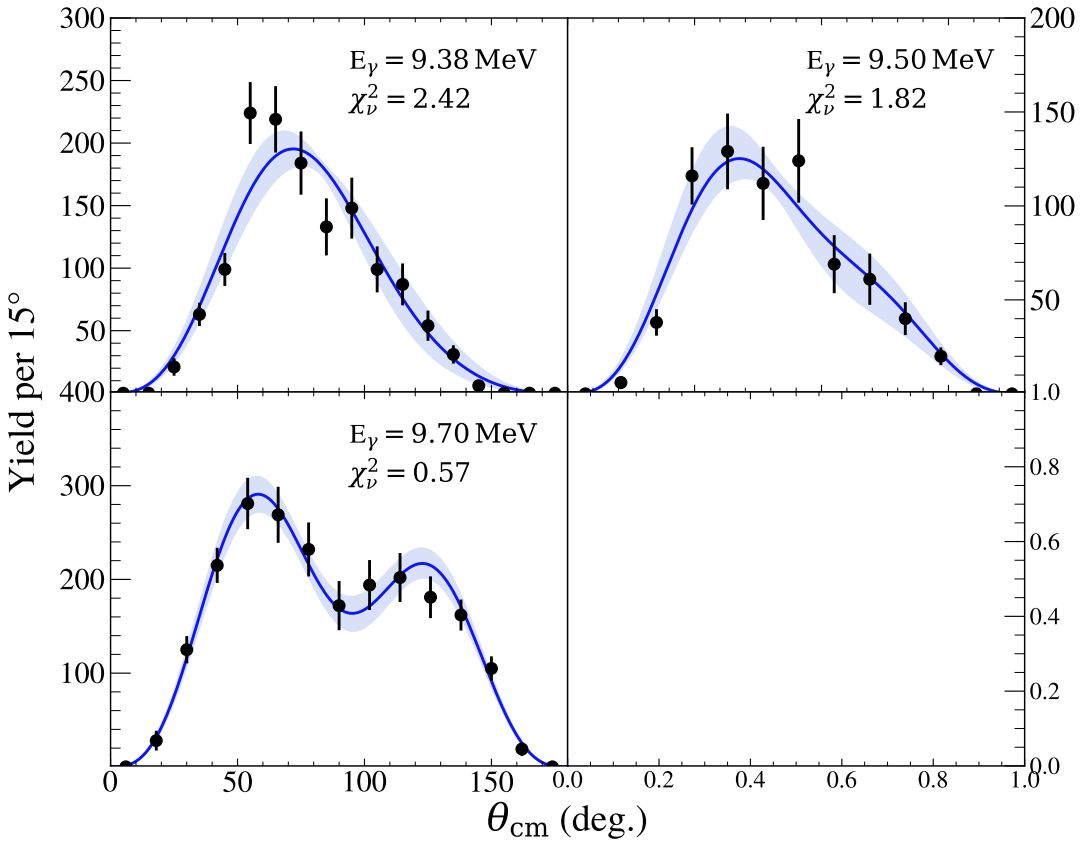

Figure 5.40: Angular Distributions Method-2: The fits to the angular distributions are shown using equation (5.5.2.2). Each panel states the reduced chi-squared metric and the nominal beam energy. The error band comes from varying the parameters within their 1σ errors.

Comparison with Theory. The extracted ϕ_{12} is shown at incident energy in figure 5.41, where it is compared with energy-averaged ϕ_{12} using equation (5.5.2.1). The good agreement here validates the previous approach of unfolding using the cross sections from reference [46].

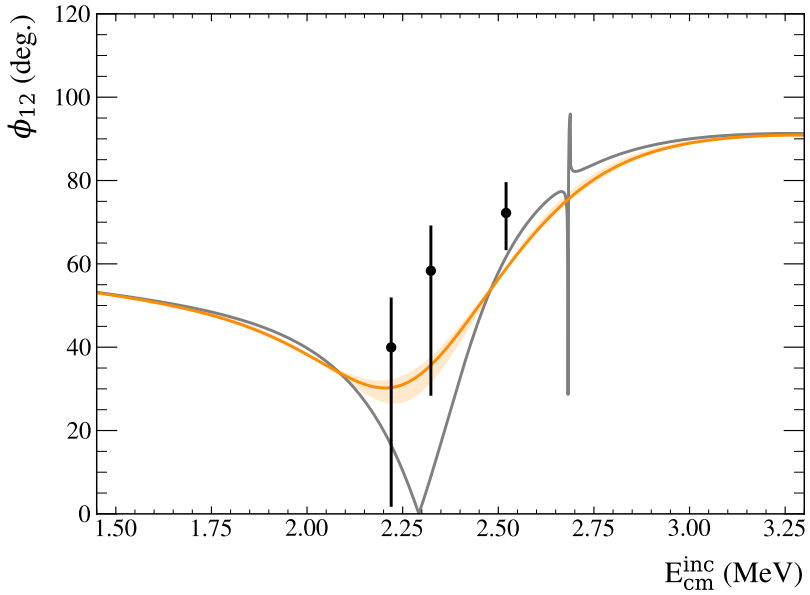

Figure 5.41: Energy-Averaged ϕ_{12} Results from Method-2: The extracted energy-averaged phase mixing angles, $\langle\phi_{12}\rangle$, from table 5.12 are plotted. They are compared with the energy-averaged theoretical predictions (orange line), obtained by convolving the underlying theory (grey line) with a Gaussian of average beam width. The error band corresponds to the range in beam widths.

5.5.3 Method-3: Beam Splitting

A final method is shown, where the data are analysed holistically; since the energies and angles are measured event-by-event in the OTPC, it is possible to combine datasets. This approach relies on the angular efficiency correction profiles being essentially constant across each nominal beam energy.

Before summing the individual datasets, a $\mu \pm 2\sigma$ cut is applied based on the fit to the unfolded HPGe profile. This cut removes a small number of events and is necessary for subsequent total cross section calculations. This is because the luminosity is distributed

across the measured beam profile, and the beam profile is known with reduced accuracy in the tails. The summed spectra after this cut are shown in figure 5.42

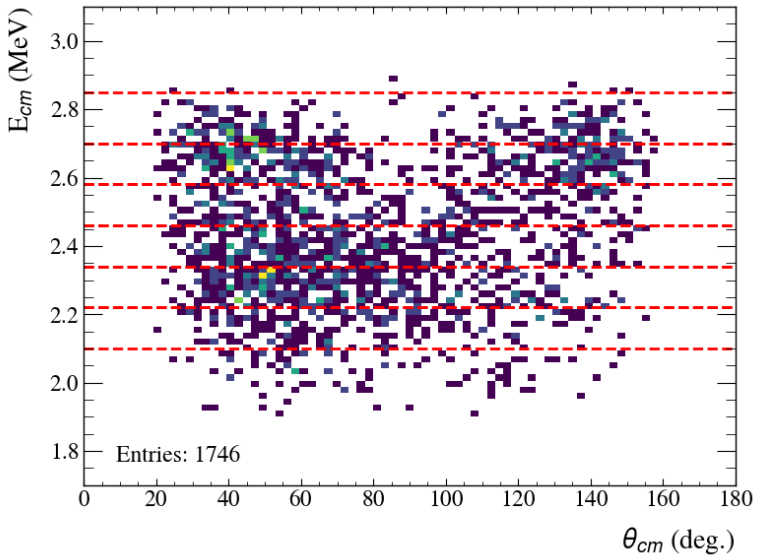

Figure 5.42: Re-summed Data in the OTPC: All beam energies have been summed after 2σ cut from the beam centroid. Slices are taken at the energies indicated by the red lines. The data in each slice are fitted using the standard partial-wave decomposition.

Slices are taken across this spectrum, with regions selected to maintain sufficient statistics for a valid fit, marked in red dotted lines. The data in these slices are projected onto the angle-axis, and fitted using the standard partial-wave decomposition of equation (5.5.0.1). The fitted data are shown in figure 5.43, with extracted fit parameters in table 5.13.

$E_{\mathrm{cm}}^{\mathrm{tpc}}$	Fit range (MeV)	$\langle\phi_{12}\rangle$ (deg.)	$\langle\frac{\sigma_2}{\sigma_1}\rangle$	Counts	Corrected counts
2.163(5)	2.08, 2.22	$50.92^{+13.80}_{-43.75}$	$0.10^{+0.14}_{-0.08}$	185	576 ± 44
2.282(4)	2.22, 2.34	$54.75^{+8.21}_{-16.07}$	$0.17^{+0.13}_{-0.10}$	324	986 ± 57
2.400(4)	2.34, 2.46	$59.64^{+7.28}_{-9.89}$	$0.19^{+0.13}_{-0.10}$	314	958 ± 56
2.517(4)	2.46, 2.58	$78.68^{+6.36}_{-6.38}$	$0.47^{+0.25}_{-0.18}$	249	725 ± 48
2.646(4)	2.58, 2.70	$76.18^{+7.30}_{-7.98}$	$4.04^{+2.81}_{-1.46}$	342	885 ± 50
2.751(4)	2.70, 2.85	$88.56^{+14.48}_{-15.57}$	$14.18^{+43.79}_{-7.84}$	253	613 ± 41

Table 5.13: Summary of Energy-Averaged Fit Parameters from Method-3: The table lists the fit parameters and their associated errors from the partial-wave decomposition of all summed datasets. The energies indicated are the centre-of-mass energies reconstructed in the OTPC, and the fit range considered.

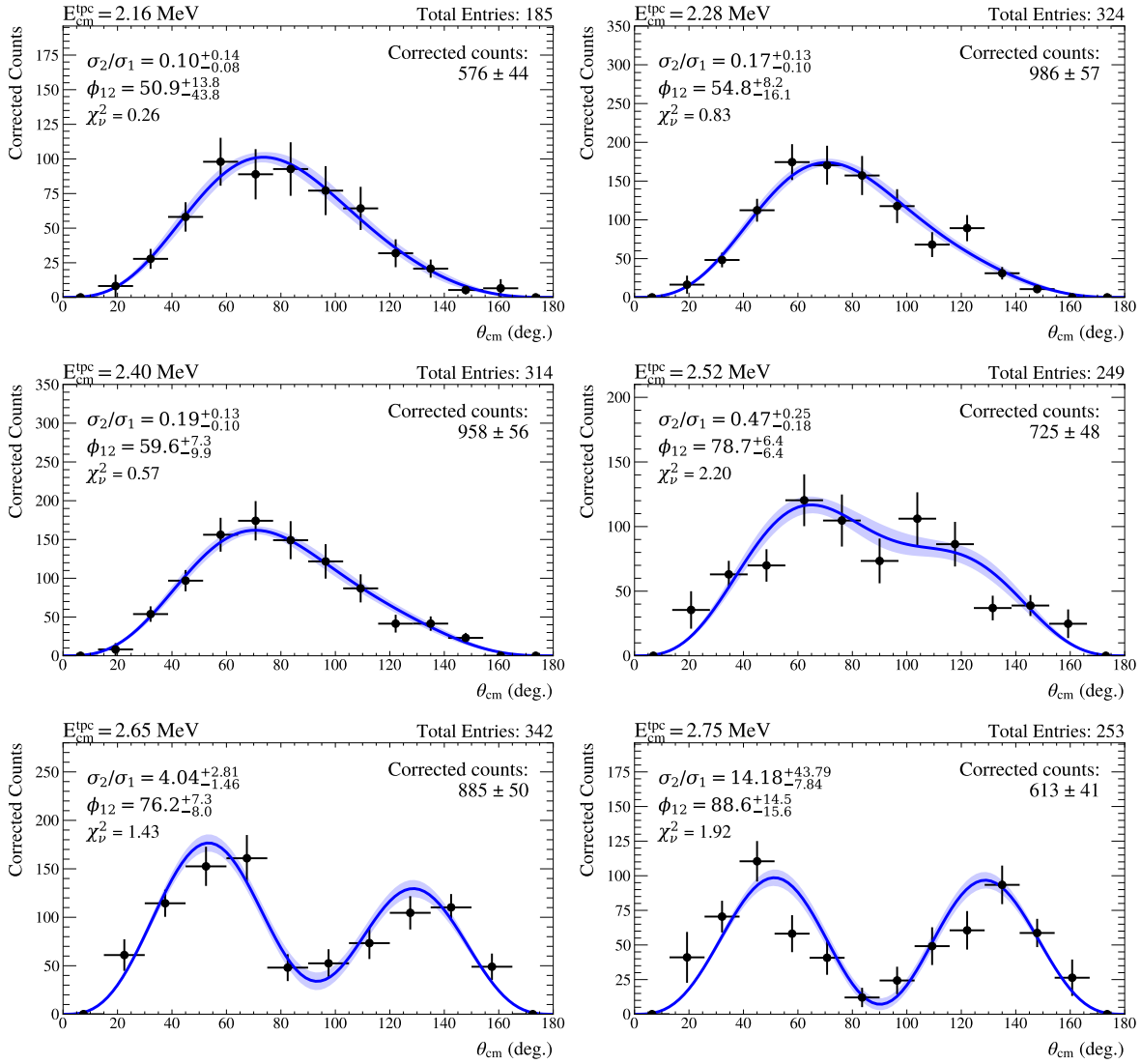

Figure 5.43: Angular Distributions Method-3: The fits to the angular distributions are shown using equation (5.5.0.1). Each panel states the best fit parameters, the reduced chi-squared metric, the centre-of-mass energy, and the total and corrected counts. The error band comes from the parameter covariance matrix.

To express the data at their OTPC reconstructed energies, new expectation values are used, as defined in appendix A.3. The extracted fit parameters are unfolded using these values; both are listed in table 5.14 and shown in figure 5.44.

$E_{\mathrm{cm}}^{\mathrm{tpc}}$	Fit range (MeV)	$f_{\phi_{12}}$	ϕ_{12} (deg.)	f_{σ_2/σ_1}	σ_2/σ_1
2.163(5)	2.08, 2.22	$1.081^{+0.014}_{-0.016}$	$55.1^{+14.9}_{-47.3}$	$1.148^{+0.029}_{-0.028}$	$0.12^{+0.16}_{-0.10}$
2.282(4)	2.22, 2.34	$0.100^{+0.008}_{-0.008}$	$5.5^{+0.9}_{-1.7}$	$0.957^{+0.006}_{-0.006}$	$0.16^{+0.12}_{-0.10}$
2.400(4)	2.34, 2.46	$0.869^{+0.019}_{-0.032}$	$51.8^{+6.4}_{-8.8}$	$0.859^{+0.023}_{-0.036}$	$0.16^{+0.11}_{-0.09}$
2.517(4)	2.46, 2.58	$0.877^{+0.020}_{-0.015}$	$69.0^{+5.8}_{-5.7}$	$0.424^{+0.088}_{-0.065}$	$0.20^{+0.12}_{-0.08}$
2.646(4)	2.58, 2.70	$0.930^{+0.001}_{-0.001}$	$70.8^{+6.8}_{-7.4}$	$0.156^{+0.009}_{-0.007}$	$0.6^{+0.4}_{-0.2}$
2.751(4)	2.70, 2.85	$1.000^{+0.003}_{-0.004}$	$88.5^{+14.5}_{-15.6}$	$0.031^{+0.003}_{-0.003}$	$0.4^{+1.4}_{-0.3}$

Table 5.14: Summary of Unfolded Fit Parameters from Method-3: The table lists the deconvolution values, and the fit parameters with their associated errors from the partial-wave decomposition after unfolding. The energies indicated are the centre-of-mass energies reconstructed in the OTPC, and the fit range considered.

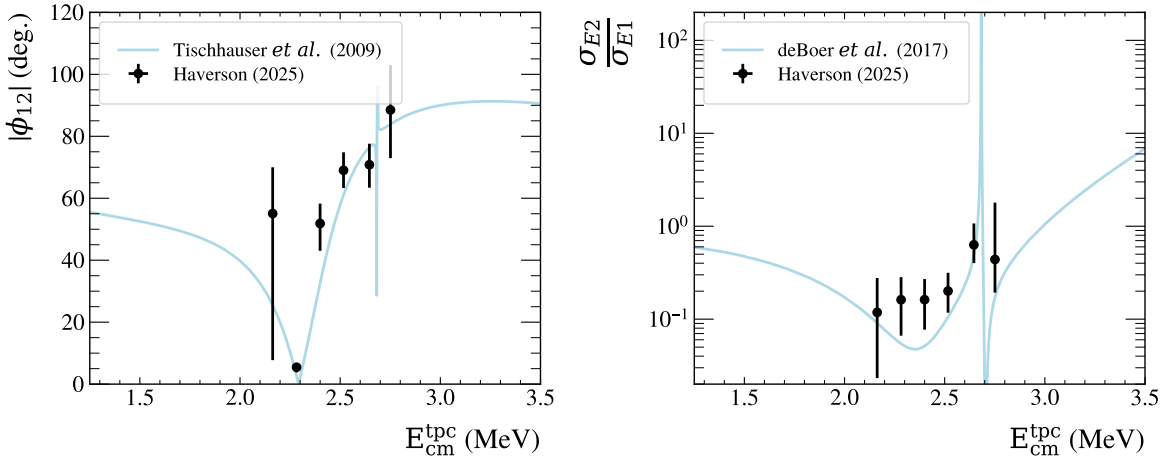

Figure 5.44: Unfolded Angular Distribution Fit Parameters from Method-3: The unfolded fit parameters, σ_2/σ_1 (**left**) and ϕ_{12} (**right**) from table 5.14 are plotted. They are both compared with the theoretical predictions (blue line).

5.5.4 Angle-integrated Cross Section

The energy-averaged $^{16}\mathrm{O}(\gamma,\alpha_0)$ cross section is obtained using the method outlined in appendix A.2, yielding the equation below

$$\langle\sigma_{\gamma\alpha_0}\rangle = \frac{N_{^{16}O}}{\mathcal{L}\ \epsilon\ f_{LT}}. \tag{5.5.4.1}$$

Here, $N_{^{16}\mathrm{O}}$ represents the β-cut-corrected number of $^{16}\mathrm{O}$ counts measured in each angular distribution, ϵ is an efficiency to correct for the various software cuts ($\sim$98%), f_{LT} accounts for the OTPC live-time corrections, and $\mathcal{L}$ is the integrated luminosity for the given run.

Live-time. The OTPC dead-time is assumed to arise primarily from the 28.4 frames/second CCD capture rate, which is calculated using the non-paralysable dead time model

$$R_{\mathrm{T}} = \frac{R_{\mathrm{M}}}{1 - R_{\mathrm{M}}\ \tau}. \tag{5.5.4.2}$$

Here, τ is the reciprocal of the maximum frame rate, R_{T} is the true rate, and R_{M} is the measured rate. Figure 5.45 shows these relations. The blue line shows the relationship of measured-to-true rate, with the black line representing live time as a percentage. The average measured frame rate was calculated for each nominal beam energy, with corresponding live-time correction factors calculated using equation 5.5.4.2 presented in table 5.15.

E_γ (MeV)	Live-time (%)
9.38	80
9.50	87
9.70	89
9.80	98

Table 5.15: Live-time in the OTPC: The live-time in the OTPC is listed as a percentage for each beam energy. The limiting factor was assumed to be the frame-rate limit of the CCD camera.

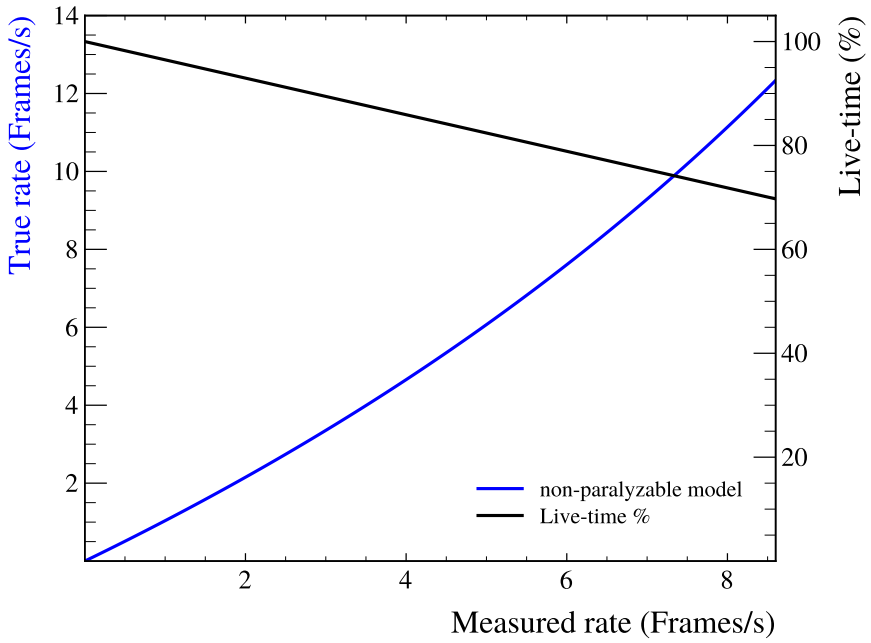

Figure 5.45: OTPC Live-time: The OTPC live-time behaviour (black line) and true rate (blue line) are shown as a function of measured rate.

Cross section. Using equation (5.5.4.1), the efficiency-corrected counts measured in each angular distribution from method-3 (listed in table 5.13), the luminosities in table 5.7, and the previously calculated live-times, the energy-averaged cross sections were calculated and are listed in table 5.16. These were subsequently unfolded using the R-matrix fit of reference [46] and converted to the capture cross section using the principle of detailed balance. The capture cross sections are shown in figure 5.46, compared with the world data.

$E_{\mathrm{cm}}^{\mathrm{tpc}}$	fit range (MeV)	$\langle\sigma_{\gamma\alpha_0}\rangle$	f_{cor}	$\sigma_{\gamma\alpha_0}$ (nb)	f_{db}	$\sigma_{\alpha\gamma_0}$ (nb)
2.163(5)	2.08, 2.22	2121^{+56}_{-52}	$0.85^{+0.03}_{-0.03}$	1802^{+78}_{-76}	$69.48^{+0.01}_{-0.01}$	$25.9^{+1.1}_{-1.1}$
2.282(4)	2.22, 2.34	3119^{+70}_{-66}	$1.029^{+0.004}_{-0.004}$	3211^{+73}_{-69}	$71.467^{+0.007}_{-0.007}$	$44.9^{+1.0}_{-1.0}$
2.400(4)	2.34, 2.46	3156^{+104}_{-98}	$1.13^{+0.02}_{-0.02}$	3561^{+128}_{-122}	$73.310^{+0.005}_{-0.005}$	$48.6^{+1.8}_{-1.7}$
2.517(4)	2.46, 2.58	2969^{+109}_{-101}	$0.84^{+0.04}_{-0.04}$	2490^{+147}_{-136}	$75.037^{+0.005}_{-0.005}$	$33.2^{+2.0}_{-1.8}$
2.646(4)	2.58, 2.70	4993^{+316}_{-281}	$0.31^{+0.01}_{-0.01}$	1534^{+111}_{-99}	$76.822^{+0.006}_{-0.006}$	$20.0^{+1.5}_{-1.3}$
2.751(4)	2.70, 2.85	5241^{+574}_{-477}	$0.165^{+0.006}_{-0.005}$	865^{+100}_{-83}	$78.191^{+0.008}_{-0.008}$	$11.1^{+1.3}_{-1.1}$

Table 5.16: Integrated Ground State Cross Sections: The energy-averaged cross section, deconvolution correction factor, detailed balance factor and both photo and capture cross sections are listed for each measured angular distribution.

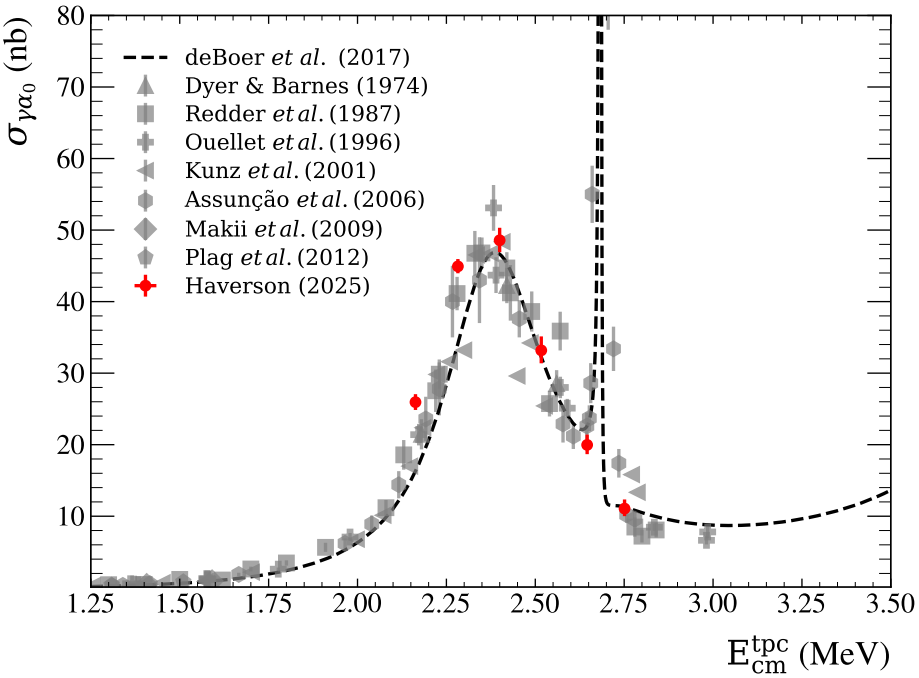

Figure 5.46: Unfolded $^{12}C(\alpha,\gamma_0)$ Angle-Integrated Cross section: The unfolded capture reaction cross section is shown against the R-matrix fit of reference [46], and the data of references [40, 41, 58–61, 63, 65].

Part III

Experiment 2: Electronic Time Projection Chamber

6

Experimental Details

The work in this part pertains to the photo-dissociation measurement of both ^{12}C and ^{16}O using the Warsaw TPC (eTPC). This section provides an overview of the eTPC, defines the coordinate system used, and outlines the run conditions.

The data used in this analysis were collected at HIγS during two campaigns in 2022, one in April and the other in August, each spanning several weeks. The former is referred to as the high-energy campaign, and the latter as the low-energy campaign. The experimental setup at HIγS is described in section 3.3. These data have been partially analysed previously [186] without automation, instead relying on hand "clicking" events.

The aim of these experiments is to provide high precision angular distributions of both the $^{12}\mathrm{C}(\alpha,\gamma)^{16}\mathrm{O}$ and $^{12}\mathrm{C}(\gamma,\alpha)^{8}\mathrm{Be}$ reactions, for both astrophysical and nuclear structure purposes.

6.1 Electronic Time Projection Chamber

The eTPC is shown photographed at HIγS in figure 6.1. The detector was designed in collaboration with the University of Warsaw, Poland, the University of Connecticut, USA, and the Extreme Light Infrastructure Nuclear Physics (ELI-NP), Romania. This detector works similarly to the OTPC in the previous analysis; it is an AT-TPC, operates at sub-atmospheric pressures, and allows for the 3D momentum reconstruction and identification of charged particles. The main difference is the use of the electronic readout, which allows to record higher precision data, and for the true pairing of the event's drift-axis information with the in-plane information, reducing the need for restrictive fiducial cuts. A full description of the eTPC can be found in reference [187]; an overview is provided here.

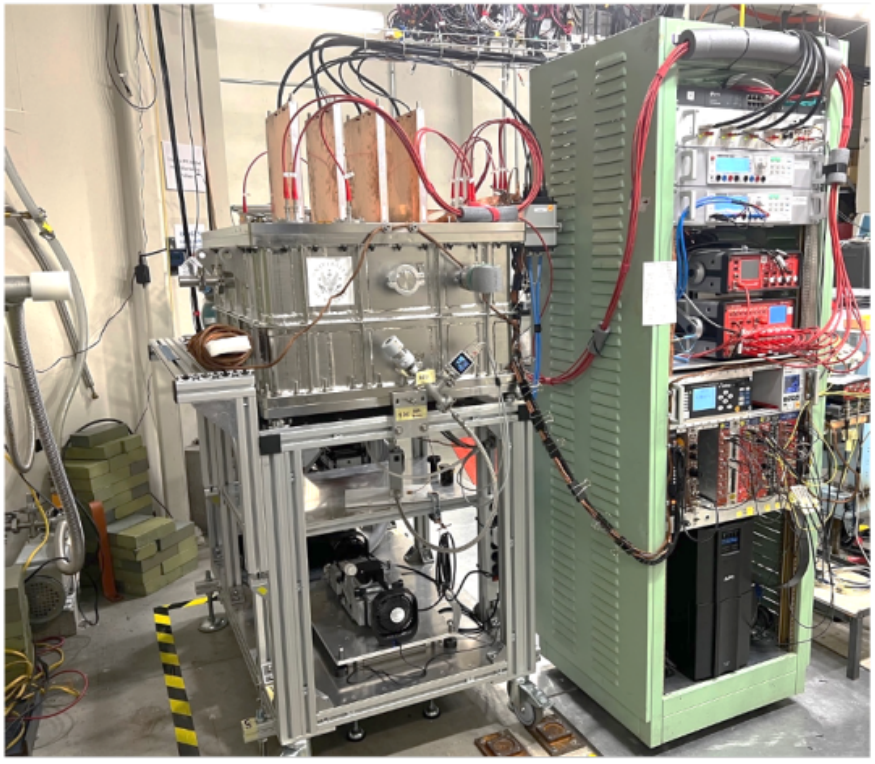

Figure 6.1: Photograph of eTPC at HIγS: Shown photographed at the HIγS Upper Target Room (UTR). Image was taken from reference [186], photo taken by Mikołaj Ćwiok, University of Warsaw.

The eTPC is used to track charged particles in its gas-filled active volume induced by photo-dissociation reactions. A cross section of the detector's low-pressure outer vessel is shown in figure 6.2, revealing various components: the internal drift chamber, the beam entrance/exit, and the front-end electronics boards mounted atop.

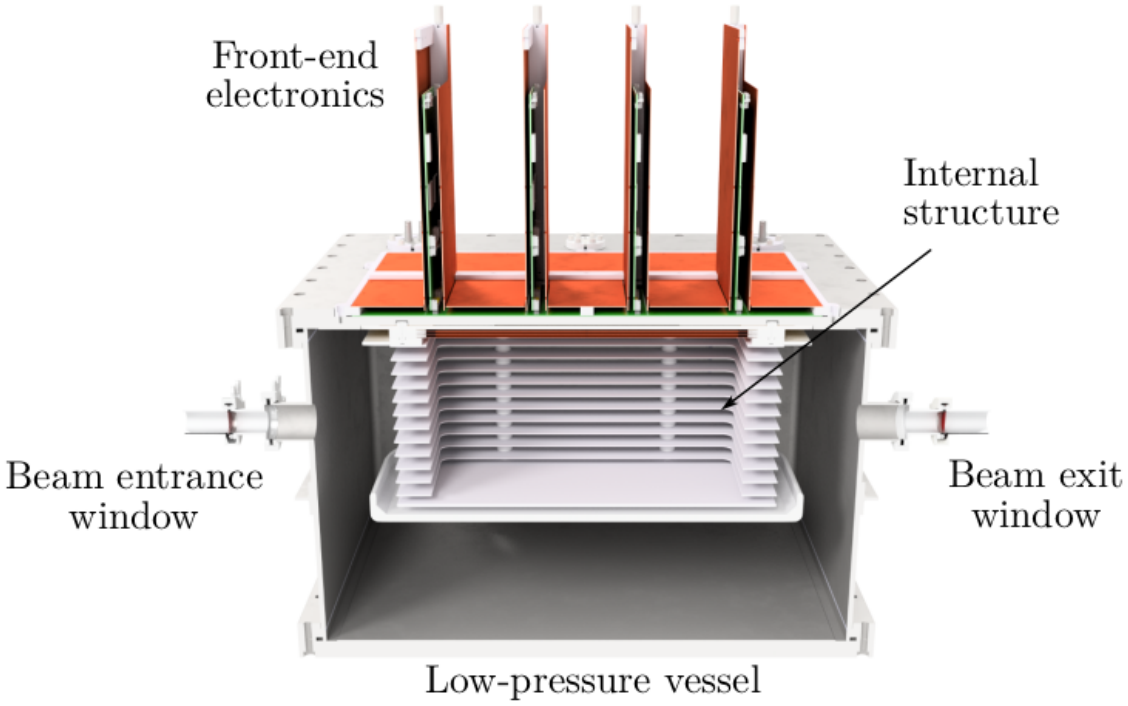

Figure 6.2: Cross Section of the eTPC Chamber: Shows the main detector components: The low-pressure vessel, drift cage, beam entrance/exit, and the front end electronics. The figure was taken from reference [187].

The main components can be broken up into four regions: the active volume, the charge multiplication region, the readout plane, and the DAQ.

6.1.1 Active Volume

Situated inside the outer vacuum vessel is the eTPC drift cage broadly defining the active area with dimensions of approximately 33(L) × 20(W) × 20(d) cm^3. The walls of the drift cage consist of twelve 2 mm thick aluminium electrodes, with a 16 mm pitch. The drift cage is enclosed by a 4 mm thick aluminium cathode plate at the bottom, and the readout plane at the atop [187]. This structure, along with the three-layer Gas

Electron Multiplier (GEM) foils and the diamond structure of the electronic readout strips, is shown flipped vertically in figure 6.3.

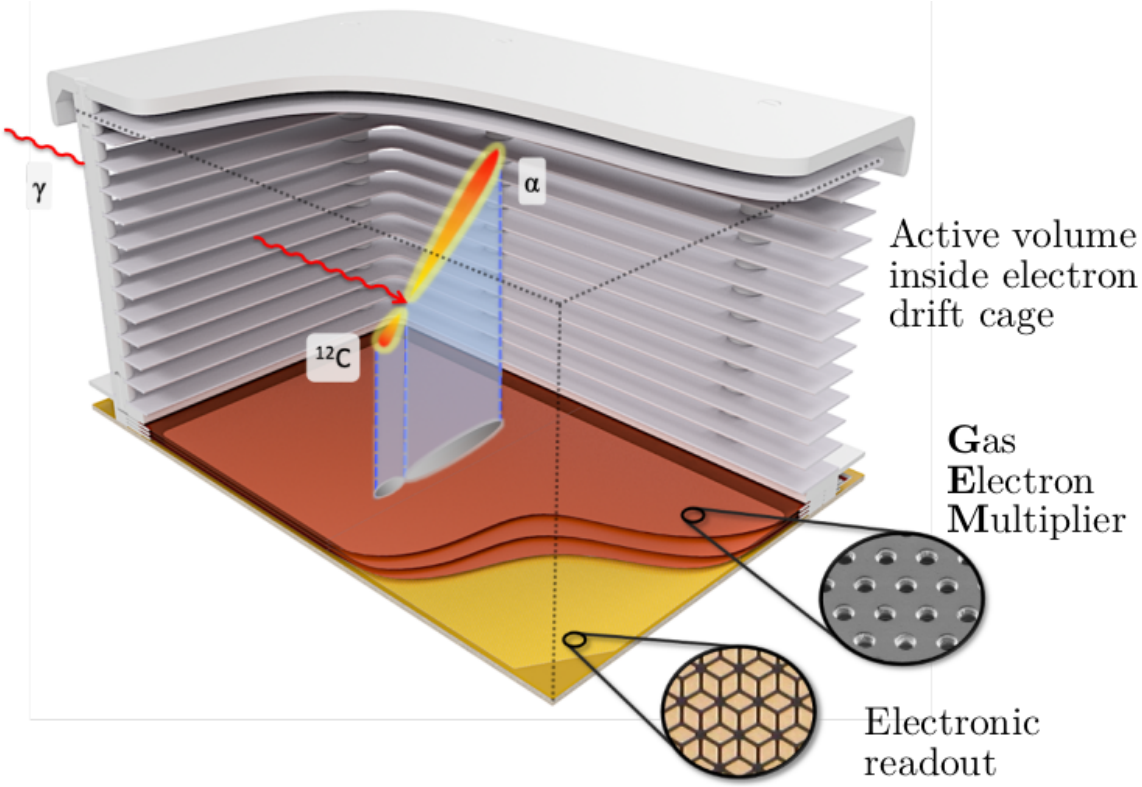

Figure 6.3: Internal Structure of the eTPC Chamber: Shows the γ beam inducing an event in the active volume (flipped vertically). The GEM foils and readout plane are shown. The figure was taken from reference [187].

6.1.2 Charge Multiplication

To record measurable signals, the electron charge cloud from events must be multiplied. To achieve this, a three-layer GEM foil [167], mounted above the drift volume, just before the readout plane, is used. Each GEM foil is made from 50 μm thick Kapton coated with a layer of copper (5 μm), with perforated holes (50 μm) at a 140 μm pitch from each other [186]. Between each successive GEM layer is a 3 mm transfer region [187]. A large bias is applied across the GEMs sufficient to cause electron avalanches. Typical operating voltages ranged from 245 to 296 V. The GEMs can be seen in figure 6.4.

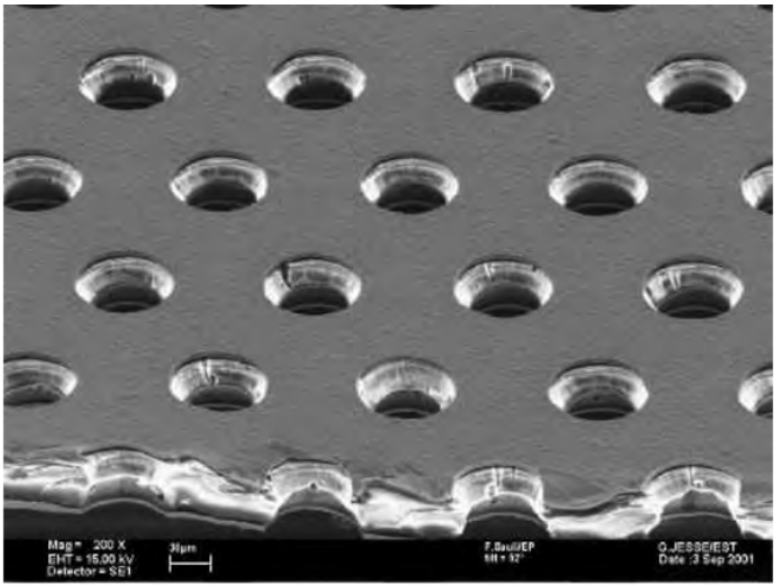

Figure 6.4: Gas Electron Multiplier Foil: Figure shows a GEM foil viewed using a microscope. The image was taken from reference [167].

6.1.3 Readout System

As noted previously, the active area is approximately 33 by 20 cm^2, defined by the outline of the field cage. The actual active area is slightly reduced because the corners of the readout plane are cut at 30°. This shape can be seen in figure 6.5. The readout plane is made from a multi-layer PCB board, with each layer of the board containing a family of interconnected diamond-shaped, gold-plated pads forming a series of "strips", denoted U,V, or W for each direction. Each family of strips is aligned along a given direction (U runs parallel to the beam), with each family oriented at 60 degrees to the previous. Each has a pitch of 1.5 mm in a given family. In total, there are 263 U-strips, 376 V-strips, and 378 W-strips, segmented across the readout plane as shown [187].

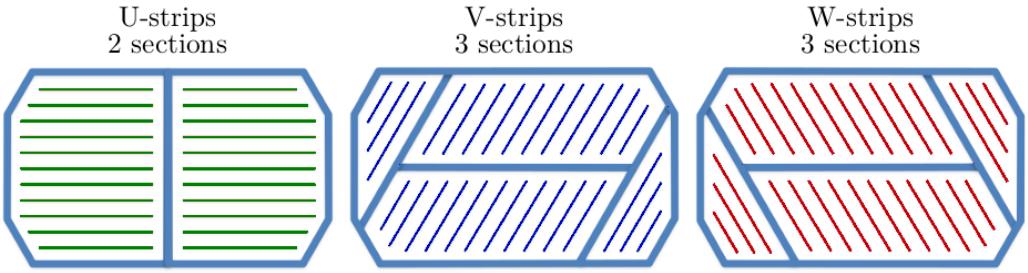

Figure 6.5: Multi-layered eTPC PCB Electronic Readout: Design of the readout plane, showing segmented strip readout. Scheme by Mikołaj Ćwiok, University of Warsaw, adapted from [186].

Signals revived from charge deposits are read on each strip independently as a function of time: $U(t)$, $V(t)$, $W(t)$, each being a different projection of the three-dimensional event. Hit localisation is achieved later in the reconstruction step by pairing charge deposits from two projections at a given common time. The crossing point of strips forms a "virtual pixel", allowing for in-plane coordinates to be reconstructed, while time provides the paired out-of-plane coordinate. The mapping between UVW space and Cartesian coordinates is explained later in the methods section.

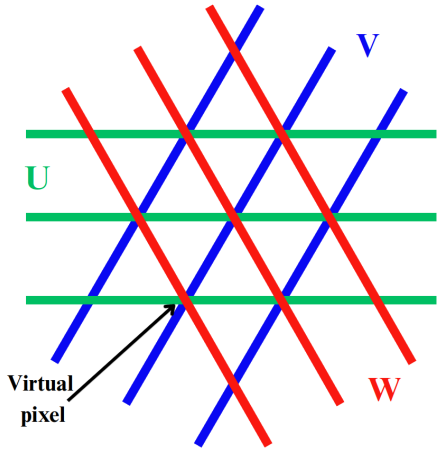

Figure 6.6: Virtual Pixel eTPC Illustration: Overlapping strips to illustrate how position determination in *det* coordinates (x,y) can be obtained by finding the crossing points of two strip families (U,V,W).

The virtual pixel structure is illustrated in figure 6.6. Note that this is a redundant coordinate system; only two projections are needed to obtain the coordinates in Cartesian space. However, the third family is useful for more complex events, as it provides

redundancy for validation.

Figure 6.7 below was adapted from reference [188] to illustrate how signals are deposited on each family of strips[1]. By using this strip readout over a pixel-based readout, the cost due to the number of channels is significantly reduced.

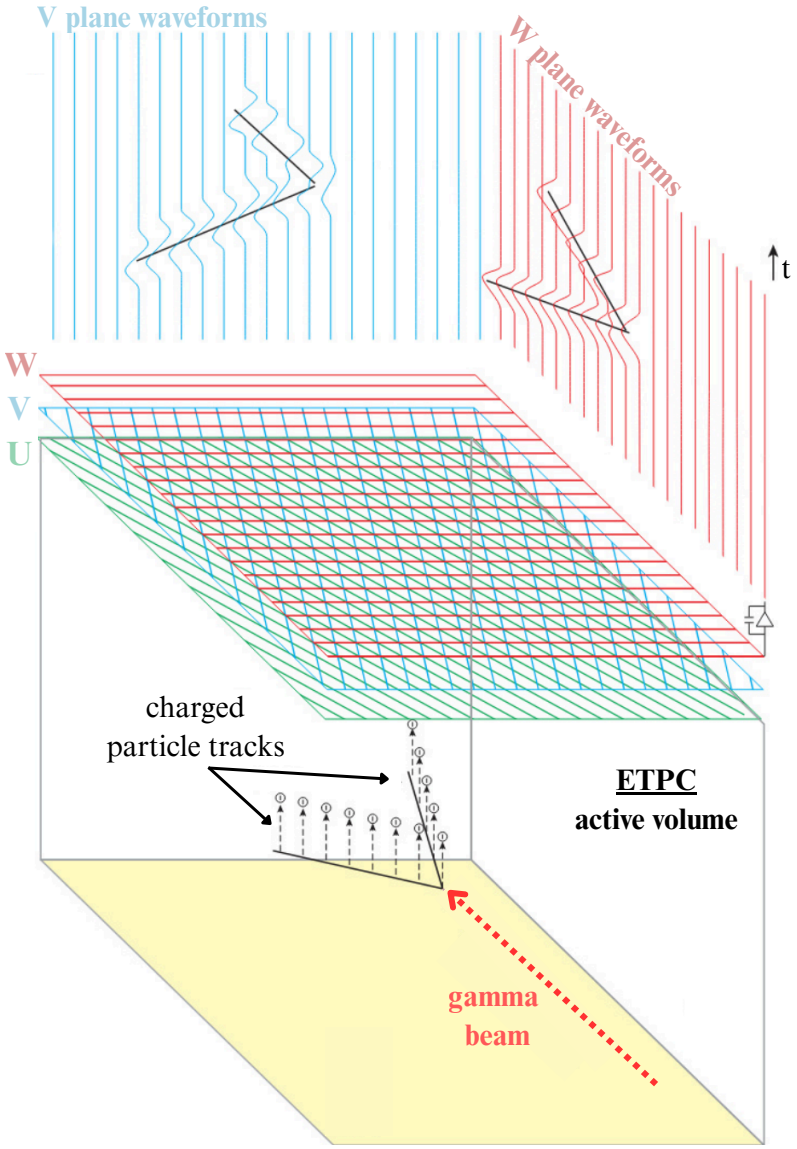

Figure 6.7: Signal Readout eTPC Illustration: Shows gamma beam inducing an event in the TPC active volume, and how signals are recorded in time for different strip families. The figure was adapted from reference [188].

[1]Note that the topology of this event is not relevant.

6.1.4 Data Acquisition System

The eTPC uses a data acquisition (DAQ) system based on General Electronics for TPCs (GET) [189]. The DAQ chain consists of several stages, starting from the UVW readout and front-end electronics, to back-end processing and data storage. Figure 6.8 provides a simplified overview of the readout chain.

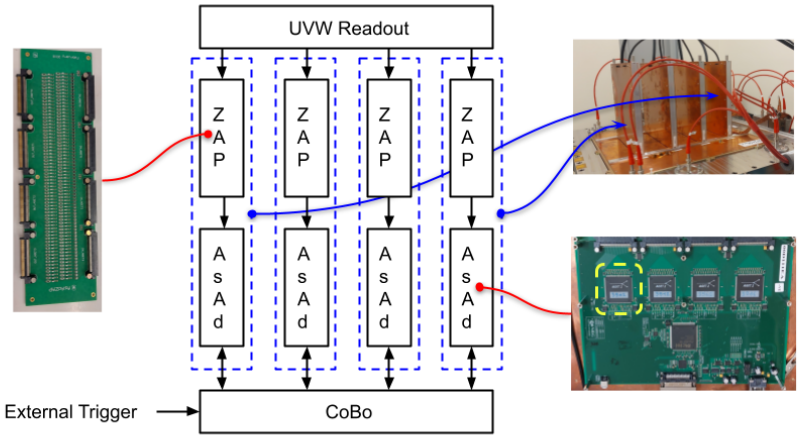

Figure 6.8: Front-end Electronics eTPC Illustration: Simplified outline of the detector readout chain, showing the path from UVW readout to Concentration Boards.

ZAP Boards. The UVW readout strips are connected to the four front-end electronics AsAd boards, mounted on top of the eTPC, via ZAP surge protection boards.

AsAd Boards. The AsAd boards are the main component in the DAQ chain. Each AsAd board is capable of providing 256 channels, and is equipped with:

- Four application-specific integrated circuit (ASIC) for GET (AGET) chips for signal shaping and amplification.
- A 4-channel, 12-bit, Analog-to-Digital Converter (ADC).
- A Field Programmable Gate Array (FPGA) circuit for board communication control.

AGET Chips. Each AGET chip has 64 physical channels and four "virtual" Fixed Pattern Noise (FPN) channels. Signals from the physical channels are amplified by a charge-sensitive amplifier (CSA) with selectable dynamic ranges of 120 fC, 240 fC, 1 pC, or 10 pC. Shaping is performed with a Sallen-Key filter, with shaping times between 70 ns and 1 μs [187]. The shaped analogue signals are stored temporarily in a Switched Capacitor Array (SCA) with 512 time buckets per channel, acting as a circular buffer operating at 1–100 MHz [190].

The FPN channels have different roles depending on the operating mode. In standard mode, they are blind to detector signals but are connected to the SCA to monitor electronic noise. In pulser calibration mode, they record the raw input step waveform, bypassing shaping.

Trigger & output. The system supports both internal and external triggers. Internal trigger mode uses signals from the last GEM layer, while external trigger mode allows for inputs from external detectors. In this experiment, internal triggering was used. Upon receiving a trigger, writing to the circular buffer is temporarily halted, and the stored analogue signals, including the 50 pre-trigger time bins, are digitised. The AsAd ADCs send data to the z-CoBo modules, which format and timestamp it before transferring it to the DAQ PC. A typical event from the four AsAd boards is approximately 1.1 MB in size [186].

6.2 Coordinate Systems

Throughout this work, two right-handed coordinate systems are used, the *det* and *beam* systems. These systems are illustrated in figure 6.9.

Beam Coordinate System. The *beam* system is the standard physics coordinate system aligned with the beam direction. In this system, z_{beam} is parallel to the beam axis, while x_{beam} and y_{beam} are perpendicular to it, with y_{beam} pointing toward the ceiling.

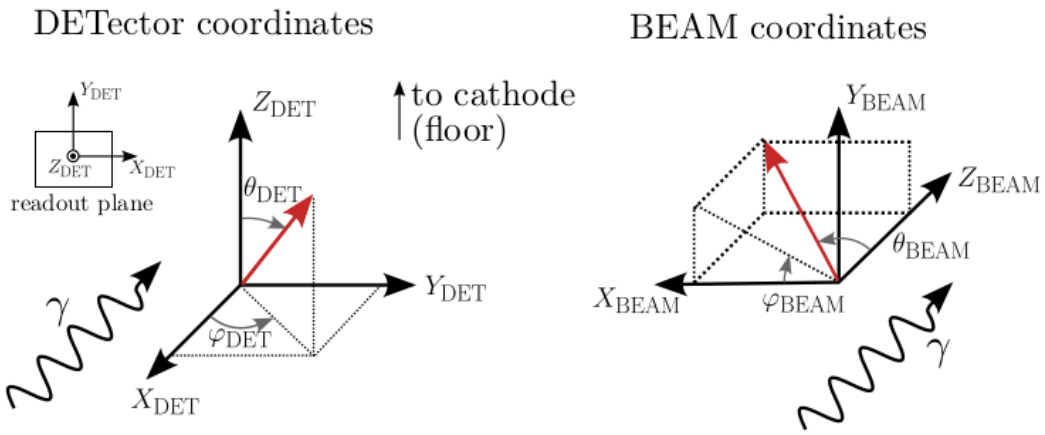

Figure 6.9: Coordinate Systems for the eTPC: Figure shows both the *det* and *beam* coordinate systems shown. The figure was taken from reference [186].

The polar coordinates in the *beam* system are defined as

$$\begin{cases} x_{beam} = r\cos(\phi_{beam})\sin(\theta_{beam}) \\ y_{beam} = r\sin(\phi_{beam})\sin(\theta_{beam}) \\ z_{beam} = r\cos(\theta_{beam}). \end{cases}$$

Det Coordinate System. The *det* system is the standard coordinate system used for event reconstruction, chosen because it aligns with the readout plane geometry. In this system, x_{det} and y_{det} lie in the readout plane, while z_{det} points out of this plane vertically downwards, anti-parallel to the drift direction. The polar coordinates in the *det* system are defined as

$$\begin{cases} x_{det} = r\cos(\phi_{det})\sin(\theta_{det}) \\ y_{det} = r\sin(\phi_{det})\sin(\theta_{det}) \\ z_{det} = r\cos(\theta_{det}) \end{cases}$$

Coordinate Transformation. To transform between these coordinate systems, the following rotation matrix is used [2],

$$\begin{pmatrix} x \\ y \\ z \end{pmatrix}_{beam} = \begin{pmatrix} 0 & -1 & 0 \\ 0 & 0 & 1 \\ -1 & 0 & 0 \end{pmatrix} \begin{pmatrix} x \\ y \\ z \end{pmatrix}_{det}$$

6.3 Experimental Overview

Data were collected from multiple beam energies, of typical FWHM $\sim$ 300 keV, spanning from $E_\gamma = 8.51$ to 13.9 MeV. These are shown for reference in figure 6.10 against the current fit to the $^{12}C(\alpha,\gamma_0)$ "world data" [46] (after applying the detailed balance factor). The beam provided in the April campaign was reported to be predominantly linearly polarised, while the August campaign was largely circularly polarised. This is later confirmed in the analysis section.

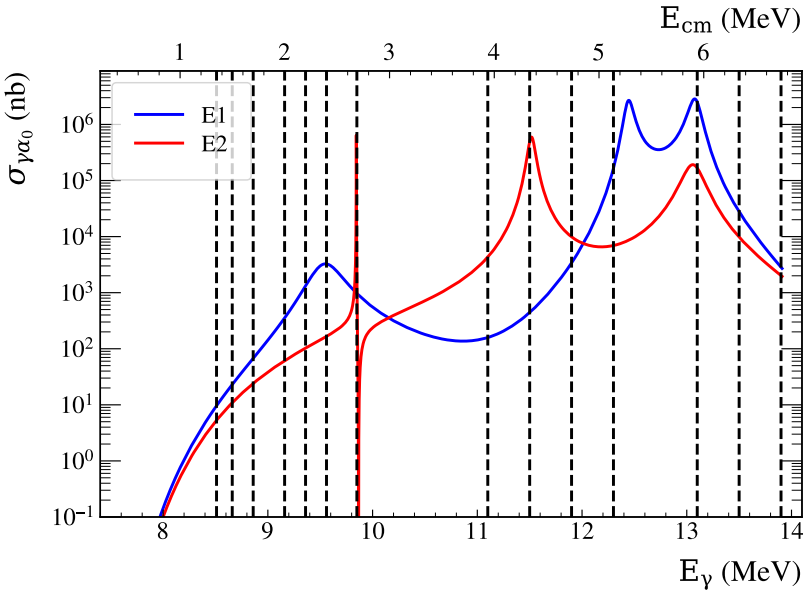

Figure 6.10: Experimental Measurement Points: Plot showing the nominal energies measured at in this experiment against the $E1$ and $E2$ cross sections for the $^{12}C(\alpha,\gamma)^{16}O$. The lineshapes were taken from reference [46].

[2] Note that this is only strictly accurate if the beam is aligned along the z direction

E_γ (MeV)	Date	Drift voltage (V)	Pressure (mbar)	Drift velocity (cm/μs)	Samp. freq. (MHz)	# events	Time (s)	Rate (cps)
8.51	Aug.	1372	130	0.390	25	54658	117167	0.47
8.66	Aug.	1372	130	0.390	25	238385	324605	0.73
8.86	Aug.	1372	130	0.390	25	164210	180677	0.91
9.16	Aug.	1568	130	0.445	25	63967	46472	1.38
9.36	Aug.	1764	130	0.500	25	57530	14815	3.88
9.56	Aug.	1764	130	0.500	25	33690	8221	4.10
9.85	Aug.	1764	130	0.500	25	36917	3490	10.58
11.1	Apr.	3332	190	0.646	25	159783	21209	7.53
11.5	Apr.	3332	190	0.646	25	247699	11742	21.10
11.9	Apr.	3332	190	0.646	25	168188	15367	10.95
12.3	Apr.	3332	190	0.646	25	253922	5070	50.08
13.1	Apr.	2744	250	0.405	12.5	284674	7417	55.25
13.5	Apr.	2744	250	0.405	12.5	567720	12682	44.77
13.9	Apr.	2744	250	0.405	12.5	528264	15059	35.1

Table 6.1: Run Parameters for the eTPC Experiment: A list of settings and information about the energies that were analysed.

The fill gas used was high-purity CO_2 of natural isotopic abundance. The pressures varied from run to run, depending on the expected energy of the events of interest. Values were either 130, 190, or 250 mbar. At each eTPC pressure, the GEM voltages were tuned to ensure sufficient amplification. The drift voltages and electronics sampling frequency were also set to ensure the full capture of the events of interest. A shaping time of 232 ns and a dynamic range of 120 fC were used constantly. All other pertinent values are listed in table 6.1. Including the drift velocities which were calculated by Magdalena Kuich (University of Warsaw) using the `MAGBOLTZ` code.

7

Methods

This section details the methods used to transform low-level measured data into high-level reconstructed physics events. It is divided into three parts: the procedure for converting raw waveforms into interpretable images; the types of events that appear in the eTPC and their general topologies; and finally, the reconstruction algorithms that enable particle identification and extraction of physical observables for the events of interest.

The reconstruction and interpretation process, which spans both the Methods and Analysis sections, are split into two stages:

Stage 1: Batch Processing was performed within the `TPCRECO` package [191], a custom-written analysis framework written by the University of Warsaw. In this analysis, the following operations are used as pre-written, since they are not specific to particular physics cases: I/O operations of raw binary files, initial waveform reconstruction, and coordinate transformations. Whereas image cleaning, event reconstruction, and the writing of high-level reconstructed objects into `ROOT` files have been custom-written for this case.

Stage 2: Event Analysis and interpretation of these files to extract physics quantities was performed outside this package, using custom-written C++ and Python codes.

7.1 Waveform Reconstruction

Once the eTPC data are extracted from their binary (GRAW) files, the raw signals can be examined channel-by-channel. They exhibit several non-ideal characteristics that require correction. These include spiking at the beginning and end of each sample, a non-linear baseline, background noise, and significant baseline differences between channels. The first three issues are illustrated in figure 7.1, which shows an "empty" raw waveform from a single physical channel, as well as the same channel averaged over 1000 events.

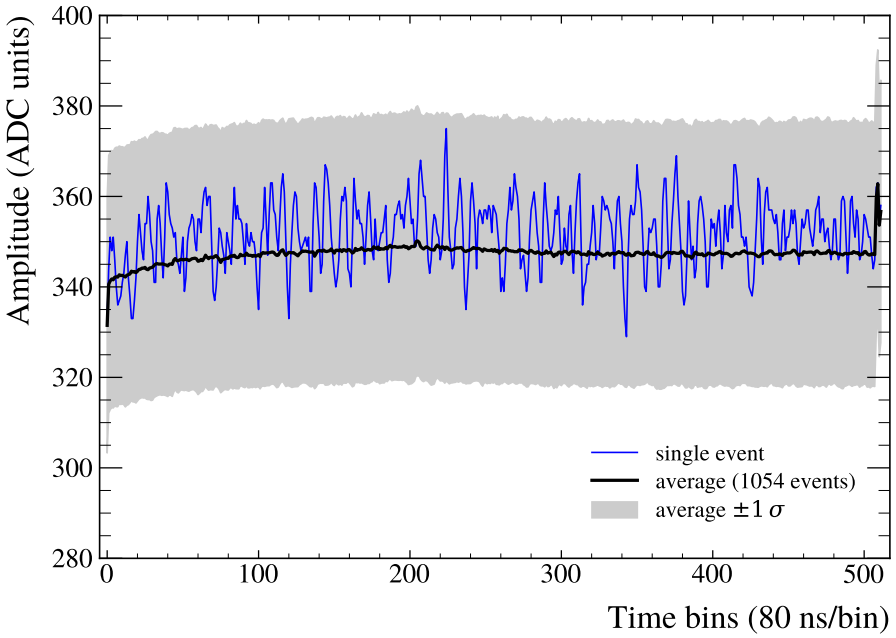

Figure 7.1: Raw eTPC Waveform: Single waveform on a given channel is shown in blue, with the average over 1K events in black, and the standard deviation in grey.

The processing steps required to transform these signals into physically meaningful waveforms are outlined by the GET collaboration [190]. This section describes and evaluates most of these corrections and outlines the process for obtaining physically meaningful images.

7.1.1 Fixed Pattern Noise

As mentioned previously, the FPN channels are not connected to any input signal, so they can be used to estimate the characteristic background from the GET electronics. In this analysis, the average background was determined for each on an AGET-by-AGET basis using all four FPN channels per AGET [1].

Figure 7.2 shows a single channel, averaged over 1000 events, before and after FPN corrections. The waveform has been scaled for visual comparison.

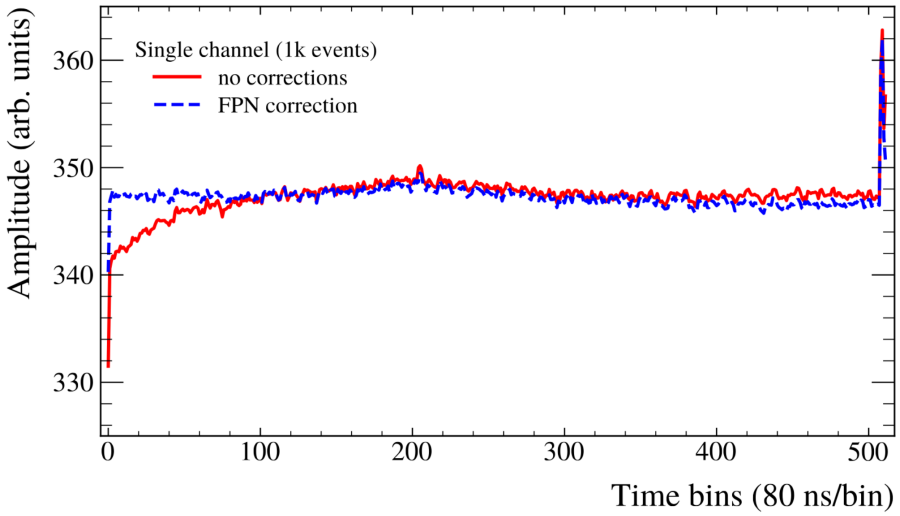

Figure 7.2: eTPC FPN Channel: Blind FPN channel shown before and after correction (approximately scaled to match amplitude).

7.1.2 Baseline Correction

The next correction addresses significant baseline differences between channels, known as baseline or pedestal correction. This variation in baseline is shown in figure 7.3.

Two correction methods are available. External pedestal runs can be used that capture empty data, triggered at a constant rate, to calculate the average background per channel over many events. Alternatively, the internal correction estimates the baseline event-by-event. Both methods consider only time bins 5-25 to avoid switching effects and real events (the trigger timing should ensure no real events occur in this region).

[1] As an alternative, one could also correct the physical channels on the AGET based on proximity to a single given FPN channel.

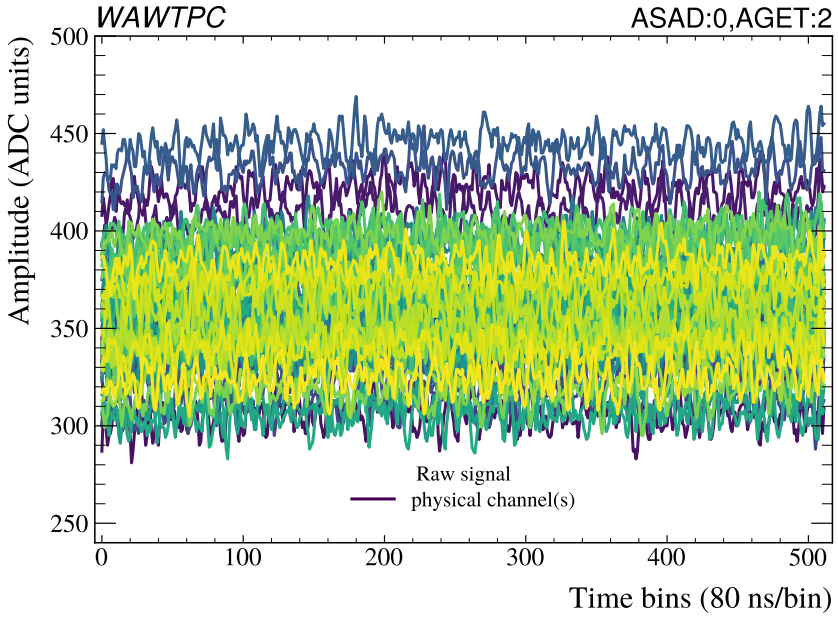

Figure 7.3: Baseline eTPC Signal Variation Before Correction: Channel-to-channel baseline differences before pedestal correction.

For this analysis, the internal method was used. Figure 7.4 shows the data from figure 7.3 after both FPN and pedestal corrections.

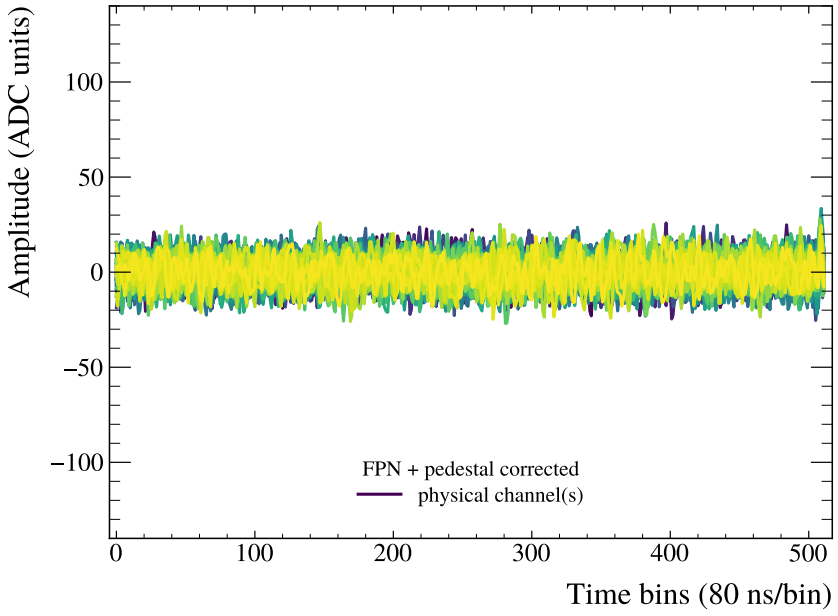

Figure 7.4: Baseline eTPC Signal Variation Post-Correction: Channel baselines following FPN and pedestal corrections.

7.1.3 Other Corrections

Additional corrections are recommended in reference [190] but are not currently included in this analysis.

Circular Buffer Memory. Circular buffer correction addresses switching effects at the signal extremes; these regions are ignored, which slightly reduces the recordable time.

Deconvolution Signal deconvolution is also recommended. This was investigated [171] but deemed not worthwhile given the trade-off between processing time and improvement gained.

7.1.4 Overview of Waveform Corrections

The effectiveness of the applied corrections is shown in figure 7.5. Here, the average of a single channel before and after all corrections is shown. Figure 7.6 shows the average noise level for each channel before and after FPN and baseline corrections. Illustrating that the noise level is not constant across channels, this is to be expected due to tolerances in the manufacturing process and differences in wire paths through the electronics resulting from the detector geometry.

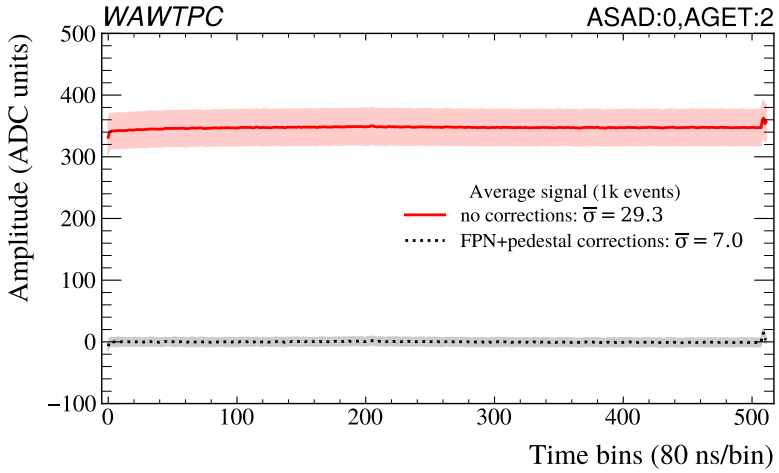

Figure 7.5: Overview of eTPC Waveform Corrections: Single channel averaged over multiple events, before and after FPN and baseline corrections.

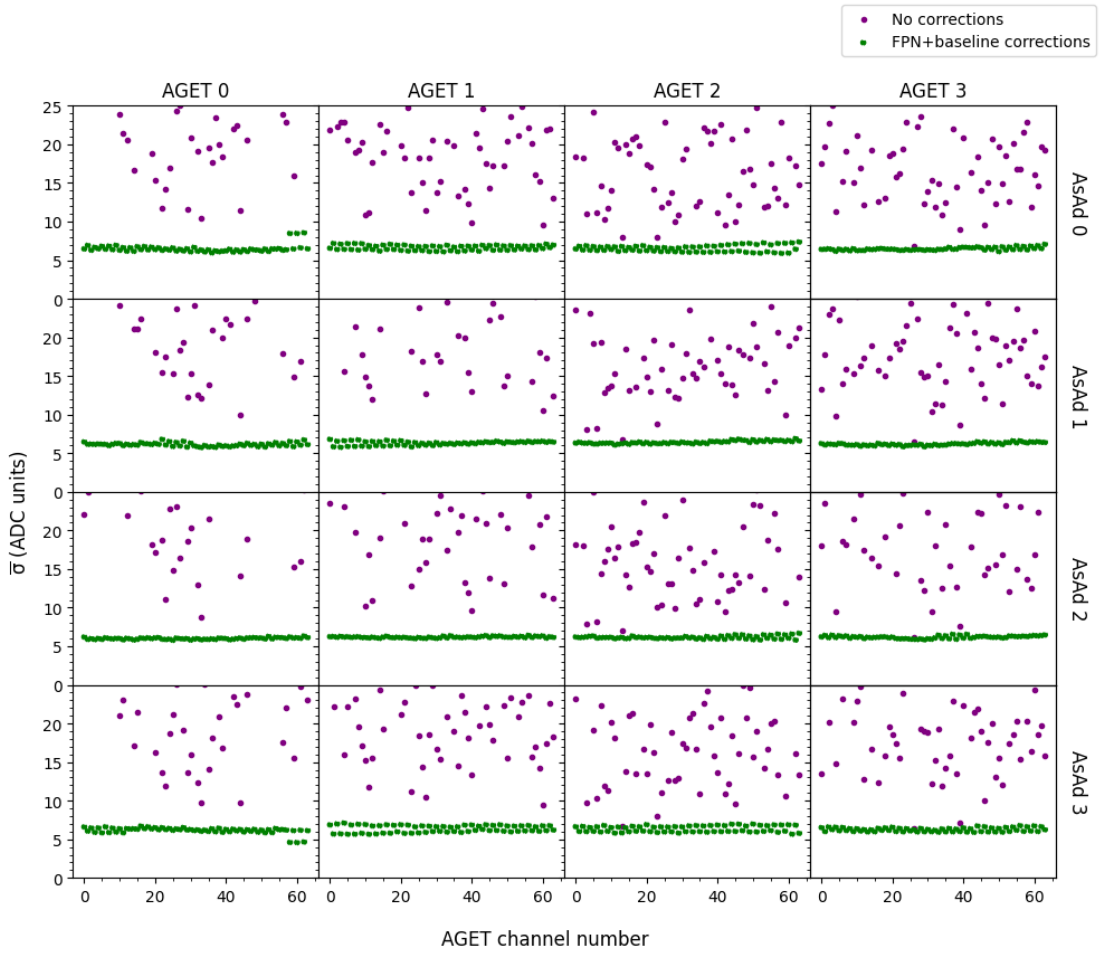

Figure 7.6: All eTPC Channel Noise Levels: Average noise level per channel before (purple) and after (green) all corrections are applied.

7.1.5 Channel Mapping

Now that the waveforms on each channel have been corrected, the data can be displayed natively as strip numbers and time bins for each projection. This representation is called "logical mapping" and is shown in figure 7.7.

To extract observables from the data, the projections must be translated into "physical mapping". The sampling rate and calculated drift velocity are used to convert the drift direction from time bins to millimetres. While the strip positions in millimetres are already known from the detector geometry. This mapping process sometimes results in a reflection, as shown in figure 7.8.

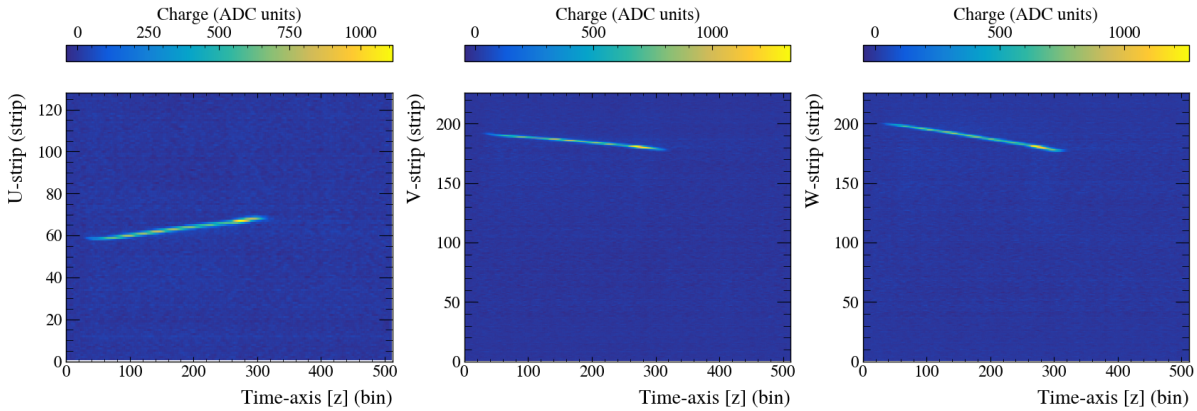

Figure 7.7: Logical eTPC channel mapping. A single "2-prong" event, shown as recorded in the eTPC across all three U, V, and W projections. The signal is displayed in terms of strip number as a function of time bin, corresponding to the raw logical mapping.

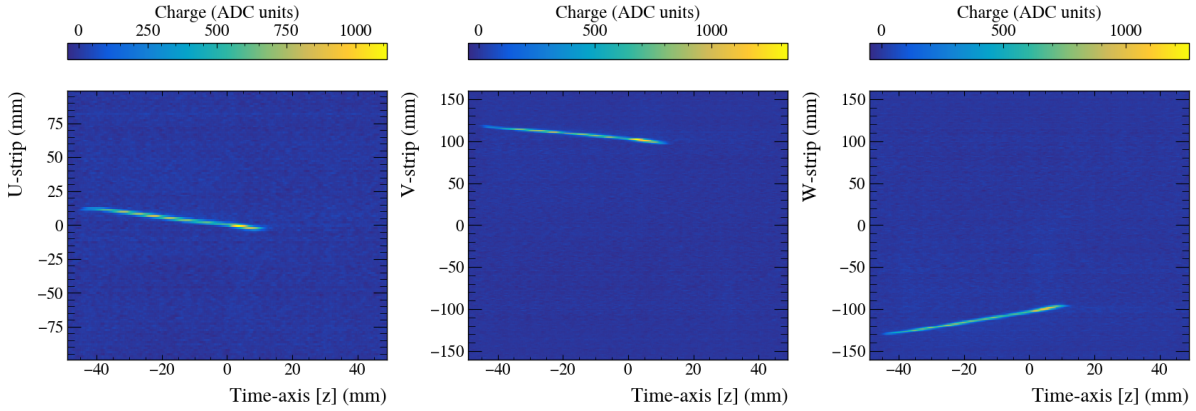

Figure 7.8: Physical eTPC channel mapping. The same "2-prong" event as shown in figure 7.7, after conversion from logical to physical mapping. Both axes of the U, V, and W projections are shown in terms of millimetres.

7.2 Event types

In order to design event reconstruction methods, one must first be aware of how events of interest and background appear in the eTPC. With CO_2 being the choice of active target, several types of beam-related events can occur. Specifically from (γ, α), (γ, n), and (γ, p) reactions on ^{16}O, ^{17}O, ^{18}O, ^{12}C, and C^{13} targets. The possible beam-related reactions are shown schematically in figure 7.9. Note that this list covers the energy range considered and is not exhaustive, but it covers the most likely events.

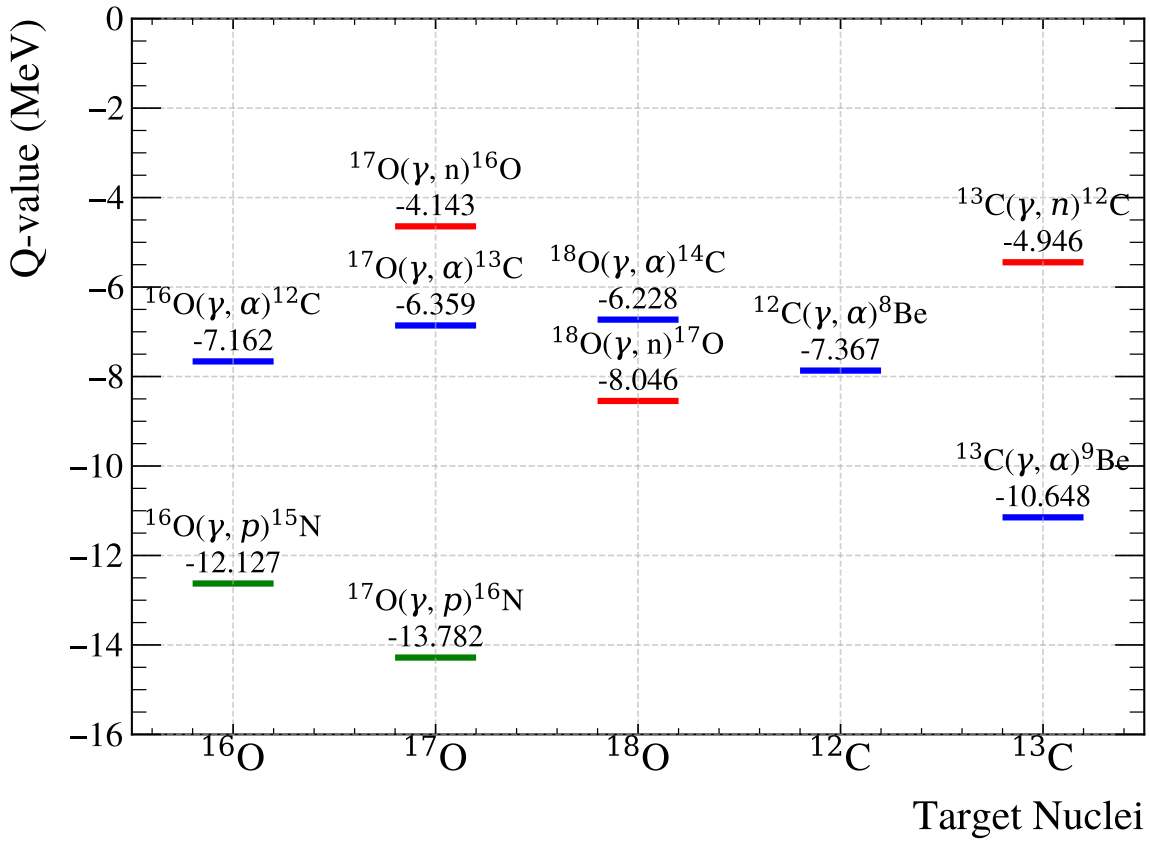

Figure 7.9: Reactions in the eTPC: Possible reactions shown as a function of target nuclei, with Q-Values on the vertical axis. The (γ, α) events are in blue, (γ, n) events in red, and (γ, p) events in green.

7.2.1 Event Topology

Event types as recorded by the eTPC can be classified by their general topology into the following classes:

- **Noise:** Events that capture electronic noise only (empty frames). As shown in figure 7.10.
- **Spots:** Events that are characterised by a single point-like charge deposit. These events are (γ, n) reactions, as shown in figure 7.11.
- **1-prong:** Events pertaining to (γ, p) reactions. Although they involve two charged particles, the heavy recoil only deposits a point-like charge. As shown in figure 7.12.
- **2-prong:** Events that leave two distinct racks, pertaining to (γ, α) events. As shown in figure 7.13.
- **3-prong:** Events that leave three tracks, these are from $(\gamma, 3\alpha)$ or $(\gamma, 3\alpha_0)$ events. As shown in figure 7.14.
- **Other:** Other rarer types of events include pile up, which are rarely seen.

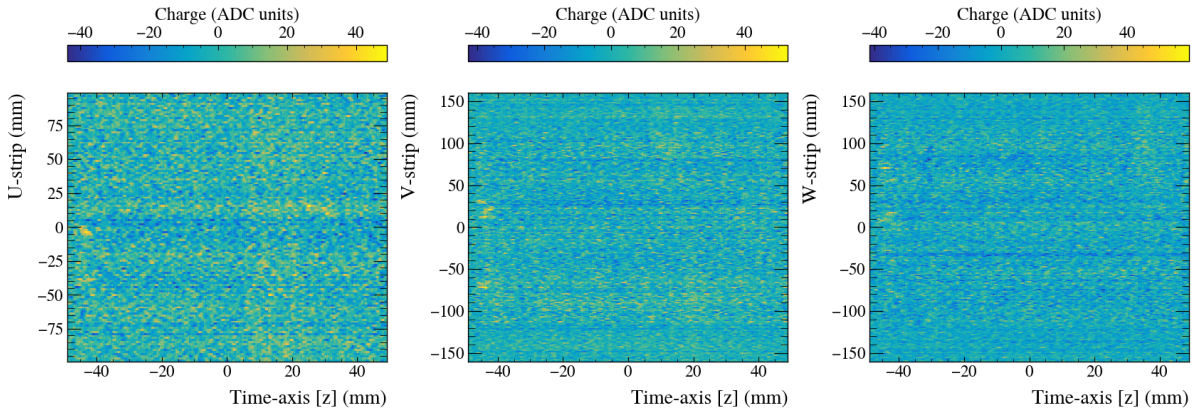

Figure 7.10: Event Classification: All physically mapped eTPC projections are shown for an electronic noise event.

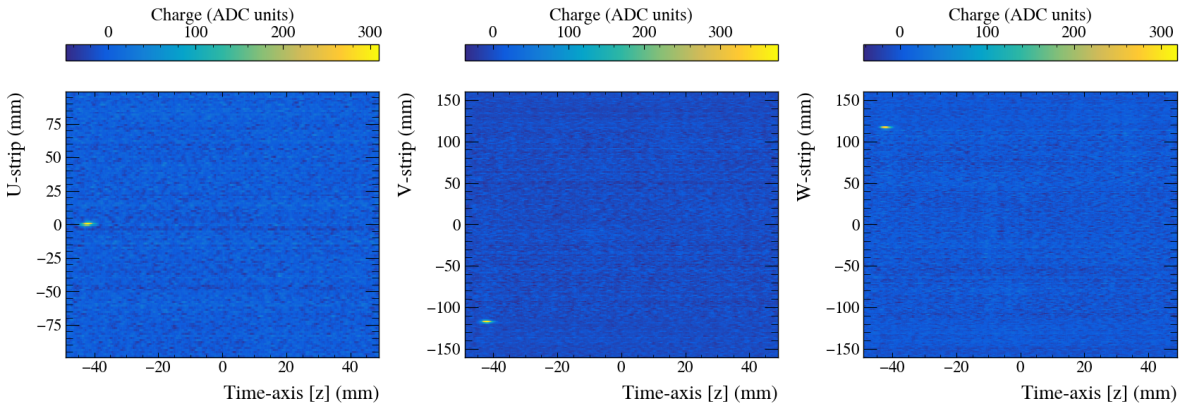

Figure 7.11: Event Classification: All physically mapped eTPC projections are shown for a spot event.

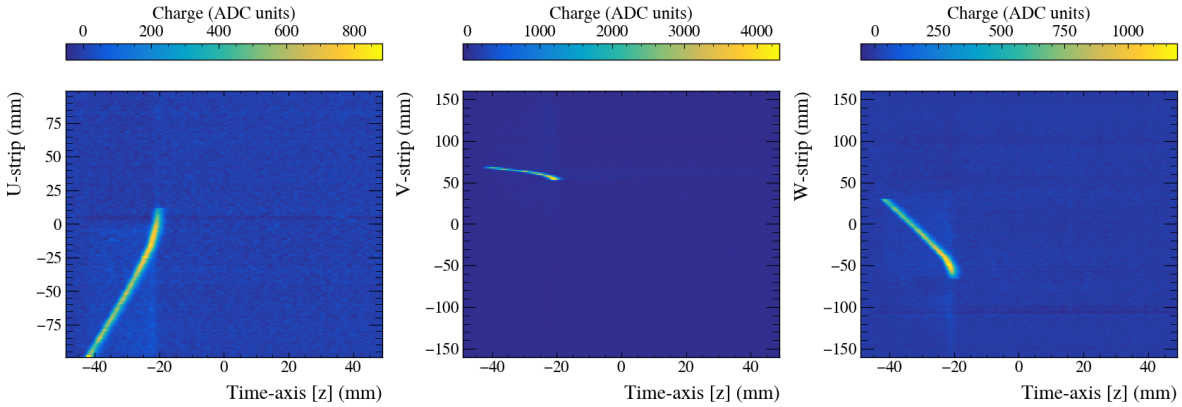

Figure 7.12: Event Classification: All physically mapped eTPC projections are shown for a 1-prong event.

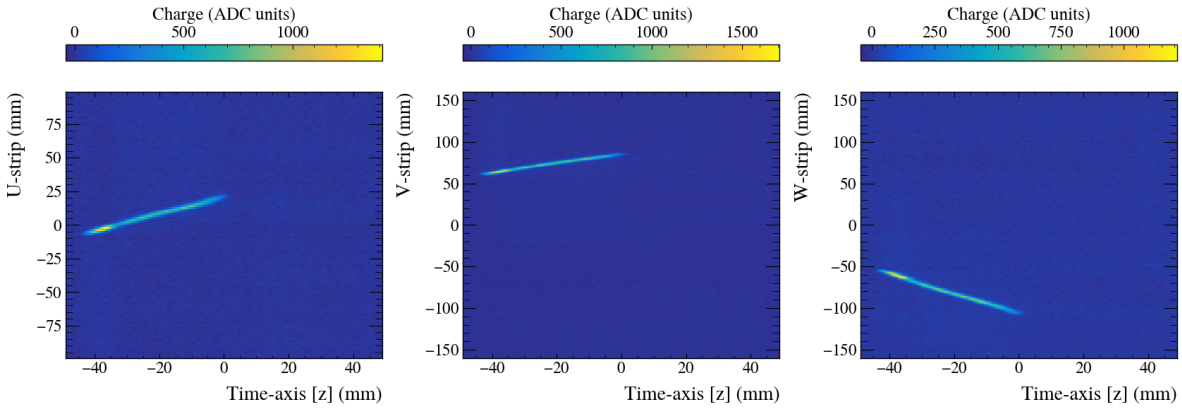

Figure 7.13: Event Classification: All physically mapped eTPC projections are shown for a 2-prong event.

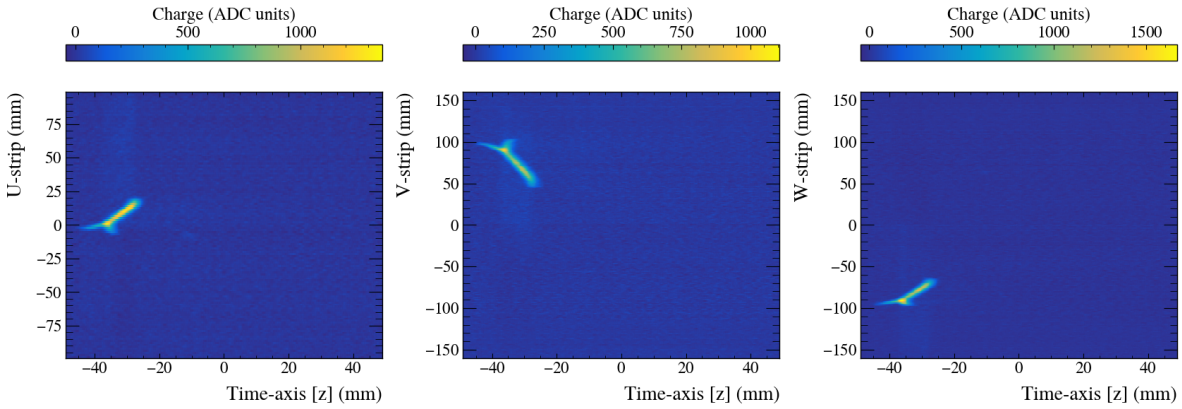

Figure 7.14: Event Classification: All physically mapped eTPC projections are shown for a 3-prong event.

7.3 Event Reconstruction

7.3.1 Image Processing

After mapping, each event was cleaned using standard image processing techniques: a pixel threshold was set at 8% of the maximum of the maximum pixel intensity, individual cluster islands were identified, then all but the largest cluster were set to zero. These steps are highlighted in each panel of figure 7.15

Two quantities are recorded at this stage:

- **Total raw charge:** charge is summed from all pixels in each projection, before cleaning.
- **Total cluster cleaned charge:** charge is summed from all pixels in each projection, after all cleaning.

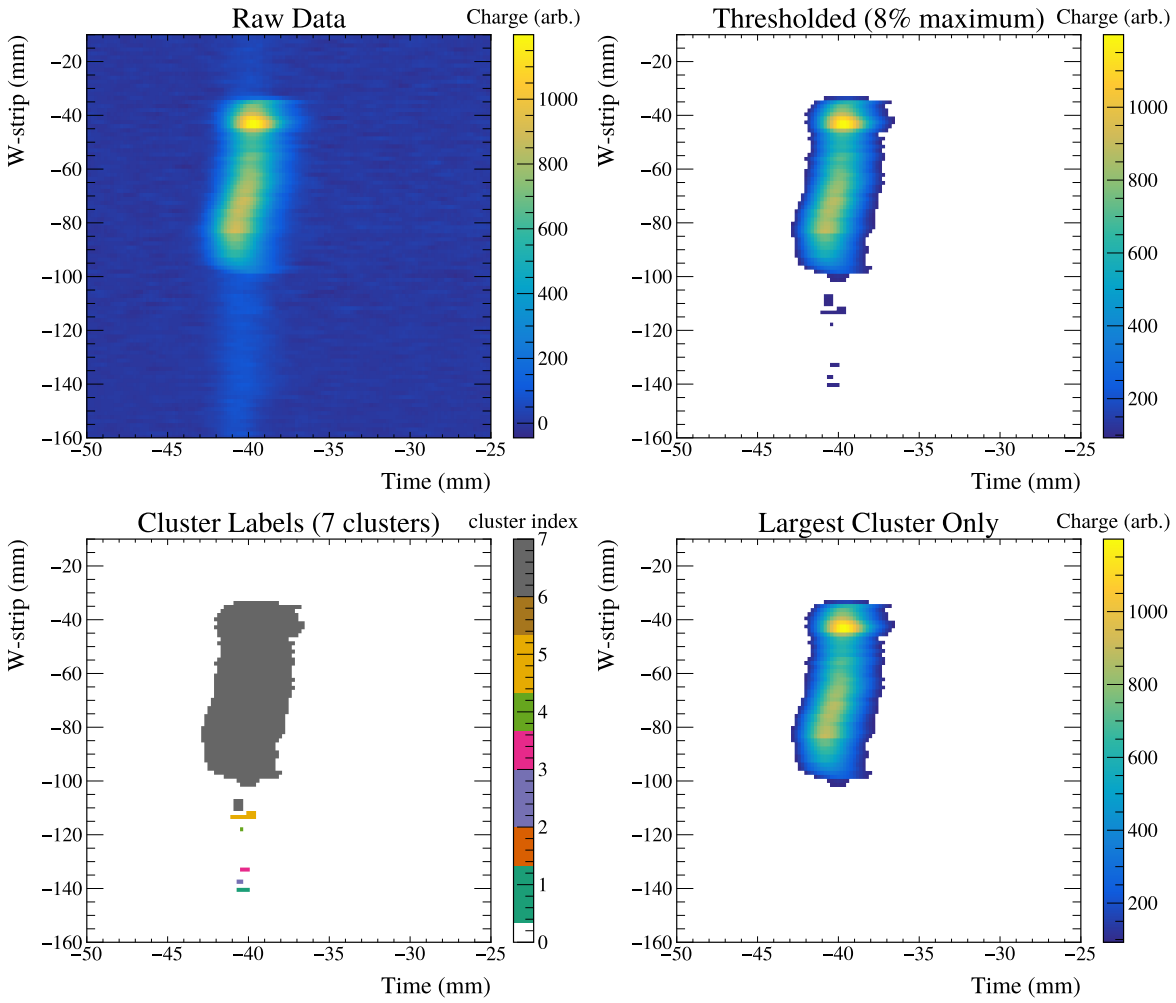

Figure 7.15: Image Cleaning in the eTPC: Event shown is a $^{16}O(\gamma, \alpha)$ event, from $E_\gamma = 9.85$ MeV. Steps taken when image cleaning. **Top-left:** Raw image (post pedestal & FPN corrections). **Top-right:** Image after applying 8% maximum pixel threshold. **Bottom-left:** cluster search identifying islands of charge. **Bottom-right:** Original image after applying the mask of the largest cluster of charge.

7.3.2 Track Reconstruction

The track reconstruction algorithm will attempt to reconstruct the two longest track lengths from a given common vertex. It works on each projection independently, extracting both the strip position (U/V/W) and the z position for each endpoint and the reaction vertex. These are later translated to Cartesian coordinates. For the following example, only the W-strip projection is shown.

First, the two most spatially separated pixels are identified. These are set as preliminary endpoints, denoted as $\mathbf{p}_1$ and $\mathbf{p}_2$, shown in the left panel of figure 7.16. The pixel containing

the most charge in the image, $\mathbf{p}_{\text{max}}$, is then located. Using the distance between $\mathbf{p}_1$, $\mathbf{p}_2$, and $\mathbf{p}_{\text{max}}$, the "ion-end" (corresponding to either a ^{12}C ion or α particle from the decay of ^{8}Be) and "alpha-end" (corresponding to α_0) can be designated as $\mathbf{p}_{\text{ion}}$ and $\mathbf{p}_\alpha$ respectively. This is shown in panel two of figure 7.16

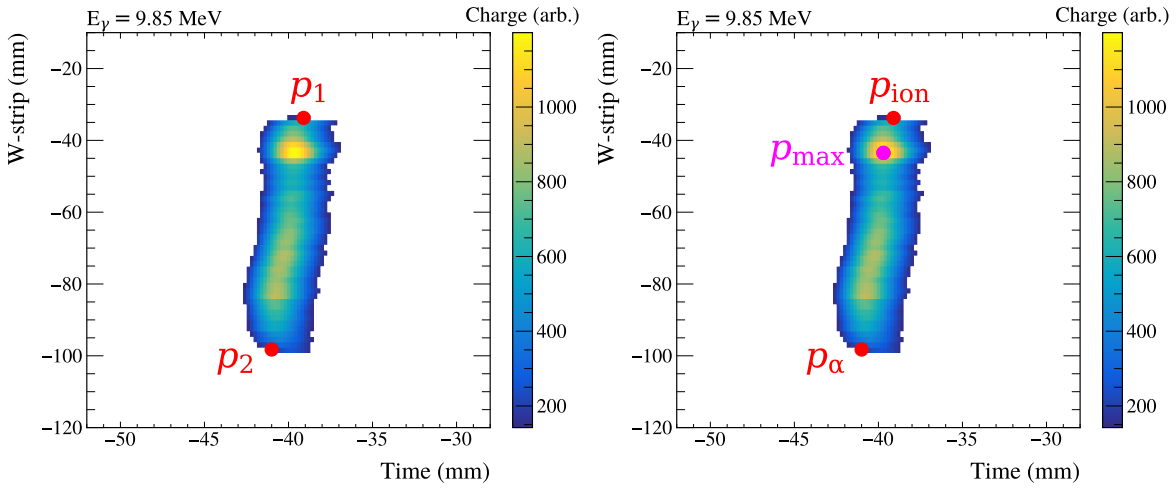

Figure 7.16: Event Reconstruction in the eTPC 1. Left: Initial endpoints $\mathbf{p_1}$ & $\mathbf{p_2}$ are identified as the maximumly separated points. **Right:** $\mathbf{p}_{\text{max}}$ is identified as the pixel with maximum charge deposition, and α and Ion end are assigned.

The vertex position $\mathbf{p}_{\text{vertex}}$ is then determined by analysing the charge distribution projected along the axis $\hat{\mathbf{v}}_{(\mathbf{p}_{\text{max}}-\mathbf{p}_\alpha)}$, which is defined as the unit vector point along $\mathbf{p}_{\text{max}}-\mathbf{p}_\alpha$. This line is shown as the dashed black line in the left panel of figure 7.17. The charge is then projected onto this line, shown in the right panel of figure 7.17. The bin containing the steepest gradient in this projection (distance from $\mathbf{p}_\alpha = 52$ mm), combined with the unit vector, $\hat{\mathbf{v}}_{(\mathbf{p}_{\text{max}}-\mathbf{p}_\alpha)}$, provides the approximate vertex location, $\mathbf{p}_{\text{vertex}}$.

The left panel of figure 7.18 shows the approximate vertex location along with both ion endpoints. To refine the selection of $\mathbf{p}_{\text{vertex}}$ and $\mathbf{p}_\alpha$, the data between these points form a subsample, which are linearly fit using χ^2 minimisation, shown in the right panel of figure 7.18. The points, $\mathbf{p}_{\text{vertex}}$ and $\mathbf{p}_\alpha$, are updated by selecting the first and last illuminated pixels along this fitted line in the subsample.

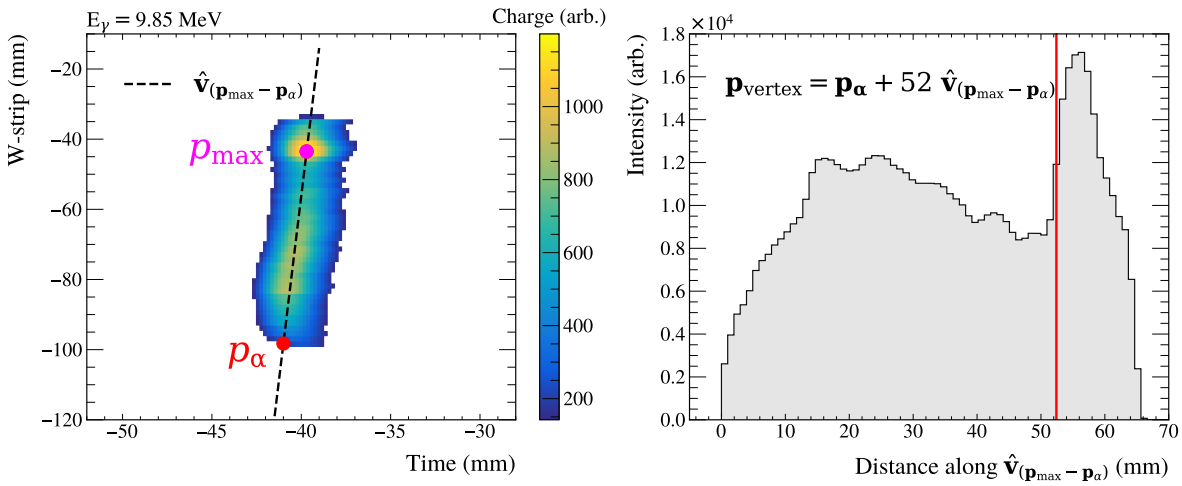

Figure 7.17: Event Reconstruction in the eTPC 2. Left: The projection line, $\hat{\mathbf{v}}_{(\mathbf{p}_{max}-\mathbf{p}_\alpha)}$, is identified as the line that passes through $\mathbf{p}_{max}$ and $\mathbf{p}_\alpha$. **Right:** Charge is projected onto $\hat{\mathbf{v}}_{(\mathbf{p}_{max}-\mathbf{p}_\alpha)}$ and the bin of maximal gradient is identified (red line).

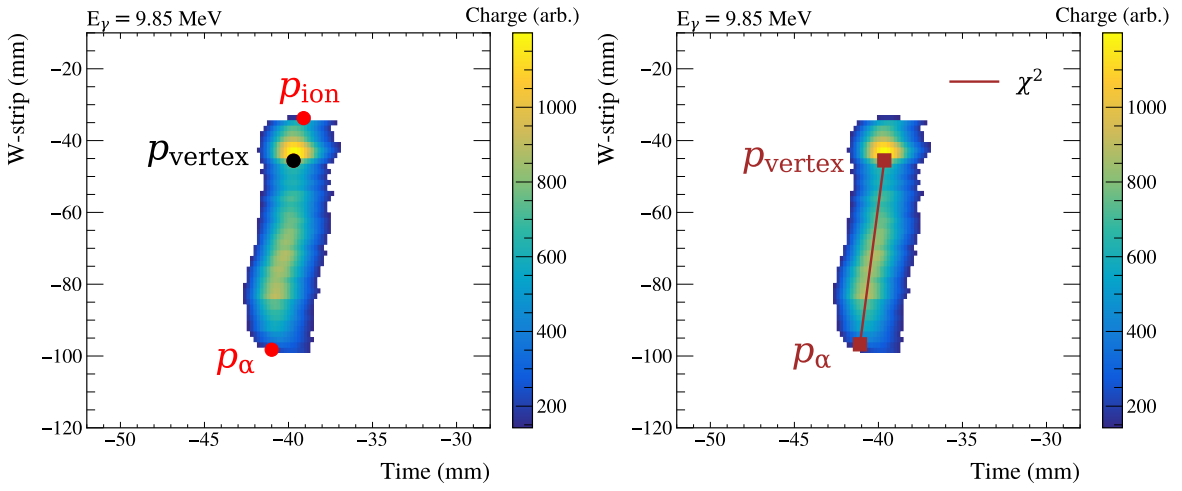

Figure 7.18: Event Reconstruction in the eTPC 3. Left: $\mathbf{p}_{vertex}$ is located. **Right:** Using the fit-line $\mathbf{p}_{vertex}$ and $\mathbf{p}_\alpha$ are updated.

Monte Carlo studies have shown that applying the same fitting procedure to refine the ion-end position is unreliable due to insufficient track length. Therefore, the initial $\mathbf{p}_{ion}$ approximation is retained.

Cartesian Coordinate Transformation

To obtain a representation of the reconstructed events in the native *det* coordinate system, the following transformation is used. Assuming that the time axis has not yet been converted and the drift velocity is given by v_d, the following transformation can be used [186]

$$\begin{pmatrix} u \\ v \\ w \\ t \end{pmatrix} = \begin{pmatrix} \cos(0) & \sin(0) & 0 \\ \cos\left(-\frac{2\pi}{3}\right) & \sin\left(-\frac{2\pi}{3}\right) & 0 \\ \cos\left(-\frac{\pi}{3}\right) & \sin\left(-\frac{\pi}{3}\right) & 0 \\ 0 & 0 & \frac{1}{v_d} \end{pmatrix} \begin{pmatrix} x_{\text{det}} \\ y_{\text{det}} \\ z_{\text{det}} \end{pmatrix}, \tag{7.3.2.1}$$

where the angles used in this matrix correspond to the orientation of the strip families.

However, the UVW readout system is redundant, meaning the transformation to detector coordinates is non-invertible when using all three projections simultaneously. To address this issue, this analysis only uses two strip families at a time, reducing the coordinate system to an invertible one [186]. A voting system was implemented to determine which two strip families to use.

Voting. Since the z-positions of the reconstructed points obtained from each projection should be the same, the optimal combination of UVW was determined by comparing those z-positions ($\mathbf{z}_{\text{vertex}}$, $\mathbf{z}_{\text{ion}}$, $\mathbf{z}_{\alpha}$). The pair of projections yielding the closest matching reconstructed z-positions was retained, and the average z-position between them was computed. This comparison was quantified through the following distance metrics

$$\begin{aligned} D_{UV} &= \sqrt{(z^U_{\text{vertex}} - z^V_{\text{vertex}})^2 + (z^U_{\text{ion}} - z^V_{\text{ion}})^2 + (z^U_{\alpha} - z^V_{\alpha})^2}, \\ D_{UW} &= \sqrt{(z^U_{\text{vertex}} - z^W_{\text{vertex}})^2 + (z^U_{\text{ion}} - z^W_{\text{ion}})^2 + (z^U_{\alpha} - z^W_{\alpha})^2}, \\ D_{VW} &= \sqrt{(z^V_{\text{vertex}} - z^W_{\text{vertex}})^2 + (z^V_{\text{ion}} - z^W_{\text{ion}})^2 + (z^V_{\alpha} - z^W_{\alpha})^2}. \end{aligned}$$

Transformation. Based on the selected projection pair, the reduced transformation matrix becomes invertible, and the following transformations can be applied.

UV Coordinate Pair:

$$\begin{pmatrix} x_{\text{det}} \\ y_{\text{det}} \\ z_{\text{det}} \end{pmatrix} = \begin{pmatrix} \cos(0) & \sin(0) & 0 \\ \cos\left(-\frac{2\pi}{3}\right) & \sin\left(-\frac{2\pi}{3}\right) & 0 \\ 0 & 0 & \frac{1}{v_d} \end{pmatrix}^{-1} \begin{pmatrix} u \\ v \\ t \end{pmatrix}. \tag{7.3.2.2}$$

UW Coordinate Pair:

$$\begin{pmatrix} x_{\text{det}} \\ y_{\text{det}} \\ z_{\text{det}} \end{pmatrix} = \begin{pmatrix} \cos(0) & \sin(0) & 0 \\ \cos\left(-\frac{\pi}{3}\right) & \sin\left(-\frac{\pi}{3}\right) & 0 \\ 0 & 0 & \frac{1}{v_d} \end{pmatrix}^{-1} \begin{pmatrix} u \\ w \\ t \end{pmatrix}. \tag{7.3.2.3}$$

VW Coordinate Pair:

$$\begin{pmatrix} x_{\text{det}} \\ y_{\text{det}} \\ z_{\text{det}} \end{pmatrix} = \begin{pmatrix} \cos\left(-\frac{2\pi}{3}\right) & \sin\left(-\frac{2\pi}{3}\right) & 0 \\ \cos\left(-\frac{\pi}{3}\right) & \sin\left(-\frac{\pi}{3}\right) & 0 \\ 0 & 0 & \frac{1}{v_d} \end{pmatrix}^{-1} \begin{pmatrix} v \\ w \\ t \end{pmatrix}. \tag{7.3.2.4}$$

7.3.3 Nominal Momentum Reconstruction

With both the ion and α track ends reconstructed in Cartesian space, momentum reconstruction can be performed. The lab-frame angles are inherently known, and energies can be obtained using `SRIM` energy-loss tables.

Depending on the hypothesis of the reaction, one can use the γ-beam energy from the HPGe detector, listed in table 8.8, to boost the particle four-momenta to the centre-of-mass frame, improving energy resolution.

Note that calibration is required to reproduce the energies of known states. Also, an angle-based correction is needed to account for reconstruction bias. Both of these corrections are outlined later.

7.3.4 Q-ratio

In addition to the reconstructed endpoints and the total event charge, a charge ratio metric, dubbed Q-ratio, was also saved at this stage. As the reconstruction method described previously extracts only two of the tracks, information is lost from the third in the case of ^{12}C decays. Due to the closeness of the Q-values of the two reactions of interest, this information was necessary to separate the two channels.

This analysis uses the unit vector defined as $\hat{\mathbf{v}}(\mathbf{p}_{\text{vertex}} - \mathbf{p}_\alpha)$, and the line perpendicular to this, defined as $\hat{\mathbf{v}}_{\perp(\mathbf{p}_{\text{vertex}} - \mathbf{p}_\alpha)}$, to separate the projections into two separate regions, as shown in figure 7.19.

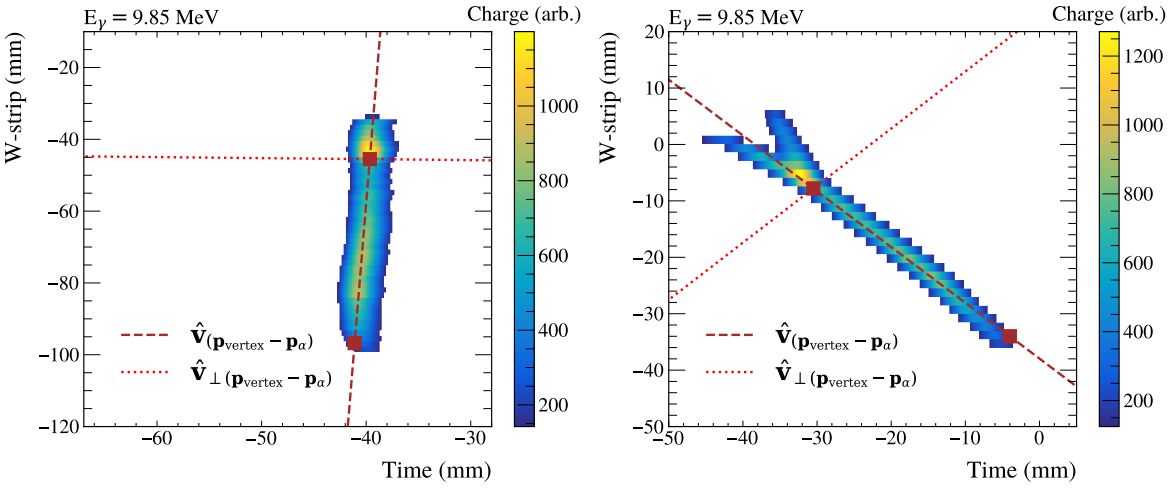

Figure 7.19: Q-ratio Image Segmentation: The line through the α endpoint and vertex is shown, as well as the line tangent to that that passes through the vertex for ^{16}O (left panel) and ^{12}C (right panel) events.

The charge is summed independently in both regions. The side that contains the α end is defined as Q_α, and the side that contains the ion end is defined as Q_{ion}. The ratio of these quantities gives

$$Q_{\text{ratio}} = \frac{Q_\alpha}{Q_{\text{ion}} + Q_\alpha}. \tag{7.3.4.1}$$

Per event, three values of this quantity are obtained − one from each UVW image independently. The Q_{ratio} value used in the analysis is the average of the two closest matching ratios.

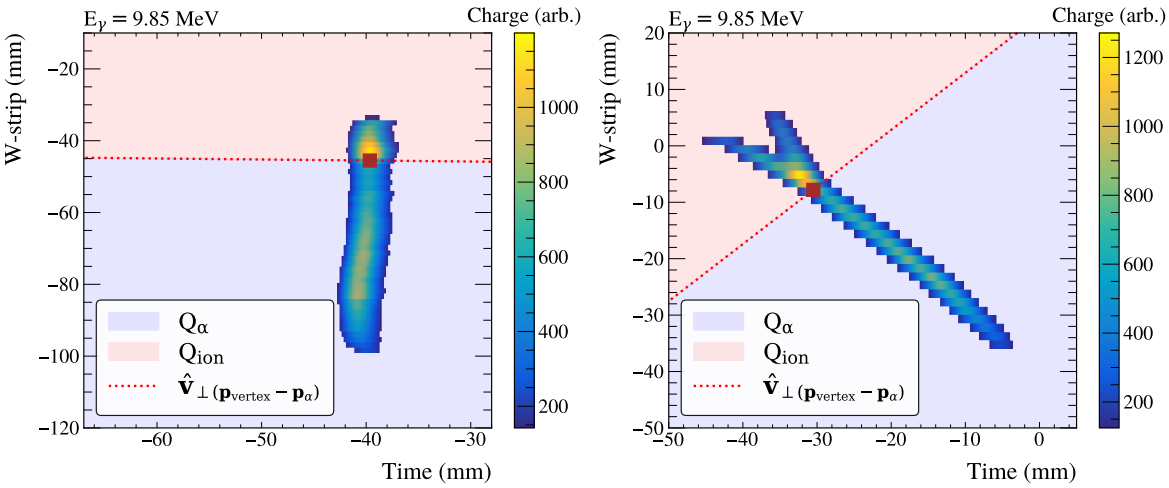

Figure 7.20: Q-ratio Extraction: The images are split into two regions, where the pixels are summed to calculate the Q-ratio, for ^{16}O (left panel) and ^{12}C (right panel) events.

8

Analysis

This chapter details the analysis steps required to extract the ^{12}C and ^{16}O photo-dissociation cross sections. First, the reconstruction corrections and resolutions in the eTPC are presented. The HIγS beam characterisation follows this, and then the data reduction cuts used to isolate ^{12}C and ^{16}O photo-dissociation events. Next, the centre-of-mass energy calibration and resolution are discussed, followed by angular efficiency corrections. The cross section normalisation procedure is then described, before the final two sections present the extracted ^{16}O and ^{12}C cross sections.

8.1 Reconstruction Corrections & Resolutions

Before detailing the complete eTPC data reduction procedure, it is essential to investigate event-by-event corrections to assess potential bias introduced by the reconstruction process. Detailed Monte-Carlo simulations were done at each nominal beam energy for both ^{12}C and

^{16}O photo-dissociation reactions, as discussed in appendix E. Both these simulated data and experimental data are used to assess these effects, and angular resolutions are also obtained.

8.1.1 Angular Reconstruction Bias

The key physical observables obtained in this analysis are derived from the angles of events relative to the beam direction. Poorly implemented reconstruction algorithms can introduce biases in these angles, thereby affecting the extracted physics results. To assess such biases, the simulated data were analysed. Since the drift velocity, a key parameter affecting track reconstruction, is known at truth-level, this study isolates biases arising solely from the reconstruction algorithm—the ability to extract endpoint and vertex positions. Events were simulated and reconstructed, and the difference between generated and reconstructed angles was tracked as a function of the reconstructed value (or its cosine).

From this process, a systematic reconstruction bias was found corresponding to the $\theta_{\text{det}}^{\text{Lab}}$ angle. This bias is shown for ^{16}O photo-dissociation events at $E_{\gamma} = 9.56$ MeV as a function of its cosine in figure 8.1. This sinusoidal behaviour, if left uncorrected, will propagate to the beam coordinates and thus bias the angular distributions. The error distributions for $\theta_{\text{det}}^{\text{Lab}}$ were fitted using a sinusoidal function to quantify the bias

$$Y(\cos\theta_{\text{DET}}) = \frac{180}{\pi} A \sin(\omega \cos\theta_{\text{DET}} + \phi) + b, \tag{8.1.1.1}$$

where A is the amplitude, ϕ the shift, ω the angular frequency, and b the offset. The fitted parameters for each nominal beam energy. and event-type are listed in appendix H. The maximum angular correction is approximately one degree. These corrections are applied to both experimental and simulated data during reconstruction, depending on the reaction channel being analysed.

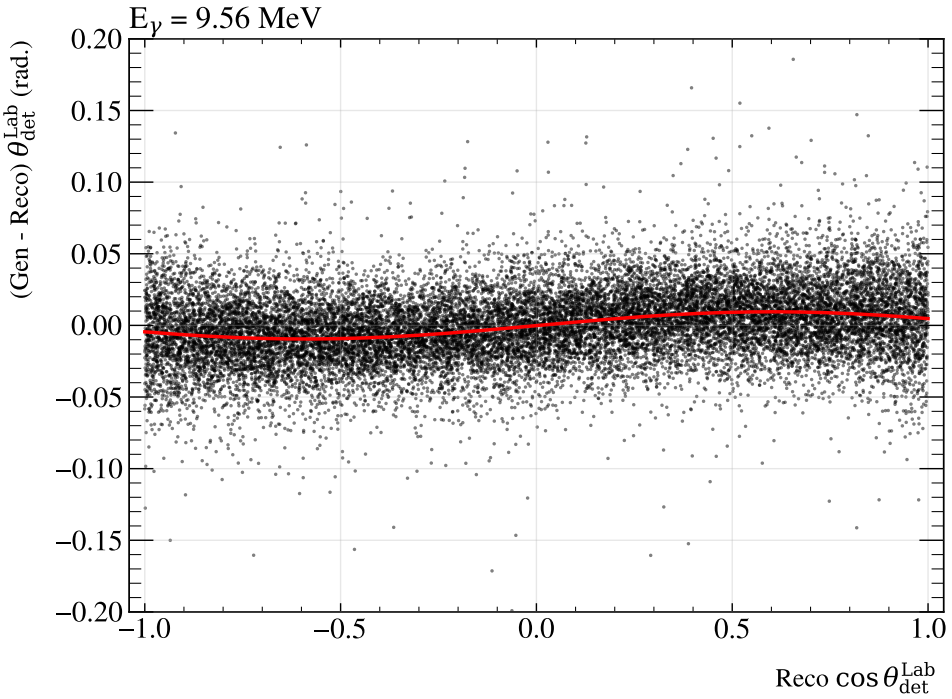

Figure 8.1: Simulated Angular Distribution Error vs. Reconstructed Value. The observed angular reconstruction bias in $\theta^{\mathrm{Lab}}_{\mathrm{det}}$ is shown for ^{16}O photo-dissociation events at $E_\gamma = 9.56$ MeV. This is quantified by fitting equation (8.1.1.1), with values listed for all energies in table H.1.

8.1.2 Angular Resolutions

With the source of the systematic bias in angular reconstruction, θ_{det}, quantified, the corrected simulated data were used to estimate the angular resolution for each nominal beam energy. The angular resolutions were obtained for each reconstructed *lab* angle, as shown in figure 8.2, by fitting a Gaussian distribution to the reconstruction error. This procedure was also done for the scattering angle in the centre-of-mass frame, $\theta^{\mathrm{cm}}_{\mathrm{beam}}$, using the nominal boost corresponding to the effective beam energy used (detailed in the beam characterisation section).

These values are not used directly in this work, as resolution effects are accounted for when applying the efficiency correction during the fitting of angular distributions later in the analysis. The values are reported in table 8.1 for both reaction channels for completeness.

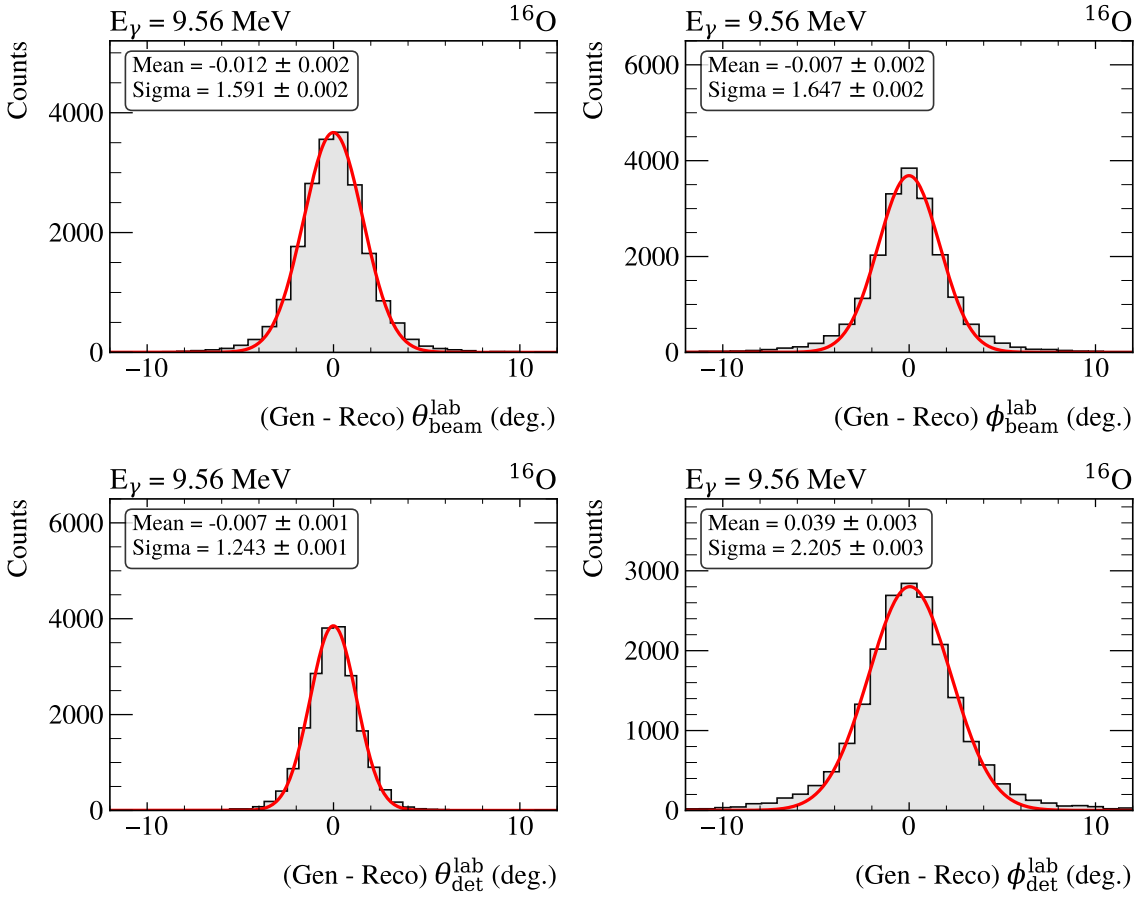

Figure 8.2: Angular Resolution from eTPC Simulations: Resolution histograms showing the difference between generated and reconstructed angles in the laboratory frame: θ_{beam} (upper left), ϕ_{beam} (upper right), θ_{det} (lower left), and ϕ_{det} (lower right). Results are shown for simulated ^{16}O photo-dissociation events at $E_\gamma = 9.56$ MeV.

E_γ (MeV)	Lab angle resolution (deg.)				CM angle resolution (deg.)
	θ_{beam}	ϕ_{beam}	θ_{det}	ϕ_{det}	θ_{beam}
			^{12}**C**		
8.51	2.945(4)	2.890(4)	2.139(2)	4.223(7)	3.5009 (4)
8.66	2.742(3)	2.652(3)	1.984(2)	3.865(6)	3.293 (5)
8.86	2.437(3)	2.444(3)	1.813(2)	3.454(5)	3.000 (4)
9.16	2.227(3)	2.231(3)	1.668(2)	3.258(5)	2.756 (4)
9.36	2.102(2)	2.061(2)	1.551(2)	3.026(4)	2.560 (3)
9.56	1.946(2)	1.925(2)	1.444(1)	2.818(4)	2.421 (3)
9.85	1.727(2)	1.769(2)	1.347(1)	2.472(3)	2.209 (3)
11.1	1.468(1)	1.422(1)	1.041(1)	2.081(2)	1.908 (2)
11.5	1.267(1)	1.277(1)	0.927(1)	1.769(2)	1.740 (2)
11.9	1.1461(9)	1.150(1)	0.8526(7)	1.612(2)	1.596 (2)
12.3	1.0398(8)	1.0482(9)	0.7645(7)	1.441(1)	1.533 (2)
13.1	1.0207(8)	0.9879(8)	0.6894(6)	1.449(1)	1.507 (1)
13.5	0.9578(7)	0.8955(7)	0.6279(7)	1.348(1)	1.431 (1)
			^{16}**O**		
8.51	2.631(3)	2.677(3)	1.996(2)	3.770(6)	3.221(5)
8.66	2.440(3)	2.355(3)	1.749(2)	3.470(5)	2.965(4)
8.86	2.163(3)	2.154(3)	1.615(2)	3.086(4)	2.682(3)
9.16	1.901(3)	1.953(2)	1.478(1)	2.684(4)	2.399(3)
9.36	1.751(2)	1.798(2)	1.346(1)	2.438(3)	2.235(3)
9.56	1.591(2)	1.647(2)	1.244(1)	2.205(3)	2.091(2)
9.85	1.323(1)	1.498(2)	1.135(1)	1.937(2)	1.867(2)
11.1	1.05823(6)	1.06170(6)	0.79497(4)	1.45777(9)	1.5415(1)
11.5	1.01058(5)	1.01745(6)	0.75868(4)	1.39367(9)	1.49960(9)
11.9	0.96125(5)	0.96240(5)	0.71675(3)	1.33415(8)	1.459913(9)
12.3	0.82312(4)	0.81730(4)	0.61392(3)	1.14853(6)	1.35408(8)
13.1	0.83594(4)	0.77769(4)	0.57346(2)	1.16484(7)	1.34285(8)
13.5	0.80713(4)	0.75530(4)	0.55618(2)	1.12743(6)	1.32130(8)

Table 8.1: Angular Resolutions from eTPC Simulations: Resolutions for the reconstructed angles of the α track were obtained from simulated data, after applying the reconstruction correction, for each nominal beam energy. Values for both ^{12}C and ^{16}O photo-dissociation reactions are given.

8.1.3 Drift Velocity Verification

The above resolutions and corrections correspond to the ideal case in which the drift velocity is known with 100% accuracy. When reconstructing experimental data, the drift velocity used in the reconstruction was obtained from `MAGBOLTZ`, as listed in table 6.1. These values do not account for non-uniformities in the electric field caused by voltage fluctuations or gas flow effects, as the simulations are relatively idealised.

To validate these assumptions, a study was conducted using experimental data. Consider an alpha track extending from the vertex to the endpoint. The components ΔX_{det}, ΔY_{det}, and ΔZ_{det} should form a deformed sphere if a narrow energy range is considered. In *det* coordinates, the beam propagates along the $-X_{\text{det}}$ direction, causing deformation along this axis due to the momentum of the γ beam. Deformation in the drift direction, however, Z_{det}, should occur only if an incorrect drift velocity is used in reconstruction, artificially lengthening or shortening the reconstructed tracks.

A projection of this sphere onto the plane normal to the beam direction for $E_\gamma = 9.56$ MeV is shown in figure 8.3. This analysis was performed for ^{16}O events after all cuts were applied to isolate that reaction channel. The resulting shape resembles a torus.

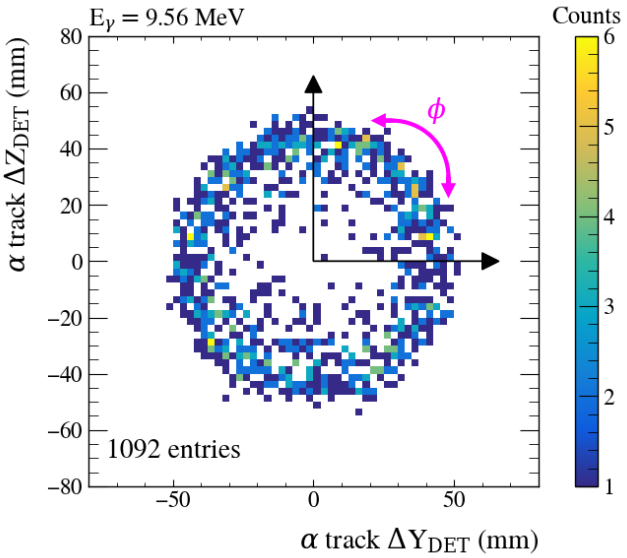

Figure 8.3: Distribution of α Tracks: The deformed torus shows the distribution of α tracks in the chamber for all ^{16}O events at $E_\gamma = 9.56$ MeV. The distribution around the torus relates to the beam polarisation.

To quantify the level of deformation, a narrow slice in reconstructed track length (event energy) was considered, and a series of slices were taken in $\theta^{\text{lab}}_{\text{beam}}$, producing concentric ellipses. These were fitted using the equation of an ellipse,

$$\frac{(\Delta Y)^2}{a^2} + \frac{(\Delta Z)^2}{b^2} = 1, \tag{8.1.3.1}$$

where a and b are the lengths of the semi-major and semi-minor axes. The fitted data for each slice are shown in figure 8.4.

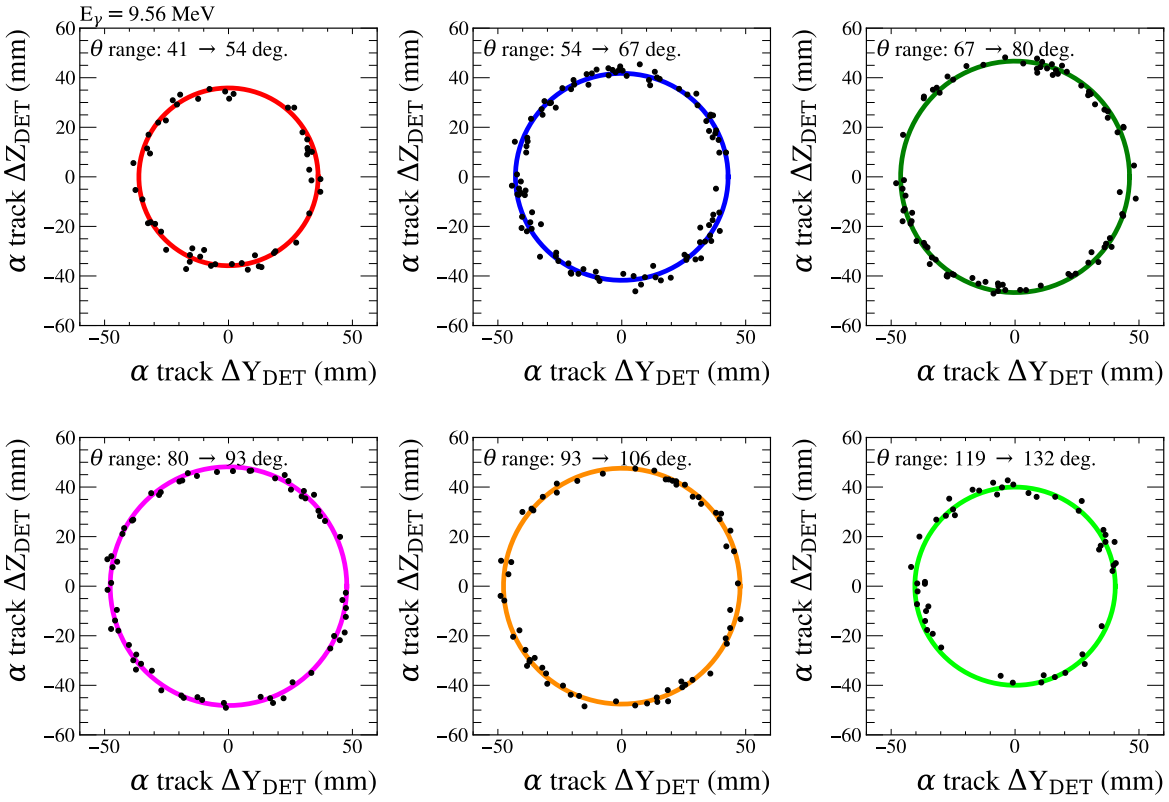

Figure 8.4: Distribution of α Tracks: A series of slices in θ_{beam} are taken, the distribution of α tracks are considered in each slice for all ^{16}O events at $E_\gamma = 9.56$ MeV. These data are then fit with an ellipse to extract the amount of deformation due to the applied drift velocity.

The drift velocity correction factor is determined from the ratio b/a. A value of $b/a > 1$ indicates that tracks are systematically too long in the z-direction, requiring the z components of track vectors to be divided by b/a. The variation of this parameter for $E_\gamma = 9.56$ MeV is shown in figure 8.5 tracked as a function of θ_{beam}.

The results for all energies are summarised in table 8.6. The data are typically only a few standard deviations from unity, indicating that nominally correct drift velocities were applied during reconstruction of the experimental data. Thus, the resolutions and corrections based on the simulated data are applicable. These minor corrections were not used in the final analysis.

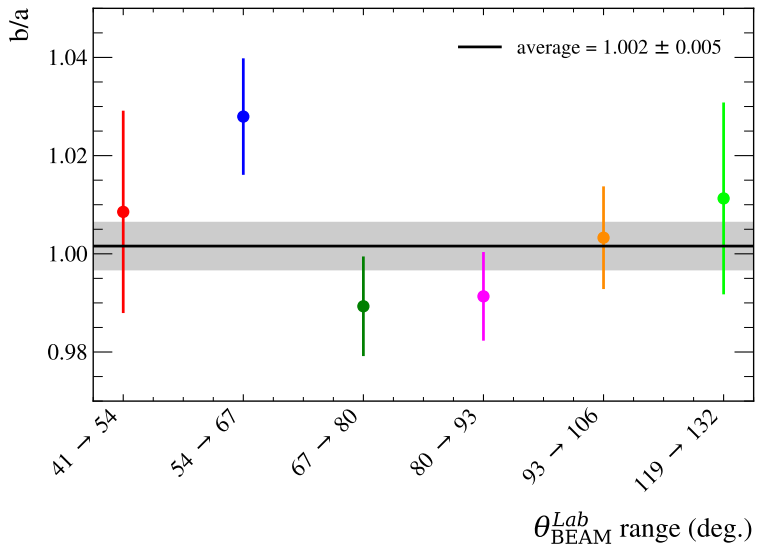

Figure 8.5: Tracking Deformation: Values of b/a for different slices in θ_{beam}, for ^{16}O events at E_γ=9.56 MeV were tracked. The weighted average value and 1σ error band are shown.

E_γ (MeV)	b/a
8.51	1.042(4)
8.66	1.020(8)
8.86	1.010(5)
9.16	0.999(3)
9.36	1.000(4)
9.56	1.002(5)
9.85	1.0112(8)
11.1	1.0031(7)
11.5	1.0032(4)
11.9	1.002(2)
12.3	1.0005(1)
13.1	0.9995(3)
13.5	1.0009(3)
13.9	0

Figure 8.6: Deformation Values: The deformation values of b/a for each nominal beam energy are tabulated.

8.1.4 Overview

The angle-based reconstruction bias correction derived from simulated data was applied when analysing the experimental data. The experimental drift velocity analysis confirms that the correct drift velocity was used in the reconstruction of the experimental data.

Additional angle-dependent non-uniformities do arise in the reconstructed events. However, this is more appropriately addressed in the data cuts section. No direct correction is applied to the data on an event-by-event basis to correct for this. Instead, the affected regions are removed entirely, and this was accounted for through an efficiency correction applied to the angular distributions.

8.2 Beam Characterisation

This section details the characterisation of the HIγS beam delivered to the eTPC, including analyses of beam energy, intensity, and alignment. The reader is referred to figure 3.5 that outlines the detectors referenced in this section.

8.2.1 Intensity

Low-Energy Calibration: Gold Foil Activation

An absolute beam intensity analysis was performed by Chiara Mazzocchi (University of Warsaw) for the low-energy measurements collected during the August campaign. Gold foils (0.75(1) inch diameter, ~ 25 μm thick) were placed downstream of the eTPC and activated by the γ-beam for a known duration. After removal from the beam each activated foil was transferred to an HPGe detector, which measured the decay rate by detecting emitted neutrons. Using the known ^{197}Au(γ, n) cross section, these measurements were used to determine the beam intensity, I_γ [192]. These values are listed in table 8.2.

E_γ(MeV)	I_γ (10^8 γ/s)
8.51	3.72 ± 0.27
8.66	3.25 ± 0.23
8.86	3.19 ± 0.23
9.16	3.83 ± 0.28
9.36	3.93 ± 0.28
9.56	3.98 ± 0.29
9.85	4.20 ± 0.30

Table 8.2: Gold Foil Beam Intensity: The absolute beam intensity values obtained from the gold foil analysis for all nominal beam energies are given.

High-Energy Calibration: Paddle Normalisation

The gold foil method was used to obtain the absolute beam intensity only at low energies during the August campaign. However, the plastic scintillator paddles, MPAD and SPAD, were used for both campaigns to measure the relative intensity. At these low energies, a relationship was established between the rates measured in the paddles and the beam

intensity determined from the gold foil analysis. This relationship was then extrapolated to higher energies to provide full intensity paddle calibrations for the April data.

SPAD Analysis. The SPAD is a 1 mm thick, in-beam, plastic scintillator paddle located after the copper attenuators. The rate measured in the SPAD, R_s, is related to the beam intensity observed in the eTPC by the unknown efficiency ϵ

$$R_s = \epsilon \; I_\gamma. \tag{8.2.1.1}$$

Thus, a calibration factor, $f_s = I_\gamma / R_s = 1/\epsilon$, is obtainable for the low-energy data, shown as the black data points in figure 8.7 and listed in table 8.3. The SPAD data used to obtain the ratio were collected with no attenuation and averaged across multiple measurements for each beam energy.

The assumption was made that the shape of the energy dependence of ϵ can be approximated using the linear attenuation coefficient of Vinyltoluene, μ, defining the prior as $\epsilon_\mu(E_\gamma)$, such that

$$R_s \propto \epsilon_\mu(E_\gamma) \; I_\gamma, \tag{8.2.1.2}$$

where $\epsilon_\mu(E_\gamma)$ is defined as

$$\epsilon_\mu(E_\gamma) = 1 - \exp(-\mu(E_\gamma)x), \tag{8.2.1.3}$$

with x being the thickness of the paddle. Therefore

$$f_s = \frac{I_\gamma}{R_s} = \frac{A}{\epsilon_\mu(E_\gamma)}. \tag{8.2.1.4}$$

Using equation (8.2.1.4) the data were fitted, and the equation extrapolated to high energy to obtain the calibration. This fit is shown as the red line in the figure, with the error band fixed as the average fractional error on the data points (9%). The fitted line is averaged over the beam profiles to obtain the calibration values for the high-energy data, listed in table 8.5.

E_γ	$f_s = I_\gamma / R_s$
8.51	12314 ± 1089
8.66	12791 ± 1266
8.86	11544 ± 1057
9.16	14067 ± 1238
9.36	13564 ± 1038
9.56	13285 ± 1222

Table 8.3: SPAD Calibration Factors: The calculated calibration factors obtained using the gold-foil activation method are listed for the SPAD.

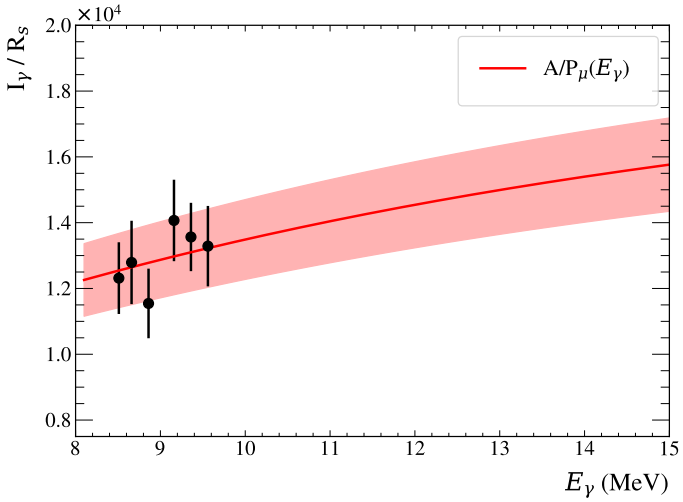

Figure 8.7: SPAD Fitted Calibration: The SPAD calibration data are shown fitted with the equation (8.2.1.4), as described in the text, to extrapolate the calibration to high energy.

MPAD Analysis. The MPAD is a 5 mm plastic scintillator located before the copper attenuators that detects Compton scattered photons from the FEL mirror at $\theta = 45° \pm 2$. Using similar logic to the SPAD analysis, the rate of photons detected in the MPAD, R_m, is proportional to

$$R_m \propto \epsilon_\mu(E_\mathrm{s})\ I_\gamma\ \sigma_c(E_\gamma), \tag{8.2.1.5}$$

where $\sigma_c(E_\gamma)$ is the Compton scattering cross section, obtained using the Klein-Nishina formula

$$\frac{d\sigma}{d\Omega}(E_\gamma, \theta) = \frac{r_e^2}{2}\left(\frac{E_s}{E_\gamma}\right)^2\left(\frac{E_s}{E_\gamma} + \frac{E_\gamma}{E_s} - \sin^2\theta\right). \tag{8.2.1.6}$$

Here r_e is the classical electron radius, and E_s is the scattered photon energy. It is noted that the effect of polarisation on the differential cross section is negligible at the energy range considered [193, 194].

The attenuation term, $\epsilon_\mu(E_\mathrm{s})$, is evaluated at the energy of the scattered photons

$$E_s(E_\gamma, \theta) = \frac{E_\gamma}{1 + \frac{E_\gamma}{m_e c^2}(1 - \cos\theta)}, \tag{8.2.1.7}$$

where m_e is the electron mass. Such that

$$\epsilon_\mu(E_\mathrm{s}) = 1 - \exp(-\mu(E_\mathrm{s})x), \tag{8.2.1.8}$$

where x is the thickness of the MPAD paddle. Therefore, the energy dependence of the calibration factor is given by

$$f_m = \frac{I_\gamma}{R_m} = \frac{A}{\epsilon_\mu(E_\mathrm{s})\ \sigma(E_\gamma)}. \tag{8.2.1.9}$$

The MPAD data used to obtain the ratio were collected with no attenuation and averaged across multiple measurements for each beam energy. These data, shown in figure 8.8 and listed in table 8.4, were fitted using equation (8.2.1.9). This fit is shown as the red line, with the error band fixed as the average error on the data points (8%). The fitted line is averaged over the high-energy beam profiles to obtain the calibration values shown in the table 8.6.

E_γ	$f_m = I_\gamma/R_m$
8.51	50089 ± 4114
8.66	50192 ± 3957
8.86	45954 ± 3683
9.16	55539 ± 4296
9.36	53758 ± 3997
9.56	52843 ± 4014

Table 8.4: MPAD Calibration Factors: The calculated calibration factors obtained using the gold foil activation method are listed for the MPAD.

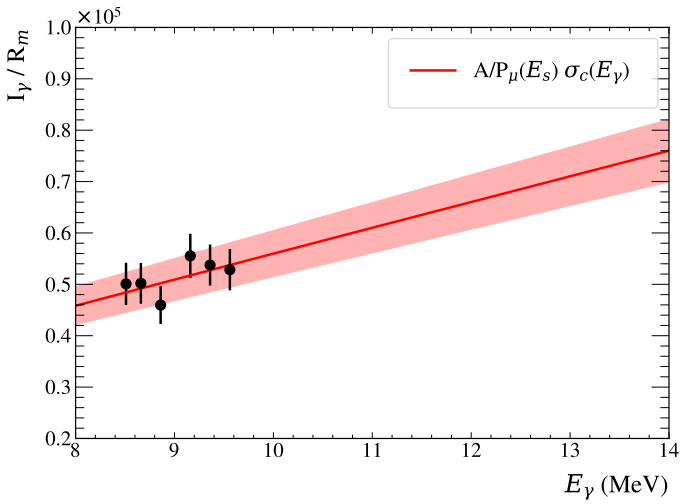

Figure 8.8: MPAD Fitted Calibration: The MPAD calibration data are shown fitted with equation (8.2.1.9), as described in the text, to extrapolate the calibration to high energy.

Calibration. In the following section, the extrapolated calibration factors are used to scale the paddle rates obtained for the high-energy campaign to full beam intensity. The intensity values, I_γ^s, obtained from the SPAD rates and calibration are given in table 8.5.

E_γ (MeV)	R_s (Hz)	f_s	I_γ^s (γ/s)
11.1	$3.25(14)\times10^4$	$1.41(13)\times10^4$	$4.58(46)\times10^8$
11.5	$3.21(14)\times10^4$	$1.43(13)\times10^4$	$4.60(46)\times10^8$
11.9	$3.26(14)\times10^4$	$1.45(13)\times10^4$	$4.72(47)\times10^8$
12.3	$2.21(8)\times10^4$	$1.47(13)\times10^4$	$3.24(31)\times10^8$
13.1	$2.60(9)\times10^3$	$1.50(14)\times10^4$	$3.92(38)\times10^7$
13.5	$1.13(5)\times10^4$	$1.52(14)\times10^4$	$1.72(17)\times10^8$
13.9	$3.00(14)\times10^4$	$1.54(14)\times10^4$	$4.61(47)\times10^8$

Table 8.5: High-energy Intensity from SPAD: The SPAD rates, calibration factor and full calibrated beam intensities are given.

In the case of the SPAD analysis, the level of attenuation is inconsequential as the SPAD will always see the same beam intensity as the eTPC, so the calibration will always hold. This is not the case for the MPAD as it is located before the attenuators. Most energies had zero attenuation, so the calibration holds as is, but two energies (E_γ =13.1 and 13.5 MeV) did use attenuators. To extract the intensity for these cases, a correction is made using the attenuation coefficient of the copper attenuators.

The linear attenuation coefficient, μ_c, of the copper attenuators was obtained in an analysis by Chiara [192]. This was achieved by tracking the ratio of attenuated counts in the large NaI(Tl) detector and the unattenuated counts in the MPAD, as a function of attenuator thickness. All μ_c values that were obtained from the first campaign are shown in the figure 8.9. The blue line is the calculated energy dependence of the linear attenuation coefficient from NIST. This was scaled to match the data, with the error band set to the average fractional error across the data points (0.2%). The difference could be attributed to impurities in the copper. This line was averaged over the beam profiles at these two energies to calculate the attenuation coefficients listed in table 8.6. The intensity values, I_γ^m, obtained from the MPAD rates and calibration are also given in table 8.6.

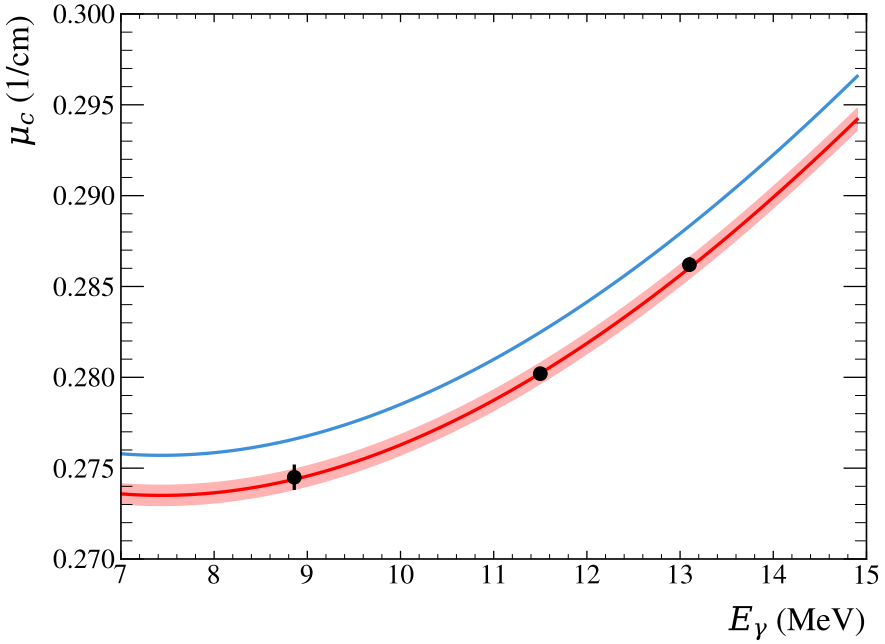

Figure 8.9: Model of the HIγS Attenuation Coefficients: The theoretical attenuation coefficient from NIST (blue) is scaled to match the experimentally obtained data (black), yielding the red line with error band set to match the average fractional error on the data points (0.2%).

E_γ (MeV)	R_m (Hz)	f_m	x (cm)	μ_c (cm^{-1})	I_γ^m (γ/s)
11.1	$5.98(25)\times10^3$	$6.16(49)\times10^4$	0	–	$3.69(33)\times10^8$
11.5	$5.92(22)\times10^3$	$6.36(51)\times10^4$	0	–	$3.77(33)\times10^8$
11.9	$6.03(26)\times10^3$	$6.56(53)\times10^4$	0	–	$3.96(36)\times10^8$
12.3	$4.33(15)\times10^3$	$6.76(54)\times10^4$	0	–	$2.93(26)\times10^8$
13.1	$4.65(14)\times10^3$	$7.16(57)\times10^4$	7.35	0.2861(5)	$4.07(35)\times10^7$
13.5	$4.62(19)\times10^3$	$7.36(59)\times10^4$	2.45	0.2878(5)	$1.68(15)\times10^8$
13.9	$5.31(15)\times10^3$	$7.55(60)\times10^4$	0	–	$4.01(34)\times10^8$

Table 8.6: MPAD Intensity: The MPAD rates, thickness of copper attenuators, averaged attenuation coefficient, and calibrated intensities are given.

Verification. The intensities from the SPAD (blue) and MPAD (green) analysis are shown in figure 8.10, where the error bars represent the statistical errors. Largely, there is good agreement with a slight systematic shift. The weighted average and statistical uncertainty at each energy are calculated, shown as the black points and error bars in figure 8.11. To account for the systematic uncertainty, the absolute distance between the averaged value and individual MPAD and SPAD measurements is calculated. This error is shown in the figure as the shaded black box, where the average paddle measurement is

expected to move. The calculated intensities and their uncertainties are given in table 8.7.

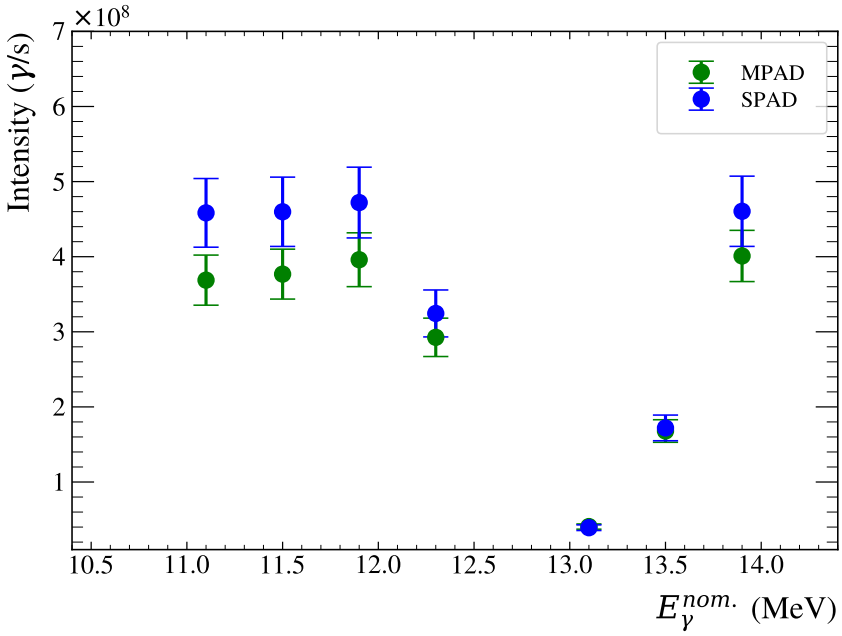

Figure 8.10: Comparison of Intensities: The beam intensities calculated from the MPAD (green) and SPAD (blue) extrapolation are compared. The data points are plotted at the nominal beam energies.

E_γ (MeV)	I_γ (γ/s)	Systematic error (γ/s)
11.1	$4.00(27)\times10^8$	$^{+6.44}_{-4.12} \times 10^7$
11.5	$4.05(27)\times10^8$	$^{+6.09}_{-3.91} \times 10^7$
11.9	$4.24(29)\times10^8$	$^{+5.60}_{-3.99} \times 10^7$
12.3	$3.05(20)\times10^8$	$^{+2.75}_{-2.35} \times 10^7$
13.1	$4.00(26)\times10^7$	$^{+2.65}_{-2.68} \times 10^6$
13.5	$1.70(11)\times10^8$	$^{+1.15}_{-1.14} \times 10^7$
13.9	$4.23(28)\times10^8$	$^{+4.76}_{-3.44} \times 10^7$

Table 8.7: eTPC Intensities: The weighted averaged beam intensities from the MPAD and SPAD extrapolation are given, with both statistical and systematic uncertainties.

The validity of calculating the intensity using the paddle extrapolation is checked using the intensities obtained by normalising the eTPC data to the $^{16}O(\gamma,\alpha_0)$ cross section of DeBoer *et al.* [46] (appendix G). These are shown in figure 8.11 as the red points, where the error bars represent the statistical uncertainty, and the shaded red box is the approximated 23% systematic uncertainty. These data points have been shifted in energy for visualisation.

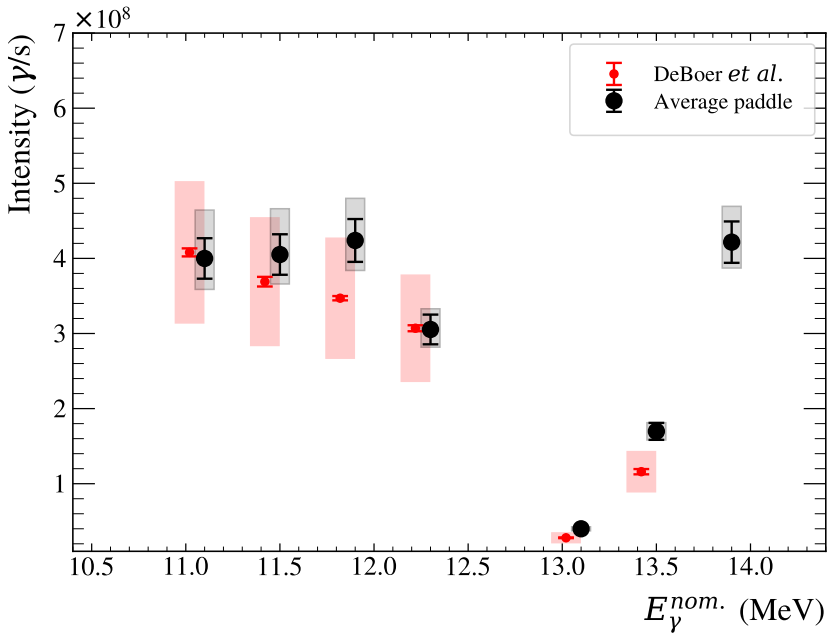

Figure 8.11: Verification of Intensities: The weighted average beam intensities from the SPAD and MPAD extrapolations (black) with decomposed statistical (bar) and systematic errors (box) are shown. These are compared with those obtained from normalising eTPC data to the $^{16}O(\gamma,\alpha_0)$ cross section of reference [46] (red) with statistical errors (bar) and systematic (box) also decomposed. The red points have been shifted in energy for visualisation.

8.2.2 Energy

Beam Profile

As with the analysis of the first experiment detailed in this thesis, for data below 10 MeV, the beam energy profile was obtained by unfolding the response of the HPGe detector using `HORST`[1] to obtain the photo-peak. The unfolded spectra are then fit with a skewed Gaussian to parametrise the energy profile, defined as

$$G(E|\xi,\omega,\alpha) = \frac{1}{\omega\sqrt{2\pi}}\exp\left[-\frac{1}{2}\left(\frac{E-\xi}{\omega}\right)^2\right]\left[1+\mathrm{erf}\left(\alpha\frac{E-\xi}{\omega\sqrt{2}}\right)\right], \tag{8.2.2.1}$$

where ξ is the location, ω is the scale, and α is the skewness parameter. This general procedure is detailed in appendix B. An example of a fitted spectrum is shown in figure 8.12.

However, no HPGe response matrix was available for beam energies above 10 MeV.

[1]Response simulated with a 10 mm diameter collimator and 20 mm beam offset.

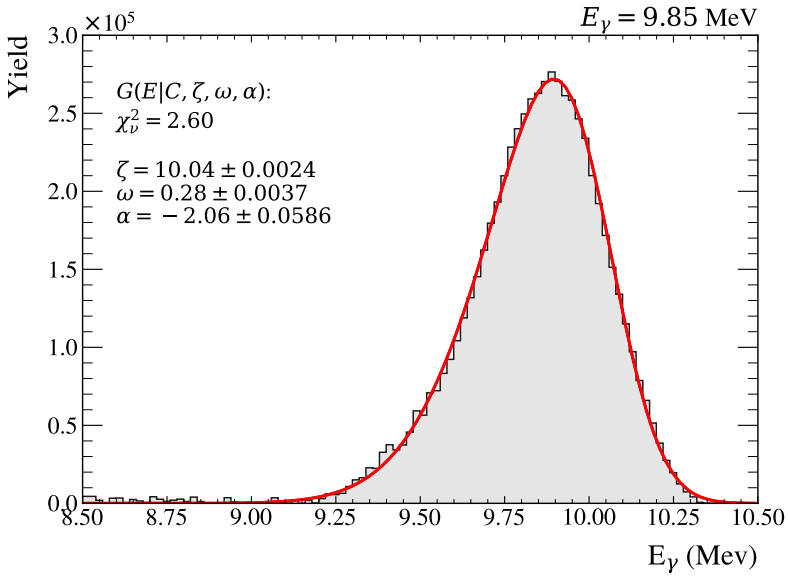

Figure 8.12: Unfolded Beam Energy Profile: A typical unfolded HPGe spectrum, from $E_\gamma = 9.85$ MeV, is fitted using χ^2 minimisation with a skewed Gaussian distribution; ξ is the location parameter, ω is the scale, and α is the skew. 1σ errors on relevant parameters are given in the figure.

Consequently, the beam profiles in this energy regime were determined through `Geant4` simulations conducted by HIγS staff. The resulting distributions are presented alongside the experimental measurements in figure 8.13.

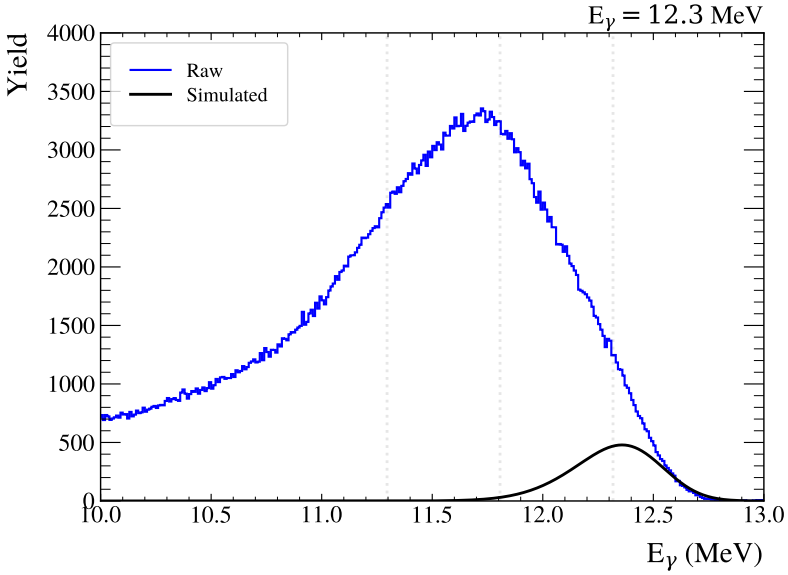

Figure 8.13: Raw and Simulated Beam Energy Profile: Raw HPGe energy spectrum (blue) compared with a simulated skewed Gaussian distribution (black) for $E_\gamma = 12.3$ MeV.

In both cases, for beam energies spanning multiple days and multiple beam energy measurements, a weighted-average unfolded spectrum was obtained using the time of the associated eTPC measurement. Fitted parameters are given in table 8.8. Note that no uncertainties were provided for the simulated spectra.

E_γ (MeV)	ζ(MeV)	ω (MeV)	α	μ (MeV)	σ (MeV)
8.51	8.68 ± 2.54 $\times10^{-3}$	0.231 ± 2.78$\times10^{-3}$	-1.64 ± 6.06$\times10^{-2}$	8.52 ± 3.5$\times10^{-3}$	0.169 ± 2.5$\times10^{-3}$
8.68	8.82 ± 2.74 $\times10^{-3}$	0.227 ± 2.94$\times10^{-3}$	-1.59 ± 6.33$\times10^{-2}$	8.67 ± 3.8$\times10^{-3}$	0.168 ± 2.7$\times10^{-3}$
8.86	9.04 ± 2.65 $\times10^{-3}$	0.247 ± 3.06$\times10^{-3}$	-1.75 ± 6.62$\times10^{-2}$	8.86 ± 3.7$\times10^{-3}$	0.178 ± 2.6$\times10^{-3}$
9.16	9.33 ± 2.81 $\times10^{-3}$	0.269± 4.12$\times10^{-3}$	-1.99 ±6.67$\times10^{-2}$	9.14 ± 4.3$\times10^{-3}$	0.189 ± 3.1$\times10^{-3}$
9.36	9.54 ± 2.53 $\times10^{-3}$	0.272± 3.55$\times10^{-3}$	-1.87 ±5.38$\times10^{-2}$	9.35 ± 3.8$\times10^{-3}$	0.193 ± 2.8$\times10^{-3}$
9.56	9.75 ± 2.14 $\times10^{-3}$	0.269± 3.09$\times10^{-3}$	-1.99 ±5.04$\times10^{-2}$	9.56 ± 3.4$\times10^{-3}$	0.189 ± 2.3$\times10^{-3}$
9.85	10.00 ± 2.56 $\times10^{-3}$	0.282± 3.91$\times10^{-3}$	-2.06 ±6.18$\times10^{-2}$	9.80 ± 4.0$\times10^{-3}$	0.196 ± 3.0$\times10^{-3}$
11.1	(11.30)	(0.267)	(-1.35)	(11.13)	(0.205)
11.5	(11.70)	(0.280)	(-1.39)	(11.52)	(0.213)
11.9	(12.11)	(0.285)	(-1.51)	(11.92)	(0.213)
12.3	(12.51)	(0.283)	(-1.68)	(12.32)	(0.206)
13.1	(13.33)	(0.307)	(-1.78)	(13.11)	(0.221)
13.5	(13.74)	(0.316)	(-1.87)	(13.52)	(0.225)

Table 8.8: Beam Energy Profiles: The skewed Gaussian fit parameters that model the beam energy profile. Entries that are black were obtained from unfolding the HPGe profile using `HORST`. Entries that are in brackets were obtained through simulation of the γ beam.

Energy Asymmetry

An interesting feature to note is that the beam energy appears to have spatial dependence. Using the eTPC, the reconstructed centre-of-mass energy spectrum (detailed later) can be viewed as a function of the reconstructed event vertex y_{det}, where y_{det} steps across the beam from one side of the eTPC to the other. Data for all ^{16}O events are shown in figure 8.14, but only beam energies of 11.1, 11.9, 13.1, and 13.5 MeV, where there are obvious features in the reaction cross section. The cause is not yet determined, but it is thought to be due to a misalignment of the collimator. Figure 8.15 shows the average E_{cm} as a function of vertex position, fitted to extract the gradient of the energy dependence.

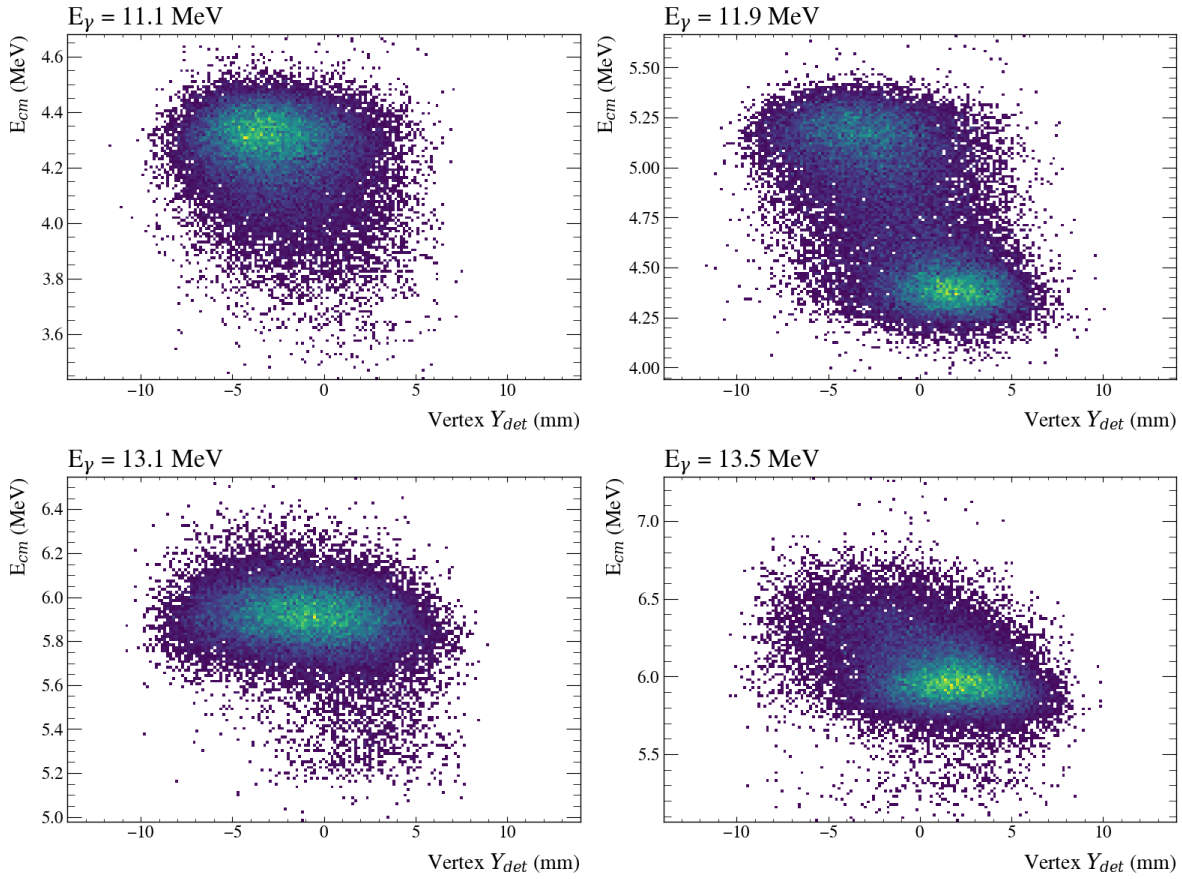

Figure 8.14: Beam Energy Asymmetry: Each panel shows the reconstructed y_{det} vertex position as a function of the calibrated centre-of-mass energy energy (explained later), for all ^{16}O events. The run identifier is located in the upper left panel of each plot.

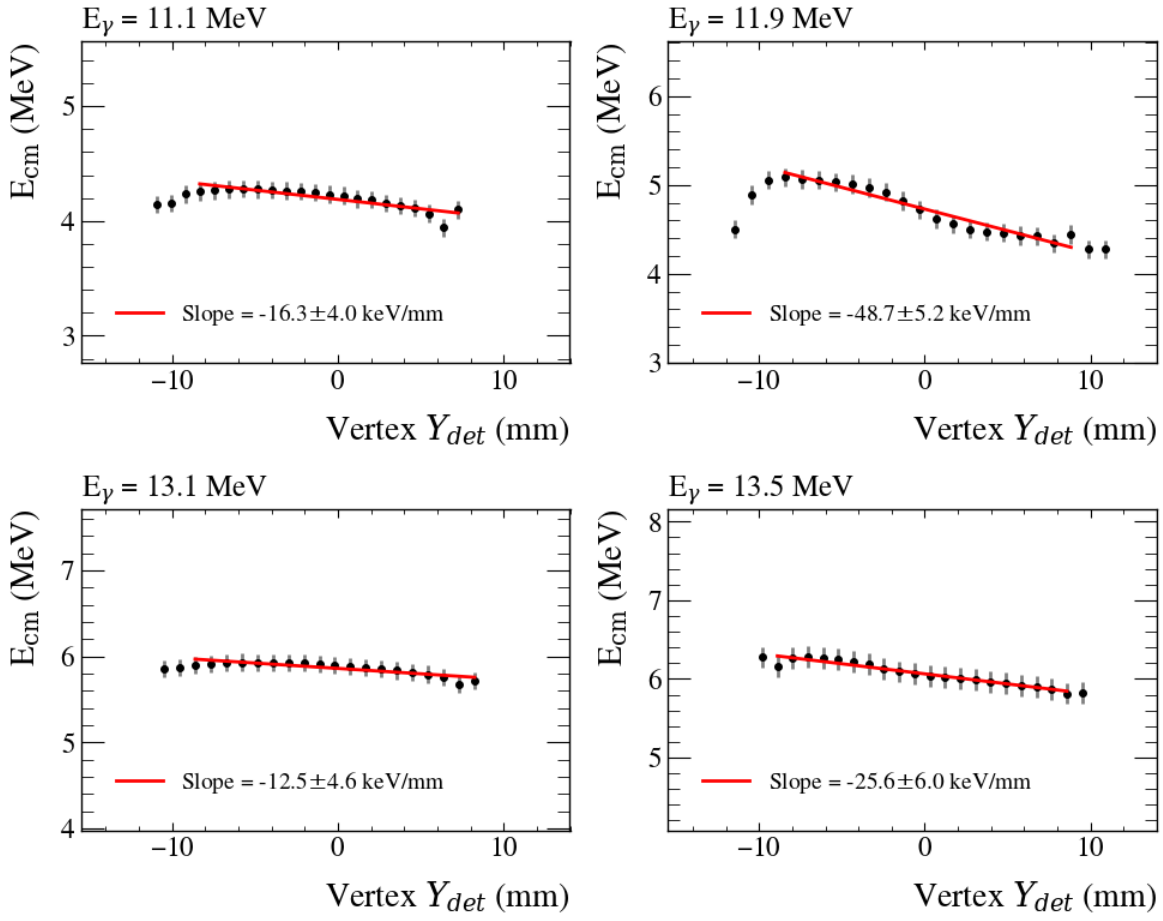

Figure 8.15: Beam Energy Asymmetry Quantification: The reconstructed average centre-of-mass energy as a function of y_{det} vertex position for all ^{16}O events at four beam energies, $E_\gamma = 11.1, 11.9, 13.1, 13.5$ MeV is shown. Linear fits (solid lines) were used to approximate the energy asymmetry across the central portion of the beam width, although non-linear behaviour is seen at the extremities. The run identifier is located in the upper left panel of each plot.

8.2.3 Alignment

Accurate beam alignment, or the ability to quantify misalignment, is an essential step in the experimental setup and analysis. The γ beam should be aligned along the $-x_{\text{det}}$ direction, and any significant deviation from this will potentially bias the results by affecting the reaction mechanics.

Online Alignment

During the experiment, initial beam alignment was achieved using a laser and subsequently verified with an external bismuth germanium oxide (BGO) gamma camera positioned downstream of the eTPC, in line with the beam entrance and exit ports. Lead plugs were placed at both ports, and the resulting shadows in the BGO images (appearing as central yellow regions) were used to confirm beam alignment. Example images from the BGO camera are shown in figure 8.16. The left panel demonstrates misalignment with the collimator, while the right panel shows proper alignment.

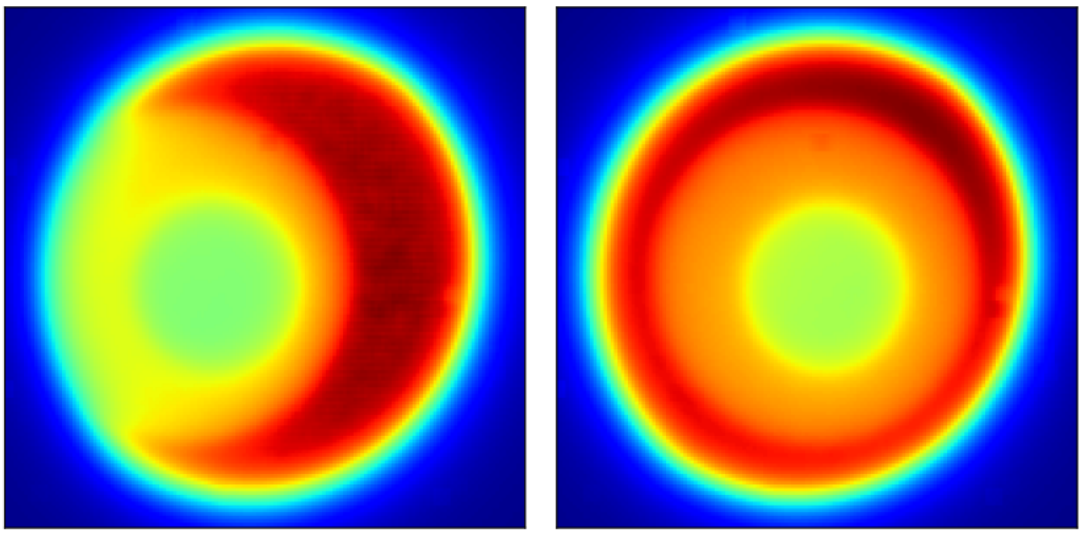

Figure 8.16: Beam Alignment using a Bismuth Germanium Oxide Camera. Left: Shows incorrect alignment of the beam with the collimator. **Right:** shows the correct alignment.

Offline Verification

Any residual beam tilt after laser and BGO alignment can be extracted from the eTPC itself by analysing the distribution of event vertices throughout the chamber. Note that since the detector operated in self-trigger mode, beam tilt analysis is restricted to the $x_{\text{det}} - y_{\text{det}}$ plane, as z_{det} is only known as a relative coordinate.

The nominal beam direction and an exaggerated tilted beam of some angle β are illustrated in figure 8.17. Experimentally extracted vertices from the ^{16}O photo-dissociation reaction measured at $E_\gamma = 9.56$ MeV are shown in figure 8.18. As the data are uniformly distributed along the beam within the considered region, the level of tilt is approximated by fitting a linear function, yielding the gradient m and offset c. The extracted fit parameters

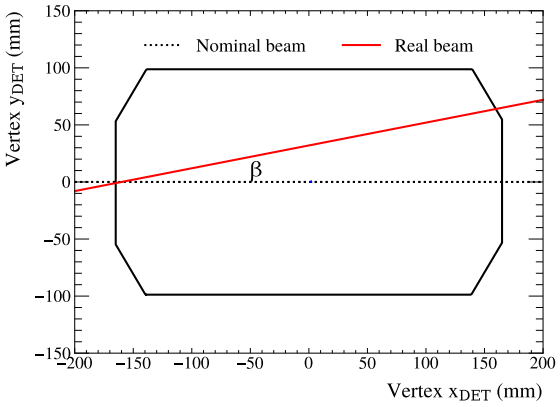

Figure 8.17: Beam Tilt Example: Plot showing an exaggerated beam tilt angle in-plane.

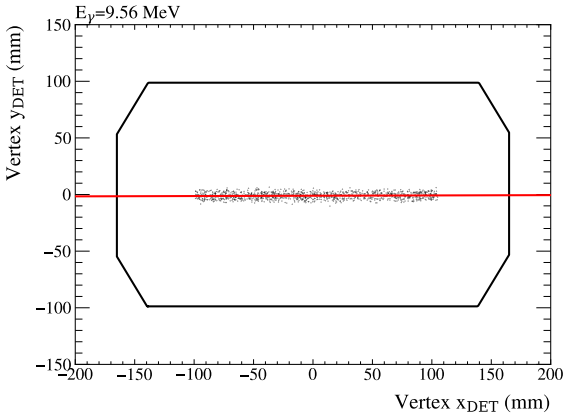

Figure 8.18: Beam Tilt Experimental: Plot showing the distribution of ^{16}O event vertices in the eTPC, used to extract beam tilt in-plane.

and calculated tilt angle, β, for all measured energies are shown in table 8.9. The beam tilt angles are consistently small, indicating good alignment throughout the experiment. Given these minimal deviations, no alignment corrections were applied to the data.

E_γ (MeV)	m	c (mm)	β (deg.)
8.51	0.002(4)	-1.4(3)	0.1(2)
8.66	0.002(2)	-1.6(1)	0.1(1)
8.86	0.003(1)	-1.29(8)	0.17(6)
9.16	0.002(1)	-1.25(7)	0.12(6)
9.36	0.003(1)	-1.32(8)	0.17(6)
9.56	0.003(2)	-1.07(9)	0.2(1)
9.85	0.002(2)	-0.9(1)	0.1(1)
11.1	0.0032(3)	-2.49(2)	0.18(2)
11.5	0.0034(2)	-1.25(1)	0.20(1)
11.9	0.0030(4)	-0.87(2)	0.17(2)
12.3	0.0028(3)	-1.9(1)	0.16(2)
13.1	0.0030(4)	-0.90(2)	0.17(2)
13.5	0.0028(5)	0.89(2)	0.16(3)

Table 8.9: Beam Tilt Parameters: The parameters for the linear model of the beam tilt are given, as well as the tilt angle β for all beam energies.

8.2.4 Polarisation

The azimuthal angular distribution of the emitted α particles from both the ^{12}C and ^{16}O photo-dissociation reactions follow a dependence due to the polarisation of the beam, which is described in detail in appendix A.3. This distribution follows the form

$$H(\phi) = 1 + f\cos(2(\phi + \phi_0)), \tag{8.2.4.1}$$

where f is the fraction of linear polarisation, and ϕ_0 defines the polarisation axis [186]. Here, $f = 0$ corresponds to purely circular polarisation, and $f = 1$ corresponds to purely linear polarisation. This equation was used to derive a PDF

$$N(\phi \,|\, f, \phi_0) = \frac{H(\phi)\,\epsilon(\phi)}{\int_{-\pi}^{\pi} H(\phi)\,\epsilon(\phi)\,d\phi}, \tag{8.2.4.2}$$

Where $\epsilon(\phi)$ is the efficiency term (defined later).

All data at each beam energy, for both the ^{12}C and ^{16}O reaction channels, were fitted independently. Two examples of mostly linear and mostly circular polarisation are shown in figure 8.19. The top panel shows data from the ^{16}O channel, and the bottom panel from ^{12}C channel.

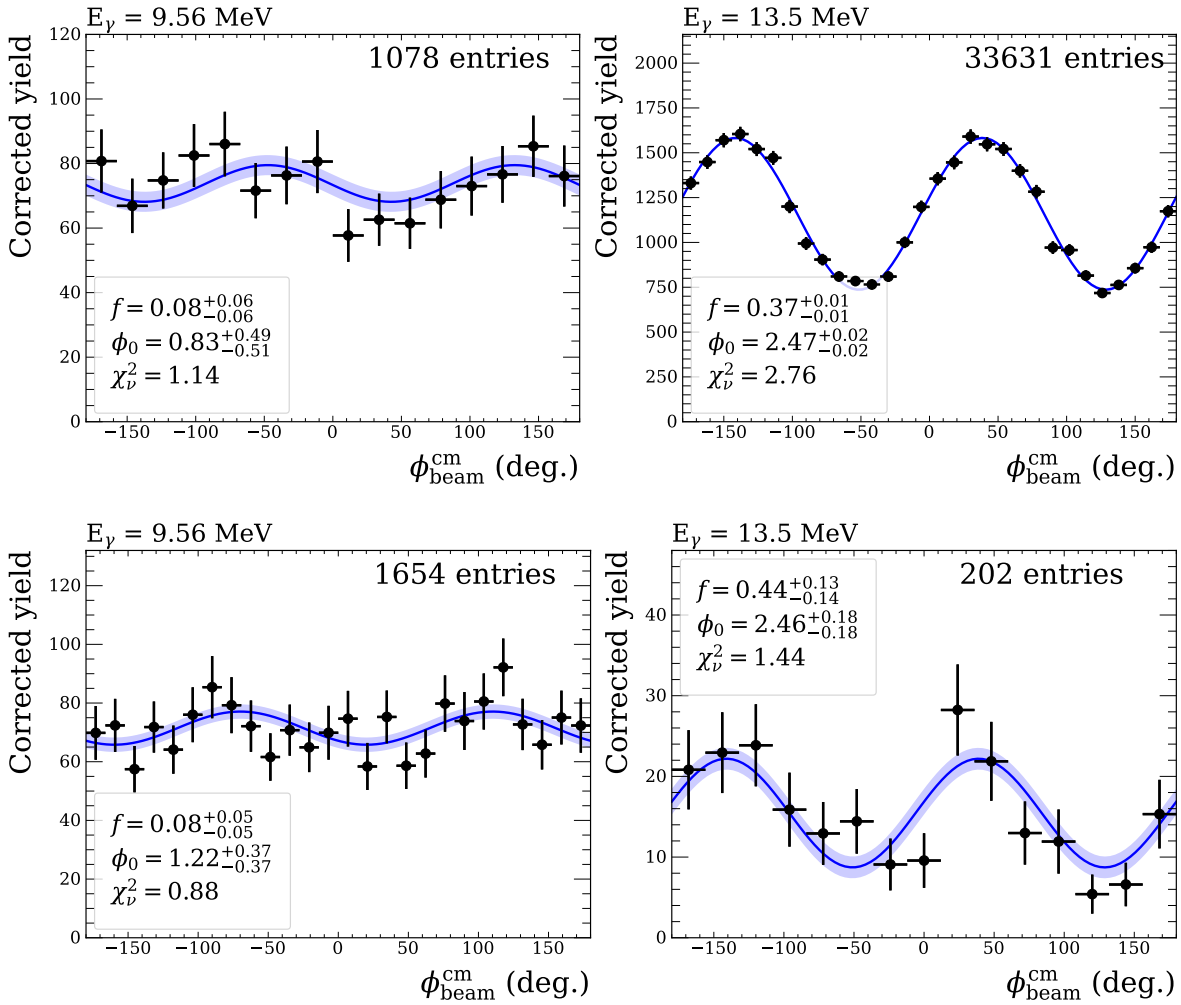

Figure 8.19: Azimuthal Angular Distributions. Top: Shows fits (of equation (8.2.4.1)) to the ^{16}O reaction channel. with the left panel showing a largely circularly polarised distribution and the right panel showing a largely linearly polarised distribution. **Bottom:** Shows fits of the same function to the ^{12}C reaction channel for the same beam energies. The same trend is observed.

Tabulated values from each fit are given in table 8.10, and the extracted parameters are shown in figure 8.20, compared with a previous analysis of the same dataset [186]. The low energies were expected to be circularly polarised, with the high energies linearly polarised, which is commensurate with what is shown here.

	^{16}O		^{12}C	
E_γ (MeV)	f	ϕ_0 (rad)	f	ϕ_0 (rad)
8.51	$0.106^{+0.210}_{-0.106}$	$1.449^{+1.693}_{-1.449}$	$0.130^{+0.089}_{-0.090}$	$1.063^{+0.389}_{-0.379}$
8.66	$0.083^{+0.085}_{-0.083}$	$0.053^{+3.088}_{-0.053}$	$0.053^{+0.038}_{-0.038}$	$1.054^{+0.400}_{-0.398}$
8.86	$0.014^{+0.069}_{-0.014}$	$1.557^{+1.585}_{-1.557}$	$0.066^{+0.031}_{-0.031}$	$0.659^{+0.248}_{-0.245}$
9.16	$0.099^{+0.058}_{-0.059}$	$0.186^{+0.310}_{-0.186}$	$0.047^{+0.034}_{-0.034}$	$1.142^{+0.397}_{-0.418}$
9.36	$0.092^{+0.059}_{-0.060}$	$0.889^{+0.352}_{-0.370}$	$0.123^{+0.044}_{-0.044}$	$0.882^{+0.189}_{-0.184}$
9.56	$0.077^{+0.064}_{-0.064}$	$0.828^{+0.492}_{-0.508}$	$0.079^{+0.052}_{-0.052}$	$1.219^{+0.366}_{-0.367}$
9.85	$0.117^{+0.085}_{-0.086}$	$0.341^{+0.414}_{-0.341}$	$0.151^{+0.073}_{-0.074}$	$1.377^{+0.268}_{-0.271}$
11.10	$0.358^{+0.011}_{-0.011}$	$2.407^{+0.016}_{-0.016}$	$0.352^{+0.031}_{-0.032}$	$2.442^{+0.047}_{-0.047}$
11.50	$0.355^{+0.007}_{-0.007}$	$2.412^{+0.010}_{-0.010}$	$0.398^{+0.057}_{-0.059}$	$2.290^{+0.081}_{-0.082}$
11.90	$0.371^{+0.011}_{-0.011}$	$2.498^{+0.015}_{-0.015}$	$0.392^{+0.057}_{-0.059}$	$2.484^{+0.081}_{-0.081}$
12.30	$0.383^{+0.007}_{-0.007}$	$2.558^{+0.010}_{-0.010}$	$0.312^{+0.147}_{-0.154}$	$2.431^{+0.257}_{-0.269}$
13.10	$0.342^{+0.012}_{-0.012}$	$2.468^{+0.018}_{-0.018}$	–	–
13.50	$0.365^{+0.011}_{-0.011}$	$2.469^{+0.016}_{-0.016}$	$0.436^{+0.127}_{-0.136}$	$2.462^{+0.179}_{-0.183}$

Table 8.10: Beam Polarisation Parameters: The polarisation parameters f and ϕ_0 for different beam energies for both ^{16}O and ^{12}C reaction channels are given.

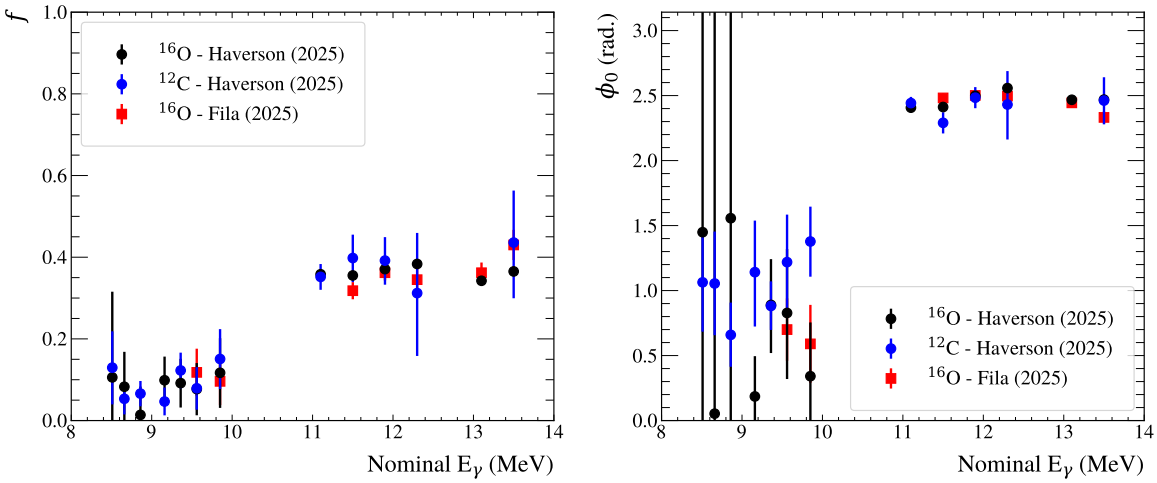

Figure 8.20: Beam Polarisation Parameter Tracking: The extracted parameters are shown for both reaction channels, compared with a previous analysis by Fila (2025) [186].

8.3 Data Reduction Cuts

This section describes the software cuts applied to isolate background-free samples of both $^{16}\mathrm{O}(\gamma,\alpha_0)$ and $^{12}\mathrm{C}(\gamma,\alpha_0)$ photo-dissociation events, as well as the steps taken to address biasing arising from the detector's fiducial volume and reconstruction methods. It is divided into four parts:

1. **General Cuts:** General cuts applied to remove background and exclude regions of non-uniform detection efficiency.

2. **Proportion of Events:** The relative proportion of $^{12}\mathrm{C}$ and $^{16}\mathrm{O}$ photo-dissociation events is obtained.

3. **Isolation of $^{16}\mathrm{O}$ Events:** Specific additional cuts used to isolate $^{16}\mathrm{O}(\gamma,\alpha_0)$ events.

4. **Isolation of $^{12}\mathrm{C}$ Events:** Specific additional cuts used to isolate $^{12}\mathrm{C}(\gamma,\alpha_0)$ events.

The cuts described in the following sections are presented in the order in which they were applied. The number of events rejected at each stage is recorded, and example plots are shown where appropriate, typically using $E_\gamma = 9.56$ MeV as a representative beam energy.

8.3.1 General Cuts

Charge Threshold

An initial energy threshold was applied to remove a large fraction of the background, which primarily consists of spots, single-prong events, and electronic noise. The energy metric used is the *cluster-cleaned total charge*, defined as the sum of all charge deposits on all strips after full image cleaning. An example of this cut is shown in figure 8.21, and the corresponding thresholds for each run are listed in table 8.11.

A subset of the data [186] were reconstructed manually, providing a small but valuable validation dataset. The threshold values were conservatively chosen based on this hand-classified sample to ensure that no $^{12}\mathrm{C}(\gamma,\alpha_0)$ or $^{16}\mathrm{O}(\gamma,\alpha_0)$ events were removed.

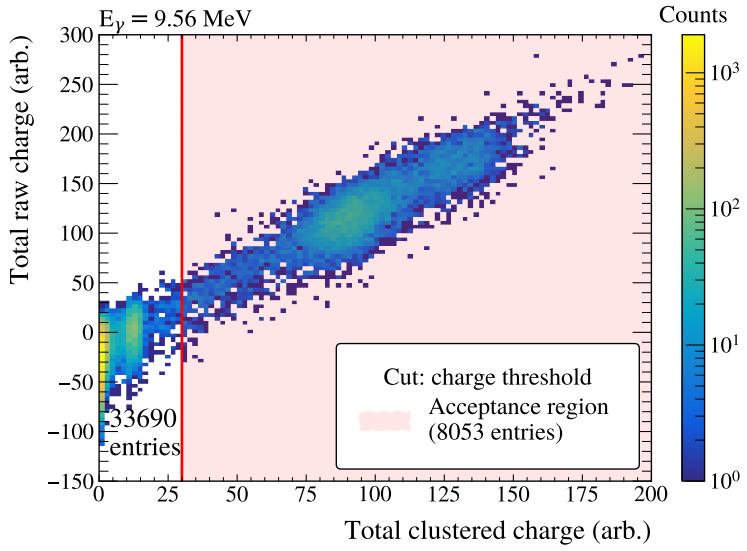

Figure 8.21: Clustered Charge Threshold Example: Two-dimensional histogram showing total charge deposited on the readout plane (y-axis) versus total charge from the main cluster (x-axis). The total entries are given, along with the acceptance region and the number of entries within that region.

Table 8.11: Clustered Charge Threshold Values: The clustered charge threshold for initial background removal at each nominal beam energy.

E_γ (MeV)	Threshold (arb.)
8.51	200000
8.66	200000
8.86	200000
9.16	300000
9.36	300000
9.56	300000
9.85	300000
11.1	150000
11.5	150000
11.9	100000
12.3	185000
13.1	100000
13.5	100000

Border padding

A condition is applied to remove any events with either an endpoint or a vertex located within 5 mm of the edge of the active area in the xy_{det}-plane, thereby excluding partially contained events from the analysis. The acceptance region defined by this cut is shown in figure 8.22, where the histogram displays the distribution of α-track endpoints.

Beam Position

A cut is applied to remove events where the vertex lies beyond a certain distance from the γ-beam axis in y_{det}, thereby excluding events that do not originate from the beam. An example of the acceptance region is shown in the left-hand panel of figure 8.23. To quantify an appropriate cut, the data were projected onto the y-axis, as shown in the right-hand panel, where a Gaussian function approximates it; A $\mu \pm 3\sigma$ cut is applied to each beam energy. The extracted parameters for all energies are listed in table 8.12.

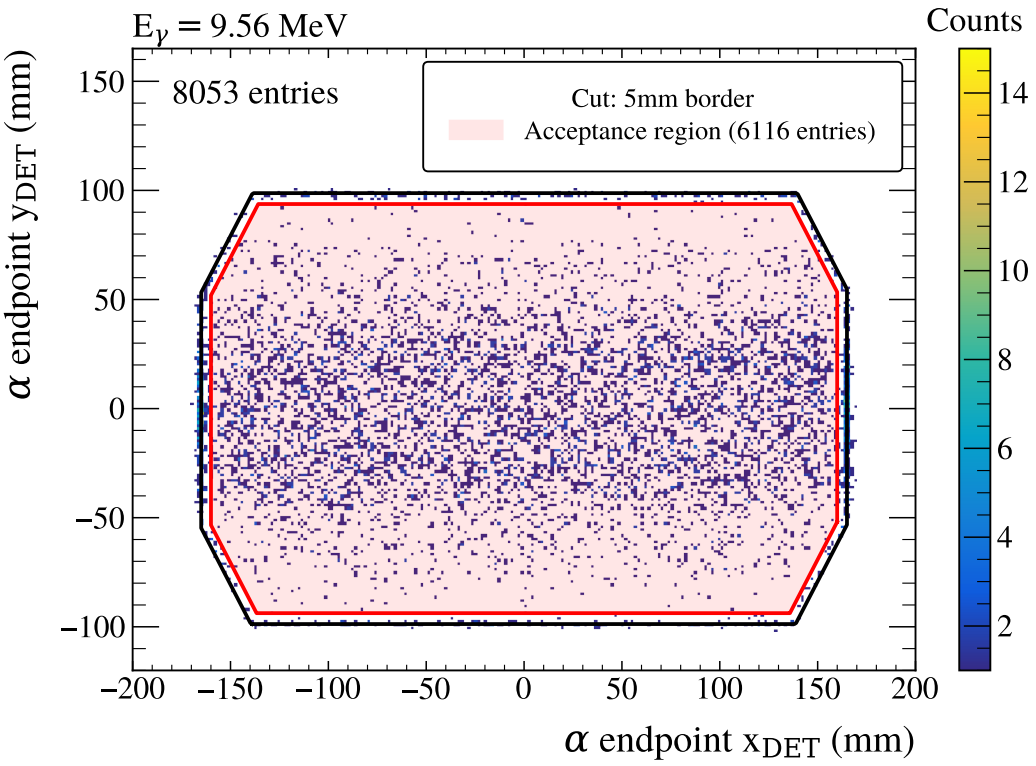

Figure 8.22: Border Padding Fiducial Cut: The α-track endpoints are shown in the xy_{det}-plane. Events that have any vertex or endpoint within 5 mm of the active area border in the xy-plane (black region) are removed. The acceptance region is shown in red.

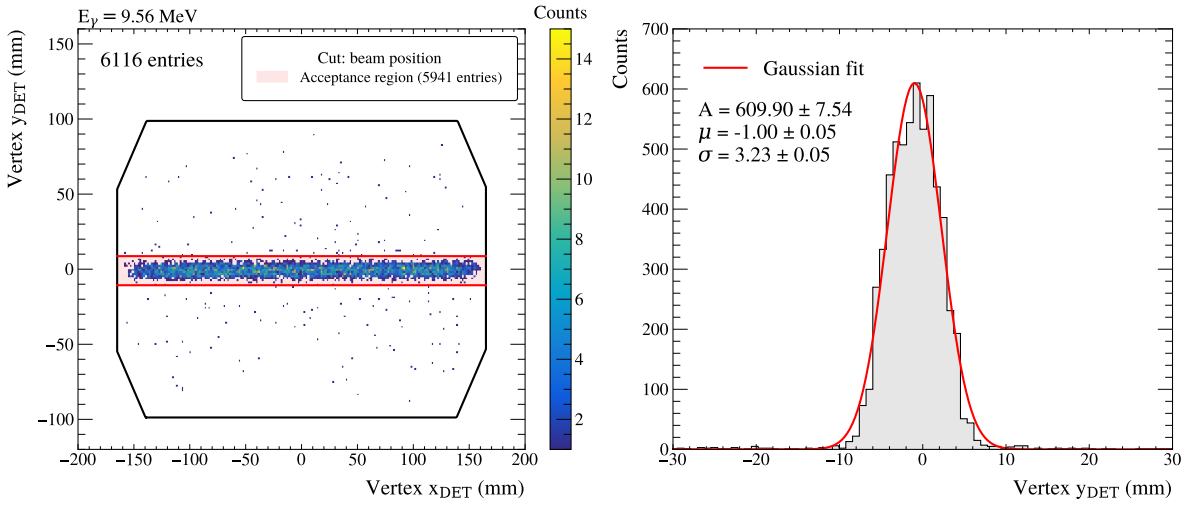

Figure 8.23: Distribution of Event Vertices. Left panel: Distribution of vertex positions within the ETPC in the xy-plane. **Right panel:** Projection of vertices onto the y-axis, fitted with a Gaussian distribution.

E_γ (MeV)	μ (mm)	σ (mm)
8.51	-1.38(3)	3.16(3)
8.66	-1.42(3)	3.14(3)
8.86	-1.32(3)	3.18(3)
9.16	-1.12(2)	3.19(3)
9.36	-1.17(4)	3.24(4)
9.56	-1.00(5)	3.23(5)
9.85	-0.84(6)	3.18(6)
11.1	-2.52(3)	2.90(3)
11.5	-1.24(2)	3.14(2)
11.9	-0.69(5)	3.74(5)
12.3	-2.01(2)	3.20(2)
13.1	-0.79(3)	3.36(3)
13.5	1.26(3)	2.94(3)

Table 8.12: Beam Position & Width: Table of parameters for the beam centre and width extracted using the reconstructed vertex positions for each energy.

Pedestal Region

As described previously, a pedestal region at the beginning of the electronics buffer is used to estimate the background. Events are rejected if any endpoint or vertex is reconstructed within this region, ensuring that the event is fully contained within said buffer.

An example of the acceptance region for this cut is shown in figure 8.24. In practice, this cut typically removes no/few events, as the detector settings were chosen such that the tracks of the reactions of interest do not extend into this region.

Drift z-span

Since the previous cut on the z-position is relative, an additional cut was applied to ensure events were not able to reach the readout plane. It is required that the α-track length of an event does not exceed half the length of the drift cage in the vertical direction. This cut is illustrated in figure 8.25.

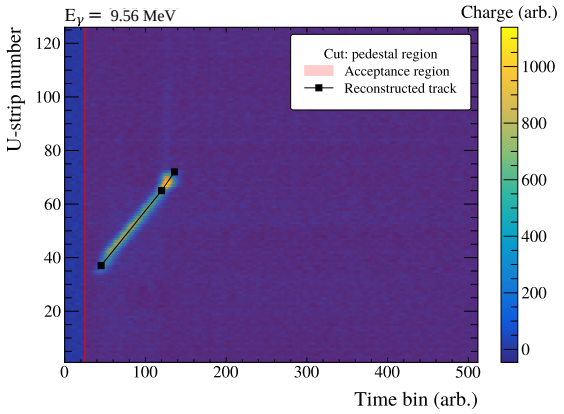

Figure 8.24: Pedestal Region Fiducial Cut: The U-projection of an event is shown, with the acceptance region highlighted in red. If any reconstructed point lay outside this region, the event was discarded.

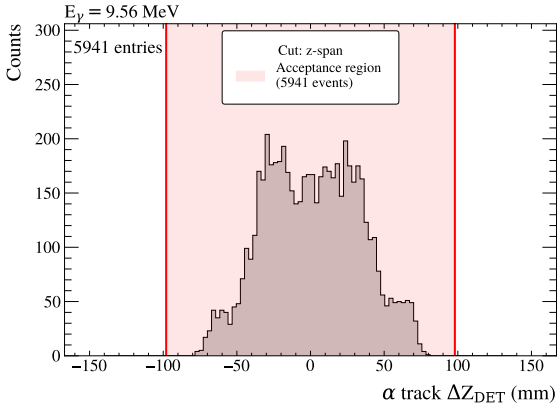

Figure 8.25: Drift z-Span Fiducial Cut: Distribution showing event span in the z_{det} direction, with the acceptance region highlighted to remove events greater than half the length of the drift volume. There were no such events at this beam energy.

Full Capture Region

The threshold and fiducial cuts described thus far remove background and ensure that the surviving events are fully contained within the detector. However, these cuts also produce a non-uniform spatial distribution of the remaining events. This occurs because the containment requirements preferentially exclude events emitted at certain angles and those with longer track lengths.

For example, consider two events originating from the same vertex position with randomly distributed emission angles near the detector boundary. The higher-energy event, which produces a longer track, is more likely to be removed than the lower-energy event. Similarly, for two events with the same track length, but located at different positions within the detector, certain emission angles may be preferentially removed. These effects introduce an angular and energy-dependent bias that must be accounted for.

This analysis avoided such biases by simply placing a cut on the vertex position along the beam axis (x_{det}). By further restricting the fiducial volume, it was ensured that the preceding cuts do not remove tracks produced at all emission angles for the maximum-probable energy of any event.

The maximum probable beam energy was estimated as $E = \mu + 2.5\sigma$, with μ and σ values taken from table 8.8. For this energy, the kinematics of the $^{16}O(\gamma, \alpha_0)$ reaction were used to calculate the α-particle lab-energy in both emission directions, aligned parallel and anti-parallel with the beam. Which was then used to determine the corresponding track lengths within the detector using `SRIM` energy-loss tables. The resulting vertex cuts, defining the new active lengths, are listed in table 8.13 [2].

An example of this cut is shown in figure 8.26, the left-hand panel provides a two-dimensional view of x_{det}-vertex vs. y_{det}-vertex, with the acceptance region drawn. The right panel shows the number of events for a given x_{det}-vertex vertex position. A clear deviation is observed outside the red acceptance region, confirming the validity of the chosen cut.

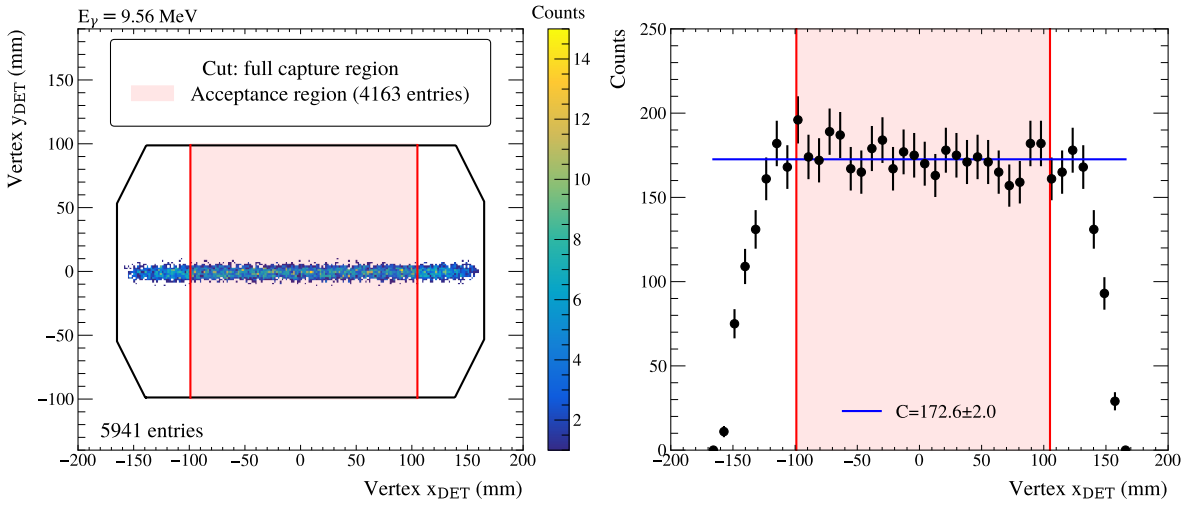

Figure 8.26: Full Capture Region Cut. Left: Shows the distribution of event vertices within the eTPC. **Right:** Shows the projection of event vertices onto the x_{det} axis. A clear deviation is seen outside the full capture region.

[2] Although optimised for the $^{16}O(\gamma, \alpha_0)$ channel the same cuts are also valid for $^{12}C(\gamma, \alpha_0)$, since this reaction produces events with shorter track lengths.

E_γ (MeV)	$\mu + 2.5\sigma$ (MeV)	E_α^{-x} (MeV)	E_α^{+x} (MeV)	-x_{beam} cut (mm)	+x_{beam} cut (mm)	active length (mm)
8.51	8.94	1.40	1.28	125	128	253
8.66	9.09	1.51	1.38	122	125	247
8.86	9.31	1.68	1.54	117	121	238
9.16	9.61	1.91	1.76	110	114	224
9.36	9.83	2.08	1.92	104	110	214
9.56	10.03	2.23	2.06	99	105	204
9.85	10.33	2.46	2.28	91	98	189
11.1	11.58	3.43	3.19	88	95	183
11.5	11.98	3.74	3.48	79	87	166
11.9	12.37	4.04	3.76	69	78	147
12.3	12.77	4.35	4.05	59	69	128
13.1	13.57	4.98	4.63	67	77	144
13.5	14.01	5.31	4.95	57	68	125

Table 8.13: Full Capture Region Parameters. Listed from left to right: The nominal beam energy, the maximum likely beam energy, the maximum alpha energy for an event pointing parallel and anti-parallel to the beam direction, the asymmetric volume cuts parallel and anti-parallel to the beam, and the corresponding total target thickness (active length). All distances are measured relative to the centre of the eTPC.

Track Length

At this stage of the analysis, the majority of the remaining events arise from the photo-dissociation of ^{12}C, ^{16}O, and $^{17/18}$O. To further isolate the $^{16}O(\gamma, \alpha_0)$ and $^{12}C(\gamma, \alpha_0)$ events, an acceptance region in reconstructed track lengths ("ion" and α particle) is defined. When visualising a two-dimensional histogram of these quantities, three distinct clusters corresponding to the aforementioned events are clearly identified, as shown in figure 8.27. A simple graphical cut is then applied to cleanly remove contributions from $^{17/18}$O. Table 8.14 lists the upper and lower cut limits, as well as the coordinates for the indents used in the cut.

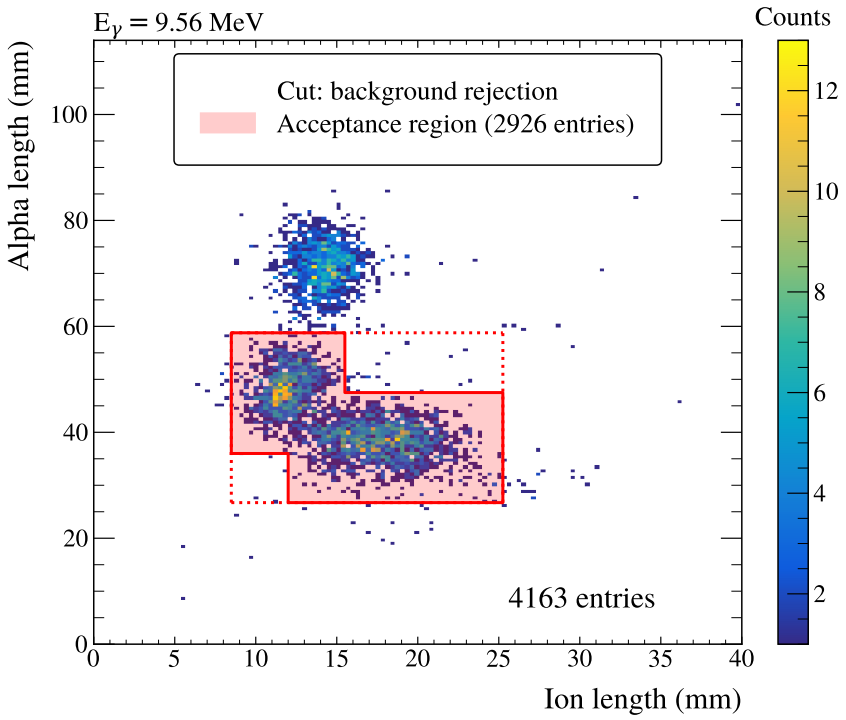

Figure 8.27: Reconstructed Track length Cut: In the "ion" vs. α track-length spectra three main regions are shown, ^{16}O, $^{17/18}$O, and ^{12}C events. An acceptance region has been placed to remove $^{17/18}$O events.

E$_\gamma$ (MeV)	α lower (mm)	α upper (mm)	Ion lower (mm)	Ion upper (mm)	upper indent [Ion, α] (mm)	lower indent [Ion, α] (mm)
8.51	14.0	34.3	6.0	19.7	(1.02 , 33.0)	(7.5 , 20.0)
8.66	16.0	38.7	5.7	21.4	(12.5 , 34.0)	(8.5 , 24.0)
8.86	19.3	42.9	6.3	22.8	(14.0 , 38.0)	(9.0 , 25.0)
9.16	22.7	49.0	6.7	24.0	(15.0 , 41.5)	(10.0 , 32.0)
9.36	24.4	52.9	7.2	24.8	(15.0 , 45.0)	(11.0 , 34.0)
9.56	26.7	58.8	8.5	25.3	(15.5 , 47.5)	(12.0 , 36.0)
9.85	32.5	59.1	8.5	26.2	(16.0 , 54.0)	(13.0 , 43.0)
11.1	34.6	75.9	7.1	22.8	(17.0 , 61.0)	(11.0 , 44.0)
11.5	43.1	80.6	6.8	24.2	(17.0 , 68.0)	(11.0 , 53.0)
11.9	50.0	95.0	6.8	24.2	(19.0 , 76.0)	(13.0 , 55.0)
12.3	55.0	101.0	7.0	28.0	(22.0 , 88.0)	(15.0 , 73.0)
13.1	52.0	96.0	6.8	35.0	(35.0 , 50.0)	(15.0 , 52.0)
13.5	50.0	105.0	7.0	30.0	(18.0 , 105.0)	(7.0 , 60.0)

Table 8.14: Track Length Cut Parameters: Acceptance region boundaries for isolating ^{16}O(γ, α_0) and ^{12}C(γ, α_0) events in [Ion track length vs α track length] space. The values in the first four columns define the rectangle; the last two columns provide coordinates for the indents of the rectangle.

Angle Cut: θ_{det}

Up to this point, all data cuts applied have been relatively conservative. However, to separate ^{16}O and ^{12}C events, more restrictive cuts on energy metrics are required, which bias the sample. In this section, the restrictive alpha energy cut, E^{α}_{cm}, is considered. To illustrate this evaluation, the $E_{\gamma} = 12.3$ MeV dataset is used. At this energy, the $^{12}\text{C}(\gamma, \alpha_0)$ cross section is very low, meaning that the data primarily consist of ^{16}O photo-dissociation events. This makes the reconstruction bias easier to observe.

The reconstructed α-particle energy in the centre-of-mass (assuming the $^{16}\text{O}(\gamma, \alpha_0)$ hypothesis, without any calibration) is plotted as functions of $\theta^{\text{lab}}_{\text{det}}$, as shown in figure 8.28. A clear reduction in reconstruction quality is observed at the extreme angles, where both quantities deviate significantly from their expected values.

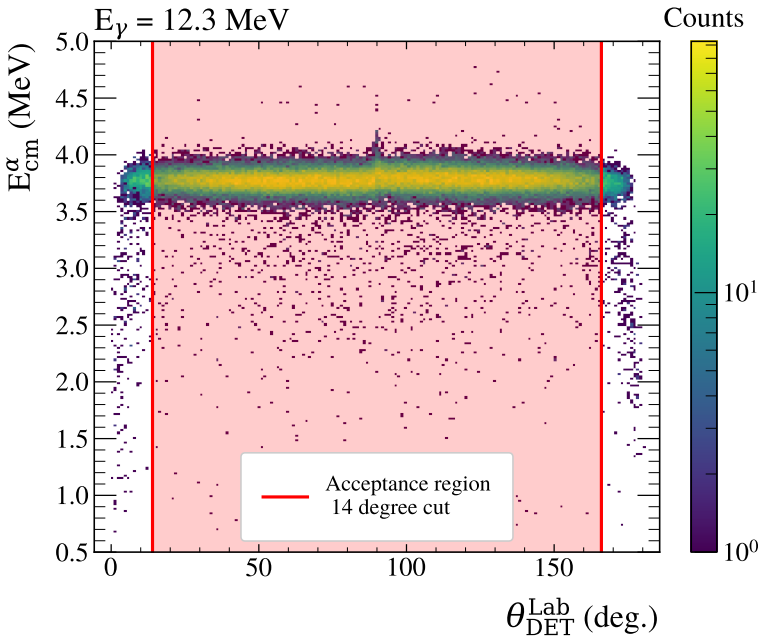

Figure 8.28: Reconstruction Bias Leading to Angle Dependent Efficiency Effects: The uncalibrated centre-of-mass energy reconstructed from the alpha particle is shown as a function of θ_{det}. An acceptance region is highlighted in red to remove poorly reconstructed events.

This reconstruction bias arises when tracks are aligned along only a few strips on the readout plane. That is, when they are approximately parallel or anti-parallel normal to it. In such cases, a plateau effect can occur on the readout strips, where the signals fail to return to baseline. An example of such an event is shown in figure 8.29, with the

affected region indicated in red. For these events, the main track-clustering algorithm fails to perform correctly, often resulting in artificially shortened or lengthened tracks and, consequently, incorrectly reconstructed energies.

This effect is not observed in the simulated data, as the electronic plateau response had not yet been implemented at the time. To ensure that only well-reconstructed events are included in the analysis, a small fiducial cut is applied to exclude these extreme angular regions. Specifically, events with $\theta_{\text{det}} < 14°$ or $\theta_{\text{det}} > 166°$ are removed, as indicated by the acceptance regions in figure 8.28. The angular bias introduced by this exclusion is later accounted for through an efficiency correction derived from the Monte Carlo simulations.

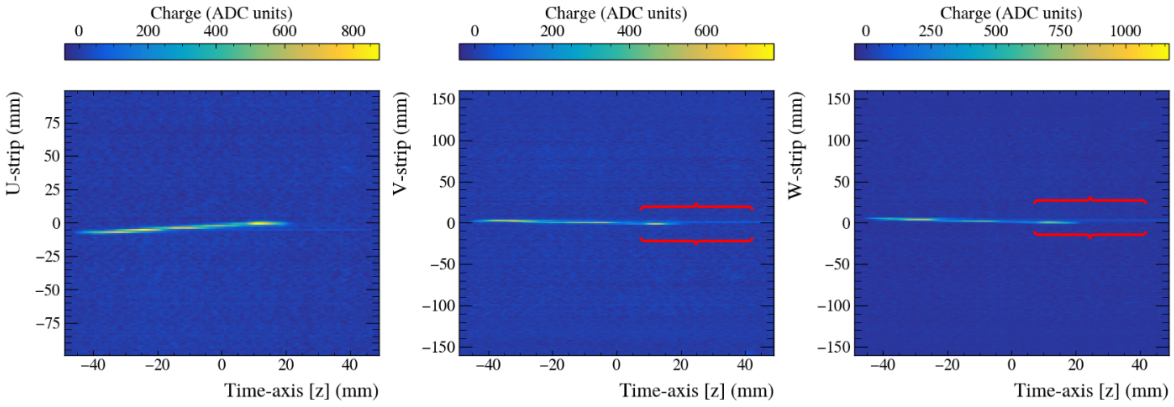

Figure 8.29: Example of a Vertical Event: A vertical $^{16}\text{O}(\gamma, \alpha)$ event is shown across all projections. The highlighted plateau (red) is responsible for the observed reconstruction error at large θ_{det} angles. A typical 2-prong event without this effect is shown in figure 7.13.

Overview

At this stage, a summary of the reduction in event statistics after each successive cut is presented in figure 8.30. The first panel shows a vertical histogram for each nominal beam energy, indicating the total number of events recorded at that energy. The central heatmap illustrates the cumulative event retention after each cut. Finally, the histogram in the rightmost panel shows the number of surviving events for each beam energy after all cuts have been applied.

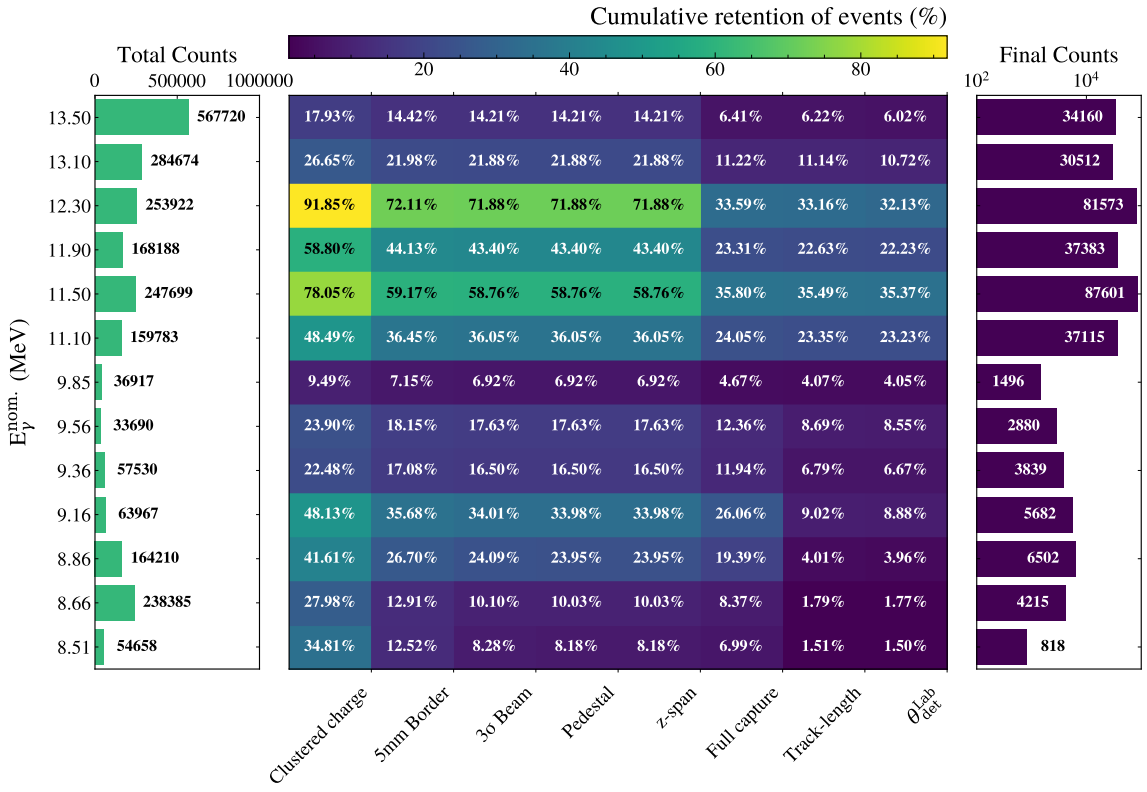

Figure 8.30: Overview of Statistics. General Cuts: A summary plot showing the total number of events, the percentage of events that remain after each cut, and the total number of remaining events after all cuts were applied.

8.3.2 Proportion of Events

At this stage in the analysis, the remaining events are mainly from $^{12}\mathrm{C}(\gamma,\alpha_0)$ and $^{16}\mathrm{O}(\gamma,\alpha_0)$. The relative proportions of these channels are quantified using the Q-ratio metric, which provides the best separation.

Definition of Q-ratio

Recall the Q-ratio is calculated as

$$Q_{\text{ratio}} = \frac{Q_\alpha}{Q_{\text{Ion}} + Q_\alpha} \tag{8.3.2.1}$$

$$\propto \frac{E_\alpha}{E_{\text{Ion}} + E_\alpha}. \tag{8.3.2.2}$$

Since $E_x = \frac{p_x^2}{2m_x}$ where p_x and m_x are the momentum and mass of particle x, it can be expressed as,

$$Q_{\text{ratio}} = \frac{\dfrac{p_\alpha^2}{2m_\alpha}}{\dfrac{p_{\text{Ion}}^2}{2m_{\text{Ion}}} + \dfrac{p_\alpha^2}{2m_\alpha}}. \tag{8.3.2.3}$$

In the centre-of-mass frame, the momenta are equal and opposite, $p_\alpha = p_{\text{Ion}} = p$, thus

$$Q_{\text{ratio}} = \frac{\dfrac{p^2}{2m_\alpha}}{\dfrac{p^2}{2m_{\text{Ion}}} + \dfrac{p^2}{2m_\alpha}} \tag{8.3.2.4}$$

$$= \frac{1/m_\alpha}{1/m_{\text{Ion}} + 1/m_\alpha} \tag{8.3.2.5}$$

$$= \frac{m_{\text{Ion}}}{m_{\text{Ion}} + m_\alpha}. \tag{8.3.2.6}$$

For a ^{12}C photo-dissociation event, the "Ion" corresponds to two α particles. Approximating the masses as $m_\alpha = 4\,\text{u}$ and $m_{\text{Ion}} = 8\,\text{u}$, the Q-ratio is

$$Q_{\text{ratio}} \simeq \frac{m_{\text{Ion}}}{m_{\text{Ion}} + m_\alpha} \simeq \frac{8}{8+4} = 0.667. \tag{8.3.2.7}$$

For a ^{16}O photo-dissociation event, the "Ion" is a ^{12}C nucleus. Taking $m_\alpha = 4\,\text{u}$ and $m_{\text{Ion}} = 12\,\text{u}$ gives

$$Q_{\text{ratio}} \simeq \frac{m_{\text{Ion}}}{m_{\text{Ion}} + m_\alpha} \simeq \frac{12}{12+4} = 0.75. \tag{8.3.2.8}$$

Q-ratio Fitting

In practice, the Q-ratio is calculated in the laboratory frame, where the incident γ momentum introduces angular dependence. This is shown for $E_\gamma = 9.56$ in figure 8.31.

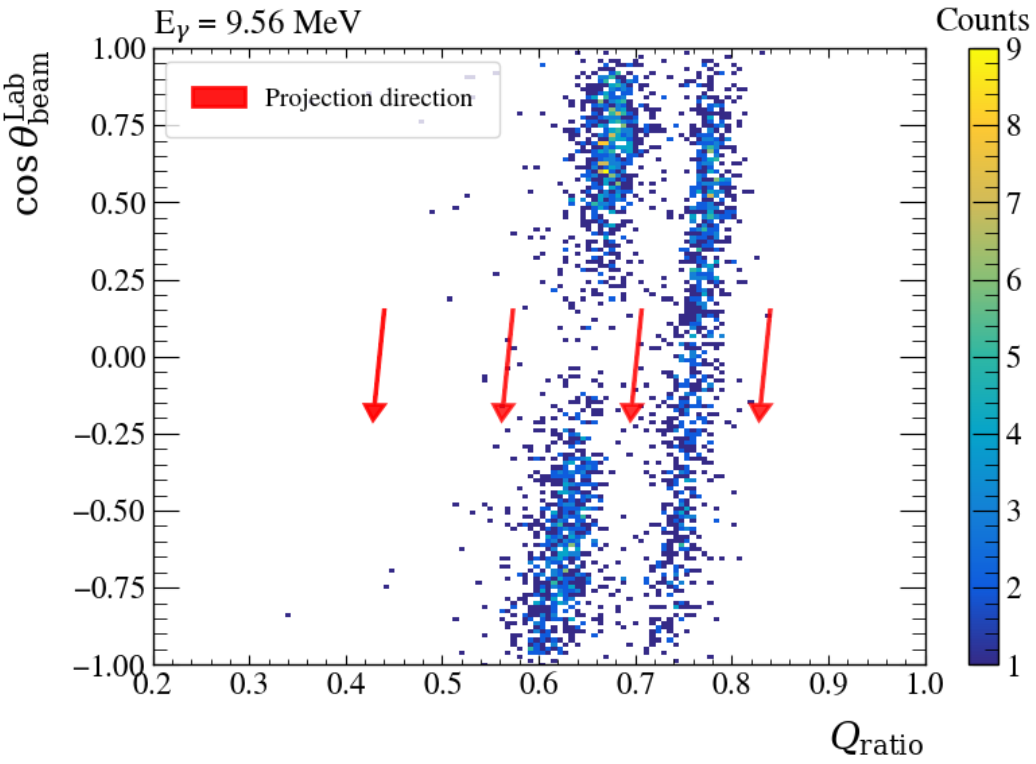

Figure 8.31: Angular Dependence of the Q-ratio: The Q-ratio metric as a function of $\cos\theta^{\text{Lab}}_{\text{beam}}$ is shown for $E_\gamma = 9.56$ MeV. The projection direction is shown in red.

To determine the relative fractions of ^{12}C and ^{16}O events, two steps are required:

1. Identify the optimal line separating the two reaction channels in Q-ratio vs. $\cos\theta^{lab}_{beam}$ space, along which the data can be projected to obtain a one-dimensional spectrum.

2. Obtain accurate Q-ratio models for each channel that can be fitted to the data to extract their relative proportions.

The simulated data for the same energy (see appendix E), shown in figure 8.32, provide labelled Q-ratio distributions for both reaction channels. A support vector machine[3] (SVM) classifier was trained on this dataset to determine the optimal separation line. Using the

[3]A supervised machine learning algorithm that finds the best separation between labelled datasets.

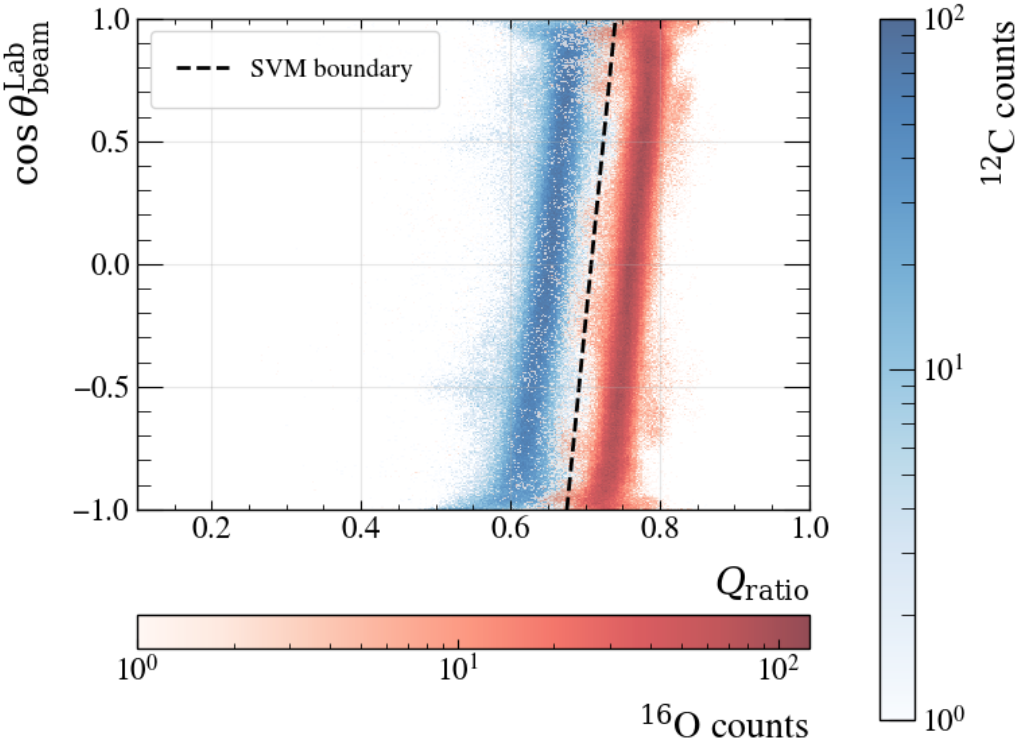

Figure 8.32: Simulated Q-ratio Separation: Simulated data for both the ^{16}O and ^{12}C reaction channels are shown separated using a support vector machine for $E_\gamma = 9.56$ MeV.

SVM-defined separation line, both the experimental and simulated data were projected tangent to this boundary. The projected simulated spectra for ^{12}C and ^{16}O were normalised and scaled independently to reproduce the experimental distribution, in order to obtain

$$f_{^{12}\mathrm{C}/^{16}\mathrm{O}} = \frac{N_{^{12}\mathrm{C}}}{N_{^{16}\mathrm{O}}}. \tag{8.3.2.9}$$

During the fit, two independent scaling parameters, $S_{^{12}\mathrm{C}}$ and $S_{^{16}\mathrm{O}}$, and an overall Gaussian smearing factor were introduced to account for small imperfections in the simulation. These corrections were typically very small[4].

Figure 8.33 shows an example of the fitted Q-ratio spectrum, while figure 8.34 displays the corresponding χ^2 variation as a function of $f_{^{12}\mathrm{C}/^{16}\mathrm{O}}$. The extracted parameters are summarised in table 8.15 for all energies.

[4]Potential causes of disagreement: slightly different `Geant4` energy-loss curves compared to reality, or the fact that z-dependent track diffusion wasn't included in the simulation.

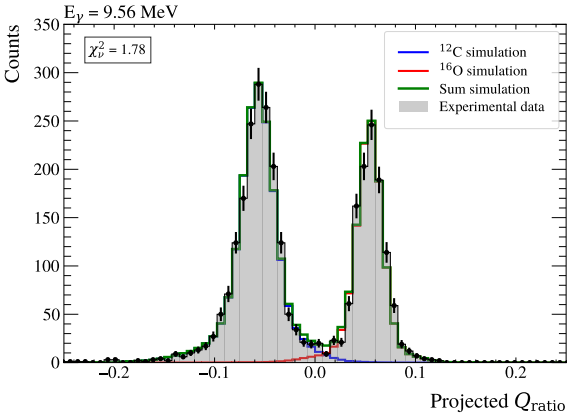

Figure 8.33: Projected Q-ratio: Simulation fitted to experimental data to extract the proportions of the remaining reaction channels at this stage of the analysis, for $E_\gamma = 9.56$ MeV.

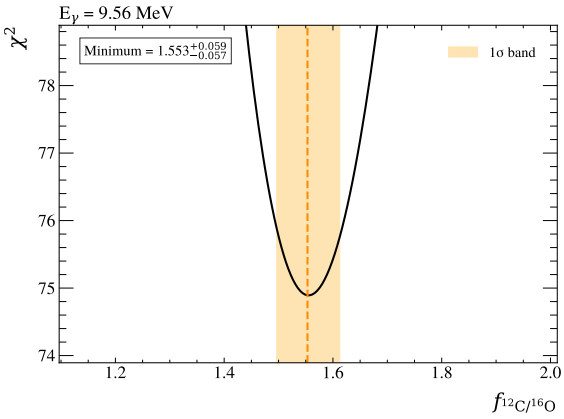

Figure 8.34: Q-ratio Error Tracking: All fit parameters were re-minimised, taking steps in $f_{^{12}\text{C}/^{16}\text{O}}$ to obtain its error, for $E_\gamma = 9.56$ MeV.

E$_\gamma$ (MeV)	$f_{^{12}\text{C}/^{16}\text{O}}$	Q^{12C}_{ratio} scaling	Q^{16O}_{ratio} scaling	Q_{ratio} Gaussian σ
8.51	$4.5^{+0.4}_{-0.4}$	1.012	1.026	0.010
8.66	$4.1^{+0.2}_{-0.2}$	1.016	1.034	0.015
8.86	$3.9^{+0.1}_{-0.1}$	1.025	1.034	0.012
9.16	$2.71^{+0.08}_{-0.08}$	1.030	1.044	0.006
9.36	$1.88^{+0.07}_{-0.06}$	1.025	1.044	0.006
9.56	$1.58^{+0.06}_{-0.06}$	1.025	1.044	0.007
9.85	$1.34^{+0.08}_{-0.06}$	1.025	1.049	0.008
11.1	$0.125^{+0.002}_{-0.002}$	1.032	1.052	0.007
11.5	$0.0149^{+0.0004}_{-0.0004}$	1.032	1.047	0.006
11.9	$0.032^{+0.001}_{-0.001}$	1.030	1.052	0.008
12.3	$0.0029^{+0.0002}_{-0.0002}$	1.029	1.053	0.009
13.1	$0.0030^{+0.0003}_{-0.0003}$	1.030	1.042	0.006
13.5	$0.0081^{+0.0005}_{-0.0005}$	1.026	1.044	0.008

Table 8.15: Parameters Comparing Simulated Q-ratio to Experimental Data: Lists the $f_{^{12}\text{C}/^{16}\text{O}}$ and associated 1σ errors, as well as the various scaling and smearing parameters.

8.3.3 Isolation of ^{16}O Events

With a handle on the proportion of events and all regions of non-uniform detection efficiency removed, the next aim is to separate the reaction channels as effectively as possible, and estimate the remaining fraction of "background" events.

Q-Ratio cut

The simulated data, after applying all Q-ratio corrections, were projected again along the tangent to their SVM separation line, with the relative counts for each reaction controlled using the minimised $f_{^{12}C/^{16}O}$ value (see table 8.15). The SVM separation line was laterally adjusted by varying its intercept: events to the left of the line were rejected, while those to the right were retained. At each step, the efficiency for maintaining ^{16}O, and the leakage of ^{12}C events were calculated. An example showing these quantities as a function of the separation line position is presented in figure 8.35. A cut position was chosen to remove the majority of carbon events while maintaining high ^{16}O efficiency. The optimal line parameters, efficiencies, and leakage fractions are summarised in table 8.16.

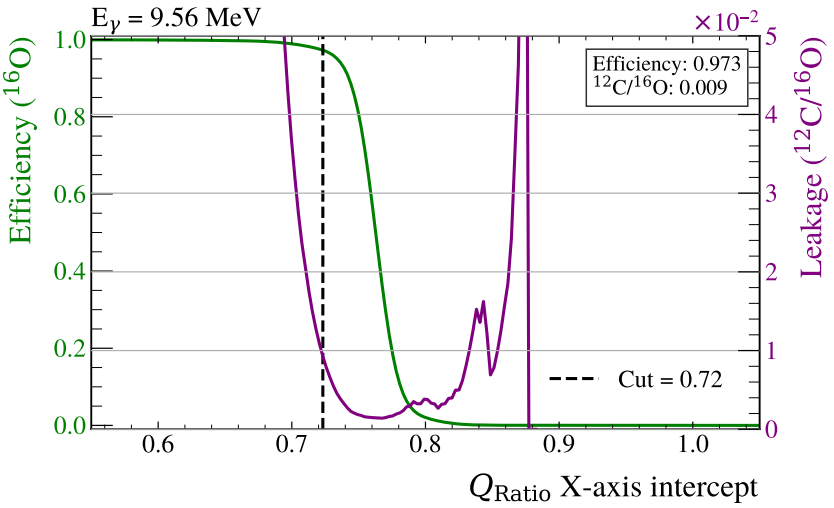

Figure 8.35: Tracking efficiency and leakage of Q-ratio cut: This plot shows the efficiency of maintaining ^{16}O events (green line and axis) and the leakage fraction of ^{12}C events (purple line and axis) as a function of x-axis intercept of the Q-Ratio separation line. An example of such a line is shown in red in figure 8.36. The dotted line in this figure indicates the selected cut position for $E_\gamma = 9.56$ MeV, with the related efficiency and leakage fraction given in the upper-right box.

E_γ (MeV)	m	c	x-axis intercept	ϵ^{16}O (%)	$L_{^{12}C/^{16}O}$
8.51	33.007	-22.986	0.696	83.1	9.62×10^{-2}
8.66	32.437	-22.788	0.703	83.7	5.81×10^{-2}
8.86	30.687	-21.475	0.700	88.7	4.92×10^{-2}
9.16	27.793	-19.533	0.703	95.4	3.63×10^{-2}
9.36	28.594	-20.405	0.714	96.5	1.87×10^{-2}
9.56	28.852	-20.866	0.723	97.3	9.26×10^{-3}
9.85	31.130	-22.444	0.721	98.5	9.17×10^{-3}
11.1	33.335	-23.589	0.708	99.7	2.00×10^{-3}
11.5	33.432	-24.040	0.719	99.7	9.35×10^{-5}
11.9	33.077	-23.803	0.720	99.7	8.51×10^{-5}
12.3	33.369	-23.930	0.717	99.7	9.94×10^{-6}
13.1	34.066	-23.990	0.704	99.7	8.41×10^{-5}
13.5	34.157	-24.327	0.712	99.6	9.52×10^{-5}

Table 8.16: Optimal Parameters for Q-ratio Separation Line: Lists the parameters for the optimal separation line for each energy, as well as the ^{16}O efficiency for the cut, and the total leakage fraction, $L_{^{12}C/^{16}O}$, at this stage of the analysis.

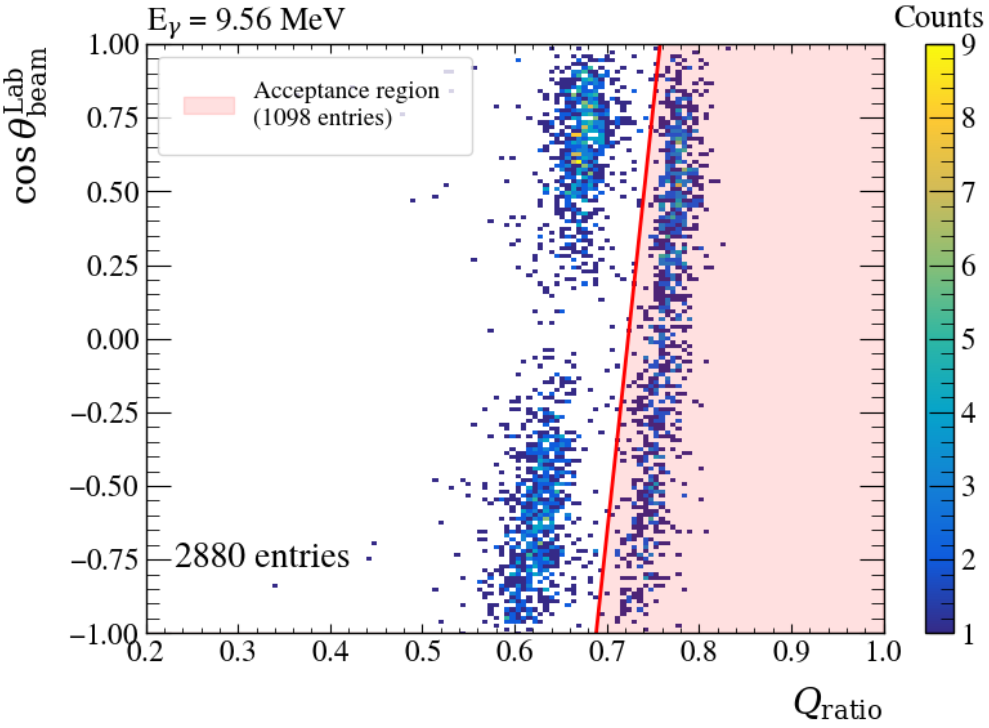

Figure 8.36: Q-ratio Data Cut for Isolating ^{16}O: The acceptance region for the optimised cut is shown in red for E_γ=9.56 MeV to isolate ^{16}O from ^{12}C events.

It should be noted that the leakage fraction, $L_{^{12}\mathrm{C}/^{16}\mathrm{O}}$, represents the total ratio of ^{12}C to ^{16}O counts at this stage of the analysis cuts, while the efficiency $\epsilon^{^{16}\mathrm{O}}$ corresponds to this cut alone. The acceptance region for an example energy is shown in figure 8.36.

Particle Energy Cut

The final cut used to isolate ^{16}O events is based on the measured centre-of-mass energies. The measured track lengths for both the ion and the α particle were converted to energies using `SRIM` tables and the two-body $^{16}\mathrm{O}(\gamma, \alpha_0)^{12}\mathrm{C}$ reaction hypothesis. These energies were then boosted to the centre-of-mass frame using the effective gamma beam energy and nominal alignment. No calibration is applied at this stage.

Verification. The experimental E^{α}_{cm} and $E^{\mathrm{Ion}}_{\mathrm{cm}}$ spectra are shown in the upper and lower panels of figure 8.37, respectively. The simulated data from the previous step, after the $\cos\theta_{det}$ vs. Q-ratio cut was applied, were scaled by the leakage fraction from table 8.16 are overlaid (typically 1-2% energy scale was applied to the simulated data). The good agreement confirms that the simulation can be used to determine an appropriate cut.

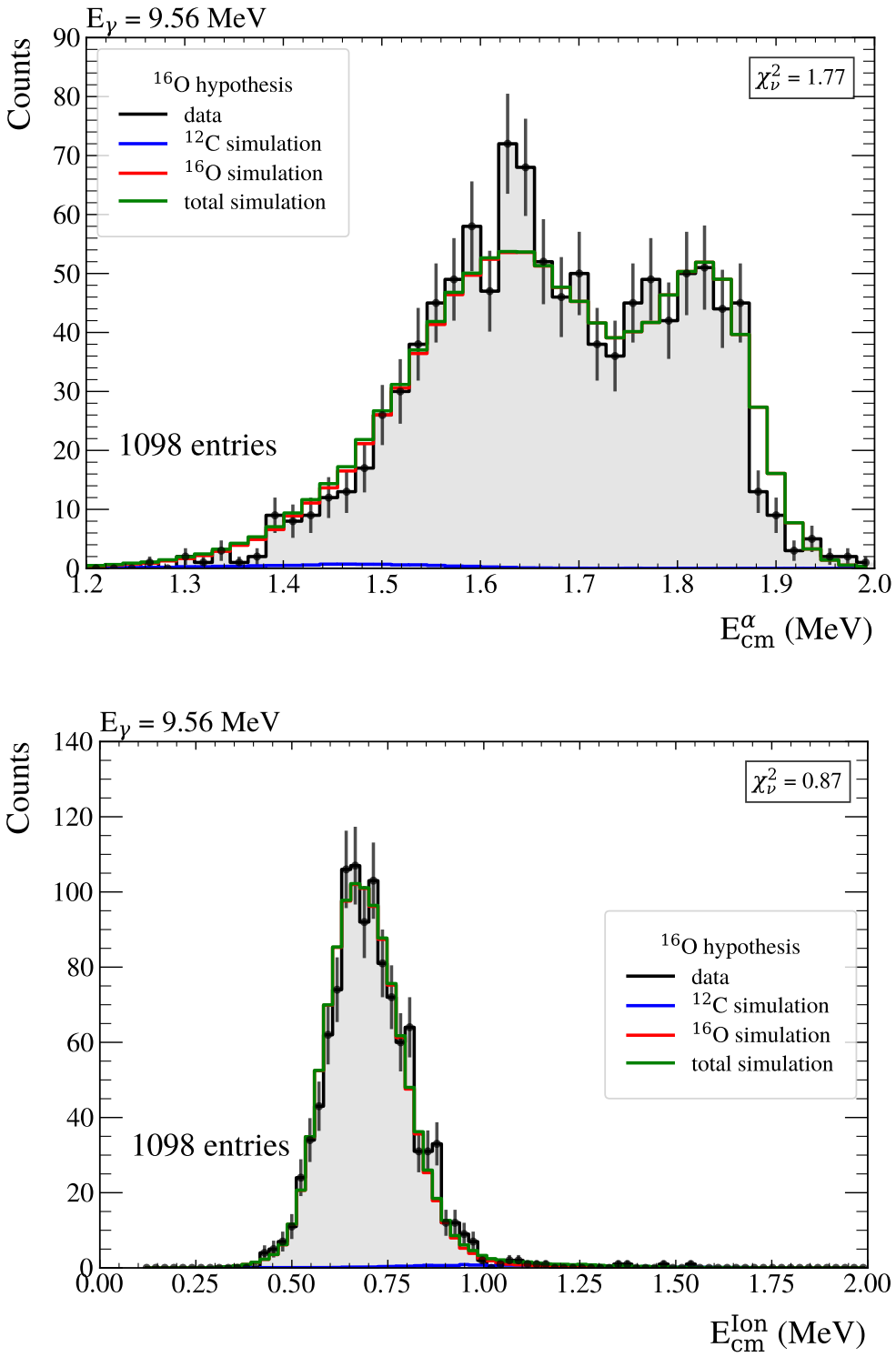

Figure 8.37: Centre-of-Mass Energy Distributions for ^{16}O: Reconstructed centre-of-mass energy distributions for α particles (top) and recoil ions (bottom), comparing experimental data (grey histograms) with Monte Carlo simulations. The simulated contributions from ^{12}C (blue) and ^{16}O (red) events are shown separately, with their sum in green. All data were reconstructed assuming the ^{16}O reaction hypothesis.

Ellipse cut. The energies were plotted in two dimensions, with simulated data as histograms and experimental data as a scatter plot, shown in figure 8.38. An elliptical gate was defined to isolate the main ^{16}O sample, defined as

$$\frac{(x-x_0)^2}{(w_x^2/2)} + \frac{(y-y_0)^2}{(w_y^2/2)} = 1, \tag{8.3.3.1}$$

where (x_0, y_0) is the centre of the ellipse, and w_x and w_y are the widths in the x and y directions, respectively. The new leakage fraction, $L^*_{^{12}\mathrm{C}/^{16}\mathrm{O}}$, and ^{16}O efficiency after this cut are given in table 8.17). Note that the leakage fraction represents the total leakage at this stage of the analysis, whereas the efficiency corresponds to this cut alone. This process provides an estimate of the remaining ^{12}C in the sample at the end of the data cuts, which is negligible at all energies.

E_γ (MeV)	x_0 (MeV)	y_0 (MeV)	w_x (MeV)	w_y (MeV)	ϵ^{16}O (%)	$L^*_{^{12}\mathrm{C}/^{16}\mathrm{O}}$
8.51	0.42	0.98	0.40	0.58	87.1	8.1×10^{-3}
8.66	0.48	1.09	0.48	0.63	94.2	8.8×10^{-3}
8.86	0.50	1.22	0.45	0.65	86.3	4.4×10^{-3}
9.16	0.59	1.45	0.55	0.65	91.3	4.6×10^{-3}
9.36	0.65	1.55	0.50	0.65	92.2	2.8×10^{-3}
9.56	0.69	1.70	0.62	0.80	96.7	1.7×10^{-3}
9.85	0.75	1.80	0.62	0.50	92.5	5.7×10^{-4}
11.1	1.30	2.85	1.75	0.97	99.5	1.2×10^{-4}
11.5	1.38	3.06	1.79	0.95	99.8	6.3×10^{-6}
11.9	1.50	3.46	2.30	1.42	99.8	1.6×10^{-5}
12.3	1.70	3.78	2.30	0.90	99.4	6.5×10^{-7}
13.1	2.19	4.15	3.10	1.25	99.8	2.7×10^{-5}
13.5	2.19	4.50	3.00	1.90	99.8	3.2×10^{-5}

Table 8.17: Elliptical Cut Parameters for Each Energy: The parameters of the ellipse cut to isolate the ^{16}O sample are given, as well as the efficiency of this cut and the total leakage fraction of ^{12}C at this stage of the analysis.

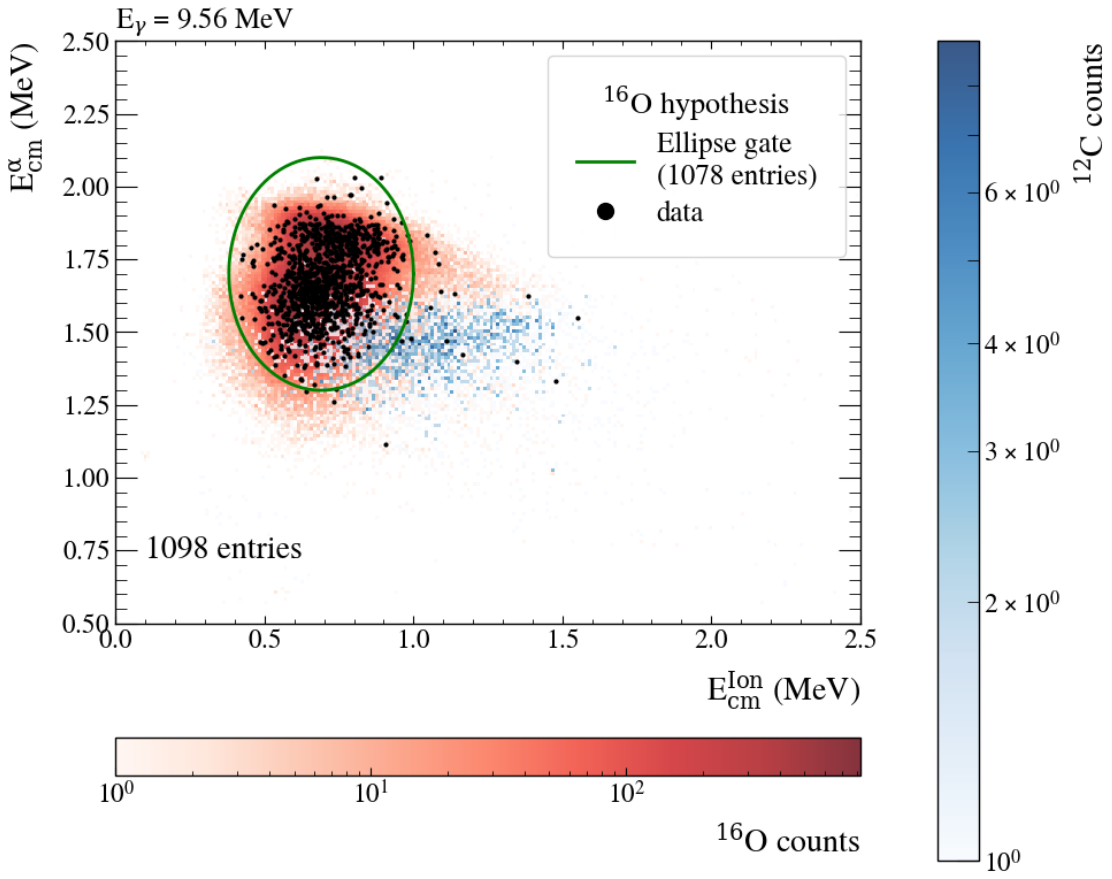

Figure 8.38: Elliptical Cut for ^{16}O Selection: Recoil Ion energy vs. α energy in the centre-of-mass frame, reconstructed assuming the ^{16}O photo-dissociation hypothesis. Experimental data (black points) are compared with Monte Carlo simulations for ^{16}O (red) and ^{12}C (blue) events. The elliptical acceptance region (green line) is positioned to gate on experimental ^{16}O events while rejecting ^{12}C background, guided by the simulation.

Overview of Entries

A summary plot is given in figure 8.39. Where the total number of events is tracked after each cut to isolate ^{16}O. The final numbers represent the final sample of ^{16}O events.

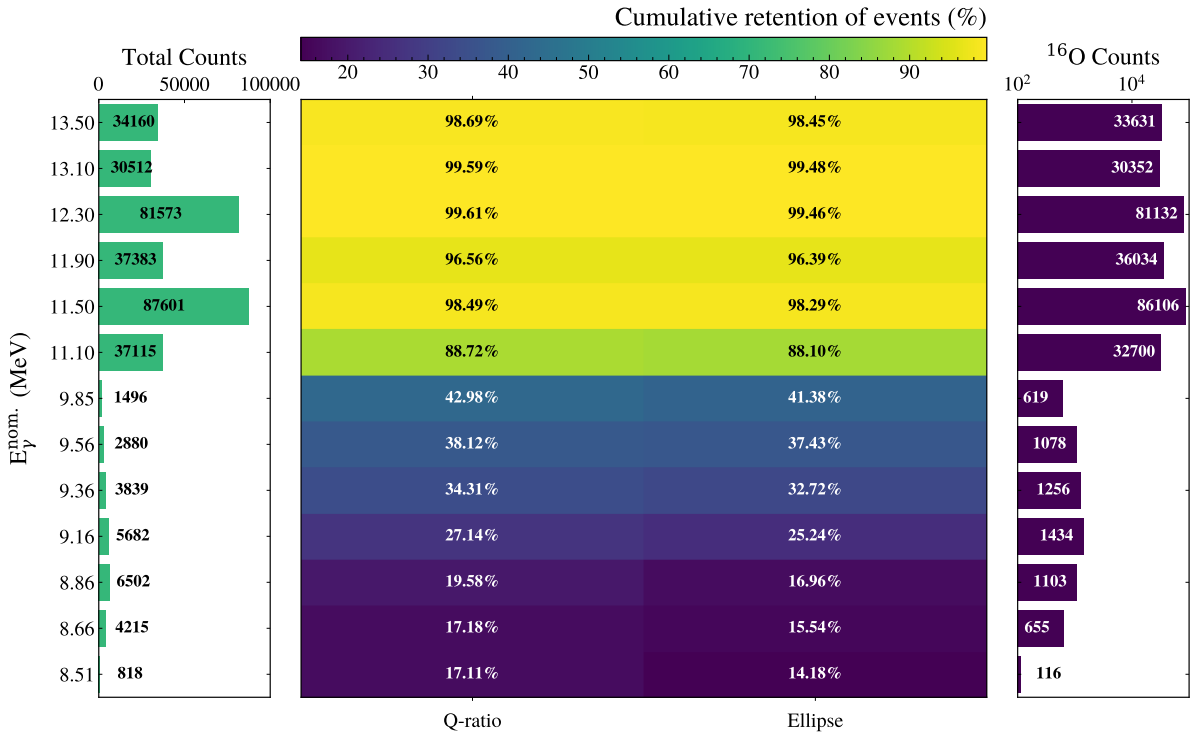

Figure 8.39: Overview of Statistics. ^{16}O: A summary plot showing the total number of events, how many events remain after each cut, and the total number of remaining events.

8.3.4 Isolation of ^{12}C Events

This step is the same as the previous, except the aim here is to remove ^{16}O events while maintaining ^{12}C. The reader is directed to read the previous section, as details are brief here.

Q-Ratio cut

The corrected simulated Q-ratio data were scaled by the fraction of counts $f_{^{12}C/^{16}O}$, and a cut position was chosen by varying the same SVM line to remove the majority of ^{16}O events while maintaining high ^{12}C efficiency. The optimal line parameters, efficiencies, and leakage fractions are summarised in table 8.18.

It should be noted that the leakage fraction, $L_{^{16}O/^{12}C}$, represents the total ratio of ^{12}C to ^{16}O counts at this stage of the analysis cuts, while the efficiency ϵ^{12C} corresponds to this cut alone. The acceptance region for an example energy is shown in figure 8.40. No data were available for $E_\gamma = 13.1$ MeV, as the cross section drops rapidly at this energy, the entire Q-ratio spectrum could be described by the model for ^{16}O.

E_γ (MeV)	m	c	x-axis intercept	ϵ^{12}C (%)	$L_{^{16}O/^{12}C}$
8.51	33.290	-22.750	0.683	97.8	0.0192
8.66	30.886	-21.684	0.702	99.1	0.0295
8.86	29.210	-20.462	0.701	99.2	0.0226
9.16	27.573	-19.564	0.710	99.4	0.0169
9.36	28.329	-20.381	0.719	99.6	0.0172
9.56	28.886	-20.965	0.726	99.5	0.0198
9.85	31.113	-22.657	0.728	99.6	0.0158
11.1	33.378	-23.620	0.708	98.4	0.0222
11.5	33.050	-22.783	0.689	91.1	0.0681
11.9	33.097	-23.063	0.697	96.4	0.0728
12.3	34.536	-23.910	0.692	94.3	0.4307
13.1	N/A	N/A	N/A	N/A	N/A
13.5	34.179	-23.663	0.6923	93.8	0.1624

Table 8.18: Table of Parameters for Best Q-Ratio Separation Line: Lists the optimal separation line for each energy. lists the ^{12}C efficiency for this cut, and the total leakage fraction, $L_{^{16}O/^{12}C}$, at this stage of the analysis.

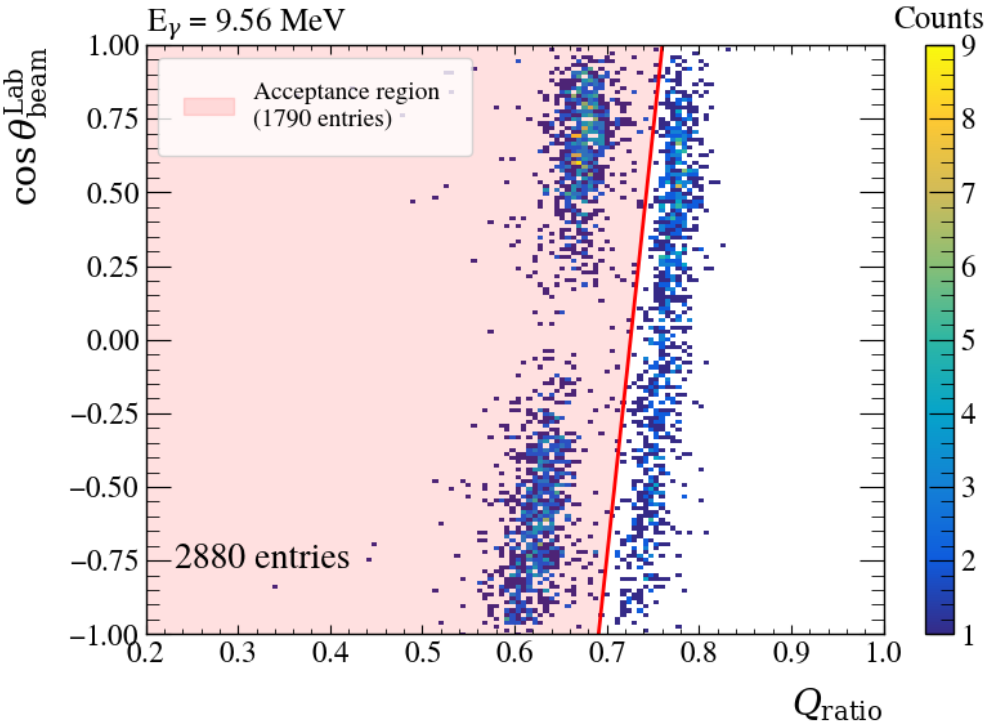

Figure 8.40: Q-Ratio Data Cut for Isolating ^{12}C: The acceptance region for the optimised cut is shown in red for E_γ=9.56 MeV to isolate ^{12}C from ^{16}O events.

Particle Energy Cut

The final cut used to isolate ^{12}C events is based on the measured centre-of-mass energies. Measured track lengths for both the ion and the α particle were converted to energies using `SRIM` tables, and still currently assuming the two-body $^{16}\mathrm{O}(\gamma,\alpha)^{12}\mathrm{C}$ reaction hypothesis. These momenta were then boosted to the centre-of-mass frame using the effective gamma beam energy and nominal alignment.

Verification. The experimental E^{α}_{cm} and $E^{\mathrm{Ion}}_{\mathrm{cm}}$ spectra are shown in the upper and lower panels of figure 8.41, respectively. The simulated data from the previous step, after the $\cos\theta_{det}$ vs. Q-ratio cut was applied, were scaled by the leakage fraction from table 8.18 and overlaid. An energy scale was applied to the simulated data, again typically 1-2%, similar to the ones used for the ^{16}O simulation. The good agreement confirms that the simulation can be used to determine an appropriate cut.

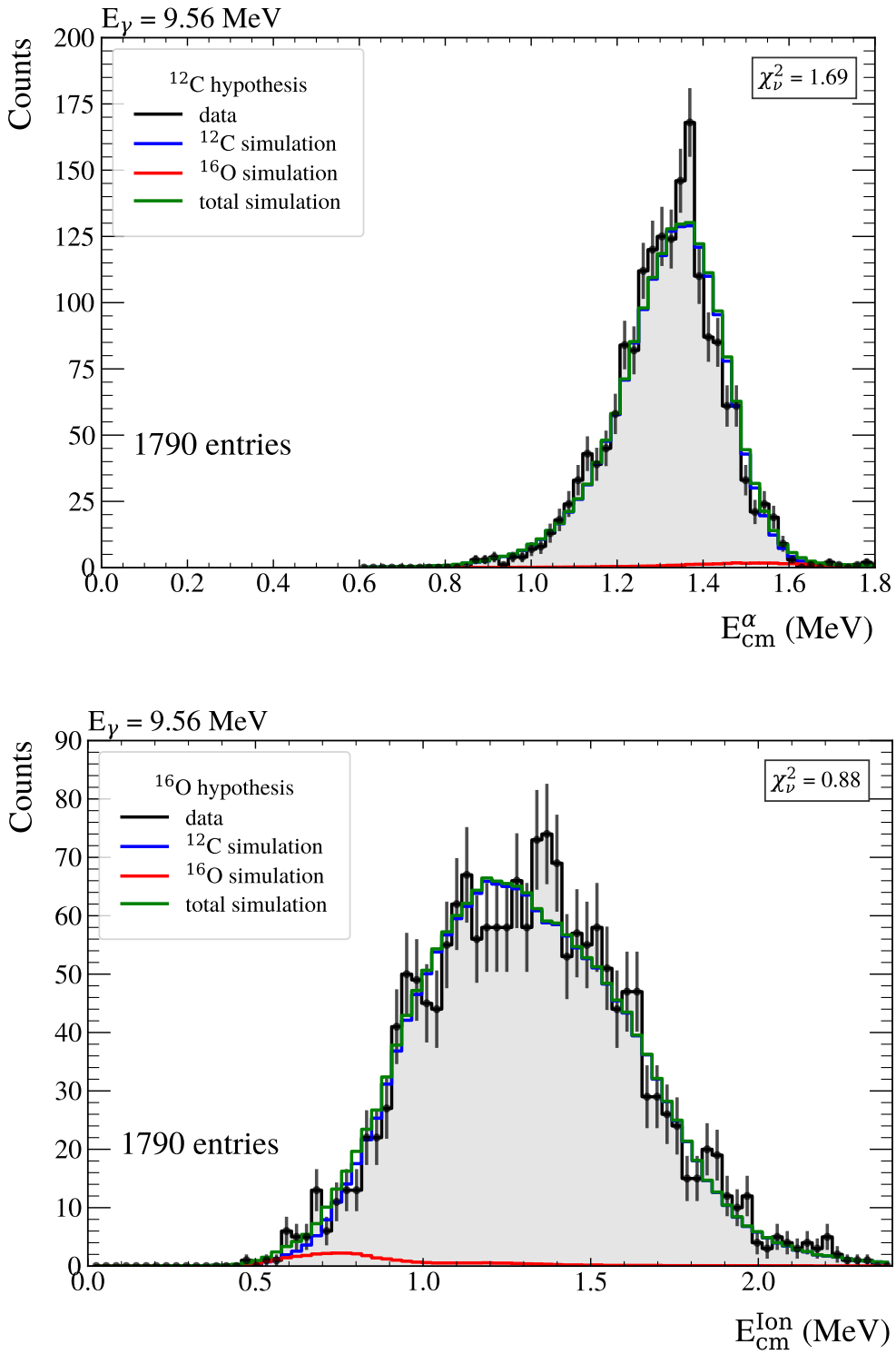

Figure 8.41: Centre-of-Mass Energy Distributions for ^{12}C: Reconstructed centre-of-mass energy distributions for α particles (top) and recoil ions (bottom), comparing experimental data (grey histograms) with Monte Carlo simulations. The simulated contributions from ^{12}C (blue) and ^{16}O (red) events are shown separately, with their sum in green. All data were reconstructed assuming the ^{16}O reaction hypothesis.

Ellipse cut. The energies were plotted in two dimensions, with simulated data as histograms and experimental data as a scatter plot, shown in figure 8.42. An elliptical gate was defined to isolate the main ^{12}C sample. The new leakage fraction, $L^*_{^{16}\mathrm{O}/^{12}\mathrm{C}}$, and ^{12}C efficiency after this cut are given in table 8.19. Note that the leakage fraction represents the total leakage at this stage of the analysis, whereas the efficiency corresponds to this cut alone. This process provides an estimate of the remaining ^{16}O in the sample after all data cuts, which is minimal.

E_γ (MeV)	x_0 (MeV)	y_0 (MeV)	w_x (MeV)	w_y (MeV)	ϵ^{12}C (%)	$L^*_{^{16}\mathrm{O}/^{12}\mathrm{C}}$
8.51	0.90	0.68	0.90	0.50	86.5	0.0117
8.66	0.95	0.74	0.95	0.55	86.5	0.0167
8.86	1.05	0.89	1.00	0.54	84.8	0.0159
9.16	1.25	1.05	1.40	0.70	92.4	0.0119
9.36	1.30	1.20	1.30	0.60	87.3	0.0093
9.56	1.40	1.30	1.30	0.66	89.6	0.0076
9.85	1.50	1.46	1.30	0.66	87.6	0.0066
11.1	2.35	2.33	2.40	0.95	97.6	0.0085
11.5	2.45	2.55	2.10	0.90	93.4	0.0150
11.9	2.70	2.90	2.30	0.80	91.2	0.0103
12.3	3.10	3.00	2.20	1.00	91.9	0.0541
13.1	N/A	N/A	N/A	N/A	N/A	N/A
13.5	4.15	4.00	3.30	1.00	95.4	0.0329

Table 8.19: Elliptical Cut Parameters for Each Energy: The parameters of the ellipse cut to isolate the ^{12}C sample are given, as well as the efficiency of this cut and the total leakage fraction of ^{16}O at this stage of the analysis.

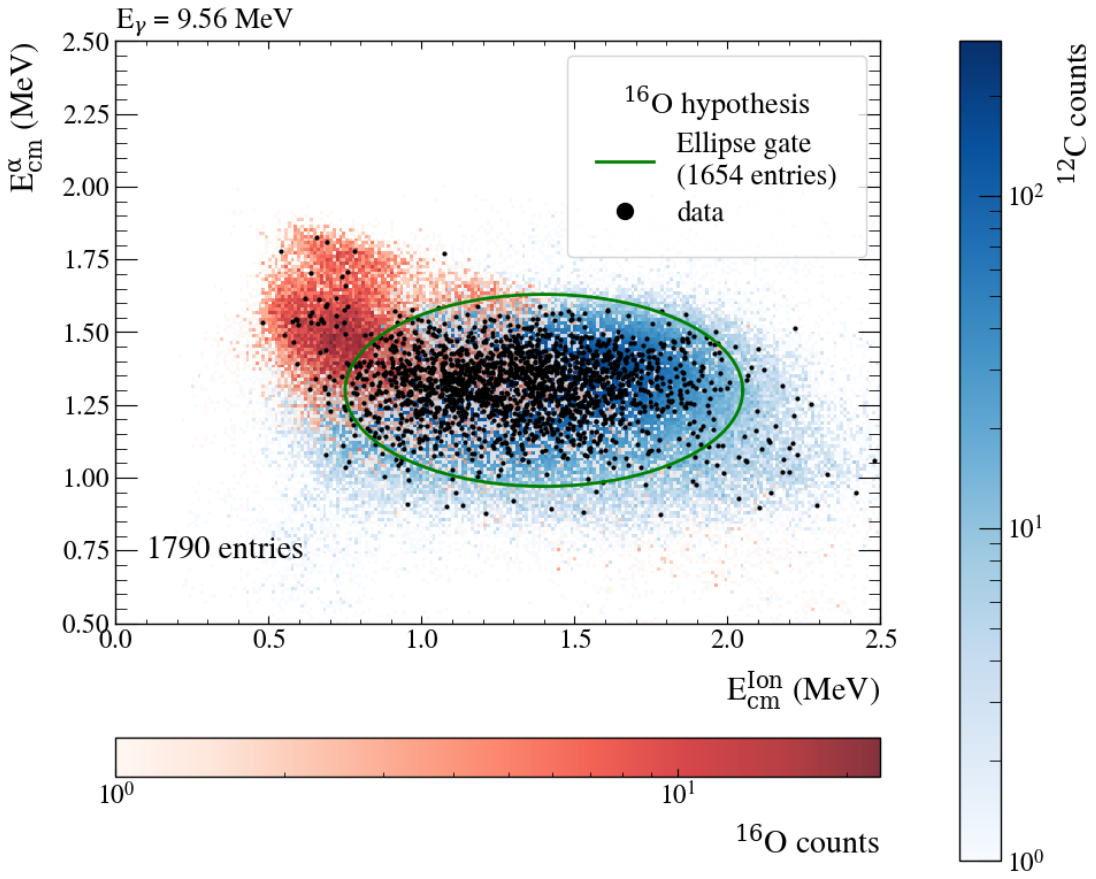

Figure 8.42: Elliptical Cut for ^{12}C Selection: Recoil Ion energy vs. α energy in the centre-of-mass frame, reconstructed assuming the ^{16}O photo-dissociation hypothesis. Experimental data (black points) are compared with Monte Carlo simulations for ^{16}O (red) and ^{12}C (blue) events. The elliptical acceptance region (green line) is positioned to gate on experimental ^{12}C events while rejecting ^{16}O background, guided by the simulation.

Overview of Entries

A summary plot is given in figure 8.43, in the same format as figure 8.30. Where the total number of events is tracked after each cut to isolate ^{12}C, the final numbers represent the final sample of ^{12}C.

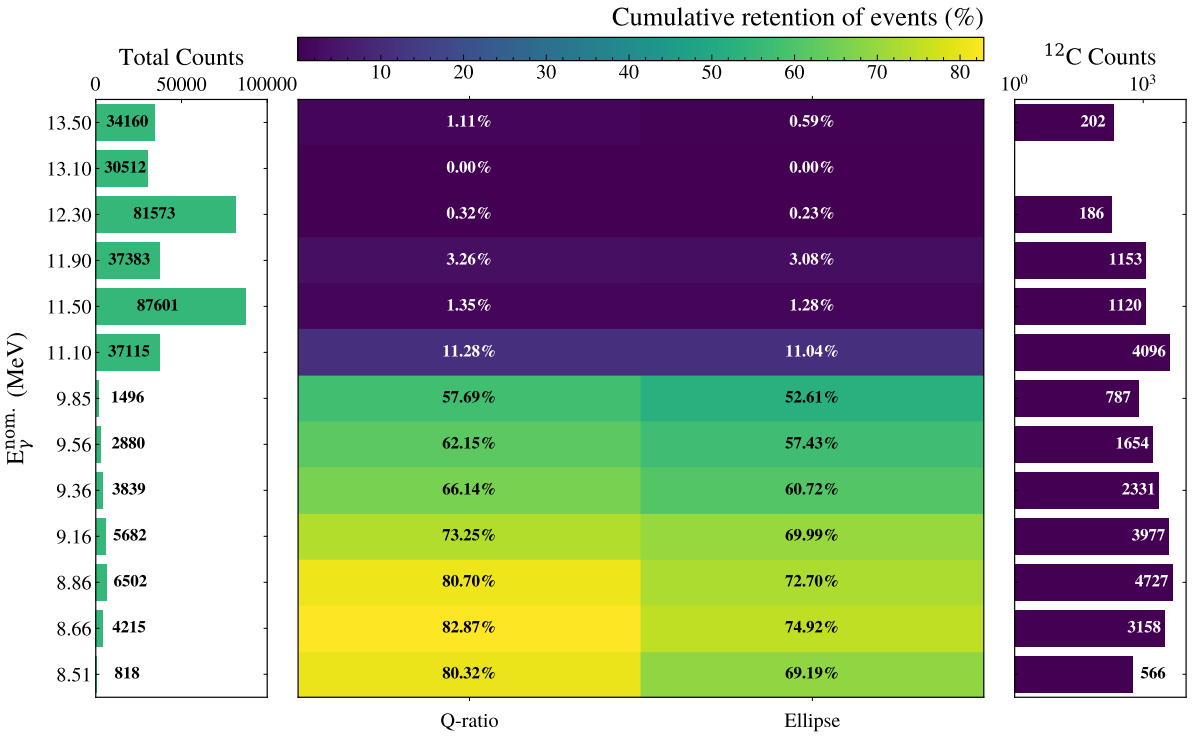

Figure 8.43: Overview of Statistics. ^{12}C: A summary plot showing the total number of events, how many events remain after each cut, and the total number of remaining events.

8.4 Energy Calibration & Resolution

Sometimes it is convenient to express the extracted fit parameters from the measured angular distributions in terms of the reconstructed centre-of-mass energy. This section details the calibration procedure and the resolution of centre-of-mass energies reconstructed in the eTPC. Please see appendix A.1 for further discussion on the details of the different definitions of energies used in this work.

In principle, the total reaction energy in the centre-of-mass can be reconstructed either by using both the individually reconstructed momenta of the ion and α tracks, or by using only the α track in combination with conservation laws. In this analysis, the second approach was adopted, as the ion track is often poorly reconstructed due to its shorter length. After converting track length to energy, these are converted to energy using `SRIM` energy-loss tables. Then, depending on the reaction mechanism, either ^{16}O or ^{12}C photo-dissociation, the α-particle momentum is boosted into the centre-of-mass frame using the mean effective γ-beam energy, and scaled by factors of approximately

16/12 or 12/8, respectively. For example, the reconstructed energies for each ^{16}O event are shown in figure 8.44.

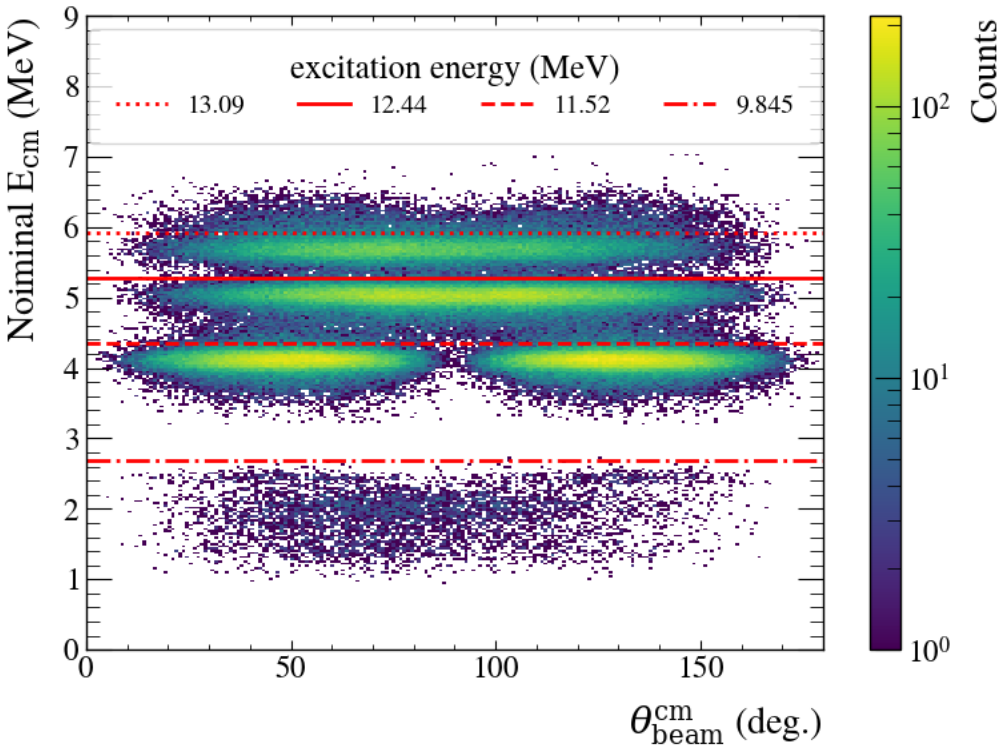

Figure 8.44: Nominal Centre-of-mass Energy vs. Scattering Angle: All ^{16}O events are plotted as uncalibrated energy vs. scattering angle. Four narrow states in ^{16}O are identified as red lines [54].

8.4.1 Calibration

The reconstructed energies, shown in figure 8.44, were consistently higher than the tabulated values. This is expected, as the track is lengthened due to diffusion. To a lesser extent, reconstruction bias also contributes. Consequently, a calibration is needed to reproduce the known energy scale. As the calibration concerns the energies from the α tracks, the same correction is expected to hold for both reaction channels.

Known excitations in ^{16}O, with values listed in table 8.20 (data from reference [54]), were used as reference points for a linear calibration. Experimental data from nominal beam energies of 13.1, 11.5, 12.45, 9.85, and 9.56 MeV were used. The narrow 2^+ state appears in both 9.85 and 9.56 MeV data sets, and was therefore fitted simultaneously.

E_x (MeV)	J^π	Γ (keV)
13.090(8)	1^-	130(5)
11.520(4)	2^+	71(3)
12.440(2)	1^-	91(6)
9.8445(5)	2^+	0.625(100)

Table 8.20: Excited States of ^{16}O: Narrow states In ^{16}O used for energy calibration are listed. The values were taken from reference [54].

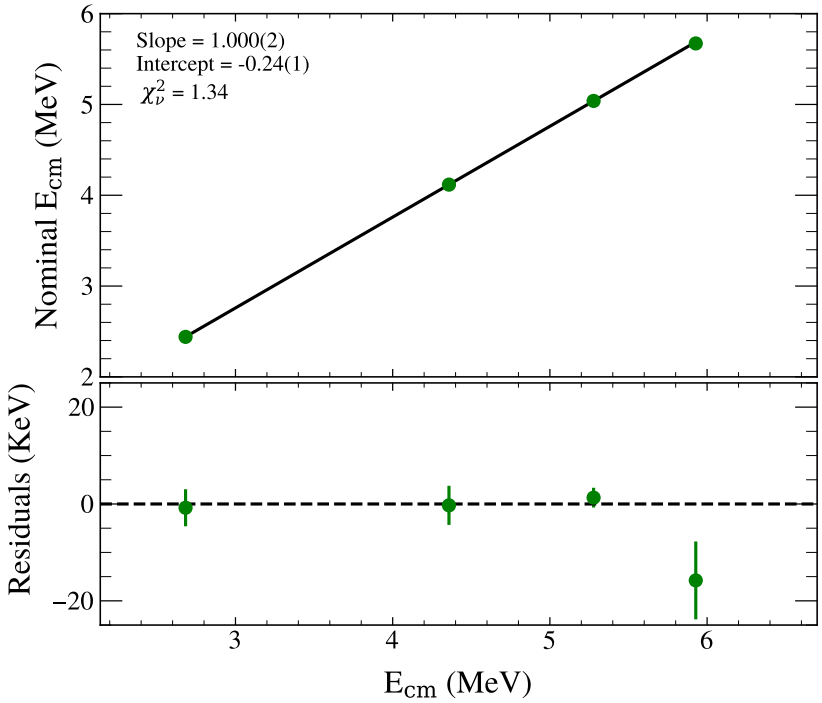

Figure 8.45: Centre-of-mass Energy Calibration: Known states in ^{16}O were used to calibrate nominal centre-of-mass energies energies to true energies centre-of-mass energies.

The fitted calibration and residuals are shown in figure 8.45. The slope is close to unity, with an intercept of ~ -240 keV, confirming a systematic overestimation of track length during reconstruction. The covariance matrix for the fit is

$$\mathrm{Cov}(m, c) = \begin{bmatrix} 5.535 \times 10^{-6} & -2.600 \times 10^{-5} \\ -2.600 \times 10^{-5} & 1.277 \times 10^{-4} \end{bmatrix},$$

where m and c denote the fitted gradient and intercept, respectively. The reconstructed ^{16}O data are shown again after calibration in figure 8.46. All fully calibrated spectra for

both ^{12}C and ^{16}O photo-dissociation reactions are shown in appendix F.

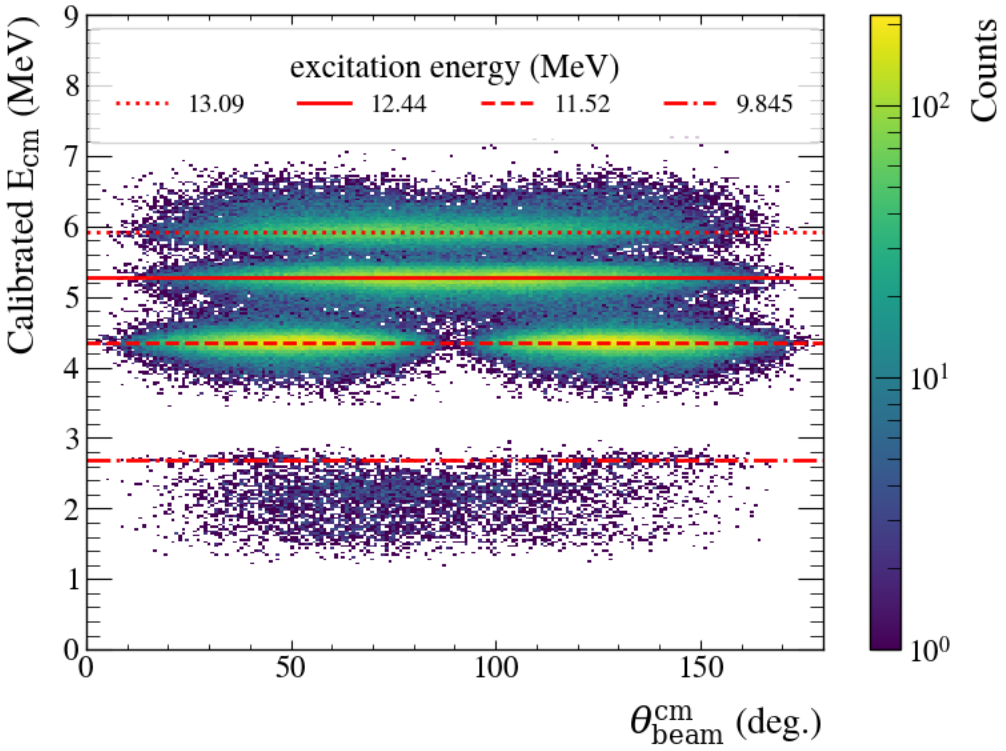

Figure 8.46: Calibrated Centre-of-mass Energy vs. Scattering Angle: All ^{16}O events are plotted as calibrated energy vs. scattering angle. Four narrow states in ^{16}O are identified as red lines [54].

8.4.2 Resolution

The post-calibration energy resolution was estimated using the narrow $J^{\pi}(2^{+})$ state in ^{16}O, which appears in both the $E_{\gamma} = 9.56$ and 9.85 MeV datasets. These were fitted simultaneously, including two additional Gaussian components to model the broad $J^{\pi}(1^{-})$ state at each energy. The resulting fit is shown in figure 8.47. From the fitted width of the $J^{\pi}(2^{+})$ state, the centre-of-mass energy resolution was determined to be $\sigma = 55(3)$ keV. This shows an improvement of approximately 15 keV compared with the hand-clicked analysis [186].

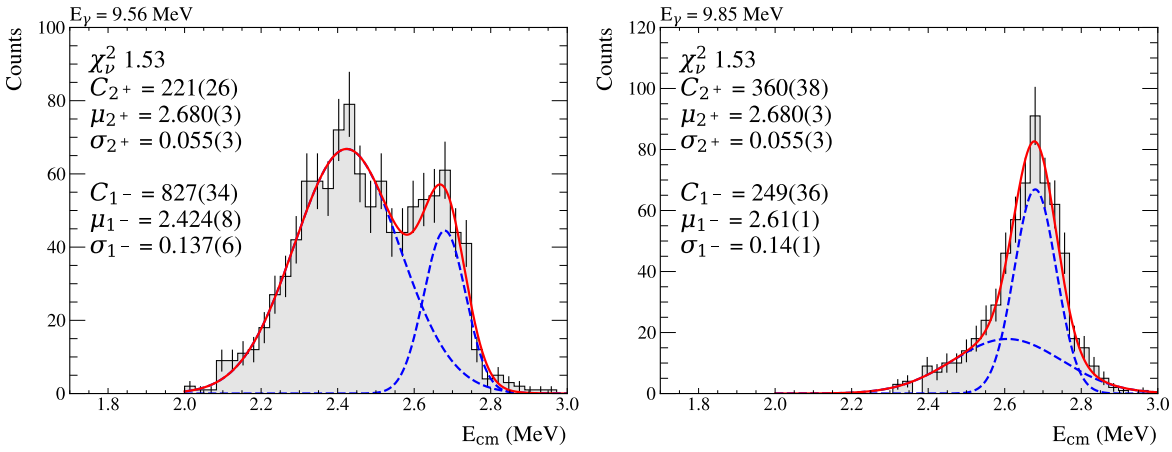

Figure 8.47: Centre-of-mass Energy Resolution: Plot shows Gaussian fits to the calibrated centre-of-mass energy spectrum, where the $J^\pi(2^+)$ centroid and width were common fit parameters across both $E_\gamma = 9.56$ and 9.85 MeV datasets. This was used to extract resolution from the observed width of the narrow $J^\pi(2^+)$ resonance.

8.5 Efficiency Correction

The last correction accounts for the angular bias introduced during data reduction. The data cuts that affect the total efficiency of each reaction channel are the ellipse cut, the Q-ratio cut, and the θ_{det} cut. To assess how these cuts bias the experimental data, they were applied to the simulated data to determine efficiency as a function of both $\cos\theta^{cm}_{\text{beam}}$ and ϕ^{cm}_{beam}. All efficiency curves shown in the following figures correspond to ^{16}O events.

The resulting efficiency distributions for $E_\gamma = 8.66$ MeV are shown in figure 8.48, the left panel showing the cosine of the scattering angle and the right panel the azimuthal angle. These were obtained by considering all events across the full beam width. These distributions were fitted with the following phenomenological models: A 13th-order polynomial for the cosine of the scattering angle, and a sum of Gaussians with a quadratic term for the azimuthal angle

$$\epsilon(\cos\theta^{cm}_{\text{beam}}) = \sum_{i=0}^{13} a_i(\cos\theta^{cm}_{\text{beam}})^i, \tag{8.5.0.1}$$

$$\epsilon(\phi^{cm}_{\text{beam}}) = a + b\phi^{cm}_{\text{beam}} + (\phi^{cm}_{\text{beam}})^2 c + \sum_{i=1}^{4} d_i \exp\left(-\frac{1}{2}\left(\frac{\phi^{cm}_{\text{beam}} - \mu_i}{\sigma_i}\right)^2\right). \tag{8.5.0.2}$$

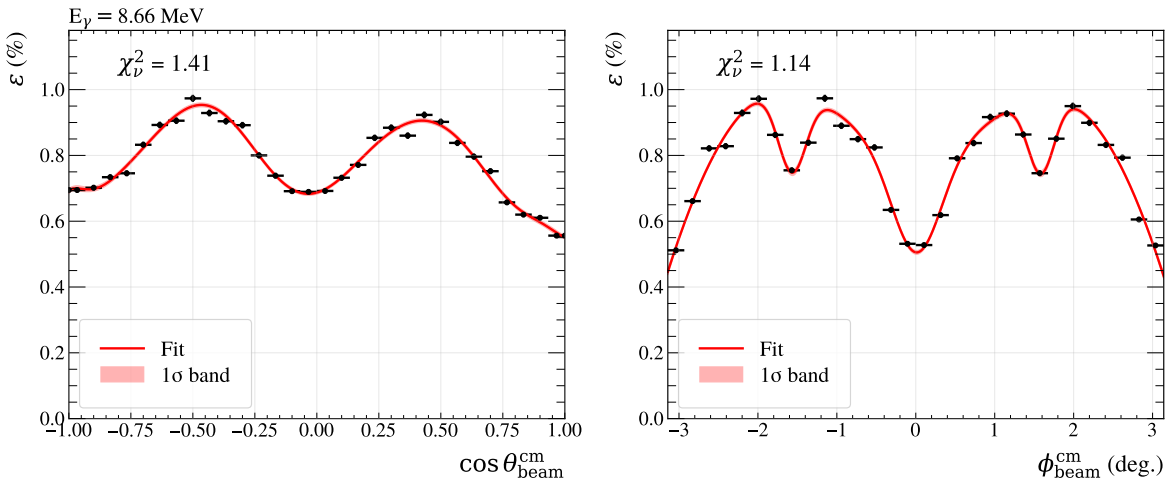

Figure 8.48: Angular Efficiency 1: Shows simulated ^{16}O centre-of-mass angular efficiency fits across the whole beam at E_γ=8.66 MeV. **Left:** Showing reconstructed $\cos\theta^{cm}_{\text{beam}}$ data after cuts (black) fitted with equation (8.5.0.1) (red) **Right:** Showing reconstructed ϕ^{cm}_{beam} data (black) fitted with equation (8.5.0.2) (red).

In some cases, when analysing $\cos\theta_{\text{beam}}$, it is favourable to split the measured angular distributions within a given beam energy into narrower energy slices. This allows for finer tracking of the energy dependence of the extracted fit parameters. It is therefore necessary to evaluate $\epsilon(\cos\theta_{\text{beam}})$ separately for each energy slice on a case-by-case basis. Figure 8.49 shows this efficiency for two such energy slices, where the higher-energy slice shows a generally higher efficiency, as there was less overlap with the other reaction channel.

It should be noted that uncertainties on the efficiency profile are not yet considered, only the central values are taken. In most cases, this is a reasonable approximation, as the uncertainty bands on the extracted fits are narrow. In future work, either a larger sample of events will be generated so that no fit is required, or a Monte Carlo procedure will be developed to extract results by varying the profile within its uncertainties.

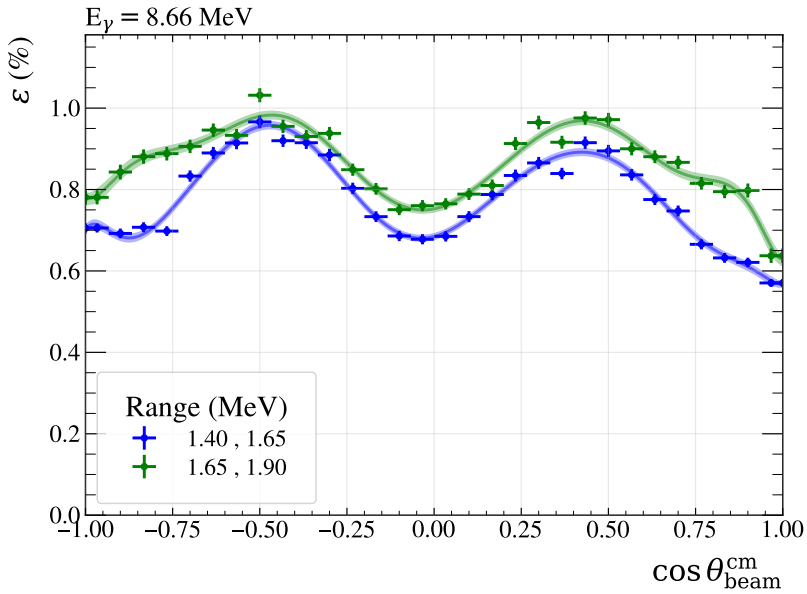

Figure 8.49: Angular Efficiency 2: Shows simulated ^{16}O centre-of-mass $\cos\theta_{\mathrm{beam}}$ angular efficiency fits using equation (8.5.0.1) for two energy slices, for E_γ=8.66 MeV.

8.6 Cross Section Normalisation

The total cross section is defined as, $\sigma = N/\mathcal{L}$, where N is the total number of events of interest and $\mathcal{L}$ is the integrated luminosity, defined as

$$\mathcal{L} = N_\gamma \, n \, x \, f_{LT}. \tag{8.6.0.1}$$

Here n is the number density of target nuclei per cubic centimetre, x is the active length of the eTPC, f_{LT} is the live-time fraction of eTPC, and N_γ is the total number of photons incident on the target. Where the latter is denied as

$$N_\gamma = I_\gamma \times t_{tpc}, \tag{8.6.0.2}$$

where I_γ is the intensity of the γ beam, and t_{tpc} is the associate eTPC measurement time.

8.6.1 General Details

Targets. The number density n is calculated from the measured gas temperature T and pressure P. First, the number of CO_2 molecules per cubic centimetre is obtained using Avagadro's constant (6.022×10^{23}), then n for each target is obtained trivially. The values for each beam energy are listed in table 8.21.

Active length. The active length considered is defined by the full capture cut from table 8.13. These lengths have been copied for convenience into table 8.21

Live-time. The live-time fraction f_{LT} accounts for the dead time of the detector. For the eTPC, the minimum time between successive events is $t_{dt} = 0.0029$ s per event. This was used to estimate the live time fraction as, $f_{LT} = 1 - (R\,t_{dt})$,, where R is the measured event rate, the live-time fractions are also given in table 8.21, for event rates calculated using values from table 6.1[5].

E_γ (MeV)	Temp. (K)	P (mbar)	Molecules / m^3	n ($^{16}O/m^3$)	n ($^{12}C/m^3$)	x (cm)	f_{LT}
8.51	24.7	130	3.16×10^{24}	6.33×10^{24}	3.16×10^{24}	25.3	0.999
8.66	24.9	130	3.16×10^{24}	6.32×10^{24}	3.16×10^{24}	24.7	0.998
8.86	24.7	130	3.16×10^{24}	6.33×10^{24}	3.16×10^{24}	23.8	0.997
9.16	24.1	130	3.17×10^{24}	6.34×10^{24}	3.17×10^{24}	22.4	0.996
9.36	24.0	130	3.17×10^{24}	6.34×10^{24}	3.17×10^{24}	21.4	0.988
9.56	24.0	130	3.17×10^{24}	6.34×10^{24}	3.17×10^{24}	20.4	0.988
9.85	22.2	130	3.19×10^{24}	6.38×10^{24}	3.19×10^{24}	18.9	0.969
11.1	22.9	190	4.65×10^{24}	9.30×10^{24}	4.65×10^{24}	18.3	0.978
11.5	22.9	190	4.65×10^{24}	9.30×10^{24}	4.65×10^{24}	16.6	0.938
11.9	24.6	190	4.62×10^{24}	9.25×10^{24}	4.62×10^{24}	14.7	0.968
12.3	24.6	190	4.62×10^{24}	9.25×10^{24}	4.62×10^{24}	12.8	0.852
13.1	24.6	250	6.08×10^{24}	1.22×10^{25}	6.08×10^{24}	14.4	0.886
13.5	24.6	250	6.08×10^{24}	1.22×10^{25}	6.08×10^{24}	12.5	0.867

Table 8.21: Summary Table of Normalisation Parameter: The table presents a summary of parameters that are used to calculate integrated luminosity: The temperature, and pressure in the eTPC, the number of targets per unit volume, the active eTPC length, and the live-time fraction are listed.

[5]This approximation was found to be reasonable in the limit of the low rates observed, as compared to the full non-paralysable model.

8.6.2 Luminosity

First, N_γ is calculated using beam intensity values from tables 8.2 and 8.7, and timing information from table 6.1, which are given again in table 8.22. The resulting luminosities, calculated using equation (8.6.0.1), are presented in table 8.23.

E_γ (MeV)	Run time (s)	I_γ (γ/s)	N_γ
8.51	1.17×10^5	$3.7(3)\ ^{+0.0}_{-0.0}\times10^8$	$4.4(3)\ ^{+0.0}_{-0.0}\times10^{13}$
8.66	3.25×10^5	$3.3(2)\ ^{+0.0}_{-0.0}\times10^8$	$1.05(8)\ ^{+0.0}_{-0.0}\times10^{14}$
8.86	1.81×10^5	$3.2(2)\ ^{+0.0}_{-0.0}\times10^8$	$5.8(4)\ ^{+0.0}_{-0.0}\times10^{13}$
9.16	4.65×10^4	$3.8(3)\ ^{+0.0}_{-0.0}\times10^8$	$1.8(1)\ ^{+0.0}_{-0.0}\times10^{13}$
9.36	1.48×10^4	$3.9(3)\ ^{+0.0}_{-0.0}\times10^8$	$5.8(4)\ ^{+0.0}_{-0.0}\times10^{12}$
9.56	8.22×10^3	$4.0(3)\ ^{+0.0}_{-0.0}\times10^8$	$3.3(2)\ ^{+0.0}_{-0.0}\times10^{12}$
9.85	3.49×10^3	$4.2(3)\ ^{+0.0}_{-0.0}\times10^8$	$1.5(1)\ ^{+0.0}_{-0.0}\times10^{12}$
11.1	2.12×10^4	$4.0(3)\ ^{+0.6}_{-0.4}\times10^8$	$8.5(6)\ ^{+1.4}_{-0.9}\times10^{12}$
11.5	1.17×10^4	$4.1(3)\ ^{+0.6}_{-0.4}\times10^8$	$4.8(3)\ ^{+0.7}_{-0.5}\times10^{12}$
11.9	1.54×10^4	$4.2(3)\ ^{+0.6}_{-0.4}\times10^8$	$6.5(5)\ ^{+0.9}_{-0.6}\times10^{12}$
12.3	5.07×10^3	$3.1(2)\ ^{+0.3}_{-0.2}\times10^8$	$1.6(1)\ ^{+0.1}_{-0.1}\times10^{12}$
13.1	7.42×10^3	$4.0(3)\ ^{+0.3}_{-0.3}\times10^7$	$3.0(2)\ ^{+0.2}_{-0.2}\times10^{11}$
13.5	1.27×10^4	$1.7(1)\ ^{+0.1}_{-0.1}\times10^8$	$2.2(1)\ ^{+0.2}_{-0.2}\times10^{12}$

Table 8.22: Intensity Values for the eTPC: N_γ calculated using beam intensity values from tables 8.2 and 8.7. Both statistical and asymmetric systematic errors are listed.

E_γ (MeV)	$\mathcal{L}_{O16}$ (cm^{-2})	$\mathcal{L}_{C12}$ (cm^{-2})
8.51	$7.0(5)\ ^{+0.0}_{-0.0} \times 10^{33}$	$3.5(3)\ ^{+0.0}_{-0.0} \times 10^{33}$
8.66	$1.6(1)\ ^{+0.0}_{-0.0} \times 10^{34}$	$8.2(6)\ ^{+0.0}_{-0.0} \times 10^{33}$
8.86	$8.7(6)\ ^{+0.0}_{-0.0} \times 10^{33}$	$4.3(3)\ ^{+0.0}_{-0.0} \times 10^{33}$
9.16	$2.5(2)\ ^{+0.0}_{-0.0} \times 10^{33}$	$1.26(9)\ ^{+0.0}_{-0.0} \times 10^{33}$
9.36	$7.8(6)\ ^{+0.0}_{-0.0} \times 10^{32}$	$3.9(3)\ ^{+0.0}_{-0.0} \times 10^{32}$
9.56	$4.2(3)\ ^{+0.0}_{-0.0} \times 10^{32}$	$2.1(2)\ ^{+0.0}_{-0.0} \times 10^{32}$
9.85	$1.7(1)\ ^{+0.0}_{-0.0} \times 10^{32}$	$8.6(6)\ ^{+0.0}_{-0.0} \times 10^{31}$
11.1	$1.4(1)\ ^{+0.2}_{-0.2} \times 10^{33}$	$7.1(5)\ ^{+1.1}_{-0.7} \times 10^{32}$
11.5	$6.9(5)\ ^{+1.0}_{-0.7} \times 10^{32}$	$3.4(2)\ ^{+0.5}_{-0.3} \times 10^{32}$
11.9	$8.6(6)\ ^{+1.1}_{-0.8} \times 10^{32}$	$4.3(3)\ ^{+0.6}_{-0.4} \times 10^{32}$
12.3	$1.6(1)\ ^{+0.1}_{-0.1} \times 10^{32}$	$7.8(5)\ ^{+0.7}_{-0.6} \times 10^{31}$
13.1	$4.6(3)\ ^{+0.3}_{-0.3} \times 10^{31}$	$2.3(2)\ ^{+0.2}_{-0.2} \times 10^{31}$
13.5	$2.8(2)\ ^{+0.2}_{-0.2} \times 10^{32}$	$1.42(9)\ ^{+0.1}_{-0.1} \times 10^{32}$

Table 8.23: Luminosity Values for the eTPC: Integrated luminosity, $\mathcal{L}$, values are calculated using values listed in tables 8.22 and 8.21, for both ^{12}C and ^{16}O photo-dissociation reaction channels. Both statistical and asymmetric systematic errors are listed.

8.7 Cross Sections of ^{16}O Photo-dissociation

To analyse these data, each nominal beam energy was evaluated independently due to the differing efficiency corrections. However, to better track the extracted cross sections, energy slices were taken in the eTPC reconstructed energy spectra. The bin size considered was motivated by several factors. To allow sufficient statistics to extract meaningful fit parameters from the partial wave decomposition. Also, only the central 2σ of the beam profile was considered, this is to avoid potential systematic errors in the beam profile at the extremes, which will affect distributing the luminosity across the eTPC data when calculating angle-integrated cross sections.

8.7.1 Angular Distributions

The data are fitted with the $E1 - E2$ mixing partial-wave decomposition, as derived in section 1.4.5. Using an unbinned negative log likelihood fitting procedure, further details are given in appendix A.3, and should be read before continuing.

The polar-angle distribution is given again here

$$\begin{aligned} W(\theta) = \sigma_{E1} W_{E1}(\cos\vartheta) + \sigma_{E2} W_{E2}(\cos\vartheta) \\ + \sqrt{\sigma_{E1}\sigma_{E2}}\cos\phi_{12}\, W_{12}(\cos\vartheta). \end{aligned} \tag{8.7.1.1}$$

This formula consists of three individual angular distributions: a pure $E1$ contribution W_{E1}, a pure $E2$ contribution W_{E2}, and the interference term W_{12}. These are defined in terms of Legendre polynomials $P_l(\cos\theta)$.

The energy ranges used for each fit and the extracted parameters are given in table 8.24. A selection of the fitted angular distribution are shown in figure 8.50, with all distributions given in appendix I. For visualisation, the efficiency curves have been applied to the data, and the fit function has been scaled to match the experimental counts. The extracted energy averaged fit parameters are shown in figure 8.51, where they are compared with the theoretical expectation values obtained as outlined in appendix A.4.

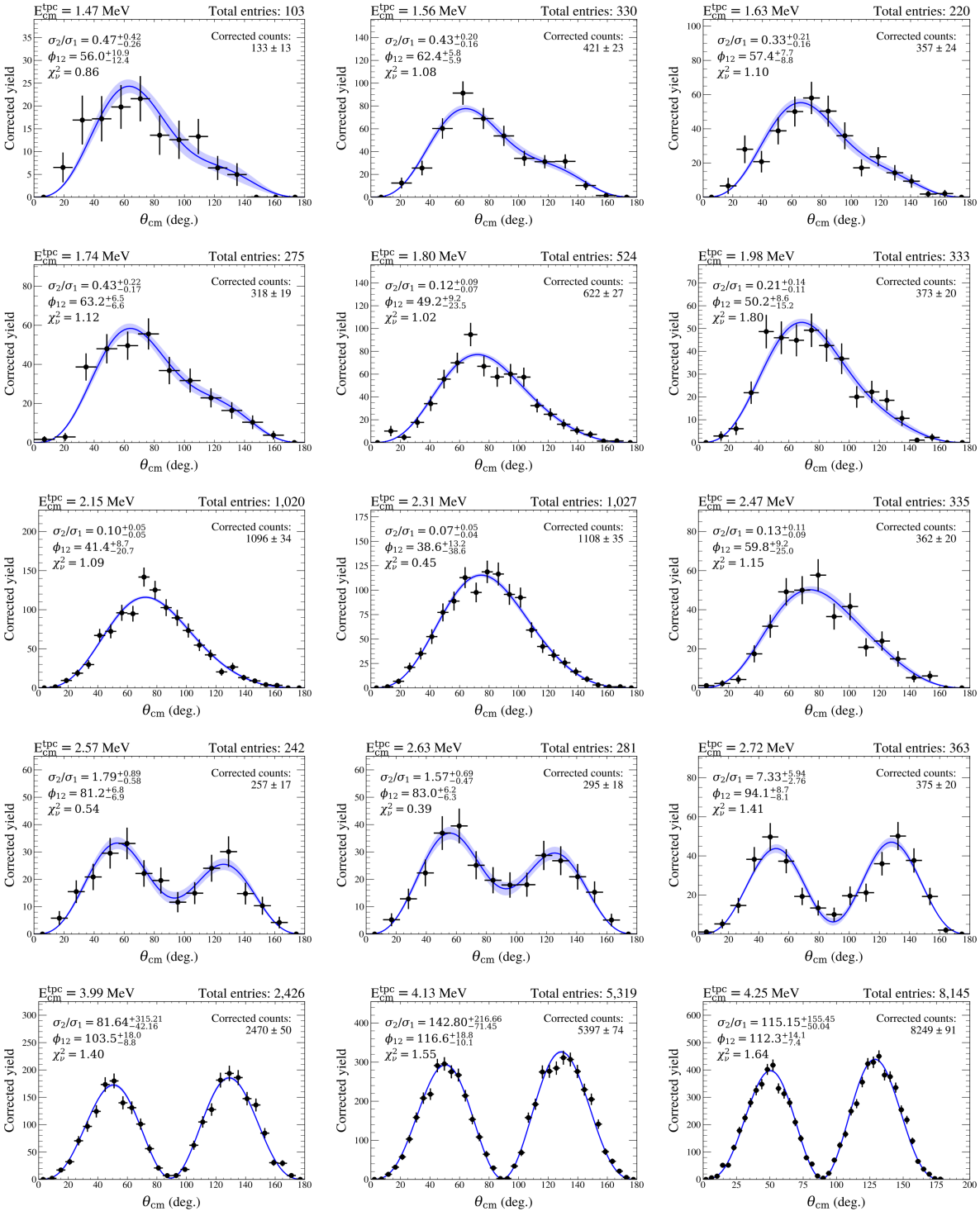

Figure 8.50: Angular Distributions of the $^{16}O(\gamma,\alpha_0)$ Reaction: Partial-wave decomposition of the reconstructed centre-of-mass polar angle. Each panel shows the fitted angular distribution, using equation (8.7.1.1). The blue band indicates the uncertainty obtained from the covariance matrix of the fit. The fit parameters, ϕ_{12} and σ_2/σ_1, and the corresponding energy of each angular distribution are provided.

$E_{\mathrm{cm}}^{\mathrm{tpc}}$ (MeV)	E_γ (MeV)	fit range (MeV)	$\langle\phi_{12}\rangle$ (deg.)	$\langle\sigma_{E2}/\sigma_{E1}\rangle$	counts	corr. counts	$\langle\sigma_{\gamma\alpha_0}\rangle$ (nb)
1.465(6)	8.51	1.25 , 1.65	$56.0\ ^{+10.9}_{-12.4}$	$0.466\ ^{+0.416}_{-0.265}$	103	133±13	27±3
1.559(3)	8.66	1.40 , 1.65	$62.4\ ^{+5.8}_{-5.9}$	$0.430\ ^{+0.205}_{-0.160}$	330	421±23	48±5
1.632(4)	8.86	1.40 , 1.70	$57.4\ ^{+7.7}_{-8.8}$	$0.328\ ^{+0.210}_{-0.157}$	220	357±24	100±10
1.739(4)	8.66	1.65 , 1.90	$63.2\ ^{+6.5}_{-6.6}$	$0.434\ ^{+0.220}_{-0.166}$	275	318±19	97±10
1.805(3)	8.86	1.70 , 1.90	$49.2\ ^{+9.2}_{-23.5}$	$0.121\ ^{+0.085}_{-0.072}$	524	622±27	184±16
1.979(3)	8.86	1.90 , 2.10	$50.2\ ^{+8.6}_{-15.2}$	$0.207\ ^{+0.136}_{-0.107}$	333	374±20	335±33
2.152(2)	9.16	2.00 , 2.30	$41.4\ ^{+8.7}_{-20.7}$	$0.103\ ^{+0.053}_{-0.047}$	1020	1096±34	980±80
2.312(2)	9.36	2.15 , 2.50	$38.6\ ^{+13.2}_{-38.6}$	$0.066\ ^{+0.051}_{-0.036}$	1027	1108±35	2568±198
2.468(3)	9.56	2.40 , 2.55	$59.8\ ^{+9.2}_{-25.0}$	$0.126\ ^{+0.115}_{-0.091}$	335	363±20	2892±266
2.575(4)	9.85	2.40 , 2.65	$81.2\ ^{+6.8}_{-6.9}$	$1.794\ ^{+0.885}_{-0.581}$	242	257±17	4059±387
2.630(4)	9.56	2.55 , 2.70	$83.0\ ^{+6.3}_{-6.3}$	$1.574\ ^{+0.689}_{-0.474}$	281	295±18	4044±380
2.719(3)	9.85	2.65 , 2.90	$94.1\ ^{+8.7}_{-8.1}$	$7.326\ ^{+5.942}_{-2.758}$	363	375±20	5217±464
3.990(1)	11.1	3.91 , 4.05	$103.5\ ^{+18.0}_{-8.8}$	$81.639\ ^{+315.212}_{-42.159}$	2426	2470±50	6687±1014
4.129(1)	11.1	4.05 , 4.19	$116.6\ ^{+18.8}_{-10.2}$	$142.802\ ^{+216.662}_{-71.448}$	5319	5397±74	17943±2634
4.2451(8)	11.1	4.19 , 4.29	$112.3\ ^{+14.1}_{-7.4}$	$115.155\ ^{+155.451}_{-50.042}$	8145	8249±91	68827±10190
4.2703(5)	11.5	4.21 , 4.31	$115.9\ ^{+11.1}_{-6.3}$	$153.456\ ^{+137.692}_{-55.317}$	19751	19964±142	185526±26725
4.3403(9)	11.9	4.26 , 4.40	$113.3\ ^{+26.3}_{-9.8}$	$203.249\ ^{+605.935}_{-108.236}$	6942	7044±85	198994±28112
4.3598(4)	11.5	4.31 , 4.41	$115.1\ ^{+9.7}_{-6.0}$	$236.466\ ^{+189.985}_{-84.727}$	36324	36808±193	296614±42621
4.4496(5)	11.5	4.41 , 4.51	$96.6\ ^{+4.6}_{-4.0}$	$132.656\ ^{+86.371}_{-42.806}$	18846	19043±139	159671±21983
4.4587(9)	11.9	4.40 , 4.54	$103.2\ ^{+5.5}_{-4.6}$	$48.593\ ^{+27.432}_{-14.740}$	5992	6065±78	70811±9710
4.547(1)	11.5	4.51 , 4.61	$95.5\ ^{+6.1}_{-5.4}$	$49.1512\ ^{+33.862}_{-16.409}$	4034	4118±65	46734±6602
4.605(1)	11.9	4.54 , 4.68	$93.5\ ^{+2.9}_{-2.9}$	$7.577\ ^{+1.753}_{-1.306}$	2852	2927±55	18384±2498
4.750(2)	11.9	4.68 , 4.82	$92.7\ ^{+2.1}_{-2.1}$	$1.374\ ^{+0.185}_{-0.163}$	2351	2445±50	11380±1498
4.893(1)	11.9	4.82 , 4.96	$91.9\ ^{+2.0}_{-2.0}$	$0.336\ ^{+0.054}_{-0.049}$	2903	3034±56	15600±2085
5.035(1)	11.9	4.96 , 5.10	$93.5\ ^{+5.2}_{-3.9}$	$0.031\ ^{+0.024}_{-0.022}$	4315	4535±69	41525±5533
5.2675(3)	12.3	5.10 , 5.40	$93.9\ ^{+8.9}_{-2.6}$	$0.004\ ^{+0.006}_{-0.004}$	67980	71302±274	903132±97314
5.557(2)	13.1	5.40 , 5.65	$80.1\ ^{+5.6}_{-9.7}$	$0.060\ ^{+0.049}_{-0.044}$	1239	1315±37	337104±36124
5.710(2)	13.1	5.65 , 5.75	$61.9\ ^{+4.1}_{-5.3}$	$0.118\ ^{+0.041}_{-0.038}$	2024	2113±47	549218±54348
5.808(1)	13.1	5.75 , 5.85	$55.8\ ^{+3.9}_{-5.3}$	$0.082\ ^{+0.023}_{-0.021}$	5848	6113±80	1047683±97495
5.857(1)	13.5	5.80 , 5.90	$55.1\ ^{+4.5}_{-6.7}$	$0.071\ ^{+0.022}_{-0.021}$	5661	5933±79	1093764±119454
5.9005(9)	13.1	5.85 , 5.95	$48.6\ ^{+5.4}_{-9.0}$	$0.051\ ^{+0.016}_{-0.015}$	9880	10362±104	1383474±134370
5.9501(9)	13.5	5.90 , 6.00	$63.1\ ^{+2.4}_{-2.8}$	$0.102\ ^{+0.020}_{-0.019}$	8192	8584±95	810910±84618
5.994(1)	13.1	5.95 , 6.05	$53.2\ ^{+7.8}_{-18.7}$	$0.031\ ^{+0.018}_{-0.017}$	7316	7692±90	938542±89085
6.046(1)	13.5	6.00 , 6.10	$72.3\ ^{+2.4}_{-2.7}$	$0.103\ ^{+0.024}_{-0.023}$	5881	6189±81	340060±32953
6.090(2)	13.1	6.05 , 6.15	$72.2\ ^{+3.3}_{-3.9}$	$0.115\ ^{+0.037}_{-0.034}$	2579	2734±54	372187±37406
6.147(1)	13.5	6.10 , 6.20	$78.2\ ^{+1.9}_{-2.0}$	$0.279\ ^{+0.043}_{-0.040}$	3591	3778±63	130157±12343
6.290(1)	13.5	6.20 , 6.40	$82.7\ ^{+1.5}_{-1.5}$	$0.614\ ^{+0.063}_{-0.058}$	4449	4629±70	52355 ±4876

Table 8.24: Cross sections of the ^{16}O(γ,α_0) Reaction: Extracted fit parameters and integrated cross sections from analysing the ^{16}O(γ,α_0) distributions. For each distribution, the reconstructed energy as measured in the eTPC, the nominal beam energy the distribution belongs to, and the fit range considered are listed. As well as the extracted energy-averaged fit parameters, where the errors represent 1σ errors obtained from the contour plots using the method in appendix A.3 to account for parameter correlation. The total counts, efficiency-corrected counts, and energy-averaged angle-integrated cross sections are also given; the error on the latter has both the statistical and systematic error contributions from the luminosity added in quadrature.

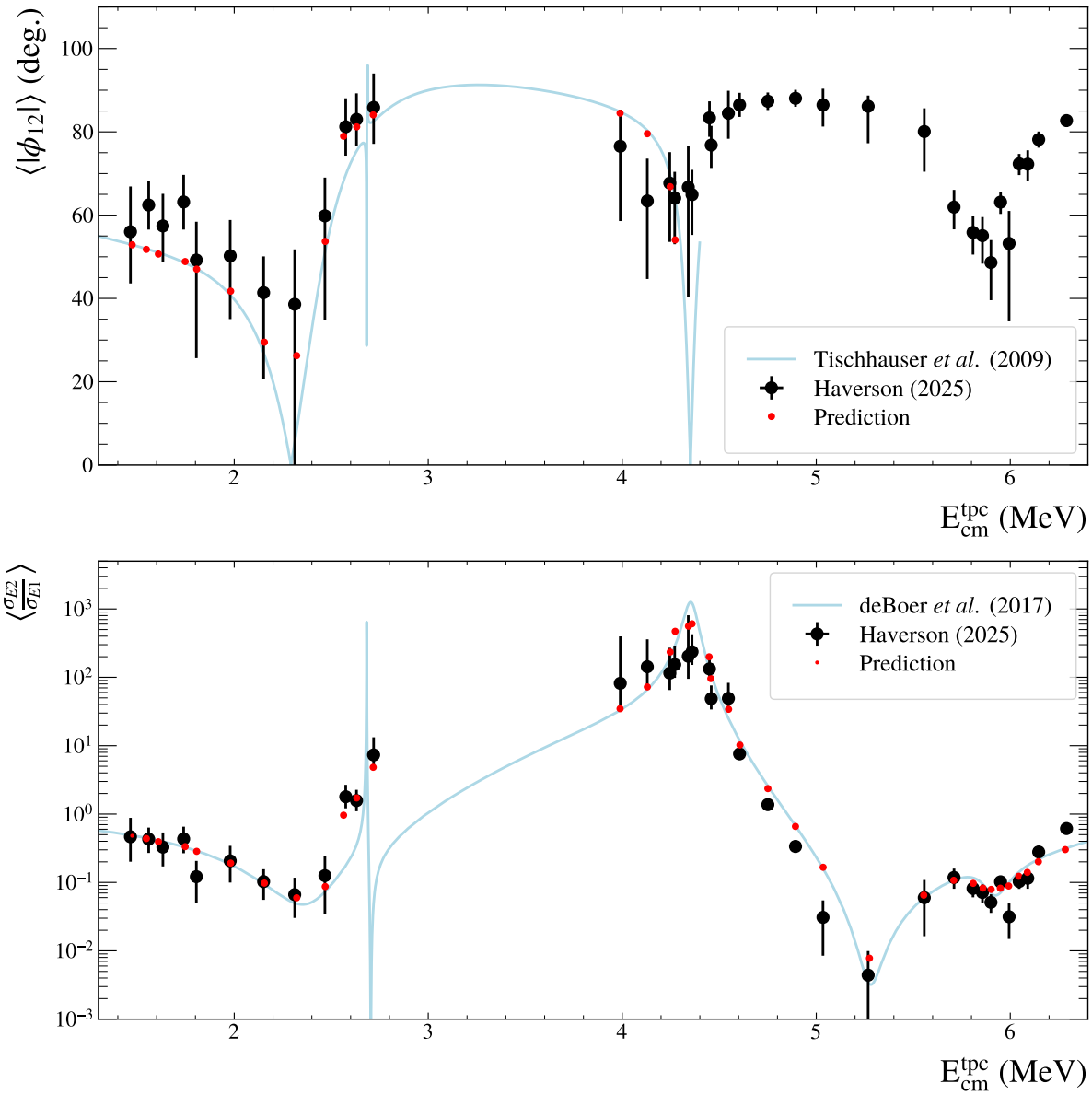

Figure 8.51: Energy-Averaged ^{16}O(γ,α_0) Fit Parameters: In both figures, the black points are the extracted fit parameters from the angular distribution analysis, plotted at the eTPC reconstructed energy, while the red points are the theoretical expectation values (appendix A.4). **Top:** This panel shows the mixing angle ϕ_{12} normalised between $0-90°$, compared with the expected values obtained using equation (1.6.1.1) and the scattering data from reference [79]. This comparison is only valid below the ~ 4.4 MeV threshold as decays will start to proceed through the first excited state in ^{12}C. **Bottom:** This panel shows the extracted ratio of cross sections, compared with the R-matrix analysis of reference [46].

Uncertainties. The 1σ statistical uncertainties on the extracted fit parameters are determined from contour plots, as detailed in appendix A.3, where the fit parameters σ_2/σ_1 and ϕ_{12} are varied simultaneously whilst tracking the log-likelihood for a change of $\frac{2.3}{2}$ (as two parameters are varied) from the minimum. This method yields the contour plots, as shown in figure 8.52 for the lowest energy $E_\gamma = 8.51$ MeV, and in figure 8.53 for $E_\gamma = 9.36$ MeV, which measures over the broad $J^\pi(1^-)$ region. The maximum and minimum values in both directions and their differences from the minimum are calculated to determine the asymmetric errors; thus, the uncertainties extracted using this approach include parameter correlations.

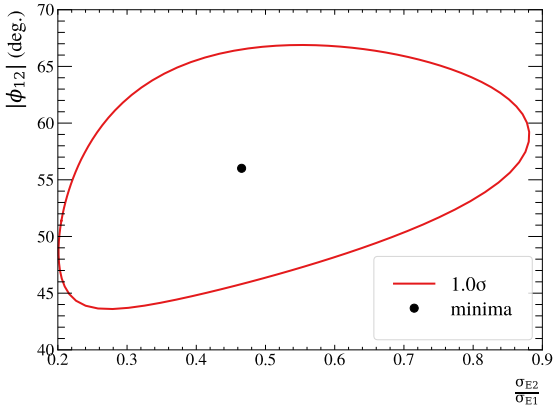

Figure 8.52: Partial-wave Decomposition Contour: The red line shows the contour tracking the 1σ errors of the fit to the $^{16}\mathrm{O}(\gamma,\alpha)$ data at $E_\gamma = 8.51$ MeV.

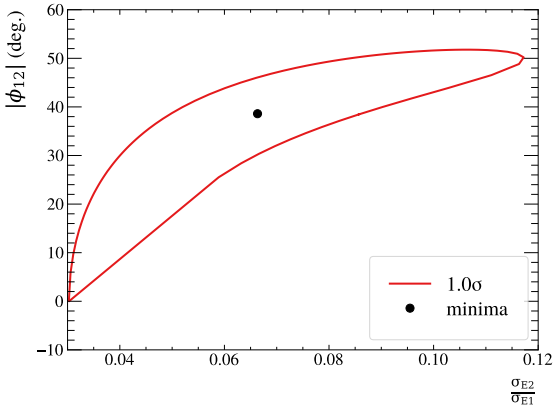

Figure 8.53: Partial-wave Decomposition Contour: The red line shows the contour tracking the 1σ errors of the fit to the $^{16}\mathrm{O}(\gamma,\alpha)$ data at $E_\gamma = 9.36$ MeV.

Unfolding. For a direct comparison with other datasets in the low-energy region, in the vicinity of the broad $J^\pi(1^-)$ state where there has been historical disagreement, theoretical expectation values are used to obtain correction factors through a deconvolution procedure detailed in appendix A.4. These correction factors are listed in table 8.25 and shown in figures 8.54 and 8.55 respectively.

$E_{\mathrm{cm}}^{\mathrm{eff}}$ (MeV)	E_γ (MeV)	Fit range (MeV)	f_{cor}^{ϕ}	ϕ_{12} (deg.)	f_{cor}^{σ}	σ_{E2}/σ_{E1}
1.465(6)	8.51	1.25 , 1.65	1.0002 ± 0.0001	$56.024\ ^{+12.413}_{-10.879}$	1.0138 ± 0.0008	$0.472\ ^{+0.268}_{-0.421}$
1.559(3)	8.66	1.40 , 1.65	1.0027 ± 0.0003	$62.598\ ^{+5.913}_{-5.828}$	1.0213 ± 0.0018	$0.439\ ^{+0.163}_{-0.209}$
1.632(4)	8.86	1.40 , 1.70	1.0069 ± 0.0008	$57.797\ ^{+8.816}_{-7.772}$	1.0434 ± 0.0044	$0.343\ ^{+0.164}_{-0.219}$
1.739(4)	8.66	1.65 , 1.90	0.9930 ± 0.0008	$62.726\ ^{+6.587}_{-6.467}$	0.9789 ± 0.0033	$0.425\ ^{+0.163}_{-0.216}$
1.805(3)	8.86	1.70 , 1.90	1.0019 ± 0.0004	$49.298\ ^{+23.589}_{-9.230}$	1.0171 ± 0.0019	$0.123\ ^{+0.073}_{-0.087}$
1.979(3)	8.86	1.90 , 2.10	0.9759 ± 0.0022	$49.007\ ^{+14.811}_{-8.412}$	0.9519 ± 0.0057	$0.197\ ^{+0.102}_{-0.130}$
2.152(2)	9.16	2.00 , 2.30	0.8992 ± 0.0028	$37.209\ ^{+18.649}_{-7.834}$	0.9635 ± 0.0013	$0.099\ ^{+0.045}_{-0.051}$
2.312(2)	9.36	2.15 , 2.50	0.3167 ± 0.0087	$12.225\ ^{+12.230}_{-4.188}$	0.8209 ± 0.0022	$0.054\ ^{+0.030}_{-0.042}$
2.468(3)	9.56	2.40 , 2.55	0.9574 ± 0.0104	$57.277\ ^{+23.919}_{-8.818}$	0.8467 ± 0.0271	$0.106\ ^{+0.077}_{-0.097}$
2.575(4)	9.85	2.40 , 2.65	0.8648 ± 0.0027	$70.249\ ^{+6.009}_{-5.914}$	0.1643 ± 0.0068	$0.295\ ^{+0.096}_{-0.146}$
2.630(4)	9.56	2.55 , 2.70	0.9289 ± 0.0009	$77.105\ ^{+5.832}_{-5.803}$	0.2080 ± 0.0038	$0.327\ ^{+0.099}_{-0.143}$
2.719(3)	9.85	2.65 , 2.90	0.9813 ± 0.0009	$92.367\ ^{+7.996}_{-8.580}$	0.0081 ± 0.0022	$0.059\ ^{+0.028}_{-0.051}$

Table 8.25: Unfolded $^{16}\mathbf{O}(\gamma,\alpha_0)$ Fit Parameters: The energy-averaged angular distribution fit parameters, from table 8.24, are deconvolved using the deconvolution factors obtained by the procedure explained in appendix A.4. Both the factors and deconvolved values are given in this table.

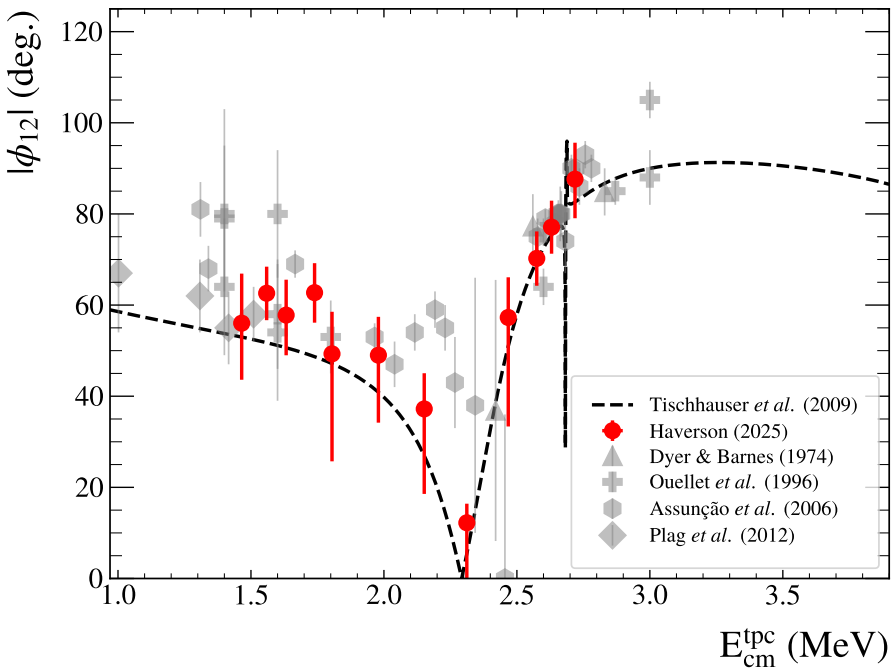

Figure 8.54: Unfolded ϕ_{12} from the $^{16}\mathbf{O}(\gamma,\alpha_0)$ Decomposition: The unfolded and normalised mixing angles from table 8.25 are shown, and compared with other datasets where ϕ_{12} is kept as a fit parameter [40, 41, 60, 65]. Also shown is the underlying prediction from reference [79].

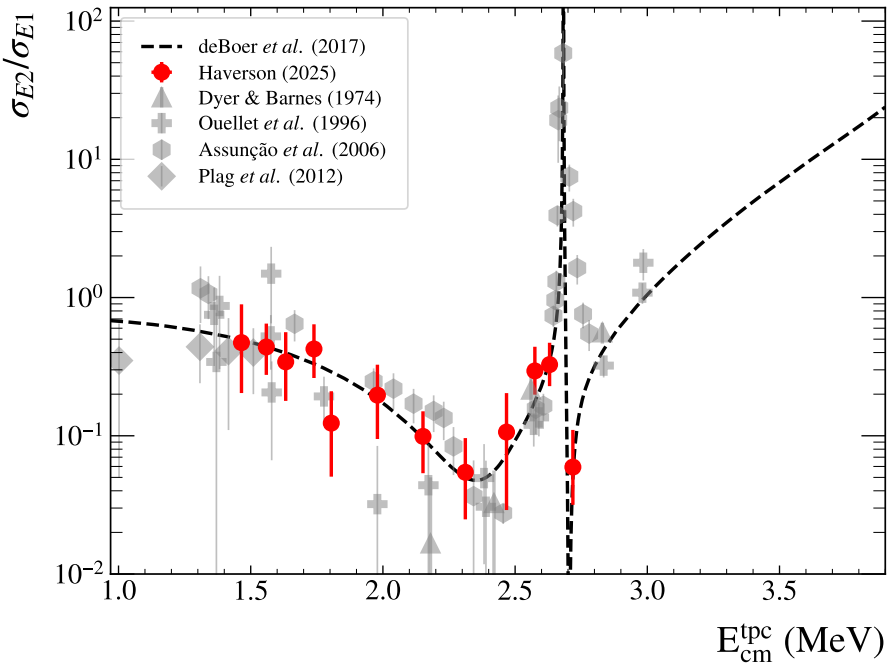

Figure 8.55: Unfolded σ_2/σ_1 from the ^{16}O(γ,α_0) Decomposition: The unfolded ratio of cross sections from table 8.25 are shown, and compared with other datasets where ϕ_{12} is kept as a fit parameter [40, 41, 60, 65]. Also shown is the underlying prediction from reference [46].

8.7.2 Angle-integrated Cross Section

The angle-integrated cross section was also evaluated for all energies. The reader is directed to appendix A.2 for a full discussion on cross section reconstruction. In brief, the total counts, $N_{^{16}\mathrm{O}}$, were obtained from the efficiency corrected angular distributions using

$$N_{^{16}\mathrm{O}} = \int_{-1}^{1} \frac{S(\cos\theta_{\mathrm{beam}})}{\epsilon(\cos\theta_{\mathrm{beam}})}\, d\cos\theta_{\mathrm{beam}}, \tag{8.7.2.1}$$

where $S(\cos\theta_{\mathrm{beam}})$ is the eTPC distribution in a given energy slice, and $\epsilon(\cos\theta_{\mathrm{beam}})$ is the corresponding efficiency curve.

The energy-averaged cross section is then obtained using

$$\langle\sigma_{\gamma\alpha}\rangle = \frac{N_{^{16}\mathrm{O}}}{\int_a^b \left[\int_{-\infty}^{\infty} \mathcal{L}\, G(E')\, \mathcal{G}(E-E')\, dE'\right] dE}, \tag{8.7.2.2}$$

where $G(E)$ is the beam profile, using parameters as listed in table 8.8, $\mathcal{G}(E)$ represents the Gaussian eTPC resolution, and the $\mathcal{L}$ is integrated luminosity, values are given in table 8.23.

The uncertainty in the cross section was determined using a Monte Carlo procedure that varied the beam profile, eTPC resolution, integrated luminosity, and energy slice within their respective statistical uncertainties. The leading contributor to the uncertainty is the uncertainty on the beam intensity. The energy-averaged cross sections are listed in table 8.24 and shown in figure 8.56 compared with energy-averaged theory.

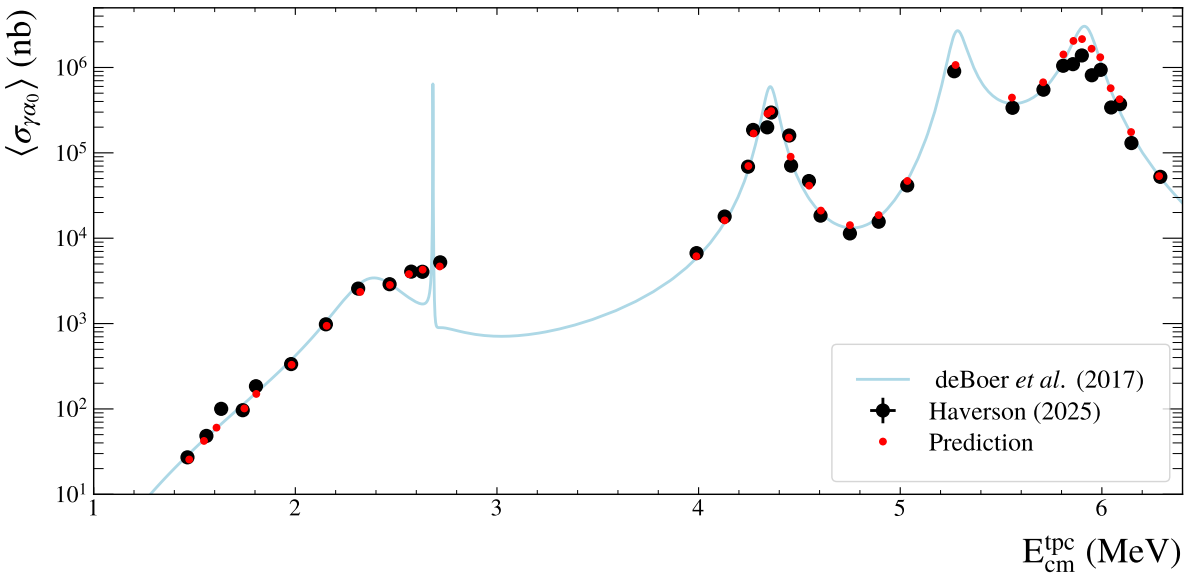

Figure 8.56: Energy-averaged angle-integrated cross sections for the $^{16}\mathbf{O}(\gamma,\alpha_0)$ reaction: The energy-averaged cross sections from table 8.24 are shown, and compared to the R-matrix fit of reference [46] (blue line) after applying detector response (red points).

Unfolding. In order to compare directly with other datasets, an unfolding procedure was used, as detailed in appendix A.2. The procedure was only used in the low-energy region where the angle-integrated cross section is well known. Then, the unfolded photodissociation cross sections were converted to the forward capture cross sections using the detailed balance factor, as calculated using equation (1.6.1.5). All values are listed in table 8.26, and the unfolded cross sections for the capture reaction are shown in figure 8.57.

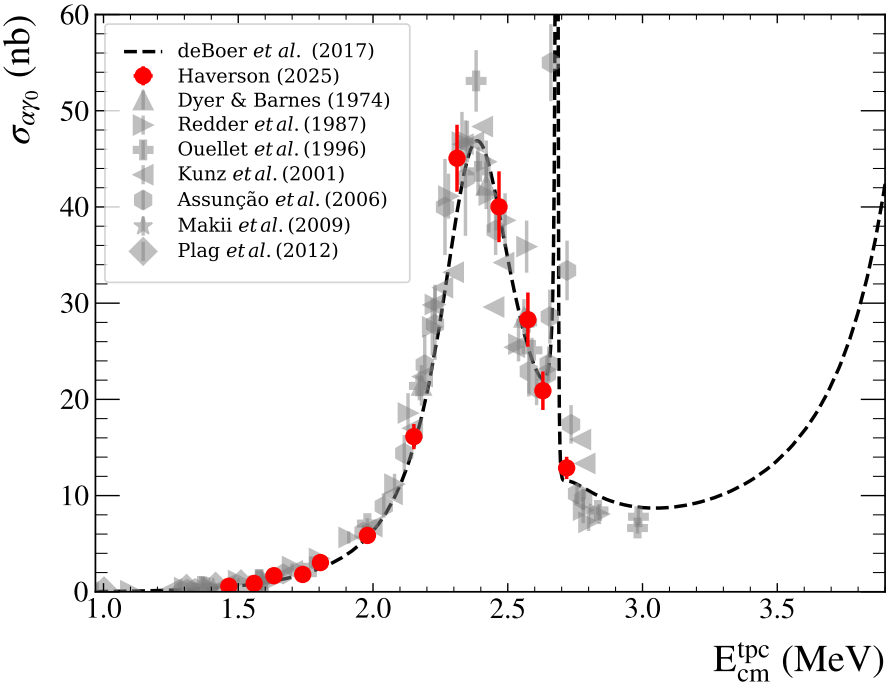

Figure 8.57: Unfolded $^{12}C(\alpha,\gamma_0)$ Cross Section: The unfolded cross section from table 8.26 are shown against other datasets of the same reaction [40, 41, 58–61, 65].

E_{cm}^{tpc} (MeV)	E_γ (MeV)	fit range (MeV)	$\langle\sigma_{\gamma\alpha_0}\rangle$ (nb)	f_{cor}	$\sigma_{\gamma\alpha_0}$ (nb)	f_{db}	$\sigma_{\alpha\gamma_0}$ (nb)
1.465(6)	1.25 , 1.65	8.51	27(3)	1.168(2)	32(4)	55.0(2)	0.58(7)
1.559(3)	1.40 , 1.65	8.66	48(5)	1.033(4)	50(5)	57.25(7)	0.87(8)
1.632(4)	1.40 , 1.70	8.86	100(10)	0.98(1)	99(10)	58.95(9)	1.7(2)
1.739(4)	1.65 , 1.90	8.66	97(10)	1.15(1)	111(11)	61.31(8)	1.8(2)
1.805(3)	1.70 , 1.90	8.86	185(16)	1.033(2)	191(16)	62.69(5)	3.0(3)
1.979(3)	1.90 , 2.10	8.86	335(33)	1.16(2)	388(38)	66.15(6)	5.9(6)
2.152(2)	2.00 , 2.30	9.16	980(80)	1.140(3)	1117(91)	69.28(3)	16(1)
2.312(2)	2.15 , 2.50	9.36	2568(198)	1.262(4)	3242(250)	71.94(3)	45(4)
2.468(3)	2.40 , 2.55	9.56	2892(266)	1.028(4)	2974(274)	74.32(5)	40(4)
2.575(4)	2.40 , 2.65	9.85	4059(387)	0.53(2)	2146(214)	75.85(6)	28(3)
2.630(4)	2.55 , 2.70	9.56	4044(380)	0.396(7)	1601(154)	76.61(5)	21(2)
2.719(3)	2.65 , 2.90	9.85	5218(464)	0.192(3)	1001(90)	77.78(4)	13(1)

Table 8.26: Angle-Integrated Cross Sections of the $^{12}C(\alpha,\gamma_0)$ Reaction: The table lists the low energy total cross sections $\sigma_{\gamma\alpha_0}$, the deconvolution factors, the deconvolved $\sigma_{\gamma\alpha_0}$ cross sections, the detailed balance factor, and the inverse $\sigma_{\alpha\gamma_0}$ cross sections.

8.8 Cross Sections of ^{12}C Photo-dissociation

To analyse these data, each nominal beam energy was considered independently. However, they were not split into finer bins using the eTPC reconstructed energy. Instead, all events were analysed at the same time, and the extracted parameters were evaluated at the effective beam energy as measured by the HPGe. This approach has two advantages: it removes complex energy-averaging effects because the luminosity is no longer distributed across the beam profile (as detailed in appendix A.2), and it also allows for easier comparison with the previously measured photo-dissociation dataset [139].

8.8.1 Angular Distributions

As before, the data were fitted with the $E1$–$E2$ mixing partial-wave decomposition, as derived in section 1.4.5, using an unbinned negative log likelihood fitting procedure. Further details are given in appendix A.3.

For convenience, the polar-angle distribution is given again here

$$\begin{aligned} W(\theta) = \sigma_{E1} W_{E1}(\cos\vartheta) + \sigma_{E2} W_{E2}(\cos\vartheta) \\ + \sqrt{\sigma_{E1}\sigma_{E2}}\cos\phi_{12}\, W_{12}(\cos\vartheta). \end{aligned} \tag{8.8.1.1}$$

This formula consists of three individual angular distributions: a pure $E1$ contribution W_{E1}, a pure $E2$ contribution W_{E2}, and the interference term W_{12}. These are defined in terms of Legendre polynomials $P_l(\cos\theta)$.

The extracted energy-averaged fit parameters and total counts are given in table 8.27, and the angular distributions are shown in figure 8.58. The statistical errors on the fit parameters were extracted in the same way as the ^{16}O analysis, by using the contour plots.

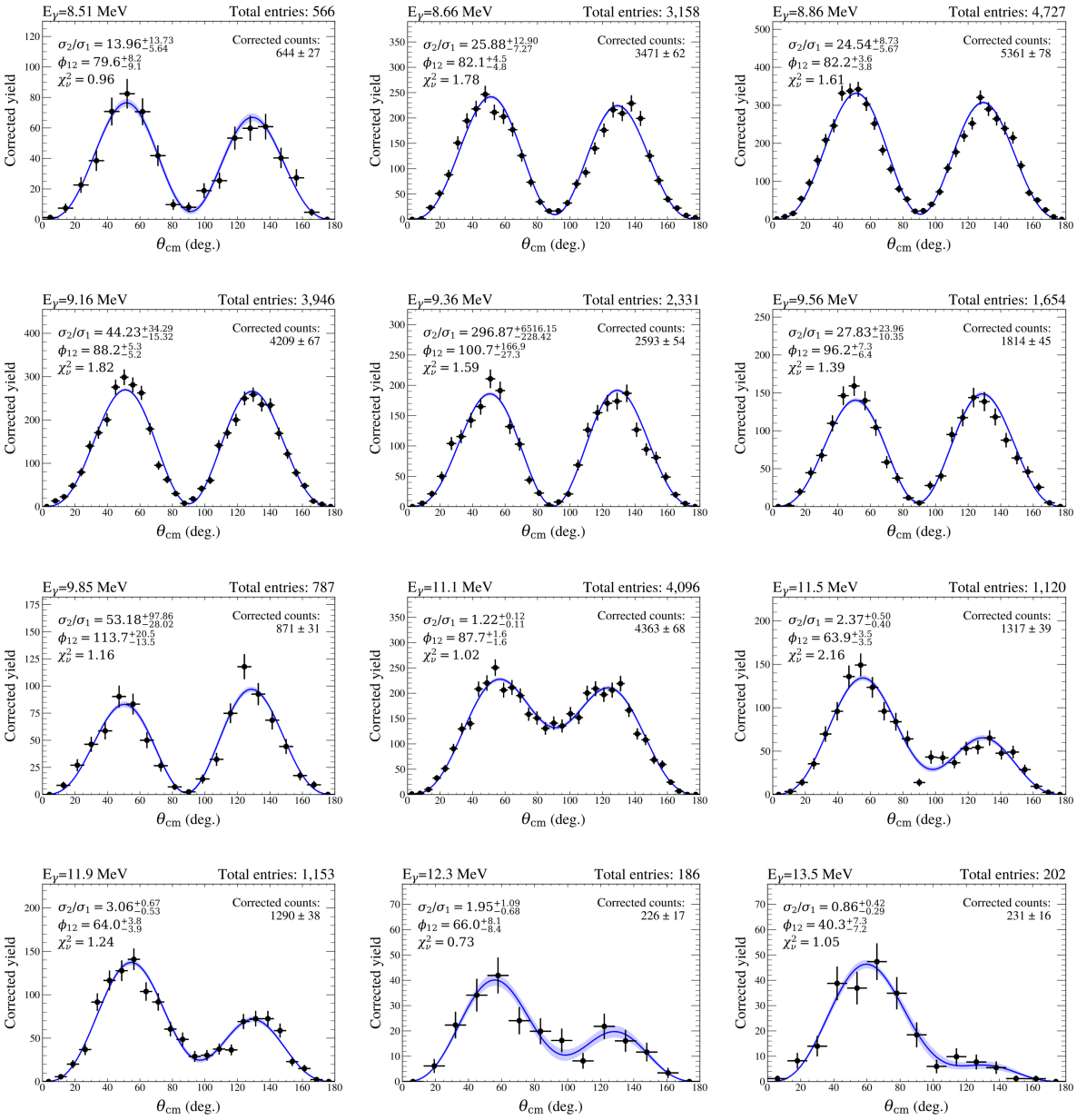

Figure 8.58: Angular Distributions of the $^{12}C(\gamma, \alpha_0)$ Reaction: Partial-wave decomposition of the reconstructed centre-of-mass polar angle. Each panel shows the fitted angular distribution, using equation (8.8.1.1). The blue band indicates the uncertainty obtained from the covariance matrix of the fit. The fit parameters, ϕ_{12} and σ_2/σ_1, and the corresponding energy of each angular distribution are provided.

E_γ (MeV)	$\langle\phi_{12}\rangle$ (deg.)	$\langle\sigma_{E2}/\sigma_{E1}\rangle$	Counts	Corrected counts
8.51	$79.6^{+8.2}_{-9.1}$	$13.96^{+13.73}_{-5.64}$	566	644±27
8.66	$82.1^{+4.5}_{-4.8}$	$25.88^{+12.90}_{-7.27}$	3158	3471±62
8.86	$82.2^{+3.6}_{-3.8}$	$24.5^{+8.73}_{-5.67}$	4727	5361±78
9.12	$88.2^{+5.3}_{-5.2}$	$44.23^{+34.29}_{-15.32}$	3946	4209±67
9.36	$100.7^{+166.9}_{-27.3}$	$296.87^{+6516.15}_{-228.42}$	2331	2593±54
9.56	$96.2^{+7.3}_{-6.4}$	$27.83^{+23.96}_{-10.35}$	1654	1814±45
9.85	$113.7^{+20.5}_{-13.5}$	$53.18^{+97.86}_{-28.02}$	787	871±31
11.1	$87.7^{+1.6}_{-1.6}$	$1.22^{+0.12}_{-0.11}$	4096	4363±68
11.5	$63.9^{+3.5}_{-3.5}$	$2.37^{+0.50}_{-0.40}$	1120	1317±39
11.9	$64.0^{+3.8}_{-3.9}$	$3.06^{+0.67}_{-0.53}$	1153	1290±38
12.3	$66.0^{+8.1}_{-8.4}$	$1.95^{+1.09}_{-0.68}$	186	226±17
13.5	$40.3^{+7.3}_{-7.2}$	$0.86^{+0.42}_{-0.29}$	202	231±16

Table 8.27: Partial-wave Decomposition of the ^{12}C(γ,α_0) Reaction: Extracted fit parameters from analysing the ^{12}C(γ,α_0) distributions. For each distribution, the nominal beam energy and the extracted energy-averaged fit parameters are listed. The errors on the fit parameters represent 1σ errors obtained from the contour plots, using the method in appendix A.4, accounting for parameter correlation. The total counts and efficiency-corrected counts are also given.

8.8.2 Angle-integrated Cross Section

The angle-integrated cross sections were calculated as $\sigma = N_{^{12}\mathrm{C}}/\mathcal{L}$, where $N_{^{12}\mathrm{C}}$ represents the total counts and $\mathcal{L}$ is the integrated luminosity. The total counts were obtained from the efficiency-corrected angular distributions using

$$N_{^{12}\mathrm{C}} = \int_{-1}^{1} \frac{S(\cos\theta_{\mathrm{beam}})}{\epsilon(\cos\theta_{\mathrm{beam}})}\, d\cos\theta_{\mathrm{beam}}, \tag{8.8.2.1}$$

where $S(\cos\theta_{\mathrm{beam}})$ is the eTPC distribution across the full width of the beam and $\epsilon(\cos\theta_{\mathrm{beam}})$ is the corresponding efficiency curve. The integrated luminosities were taken from table 8.23. The results are given in table 8.28, with the quoted uncertainties being statistical, and calculated using the same Monte Carlo procedure as the ^{16}O data. The decomposed cross sections are listed in the same table.

E_γ (MeV)	$\langle\sigma_{\gamma\alpha_0}\rangle$ (μb)	$\langle\sigma^{E1}_{\gamma\alpha_0}\rangle$ (μb)	$\langle\sigma^{E2}_{\gamma\alpha_0}\rangle$ (μb)	low frac. (%)	up frac. (%)
8.51	0.185 ± 0.016	$0.012\ ^{+0.011}_{-0.005}$	$0.172\ ^{+0.018}_{-0.015}$	0.0	0.0
8.66	0.422 ± 0.032	$0.016\ ^{+0.008}_{-0.004}$	$0.407\ ^{+0.031}_{-0.031}$	0.0	0.0
8.86	1.239 ± 0.093	$0.049\ ^{+0.017}_{-0.011}$	$1.191\ ^{+0.091}_{-0.090}$	0.0	0.0
9.12	3.564 ± 0.263	$0.079\ ^{+0.060}_{-0.027}$	$3.485\ ^{+0.264}_{-0.258}$	0.0	0.0
9.36	6.642 ± 0.510	$0.022\ ^{+0.488}_{-0.017}$	$6.620\ ^{+0.704}_{-0.508}$	0.0	0.0
9.56	8.681 ± 0.659	$0.301\ ^{+0.251}_{-0.110}$	$8.380\ ^{+0.683}_{-0.645}$	0.0	0.0
9.85	10.183 ± 0.805	$0.188\ ^{+0.340}_{-0.098}$	$9.995\ ^{+0.860}_{-0.796}$	0.0	0.0
11.1	6.180 ± 0.424	$2.783\ ^{+0.245}_{-0.237}$	$3.397\ ^{+0.279}_{-0.272}$	10.3	16.1
11.5	3.827 ± 0.279	$1.135\ ^{+0.189}_{-0.159}$	$2.692\ ^{+0.260}_{-0.239}$	9.7	15.0
11.9	3.014 ± 0.220	$0.742\ ^{+0.134}_{-0.111}$	$2.272\ ^{+0.206}_{-0.192}$	9.4	13.2
12.3	2.899 ± 0.285	$0.983\ ^{+0.376}_{-0.245}$	$1.916\ ^{+0.409}_{-0.293}$	7.7	9.0
13.5	1.628 ± 0.155	$0.875\ ^{+0.213}_{-0.162}$	$0.753\ ^{+0.209}_{-0.156}$	6.7	6.8

Table 8.28: Angle-Integrated Cross Section of the ^{12}C(γ,α_0) Reaction: The table lists the total angle-integrated, $E1$ and $E2$ cross sections. The error on the cross section has only the statistical contributions from the luminosity propagated; the systematic contributions are listed as fractional errors.

The cross sections and extracted fit parameters are shown in figure 8.59, plotted at the effective beam energy from table 8.8. The top-left panel shows ϕ_{12}, the top-right shows σ_{E2}/σ_{E1}, the bottom-left shows the angle-integrated cross section, and the bottom-right shows the decomposed $E1$ and $E2$ cross sections.

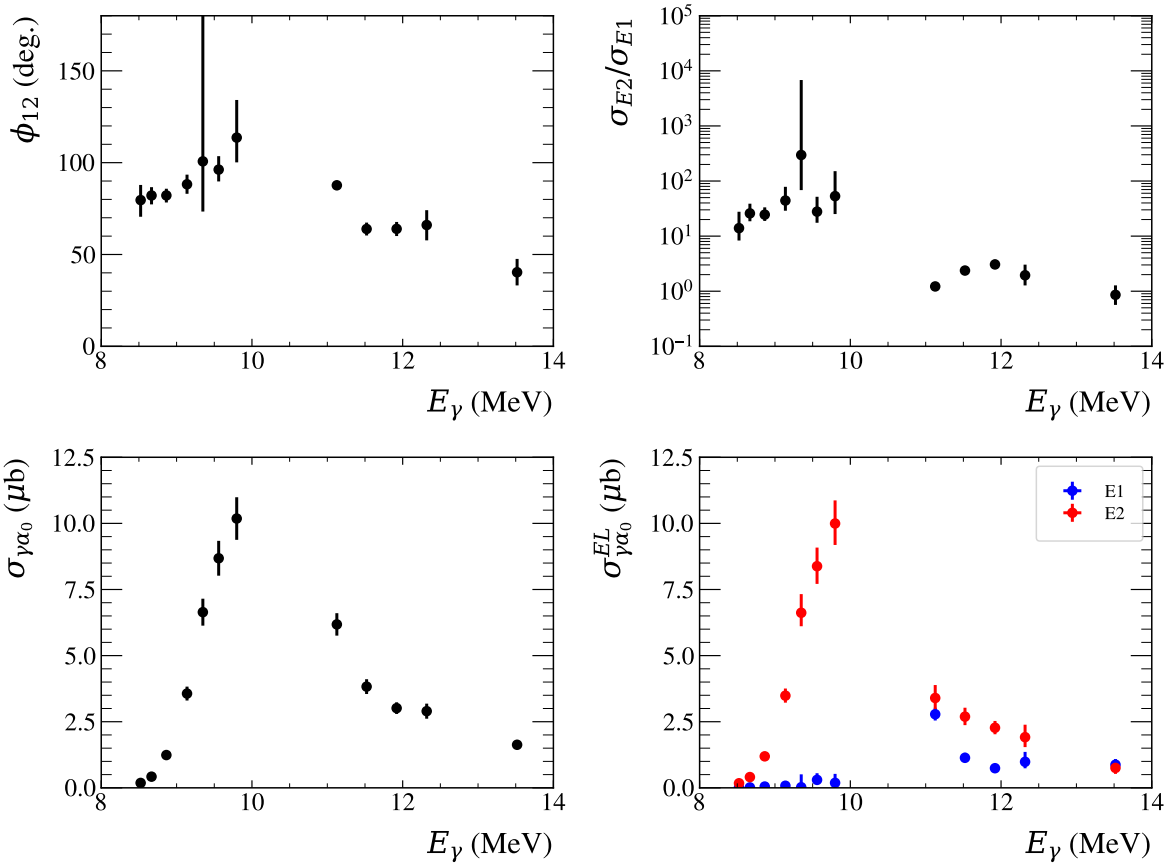

Figure 8.59: Energy-Averaged Cross Sections of the ^{12}C(γ,α) Reaction. Top-left: Shows the extracted $E1-E2$ mixing phase angle ϕ_{12}. **Top-right:** Shows the extracted ratio of cross sections, σ_2/σ_1. **Bottom-left:** Shows the calculated total cross section. **Bottom-right:** Shows the decomposed total cross section into $E1$ and $E2$ components. All plots show statistical errors only.

8.8.3 R-matrix Fitting

To extract resonance information from the cross sections in table 8.27, the R-matrix formalism is used. This is discussed in section 1.4.4 in terms of radiative capture, by applying the detailed balance factor, the following single-level formalism is obtained for the (γ,α_0) reactions decaying into nuclei of $J^\pi(0^+)$

$$\sigma(E) = \frac{\pi}{k_\gamma^2}\frac{2J_{C^*}+1}{2}\frac{\Gamma_{\lambda\alpha}\Gamma_{\lambda\gamma}}{(E-E_\lambda-\Delta_\lambda(E))^2+\Gamma_\lambda^2/4}. \tag{8.8.3.1}$$

To supplement those data, the values from the thesis of Zimmerman [140] are fitted simultaneously. However, each dataset requires specific treatment due to differences in

experimental conditions and analysis methods.

Treatment of the Zimmerman Dataset

Before fitting, a correction to Zimmerman's efficiency values is required. Zimmerman applied efficiency corrections to his total cross sections using a single scaling factor at each beam energy. This factor was used to correct for the loss of events due to his β angle fiducial cut in the OTPC. He would simulate data using the extracted fit function, place the β cut, and evaluate the total fraction of events lost.

Upon re-examination of this procedure, it was found that the solid angle term was omitted during the Monte Carlo sampling. Figure 8.60 demonstrates this issue by comparing three sets of efficiency values. The original single value reported by Zimmerman (black square), values recalculated using the suspected method without the solid angle term (blue circles), and values recalculated using the correct method, including the solid angle term (orange points). Good agreement with Zimmerman's value is obtained when the solid angle term is omitted, confirming the suspected omission [6].

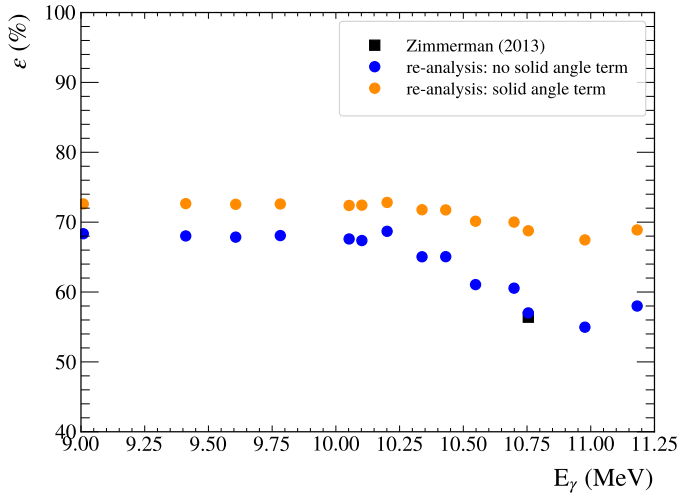

Figure 8.60: Zimmerman Efficiency Calculations: The black square shows the singular OTPC efficiency value given in reference [140]. The blue circles show the efficiency values recalculated in this analysis using the suspected incorrect method, omitting the solid angle term. The orange points show the correct method, which includes the solid angle term.

[6] To recalculate these a $10 < \beta < 55$ cut, and a θ resolution of $5°$ was used

To correct for this, the Zimmerman data are scaled by the ratio ϵ_b/ϵ_k during fitting, where ϵ_b is Zimmerman's recalculated efficiency correction and ϵ_k is the correct efficiency correction. Additionally, a common scale factor (nuisance parameter) f_b is introduced as a fit parameter, allowing all of Zimmerman's data points to vary by the same multiplicative factor. This accounts for systematic beam intensity uncertainty in the measurement. The normalisation of the present work is considered more reliable due to its agreement with the well-established low-energy ^{12}C(α,γ_0)^{16}O cross section.

The experimental resolution for the Zimmerman dataset is modelled using a Gaussian with beam energy spread of $\sigma = 190$ keV.

Treatment of the Present Dataset

For the data presented in this thesis, the experimental response function varies with beam energy. At each energy point, the intrinsic lineshape is convolved with a different skewed Gaussian function, with parameters given in table 8.8.

An additional systematic uncertainty arises from the high-energy normalisation procedure above and including $E_\gamma = 11.1$ MeV. This uncertainty is accounted for by introducing scale factors, f_k^n, which act as nuisance parameters applied to each datapoint of energy n. During fitting, each f_k^n is constrained to vary within the fractional uncertainties listed in table 8.28, centred at unity.

Fitting Procedure for the 2_2^+ State

The $J_n^\pi(2_2^+)$ resonance was fitted using single-level R-matrix formalism, as defined in equation (8.8.3.1), by minimising χ^2 using the `Minuit` package. The resonance is characterised by three *formal* parameters: the resonance energy E_λ, the radiative width $\Gamma_{\lambda\gamma}$, and the α-particle width $\Gamma_{\lambda\alpha}$. The boundary condition was set to zero.

The sensitivity to the channel radius ($a_c = r_0(A_1^{1/3} + A_2^{1/3})$) was found by performing fits while varying r_0 over a range of values and examining the χ^2 score. Figure 8.61 shows this variation, from which the central value and its 1σ errors were determined to be $r_0 = 2.37^{+0.08}_{-0.05}$ fm.

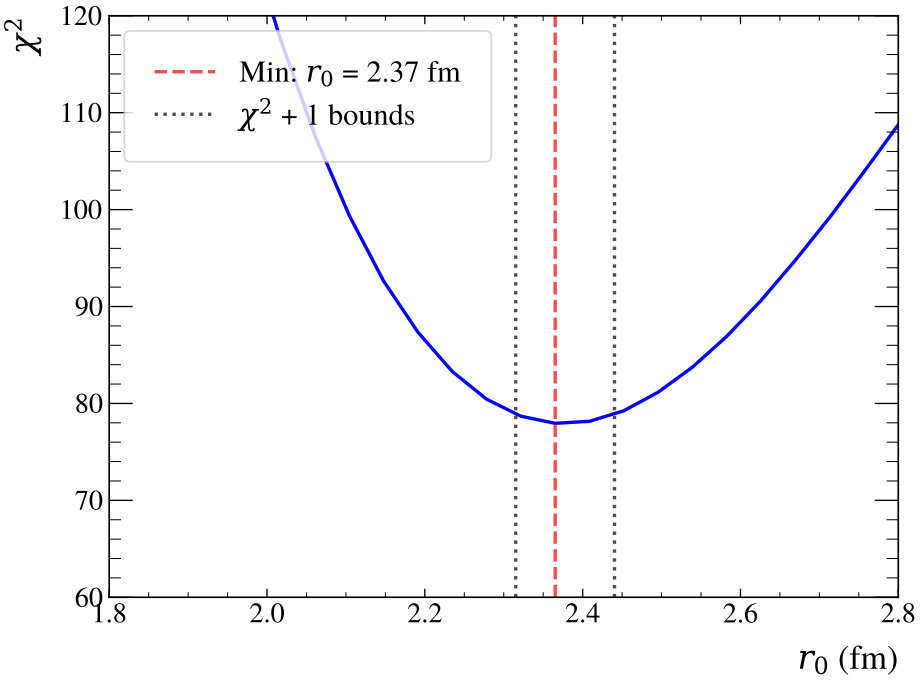

Figure 8.61: Channel Radius Sensitivity Scan for $J^\pi_n(2^+_2)$ State: The dependence of the goodness-of-fit metric, χ^2, on the channel radius is shown by scanning over r_0 values, when fitting the $J^\pi_n(2^+_2)$ resonance.

With r_0 fixed at 2.37 fm, the final fit yields the nuisance parameters: $f_k^{11.1} = 1.16$, $f_k^{11.5} = 1.15$, $f_k^{11.9} = 1.13$, $f_k^{12.3} = 1.09$, $f_k^{13.5} = 1.07$, and $f_b = 1.40$. The *formal* fit parameters are given in table 8.29. The goodness-of-fit score $\chi^2_\nu = 3.4$ was obtained by considering only the model parameters (not the nuisance parameters) when calculating the degrees of freedom.

J^π_n	E_λ (MeV)	$\Gamma_{\lambda\alpha}$ (MeV)	$\Gamma_{\lambda\gamma}$ (MeV)	χ^2_ν
2^+_2	9.76(2)	1.16(4)	$112(4)\times10^{-9}$	3.4
$r_0 = 2.37, B = 0$				

Table 8.29: Formal R-matrix Parameters the ^{12}C $J^\pi_n(2^+_2)$ State:. The *formal* resonance parameters extracted from the fit. Uncertainties in brackets are statistical, obtained from the fit covariance matrix.

Figure 8.62 presents the fitted results. The left panel shows Zimmerman's data (orange), whilst the right panel shows the present data (black). In both panels, the

solid blue line shows the intrinsic R-matrix lineshape, and the blue points represent the intrinsic lineshape after applying experimental effects.

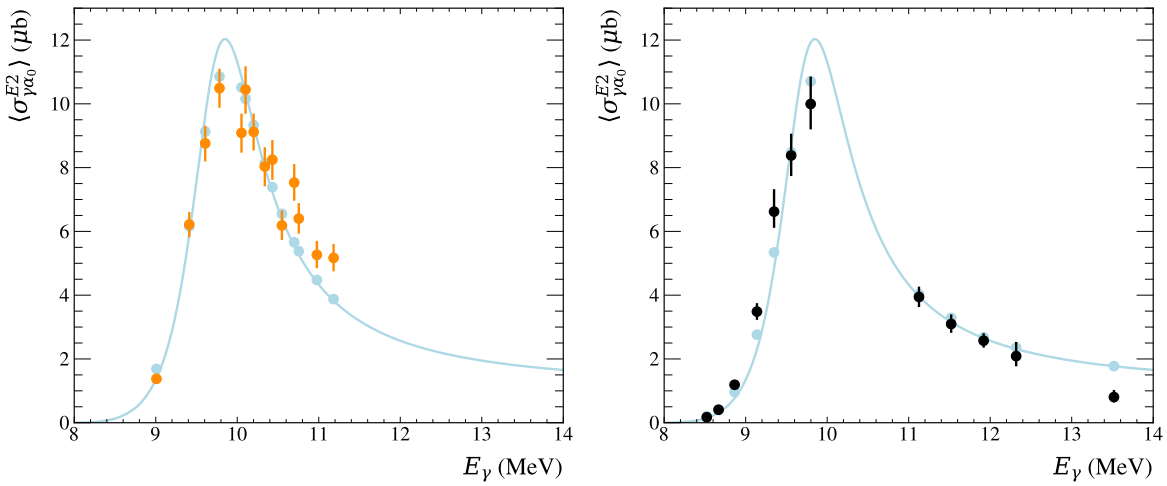

Figure 8.62: Simultaneous Fit to $J^\pi_n(2^+_2)$ State in ^{12}C: Zimmerman data (left, orange) and present work (right, black) are plotted at the effective beam energy. Blue points show the fitted cross section after applying experimental responses, whilst the solid line shows the intrinsic R-matrix lineshape. The total goodness-of-fit is χ^2_ν=3.4. It is noted that some data points have been scaled, and the error bars are statistical only.

To obtain physically meaningful parameters, the *formal* parameters were converted to *observed* parameters using the Thomas approximation (equations (1.4.4.11), (1.4.4.12), (1.4.4.13)). The resulting parameters are listed in table 8.30. The statistical errors (shown in brackets) were propagated from the fit covariance matrix. To assess systematic uncertainties due to the channel radius, all model parameters were fixed and r_0 was varied within its 1σ errors ($2.32 < r_0 < 2.45$ fm). Each *observed* parameter was tracked as a function of r_0, as shown in figure 8.63. The asymmetric systematic errors were determined from the maximum deviation of each parameter from its central value over this range.

J_n^π	E_R (MeV)	Γ_α (MeV)	Γ_γ (MeV)	χ^2_ν
2_2^+	$9.89(2)\ ^{+0.01}_{-0.02}$	$1.05(4)^{+0.04}_{-0.06}$	$101(3)^{+0.9}_{-1.3}\times10^{-9}$	3.4
$r_0 = 2.37, B = 0$				

Table 8.30: Observed R-matrix Parameters for the ^{12}C $J_n^\pi(2_2^+)$ State: The *observed* resonance parameters obtained from the *formal* parameters listed in table 8.29. Uncertainties in brackets are statistical, obtained from the fit covariance matrix. The asymmetric uncertainties are systematic, obtained by varying r_0 within its 1σ range.

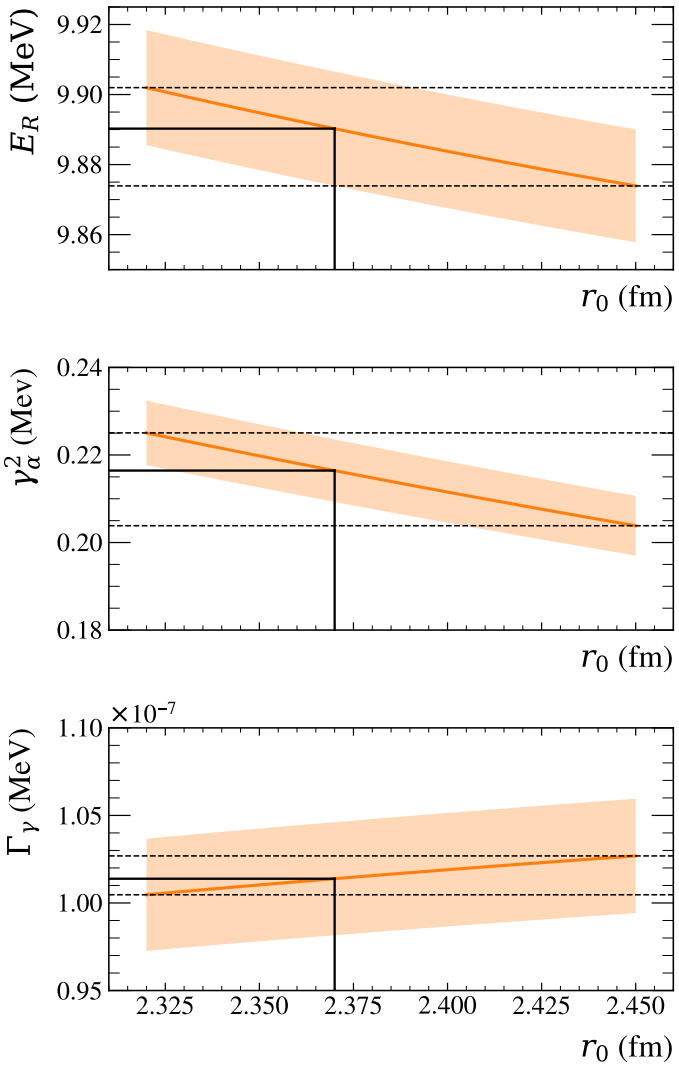

Figure 8.63: Channel Radius Sensitivity of Observed Parameters for the $J_n^\pi(2_2^+)$ State: The dependence of the *observed* parameters (orange line) on the channel radius is shown for E_R (upper), γ_α^2 (middle), and Γ_γ (lower). The shaded band shows the statistical error as a function of r_0. The vertical black line indicates the best-fit value at $r_0 = 2.37$ fm, and the dotted vertical lines indicate the 1σ bounds used to determine systematic errors.

Fitting Procedure for the 1^-_1 State

The $J^\pi_n(1^-_1)$ resonance requires a slightly different treatment; a two-level R-matrix formalism was used. One level to model the resonance of interest, and a second level added phenomenologically to account for background contributions. The two levels were summed incoherently, and the boundary condition was set to zero. All nuisance parameters, f^n_k and f_b, were fixed at their values as determined from the fit to the $J^\pi_n(2^+_2)$ state.

Similarly to before, the sensitivity to r_0 was investigated by performing fits over a range of values and examining the χ^2 score. Figure 8.64 shows this variation, from which the central value and its 1σ errors were determined to be $r_0 = 1.25^{+0.33}_{-0.23}$ fm.

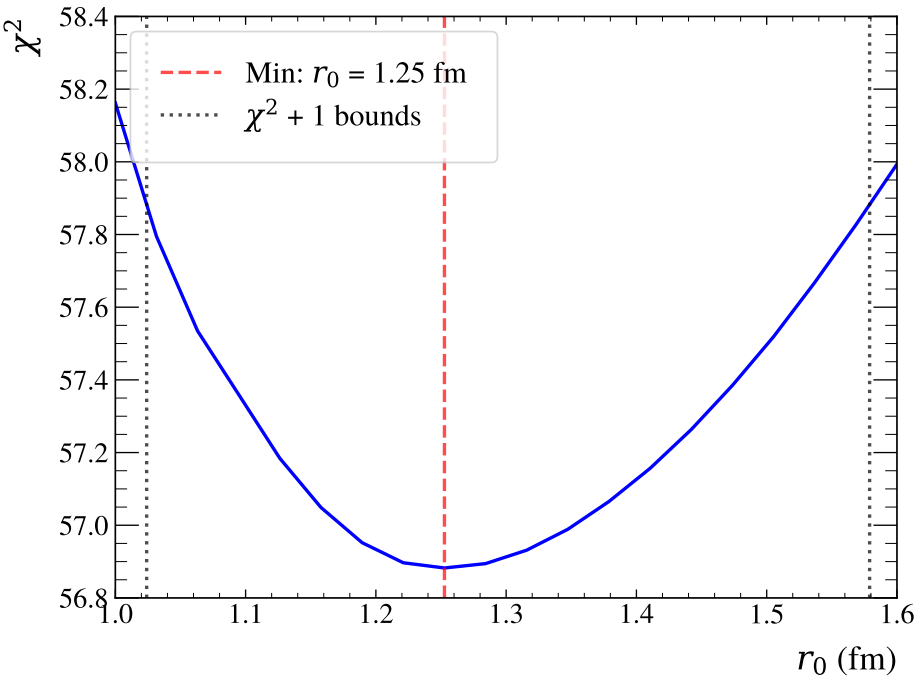

Figure 8.64: Channel Radius Sensitivity Scan for $J^\pi_n(1^-_1)$ State: The dependence of the goodness-of-fit metric, χ^2, on the channel radius is shown by scanning over r_0 values, when fitting the $J^\pi_n(1^-_1)$ resonance.

With r_0 fixed at 1.25 fm the resulting fit yielded a goodness-of-fit score of $\chi^2_\nu = 2.2$. The *formal* parameters for the resonance of interest are given in table 8.31. The fitted results are shown in figure 8.65, using the same layout as previously described. The background centroid is located $\sim$ 23 MeV. However, large correlations are observed among the background-level parameters, preventing definitive conclusions. This is not

unexpected, as the background level is included purely to improve the fit quality rather than to represent a specific physical state.

J^π_n	E_λ (MeV)	$\Gamma_{\lambda\alpha}$ (MeV)	$\Gamma_{\lambda\gamma}$ (MeV)	χ^2_ν
1^-_1	10.88(1)	0.19(4)	32(2) $\times 10^{-9}$	2.2
$r_0 = 1.25, B = 0$				

Table 8.31: Formal R-matrix Parameters the ^{12}C $J^\pi_n(1^+_1)$ State:. The *formal* resonance parameters extracted from the fit. Uncertainties in brackets are statistical, obtained from the fit covariance matrix.

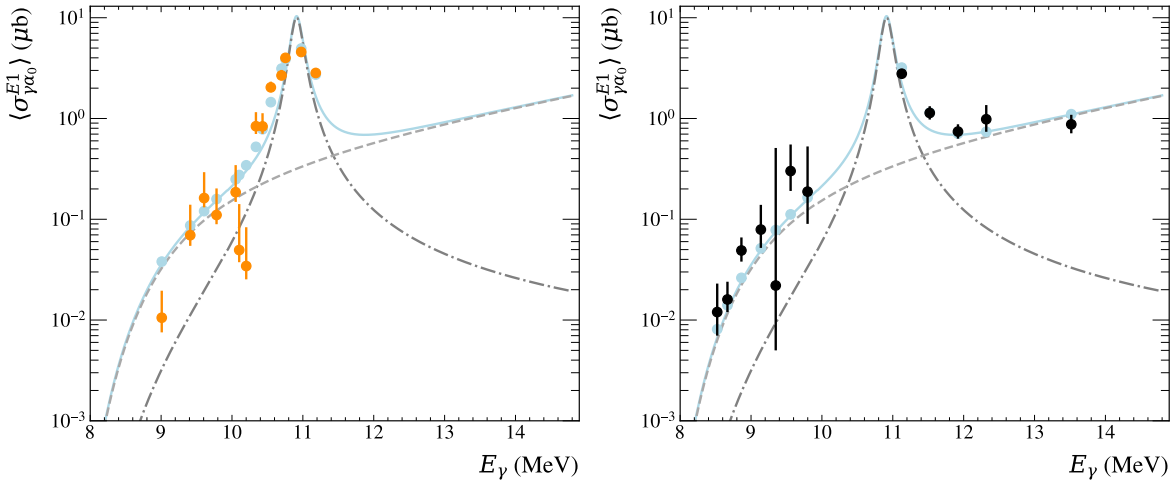

Figure 8.65: Simultaneous Fit to $J^\pi_n(1^-_1)$ State in ^{12}C: Zimmerman data (left, orange) and present work (right, black) are plotted at the effective beam energy. Blue points show the fitted cross section after applying experimental responses, whilst the solid line shows the intrinsic R-matrix lineshape. The total goodness-of-fit is χ^2_ν=2.2. It is noted that some data points have been scaled, and the error bars are statistical only.

Again, the *formal* parameters were converted to *observed* parameters using the Thomas approximation (equations (1.4.4.11), (1.4.4.12), (1.4.4.13)). The resulting parameters are listed in table 8.32. Statistical errors (shown in brackets) were propagated from the fit covariance matrix. To assess systematic uncertainties due to the channel radius, all model parameters were fixed, and r_0 was varied within its 1σ errors ($1.02 < r_0 < 2.58$ fm). Each *observed* parameter was tracked as a function of r_0, as shown in figure 8.66. The asymmetric systematic errors were determined from the maximum deviation of each parameter from its central value over this range.

J^π_n	E_R (MeV)	Γ_α (MeV)	Γ_γ (MeV)	χ^2_ν
1^-_1	$10.91(1)\ ^{+0.04}_{-0.02}$	$0.19(4)\ ^{+0.10}_{-0.07}$	$31(2)^{+0.3}_{-0.4} \times 10^{-9}$	2.2
$r_0 = 1.25, B = 0$				

Table 8.32: Observed R-matrix Parameters for the ^{12}C $J^\pi_n(1^-_1)$ State: The *observed* resonance parameters obtained from the *formal* parameters listed in table 8.31. Uncertainties in brackets are statistical, obtained from the fit covariance matrix. The asymmetric uncertainties are systematic, obtained by varying r_0 within its 1σ range.

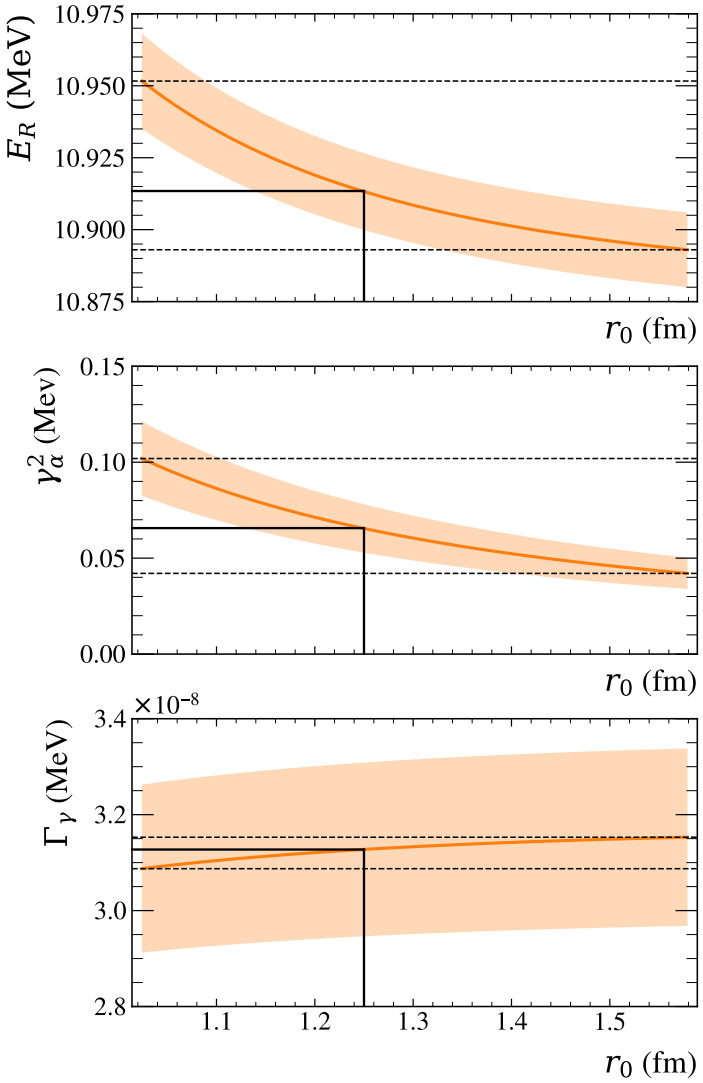

Figure 8.66: Channel Radius Sensitivity of Observed Parameters for the $J^\pi_n(1^-_1)$ State: The dependence of the *observed* parameters (orange line) on the channel radius is shown for E_R (upper), γ^2_α (middle), and Γ_γ (lower). The shaded band shows the statistical error as a function of r_0. The vertical black line indicates the best-fit value at $r_0 = 1.25$ fm, and the dotted vertical lines indicate the 1σ bounds used to determine systematic errors.

Final Results

Figure 8.67 presents the final fitted results after unfolding the data using the experimental resolution, allowing for direct comparison of both datasets with the intrinsic R-matrix lineshape. The shaded bands represent the 1σ uncertainty derived from the fit covariance matrix. Relevant *observed* resonance parameters for both the $J^\pi_n(2^+_2)$ and $J^\pi_n(1^-_1)$ states are listed again for convenience in in table 8.33. Also listed are the dimensionless reduced width and the reduced transmission probability, defined below.

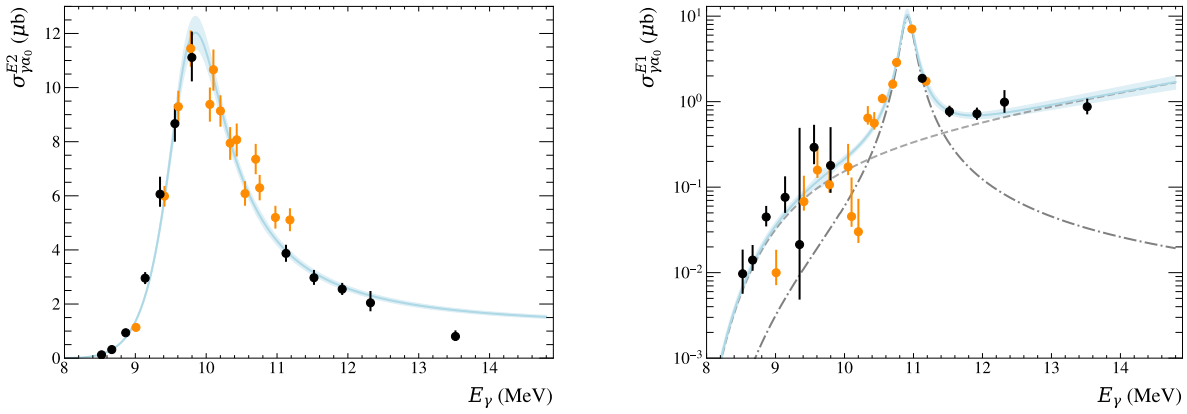

(a) $J^\pi_n(2^+_2)$ state **(b)** $J^\pi_n(1^-_1)$ state

Figure 8.67: Fits to the Deconvolved Cross Section for the $J^\pi_n(2^+_2)$ and $J^\pi_n(1^-_1)$ States: The experimental data (points) from Zimmerman (orange) and this analysis (black) are plotted at the effective beam energy after deconvolution of the experimental response and compared with the intrinsic R-matrix lineshape (solid line). The shaded bands represent the 1σ uncertainty from the covariance matrix. It is noted that some data points have been scaled, and the error bars are statistical only.

J^π	E_R (MeV)	Γ_α (MeV)	γ^2_α (MeV)	θ^2_α	Γ_γ (MeV)	$B(EL)$ (e^2 fm^{2L})	$B(EL)$ (W.u.)	χ^2_ν
2^+_2	$9.89\ ^{+0.02}_{-0.02}$	$1.05\ ^{+0.05}_{-0.07}$	$0.22\ ^{+0.01}_{-0.01}$	$0.67\ ^{+0.03}_{-0.05}$	$101\ ^{+3}_{-4} \times 10^{-9}$	$1.91\ ^{+0.06}_{-0.07}$	$1.17\ ^{+0.04}_{-0.04}$	3.4
1^-_1	$10.91\ ^{+0.04}_{-0.02}$	$0.19\ ^{+0.1}_{-0.08}$	$0.07\ ^{+0.04}_{-0.03}$	$0.06\ ^{+0.03}_{-0.02}$	$31\ ^{+2}_{-2} \times 10^{-9}$	$33\ ^{+2}_{-2} \times 10^{-6}$	$97\ ^{+6}_{-6} \times 10^{-6}$	2.2
$r_0 = 1.25$ fm (1^-_1); $r_0 = 2.37$ fm (2^+_2)								

Table 8.33: Overview of Extracted *observed* Parameters for Fits to the ^{12}C Data: Fitted and related parameters for the $J^\pi_n(1^-_1)$ and $J^\pi_n(2^+_2)$ resonances in ^{12}C. The uncertainties quoted have statistical and systematic errors added in quadrature from tables 8.30 and 8.32.

Alpha width. The reduced alpha width, γ_α^2, can then be expressed in terms of the ratio to the so-called Wigner limit, γ_w^2, dubbed the dimensionless reduced width, $\theta_\alpha^2 = \gamma_\alpha^2/\gamma_w^2$ [195].

The Wigner limit, γ_w^2, as calculated below, gives the reduced width expected for perfect cluster formation

$$\gamma_w^2 = \frac{3}{2}\frac{\hbar^2}{\mu\ a_c^2}. \tag{8.8.3.2}$$

It is generally considered that $\theta^2 > 0.1$ indicates significant clustering (preformation) [196].

Gamma width. The γ width, Γ_γ, can be expressed in terms of the reduced transition probability using equation (1.4.4.5) to determine $B(E1 : 1_1^- \rightarrow 0_1^+)$ and $B(E2 : 2_2^+ \rightarrow 0_1^+)$, in units $\mathrm{e^2fm^2}L$. These values are also represented in terms of Weisskopf units (W.u) [31], where the Weisskopf single-particle estimates for the reduced transition probabilities are defined as [19]

$$B_\mathrm{w}(EL) = \frac{(1.2)^{2L}}{4\pi}\left(\frac{3}{L+3}\right)^2 A^{2L/3}\, e^2\mathrm{fm}^{2L}. \tag{8.8.3.3}$$

Here, A is the mass of the compound nucleus, and L is the multipolarity of the transition. For $A = 12$, this yields $B_\mathrm{w}(E2) = 1.63\ \mathrm{e^2fm^4}$ and $B_\mathrm{w}(E1) = 0.34\ \mathrm{e^2fm^2}$.

These estimates represent the reduced transmission probability between two states caused by the motion of a single nucleon. Therefore, if $B(EL)$ is close to one W.u., it could be thought to be single-particle in nature. In contrast, if it is many W.u., the transition can be considered to occur from collective motion.

Part IV

Conclusions

9

Summary

9.1 The $^{16}\mathbf{O}(\gamma, \alpha_0)$ Reaction

A new method of analysing the astrophysical $^{12}\mathrm{C}(\alpha, \gamma_0)$ reaction using TPCs and γ beams has been developed, which has several advantages over directly measuring the capture reaction. These include the benefit of having no background induced through the $^{13}\mathrm{C}(\alpha, n)$ reaction, a cross section boosted by the principle of detailed balance, and full kinematic information event-by-event, which allows for precise high-statistics detailed angular distributions.

This work has shown, for the first time, an extracted phase mixing angle (ϕ_{12}) in unambiguous agreement with predictions of quantum scattering theory, a long-standing issue in the field. This has been verified using two different TPC detectors with different readout technologies and different active gas target compositions, as shown in figure 9.1.

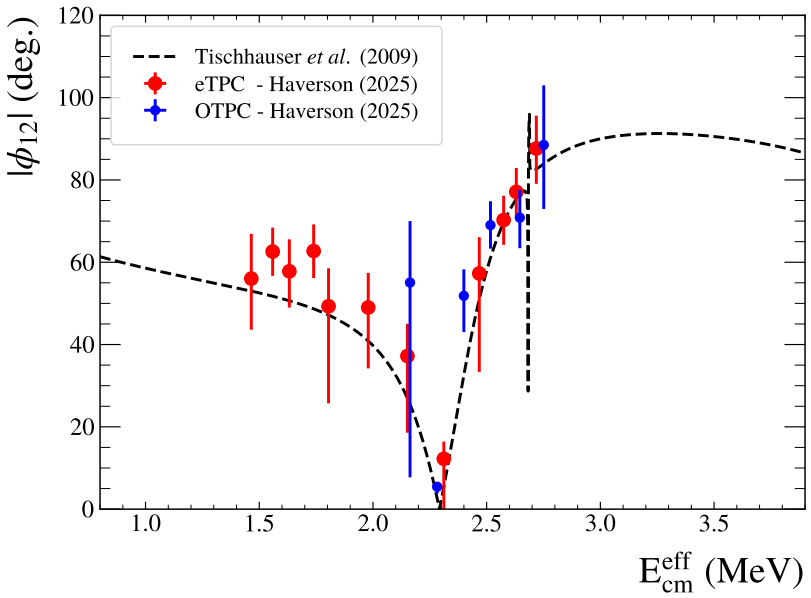

Figure 9.1: Unfolded ϕ_{12} Parameter: Both the ϕ_{12} results from the OTPC (blue) and eTPC (red) are shown unfolded and compared with values calculated from the elastic scattering phase shifts of Tischauser*et al.* [79] (black dashed line).

This provides evidence that these data are of good enough quality to be included in an extrapolation to the Gamow window; the extracted ratios of cross sections (σ_2/σ_1) are shown compared to the current global fit of DeBoer *et al.* [46] in figure 9.2. In the past, earlier datasets have shown that "fixing" ϕ_{12} changes the partial cross sections significantly. The reason for this discrepancy should be identified before such data are used for extrapolations.

These data have also been benchmarked against reliable world data by reproducing the well-constrained low-energy angle-integrated ground-state cross section, as shown in figure 9.3.

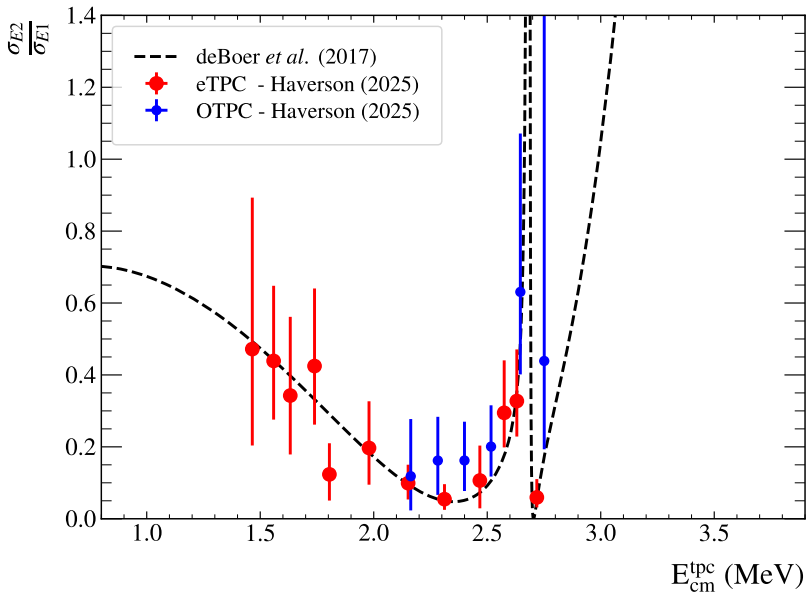

Figure 9.2: Unfolded ϕ_{12} Parameter: Both the σ_2/σ_1 results from the OTPC (blue) and eTPC (red) are shown unfolded and compared with values from R-matrix fit of DeBoer *et al.* [46] (black dashed line).

The eTPC data are also be valuable for constraining the high-energy cross section, which affects the extrapolation to low energy. This is particularly the case in the off-resonance region, as highlighted in figure 9.4. The extracted σ_2/σ_1 values (black points) are compared with the energy-averaged fit to the world data (the blue line is intrinsic, and the red points include energy-averaging resolution effects). There is, on average, a 70% difference between current experimental values and those of the global R-matrix fit of deBoer *et al.* [46] between E_{cm}=4.3 and 5.3 MeV. This may not be hard to explain as the off-resonance region is constrained only by the on-resonance data of Brochard *et al.* [64] and Schürmann *et al.* [63] (shown in figure G.2). This could indicate the background term used in the R-matrix fit to the world data is likely not correct. As noted by Brune [197], the choice of background term will affect the extrapolation to stellar conditions, and hence a revision of the fit to include the new data in this region is potentially of high importance.

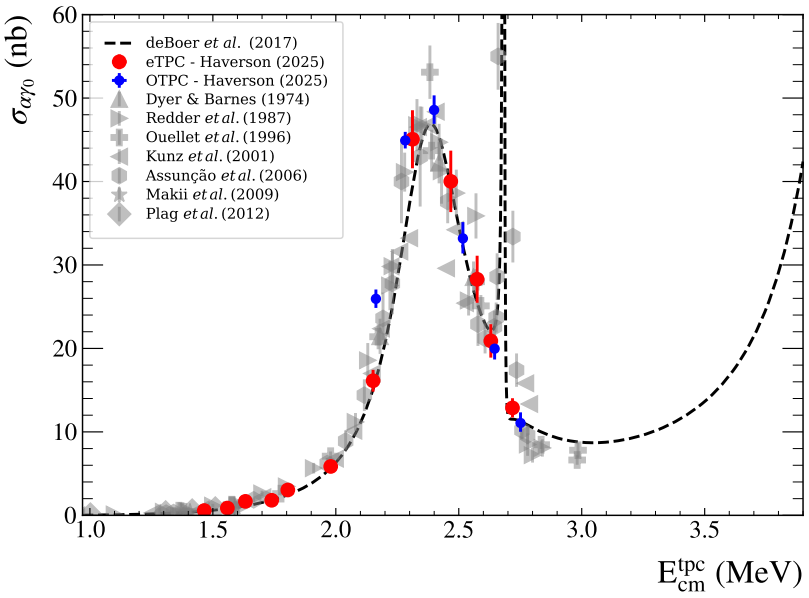

Figure 9.3: Unfolded Angle-Integrated Cross Section: Both the $\sigma_{\alpha\gamma_0}$ cross sections from the OTPC (blue) and eTPC (red) are shown unfolded, compared with the current R-matrix fit to the world data [46] (black dashed line), and previous datasets [41, 58–61, 63, 65].

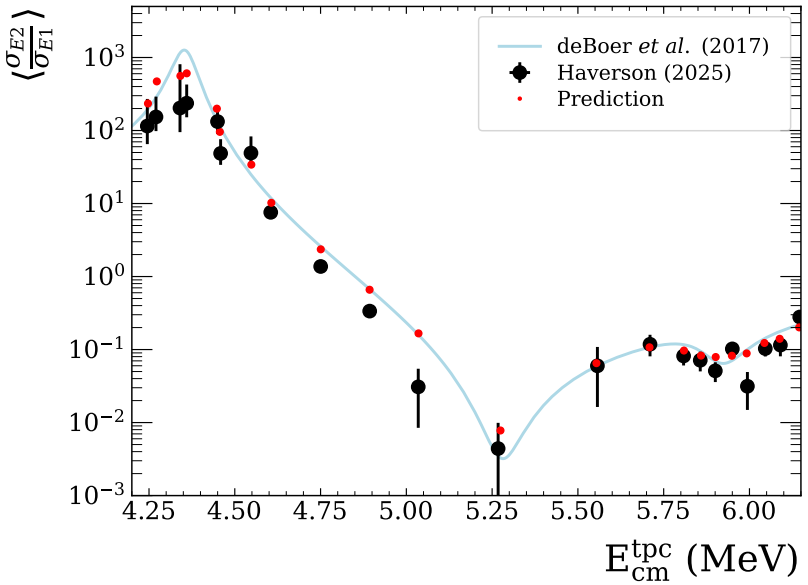

Figure 9.4: High-Energy Partial ^{16}O(γ, α_0) Cross Sections: This shows the ratio of cross sections, σ_{E2}/σ_{E1}, from the global R-matrix fit as both the intrinsic lineshape (light blue) and energy-averaged points (red), compared with the energy-averaged eTPC data (black points). An average percentage difference of $\sim 70\%$ is noted in the off-resonance region between E_{cm}=4.3-5.3 MeV.

9.2 The $^{12}C(\gamma, \alpha_0)$ Reaction

This analysis continued the photo-dissociation measurements of ^{12}C by Zimmerman *et al.* [139, 140] to higher energies. This was to measure the full lineshape of the previously discovered $J^{\pi}_n(2^+_2)$ state and to search for a higher energy $J^{\pi}_n(2^+_3)$ state, predicted by the ACM to belong to the so-called bending-band.

An R-matrix analysis was performed on the $E2$ and $E1$ partial cross sections, where they were modelled as a single broad $J^{\pi}(2^+)$ resonance and two $J^{\pi}(1^-)$ resonances, one of which modelled a broad non-interfering background. The $^{12}C(\gamma, \alpha_0)$ datasets of this analysis and those of Zimmerman [140] were analysed together. The data of Zimmerman required a correction to account for their incorrectly calculated fiducial volume correction.

A sensitivity study was performed on both the $J^{\pi}_n(2^+_2)$ and $J^{\pi}_n(1^-_1)$ states to identify the channel radius ($a_c = r_0(A_1^{1/3} + A_2^{1/3})$) that provides the best fit. A typical r_0 of 1.25 was found for the $J^{\pi}_n(1^-_1)$ state, and was well modelled by including the low-energy tail of a broad high-energy resonance, possibly the Giant Dipole Resonance (GDR) [198, 199]. In contrast, the $J^{\pi}_n(2^+_2)$ state required a very large $r_0 = 2.37$, and was well modelled by a single resonance. There is no compelling evidence for the existence of the $J^{\pi}_n(2^+_3)$ state in the given energy range.

Structural Interpretation

The large r_0 required is not inconsistent with predictions for the $J^{\pi}_n(2^+_2)$ state. It is believed to be an excitation of the Hoyle state, predicted by the ACM to have, on average, due to the oscillations of the breathing mode, a larger radius than states belonging to the ground state band. This is furthermore supported by Barker and Treacy [200], who showed that to reproduce the properties of the Hoyle state, they needed to use an elevated r_0 of 1.8. The extracted dimensionless reduced width of the $J^{\pi}_n(2^+_2)$ was found to be $0.67^{+0.03}_{-0.05}$, which is a considerable percentage of the Wigner limit, indicating a significant degree of α preformation. This also tracks with what has been extracted from measurements of the alpha width of the Hoyle state. In their review paper, Freer and Fynbo [104] conclude that the Hoyle state has a dimensionless reduced width of 1. The similarity

between this and the extracted dimensionless reduced width of the $J^{\pi}_{n}(2^{+}_{2})$ indicates that these states could have a similar intrinsic structure.

Further insight into the structure of the $J^{\pi}_{n}(2^{+}_{2})$ can be obtained by analysing energy-spin systematics. Both the rotational bands of the Hoyle state [54] and the ground state [54, 201] are shown in figure 9.5, where the resonance energy for the $J^{\pi}_{n}(2^{+}_{2})$ obtained in this work was included in the Hoyle band. By performing a simple linear fit, the moment of inertia is extracted for both rotational bands, using $E(J) = E_0 + \frac{\hbar^2}{2\mathcal{I}}J(J+1)$. The extracted moments of inertia are $I = 4.7 \times 10^{-56} \pm 2.2 \times 10^{-60}$ kg m^2 for the ground state band and $I = 9.7 \times 10^{-56} \pm 8.0 \times 10^{-58}$ kg m^2 for the Hoyle band. This agrees well with the prediction of reference [120], which states that the moment of inertia of the Hoyle band should be a factor of two larger than that of the ground state band.

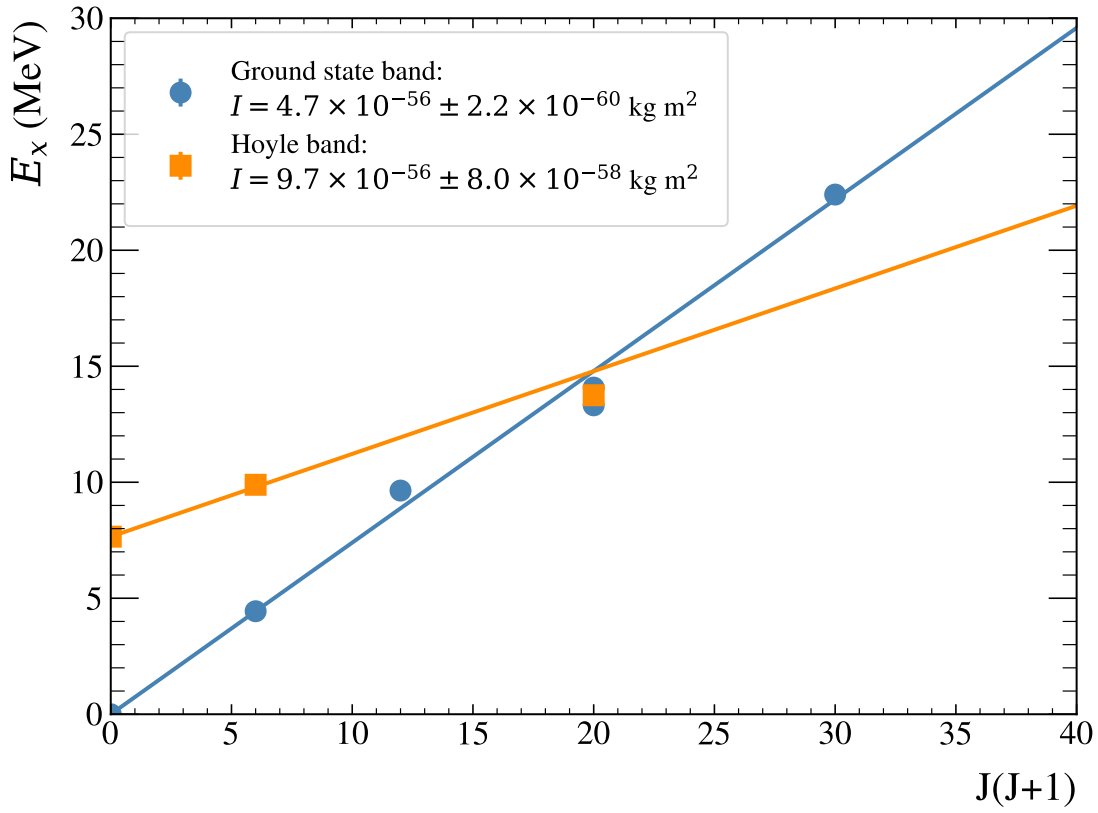

Figure 9.5: Rotational Bands of ^{12}C: The energy-spin systematics of the ground state and Hoyle state rotational bands are shown, with the moment of inertia of both labelled in the plot. The parameters for the $J^{\pi}_{n}(2^{+}_{2})$ resonance found in this work were included in the Hoyle band.

Comparison with Theory

One observable that many structure models predict is the reduced transmission probability, $B(E2)$. For example, predictions exist from *ab initio* calculations such as antisymmetrised molecular dynamics (AMD) and lattice effective field theory (L-EFT), as well as alpha condensate models such as the Tohsaki-Horiuchi-Schuck-Roṗke (THSR) wave function approach and the microscopic cluster generator coordinate method (GCM). However, it is unfortunately not predicted by the ACM because interband transitions are not yet calculable in this model [202]. Each approach makes predictions for the transition from the $J^{\pi}_{n}(2^{+}_{2})$ to the ground state of ^{12}C, and these are compared with the experimental result from this work in table 9.1. There is good agreement with Epelbaum *et al.* as well as with the alpha condensate calculation of Funaki.

Theory	Ref.	$B(E2 : 2^{+}_{2} \rightarrow 0^{+}_{1})$ (e^2 fm^4)
Microscopic Cluster	Descouvemont *et al.*(1987) [203]	4.1
AMD	Kanada-En'yo (2009) [204, 205]	0.4
L-EFT	Epelbaum *et al.*(2012) [115]	2(1)
α condensate model	Funaki (2015) [206]	2.0-2.5
Faddeev 3-body formalism	Ishikawa (2025) [207]	0.62-5.4
Experiment	**This Work**	$1.91^{+0.06}_{-0.07}$

Table 9.1: Theoretical Predications of Reduced Transmission Probability: Values of $B(E2 : 2^{+}_{2} \rightarrow 0^{+}_{1})$ predicted from different models of ^{12}C are compared with this analysis.

Comparison with Previous Experiments

A comparison with previous experimental measurements of the $J^{\pi}_{n}(2^{+}_{2})$ state is made in figure 9.6, with values provided in table 9.2. Overall, there is good agreement with Itoh *et al.* [113, 124] and the latest scattering measurement of Li *et al.* [131] in terms of both total width and resonance energy.

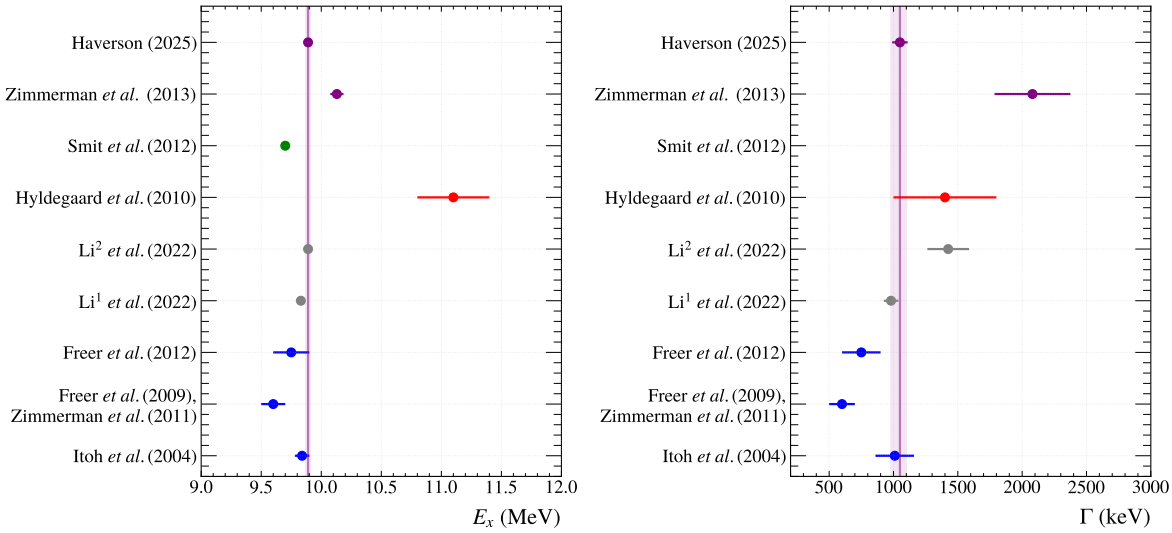

Figure 9.6: Resonance Parameters of the $J^\pi(2_2^+)$ State in ^{12}C : Excitation energy, E_x, and total width, Γ, for this resonance are plotted from various studies. The purple vertical line indicates the values and uncertainty from this work. The superscripts for the Li *et al.* measurements indicate different interference scenarios explained in reference [131]. All references are given in table 9.2.

Study	E_x (MeV)	Γ (keV)
Itoh *et al.*(2004) [113, 124]	9.84 ± 0.06	1010 ± 150
Freer *et al.*(2009) [126], Zimmerman *et al.*(2011) [129]	9.60 ± 0.10	600 ± 100
Freer *et al.*(2012) [130]	9.75 ± 0.15	750 ± 150
Li^1 *et al.*(2022) [131]	9.830 ± 0.033	981 ± 56
Li^2 *et al.*(2022) [131]	9.890 ± 0.011	1425 ± 162
Hyldegaard *et al.*(2010) [135]	11.10 ± 0.30	1400 ± 400
Smit *et al.*(2012) [137]	9.70	—
Zimmerman *et al.*(2013)[140]	$10.13^{+0.06}_{-0.05}$	2080^{+330}_{-260}
Haverson (2025)	9.89(2)	1050^{+50}_{-70}

Table 9.2: Resonance Parameters of the ^{12}C 2_2^+ State: Excitation energy, E_x, and total width, Γ, for this level are listed from various studies. The superscripts for the Li *et al.* measurements indicate different interference scenarios.

10

Outlook

The work done here, at low energies, demonstrates the viability of this method for conducting measurements at lower astrophysical energies closer to the Gamow window for the $^{12}\mathrm{C}(\gamma, \alpha_0)$ reaction. Furthermore, it has the potential to describe the resonance structure of both $^{12}\mathrm{C}$ and $^{16}\mathrm{O}$ at higher energies, where it is less well known.

The analysis of the eTPC data could also be improved by running a larger number of more realistic simulations, these could include effects such as the electronics plateau effect (which has since been added), z-dependent electron diffusion during drift, and realistic noise models. This would facilitate data correction rather than applying the angular fiducial cut. Although minimal, removing this cut would retain additional statistics.

Machine learning methods for event classification and reconstruction are well-suited to TPC data, and a preliminary study into this was previously published by the author of this thesis [171]. However, a current limitation is the lack of training data to reliably cover the full variation of event topologies. With upgraded simulations, studies could be performed by training models on realistic simulated data and applying them to analyse

experimental events. This could significantly improve the reconstruction of more complex events, such as wide open-angle ^{12}C decays through the ^{8}Be excited state. The development of additional algorithms, whether using classical approaches or machine learning, would be needed to study these events due to their three-pronged topology. This would allow them to be analysed using Dalitz plots. This decay mode is particularly useful as the restriction to natural parity states does not apply.

There is a scheduled continuation experiment at HIγS in summer 2026 using the eTPC with a CO_2 target, with higher beam intensities than presented here. It is recommended that additional measurements be taken at $E_\gamma \sim 10$ MeV to cover the on-resonance region in ^{12}C, enabling an independent analysis of the $J^\pi_n(2^+_2)$ and $J^\pi_n(1^-_1)$ states. This energy also corresponds to an off-resonance region in ^{16}O, where few measurements exist, and the R-matrix fit is poorly constrained. For future experiments at HIγS, it is important that HPGe response matrices are obtained and validated for use above $E_\gamma = 10$ MeV, enabling the unfolding procedure for accurate beam energy determination. Future experiments at ELI-NP are also expected to achieve even higher beam intensities, enabling measurements at lower, more astrophysically relevant energies for the ^{12}C(α, γ_0) reaction.

Unlike the ^{12}C photo-dissociation data, where a simple one- or two-level R-matrix fit might suffice to model the level structure, this is certainly not the case for the ^{16}O photo-dissociation data. To obtain a reliable extrapolation to the Gamow window from these data, a more sophisticated approach is needed. To better constrain the fit and make the most of the eTPC's full kinematic reconstruction capabilities, an unbinned log-likelihood analysis in both energy and angle should be adopted. This would require significant modification of current codes, such as `AZURE2` [38]. Currently, these codes are optimised for traditional experiments with simple energy resolution effects and don't yet account for the unique TPC energy-averaging effects.

Appendices

A

Operating TPCs in Broad γ Beams

This thesis presents multiple analyses using different TPCs in γ beams to study the cross sections of photo-dissociation reactions producing $J^{\pi}(0^{+})$ nuclei. To avoid repetition, the general analysis methods and technical considerations are defined here. Several technical issues arise that must be addressed, particularly surrounding effective energies and the comparison of extracted observables. For this appendix, please note the following notation:

- † superscript will denote a theoretical expectation value.
- $\langle X \rangle$ denotes that the quantity inside the brackets is an energy-averaged parameter
- Energy dependence is explicit: $\langle X(E) \rangle$ versus $\langle X \rangle$
- $\sigma_{\gamma\alpha}$ and $\sigma_{\alpha\gamma}$ denote the direct from/to ground state photo-dissociation and radiative capture reaction cross sections, respectively.
- The model of the underlying cross section used here, $\sigma^{\dagger}_{\gamma\alpha}(E)$, is taken from reference [46].

A.1 Effective Energies

Because γ beams generated at HIγS at the energies considered, are typically broad, reactions occur over a wide range of energies for a given nominal beam energy. Thus an effective energy parameter must be defined.

Historically [97, 139, 140], data were not evaluated using TPC-reconstructed energies, but rather a single measurement was taken across the full width of the beam. In this case, the energy measurement was achieved using an external HPGe detector to measure the γ beam profile (see appendix B).

A.1.1 Incident Centre-of-mass Energy

The effective incident energy is defined as

$$E_{\mathrm{cm}}^{\mathrm{inc}} = \frac{\int_0^\infty E\, G(E)\, dE}{\int_0^\infty G(E)\, dE}. \tag{A.1.1.1}$$

Where $G(E)$ is the experimentally obtained γ beam energy profile shifted approximately by the Q-value [1]. This is simply the weighted average of the distribution.

A.1.2 Effective Centre-of-mass Energy

An alternative is to present data at the effective centre-of-mass energy, which accounts for the energy dependence of the reaction cross section. This is defined as

$$E_{\mathrm{cm}}^{\mathrm{eff}} = \frac{\int_0^\infty E\, G(E)\, \sigma_{\gamma\alpha}^{\dagger}(E)\, dE}{\int_0^\infty G(E)\, \sigma_{\gamma\alpha}^{\dagger}(E)\, dE}, \tag{A.1.2.1}$$

where $\sigma_{\gamma\alpha}^{\dagger}(E)$ is the theoretical expectation for the total reaction cross section.

[1] The full calculation accounts for the tiny, (sub) keV recoil energy of the target nucleus, but this was found to be negligible in all cases in comparison with other experimental errors.

A.1.3 TPC-reconstructed Effective Energy

One improvement in this analysis is the ability to calibrate the spectra measured in the TPC, enabling event-by-event energy reconstruction. This removes the previous limitation imposed by the broad beam width, with the analysis now constrained by statistics and reconstruction resolution. By selecting energy slices between limits a and b, the effective energy of events measured in an energy slice by the TPC has an expectation value of

$$E_{\mathrm{cm}}^{\mathrm{tpc}} = \frac{\int_a^b E \left[\int_0^\infty G(E')\, \sigma_{\alpha\gamma}^{\dagger}(E')\, \mathcal{G}(E - E')\, dE' \right] dE}{\int_a^b \left[\int_0^\infty G(E')\, \sigma_{\alpha\gamma}^{\dagger}(E')\, \mathcal{G}(E - E')\, dE' \right] dE}. \tag{A.1.3.1}$$

Here $\mathcal{G}(E - E')$ applies a Gaussian response representing the TPC resolution (assuming that the resolution of the TPC does not depend on energy).

This resolution term is a slight nuisance when slices are taken in the TPC spectrum and effective energies are calculated, as these do not always approach the true effective energy, given by equation (A.1.2.1). The degree of this effect is shown in figure A.1. Each panel shows the difference in energy from equation (A.1.2.1) and equation (A.1.3.1) for various bin sizes, with each panel using a different TPC resolution, as noted in the title. The beam profile and cross section that was used is shown later in figure A.2.

What is made clear is that the difference in effective energies is exacerbated by larger bin sizes, the width of the TPC reconstruction resolution, and the location of rapidly changing resonances. It is important to be aware of the differences when plotting results. Comparison with theory needs to be done at the appropriate energy.

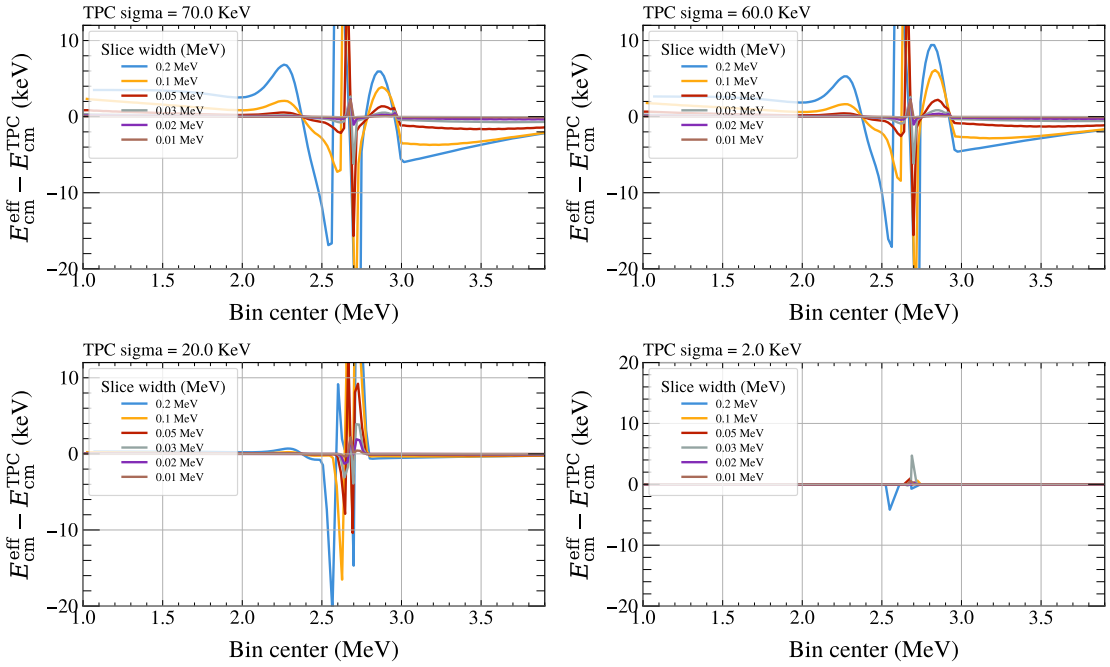

Figure A.1: TPC Resolution Effects: Comparison of TPC reconstructed effective energies with true effective energy for different bin sizes and reconstruction resolutions, plotted at the bin centre.

A.2 Angle-integrated Cross Section

The formalism for obtaining the angle-integrated photo-dissociation cross section under the assumption of perfect energy resolution is relatively simple. Divide the number of events of interest over a given energy range, N, by the integrated luminosity over the same energy range, $\mathcal{L}$, such that $\sigma_{\gamma\alpha} = \frac{N}{\mathcal{L}}$. Here $\mathcal{L} = N_\gamma nx$, where N_γ represents the number of photons in the beam incident on the TPC, x is the target thickness, and n is the number density of target nuclei.

A.2.1 Single Measurement

One can measure a single effective cross section per beam energy. This procedure is shown in figure A.2. A typical beam profile is shown in green, and a model of the cross section, $\sigma^{\dagger}_{\gamma\alpha}(E)$, is in black. The effective cross section measured from this procedure is shown as the green data point plotted at the effective energy from equation (A.1.2.1).

The expectation value for the effective cross section is obtained using

$$\langle \sigma^{\dagger}_{\gamma\alpha} \rangle = \frac{\int_0^{\infty} \sigma^{\dagger}_{\gamma\alpha}(E)\, G(E)\, dE}{\int_0^{\infty} G(E)\, dE}. \tag{A.2.1.1}$$

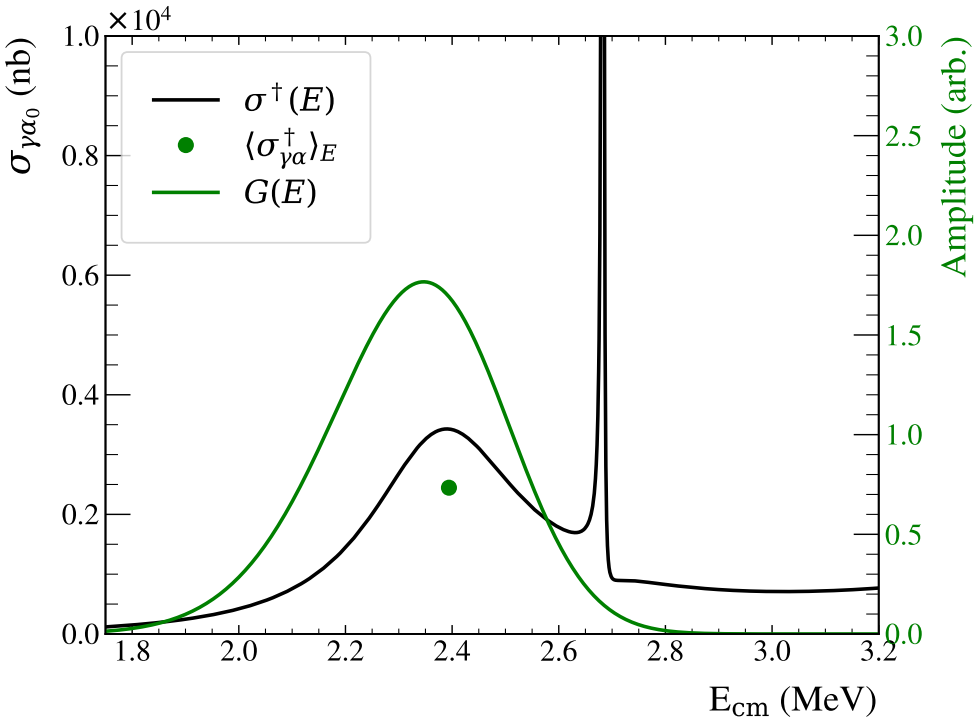

Figure A.2: Single Measurement Effective Cross Section: The plot shows the $^{16}\mathrm{O}(\gamma, \alpha_0)$ cross section in black, a typical γ beam profile in green, and the effective cross section measured across the beam as the green point.

When this energy-averaged cross section is obtained experimentally to compare with the underlying intrinsic cross section, a deconvolution/unfolding method can be used. The full procedure is outlined in [185]. In brief, a correction factor, f_{cor}, is obtained by applying detector effects to the underlying cross section, and taking a ratio of the true cross section at the effective energy

$$f_{\mathrm{cor}} = \frac{\sigma^{\dagger}_{\gamma\alpha}(E^{\mathrm{eff}}_{\mathrm{cm}})}{\langle \sigma^{\dagger}_{\gamma\alpha} \rangle}. \tag{A.2.1.2}$$

This multiplicative factor will bring the green point in figure A.2 to the cross section at

the effective energy. Therefore, the deconvolved cross section is obtained as

$$\sigma_{\gamma\alpha} = \frac{N}{\mathcal{L}} f_{\text{cor}} \tag{A.2.1.3}$$

At this stage, it is possible to calculate the detailed balance, f_{db}, evaluated at the effective energy to convert the cross section to the forward radiative capture reaction.

$$\sigma_{\alpha\gamma} = \frac{\sigma_{\gamma\alpha}}{f_{db}(E_{\text{cm}}^{\text{eff}})} \tag{A.2.1.4}$$

A.2.2 Fine Splitting

By reconstructing the centre-of-mass energy of each event measured in the TPC, it is possible to circumvent the limitation of a single measurement per beam energy. One can use the shape of the beam profile to distribute the luminosity across the TPC spectrum, thus obtaining a finely binned cross section measurement with reduced energy-averaging effects.

Formalism. Let the distribution of events measured in the TPC, assuming 100% efficiency, be denoted as $S(E)$. This has an expectation value of

$$S^{\dagger}(E) = \int_{-\infty}^{\infty} \mathcal{L}\, G(E')\, \sigma_{\gamma\alpha}^{\dagger}(E')\, \mathcal{G}(E - E')\, dE', \tag{A.2.2.1}$$

where $\mathcal{G}(E - E')$ represents the Gaussian TPC resolution (60 keV for this example).

Since experimentally, $S(E)$ and $G(E)$ are obtained independently, a convenient approximate way to extract the cross section is by dividing the two quantities

$$\langle \sigma_{\gamma\alpha}(E) \rangle = \frac{S(E)}{\displaystyle\int_{-\infty}^{\infty} \mathcal{L}\, G(E')\, \mathcal{G}(E - E')\, dE'}. \tag{A.2.2.2}$$

Inspecting this relation using the expectation values of the relevant quantities gives,

$$\langle \sigma_{\gamma\alpha}^{\dagger}(E) \rangle = \frac{\displaystyle\int_{-\infty}^{\infty} \mathcal{L}\, G(E')\, \sigma^{\dagger}(E')\, \mathcal{G}(E - E')\, dE'}{\displaystyle\int_{-\infty}^{\infty} \mathcal{L}\, G(E')\, \mathcal{G}(E - E')\, dE'}. \tag{A.2.2.3}$$

It is clear from the above equations that what is obtained experimentally does not result in a simple Gaussian energy-averaging of the underlying cross section.

Under the assumption that the beam profile $G(E)$ is constant (flat beam distribution), it can be factored out of the integrals above. In this limit, the reconstructed cross section does indeed reduce to a simple convolution of the underlying cross section with the TPC resolution

$$\langle \sigma^{\dagger}_{\gamma\alpha}(E) \rangle \simeq \int_{-\infty}^{\infty} \sigma^{\dagger}_{\gamma\alpha}(E')\, \mathcal{G}(E - E')\, dE'. \tag{A.2.2.4}$$

This is shown in figure A.3 where the simple Gaussian energy-averaged cross section, denoted in the legend as $\sigma_{\gamma\alpha} \circledast \mathcal{G}(E)$, is plotted at E^{eff}_{cm}. Compared with the expectation value for the TPC-reconstructed cross section, $\langle \sigma^{\dagger}_{\gamma\alpha}(E) \rangle$, plotted at E^{tpc}_{cm} (as would be done experimentally). Case 1 corresponds to a uniform beam, and Case 2 corresponds to the realistic beam profile shown in figure A.2[2].

[2]A previous analysis [186] applied numerical unfolding methods to remove the effects of the TPC resolution. However, those methods outlined in that thesis were not reproducible here to reconstruct the shape of known resonances accurately enough.

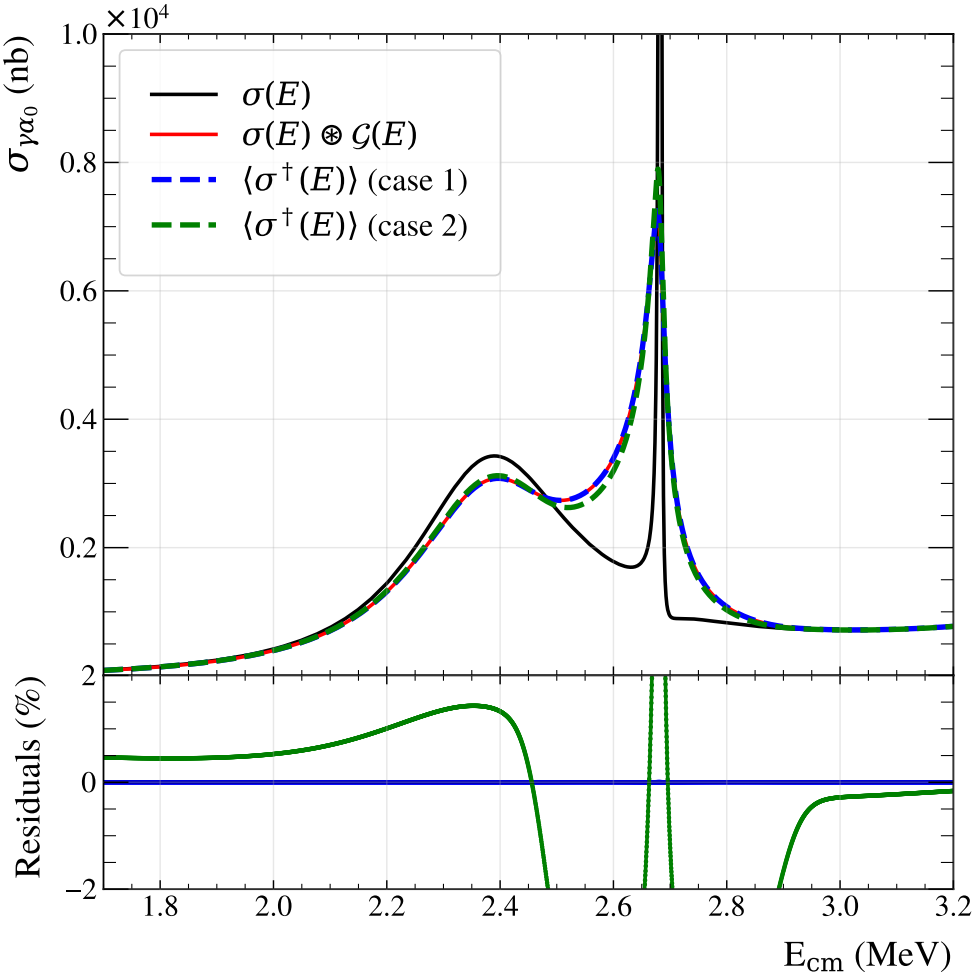

Figure A.3: TPC Resolution Effect on Extracting Cross Sections. Upper: Shows the intrinsic cross section (in black), compared with the expectation values of the reconstruction using the fine splitting formalism (green dotted line), to illustrate that it is not a simple Gaussian smearing of the intrinsic cross section (red line). For completeness, the case where the reconstruction approaches a simple Gaussian smearing, using a flat beam profile, is shown in blue. **Lower:** Shows the residuals of the quantities discussed compared to the intrinsic cross section.

In practice. Measurements in the TPC are subject to finite bin size effects in addition to the resolution described above. While it is clear that a correction is needed, the underlying cross section can be reproduced provided the detector response is well understood. However, this method fundamentally relies on having a model of the underlying cross section. For ^{16}O photo-dissociation, existing theoretical models are adequate, due to the wealth of total $^{12}\mathrm{C}(\alpha,\gamma)^{16}\mathrm{O}$ cross section measurements. This is not the case for the ^{12}C photo-dissociation cross section. A more appropriate approach would be to use R-matrix theory, where all detector responses are applied to an underlying model that is varied to best match the experimental data. This is, in fact, what was performed for the ^{12}C analysis in this work, since the R-matrix model was a simple single-level fit and data were not split across the width of the beam to simplify the response. However, such an R-matrix approach for ^{16}O analysis was beyond the scope of this thesis.

The formalism for fine splitting with finite bin sizes used in the ^{16}O analysis is presented below. The effective cross section was reconstructed from the data for a given energy bin from a to b using

$$\langle\sigma_{\gamma\alpha}\rangle = \frac{\int_a^b S(E)\,dE}{\int_a^b \left[\int_{-\infty}^{\infty} \mathcal{L}\,G(E')\,\mathcal{G}(E-E')\,dE'\right] dE}. \tag{A.2.2.5}$$

This quantity is evaluated at the TPC reconstructed energy (expectation values are given by equation (A.1.3.1)).

The correction factor is then evaluated by defining the expectation value for the given slice

$$\langle\sigma^{\dagger}_{\gamma\alpha}\rangle = \frac{\int_a^b \left[\int_{-\infty}^{\infty} \mathcal{L}\,G(E')\,\sigma^{\dagger}_{\gamma\alpha}(E')\,\mathcal{G}(E-E')\,dE'\right]}{\int_a^b \left[\int_{-\infty}^{\infty} \mathcal{L}\,G(E')\,\mathcal{G}(E-E')\,dE'\right] dE}, \tag{A.2.2.6}$$

which reduces to

$$\langle\sigma^{\dagger}_{\gamma\alpha}\rangle = \frac{\int_a^b \left[\int_{-\infty}^{\infty} G(E')\,\sigma^{\dagger}_{\gamma\alpha}(E')\,\mathcal{G}(E-E')\,dE'\right]}{\int_a^b \left[\int_{-\infty}^{\infty} G(E')\,\mathcal{G}(E-E')\,dE'\right] dE}. \tag{A.2.2.7}$$

Similarly, the correction is given by

$$f_{\rm cor} = \frac{\sigma^{\dagger}_{\gamma\alpha}(E^{\rm tpc}_{\rm cm})}{\langle\sigma^{\dagger}_{\gamma\alpha}\rangle}, \tag{A.2.2.8}$$

ans at this stag one may calculate the detailed balance, f_{db}, evaluated at the effective energy to convert the cross section to the forward radiative capture reaction.

$$\sigma_{\alpha\gamma} = \frac{\sigma_{\gamma\alpha}}{f_{db}(E^{\rm tpc}_{\rm cm})} \tag{A.2.2.9}$$

A.3 Angular distributions of Spin-zero Nuclei

This section reviews the polar and azimuthal angular dependence of photo-dissociation reactions concerning $J^{\pi}(0^{+})$ nuclei, and how these are used to extract observables from the data. All angles θ and ϕ are defined in the centre-of-mass frame of the standard physics coordinate system: θ is the polar angle measured from the z-axis, and ϕ is the azimuthal angle about the z-axis.

The full differential cross section for such a reaction [92] can be factorised into a polar (θ) and azimuthal (ϕ) dependence

$$\left.\frac{d\sigma_{\gamma\alpha_0}}{d\Omega}\right|_{\theta,\phi} \propto H(\phi)\, W(\theta), \tag{A.3.0.1}$$

where $W(\theta)$ describes the polar angle dependence determined by the J^{π} of the states probed and their interference, and $H(\phi)$ contains the azimuthal dependence due to the beam polarisation.

A.3.1 Polar Angle, θ

Using the partial-wave expansion as detailed in section 1.4.5, the polar-angle distribution is given by

$$\begin{aligned} W(\theta) = \sigma_{E1} W_{E1}(\cos\vartheta) + \sigma_{E2} W_{E2}(\cos\vartheta) \\ + \sqrt{\sigma_{E1}\sigma_{E2}}\cos\phi_{12}\, W_{12}(\cos\vartheta). \end{aligned} \tag{A.3.1.1}$$

The individual angular distributions W_{E1}, W_{E2}, and the interference term W_{12} are defined in terms of Legendre polynomials $P_l(\cos\theta)$ as follows

$$\begin{aligned} W_{E1}(\cos\theta) &= P_0(\cos(\theta)) - P_2(\cos(\theta)) \\ W_{E2}(\cos\theta) &= P_0(\cos(\theta)) + \frac{5}{7}P_2(\cos(\theta)) - \frac{12}{7}P_4(\cos(\theta)) \\ W_{12}(\cos\theta) &= \frac{6}{\sqrt{5}}\left(P_1(\cos(\theta)) - P_3(\cos(\theta))\right), \end{aligned}$$

where the Legendre polynomials $P_l(\cos\theta)$ of order l are explicitly given in table A.1.

l	$P_l(\cos(\theta))$
0	1
1	$\cos(\theta)$
2	$\frac{1}{2}(3\cos^2(\theta) - 1)$
3	$\frac{1}{2}(5\cos^3(\theta) - 3\cos(\theta))$
4	$\frac{1}{8}(35\cos^4(\theta) - 30\cos^2(\theta) + 3)$

Table A.1: Legendre Polynomials: A table of Legendre polynomials of order 0 to 4.

A.3.2 Azimuthal Angle, ϕ

The azimuthal distribution $H(\phi)$ arises from the polarisation of the incident γ beam, and is given by

$$H(\phi) = 1 + f\cos(2(\phi + \phi_0)) \tag{A.3.2.1}$$

where f is the fraction of linear polarisation, and ϕ_0 defines the polarisation axis [186]. Where $f = 0$ corresponds to purely circular polarisation, and $f = 1$ corresponds to purely linear polarisation.

A.3.3 Probability Density Functions

To extract physical observables from the measured angular distributions, the theoretical differential cross section must be converted into the expected counts per detector bin. The number of detected events in a given angular bin is proportional to the differential cross section times the solid angle of the bin. In spherical coordinates, the solid angle element is

$$d\Omega = \sin\theta \, d\theta \, d\phi. \tag{A.3.3.1}$$

Using equation (A.3.0.1) the expected counts in a small bin of size $d\theta$ and $d\phi$ are

$$dN(\theta, \phi) \propto \frac{d\sigma}{d\Omega}(\theta, \phi) \, d\Omega = H(\phi) \, W(\theta) \, \sin\theta \, d\theta \, d\phi. \tag{A.3.3.2}$$

Counts per θ bin. Integrating over all azimuthal angles gives the counts in a θ-bin

$$\begin{aligned} N(\theta) &\propto \int_{-\pi}^{\pi} dN(\theta, \phi) \\ &\propto W(\theta) \, \sin\theta \, d\theta \int_{-\pi}^{\pi} H(\phi) \, d\phi \\ &\propto W(\theta) \, \sin\theta \, d\theta. \end{aligned} \tag{A.3.3.3}$$

Counts per ϕ bin. Similarly, integrating over the polar angle gives the counts in a ϕ-bin

$$\begin{aligned} N(\phi) &\propto \int_{0}^{\pi} dN(\theta, \phi) \\ &\propto H(\phi) \, d\phi \int_{0}^{\pi} W(\theta) \, \sin\theta \, d\theta \\ &\propto H(\phi) \, d\phi. \end{aligned} \tag{A.3.3.4}$$

To extract information from the angular distributions, Probability Density Functions (PDF) for both θ and ϕ are constructed. The detector efficiency profiles, $\epsilon(\theta)$ and $\epsilon(\phi)$, are

applied directly to the PDFs before normalising to unity when fitting data, if appropriate.

Polar angle distribution. The PDF fitted to the data to extract information from the polar angle is given as

$$N\left(\theta \mid \frac{\sigma_{E2}}{\sigma_{E1}}, \phi_{12}\right) = \frac{W(\theta)\,\epsilon(\theta)\,\sin\theta}{\int_0^\pi W(\theta)\,\epsilon(\theta)\,\sin\theta\,d\theta}. \tag{A.3.3.5}$$

Where it has been re-parameterised in terms of the ratio of cross sections to improve fit stability.

Azimuthal angle distribution. The PDF fitted to the data to extract information from the azimuthal angle is given as

$$N(\phi \mid f, \phi_0) = \frac{H(\phi)\,\epsilon(\phi)}{\int_{-\pi}^\pi H(\phi)\,\epsilon(\phi)\,d\phi}. \tag{A.3.3.6}$$

A.3.4 Fitting Scheme & Error Estimation

To fit the data, either a one-degree binned or unbinned negative log-likelihood (NLL) minimisation was used. Similar to standard χ^2 fitting, the best-fit parameters are obtained by minimising a cost function, ℓ, which is the negative log-likelihood $-\ln\mathcal{L}$, defined as

$$\ell = -\ln\mathcal{L} = -\sum_i \ln f(x_i \mid \theta), \tag{A.3.4.1}$$

where $f(x_i \mid \theta)$ is the PDF evaluated at the observed data points x_i, given the model parameters θ.

Error estimation. The uncertainties on the fitted parameters are estimated by varying the parameters around their best-fit values and evaluating the change in ℓ for a given confidence interval. This approach is based on Wilks' theorem, which states that in the large-sample limit, the likelihood ratio test statistic, t, follows a χ^2 distribution,

where the test statistic is defined as

$$t = 2[\ell - \ell_{\text{min}}]. \tag{A.3.4.1}$$

Rearranging this gives,

$$\ell - \ell_{\text{min}} = \frac{1}{2}t, \tag{A.3.4.2}$$

where the value of t depends on the number of parameters being varied and the desired confidence level [208].

In the case of varying one parameter at a time, 1σ confidence intervals correspond to $t = 1.00$, meaning the negative log-likelihood increases by 0.5 from its minimum. However, when varying multiple parameters simultaneously, larger values of t are required. Table A.2 shows the values of t needed to obtain different confidence levels for varying numbers of fit parameters.

Confidence Level	**t**				
	$n = 1$	$n = 2$	$n = 3$	$n = 4$	$n = 5$
1 σ	1.00	2.30	3.53	4.72	5.89
2 σ	2.71	4.61	6.25	7.78	9.24
3 σ	3.84	5.99	7.82	9.49	11.1
4 σ	6.63	9.21	11.3	13.3	15.1

Table A.2: Log-likelihood confidence levels: The required test statistic values for obtaining confidence regions when varying multiple parameters. The table values were obtained from reference [208].

A.4 Energy Averaging of Fit Parameters

A.4.1 Single Measurement

In the case where all data are considered across the width of the beam, and the energy is obtained from the unfolded beam profile, equation (A.1.1.1), the theoretical expectation values for the extracted partial cross sections, σ_L, is defined as

$$\langle \sigma_L^\dagger \rangle = \frac{\int_0^\infty \sigma_L^\dagger(E)\, G(E)\, dE}{\int_0^\infty G(E)\, dE}, \tag{A.4.1.1}$$

where $\sigma_L(E)$ is a model of the underlying partial cross section of angular momentum L.

As the cosine of the phase angle, ϕ_{12}, appears in the cross term of equation (A.3.1.1), the energy dependence of the partial cross sections must be accounted for, as discussed in reference [185]. This leads to the following expression

$$\langle \cos\phi_{12}^\dagger \rangle = \frac{\int_0^\infty \cos\phi_{12}^\dagger(E) \sqrt{\sigma_1^\dagger(E)\, \sigma_2^\dagger(E)}\, G(E)\, dE}{\sqrt{\langle \sigma_1^\dagger \rangle \langle \sigma_2^\dagger \rangle} \int_0^\infty G(E)\, dE}. \tag{A.4.1.2}$$

A.4.2 Fine Splitting

To present the data at their measured TPC energy, one needs to account for the TPC response; the following expectation values are defined

$$\langle \sigma_L^\dagger \rangle = \frac{\int_a^b \left[\int_{-\infty}^\infty \sigma_L^\dagger(E')\, G(E')\, \mathcal{G}(E - E')\, dE' \right] dE}{\int_a^b \left[\int_{-\infty}^\infty G(E')\, \mathcal{G}(E - E')\, dE' \right] dE}, \tag{A.4.2.1}$$

and

$$\langle \cos\phi_{12}^\dagger \rangle = \frac{\int_a^b \left[\int_{-\infty}^\infty \cos\phi_{12}^\dagger(E') \sqrt{\sigma_1^\dagger(E')\, \sigma_2^\dagger(E')}\, G(E')\, \mathcal{G}(E - E')\, dE' \right] dE}{\sqrt{\langle \sigma_1^\dagger \rangle \langle \sigma_2^\dagger \rangle} \int_a^b \left[\int_{-\infty}^\infty G(E')\, \mathcal{G}(E - E')\, dE' \right] dE}. \tag{A.4.2.2}$$

A.4.3 Correction Factor

For comparison with data, it is possible to apply a correction factor (for the fine splitting case, these would be evaluated at E_{cm}^{tpc})

$$f_{\rm cor} = \frac{\cos\phi_{12}^{\dagger}(E_{\rm cm}^{\rm tpc})}{\langle\cos\phi_{12}^{\dagger}(E)\rangle}, \tag{A.4.3.1}$$

or

$$f_{\rm cor} = \frac{\sigma_L^{\dagger}(E_{\rm cm}^{\rm tpc})}{\langle\sigma_L^{\dagger}\rangle}. \tag{A.4.3.2}$$

B

γ-beam Unfolding & Fitting

At HIγS, the beam energy profiles are measured by directing a heavily attenuated beam onto a HPGe detector, producing spectra such as that shown in figure B.1a.

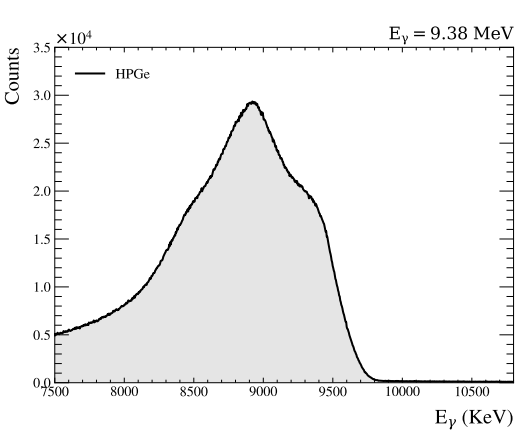

(a) Raw HPGe Spectrum: Raw spectrum measured during the OTPC experiment.

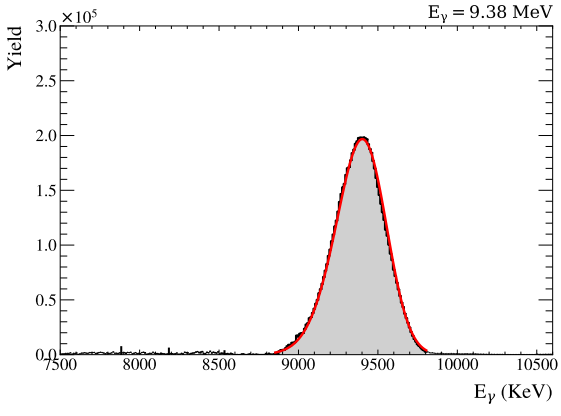

(b) Unfolded spectrum: Unfolded spectrum, measured during the OTPC experiment, using the `HORST` code.

Figure B.1: HPGe spectra: side-by-side comparison of raw and unfolded spectra.

The photo-peak, as shown, is typically overlapped by escape peaks and Compton

background. To extract the true photo-peak, an unfolding procedure is applied using `HORST` [181]. This requires two inputs: the measured 1D HPGe spectrum and a 2D simulated response matrix, obtained from a `Geant4` simulation of the HPGe detector stationed in the UTR. Key parameters for the simulation include the diameter of the collimator used, and the physical offset of the HPGE detector from the beam centre.

The algorithm estimates initial parameters for the underlying γ beam distribution, then iteratively convolves trial distributions with the detector response and fits the result to the measured data. The iteration with the lowest χ^2 yields the unfolded spectrum.

The unfolded spectra were then fitted with skewed Gaussian distributions, defined as,

$$G(x \,|\, \xi, \omega, \alpha) = \frac{1}{\omega\sqrt{2\pi}} \exp\Big[-\frac{1}{2}\Big(\frac{x-\xi}{\omega}\Big)^2\Big]\Big[1 + \operatorname{erf}\Big(\alpha\frac{x-\xi}{\omega\sqrt{2}}\Big)\Big],$$

where ξ represents the location parameter, ω the scale parameter, and α the shape parameter controlling the skewness. The mean (μ) and standard deviation (σ) of the distribution are obtained by

$$\mu = \xi + \omega\delta\sqrt{\frac{2}{\pi}}, \quad \sigma = \omega\sqrt{1 - \frac{2\delta^2}{\pi}},$$

where

$$\delta = \frac{\alpha}{\sqrt{1+\alpha^2}}.$$

C

OTPC: Simple $^{12}C(\alpha, \gamma_0)$ Model

A selection of the world data for the $^{12}C(\alpha, \gamma_0)$ reaction [40, 41, 58–61, 65, 97] were analysed using a two-level non-interfeering R-matrix matrix approximation. The narrow $J^\pi(2^+)$ resonance parameters were fixed using values from literature [46, 54], while the broader $J^\pi(1^-)$ resonance was fitted using `AZURE2` [38]. Figure C.1 shows the resulting fit to the capture cross section data, with the fit parameters detailed in table C.1. The fit used a channel radius of 5 fm. It is important to highlight that this fit and the extracted parameters have limited use. It was a purely phenomenological exercise used to estimate the shape of the cross section in the observed region, for use in the OTPC analysis (experiment 1) in this thesis.

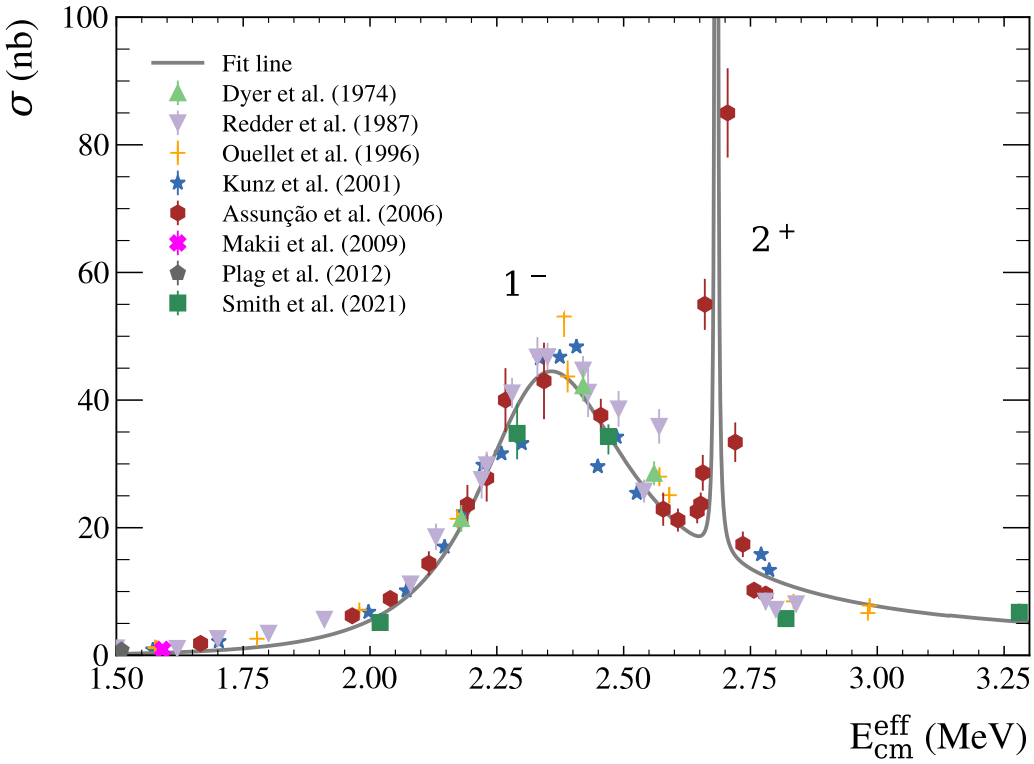

Figure C.1: Simple Fit to $^{12}C(\alpha,\gamma_0)$ Data: A simple fit to the $^{12}C(\alpha,\gamma_0)$ world data is shown, using a non-interfering two-level approximation. This figure was taken from reference [178].

J^π	Energy (MeV)	Γ_γ (eV)	Γ_α (keV)
1^-	**9.55**	**0.0168**	**427**
2^+	9.84	0.0057	0.620

Table C.1: Resonance Parameters for Simple $^{12}C(\alpha,\gamma_0)$ Model: Fit parameters in bold font were obtained through minimisation, the remaining were fixed from literature.

D

OTPC: Monte-Carlo Efficiency Profile

When fitting the θ_{cm} angular distributions in the OTPC, an efficiency correction profile is required. This profile accounts for both the loss of events in each angular bin due to the β angle cuts ($\beta_{\mathrm{Lab}} < 20$ and $\beta_{\mathrm{Lab}} > 42$), and for resolution effects arising from reconstruction biases and angular straggling. To generate the profile, a Monte Carlo simulation was used, with the basic procedure outlined below.

1. Angles were isotropically generated in the centre-of-mass frame to obtaib θ_{cm} and ϕ_{cm}.

2. These were boosted to the laboratory frame using the average γ energy, obtaining θ_{Lab} and ϕ_{Lab}.

3. The tangent unit vector aligned with these angles was defined, and was subsequently rotated randomly due to the straggle contribution about its own axis, estimated using `SRIM`.

D. OTPC: Monte-Carlo Efficiency Profile

4. The straggle corrected angles were converted to the native OTPC coordinate system, to obtain α_{Lab} and β_{Lab}.

5. The known angular resolutions were applied to α_{Lab} and β_{Lab} .

6. The same β_{Lab} cuts applied to the experimental data were applied here.

7. The new α_{Lab} and β_{Lab} were combined to obtain θ_{Lab}.

8. Then θ_{Lab} was boosted to the centre-of-mass frame, obtaining θ'_{cm} using the average γ beam energy.

9. Finally θ'_{cm} and the generated θ_{cm} are binned and divided to obtain the efficiency profile $\epsilon(\theta)$.

An example efficiency curve is shown in figure D.1. The left panel shows the generator level centre-of-mass angles, θ_{cm} (in black), and the centre-of-mass angles after cuts and smearing, θ'_{cm} (in red); the right panel shows the efficiency profile obtained from these data.

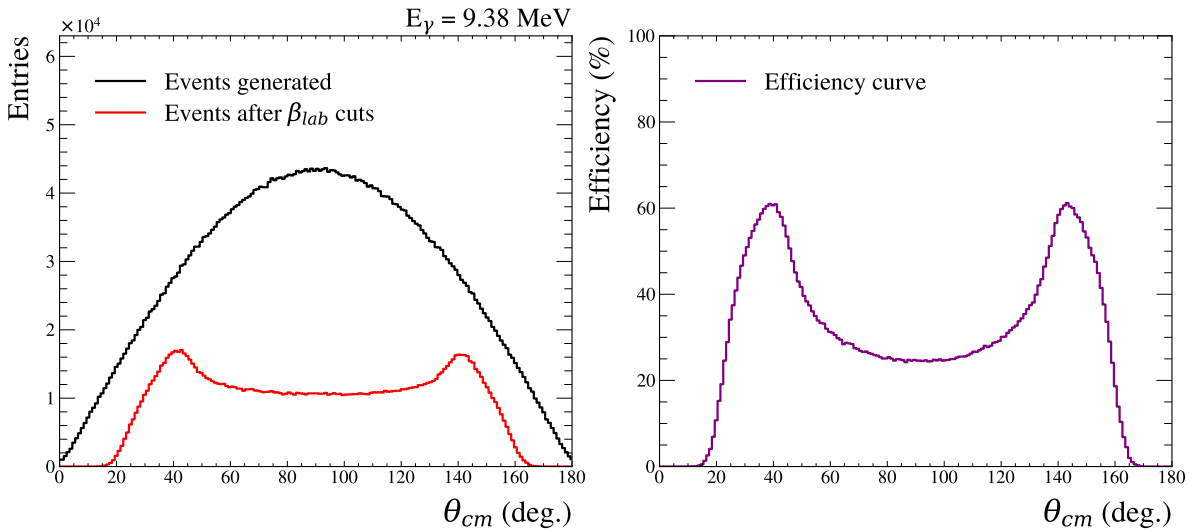

Figure D.1: Scattering Angle Efficiency Correction for the OTPC: The OTPC efficiency curve analysis for E_γ=9.38 MeV is presented. This procedure accounts for both fiducial cuts and resolution effects. **Left:** The generator level angles (black) and the angles after applying cuts and resolution (red) are displayed. **Right:** The efficiency curve, obtained by dividing these two quantities, is provided. The procedure to obtain this profile is explained in detail in the text.

E

eTPC: Monte-Carlo

Realistic simulated datasets were used in this work for various purposes, including determining resolutions and efficiencies of the experimental data measured with the eTPC. Two synthetic datasets were generated for each nominal beam energy: one simulating the two-body $^{16}\mathrm{O}(\gamma,\alpha_0)^{12}\mathrm{C}$ reaction, and the other the three-body $^{12}\mathrm{C}(\gamma,\alpha_0)^{8}\mathrm{Be}$ reaction. Both datasets contain approximately 200,000 events each, limited by computational overheads; An example simulated $^{16}\mathrm{O}(\gamma,\alpha_0)$ event is shown in figure E.1.

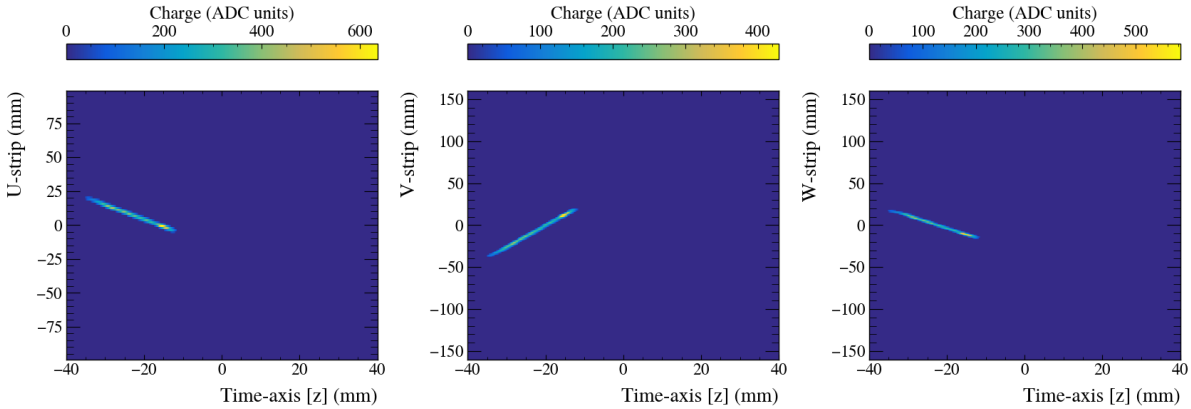

Figure E.1: eTPC Simulated data: A simulated ^{16}O photo-dissociation event shown for all three projections.

Overview. The Monte-Carlo package used in this work forms a part of the `TPCRECO` software suite. The simulation uses a modular framework where independent modules pass information through a shared `ModuleExchangeSpace`. The chain used in this analysis consists of the following key modules:

- **Generator**: Creates truth-level primary events with realistic kinematics.
- **GeantSim**: Applies `Geant4` response, accounting for primary ion straggling, range, and energy loss.
- **TriggerSimulator**: Simulates the self-triggering mode of the TPC by shifting the event such that the first z position of the track that would reach the readout plane is now at the trigger position.
- **TrackTruncator**: Ensures events are contained within the detectors' active volume and within the GET electronics time buffer.
- **TPCDigitizerSRC**: Applies detector response, including both diffusion and GET electronics response.
- **EventFileExporter**: Outputs the simulated data in ROOT format.

The **Generator** module creates primary events sampling beam energies from the measured γ beam energy profiles, parameters were taken from table 8.8. The cross section

for the ^{16}O reaction was taken from [46]. For the ^{12}C reaction, the low energy cross section data came from [140], and in the high energy region, a flat cross section was assumed due to lack of available data[1]. Event vertices are distributed uniformly along the beam direction within the central 200 mm of the chamber. Event kinematics are calculated in the centre-of-mass frame, with isotropic angular distributions for the decay products, then boosted to the laboratory frame and rotated to the detector coordinate system.

The **GeantSim** module tracks the primary particles through the detector geometry using `Geant4`. This provides a realistic response of the primary ions' range and straggle in the CO_2 gas, where the pressure is selected to match the experimental conditions. The **TriggerSimulator** then applies the experimental triggering logic, identifying when the first ionisation would reach the readout plane and shifting the event timing accordingly.

Events are processed by the **TrackTruncator** to ensure full containment within both the detector active volume and the GET electronics time window. The **TPCDigitizerSRC** module is then used to apply the further detector response. Ionisation is generated along the primary ion tracks, then diffused according to `Garfield++` calculations. The diffusion parameters, d, were simulated at each of the TPC working points; the transverse and longitudinal diffusion coefficients for each experimental setting are shown in figure E.2. Using these coefficients, the diffusion standard deviation is obtained by $\sigma = d\sqrt{h}$, where h is taken to be half the chamber length. The resulting charge clouds are projected onto the UVW readout strips, accounting for the diamond structure of the pads, where the GET electronics response is also applied using equation E.0.0.1,

$$h(t) = A \cdot \exp\left(-3\frac{t}{\tau}\right) \cdot \left(\frac{t}{\tau}\right)^3 \cdot \sin\left(\frac{t}{\tau}\right), \tag{E.0.0.1}$$

where τ is the peaking time, and A is related to the gain and of the GET electronics [190]. Examples of the get response are shown in figure E.3.

[1]The energy dependence of the simulation is less critical in the high energy region, as event separation in the experimental data is better resolved.

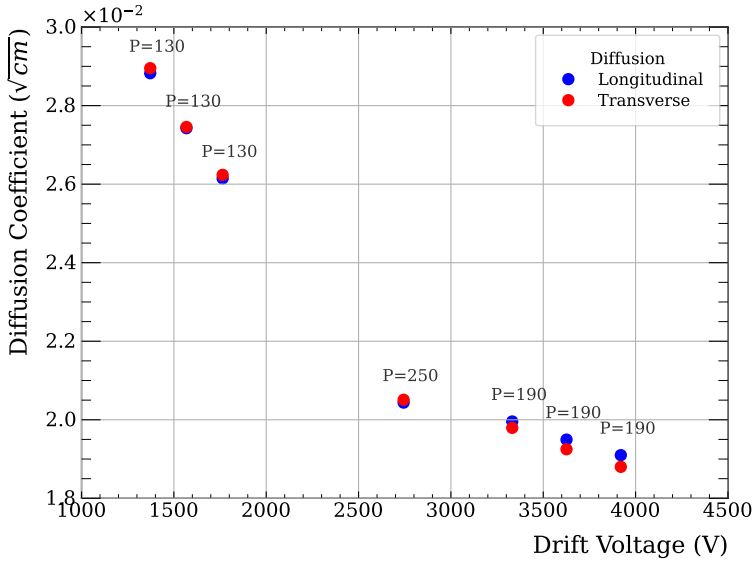

Figure E.2: Simulated Diffusion Coefficients: Transverse (red) and longitudinal (blue) diffusion coefficients for different experimental settings obtained from `Garfield++` simulations. The pressure of each point is indicated in the figure.

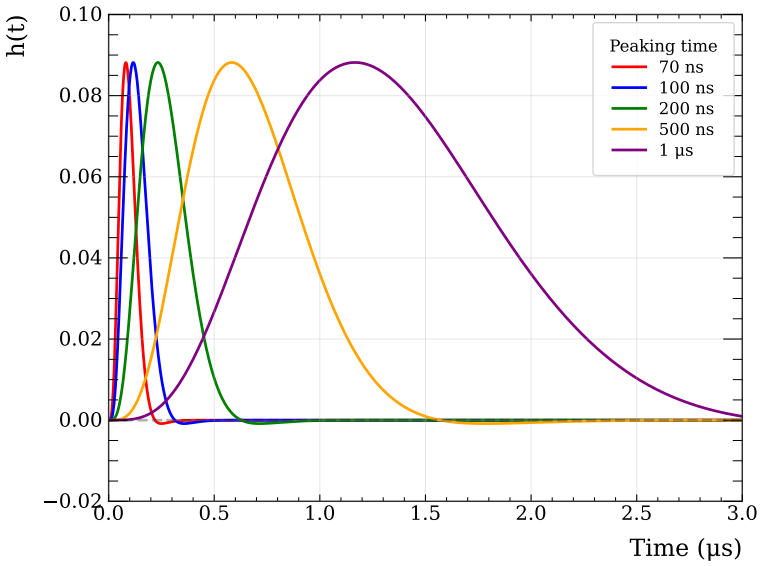

Figure E.3: Response Function Approximation for the eTPC: The GET electronics response function showing the characteristic pulse shape with delayed peak and damped oscillations for different shaping time parameters.

Finally, the **EventFileExporter** can be used to save the events in ROOT format. These simulated data are then processed using identical reconstruction algorithms as the experimental data.

Calibration. To use these simulated data to analyse the experimental, it was essential to verify that both datasets have approximately the same centre-of-mass calibration. The comparison of these is shown in figure E.4

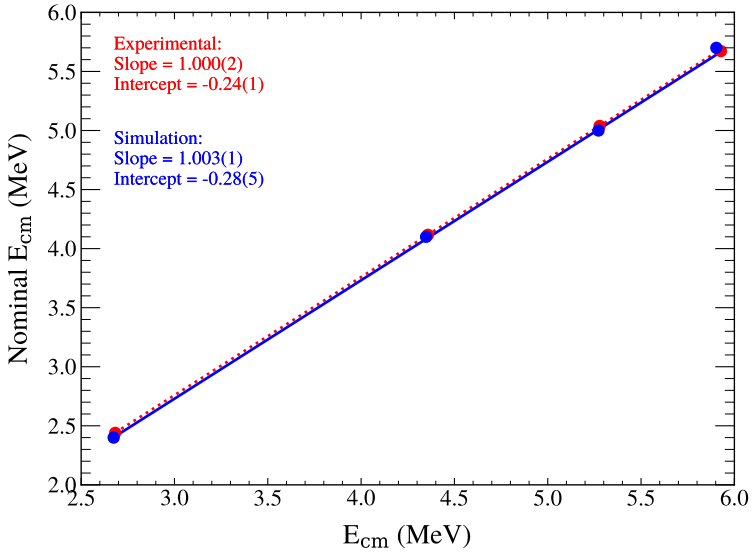

Figure E.4: Simulation Calibration Comparison in the eTPC: Comparison of the simulation and experimental centre-of-mass linear energy calibration.

F

eTPC: Reconstructed Spectra

The fully calibrated centre-of-mass energy spectra, reconstructed using the eTPC, are shown for both ^{16}O (figure F.1) and ^{12}C (figure F.2) photo-dissociation reactions. Each panel shows a different nominal beam energy, where the blue curves represent the incident beam energy profiles. These are included to highlight the eTPCs ability to overcome the limitations of the broad γ beam.

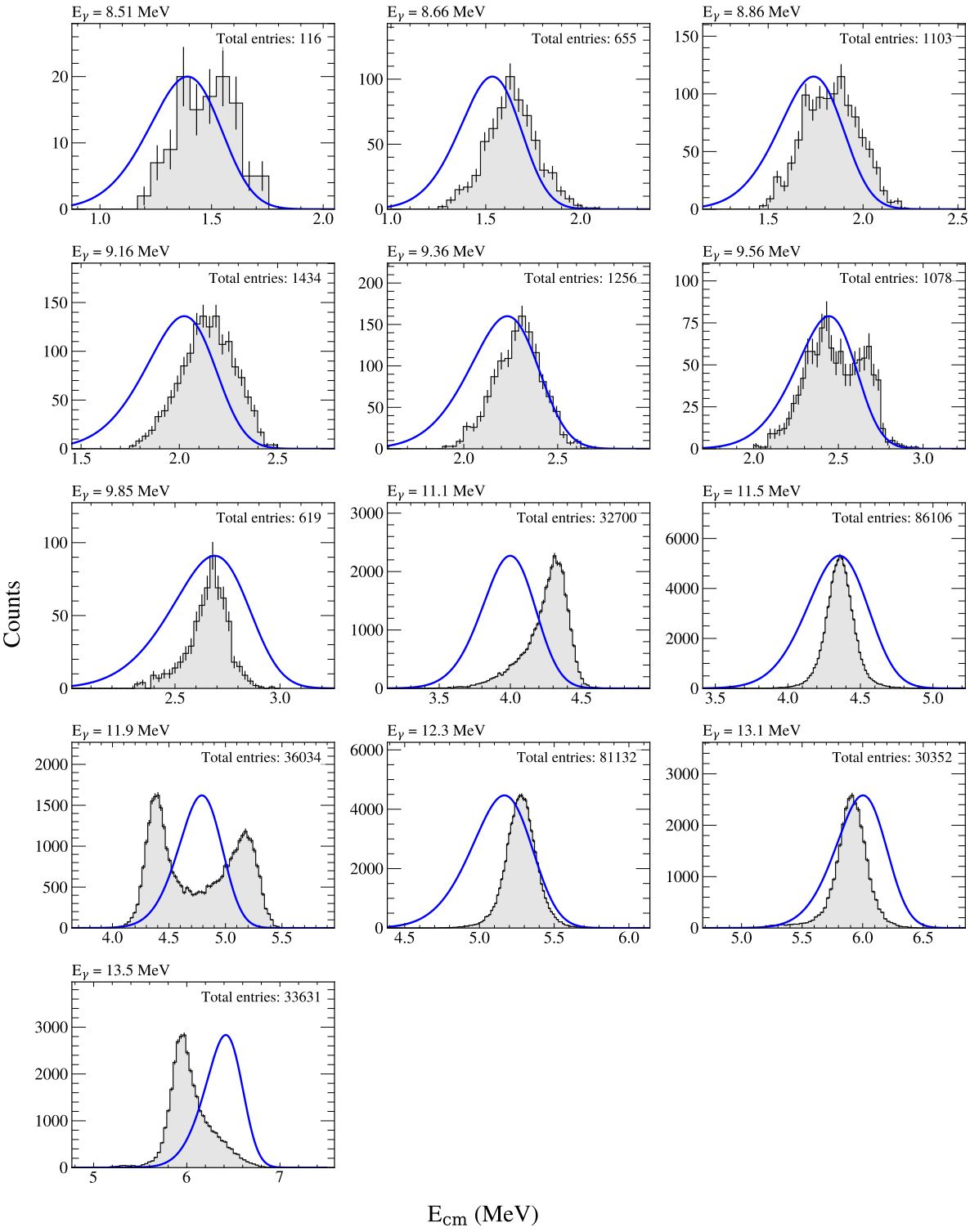

Figure F.1: Calibrated ^{16}O Centre-of-mass Spectra: Each panel shows the reconstructed ^{16}O centre-of-mass energy distributions in grey, with the unfolded beam profile shifted by the reaction Q-value in blue. This is included to highlight the eTPCs ability to overcome the limitations of the broad γ beam.

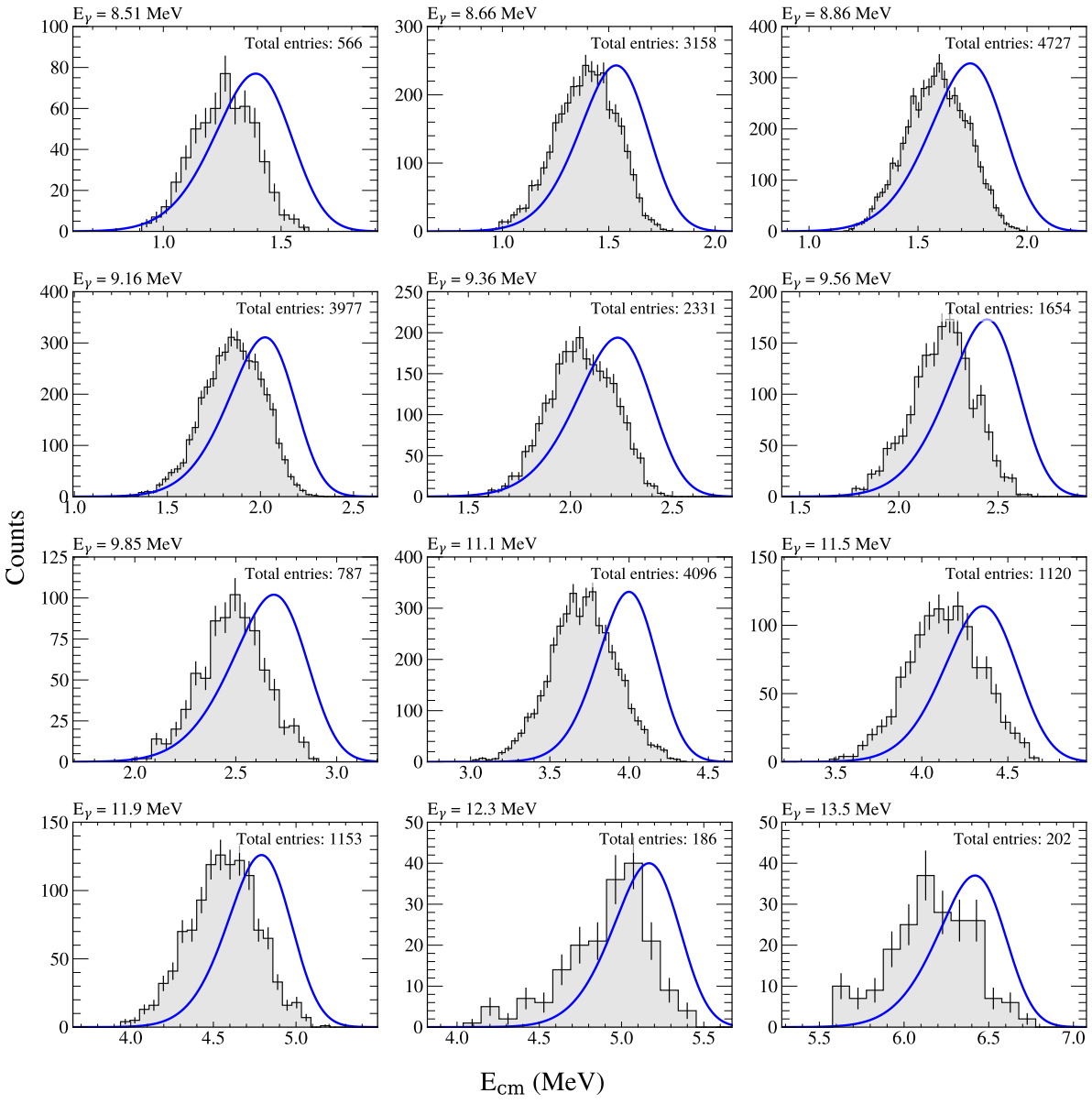

Figure F.2: Calibrated ^{12}C Centre-of-mass Spectra: Each panel shows the reconstructed ^{12}C centre-of-mass energy distributions in grey, with the unfolded beam profile shifted by the reaction Q-value in blue. This is included to highlight the eTPCs ability to overcome the limitations of the broad γ beam.

G

eTPC: Intensity Verification

In order to verify beam intensity measurements, the relatively well-known $^{16}\mathrm{O}(\gamma,\alpha_0)$ cross section was used to obtain the beam intensity from the ^{16}O counts in the eTPC. The total number of ^{16}O counts, $N_{^{16}\mathrm{O}}(E)$, is obtained by efficiency-correcting the eTPC spectra at each given beam energy, $S(E,\cos\theta_{\mathrm{beam}})$

$$N_{^{16}\mathrm{O}}(E) = \int_{-1}^{1} \frac{S(E,\cos\theta_{\mathrm{beam}})}{\epsilon(\cos\theta_{\mathrm{beam}})} d\cos\theta_{\mathrm{beam}}, \tag{G.0.0.1}$$

where $\epsilon(\cos\theta_{\mathrm{beam}})$ is the corresponding efficiency curve. This is fitted with the following model

$$C(E|\zeta,\omega,\alpha) = \psi\, I_\gamma \int_{-\infty}^{\infty} \sigma_{\gamma\alpha_0}(E')\, G(E'|\zeta,\omega,\alpha)\, g(E-E')\, dE', \tag{G.0.0.2}$$

using χ^2 minimisation, to extract the beam intensity I_γ. Here $\psi = n\,x\,f_{\mathrm{LT}}\,t_{\mathrm{TPC}}$ is an amplitude term fixed using values from table 8.21, n is the number of targets per unit

volume, x is the active length of the TPC, f_{LT} is the live-time of the TPC, and t_{TPC} is the measurement time. The beam profile is denoted by $G(E)$, which has values taken from table 8.8, and $g(E)$ denotes the eTPC resolution.

For the low-energy data, the skewed Gaussian parameters were fixed at their central values (when allowed to vary, minimal deviation was observed, confirming the validity of the unfolding procedure). For the high-energy data, the beam parameters were allowed to vary by 5%, since these distributions were obtained via simulation and no errors were quoted. The minimisation was constrained to ensure that the resulting distributions remained physically realistic, i.e, consistent with the raw measured HPGe spectra. The eTPC resolution was constrained within its measured uncertainty. Two examples of the fitted efficiency-corrected ^{16}O spectra are shown in figure G.1, the left panel shows $E_\gamma = 9.56$ MeV and the right panel $E_\gamma = 11.5$ MeV.

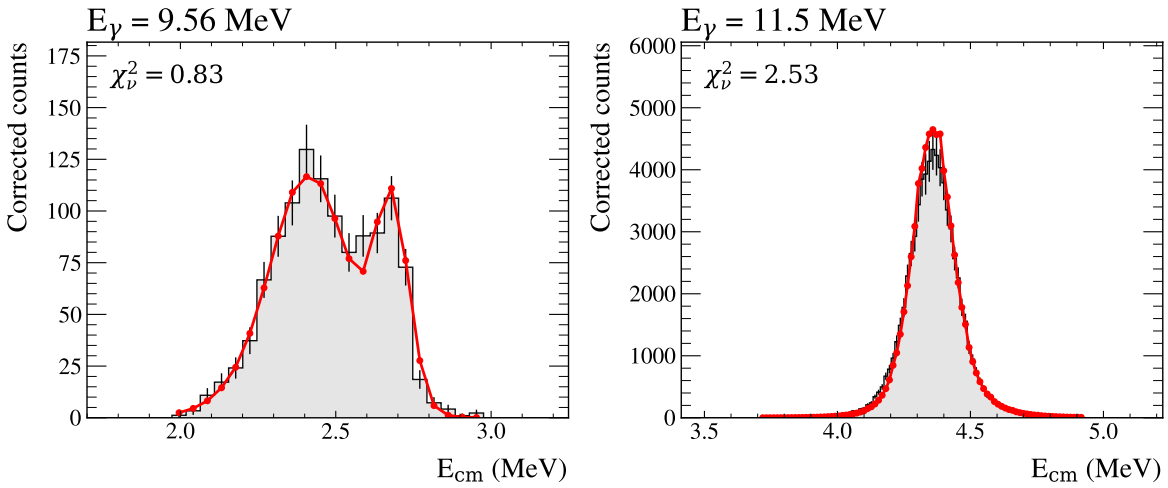

Figure G.1: Fitted Centre-of-Mass Energy Spectra: The calibrated centre-of-mass ^{16}O energy spectra (grey histograms) are fitted with the cross section model of reference [46], folded with the beam profile, and convolved with the eTPC resolution (red line). This procedure yielded beam intensities for each nominal beam energy, listed in table G.1.

In the fitting procedure, there was no consideration of any error in the cross section model, as this is not provided. The cross section model of reference [46] is constrained at high energies by the data of Brochard *et al.* [64] and Schurmann *et al.* [63]. These data, shown in figure G.2, were used to calculate the average percentage difference between

the model and their measurements. This was found to be 23%, which is an estimate of the systematic error on the model at high energies.

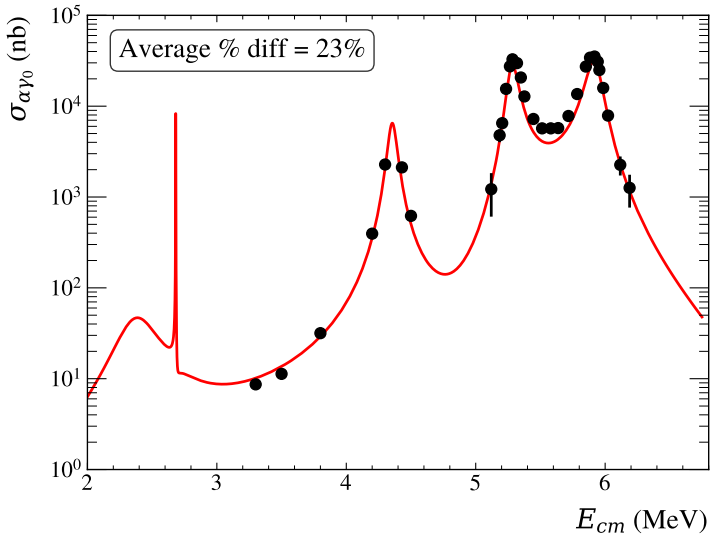

Figure G.2: Cross Section Error Estimation: R-matric fit to the world data of the $^{12}C(\alpha,\gamma_0)$ reaction [46]. The high energy data points shown are from Brochard *et al.* [64], and Schurmann *et al.* [63]. The average percentage error between the fit line and the data points has been found to be 23%.

The beam intensity values from this analysis are listed in table G.1.

E_γ (MeV)	I_γ (γ/s)
8.51	$3.67 \times 10^8 \pm 3.65 \times 10^7$
8.66	$3.36 \times 10^8 \pm 1.37 \times 10^7$
8.86	$3.58 \times 10^8 \pm 1.15 \times 10^7$
9.16	$3.87 \times 10^8 \pm 1.05 \times 10^7$
9.36	$3.93 \times 10^8 \pm 1.18 \times 10^7$
9.56	$3.67 \times 10^8 \pm 1.15 \times 10^7$
11.1	$4.08 \times 10^8 \pm 5.35 \times 10^6$
11.5	$3.69 \times 10^8 \pm 6.42 \times 10^6$
11.9	$3.47 \times 10^8 \pm 2.86 \times 10^6$
12.3	$3.07 \times 10^8 \pm 3.99 \times 10^6$
13.1	$2.80 \times 10^7 \pm 5.18 \times 10^5$
13.5	$1.16 \times 10^8 \pm 3.51 \times 10^6$

Table G.1: Beam Intensity Verification Values: The optimised values for beam intensity from the minimisation procedure to the $^{12}C(\alpha,\gamma)$ cross section are listed. The uncertainties shown are statistical; energies 11.1 MeV and above have an additional 23% systematic uncertainty due to the normalisation procedure.

H

eTPC: Angular Reconstruction Bias

The reconstruction bias of the $\theta_{\mathrm{det}}^{\mathrm{Lab}}$ angle is obtained by reconstructing simulated data, as described in section 8.1.1. It is parametrised using the following equation

$$Y(\cos\theta_{\mathrm{DET}}) = \frac{180}{\pi} A \sin(\omega \cos\theta_{\mathrm{DET}} + \phi) + b, \tag{H.0.0.1}$$

where A is the amplitude, ϕ the shift, ω the angular frequency, and b the offset. All values for both reaction channels are listed in table H.1.

E_γ (MeV)	A	ω	ϕ	b
		^{12}**C**		
8.51	0.01954(5)	1.87(9)	-0.07(4)	0.0011(5)
8.66	0.01718(4)	1.95(9)	-0.03(4)	0.0004(4)
8.86	-0.0145(3)	-2.20(8)	0.03(4)	-0.0001(3)
9.16	-0.0131(3)	-2.39(6)	-0.02(3)	0.0004(3)
9.36	-0.0118(3)	-2.60(6)	-0.01(3)	0.0000(2)
9.56	-0.0105(3)	-2.45(7)	-0.07(3)	-0.0003(2)
9.85	-0.0094(3)	-2.52(7)	-0.04(3)	-0.0001(2)
11.1	-0.0105(2)	-2.69(4)	0.02(2)	0.0001(2)
11.5	-0.0099(2)	-2.81(4)	-0.02(2)	-0.0000(1)
11.9	-0.0093(2)	-2.83(3)	-0.02(2)	0.0002(1)
12.3	-0.0082(2)	-2.73(4)	0.02(2)	-0.0000(1)
13.1	-0.0082(1)	-2.84(3)	-0.01(2)	0.0002(1)
13.5	-0.0075(1)	-2.81(3)	-0.00(2)	0.00026(9)
		^{16}**O**		
8.51	0.0164(5)	1.8(1)	-0.05(4)	0.0004(5)
8.66	-0.0149(3)	-2.33(6)	-0.02(3)	-0.0005(3)
8.86	-0.0140(3)	-2.28(6)	0.03(3)	0.0003(6)
9.16	-0.0115(3)	-2.37(7)	0.04(3)	-0.00008(2)
9.36	-0.0101(3)	-2.52(6)	-0.01(3)	0.0002(2)
9.56	-0.0095(2)	-2.64(6)	0.02(3)	0.000(2)
9.85	-0.0087(2)	-2.59(6)	0.00(3)	-0.0001(2)
11.1	-0.00873(3)	-2.555(8)	-0.028(4)	0.00008(2)
11.5	-0.00834(3)	-2.563(8)	-0.033(4)	0.00014(2)
11.9	-0.00768(3)	-2.496(9)	-0.022(5)	0.00022(2)
12.3	-0.00589(2)	-2.45(1)	-0.067(5)	0.00025(2)
13.1	-0.00582(2)	-2.587(1)	-0.049(5)	0.00016(2)
13.5	-0.00545(2)	-2.54(1)	-0.059(5)	0.00016(2)

Table H.1: Angular Bias Parametrised: The parameters corresponding to equation (H.0.0.1) used for correcting the reconstructed $\theta_{\text{det}}^{\text{Lab}}$ angles for both ^{12}C and ^{16}O photo-dissociation reactions are given. Here A is an amplitude, ϕ a shift, ω an angular frequency, and b an offset.

I

eTPC: ^{16}O Angular Distributions

All angular distributions from the analysis of the photo-dissociation of ^{16}O are shown here in figures I.1 I.2 I.3. Each panel lists the effective reconstructed energy, extracted fit parameters, and total counts and corrected counts. All values are tabulated in table 8.24. The fit function is given again here for convenience

$$\begin{aligned} W(\theta) = \sigma_{E1} W_{E1}(\cos\vartheta) + \sigma_{E2} W_{E2}(\cos\vartheta) \\ + \sqrt{\sigma_{E1}\sigma_{E2}}\cos\phi_{12}\, W_{12}(\cos\vartheta). \end{aligned} \tag{I.0.0.1}$$

This formula consists of three individual angular distributions: a pure $E1$ contribution W_{E1}, a pure $E2$ contribution W_{E2}, and the interference term W_{12}. These are defined in terms of Legendre polynomials $P_l(\cos\theta)$.

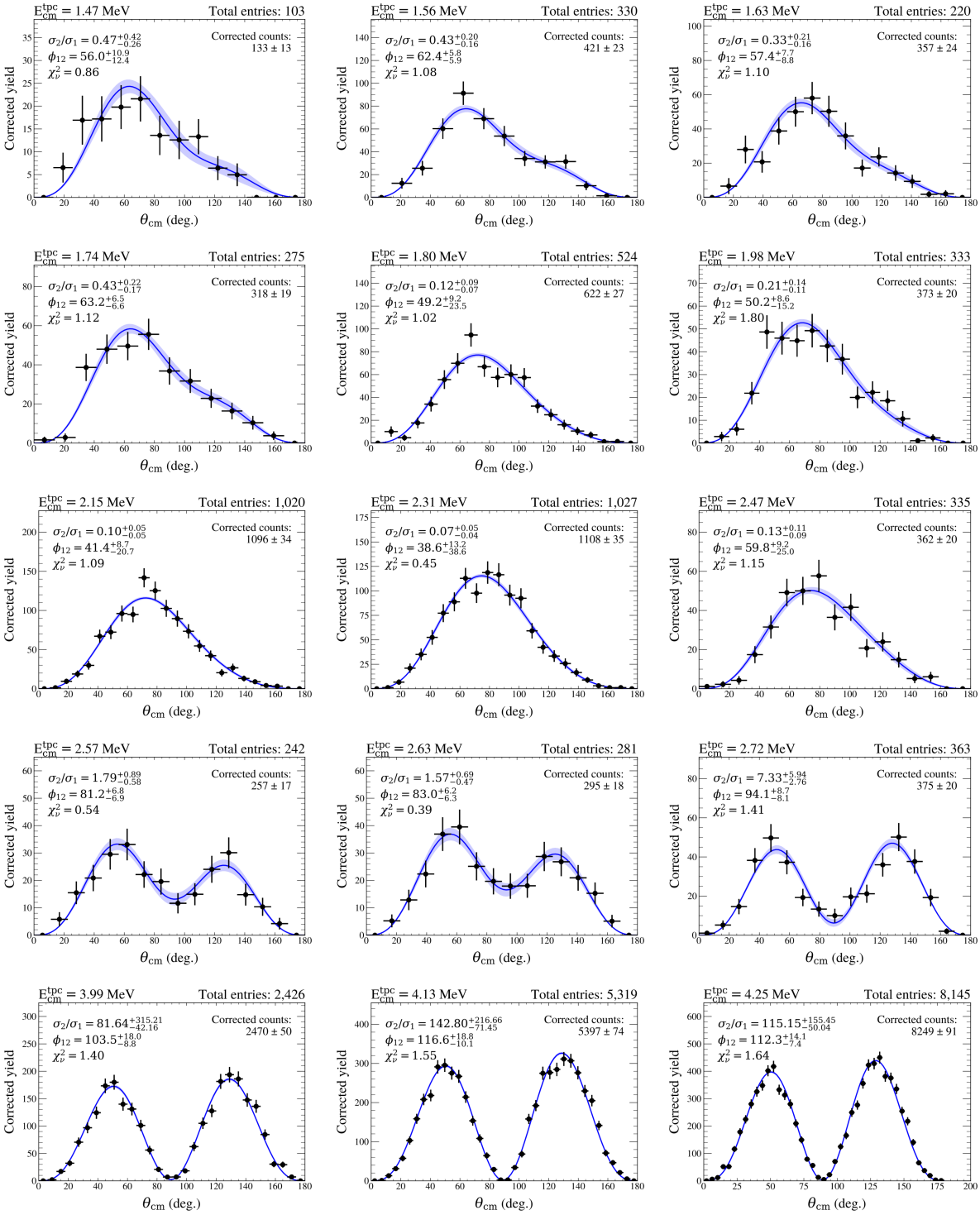

Figure I.1: Angular Distributions of the $^{16}O(\gamma, \alpha_0)$ Reaction - page 1: Partial-wave decomposition of the reconstructed centre-of-mass polar angle. Each panel shows the fitted angular distribution, using equation (I.0.0.1). The blue band indicates the uncertainty obtained from the covariance matrix of the fit. The fit parameters, ϕ_{12} and σ_2/σ_1, and the corresponding energy of each angular distribution are provided.

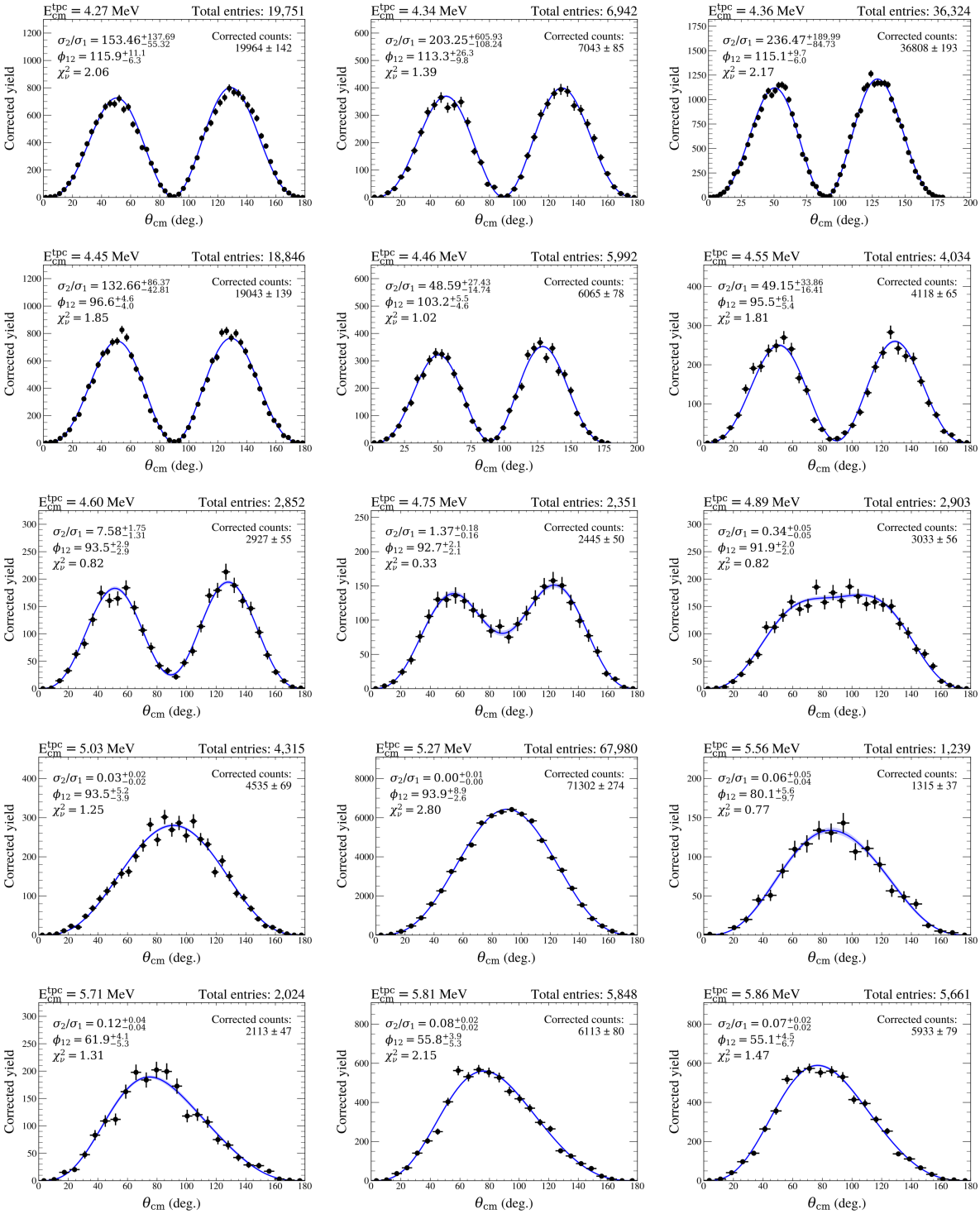

Figure I.2: Angular Distributions of the $^{16}O(\gamma, \alpha_0)$ Reaction - page 2: Partial-wave decomposition of the reconstructed centre-of-mass polar angle. Each panel shows the fitted angular distribution, using equation (I.0.0.1). The blue band indicates the uncertainty obtained from the covariance matrix of the fit. The fit parameters, ϕ_{12} and σ_2/σ_1, and the corresponding energy of each angular distribution are provided.

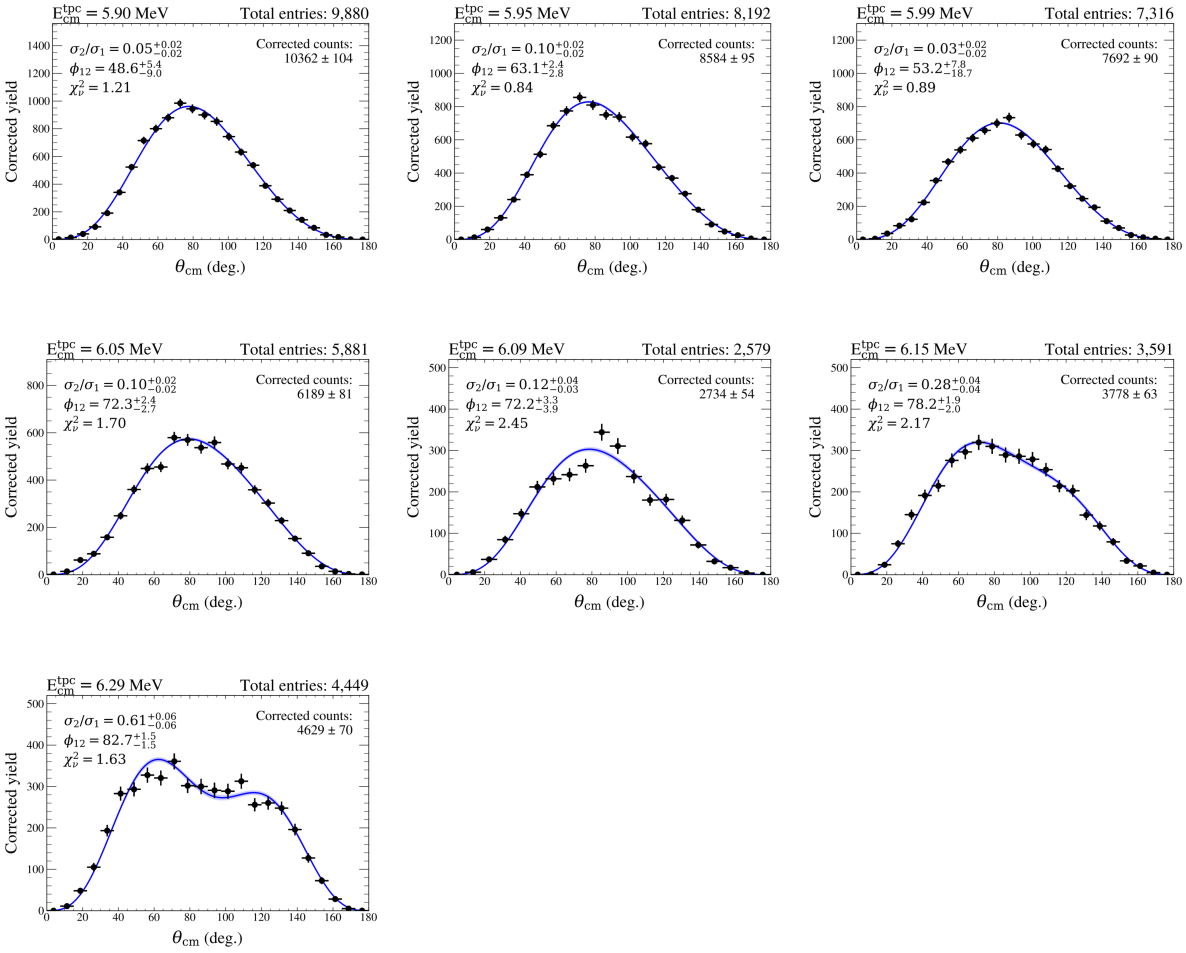

Figure I.3: Angular Distributions of the $^{16}O(\gamma, \alpha_0)$ Reaction - page 3: Partial-wave decomposition of the reconstructed centre-of-mass polar angle. Each panel shows the fitted angular distribution, using equation (I.0.0.1). The blue band indicates the uncertainty obtained from the covariance matrix of the fit. The fit parameters, ϕ_{12} and σ_2/σ_1, and the corresponding energy of each angular distribution are provided.

References

[1] Claus E. Rolfs and William S. Rodney. *Cauldrons in the cosmos : nuclear astrophysics*. 1988.

[2] E. P. Berni Ann Thushari Masa-aki Hashimoto Riou Nakamura and Kenzo Arai. *Big-Bang Nucleosynthesis: Thermonuclear History in the Early Universe*. SpringerBriefs in Physics. Springer Singapore, 2018. DOI: 10.1007/978-981-13-2935-7.

[3] Bertulani, C.A., chintak, Shubh and Mukhamedzhanov, A.M. 'Cosmological Lithium Problems'. In: *EPJ Web Conf.* 184 (2018), p. 01002. DOI: 10.1051/epjconf/201818401002. URL: https://doi.org/10.1051/epjconf/201818401002.

[4] Planck Collaboration et al. 'Planck 2015 results - XIII. Cosmological parameters'. In: *AA* 594 (2016), A13. DOI: 10.1051/0004-6361/201525830. URL: https://doi.org/10.1051/0004-6361/201525830.

[5] A. Aprahamian, K. Langanke and M. Wiescher. 'Nuclear structure aspects in nuclear astrophysics'. In: *Progress in Particle and Nuclear Physics* 54.2 (2005), pp. 535–613. DOI: https://doi.org/10.1016/j.ppnp.2004.09.002. URL: https://www.sciencedirect.com/science/article/pii/S0146641004001103.

[6] Richard H. Cyburt et al. 'Big bang nucleosynthesis: Present status'. In: *Rev. Mod. Phys.* 88 (1 Feb. 2016), p. 015004. DOI: 10.1103/RevModPhys.88.015004. URL: https://link.aps.org/doi/10.1103/RevModPhys.88.015004.

[7] F. Spite and M. Spite. 'Abundance of lithium in unevolved stars and old disk stars : Interpretation and consequences.' In: 115 (Nov. 1982), pp. 357–366.

[8] Sbordone, L. et al. 'The metal-poor end of the Spite plateau - I. Stellar parameters, metallicities, and lithium abundances'. In: *AA* 522 (2010), A26. DOI: 10.1051/0004-6361/200913282. URL: https://doi.org/10.1051/0004-6361/200913282.

[9] C. A. Bertulani, A. M. Mukhamedzhanov and Shubhchintak. 'The cosmological lithium problem revisited'. In: *AIP Conference Proceedings* 1753.1 (July 2016), p. 040001. DOI: 10.1063/1.4955357. eprint: https://pubs.aip.org/aip/acp/article-pdf/doi/10.1063/1.4955357/13110440/040001_1_online.pdf. URL: https://doi.org/10.1063/1.4955357.

[10] E. Margaret Burbidge et al. 'Synthesis of the Elements in Stars'. In: *Rev. Mod. Phys.* 29 (4 Oct. 1957), pp. 547–650. DOI: 10.1103/RevModPhys.29.547. URL: https://link.aps.org/doi/10.1103/RevModPhys.29.547.

[11] M Arnould and K Takahashi. 'Nuclear astrophysics'. In: *Reports on Progress in Physics* 62.3 (Mar. 1999), p. 395. DOI: 10.1088/0034-4885/62/3/003. URL: https://iopscience.iop.org/article/10.1088/0034-4885/62/3/003.

[12] Jhon Yana Galarza et al. 'Explosive nucleosynthesis of a metal-deficient star as the source of a distinct odd-even effect in the solar twin HIP 11915'. In: *Monthly Notices of the Royal Astronomical Society: Letters* 502.1 (Jan. 2021), pp. L104–L109. DOI: 10.1093/mnrasl/slab010. eprint: https://academic.oup.com/mnrasl/article-pdf/502/1/L104/54638783/slab010.pdf. URL: https://doi.org/10.1093/mnrasl/slab010.

[13] K Lodders, H Palme and HP Gail. '4.4 Abundances of the elements in the Solar System'. In: *Solar system* (2009), pp. 712–770.

[14] H. Palme, K. Lodders and A. Jones. 'Solar System Abundances of the Elements'. In: *Planets, Asteriods, Comets and The Solar System*. Ed. by Andrew M. Davis. Vol. 2. 2014, pp. 15–36.

[15] H. Reeves, W. Fowler and F. Hoyle. 'Galactic Cosmic Ray Origin of Li, Be and B in Stars'. In: *Nature* 226 (1970), pp. 727–729. DOI: 10.1038/226727a0.

[16] Hubert Reeves. 'On the origin of the light elements ($Zlt; 6$)'. In: *Rev. Mod. Phys.* 66 (1 Jan. 1994), pp. 193–216. DOI: 10.1103/RevModPhys.66.193. URL: https://link.aps.org/doi/10.1103/RevModPhys.66.193.

[17] C. C. King, P. Demarque and E. M. Green. 'Isochrone Fitting of Color Magnitude Diagrams of Old Star Clusters - Implications for Stellar Ages'. In: *Calibration of Stellar ages*. Jan. 1988, pp. 211–216.

[18] ESA/Hubble NASA. *Messier 5*. Hubble Space Telescope, NASA Science. [Accessed: 26/09/2026]. URL: https://science.nasa.gov/mission/hubble/science/explore-the-night-sky/hubble-messier-catalog/messier-5.

[19] Christian Iliadis. *Nuclear Physics of Stars*. 2nd, Revised and Enlarged. Wiley-VCH, Apr. 2015.

[20] Francis LeBlanc. *An Introduction to Stellar Astrophysics*. 2010.

[21] E. G. Adelberger et al. 'Solar fusion cross sections. II. The *pp* chain and CNO cycles'. In: *Rev. Mod. Phys.* 83 (1 Apr. 2011), pp. 195–245. DOI: 10.1103/RevModPhys.83.195. URL: https://link.aps.org/doi/10.1103/RevModPhys.83.195.

[22] C. A. Bertulani. *Nuclear Reactions*. 2010. arXiv: 0908.3275 [nucl-th]. URL: https://arxiv.org/abs/0908.3275.

[23] Daniel B. Sayre. 'Measurement of the 2.68-MeV Resonance Interference and R-Matrix Analysis of the $^{12}C(\alpha, \gamma_0)^{16}O$ Reaction'. PhD thesis. Ohio University, June 2011.

[24] Moshe Gai. 'Nuclear structure and the fate of core collapse (Type II) supernova'. In: *Nuclear Physics A* 928 (2014). Special Issue Dedicated to the Memory of Gerald E Brown (1926-2013), pp. 313–318. DOI: https://doi.org/10.1016/j.nuclphysa.2014.05.004. URL: https://www.sciencedirect.com/science/article/pii/S0375947414001195.

[25] Stéphane Blondin. *Type Ia supernovae*. 2025. arXiv: 2411.09740 [astro-ph.HE]. URL: https://arxiv.org/abs/2411.09740.

[26] Kate Maguire. 'Type Ia Supernovae'. In: *Handbook of Supernovae*. Ed. by Athem W. Alsabti and Paul Murdin. Cham: Springer International Publishing, 2017, pp. 293–316. DOI: 10.1007/978-3-319-21846-5_36. URL: https://doi.org/10.1007/978-3-319-21846-5_36.

[27] M. M. Phillips. 'The Absolute Magnitudes of Type IA Supernovae'. In: 413 (Aug. 1993), p. L105. DOI: 10.1086/186970.

[28] P. Höflich et al. 'SECONDARY PARAMETERS OF TYPE Ia SUPERNOVA LIGHT CURVES'. In: *The Astrophysical Journal* 710.1 (Jan. 2010), p. 444. DOI: 10.1088/0004-637X/710/1/444. URL: https://doi.org/10.1088/0004-637X/710/1/444.

[29] Juan Garcia-Bellido. *Modern Cosmology*. 2004. arXiv: hep-ph/0407111 [hep-ph]. URL: https://arxiv.org/abs/hep-ph/0407111.

[30] Faïrouz Hammache and Nicolas de Séréville. 'Transfer Reactions As a Tool in Nuclear Astrophysics'. In: *Frontiers in Physics* Volume 8 - 2020 (2021). DOI: 10.3389/fphy.2020.602920. URL: https://www.frontiersin.org/journals/physics/articles/10.3389/fphy.2020.602920.

[31] John M. Blatt and Victor F. Weisskopf. *Theoretical Nuclear Physics*. New York, NY: Springer, 1979. DOI: 10.1007/978-1-4612-9959-2.

[32] George Gamow. 'Zur Quantentheorie des Atomkernes'. In: *Zeitschrift für Physik* 51 (1928), pp. 204–212. DOI: 10.1007/BF01343196.

[33] G. Breit and M. E. Ebel. 'Nucleon Transfer and Virtual Coulomb Excitation'. In: *Phys. Rev.* 104 (4 Nov. 1956), pp. 1030–1046. DOI: 10.1103/PhysRev.104.1030. URL: https://link.aps.org/doi/10.1103/PhysRev.104.1030.

[34] Kenneth S. Krane. *Introductory Nuclear Physics*. John Wiley & Sons, 1987.

[35] A. M. Lane and R. G. Thomas. 'R-Matrix Theory of Nuclear Reactions'. In: *Rev. Mod. Phys.* 30 (2 Apr. 1958), pp. 257–353. DOI: 10.1103/RevModPhys.30.257. URL: https://link.aps.org/doi/10.1103/RevModPhys.30.257.

[36] E. P. Wigner and L. Eisenbud. 'Higher Angular Momenta and Long Range Interaction in Resonance Reactions'. In: *Phys. Rev.* 72 (1 July 1947), pp. 29–41. DOI: 10.1103/PhysRev.72.29. URL: https://link.aps.org/doi/10.1103/PhysRev.72.29.

[37] P Descouvemont and D Baye. 'The R-matrix theory'. In: *Reports on Progress in Physics* 73.3 (Feb. 2010), p. 036301. DOI: 10.1088/0034-4885/73/3/036301. URL: https://doi.org/10.1088/0034-4885/73/3/036301.

[38] Joint Institute for Nuclear Astrophysics (JINA). *AZURE R-Matrix Program*. https://azure.nd.edu/. 2025.

[39] R.W. Carr and J.E.E. Baglin. 'Table of angular-distribution coefficients for (Gamma, particle) and (particle, gamma) reactions'. In: *Atomic Data and Nuclear Data Tables* 10.2 (1971), pp. 143–204. DOI: https://doi.org/10.1016/S0092-640X(71)80042-6. URL: https://www.sciencedirect.com/science/article/pii/S0092640X71800426.

[40] P. Dyer and C. A. Barnes. 'The ^{12}C(α,γ)^{16}O reaction and stellar helium burning'. In: *Nucl. Phys. A* 233 (1974), p. 495.

[41] M. Assunção et al. '$E1$ and $E2$ S factors of $^{12}\mathrm{C}(\alpha,\gamma_0)^{16}\mathrm{O}$ from γ-ray angular distributions with a 4 π-detector array'. In: *Phys. Rev. C* 73 (5 May 2006), p. 055801. DOI: 10.1103/PhysRevC.73.055801. URL: https://link.aps.org/doi/10.1103/PhysRevC.73.055801.

[42] William A. Fowler. 'Experimental and theoretical nuclear astrophysics: the quest for the origin of the elements'. In: *Rev. Mod. Phys.* 56 (2 Apr. 1984), pp. 149–179. DOI: 10.1103/RevModPhys.56.149. URL: https://link.aps.org/doi/10.1103/RevModPhys.56.149.

[43] Adam G. Riess et al. 'Observational Evidence from Supernovae for an Accelerating Universe and a Cosmological Constant'. In: *The Astronomical Journal* 116.3 (Sept. 1998), p. 1009. DOI: 10.1086/300499. URL: https://doi.org/10.1086/300499.

[44] DES Collaboration et al. *The Dark Energy Survey: Cosmology Results With 1500 New High-redshift Type Ia Supernovae Using The Full 5-year Dataset*. 2025. arXiv: 2401.02929 [astro-ph.CO]. URL: https://arxiv.org/abs/2401.02929.

[45] R. Farmer et al. 'Constraints from Gravitational-wave Detections of Binary Black Hole Mergers on the 12C(,)16O Rate'. In: *The Astrophysical Journal Letters* 902.2 (Oct. 2020), p. L36. DOI: 10.3847/2041-8213/abbadd. URL: https://doi.org/10.3847/2041-8213/abbadd.

[46] R. J. deBoer et al. 'The $^{12}\mathbf{C}(\alpha,\gamma)^{16}\mathbf{O}$ reaction and its implications for stellar helium burning'. In: *Rev. Mod. Phys.* 89 (3 Sept. 2017), p. 035007. DOI: 10.1103/RevModPhys.89.035007. URL: https://link.aps.org/doi/10.1103/RevModPhys.89.035007.

[47] Oliver Sølund Kirsebom. '^{12}C and the triple- reaction rate'. In: *Journal of Physics: Conference Series* 436.1 (Apr. 2013), p. 012072. DOI: 10.1088/1742-6596/436/1/012072. URL: https://doi.org/10.1088/1742-6596/436/1/012072.

[48] Y. Xu et al. 'NACRE II: an update of the NACRE compilation of charged-particle-induced thermonuclear reaction rates for nuclei with mass number A<16'. In: *Nuclear Physics A* 918 (2013), pp. 61–169. DOI: https://doi.org/10.1016/j.nuclphysa.2013.09.007. URL: https://www.sciencedirect.com/science/article/pii/S0375947413007409.

[49] Thomas A. Weaver and S. E. Woosley. 'Nucleosynthesis in massive stars and the 12C(,)16O reaction rate'. In: *Physics Reports* 227.1–2 (1993), pp. 65–96. DOI: 10.1016/0370âĂŠ1573(93)90058âĂŠL. URL: https://doi.org/10.1016/0370%E2%80%911573(93)90058%E2%80%91L.

[50] F. Hoyle. 'On Nuclear Reactions Occuring in Very Hot STARS.I. the Synthesis of Elements from Carbon to Nickel.' In: 1 (Sept. 1954), p. 121. DOI: 10.1086/190005.

[51] J de Boer R et al. 'The ^{12}C(α,γ)^{16}O reaction, in the laboratory and in the stars'. In: *The European Physical Journal A* 61.4 (2025), p. 70. DOI: 10.1140/epja/s10050-025-01537-1.

[52] E. K. Warburton and J. Weneser. 'The Role of Isospin in Electromagnetic Transitions'. In: *Isospin in Nuclear Physics*. Ed. by D. H. Wilkinson. Amsterdam: North-Holland Publishing Company, 1969.

[53] Sukhendusekhar Sarkar. 'A method for semi-empirical calculation of isospin mixing probability in nuclei'. In: *Journal of Physics G: Nuclear and Particle Physics* 51.6 (Apr. 2024), p. 065103. DOI: 10.1088/1361-6471/ad3b27. URL: https://doi.org/10.1088/1361-6471/ad3b27.

[54] TUNL Nuclear Data Evaluation Project. *TUNL Nuclear Data Evaluation*. https://nucldata.tunl.duke.edu/. Accessed: 30-11-2025. 2025.

[55] L. Gialanella et al. 'The E1 capture amplitude in ^{12}C(α,γ_0)^{16}O'. In: *Eur. Phys. J. A* 11 (2001), p. 357.

[56] M. Fey. 'Im Brennpunkt der Nuklearen Astrophysik: Die Reaktion ^{12}C(α, γ)^{16}O'. PhD thesis. Universität Stuttgart, 2004.

[57] R. M. Kremer et al. 'Coincidence measurement of the ^{12}C(α,γ)^{16}O cross section at low energies'. In: *Phys. Rev. Lett.* 60 (15 Apr. 1988), pp. 1475–1478. DOI: 10.1103/PhysRevLett.60.1475. URL: https://link.aps.org/doi/10.1103/PhysRevLett.60.1475.

[58] R. Kunz et al. '$^{12}C(\alpha,\gamma)^{16}O$: The Key Reaction in Stellar Nucleosynthesis'. In: *Phys. Rev. Lett.* 86 (15 Apr. 2001), pp. 3244–3247. DOI: 10.1103/PhysRevLett.86.3244. URL: https://link.aps.org/doi/10.1103/PhysRevLett.86.3244.

[59] H. Makii et al. '$E1$ and $E2$ cross sections of the ^{12}C(α,γ_0)^{16}O reaction using pulsed α beams'. In: *Phys. Rev. C* 80 (6 Dec. 2009), p. 065802. DOI: 10.1103/PhysRevC.80.065802. URL: https://link.aps.org/doi/10.1103/PhysRevC.80.065802.

[60] J. M. L. Ouellet et al. '^{12}C(α,γ)^{16}O cross sections at stellar energies'. In: *Phys. Rev. C* 54 (4 Oct. 1996), pp. 1982–1998. DOI: 10.1103/PhysRevC.54.1982. URL: https://link.aps.org/doi/10.1103/PhysRevC.54.1982.

[61] A. Redder et al. 'The $^{12}C(\alpha, \gamma)^{16}O$ cross section at stellar energies'. In: *Nuclear Physics A* 462.2 (1987), pp. 385–412. DOI: https://doi.org/10.1016/0375-9474(87)90555-0. URL: https://www.sciencedirect.com/science/article/pii/0375947487905550.

[62] G. Roters et al. 'The E1 and E2 capture amplitudes in $^{12}C(\alpha,\gamma_0)^{16}O$'. In: *Eur. Phys. J. A* 6 (1999), p. 451.

[63] D. Schürmann et al. 'Study of the 6.05 MeV cascade transition in $^{12}C(\alpha,\gamma)^{16}O$'. In: *Physics Letters B* 703.5 (2011), pp. 557–561. DOI: https://doi.org/10.1016/j.physletb.2011.08.061. URL: https://www.sciencedirect.com/science/article/pii/S0370269311010094.

[64] 'Numéro'. In: *Journal de Physique* 34.5-6 (mai-juin 1973), pp. 363–367. DOI: 10.1051/jphys:01973003405-6036300. URL: https://doi.org/10.1051/jphys:01973003405-6036300.

[65] R. Plag et al. '$^{12}C(\alpha,\gamma)^{16}O$ studied with the Karlsruhe 4π BaF_2 detector'. In: *Phys. Rev. C* 86 (1 July 2012), p. 015805. DOI: 10.1103/PhysRevC.86.015805. URL: https://link.aps.org/doi/10.1103/PhysRevC.86.015805.

[66] Z. Zhao et al. 'Astrophysical S factor of $^{12}C(\alpha,\gamma)^{16}O$ from the beta-delayed alpha-particle emission of ^{16}N'. In: *Phys. Rev. Lett.* 70 (14 Apr. 1993), pp. 2066–2069. DOI: 10.1103/PhysRevLett.70.2066. URL: https://link.aps.org/doi/10.1103/PhysRevLett.70.2066.

[67] L. Buchmann et al. 'β-delayed α spectrum of ^{16}N and the $^{12}C(\alpha,\gamma)^{16}O$ cross section at low energies'. In: *Phys. Rev. Lett.* 70 (6 Feb. 1993), pp. 726–729. DOI: 10.1103/PhysRevLett.70.726. URL: https://link.aps.org/doi/10.1103/PhysRevLett.70.726.

[68] R. E. Azuma et al. 'Constraints on the low-energy E1 cross section of $^{12}C(\alpha,\gamma)^{16}O$ from the β-delayed α spectrum of ^{16}N'. In: *Phys. Rev. C* 50 (2 Aug. 1994), pp. 1194–1215. DOI: 10.1103/PhysRevC.50.1194. URL: https://link.aps.org/doi/10.1103/PhysRevC.50.1194.

[69] R. H. France III et al. 'Further measurement of the β-delayed α-particle emission of ^{16}N'. In: *Phys. Rev. C* 75 (6 June 2007), p. 065802. DOI: 10.1103/PhysRevC.75.065802. URL: https://link.aps.org/doi/10.1103/PhysRevC.75.065802.

[70] X. D. Tang et al. 'Determination of the $E1$ component of the low-energy ^{12}C$(\alpha,\gamma)^{16}$O cross section'. In: *Phys. Rev. C* 81 (4 Apr. 2010), p. 045809. DOI: 10.1103/PhysRevC.81.045809. URL: https://link.aps.org/doi/10.1103/PhysRevC.81.045809.

[71] X. D. Tang et al. 'New Determination of the Astrophysical S Factor S_{E1} of the ^{12}C$(\alpha,\gamma)^{16}$O Reaction'. In: *Phys. Rev. Lett.* 99 (5 Aug. 2007), p. 052502. DOI: 10.1103/PhysRevLett.99.052502. URL: https://link.aps.org/doi/10.1103/PhysRevLett.99.052502.

[72] H.M. Loebenstein et al. 'Angular distributions of deuterons from ^{6}Li(^{12}C, d)^{16}O*'. In: *Nuclear Physics A* 91.3 (1967), pp. 481–494. DOI: https://doi.org/10.1016/0375-9474(67)90568-4. URL: https://www.sciencedirect.com/science/article/pii/0375947467905684.

[73] F. Pühlhofer et al. 'Investigation of the reaction ^{12}C(^{7}Li, t)^{16}O'. In: *Nuclear Physics A* 147.2 (1970), pp. 258–272. DOI: https://doi.org/10.1016/0375-9474(70)90266-6. URL: https://www.sciencedirect.com/science/article/pii/0375947470902666.

[74] M. E. Cobern, D. J. Pisano and P. D. Parker. 'Alpha-transfer reactions in light nuclei. III. $(^{7}\mathrm{Li}, t)$ stripping reaction'. In: *Phys. Rev. C* 14 (2 Aug. 1976), pp. 491–505. DOI: 10.1103/PhysRevC.14.491. URL: https://link.aps.org/doi/10.1103/PhysRevC.14.491.

[75] F.D. Becchetti et al. '^{12}C(^{6}Li, d)^{16}Oat E(Li) = 90 MeV'. In: *Nuclear Physics A* 344.2 (1980), pp. 336–350. DOI: https://doi.org/10.1016/0375-9474(80)90682-X. URL: https://www.sciencedirect.com/science/article/pii/037594748090682X.

[76] F.D. Becchetti et al. '^{12}C(^{7}Li, t)^{16}O and stellar helium fusion'. In: *Nuclear Physics A* 305.1 (1978), pp. 293–312. DOI: https://doi.org/10.1016/0375-9474(78)90179-3. URL: https://www.sciencedirect.com/science/article/pii/0375947478901793.

[77] F. D. Becchetti, J. Jänecke and C. E. Thorn. '^{12}C(^{6}Li, d)^{16}O and ^{16}O(^{6}Li, d)^{20}Ne at E(^{6}Li) = 42 MeV'. In: *Nucl. Phys. A* 305 (1978), p. 313.

[78] C. R. Brune et al. 'Sub-Coulomb α Transfers on ^{12}C and the $^{12}C(\alpha,\gamma)^{16}O$ S Factor'. In: *Phys. Rev. Lett.* 83 (20 Nov. 1999), pp. 4025–4028. DOI: 10.1103/PhysRevLett.83.4025. URL: https://link.aps.org/doi/10.1103/PhysRevLett.83.4025.

[79] P. Tischhauser et al. 'Measurement of elastic $^{12}\mathrm{C} + \alpha$ scattering: Details of the experiment, analysis, and discussion of phase shifts'. In: *Phys. Rev. C* 79 (5 May 2009), p. 055803. DOI: 10.1103/PhysRevC.79.055803. URL: https://link.aps.org/doi/10.1103/PhysRevC.79.055803.

[80] R. Plaga et al. 'The scattering of alpha particles from 12C and the ^{12}C(α,γ)^{16}O stellar reaction rate'. In: *Nuclear Physics A* 465.2 (1987), pp. 291–316. DOI: https://doi.org/10.1016/0375-9474(87)90436-2. URL: https://www.sciencedirect.com/science/article/pii/0375947487904362.

[81] D'agostino Bruno et al. 'Experimental study of the α-^{12}C elastic scattering. R-matrix analysis of the phase shifts and ^{16}O levels'. In: *Nuov Cim A* 27.1 (1975).

[82] J. D. Larson and R. H. Spear. 'Gamma radiation from the alpha particle bombardment of ^{12}C'. In: *Nucl. Phys.* 56 (1964), p. 497.

[83] J.W. Hammer et al. 'New determination of the ^{12}C(α, γ)^{16}O reaction rate from -ray angular distribution measurements'. In: *Nuclear Physics A* 752 (2005). Proceedings of the 22nd International Nuclear Physics Conference (Part 2), pp. 514–521. DOI: https://doi.org/10.1016/j.nuclphysa.2005.02.056. URL: https://www.sciencedirect.com/science/article/pii/S0375947405002083.

[84] J.W. Hammer et al. 'E1 and E2 capture cross section and astrophysical reaction rate of the key reaction ^{12}C(α,γ)^{16}O'. In: *Nuclear Physics A* 758 (2005). Nuclei in the Cosmos VIII, pp. 363–366. DOI: https://doi.org/10.1016/j.nuclphysa.2005.05.066. URL: https://www.sciencedirect.com/science/article/pii/S0375947405007153.

[85] K. U. Kettner et al. 'The ^{4}He(^{12}C, γ)^{16}O reaction at stellar energies'. In: *Z. Phys. A* 308 (1982), p. 73.

[86] H. et al. Yamaguchi. 'Direct measurement of ^{12}C+^{4}He→^{16}O+γ total cross section at Ecm=1.2 MeV'. In: *AIP Conf. Proc.* Vol. 1594. 2014, p. 229.

[87] R. J. Jaszczak, J. H. Gibbons and R. L. Macklin. '^{12}C(α,γ)^{16}O Capture Cross Section Below 3.2 MeV'. In: *Phys. Rev. C* 2 (1970), p. 63.

[88] C. Matei et al. 'Measurement of the Cascade Transition via the First Excited State of ^{16}O in the ^{12}C$(\alpha,\gamma)^{16}$O Reaction, and Its S Factor in Stellar Helium Burning'. In: *Phys. Rev. Lett.* 97 (24 Dec. 2006), p. 242503. DOI: 10.1103/PhysRevLett.97.242503. URL: https://link.aps.org/doi/10.1103/PhysRevLett.97.242503.

[89] C. Matei, C. R. Brune and T. N. Massey. 'Measurements of branching ratios from the 7.12-MeV state in ^{16}O and the ^{12}C$(\alpha,\gamma)^{16}$O reaction cross section'. In: *Phys. Rev. C* 78 (6 Dec. 2008), p. 065801. DOI: 10.1103/PhysRevC.78.065801. URL: https://link.aps.org/doi/10.1103/PhysRevC.78.065801.

[90] F. C. Barker. 'The ^{12}C(α,γ)^{16}O Cross Section at Stellar Energies'. In: *Australian Journal of Physics* 40 (1987), pp. 25–38.

[91] F. C. Barker and T. Kajino. 'The ^{12}C(α,γ)^{16}O Cross Section at Low Energies'. In: *Australian Journal of Physics* 44 (1991), pp. 369–396.

[92] C. R. Brune. 'Electric-multipole interference effects in the ^{12}C$(\alpha,\gamma_0)^{16}$O reaction'. In: *Phys. Rev. C* 64 (5 Oct. 2001), p. 055803. DOI: 10.1103/PhysRevC.64.055803. URL: https://link.aps.org/doi/10.1103/PhysRevC.64.055803.

[93] L. D. Knutson. 'Watson's theorem for low-energy $p-d$ radiative capture'. In: *Phys. Rev. C* 59 (4 Apr. 1999), pp. 2152–2161. DOI: 10.1103/PhysRevC.59.2152. URL: https://link.aps.org/doi/10.1103/PhysRevC.59.2152.

[94] Kenneth M. Watson. 'Some General Relations between the Photoproduction and Scattering of π Mesons'. In: *Phys. Rev.* 95 (1 July 1954), pp. 228–236. DOI: 10.1103/PhysRev.95.228. URL: https://link.aps.org/doi/10.1103/PhysRev.95.228.

[95] Moshe Gai. 'Ambiguities in the rate of oxygen formation during stellar helium burning in the $^{12}C(\alpha,\gamma)$ reaction'. In: *Phys. Rev. C* 88 (6 Dec. 2013), p. 062801. DOI: 10.1103/PhysRevC.88.062801. URL: https://link.aps.org/doi/10.1103/PhysRevC.88.062801.

[96] Kevin Ching Wei Li. 'Helium burning and nuclear clustering: recent studies and constraints from direct reactions'. In: *European Nuclear Physics Conference 2025*. Caen, France, Sept. 2025.

[97] R. Smith et al. 'Precision measurements on oxygen formation in stellar helium burning with gamma-ray beams and a Time Projection Chamber'. In: *Nature Communications* 12 (2021), p. 5920.

[98] U. Von Wimmersperg et al. 'A test of time reversal invariance through detailed balance of the reaction 12C(,)16O'. In: *Physics Letters B* 33.4 (1970), pp. 291–293. DOI: https://doi.org/10.1016/0370-2693(70)90272-8. URL: https://www.sciencedirect.com/science/article/pii/0370269370902728.

[99] C. A. Baur G. Bertulani and H. Rebel. 'Coulomb dissociation as a source of information on radiative capture processes of astrophysical interest'. In: *Nuclear Physics A* 458.1 (1986), pp. 188–204. DOI: 10.1016/0375-9474(86)90290-3.

[100] F. Ajzenberg-Selove. 'Energy levels of light nuclei A = 16-17'. In: *Nuclear Physics A* 460 (1986), pp. 1–110.

[101] E. E. Salpeter. 'Nuclear Reactions in Stars Without Hydrogen.' In: 115 (Mar. 1952), pp. 326–328. DOI: 10.1086/145546.

[102] E. J. Öpik. 'Stellar Models with Variable Composition. II. Sequences of Models with Energy Generation Proportional to the Fifteenth Power of Temperature'. In: *Proceedings of the Royal Irish Academy. Section A: Mathematical and Physical Sciences* 54 (1951), pp. 49–77. URL: http://www.jstor.org/stable/20488524 (retrieved 5/11/2025).

[103] F. Hoyle. 'On Nuclear Reactions Occuring in Very Hot STARS.I. the Synthesis of Elements from Carbon to Nickel.' In: 1 (Sept. 1954), p. 121. DOI: 10.1086/190005.

[104] M. Freer and H.O.U. Fynbo. 'The Hoyle state in 12C'. In: *Progress in Particle and Nuclear Physics* 78 (2014), pp. 1–23. DOI: https://doi.org/10.1016/j.ppnp.2014.06.001. URL: https://www.sciencedirect.com/science/article/pii/S0146641014000453.

[105] D. N. F. Dunbar et al. 'The 7.68-Mev State in C^{12}'. In: *Phys. Rev.* 92 (3 Nov. 1953), pp. 649–650. DOI: 10.1103/PhysRev.92.649. URL: https://link.aps.org/doi/10.1103/PhysRev.92.649.

[106] C. W. Cook et al. 'B^{12}, C^{12}, and the Red Giants'. In: *Phys. Rev.* 107 (2 July 1957), pp. 508–515. DOI: 10.1103/PhysRev.107.508. URL: https://link.aps.org/doi/10.1103/PhysRev.107.508.

[107] Zifeng Luo et al. 'Radiative decay branching ratio of the Hoyle state'. In: *Phys. Rev. C* 109 (2 Feb. 2024), p. 025801. DOI: 10.1103/PhysRevC.109.025801. URL: https://link.aps.org/doi/10.1103/PhysRevC.109.025801.

[108] T. Kibédi et al. 'Radiative Width of the Hoyle State from γ-Ray Spectroscopy'. In: *Phys. Rev. Lett.* 125 (18 Oct. 2020), p. 182701. DOI: 10.1103/PhysRevLett.125.182701. URL: https://link.aps.org/doi/10.1103/PhysRevLett.125.182701.

[109] W. Paulsen et al. 'Remeasuring the γ-decay branching ratio of the Hoyle state'. In: *Phys. Rev. C* 112 (1 July 2025), p. 015803. DOI: 10.1103/2h2s-sbyx. URL: https://link.aps.org/doi/10.1103/2h2s-sbyx.

[110] L. R. Hafstad and E. Teller. 'The Alpha-Particle Model of the Nucleus'. In: *Phys. Rev.* 54 (9 Nov. 1938), pp. 681–692. DOI: 10.1103/PhysRev.54.681. URL: https://link.aps.org/doi/10.1103/PhysRev.54.681.

[111] Kiyomi Ikeda, Noboru Takigawa and Hisashi Horiuchi. 'The Systematic Structure-Change into the Molecule-like Structures in the Self-Conjugate 4n Nuclei'. In: *Progress of Theoretical Physics Supplement* E68 (July 1968), pp. 464–475. DOI: 10.1143/PTPS.E68.464. eprint: https://academic.oup.com/ptps/article-pdf/doi/10.1143/PTPS.E68.464/5216547/E68-464.pdf. URL: https://doi.org/10.1143/PTPS.E68.464.

[112] H. Morinaga. 'Interpretation of Some of the Excited States of $4n$ Self-Conjugate Nuclei'. In: *Phys. Rev.* 101 (1 Jan. 1956), pp. 254–258. DOI: 10.1103/PhysRev.101.254. URL: https://link.aps.org/doi/10.1103/PhysRev.101.254.

[113] M. Itoh et al. 'Candidate for the 2^+ excited Hoyle state at $E_x \sim 10$ MeV in ^{12}C'. In: *Phys. Rev. C* 84 (5 Nov. 2011), p. 054308. DOI: 10.1103/PhysRevC.84.054308. URL: https://link.aps.org/doi/10.1103/PhysRevC.84.054308.

[114] Robert Roth et al. 'Similarity-Transformed Chiral $NN + 3N$ Interactions for the Ab Initio Description of ^{12}**C** and ^{16}**O**'. In: *Phys. Rev. Lett.* 107 (7 Aug. 2011), p. 072501. DOI: 10.1103/PhysRevLett.107.072501. URL: https://link.aps.org/doi/10.1103/PhysRevLett.107.072501.

[115] Evgeny Epelbaum et al. 'Structure and Rotations of the Hoyle State'. In: *Phys. Rev. Lett.* 109 (25 Dec. 2012), p. 252501. DOI: 10.1103/PhysRevLett.109.252501. URL: https://link.aps.org/doi/10.1103/PhysRevLett.109.252501.

[116] M. Chernykh et al. 'Structure of the Hoyle State in ^{12}C'. In: *Phys. Rev. Lett.* 98 (3 Jan. 2007), p. 032501. DOI: 10.1103/PhysRevLett.98.032501. URL: https://link.aps.org/doi/10.1103/PhysRevLett.98.032501.

[117] A. Tohsaki et al. 'Alpha Cluster Condensation in ^{12}C and ^{16}O'. In: *Phys. Rev. Lett.* 87 (19 Oct. 2001), p. 192501. DOI: 10.1103/PhysRevLett.87.192501. URL: https://link.aps.org/doi/10.1103/PhysRevLett.87.192501.

[118] R. Bijker and F. Iachello. 'Cluster states in nuclei as representations of a U($\nu + 1$) group'. In: *Phys. Rev. C* 61 (6 May 2000), p. 067305. DOI: 10.1103/PhysRevC.61.067305. URL: https://link.aps.org/doi/10.1103/PhysRevC.61.067305.

[119] R. Bijker and F. Iachello. 'The Algebraic Cluster Model: Three-Body Clusters'. In: *Annals of Physics* 298.2 (2002), pp. 334–360. DOI: https://doi.org/10.1006/aphy.2002.6255. URL: https://www.sciencedirect.com/science/article/pii/S000349160296255X.

[120] D. J. Marín-Lámbarri et al. 'Evidence for Triangular $\mathcal{D}_{3h}$ Symmetry in ^{12}C'. In: *Phys. Rev. Lett.* 113 (1 June 2014), p. 012502. DOI: 10.1103/PhysRevLett.113.012502. URL: https://link.aps.org/doi/10.1103/PhysRevLett.113.012502.

[121] M. Freer et al. 'Evidence for a new ^{12}C state at 13.3 MeV'. In: *Phys. Rev. C* 83 (3 Mar. 2011), p. 034314. DOI: 10.1103/PhysRevC.83.034314. URL: https://link.aps.org/doi/10.1103/PhysRevC.83.034314.

[122] X. Aslanoglou and K. W. Kemper. '^{3}He cluster structure of ^{12}C'. In: *Phys. Rev. C* 34 (5 Nov. 1986), pp. 1649–1653. DOI: 10.1103/PhysRevC.34.1649. URL: https://link.aps.org/doi/10.1103/PhysRevC.34.1649.

[123] G. M. Reynolds, D. E. Rundquist and R. M. Poichar. 'Study of C^{12} States Using the $B^{11}(He^3, d)C^{12}$ Reaction'. In: *Phys. Rev. C* 3 (2 Feb. 1971), pp. 442–447. DOI: 10.1103/PhysRevC.3.442. URL: https://link.aps.org/doi/10.1103/PhysRevC.3.442.

[124] M. Itoh et al. 'Study of the cluster state at E_x=10.3 MeV in ^{12}C'. In: *Nuclear Physics A* 738 (2004). Proceedings of the 8th International Conference on Clustering Aspects of Nuclear Structure and Dynamics, pp. 268–272. DOI: https://doi.org/10.1016/j.nuclphysa.2004.04.044. URL: https://www.sciencedirect.com/science/article/pii/S0375947404005834.

[125] M Fujiwara et al. 'Magnetic spectrometer Grand Raiden'. In: *Nuclear Instruments and Methods in Physics Research Section A: Accelerators, Spectrometers, Detectors and Associated Equipment* 422.1 (1999), pp. 484–488. DOI: https://doi.org/10.1016/S0168-9002(98)01009-2. URL: https://www.sciencedirect.com/science/article/pii/S0168900298010092.

[126] M. Freer et al. '2^+ excitation of the ^{12}C Hoyle state'. In: *Phys. Rev. C* 80 (4 Oct. 2009), p. 041303. DOI: 10.1103/PhysRevC.80.041303. URL: https://link.aps.org/doi/10.1103/PhysRevC.80.041303.

[127] Iyabo Usman. 'High Energy-Resolution Experiments with the K600 Magnetic Spectrometer at Intermediate Energies'. In: *Exciting Interdisciplinary Physics. Quarks and Gluons / Atomic Nuclei / Relativity and Cosmology / Biological Systems*. Ed. by Walter Greiner. 2013, pp. 163–174. DOI: 10.1007/978-3-319-00047-3_14.

[128] R. Neveling et al. 'High energy-resolution zero-degree facility for light-ion scattering and reactions at iThemba LABS'. In: *Nuclear Instruments and Methods in Physics Research Section A: Accelerators, Spectrometers, Detectors and Associated Equipment* 654.1 (2011), pp. 29–39. DOI: https://doi.org/10.1016/j.nima.2011.06.077. URL: https://www.sciencedirect.com/science/article/pii/S0168900211012460.

[129] W. R. Zimmerman et al. 'Further evidence for the broad 2_2^+ state at 9.6 MeV in ^{12}C'. In: *Phys. Rev. C* 84 (2 Aug. 2011), p. 027304. DOI: 10.1103/PhysRevC.84.027304. URL: https://link.aps.org/doi/10.1103/PhysRevC.84.027304.

[130] M. Freer et al. 'Consistent analysis of the 2^+ excitation of the ^{12}C Hoyle state populated in proton and α-particle inelastic scattering'. In: *Phys. Rev. C* 86 (3 Sept. 2012), p. 034320. DOI: 10.1103/PhysRevC.86.034320. URL: https://link.aps.org/doi/10.1103/PhysRevC.86.034320.

[131] K. C. W. Li et al. 'Multiprobe study of excited states in ^{12}C: Disentangling the sources of monopole strength between the energy of the Hoyle state and $E_x = 13$ MeV'. In: *Phys. Rev. C* 105 (2 Feb. 2022), p. 024308. DOI: 10.1103/PhysRevC.105.024308. URL: https://link.aps.org/doi/10.1103/PhysRevC.105.024308.

[132] P. Adsley et al. 'CAKE: the coincidence array for K600 experiments'. In: *Journal of Instrumentation* 12.02 (Feb. 2017), T02004. DOI: 10.1088/1748-0221/12/02/T02004. URL: https://doi.org/10.1088/1748-0221/12/02/T02004.

[133] C.Aa. Diget et al. 'Properties of the ^{12}C 10 MeV state determined through -decay'. In: *Nuclear Physics A* 760.1 (2005), pp. 3–18. DOI: https://doi.org/10.1016/j.nuclphysa.2005.05.159. URL: https://www.sciencedirect.com/science/article/pii/S0375947405008602.

[134] Hans O. U. Fynbo et al. 'Revised rates for the stellar triple- process from measurement of ^{12}C nuclear resonances'. In: *Nature* 433.7022 (2005), pp. 136–139. DOI: 10.1038/nature03219.

[135] S. Hyldegaard et al. 'R-matrix analysis of the β decays of ^{12}N and ^{12}B'. In: 81.2, 024303 (Feb. 2010), p. 024303. DOI: 10.1103/PhysRevC.81.024303.

[136] C. R. Brune. 'Alternative parametrization of R-matrix theory'. In: *Phys. Rev. C* 66 (4 Oct. 2002), p. 044611. DOI: 10.1103/PhysRevC.66.044611. URL: https://link.aps.org/doi/10.1103/PhysRevC.66.044611.

[137] F. D. Smit et al. 'No evidence of an 11.16 MeV 2^+ state in ^{12}C'. In: *Phys. Rev. C* 86 (3 Sept. 2012), p. 037301. DOI: 10.1103/PhysRevC.86.037301. URL: https://link.aps.org/doi/10.1103/PhysRevC.86.037301.

[138] M. Alcorta et al. 'Properties of ^{12}C resonances determined from the ^{10}B(^{3}He,$p\alpha\alpha\alpha$) and ^{11}B(^{3}He,$d\alpha\alpha\alpha$) reactions studied in complete kinematics'. In: *Phys. Rev. C* 86 (6 Dec. 2012), p. 064306. DOI: 10.1103/PhysRevC.86.064306. URL: https://link.aps.org/doi/10.1103/PhysRevC.86.064306.

[139] W. R. Zimmerman et al. 'Unambiguous Identification of the Second 2^+ State in ^{12}**C** and the Structure of the Hoyle State'. In: *Phys. Rev. Lett.* 110 (15 Apr. 2013), p. 152502. DOI: 10.1103/PhysRevLett.110.152502. URL: https://link.aps.org/doi/10.1103/PhysRevLett.110.152502.

[140] William R. Zimmerman. 'Direct Observation of the Second 2+ State in 12C'. PhD thesis. university of connecticut, 2013.

[141] Charles Thomson Rees Wilson. 'On an expansion apparatus for making visible the tracks of ionising particles in gases and some results obtained by its use'. In: *Proceedings of the Royal Society of London. Series A* 87 (1912), pp. 277–292. DOI: 10.1098/rspa.1912.0081.

[142] N. N. Das Gupta and S. K. Ghosh. 'A Report on the Wilson Cloud Chamber and Its Applications in Physics'. In: *Rev. Mod. Phys.* 18 (2 Apr. 1946), pp. 225–290. DOI: 10.1103/RevModPhys.18.225. URL: https://link.aps.org/doi/10.1103/RevModPhys.18.225.

[143] Charles T. R. Wilson. *On the cloud method of making visible ions and the tracks of ionizing particles. Nobel Lecture*, December 12, 1927. Nobel Lecture. 1927.

[144] Carl D. Anderson. 'The Positive Electron'. In: *Phys. Rev.* 43 (6 Mar. 1933), pp. 491–494. DOI: 10.1103/PhysRev.43.491. URL: https://link.aps.org/doi/10.1103/PhysRev.43.491.

[145] Paul Adrien Maurice Dirac. 'Quantised singularities in the electromagnetic field'. In: *Proceedings of the Royal Society of London. Series A* 133 (1931), pp. 60–72. DOI: 10.1098/rspa.1931.0130.

[146] G. Danby et al. 'Observation of High-Energy Neutrino Reactions and the Existence of Two Kinds of Neutrinos'. In: *Phys. Rev. Lett.* 9 (1 July 1962), pp. 36–44. DOI: 10.1103/PhysRevLett.9.36. URL: https://link.aps.org/doi/10.1103/PhysRevLett.9.36.

[147] G. Charpak et al. 'The use of multiwire proportional counters to select and localize charged particles'. In: *Nuclear Instruments and Methods* 62.3 (1968), pp. 262–268. DOI: 10.1016/0029-554X(68)90371-6.

[148] Georges Charpak. *Electronic Imaging of Ionizing Radiation with Limited Avalanches in Gases*. Nobel Lecture. CERN, Geneva, Switzerland, Dec. 1992.

[149] Fabio Sauli. *Gaseous Radiation Detectors: Fundamentals and Applications*. 978-1-009-29121-7 P. Geneva, Switzerland: European Organization for Nuclear Research (CERN), 2025.

[150] A. H. Walenta, J. Heintze and B. Schuerlein. 'The multiwire drift chamber, a new type of proportional wire chamber'. In: *Nucl. Instrum. Meth.* 92 (1971), pp. 373–380. DOI: 10.1016/0029-554X(71)90413-7.

[151] David R. Nygren. 'Proposal to investigate the feasibility of a novel concept in particle detection'. In: (1974).

[152] H J Hilke. 'Time projection chambers'. In: *Reports on Progress in Physics* 73.11 (Oct. 2010), p. 116201. DOI: 10.1088/0034-4885/73/11/116201. URL: https://dx.doi.org/10.1088/0034-4885/73/11/116201.

[153] Glenn F. Knoll. *Radiation Detection and Measurement*. John Wiley & Sons, 2010.

[154] William R. Leo. *Techniques for Nuclear and Particle Physics Experiments: A How-to Approach*. Springer, 1994.

[155] E. Rutherford. 'LXXIX. The scattering of and particles by matter and the structure of the atom'. In: *The London, Edinburgh, and Dublin Philosophical Magazine and Journal of Science* 21.125 (1911), pp. 669–688. DOI: 10.1080/14786440508637080. eprint: https://doi.org/10.1080/14786440508637080. URL: https://doi.org/10.1080/14786440508637080.

[156] Gerald R. Lynch and Orin I. Dahl. 'Approximations to multiple Coulomb scattering'. In: *Nucl. Instrum. Meth. B* 58 (1991), pp. 6–10. DOI: 10.1016/0168-583X(91)95671-Y.

[157] N. Bohr. 'II. On the theory of the decrease of velocity of moving electrified particles on passing through matter'. In: *The London, Edinburgh, and Dublin Philosophical Magazine and Journal of Science* 25.145 (1913), pp. 10–31. DOI: 10.1080/14786440108634305. eprint: https://doi.org/10.1080/14786440108634305. URL: https://doi.org/10.1080/14786440108634305.

[158] N. Bohr. 'LX. On the decrease of velocity of swiftly moving electrified particles in passing through matter'. In: *The London, Edinburgh, and Dublin Philosophical Magazine and Journal of Science* 30.178 (1915), pp. 581–612. DOI: 10.1080/14786441008635432. eprint: https://doi.org/10.1080/14786441008635432. URL: https://doi.org/10.1080/14786441008635432.

[159] James F. Ziegler, M.D. Ziegler and J.P. Biersack. 'SRIM – The stopping and range of ions in matter (2010)'. In: *Nuclear Instruments and Methods in Physics Research Section B: Beam Interactions with Materials and Atoms* 268.11 (2010). 19th International Conference on Ion Beam Analysis, pp. 1818–1823. DOI: https://doi.org/10.1016/j.nimb.2010.02.091. URL: https://www.sciencedirect.com/science/article/pii/S0168583X10001862.

[160] CERN. *Garfield++ – Simulation of Gaseous Detectors*. https://gitlab.cern.ch/garfield/garfieldpp. Accessed: 15 July 2025.

[161] David R. Nygren. 'Origin and development of the TPC idea'. In: *Nuclear Instruments and Methods in Physics Research Section A: Accelerators, Spectrometers, Detectors and Associated Equipment* 907 (2018). Advances in Instrumentation and Experimental Methods (Special Issue in Honour of Kai Siegbahn), pp. 22–30. DOI: https://doi.org/10.1016/j.nima.2018.07.015. URL: https://www.sciencedirect.com/science/article/pii/S0168900218308477.

[162] M Gai et al. 'An optical readout TPC (O-TPC) for studies in nuclear astrophysics with gamma-ray beams at HIS1'. In: *Journal of Instrumentation* 5.12 (Dec. 2010), P12004. DOI: 10.1088/1748-0221/5/12/P12004. URL: https://doi.org/10.1088/1748-0221/5/12/P12004.

[163] Ćwiok, Mikołaj et al. 'Studies of photo-nuclear reactions at astrophysical energies with an active-target TPC'. In: *EPJ Web Conf.* 279 (2023), p. 04002. DOI: 10.1051/epjconf/202327904002. URL: https://doi.org/10.1051/epjconf/202327904002.

[164] Yassid Ayyad et al. 'Novel particle tracking algorithm based on the Random Sample Consensus Model for the Active Target Time Projection Chamber (AT-TPC)'. In: *Nuclear Instruments and Methods in Physics Research Section A: Accelerators, Spectrometers, Detectors and Associated Equipment* 880 (2018), pp. 166–173. DOI: https://doi.org/10.1016/j.nima.2017.10.090. URL: https://www.sciencedirect.com/science/article/pii/S0168900217311798.

[165] D. Karlen, P. Poffenberger and G. Rosenbaum. 'TPC performance in magnetic fields with GEM and pad readout'. In: *Nuclear Instruments and Methods in Physics Research Section A: Accelerators, Spectrometers, Detectors and Associated Equipment* 555.1 (2005), pp. 80–92. DOI: https://doi.org/10.1016/j.nima.2005.09.008. URL: https://www.sciencedirect.com/science/article/pii/S0168900205018140.

[166] P. Agnes et al. 'Sensitivity projections for a dual-phase argon TPC optimized for light dark matter searches through the ionization channel'. In: *Phys. Rev. D* 107 (11 June 2023), p. 112006. DOI: 10.1103/PhysRevD.107.112006. URL: https://link.aps.org/doi/10.1103/PhysRevD.107.112006.

[167] Fabio Sauli. 'The gas electron multiplier (GEM): Operating principles and applications'. In: *Nuclear Instruments and Methods in Physics Research Section A: Accelerators, Spectrometers, Detectors and Associated Equipment* 805 (2016). Special Issue in memory of Glenn F. Knoll, pp. 2–24. DOI: https://doi.org/10.1016/j.nima.2015.07.060. URL: https://www.sciencedirect.com/science/article/pii/S0168900215008980.

[168] G Charpak et al. 'Micromegas, a multipurpose gaseous detector'. In: *Nuclear Instruments and Methods in Physics Research Section A: Accelerators, Spectrometers, Detectors and Associated Equipment* 478.1 (2002). Proceedings of the ninth Int.Conf. on Instrumentation, pp. 26–36. DOI: https://doi.org/10.1016/S0168-9002(01)01713-2. URL: https://www.sciencedirect.com/science/article/pii/S0168900201017132.

[169] E. Koshchiy et al. 'Texas Active Target (TexAT) detector for experiments with rare isotope beams'. In: *Nuclear Instruments and Methods in Physics Research Section A: Accelerators, Spectrometers, Detectors and Associated Equipment* 957 (2020), p. 163398. DOI: https://doi.org/10.1016/j.nima.2020.163398. URL: https://www.sciencedirect.com/science/article/pii/S0168900220300073.

[170] G. Mazzitelli et al. '50 litres TPC with sCMOS-based optical readout for the CYGNO project'. In: *Nuclear Instruments and Methods in Physics Research Section A: Accelerators, Spectrometers, Detectors and Associated Equipment* 1045 (2023), p. 167584. DOI: https://doi.org/10.1016/j.nima.2022.167584. URL: https://www.sciencedirect.com/science/article/pii/S0168900222008762.

[171] K. C. Z. Haverson et al. 'A ResNeXt50-based convolution neural network for nuclear reaction classification in an active target TPC detector'. In: *Il Nuovo Cimento C* 48.1 (2025). WPCF-Resonance 2023, p. 17. DOI: 10.1393/ncc/i2025-25017-2.

[172] Huangkai Wu et al. 'Machine learning method for 12C event classification and reconstruction in the active target time-projection chamber'. In: *Nuclear Instruments and Methods in Physics Research Section A: Accelerators, Spectrometers, Detectors and Associated Equipment* 1055 (2023), p. 168528. DOI: https://doi.org/10.1016/j.nima.2023.168528. URL: https://www.sciencedirect.com/science/article/pii/S0168900223005181.

[173] Henry R. Weller et al. 'Research opportunities at the upgraded HIγS facility'. In: *Progress in Particle and Nuclear Physics* 62.1 (2009), pp. 257–303. DOI: https://doi.org/10.1016/j.ppnp.2008.07.001. URL: https://www.sciencedirect.com/science/article/pii/S0146641008000434.

[174] K. P. Schäfers et al. 'High-Resolution Small Animal Imaging'. In: *Comprehensive Biomedical Physics*. Vol. 1. Reference Module in Biomedical Sciences. 2014. Chap. 1.10, pp. 181–211. DOI: 10.1016/B978-0-444-53632-7.00110-6. URL: https://doi.org/10.1016/B978-0-444-53632-7.00110-6.

[175] R.E. Pywell et al. 'Photon flux monitor for a mono-energetic gamma ray source'. In: *Nuclear Instruments and Methods in Physics Research Section A: Accelerators, Spectrometers, Detectors and Associated Equipment* 606.3 (2009), pp. 517–522. DOI: https://doi.org/10.1016/j.nima.2009.04.014. URL: https://www.sciencedirect.com/science/article/pii/S0168900209007876.

[176] M Gai et al. 'An optical readout TPC (O-TPC) for studies in nuclear astrophysics with gamma-ray beams at HIγS'. In: *Journal of Instrumentation* 5.12 (Dec. 2010), P12004. DOI: 10.1088/1748-0221/5/12/P12004. URL: https://dx.doi.org/10.1088/1748-0221/5/12/P12004.

[177] R. Smith et al. 'Stringent upper limit on the direct 3α decay of the Hoyle state in ^{12}C'. In: *Phys. Rev. C* 101 (2 Feb. 2020), p. 021302. DOI: 10.1103/PhysRevC.101.021302. URL: https://link.aps.org/doi/10.1103/PhysRevC.101.021302.

[178] K. C. Z. Haverson et al. 'Background-free 12C(α,γ) angular distribution measurements with a time projection chamber operating in Gamma beams.' Jan. 2026. DOI: 10.1038/s42005-025-02458-7. URL: https://doi.org/10.1038/s42005-025-02458-7.

[179] S. F. Biagi. 'A multiterm Boltzmann analysis of drift velocity, diffusion, gain and magnetic-field effects in argon-methane-water-vapour mixtures'. In: *Nuclear Instruments and Methods in Physics Research Section A: Accelerators, Spectrometers, Detectors and Associated Equipment* 283.3 (1989), pp. 716–722. DOI: 10.1016/0168-9002(89)91446-0.

[180] Alfredo G. Cocco. 'Results from CHORUS experiment at CERN'. In: *Physics Reports* 307.1 (1998), pp. 319–324. DOI: https://doi.org/10.1016/S0370-1573(98)00040-4. URL: https://www.sciencedirect.com/science/article/pii/S0370157398000404.

[181] U. Friman-Gayer. *Horst*. https://github.com/u-eff-gee/Horst. Accessed: 2025-01-22.

[182] M. J. Berger et al. *XCOM: Photon Cross Sections Database*. [Online]. 2010.

[183] Rob Pywell. 'Calibration of the 5-paddle Flux Monitor'. University of Saskatchewan Subatomic Physics Internal Report SPIR 140. Nov. 2008.

[184] Sean Finch. *Private communication*. April 3, 2024. 2024.

[185] Carl R. Brune and Daniel B. Sayre. 'Energy deconvolution of cross-section measurements with an application to the 12C(,)16O reaction'. In: *Nuclear Instruments and Methods in Physics Research Section A: Accelerators, Spectrometers, Detectors and Associated Equipment* 698 (2013), pp. 49–59. DOI: https://doi.org/10.1016/j.nima.2012.09.023. URL: https://www.sciencedirect.com/science/article/pii/S0168900212010704.

[186] M. Fila. 'Study of ^{16}O(γ, α)^{12}C nuclear reaction with the Warsaw TPC detector'. PhD thesis. University of Warsaw, 2023.

[187] Mikolaj Ćwiok *et al.* 'Warsaw Active-Target TPC: A new detector for photonuclear reactions studies at astrophysical energies'. In: *EPJ Web of Conferences*. Vol. 290. European Nuclear Physics Conference (EuNPC 2022), Section P1 Accelerators and Instrumentation, Published online 08 December 2023. 2023, p. 01004. DOI: 10.1051/epjconf/202329001004. URL: https://doi.org/10.1051/epjconf/202329001004.

[188] R. Acciarri et al. 'Design and construction of the MicroBooNE detector'. In: *Journal of Instrumentation* 12.02 (Feb. 2017), P02017. DOI: 10.1088/1748-0221/12/02/P02017. URL: https://doi.org/10.1088/1748-0221/12/02/P02017.

[189] E.C. Pollacco et al. 'GET: A generic electronics system for TPCs and nuclear physics instrumentation'. In: *Nuclear Instruments and Methods in Physics Research Section A: Accelerators, Spectrometers, Detectors and Associated Equipment* 887 (2018), pp. 81–93. DOI: https://doi.org/10.1016/j.nima.2018.01.020. URL: https://www.sciencedirect.com/science/article/pii/S0168900218300342.

[190] J. Giovinazzo et al. 'GET electronics samples data analysis'. In: *Nuclear Instruments and Methods in Physics Research Section A: Accelerators, Spectrometers, Detectors and Associated Equipment* 840 (2016), pp. 15–27. DOI: https://doi.org/10.1016/j.nima.2016.09.018. URL: https://www.sciencedirect.com/science/article/pii/S0168900216309408.

[191] WarsawTPC. *TPCReco*. https://github.com/WarsawTPC/TPCReco. [Source code, GitHub]. 2025. URL: https://github.com/WarsawTPC/TPCReco.

[192] Chiara Mazzocchi. *Beam Intensity Analysis of April and August Runs at HIγS in 2022*. Internal report. University of Warsaw, Mar. 2024.

[193] R. K. Hobbie and B. J. Roth. *Intermediate Physics for Medicine and Biology*. 4th ed. Biological and Medical Physics: Biomedical Engineering. Springer.

[194] R. K. Hobbie and B. J. Roth. *Klein-Nishina Formula for Polarized Photons*. Blog post. Sept. 2021. URL: https://hobbieroth.blogspot.com/2021/09/klein-nishina-formula-for-polarized.html.

[195] T. Teichmann and E. P. Wigner. 'Sum Rules in the Dispersion Theory of Nuclear Reactions'. In: *Phys. Rev.* 87 (1 July 1952), pp. 123–135. DOI: 10.1103/PhysRev.87.123. URL: https://link.aps.org/doi/10.1103/PhysRev.87.123.

[196] D. Torresi et al. 'Evidence for $^{15}\mathrm{O} + \alpha$ resonance structures in $^{19}\mathrm{Ne}$ via direct measurement'. In: *Phys. Rev. C* 96 (4 Oct. 2017), p. 044317. DOI: 10.1103/PhysRevC.96.044317. URL: https://link.aps.org/doi/10.1103/PhysRevC.96.044317.

[197] Carl R. Brune et al. *$^{16}O(\gamma, \alpha)^{12}C$ Above $E_\gamma = 10$ MeV*. HIγS PAC Proposal. Unpublished. High Intensity Gamma-ray Source, Triangle Universities Nuclear Laboratory, May 2014.

[198] Yoshiko Kanada-En'yo. 'Isoscalar monopole and dipole excitations of cluster states and giant resonances in ^{12}C'. In: *Phys. Rev. C* 93 (5 May 2016), p. 054307. DOI: 10.1103/PhysRevC.93.054307. URL: https://link.aps.org/doi/10.1103/PhysRevC.93.054307.

[199] W. B. He et al. 'Dipole oscillation modes in light α-clustering nuclei'. In: *Phys. Rev. C* 94 (1 July 2016), p. 014301. DOI: 10.1103/PhysRevC.94.014301. URL: https://link.aps.org/doi/10.1103/PhysRevC.94.014301.

[200] F.C Barker and P.B Treacy. 'Nuclear levels near thresholds'. In: *Nuclear Physics* 38 (1962), pp. 33–49. DOI: https://doi.org/10.1016/0029-5582(62)91014-3. URL: https://www.sciencedirect.com/science/article/pii/0029558262910143.

[201] Ogloblin. AA et al. 'Rotational band in ^{12}C based on the Hoyle state'. In: *EPJ Web of Conferences* 66 (2014). INPC 2013 – International Nuclear Physics Conference, p. 02074. DOI: 10.1051/epjconf/20146602074. URL: https://doi.org/10.1051/epjconf/20146602074.

[202] R Bijker and O A Díaz-Caballero. 'Electromagnetic transitions in the algebraic cluster model'. In: *Physica Scripta* 92.12 (Oct. 2017), p. 124001. DOI: 10.1088/1402-4896/aa9242. URL: https://doi.org/10.1088/1402-4896/aa9242.

[203] P. Descouvemont and D. Baye. 'Microscopic theory of the ^{8}Be(α,γ)^{12}C reaction in a three-cluster model'. In: *Phys. Rev. C* 36 (1 July 1987), pp. 54–59. DOI: 10.1103/PhysRevC.36.54. URL: https://link.aps.org/doi/10.1103/PhysRevC.36.54.

[204] Yoshiko Kanada-En'yo. 'The Structure of Ground and Excited States of ^{12}C'. In: *Progress of Theoretical Physics* 121.4 (Apr. 2009), pp. 895–895. DOI: 10.1143/PTP.121.895. eprint:

https://academic.oup.com/ptp/article-pdf/121/4/895/5455093/121-4-895.pdf. URL: https://doi.org/10.1143/PTP.121.895.

[205] Dao T. Khoa, Do Cong Cuong and Yoshiko Kanada-En'yo. 'Hindrance of the excitation of the Hoyle state and the ghost of the 2_2^+ state in ^{12}C'. In: *Physics Letters B* 695.5 (2011), pp. 469–475. DOI: https://doi.org/10.1016/j.physletb.2010.11.061. URL: https://www.sciencedirect.com/science/article/pii/S0370269310013365.

[206] Y. Funaki. 'Hoyle band and α condensation in ^{12}C'. In: *Phys. Rev. C* 92 (2 Aug. 2015), p. 021302. DOI: 10.1103/PhysRevC.92.021302. URL: https://link.aps.org/doi/10.1103/PhysRevC.92.021302.

[207] Souichi Ishikawa. 'Low-energy ^{12}C continuum states in a three-α model'. In: *Phys. Rev. C* 112 (1 July 2025), p. 014606. DOI: 10.1103/3rkb-tzr3. URL: https://link.aps.org/doi/10.1103/3rkb-tzr3.

[208] Glen Cowan. *Statistical Data Analysis*. Oxford: Clarendon Press, 1998.